2018

Reconstructing past and present chemical weathering conditions via lithium isotopes

Leo Rothacker
University of Wollongong

Reconstructing past and present chemical weathering conditions via lithium isotopes

A thesis submitted in partial fulfilment of the requirements for the degree of

Doctor of Philosophy

from

University of Wollongong

by

LEO ROTHACKER

School of Earth and Environmental Sciences,

Faculty of Science Medicine and Health,

April 2018

UNIVERSITY OF WOLLONGONG AUSTRALIA

Abstract

Continental weathering processes not only shape the Earth's surface but may also play a significant role in regulating global climate. Over geologic time scales, one of the major controls on atmospheric CO_2 is continental silicate weathering, where carbon dioxide is consumed during weathering reactions. However, the coupling between CO_2 consumption via silicate weathering and climate is still poorly understood. Even less is known how weathering-related CO_2 consumption responds to climatic oscillations. Besides silicate weathering and its importance on the atmospheric CO_2 cycle, weathering processes are directly related to soil formation. Soils are key environmental resource, which sustains most life on land. Understanding how soil formation responds to climatic oscillations and human impact via agricultural practises is of critical importance. To fully comprehend the environmental controls on chemical weathering, a reliable proxy is essential. In this PhD thesis, lithium (Li) isotopes, a non-traditional chemical weathering proxy, is applied to two contrasting environmental settings: a river basin and a lake catchment. These contrasting environments were chosen to test how Li isotopes evolve spatially and temporally in a relatively large-scale river in contrast to a small-scale lacustrine setting.

The main study site of this PhD is the Murrumbidgee River Basin (south-east Australia) and its palaeo-channels, which record environmental changes over the last glacial cycle (100,000 years). The Li isotope proxy is applied to sediment (clay-sized fraction), bedrock, and water samples. The objective is to elucidate present chemical weathering at the Murrumbidgee River Basin and how weathering reactions have changed in the past 100,000 years in response to climatic/hydrologic variations. Results show that the upper catchment of the Murrumbidgee River consists of various weathering regimes and the current weathering regime of the Murrumbidgee River can be characterised as 'supply-limited', which corresponds to high weathering intensities. Sediments from palaeo-channel deposits show that weathering conditions during the last glacial cycle were tightly coupled with hydrological parameters. Low weathering intensities prevailed during oxygen isotope stage (OIS) 5 and 3, a time associated with a warm and wet climate. During this time, weathering reactions were limited due to high erosion rates. From OIS 3 until present, the Li isotope composition of the sediment record indicates higher weathering intensities as a possible response to an increasingly drier climate, which decreased erosion rates in the Murrumbidgee River Basin and allowed longer water-rock

reaction times. The Li isotope data suggest that the weathering regime of the Murrumbidgee River Basin shifted from an intermediate weathering intensity to a high weathering intensity within a geological short time period (< 20,000 years) as a consequence of a weaker hydrological activity. These results show that chemical weathering reactions in the Murrumbidgee River Basin are tightly coupled with hydroclimatic variations.

A sediment record from Lake Dojran (Greece/Macedonia, FYROM), which covers environmental changes over the past 12,300 years, were analysed for Li and uranium (U) isotopes. Here, the Li and U isotope composition of the <63 µm fraction was used to infer changes in soil development and soil erosion, respectively. For most of the past 12,300 years soil erosion and development were impacted differently by natural climate variability: short-lived (<1,000 years) climatic shifts had no effect on soil development but impacted soil erosion. This decoupling disappeared between 3,500 and 3,100 years ago, when the sedimentary record suggests an unprecedented erosion event associated with the development of agriculture in the region. These results show unambiguously how differently soils evolved under natural climate variability (between 12,300 and 3,500 years ago) and later in response to intensifying human impact. The transition from *natural* to *anthropogenic* landscape started just before, or at, the onset of the Greek 'Dark Ages' (~3,200 cal yr BP). This could represent the earliest recorded sign of a negative feedback between civilisation and environmental impact, where the development of regional trade impacted soil resources, which in turn resulted in a slowdown of civilisation expansion.

Analytical techniques applied are:

- Multi-Collector Inductively-Coupled-Plasma Mass Spectrometry (MC ICP-MS)
    - Li isotopes, neodymium (Nd) isotopes
    - U isotopes (not done by L.R.)
- Quadrupole Inductively-Coupled-Plasma Mass Spectrometry (Q ICP-MS)
    - Major and trace elements
- Particle size analysis
- X-Ray Diffraction (XRD) analysis

Other methods included:

- Separation of clay-sized fraction from sediments applying centrifuge techniques

- Rock cutting and crushing using a laboratory disc mill
- Chemical dissolution of geological samples with HF, HNO_3, HCl, and aqua regia
- Ion exchange chromatography to purify Nd, Li, and U (not done by L.R.)
    - Automated chromatography procedure with the Elemental Scientific prepFAST-MC™, developed for Nd and partly for Li isotopes

All analyses, except for U isotopes and XRD, were undertaken by L.R. New methods, such as ion exchange chromatography protocols for Nd and Li, Nd and Li analyses on the MC ICP-MS, clay-sized fraction separation, and rock dissolution protocols were developed by L.R.

Acknowledgements

I would like to thank my supervisors Anthony Dosseto, Nathalie Vigier, and Allan Chivas for their support during my PhD, and for teaching me isotope geochemistry. Many thanks to all friends, colleagues, and technical staff at the University of Wollongong who helped, guided, or assisted me in any way during my PhD.

I would like to acknowledge the Australian Research Council Discovery grant (ARC) DP140100354 to Anthony Dosseto, the Australian Postgraduate Award (APA), as well as the International Postgraduate Tuition Award (IPTA).

I, Leo Rothacker, declare that this thesis, submitted in partial fulfilment of the requirements for the award of Doctor of Philosophy, in the School of Earth and Environmental Sciences, University of Wollongong, is wholly my own work unless otherwise reference or acknowledged. The document has not been submitted for qualifications at any other academic institution.

Leo Rothacker

April 2018.

Abbreviations

ACC	Antarctic Circumpolar Current
BP	Before Present
CIA	Chemical Index of Alteration
D	Denudation rate (t/km^2/yr)
DEM	Digital Elevation Model
E	Erosion rate (t/km^2/yr)
EAC	East Australian Current
ENSO	El Niño-Southern Oscillation
GDR	Great Dividing Range
IPWP	Indo-Pacific Warm Pool
ITCZ	Intertropical Convergence Zone
ITF	Indonesian Throughflow
LC	Leeuwin Current
LDPE	Low-Density Polyethylene
LGM	Last Glacial Maximum
MC ICP-MS	Multicollector Inductively Coupled Plasma Mass Spectrometry
MCE	Mixed Cellulose Ester
MJO	Madden-Julian Oscillation
MORB	Mid-Ocean Ridge Basalt
NOA	North Atlantic Oscillation
NSW	New South Wales
OIS	Oxygen Isotope Stage
OSL	Optically-Stimulated Luminescence
PF	Polar Front
PSD	Particle Size Distribution
Q ICP-MS	Quadrupole Inductively Coupled Plasma Mass Spectrometry
R	Ruxton Ratio
RBS	River Bed Sands
REE	Rare Earth Elements
SAF	Subantarctic Front

SAM	Southern Annular Mode
SEC	South Equatorial Current
SEM	Secondary Electron Multiplier
SPM	Suspended Sediment Particles
SST	Sea Surface Temperature
STF	Subtropical Front
STR	Sub-Tropical Ridge
TDS	Total Dissolved Solids
TF	Tasmanian Front
TL	Thermo-Luminescence
UCC	Upper Continental Crust
V	Vogt's residual index
W	Weathering rate ($t/km^2/yr$)
WIP	Weathering Index of Parker
XRD	X-Ray diffraction
XRF	X-Ray Fluorescence
δ^7Li_{clay}	δ^7Li composition of the clay-sized fraction
δ^7Li_{diss}	δ^7Li composition of the river dissolved load

Table of Contents

Table of figures

Table of tables

1 Introduction

Continental weathering processes not only shape the Earth's surface but may also play a significant role in regulating global climate. Early work by Urey and Korff (1952) suggested that, over geologic time scales, one of the major controls of atmospheric CO_2 is continental silicate weathering, where carbon dioxide is consumed during weathering reactions. The main drivers of weathering rates are climate and tectonic uplift (Raymo and Ruddiman, 1992; Gaillardet et al., 1999; West et al., 2005). Pioneering work from Walker et al. (1981) suggested that there is a link between tectonics and climate. Modelling studies have shown that a change in continental relief by mountain building may promote silicate weathering rates and therefore decrease atmospheric CO_2 (Walker et al., 1981; Berner et al., 1983; Broecker and Sanyal, 1998). For example, late Cenozoic tectonic uplift, mainly the Himalaya orogenesis, is thought to have enhanced physical erosion and monsoonal rainfall. Consequently, more atmospheric CO_2 was consumed via accelerated silicate weathering rates. This coincided with a post-Eocene decline in atmospheric CO_2, which resulted in a global cooling (Raymo and Ruddiman, 1992). However, silicate weathering is not only controlled by tectonic processes, but also by climate itself (Raymo and Ruddiman, 1992; Gaillardet et al., 1999; West et al., 2005; Koppes and Montgomery, 2009). Climates characterised with high annual rainfall may increase physical erosion which promotes continental weathering and therefore causes a draw-down in atmospheric carbon dioxide. This negative feedback between climate and weathering may serve as an explanation why Earth's climate has remained relatively stable throughout most geological periods and allows for the existence of life (Broecker and Sanyal, 1998).

However, the coupling between CO_2 consumption via silicate weathering and climate is still poorly understood. Even less is known how weathering-related CO_2 consumption responds to climatic oscillations. On millennial timescales, chemical weathering affects the carbonate saturation level of the oceans by taking up atmospheric CO_2 via carbonate formation (Archer et al., 2000). Furthermore, it is debated that weathering may act as a CO_2 sink over the century timescale (Raymond et al., 2008; Gislason et al., 2009; Goddéris et al., 2013). Studies have also suggested the potential CO_2 consumption flux by accelerated continental weathering caused by global warming and land-use changes (Raymond et al., 2008; Gislason et al., 2009; Beaulieu et al., 2012). Artificial weathering strategies on terrestrial landscapes have been proposed to counter-balance accelerated

anthropogenic CO_2 emissions, which could potentially lower atmospheric CO_2 by 30-300 ppm by 2100 (Taylor et al., 2016).

The response of weathering rates to climatic variability is highly debated. Furthermore, the timescale at which chemical weathering interacts with climate is still unknown. Over short time timescales, thousands of years, weathering is thought to respond to hydrological fluctuations. For example, during the Holocene in central Africa, high weathering rates were linked to wet phases, while low weathering rates persist during dry phases (Bayon et al., 2012). Global short-lived climatic events such as the 8.2 kilo year event (Barber et al., 1999), which lasted for several hundred years, do not seem to have significantly affected the weathering environment. Over long timescales (several million years), chemical weathering appears to correspond to climatic trends: a sediment record from the northern South China Sea shows that during the Miocene, 20 – 15 million years ago, long-term intense weathering periods were linked to climatic optima. In contrast, a weakening of chemical weathering largely corresponds to climate cooling (Clift et al., 2014). Furthermore, Vance et al. (2009) suggested that changes in Quaternary chemical weathering rates are a direct consequence of periodic glaciations. They propose that, after the last deglaciation, the chemical weathering flux has remained far from equilibrium and has been two to three times the average for an entire late Quaternary glacial cycle.

Besides silicate weathering and its importance on the atmospheric CO_2 cycle, weathering processes are directly related to soil formation. Soils are a key environmental resource, which sustains most life on land. During weathering, the solid rock breaks down and secondary minerals such as clays are being formed. These weathering products build an essential part of soil systems. Soil dynamics are extremely sensitive to climate, vegetation type and distribution, human activity, and tectonic activity (Dosseto et al., 2010). In order to sustain soil resources, it is essential to understand how soil formation has responded to climatic variability and human activity. Agricultural practices have been shown to cause an imbalance between soil erosion and production. As a consequence, the longevity of major civilisations could be linked to the depletion of soil resources (Montgomery, 2007). In the geologic record, a first human impact on the weathering environment has been evident as early as the Iron Age in several parts of the world (Bayon et al., 2012; Hu et al., 2013; Francke et al., 2013; Wan et al., 2015). However, until today, a quantification of when humans have had a significant impact on natural soil systems has remained difficult.

To fully comprehend the environmental controls on chemical weathering, a reliable proxy is essential. A classic chemical weathering proxy is the Chemical Index of Alteration (CIA), first proposed by Nesbitt and Young (1982). It is based on the assumption that the dominant processes during chemical weathering is the degradation of feldspars and the formation of clay minerals (Goldberg and Humayun, 2010). The applicability of this proxy, however, can be limited by sediments which are rich in carbonates. Post-depositional K^+ infiltration as well as the inheritance of clays from the surrounding sediments must be considered. Furthermore, it also assumes that Al_2O_3 remains immobile during weathering, which is not true during soil formation. Other commonly used proxies for reconstructing chemical alteration are the element ratios such as K/Al and K/Rb. Potassium is highly mobile in water, while Al and Rb are less mobile due to the breakdown of minerals. Limiting factors of these proxies are that K is enriched under moderate chemical weathering conditions and becomes depleted under more intense weathering as K-feldspars break down (Clift et al., 2014).

Due to the limitations of these classic approaches, a more reliable weathering proxy is crucial. In recent years, it was discovered that many light-isotope systems show isotope fractionation during weathering processes. This PhD project focuses on exploring lithium (Li) isotopes as a novel tool to reconstruct present and past continental weathering conditions. During weathering, Li isotopes (^{7}Li, ^{6}Li) fractionate, whereby ^{6}Li is preferentially incorporated into clay minerals, in turn enriching ^{7}Li in surface waters (Pistiner and Henderson, 2003; Kısakürek et al., 2004; Vigier et al., 2008). Tracing weathering reactions with Li isotopes has several advantages compared to other proxies: Li is not i) influenced by redox reactions ii) part of atmospheric, biological or hydrological cycles iii) affected by mineral sorting (Burton and Vigier, 2012). Furthermore, Li is highly enriched in silicate minerals relative to carbonates which allows the reconstruction of solely silicate weathering conditions (Kısakűrek et al., 2005). Compared to other isotope proxies, ^{6}Li and ^{7}Li have the largest relative mass difference (~16 %) of any isotope pair aside from hydrogen and deuterium (Burton and Vigier, 2012), and which produces a large range of isotope signatures. This makes Li isotopes potentially excellent proxies for precisely reconstructing present and past silicate weathering conditions. On terrestrial systems, this proxy has mostly been applied to assess modern weathering conditions in large river systems (Huh et al., 1998; Huh et al., 2001; Kısakűrek et al., 2005; Vigier et al., 2009; Dellinger et al., 2015; Pogge von

Strandmann et al., 2017a). So far, only a few studies exist where Li isotopes were applied to evaluate past chemical weathering conditions on continental records (Pogge von Strandmann et al., 2013; Dosseto et al., 2015; Pogge von Strandmann et al., 2017b; Pogge von Strandmann et al., 2017c; Bastian et al., 2017).

One part of this PhD project aims to assess continental past and present weathering conditions in response to climate fluctuations over the last glacial cycle (100,000 years) in the Murrumbidgee River catchment (south-eastern Australia). To evaluate the palaeo weathering environment and how the weathering signal is transferred from source to sink, sediments from the modern Murrumbidgee River were comprehensively investigated. Li isotope ratios were measured on the <2 µm grain size fraction, separated from river bank sand deposits. Furthermore, the neodymium (Nd) isotope composition was measured on a selection of samples to evaluate a change in sediment provenance over time. Data from the current weathering regime give insight on the potential effect of lithology and assess whether the ratio $^{7}Li/^{6}Li$ evolves during transport. With the understanding of the modern weathering regime, weathering conditions in south-east Australia over the last glacial cycle are evaluated. For this, four palaeo-channel sediment archives with deposition ages ranging from ~13,000 to ~105,000 years (Page et al., 1996) were analysed. The clay-sized fraction (<2 µm) was separated from these sediments and Li isotope ratios were measured. Results of these palaeo-channel deposits show how the weathering regime in south-east Australia responded to environmental changes over the last glacial cycle.

A lacustrine sediment core record was chosen as a second study for this PhD project. The sediment core, retrieved from Lake Dojran (Macedonia/Greece), records environmental conditions over the past 12,300 years. A multi proxy geochemical approach, Li and uranium (U) isotopes, was applied to Lake Dojran sediments to reconstruct the Holocene soil environment. Li isotopes and U isotopes were measured on the <63 µm fraction and are used to infer soil formation and soil erosion, respectively. It is discussed how soil development and erosion responded to long- (>1,000 years) and short-term (<1,000 years) climatic variations over the past 12,300 years. Furthermore, the impact ancient Greek civilisations had on the natural soil environment is demonstrated.

A large variety of sample types was analysed for this project. These include bedrock, dust, bulk sediments, clay sized fractions (<2 µm), river waters, and individually picked minerals. All samples were chemically dissolved, and Li and Nd were concentrated using

cation exchange chromatography. Isotope ratios were measured using a Multiple Collector Inductively Coupled Plasma Mass Spectrometer (MC ICP-MS). Element concentrations were determined using a Quadrupole Inductively Coupled Plasma Mass Spectrometer (Q ICP-MS). Other measuring techniques applied on selected samples were: analysis of particle size distribution (PSD), and X-Ray Diffraction (XRD) to detect individual mineral phases. Except for XRD measurements, all analyses were conducted by Leo Rothacker and several of the isotopic methods and protocols were developed by him.

This PhD project aims at validating the use of Li isotope in sediment deposits as a proxy for chemical weathering reactions. With the combination of other geochemical weathering proxies, the present and palaeo weathering regime of two independent study locations is evaluated. Ultimately, the control of climate and human land-use on natural weathering environments over the last glacial cycle in south-east Australia, and during the Holocene in Greece/Macedonia is determined.

Following the introduction chapter 1, the thesis is divided into 9 more chapters. Chapter 2 encompasses a detailed literature review of active debates regarding the feedback between weathering and global climate. Furthermore, a variety of chemical weathering proxies that aid in understanding past and present continental weathering reactions are described in chapter 2. Details concerning stable isotope fractionation and applications and limitations of the Li isotope proxy as a chemical weathering index is discussed in chapter 3. Chapter 4 informs about the climatic setting of Australia with emphasis on South-East Australia and the Murrumbidgee River Basin. A geographical and geological description of the Murray Darling Basin is given in chapter 5. Furthermore, this chapter also discusses the formation processes of palaeo-channels in the Riverine Plain. Field methods and study site descriptions for the Murrumbidgee River project and the Lake Dojran project are given in chapter 6. The Murrumbidgee River study is presented in chapter 7, followed by the Lake Dojran study in chapter 8. Analytical methods applied during this PhD are in detail shown in chapter 9. Finally, the thesis conclusions are given in chapter 10.

References

Archer, D., Winguth, A., Lea, D. & Mahowald, N. 2000. What caused the glacial/interglacial atmosphericp CO_2 cycles? *Reviews of Geophysics,* 38**,** 159-189.

Barber, D. C., Dyke, A., Hillaire-Marcel, C., Jennings, A. E., Andrews, J. T., Kerwin, M. W., Bilodeau, G., Mcneely, R., Southon, J., Morehead, M. D. & Gagnon, J.-M. 1999. Forcing of the cold event of 8,200 years ago by catastrophic drainage. *Nature,* 400**,** 344-348.

Bastian, L., Revel, M., Bayon, G., Dufour, A. & Vigier, N. 2017. Abrupt response of chemical weathering to Late Quaternary hydroclimate changes in northeast Africa. *Scientific Reports,* 7**,** 44231.

Bayon, G., Dennielou, B., Etoubleau, J., Ponzevera, E., Toucanne, S. & Bermell, S. 2012. Intensifying weathering and land use in Iron Age Central Africa. *Science,* 335**,** 1219-1222.

Beaulieu, E., Goddéris, Y., Donnadieu, Y., Labat, D. & Roelandt, C. 2012. High sensitivity of the continental-weathering carbon dioxide sink to future climate change. *Nature Climate Change,* 2**,** 346-349.

Berner, R. A., Lasaga, A. C. & Garrels, R. M. 1983. The carbonate-silicate geochemical cycle and its effect on atmospheric carbon dioxide over the past 100 million years. *American Journal of Science,* 283**,** 641-683.

Broecker, W. S. & Sanyal, A. 1998. Does atmospheric CO_2 police the rate of chemical weathering? *Global Biogeochemical Cycles,* 12**,** 403-408.

Burton, K. W. & Vigier, N. 2012. Lithium Isotopes as Tracers in Marine and Terrestrial Environments. *In:* Baskaran, M. (ed.) *Handbook of Environmental Isotope Geochemistry: Vol I.* Berlin, Heidelberg: Springer Berlin Heidelberg, 41-59.

Clift, P. D., Wan, S. & Blusztajn, J. 2014. Reconstructing chemical weathering, physical erosion and monsoon intensity since 25 Ma in the northern South China Sea: a review of competing proxies. *Earth-Science Reviews,* 130**,** 86-102.

Dellinger, M., Gaillardet, J., Bouchez, J., Calmels, D., Louvat, P., Dosseto, A., Gorge, C., Alanoca, L. & Maurice, L. 2015. Riverine Li isotope fractionation in the Amazon River basin controlled by the weathering regimes. *Geochimica et Cosmochimica Acta,* 164**,** 71-93.

Dosseto, A., Hesse, P., Maher, K., Fryirs, K. & Turner, S. 2010. Climatic and vegetation control on sediment dynamics during the last glacial cycle. *Geology,* 38**,** 395-398.

Dosseto, A., Vigier, N., Joannes-Boyau, R. C., Moffat, I., Singh, T. & Srivastava, P. 2015. Rapid response of silicate weathering rates to climate change in the Himalaya. *Geochemical Perspectives Letters,* 1**,** 10-19.

Francke, A., Wagner, B., Leng, M. J. & Rethemeyer, J. 2013. A Late Glacial to Holocene record of environmental change from Lake Dojran (Macedonia, Greece). *Climate of the Past,* 9**,** 481-498.

Gaillardet, J., Dupré, B., Louvat, P. & Allègre, C. 1999. Global silicate weathering and CO_2 consumption rates deduced from the chemistry of large rivers. *Chemical Geology,* 159**,** 3-30.

Gislason, S. R., Oelkers, E. H., Eiriksdottir, E. S., Kardjilov, M. I., Gisladottir, G., Sigfusson, B., Snorrason, A., Elefsen, S., Hardardottir, J., Torssander, P. & Oskarsson, N. 2009. Direct evidence of the feedback between climate and weathering. *Earth and Planetary Science Letters,* 277**,** 213-222.

Goddéris, Y., Brantley, S. L., François, L. M., Schott, J., Pollard, D., Déqué, M. & Dury, M. 2013. Rates of consumption of atmospheric CO_2 through the weathering of loess during the next 100 yr of climate change. *Biogeosciences,* 10**,** 135-148.

Goldberg, K. & Humayun, M. 2010. The applicability of the Chemical Index of Alteration as a paleoclimatic indicator: An example from the Permian of the Paraná Basin, Brazil. *Palaeogeography, Palaeoclimatology, Palaeoecology,* 293**,** 175-183.

Hu, D., Clift, P. D., Böning, P., Hannigan, R., Hillier, S., Blusztajn, J., Wan, S. & Fuller, D. Q. 2013. Holocene evolution in weathering and erosion patterns in the Pearl River delta. *Geochemistry, Geophysics, Geosystems,* 14**,** 2349-2368.

Huh, Y., Chan, L.-H., Zhang, L. & Edmond, J. M. 1998. Lithium and its isotopes in major world rivers: implications for weathering and the oceanic budget. *Geochimica et Cosmochimica Acta,* 62**,** 2039-2051.

Huh, Y., Chan, L.-H. & Edmond, J. M. 2001. Lithium isotopes as a probe of weathering processes: Orinoco River. *Earth and Planetary Science Letters,* 194**,** 189-199.

Kısakürek, B., Widdowson, M. & James, R. H. 2004. Behaviour of Li isotopes during continental weathering: the Bidar laterite profile, India. *Chemical Geology,* 212**,** 27-44.

Kısakűrek, B., James, R. H. & Harris, N. B. 2005. Li and δ^7Li in Himalayan rivers: proxies for silicate weathering? *Earth and Planetary Science Letters,* 237**,** 387-401.

Koppes, M. N. & Montgomery, D. R. 2009. The relative efficacy of fluvial and glacial erosion over modern to orogenic timescales. *Nature Geoscience,* 2**,** 644-647.

Montgomery, D. R. 2007. Soil erosion and agricultural sustainability. *Proceedings of the National Academy of Sciences,* 104**,** 13268-13272.

Nesbitt, H. & Young, G. 1982. Early Proterozoic climates and plate motions inferred from major element chemistry of lutites. *Nature,* 299**,** 715-717.

Page, K., Nanson, G. & Price, D. 1996. Chronology of Murrumbidgee river palaeochannels on the Riverine Plain, southeastern Australia. *Journal of Quaternary Science,* 11**,** 311-326.

Pistiner, J. S. & Henderson, G. M. 2003. Lithium-isotope fractionation during continental weathering processes. *Earth and Planetary Science Letters,* 214**,** 327-339.

Pogge Von Strandmann, P. A., Jenkyns, H. C. & Woodfine, R. G. 2013. Lithium isotope evidence for enhanced weathering during Oceanic Anoxic Event 2. *Nature Geoscience,* 6**,** 668-672.

Pogge Von Strandmann, P. A., Frings, P. J. & Murphy, M. J. 2017a. Lithium isotope behaviour during weathering in the Ganges Alluvial Plain. *Geochimica et Cosmochimica Acta,* 198**,** 17-31.

Pogge Von Strandmann, P. A., Vaks, A., Bar-Matthews, M., Ayalon, A., Jacob, E. & Henderson, G. M. 2017b. Lithium isotopes in speleothems: Temperature-controlled variation in silicate weathering during glacial cycles. *Earth and Planetary Science Letters,* 469**,** 64-74.

Pogge Von Strandmann, P. A., Desrochers, A., Murphy, M., Finlay, A., Selby, D. & Lenton, T. 2017c. Global climate stabilisation by chemical weathering during the Hirnantian glaciation. *Geophysical Research Letters.,* 3**,** 230-237.

Raymo, M. & Ruddiman, W. F. 1992. Tectonic forcing of late Cenozoic climate. *Nature,* 359**,** 117-122.

Raymond, P. A., Oh, N. H., Turner, R. E. & Broussard, W. 2008. Anthropogenically enhanced fluxes of water and carbon from the Mississippi River. *Nature,* 451**,** 449-52.

Taylor, L. L., Quirk, J., Thorley, R. M., Kharecha, P. A., Hansen, J., Ridgwell, A., Lomas, M. R., Banwart, S. A. & Beerling, D. J. 2016. Enhanced weathering strategies for stabilizing climate and averting ocean acidification. *Nature Climate Change,* 6**,** 402-406.

Urey, H. C. & Korff, S. A. 1952. The planets: their origin and development. *Physics Today,* 5**,** 12-12.

Vance, D., Teagle, D. A. & Foster, G. L. 2009. Variable Quaternary chemical weathering fluxes and imbalances in marine geochemical budgets. *Nature,* 458**,** 493-496.

Vigier, N., Decarreau, A., Millot, R., Carignan, J., Petit, S. & France-Lanord, C. 2008. Quantifying Li isotope fractionation during smectite formation and implications for the Li cycle. *Geochimica et Cosmochimica Acta,* 72**,** 780-792.

Vigier, N., Gislason, S. R., Burton, K., Millot, R. & Mokadem, F. 2009. The relationship between riverine lithium isotope composition and silicate weathering rates in Iceland. *Earth and Planetary Science Letters,* 287**,** 434-441.

Walker, J. C., Hays, P. & Kasting, J. F. 1981. A negative feedback mechanism for the long-term stabilization of Earth's surface temperature. *Journal of Geophysical Research: Oceans,* 86**,** 9776-9782.

Wan, S., Toucanne, S., Clift, P. D., Zhao, D., Bayon, G., Yu, Z., Cai, G., Yin, X., Révillon, S. & Wang, D. 2015. Human impact overwhelms long-term climate control of weathering and erosion in southwest China. *Geology,* 43**,** 439-442.

West, A. J., Galy, A. & Bickle, M. 2005. Tectonic and climatic controls on silicate weathering. *Earth and Planetary Science Letters,* 235**,** 211-228.

2 Feedback between weathering and global climate

2.1 Active debates concerning large timescales

Over geologic timescales, a major control on atmospheric CO_2, and therefore global climate, is represented by continental silicate weathering, where carbon dioxide is consumed during weathering processes (Urey and Korff, 1952). The chemical principle that sequesters carbon dioxide during weathering occurs in a series of reactions:

$$CO_{2\,(gas)} + H_2O_{(aq)} = H_2CO_{3(sol)} = H^+ + HCO^-_{3(aq)} \quad (1)$$

$$Mg_2SiO_{4(sol)} + 4H^+_{(aq)} = 2Mg^{2+}_{(aq)} + H_4SiO_{4(aq)} \quad (2)$$

$$2Mg^{2+}_{(aq)} + HCO^-_{3(aq)} = MgCO_{3(sol)} + H^+_{(aq)} \quad (3)$$

Reaction (1) shows how atmospheric $CO_{2(gas)}$ dissolves in water to form $H_2CO_{3(sol)}$ (carbonic acid). The former disassociates into H^+ and HCO_3^-. In the following reaction (2), the acidic solution interacts with silicate minerals, in this case forsterite ($Mg_2SiO_{4(sol)}$). The mineral dissolves in the acid, leaving Mg^{2+} and silicic acid (H_4SiO_4) in the aqueous phase. In the final reaction (3), Mg^{2+} and HCO_3^- react to form magnesium carbonate ($MgCO_{3(sol)}$). This series of reactions demonstrates how atmospheric CO_2 is consumed via weathering processes and how it can be further sequestrated by the precipitation of carbonates in the ocean. The current global CO_2 consumption via silicate weathering are estimated to be 11.93 x 10^{12} mol/yr (Moon et al., 2014).

While it is well known that chemical weathering reactions consume atmospheric carbon dioxide, the coupling between controls of silicate weathering at large scale is still highly debated. For instance, pioneering work by Walker et al. (1981) suggested that climate is closely linked to tectonics where continental relief by mountain building may promote silicate weathering rates and therefore decrease atmospheric CO_2 (Walker et al., 1981; Berner et al., 1983; Broecker and Sanyal, 1998). The reason for this claim was the post-Eocene decline in atmospheric carbon dioxide, which coincided with late Cenozoic tectonic uplift, mainly the Himalaya orogeny. Tectonic forces are thought to have exposed fresh, unweathered rocks which were readily weathered at accelerated rates. Furthermore,

monsoonal rainfall must have followed the large-scale uplift, which likewise boosted physical erosion rates. Consequently, an increased amount of atmospheric CO_2 would have been consumed via chemical weathering which resulted in a global cooling (Raymo et al., 1988). This hypothesis caused much controversy, in particular, without any feedback to this process, all the atmospheric CO_2 would be consumed in a few million years only. Molnar and England (1990) argued that an increase in erosion would have caused an isostatic rebound, which in turn, would have altered the distribution of elevations by making mountain ranges even higher. This shift in regional land-mass could have greatly reduced temperatures by increasing continental chemical weathering rates. This feedback mechanism was proposed as an alternative explanation to the CO_2 consumption via silicate weathering for the observed climate cooling since the Cenozoic tectonic uplift (Molnar and England, 1990). Both hypotheses by Raymo et al. (1988) and Molnar and England (1990) were taken into consideration by Raymo and Ruddiman (1992) and they proposed that a combination must have caused a decline in atmospheric CO_2 over the past 40 Ma. This debate initiated an interest to disentangle the interactions between silicate weathering, climate and tectonics. It was found that chemical and physical erosion rates are not governed by any single parameter, but multiple factors need to be considered in order to estimate silicate weathering rates (West et al., 2005). The chemistry of dissolved loads from large rivers revealed that there is a coupling between physical erosion (i.e. the mechanical breakdown of rocks) and chemical weathering (i.e. the chemical breakdown of rocks). The highest chemical weathering rates were observed for rivers that drain areas of active physical denudation of continental rocks (Gaillardet et al., 1999). Similar observations were made by West et al. (2005), who proposed that chemical weathering scales directly with the erosion rate. Therefore, in tectonically active regions, where physical denudation is high, CO_2 consumption via chemical weathering is enhanced. Modelling results confirmed this hypothesis and show that during increasing denudation (low residence times) and the subsequent exposure of fresh minerals, silicate weathering may be accelerated (Hilley et al., 2010). The same authors also found that the duration at which these fresh minerals are exposed to fluids is another control regulating chemical weathering rates. Other experiments showed that temperature plays less of a role in controlling the chemical alteration of rocks. Instead, it is mainly controlled by runoff and water-rock exposure times, which highlights the importance of the hydrologic component in controlling continental weathering (Maher and Chamberlain, 2014). A

study by Berner and Kothavala (2001) showed that during the Devonian, where large vascular plants were abundant on continents, plants mediated chemical weathering rates by accelerating rock weathering. Therefore, biological activity is another factor governing continental weathering. Ocean records, which generally reflect a global average of Earth surface processes, have shown that erosion and chemical weathering rates have been relatively constant over the past ~10 Ma, and therefore Cenozoic cooling cannot be linked to silicate weathering (Willenbring and von Blanckenburg, 2010). The same conclusions were drawn by von Blanckenburg et al. (2015a), who found that while there was large regional variability in weathering between glacial and interglacial periods over the past 600,000 years, this variability was insufficient to shift global weathering fluxes. Furthermore, they showed that weathering remained remarkably constant over the past 2 Ma, which implies that silicate weathering played a minor role in controlling the long-term carbon cycle over this period. The timescale at which weathering fluxes equilibrate with environmental/climate changes over the past is another uncertainty that is yet to be fully understood. Studies suggested that on modern Earth, the chemical weathering flux is far from equilibrium and about two to three times higher than the average for an entire Quaternary glacial cycle (Vance et al., 2009).

2.2 Chemical weathering concerning short timescales

Over short geological timescales (e.g. 1,000 - 100,000 years), weathering is sensitive to abrupt changes in climate and hydrological cycles. Warm temperatures are generally associated with a more intense hydrological cycle, which is thought to increase the continental weathering flux (von Blanckenburg et al., 2015a). However, direct evidence for this is still scarce. Jin et al. (2006) found that chemical weathering reactions, at a lake catchment in northern China, followed the Holocene climatic evolution, where during warm and humid conditions, chemical weathering rates were enhanced and during short-lived cooling events (~500 years), weathering rates declined. Other studies suggested that there are only small changes in the global weathering flux in response to short-term climate change (Bluth and Kump, 1994; Munhoven, 2002). It was proposed that, over the Holocene, only large floodplains record a significant change in weathering flux in response to short-term (<21,000 years) climate shifts (Lupker et al., 2013). Foster and Vance (2006) showed that in the North Atlantic Region, during glacial periods, where cold and dry conditions persist, chemical weathering rates are two to three times lower than during interglacial periods. However, due to low sea levels during glacial periods,

more carbonates on continental shelves are exposed to weathering, which again counter-balance the weathering flux. Consequently, over glacial/interglacial periods, chemical weathering and associated CO_2 consumption is thought to remain relatively constant.

To disentangle the many controversies of the long- and short-term interactions between climate, tectonics, and weathering, reliable methods for reconstructing palaeo chemical weathering rates are essential.

2.3 Chemical weathering proxies based on sediment analyses

During weathering, the source rock decomposes and experiences a mass loss in chemical elements. This process results in the formation of a weathering product, where primary minerals break down to form secondary phases such as clays and Fe-oxides. An example for this is the reaction of orthoclase to kaolinite during hydrolysis:

$$2KAlSi_3O_8 + 2H^+ + 9H_2O \rightarrow H_4Al_2Si_2O_9 + 4H_4SiO_4 + 2K^+ \qquad (4)$$

Equation (4) demonstrates the loss/transfer of K^+ during weathering. In this example, K^+ is readily exported in aqueous solution, therefore leaving the source mineral, in this case orthoclase, depleted in potassium. The rate at which a source rock weathers can be estimated in the source rock or the weathering product using geochemical proxies. However, chemical weathering is controlled by many factors including the bedrock type, climate, topographic/tectonic settings, soil development, vegetation, and human activity (Li and Yang, 2010). Due to the large number of controls, reconstructing chemical weathering conditions remains challenging and one single proxy may not reflect the 'real' weathering conditions. In the next sections, several chemical weathering proxies are reviewed, and their limitations are discussed. These proxies include:

- Mobile-immobile element ratios (e.g. K/Al, Na/Al, K/Rb)
- Vogt's residual index 'V' (Vogt, 1927)
- Ruxton Ratio 'R' (Ruxton, 1968)
- Weathering Index of Parker 'WIP' (Parker, 1970)
- Clay mineralogy
- The Chemical Index of Alteration 'CIA' (Nesbitt and Young, 1982)

- Pb isotopes
- Nd isotopes
- Hf isotopes
- Meteoric $^{10}Be/^{9}Be$
- $^{87}Sr/^{86}Sr$

2.3.1 Mobile-immobile element ratios in small or monolithological systems

A simple but commonly used approach to reconstruct rock alteration processes is to utilise alkali and alkaline earth compositional changes such as ratios: K/Al, Na/Al or K/Rb (Nesbitt and Markovics, 1980; Dupré et al., 1996). During weathering, the source rock experiences a loss in chemical elements, which is removed by solution. This was demonstrated by Louvat and Allègre (1997), who found a complementary relationship between dissolved and suspended loads in a monolithological setting on the island of Réunion (Figure 1).

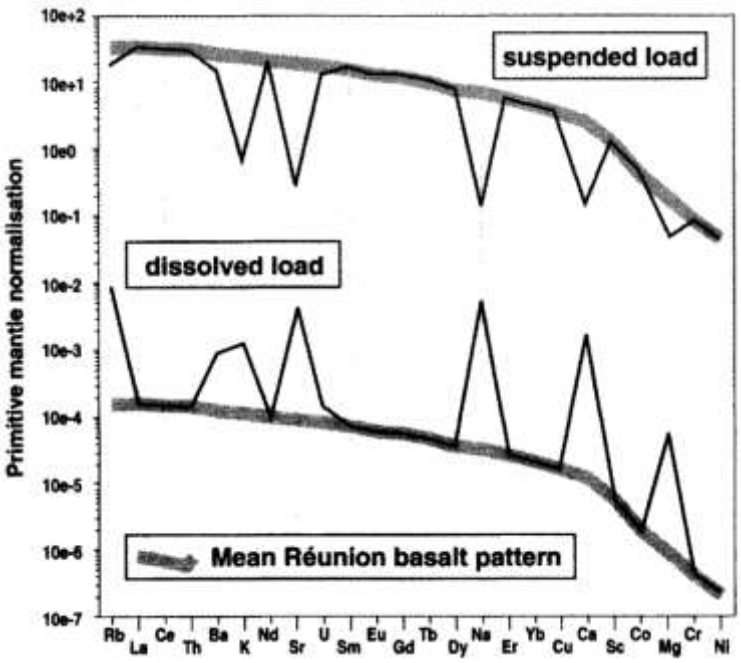

Figure 1: Mass budget relationship between suspended and dissolved loads from rivers on the Réunion island. The Y-axis shows the primitive mantle normalisation for both suspended and dissolved loads. Shaded lines are the mean basalt patterns (undiluted for suspended load and very diluted for dissolved load. Dissolved loads show element enrichments for soluble elements, whereas suspended loads show depletion for these elements. Insoluble elements show the same pattern for both suspended and dissolved loads. Source: Louvat and Allègre (1997).

Soluble elements, such as K and Na, are enriched in dissolved loads compared to the respective suspended load. In contrast, elements such as Eu and Gd show the same pattern as the mean Réunion basalt pattern for both dissolved and suspended loads, implying that, in rivers from Réunion island, these elements are insoluble compared to e.g. K and Na. The ratio mobile/immobile elements in the weathering products can therefore indicate the degree of chemical weathering. The mobility of an element during weathering can be roughly estimated via the ionic potential (z/r), where z is the ionic charge and r is the ionic radius (Figure 2).

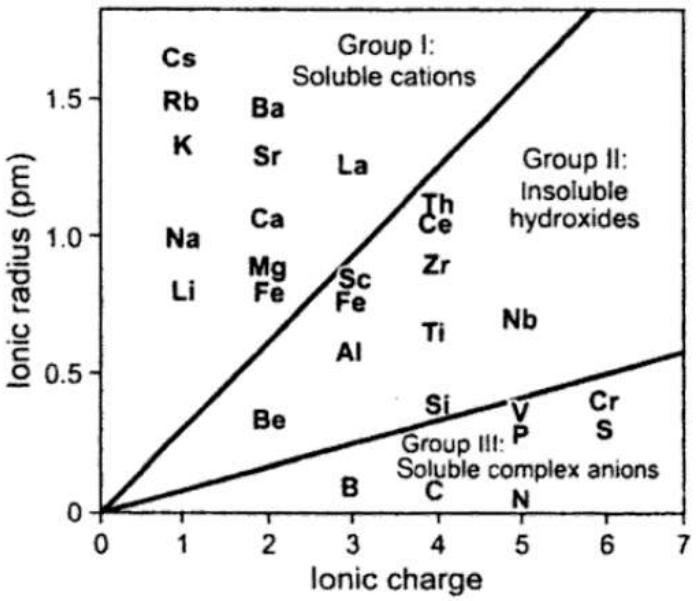

Figure 2: Ionic potentials of various elements divided into three groups (soluble cations, insoluble hydroxides, and soluble complex anions). Source: Randall and Anderson (2005).

For instance, the weathering flux can be calculated by comparing the elemental concentration of the sediment or soil sample to the (unweathered) parent rock (Dupré et al., 1996; Gaillardet et al., 1999). Low ratios of K/Al in saprolites (chemically weathered rocks which form in the lower zones of soil horizons) are generally associated with intense weathering conditions. However, K remains enriched during moderate degrees of chemical weathering, but during more intense weathering K-feldspar breaks down and therefore becomes depleted (Blaxland, 1974; Nesbitt et al., 1997). Hence, the interpretation of K/Al ratios in a sediment can be problematic (Clift et al., 2014). Rubidium, even though considered as soluble cation according to Figure 2, is considered immobile during weathering and mostly shows to be concentrated in clay-dominated

portions of a weathering profile relative to the mobile phase e.g. potassium. Although, under extreme conditions, even Rb ions are readily removed from clay minerals (Kronberg et al., 1979).

2.3.2 Vogt's Residual Index 'V'

The very first geochemical weathering index was suggested by Vogt (1927), termed the Vogt's Residual Index 'V'. The formula to calculate V is:

$$\frac{Al_2O_3 + K_2O}{MgO + CaO + Na_2O} \quad (5)$$

where Al_2O_3, K_2O, MgO, CaO, and Na_2O are in molecular proportions. Essentially, V is the ratio of immobile to mobile major elements, except that the numerator comprises mobile and immobile element phases (Burke et al., 2007). This index was used to determine the degree of weathering of Quaternary clay deposits. The comparison of V between moraine clays and marine clay deposits showed that moraine clays were more weathered than marine clays (Roaldset, 1972). Increasing V values are interpreted as more intense weathering during low pH conditions. However, V only gives valuable information if aluminium is an immobile phase during weathering, which is not always the case (Price and Velbel, 2003). This proxy may be challenging to use when applied to heterogenous weathered regolith. A study by Kim and Park (2003) showed a poor correlation between V and a petrographically determined weathering grade in granites. Furthermore, Burke et al. (2007) suggested that V is only applicable on small scale weathering profiles and over a large distance, the V index is less effective than the CIA and PI in recording the chemical weathering intensity.

2.3.3 Ruxton Ratio 'R'

Another weathering index was proposed by Ruxton (1968), later termed the Ruxton Ratio 'R' or simply the silicon-aluminium ratio (SA). This weathering proxy is restricted to weathering profiles developed on intermediate to acidic bedrock. The Ruxton Ratio is calculated as follows: SiO_2/Al_2O_3. It assumes constant sesquioxide content (an oxide in which oxygen is present in the ratio of three atoms to two of another element) during weathering and kaolinite and/or allophane weathering products. Furthermore, the Ruxton

ratio considers alumina and other sesquioxides to be immobile phases during weathering and relates silica loss to total-element loss (Price and Velbel, 2003). The validity of this proxy was tested on weathering profiles developed on 64 volcanic rocks and 48 igneous and metamorphic rocks from humid areas. Results showed that the ratio R correlated well with total-element loss (Figure 3) (Ruxton, 1968).

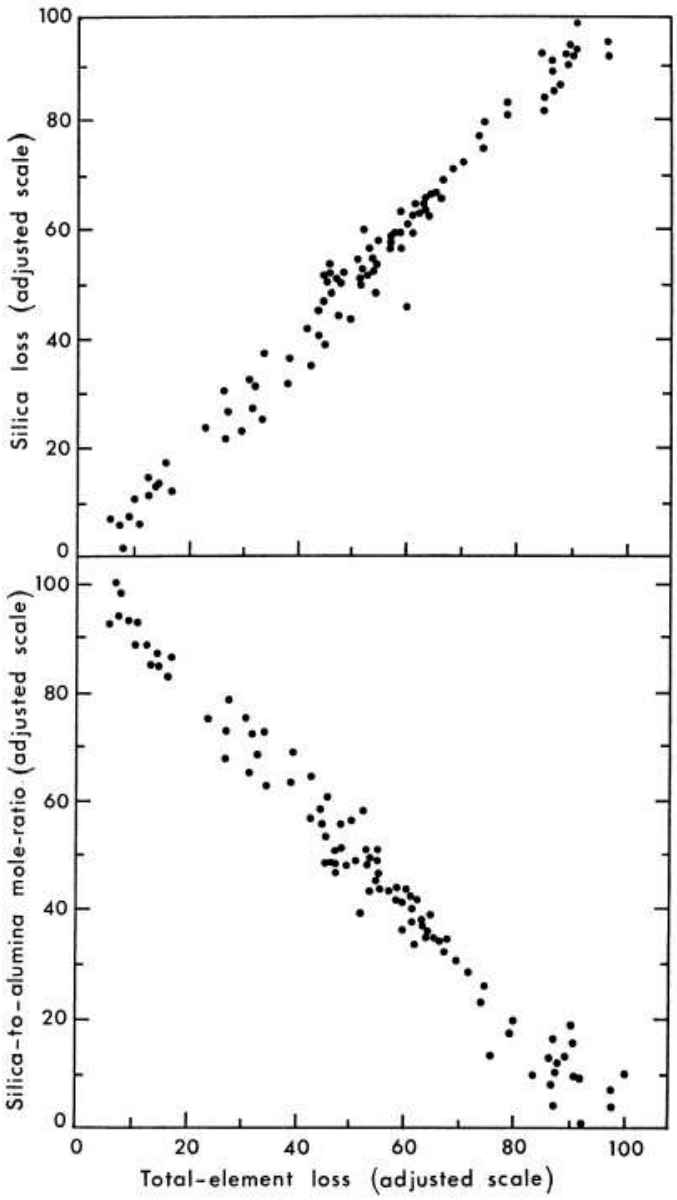

Figure 3: Top: Silica loss plotted against total-element loss, assuming Al remains constant during weathering. Bottom: Si/Al mole ratio against total-element loss. Source: Ruxton (1968).

Another study revealed that R correlates well with pH (Burke et al., 2007). However, the silica to alumina ratio may not be suitable as a weathering index for basic and ultrabasic

rocks. The index does not include feldspar weathering and only takes into account secondary minerals which contain aluminium. Furthermore, sesquioxides and/or silica in rocks found in strongly seasonal savannas or more arid areas tend to migrate and precipitate through the weathering profile, which makes the ratio R less suitable as a weathering index. The ratio Al/Si is commonly used as an index of mixing between clays and sands, rather than a proxy for chemical alteration (Van Daele et al., 2014).

2.3.4 Weathering Index of Parker (WIP)

In 1970, Parker (Parker, 1970) introduced a different weathering index, named the Weathering Index of Parker (WIP):

$$WIP = 100 \times \left(\frac{2Na_2O}{0.35} + \frac{MgO}{0.9} + \frac{2K_2O}{0.25} + \frac{CaO}{0.7}\right) \quad (6)$$

where Na_2O, MgO, K_2O, and CaO are in molecular proportions and the coefficients are based on strengths of the element-to-oxygen bonds (Parker, 1970). This index takes the proportions of Na, K, Mg, and Ca into account, which are the most mobile major elements in silicate rocks. Small WIP values indicate strong chemical weathering and generally correlate well with low pH values. Furthermore, based on their bond strengths with oxygen, individual mobilities of the aforementioned elements are accounted for. In contrast to the Ruxton Ratio, the WIP does not assume constant sesquioxide concentrations during weathering, and compared to the V index, it can be applied to heterogeneous weathered profiles (Price and Velbel, 2003). The WIP can be applied to acid, intermediate and basic igneous rocks, but cannot be utilised on highly weathered materials, because its formulation includes only mobile alkali and alkaline elements (Eswaran et al., 1973). Studies have shown that the WIP correlates well with the Chemical Index of Alteration (CIA) (see Section 2.3.5), but unlike the CIA, WIP does not seem to be affected by the sediment grain size (Shao et al., 2012). In contrast to the Ruxton Ratio, Burke et al. (2007) found poor correlation between WIP and pH weathering intensity trends.

2.3.5 The Chemical Index of Alteration (CIA)

The most widely recognised proxy to trace chemical alteration processes is the Chemical Index of Alteration (CIA) (Nesbitt and Young, 1982). It as a tool to measure the degree of chemical weathering and has been commonly used to study palaeo-soils. Under humid conditions, Na^+, K^+ and Ca^{2+} are readily leached which results in the concentration of Al and Si in the residue. The CIA is calculated via

$$\text{CIA} = \left(\frac{Al_2O_3}{Al_2O_3+CaO^*+Na_2O+K_2O}\right) \times 100 \quad (7)$$

where Al_2O_3, CaO, Na_2O, and K_2O are in molecular proportions and CaO* is the calcium content of silicate, which is based on the assumption that the dominant process during chemical weathering is the degradation of feldspars and the formation of clay minerals (Goldberg and Humayun, 2010). Kaolinite has a CIA of 100, which is associated with the highest degree of weathering. Illite is between 75 and 90, muscovite at 75, feldspars at 50. Fresh, unweathered rocks such as basalts have CIA values between 30 and 45, granites and granodiorite between 55 and 45 (Nesbitt and Young, 1982; Fedo et al., 1995). The CIA has been applied in numerous studies to evaluate the relationship between runoff and silicate weathering rates. Several studies have demonstrated that runoff represents the most important control of silicate weathering (Grantham and Velbel, 1988; Pinet and Souriau, 1988; Summerfield and Hulton, 1994; Ludwig and Probst, 1998; Gaillardet et al., 1999; West et al., 2005). However, a compilation of CIA values of sediments from large river drainage basins do not significantly correlate with runoff data (Li and Yang, 2010). The authors explain that this might be because the CIA in sediments is not a direct indicator of chemical weathering rates in the present catchment, but rather reflects an integrated weathering history through sediment formation. Hence, this proxy may not be useful in all sample types. The main limitation of the CIA is that it can be limited by sediments which are rich in carbonates. This means that this proxy cannot be applied to carbonate-rich (>30% carbonate) sediments, unless all carbonates are removed prior. Post-depositional K^+ addition via diagenetic illitisation, metamorphism, or metasomatism, as well as the inheritance of clays from sedimentary rocks in the source area must be considered. For example, the amount of clay in a sediment sample may not be directly linked to the weathering rate. This proxy also assumes that Al_2O_3 remains

immobile during weathering, which is not always the case during soil formation or extreme cases of weathering (Goldberg and Humayun, 2010).

2.3.6 Clay mineralogy as an index of chemical weathering reactions

The clay mineralogy of sediment deposits may also reflect chemical weathering reactions in response to specific environmental conditions. Clay minerals such as smectite, illite, and kaolinite are formed during weathering. Soils in tropical regions have been shown to dominantly form clays from the kaolin group (Thiry, 2000), while in dry regions, where chemical weathering is less intense due to limited water, soils are rich in smectite and illite (Asikainen et al., 2007; Clift et al., 2014). The ratio between smectite and kaolinite can therefore serve as a proxy for reconstructing the chemical weathering regime relative to climate. The clay mineral content is also related to the source rock and the amount of rainfall. For example, smectite (montmorillonite) in soils formed from basic igneous rocks remains relatively stable at high rainfalls compared to smectite in soils formed from basic igneous rocks (Figure 4). Furthermore, only acid igneous rocks can form illite at any rainfall (Singer, 1980). The clay mineral assemblage may also be a function of hill slope. Kaolinite has been shown to preferentially develop on gently sloping soils, whereas smectites are mainly formed in depressions (Kantor and Schwertmann, 1974). Furthermore, the clay mineralogy reflects palaeo humidity (Thamban and Rao, 2005): the ratio kaolinite/illite has been used in continental weathering profiles to reconstruct relative precipitation rates (Chamley, 2013). The main difficulty in using the clay mineral assemblage to infer chemical weathering conditions is that it relies on the assumption that all variables in the weathering environment, except climate, are equal (Kantor and Schwertmann, 1974), and that post-depositional alternation processes are negligible.

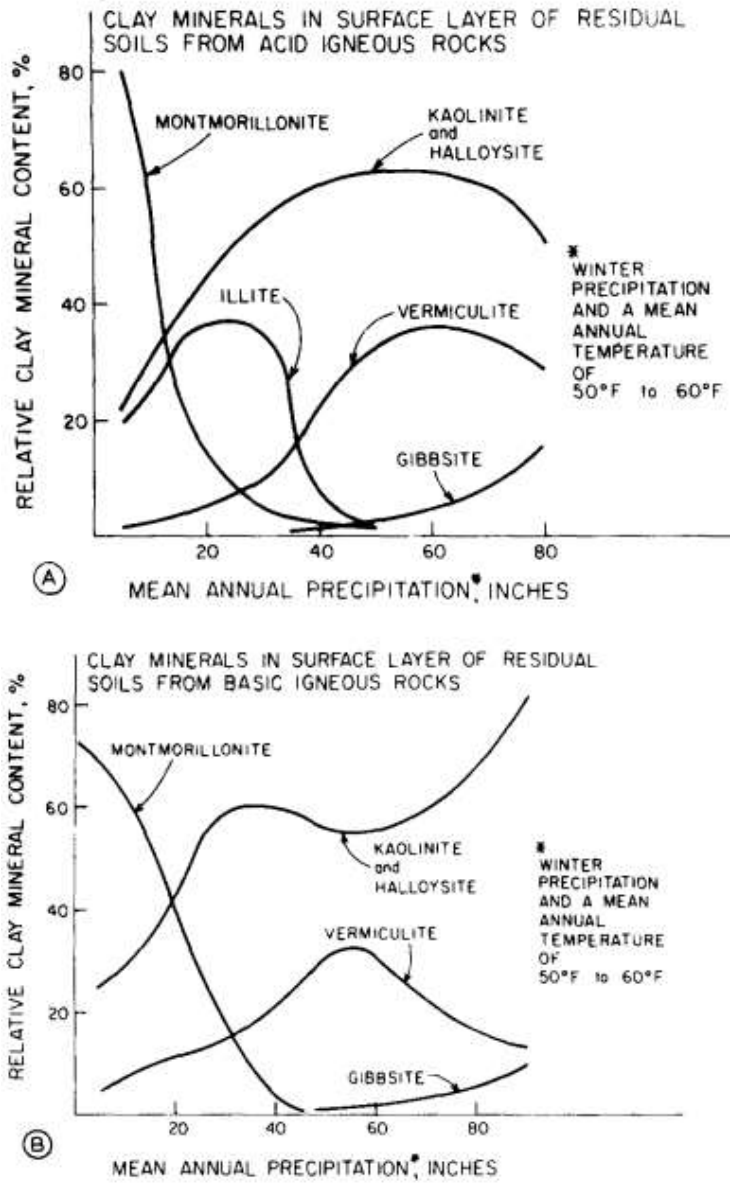

Figure 4: Distribution of clay mineral type in soil surfaces layers relative to mean annual precipitation. A) Soils formed on acid igneous rocks. B) Soils formed on basic igneous rocks. Source: Kantor and Schwertmann (1974).

2.3.7 Recent development of new isotope weathering tracers

During the last decade, several 'non-traditional' stable isotopes have been suggested as proxies for chemical weathering reactions. Among these are Li (^{7}Li, ^{6}Li) and B (^{11}B, ^{10}B), which play vital parts during soil-formation, and have shown to be subject to significant isotope fractionation during low temperature weathering reactions (Schmitt et al., 2012). The Li isotope proxy and its application as a chemical weathering tracer is in detail discussed in Chapter 3.

Boron isotopes

Boron is an essential nutrient for plants (Cividini et al., 2010) and its isotopes (^{11}B, ^{10}B) can be used to trace bio-geochemical reactions. In comparison to carbonates, silicate rocks contain moderate to high concentrations of B because of substitution with Si and Al. Large isotopic fractionation occurs during clay formation at low and high temperatures. The isotopic composition of B is not directly influenced by vegetation, but rather by local sources such as minerals, soils, and soil solutions. During root absorption, B isotopes have shown to encompass isotopic fractionation, but studies have suggested that this isotopic shift is minor compared to weathering-related fractionation (Schmitt et al., 2012). In the Mackenzie Basin, B isotopes have been applied to reconstruct silicate weathering reactions, where it was found that $^{11}B/^{10}B$ of river dissolved loads inversely correlated with the annual runoff, indicating that B may be used to trace erosion processes in river systems (Lemarchand and Gaillardet, 2006).

Ca isotopes

Two main mechanisms are known that fractionate Ca isotopes (^{40}Ca, ^{42}Ca, ^{43}Ca, ^{44}Ca, ^{46}Ca, ^{48}Ca): the light isotopes of Ca are enriched in the solid phase (e.g. calcite) during precipitation from solution (Tipper et al., 2006), and large Ca isotope fractionation occurs during plant uptake, where roots are enriched in the lighter isotopes. This was demonstrated in small-scale watersheds, where ^{40}Ca was generally concentrated in vegetation relative to surrounding soil solutions, soil leachates, and bulk soil samples (Schmitt et al., 2012). The Ca isotope proxy has been applied in several studies to investigate the role of weathering reactions coupled with biological activity.

Mg isotopes

Recent studies have shown that Mg isotopes (^{24}Mg, ^{25}Mg, ^{26}Mg) may be used to trace weathering processes. Silicate rocks are uniform in their $^{26}Mg/^{24}Mg$ isotope ratio and differ significantly from that of carbonates. Therefore, the Mg isotope composition of surface waters may be used to differentiate the silicate and carbonate weathering endmembers (Tipper et al., 2006; von Strandmann et al., 2008; Tipper et al., 2008). During weathering, systematic enrichment of the heavy Mg isotopes are observed in secondary mineral phases and the $^{26}Mg/^{24}Mg$ isotope ratio in soil profiles have been linked to the amount of smectite (Tipper et al., 2010). Furthermore, Mg isotopes fractionate during plant growth, which is evident through the enrichment of heavy Mg isotopes in trees and grasses compared to the soil exchangeable fraction (Schmitt et al.,

2012). Therefore, the Mg isotope proxy is a potential tool for tracing silicate weathering and plant-mineral interactions.

2.3.8 Tracing palaeo variations of continental weathering using 'classical' isotope tracers

Isotopic variations of trace metals with relatively short residence times in the oceans, such as Hf ($^{176}Hf/^{177}Hf$), Pb ($^{206}Pb/^{204}Pb$), and Nd ($^{143}Nd/^{144}Nd$), Sr ($^{87}Sr/^{88}Sr$), and Be ($^{10}Be/^{9}Be$) isotopes have been shown to reflect continental weathering reactions (Frank, 2002). These metals enter the oceans through three main pathways: riverine, aeolian, or hydrothermal activity on the seafloor. Figure 5 shows the pathway of each of the aforementioned trace metals from their sources into the ocean.

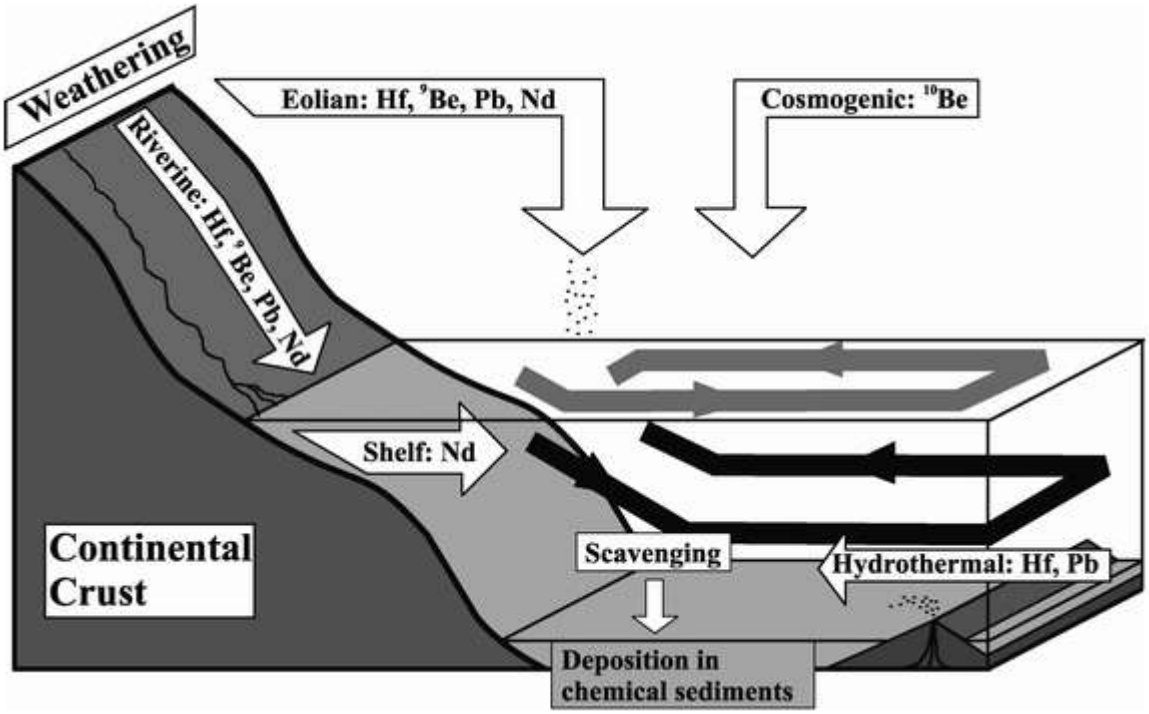

Figure 5: Pathways of Hf, Be, Pb, and Nd from their sources into the ocean. Three main sources of particulate and dissolved trace metals for the ocean are shown: riverine, aeolian, and hydrothermal. Shaded circulating bands represent deep-water circulation that cause mixing of dissolved metals. Source: Frank (2002).

Neodymium isotopes

A common proxy to trace long-term changes in the weathering source is Nd isotopes (Frank, 2002). The most important source of Nd in the oceans is the riverine input, especially in areas where strong chemical weathering persists. The isotopes of interest for

reconstructing variations in the continental weathering source are ^{143}Nd and ^{144}Nd. Fractionation of Nd isotopes is thought to not occur during weathering and dissolution processes of detrital material and the $^{143}Nd/^{144}Nd$ remains constant (Goldstein et al., 1984). Only a few studies show evidence for isotope fractionation effects accompanying weathering and mineral dissolution (Öhlander et al., 2000; von Blanckenburg and Nägler, 2001; Andersson et al., 2001). However, these effects are not considered to be of quantitative importance (Frank, 2002). Therefore, the Nd isotope composition of waters directly reflect the isotopic composition of the source rock, which depending on type and age can vary greatly. This implies that Nd isotopes do not reflect the weathering processes but rather changes in source. For example, weathering of continental rocks of Proterozoic or Archean age surrounding the North Atlantic produce waters with relatively low $^{143}Nd/^{144}Nd$ ratios. In contrast, island arc rocks around the Pacific Ocean produce waters with much higher $^{143}Nd/^{144}Nd$ ratios. The global average ocean residence time of Nd in deep waters is estimated around 600 to 2,000 years (Jeandel, 1993; Jeandel et al., 1995; Tachikawa et al., 1999). The Nd isotope composition of waters (or sediments) have been applied as a proxy to reconstruct changes in weathering sources or its spatial variability in the past (Sun, 2005; Singh et al., 2008; Dou et al., 2016; Bayon et al., 2017). For example, variations in Nd isotope ratios of planktonic foraminifera from the Bay of Bengal show significant correlations with monsoonal circulation (Burton and Vance, 2000). In summary, while the Nd isotope proxy does not reflect the intensity of weathering reactions, it can inform us of variations in the weathering source, which may be accompanied with changes in weathering regimes.

Hafnium isotopes

Similar to Nd, Hf does not exhibit isotope fractionation during continental weathering while the isotopic composition ($^{176}Hf/^{177}Hf$) varies greatly between different source rocks. The residence time of Hf at 1,500 to 2,000 years is slightly higher than that for Nd and in contrast to Nd, Hf is mostly concentrated in heavy minerals. Because of the similar behaviour between Hf and Nd during weathering, often a combination between the two proxies is utilised to study palaeo variations in weathering source (e.g. van de Flierdt et al. (2002); Bayon et al. (2009)). However, because of strong incongruent weathering effects of zircons from the continental crust, a direct coupling between Nd and Hf isotopes is not always present (Bayon et al., 2016). The Hf isotope proxy was applied by Bayon et al. (2009) to marine sediments off the Congo River mouth and other parts of the SE

Atlantic Ocean. The authors found that continental silicate weathering results in erosion products with distinctive Hf isotope signatures and that $^{176}Hf/^{177}Hf$ of marine sediments reflect that of the source rock. Similarly to Nd isotopes, the Hf isotope proxy has also been applied to identify changes in weathering regime and sediment transport (e.g. Dausmann et al. (2015)).

Pb isotopes

Rivers are the main source of Pb to the ocean, where it has an average residence time of 50 years in the Atlantic and 200 – 400 years in the Pacific Ocean (Frank, 2002). Dust input only accounts for 10-12 % of the dissolved Pb budget in the ocean (Chow and Patterson, 1962). Pb isotopes fractionate during weathering of continental rocks, which means that the isotope composition changes. Compared to the non-radiogenic isotope ^{204}Pb, the radiogenic Pb isotopes (^{206}Pb, ^{207}Pb, ^{208}Pb) are produced within the rocks by decay of U and Th. This decay results in radiation which damages the crystal structure of a mineral and causes the daughter isotopes to be loosely bound and easily mobilised during weathering (Erel et al., 1994; Jones et al., 2000; Frank, 2002). Therefore, during weathering of continental rocks and minerals, the solution transported towards the sink (the ocean) has Pb isotope ratios different to those of the source rocks (von Blanckenburg and Nägler, 2001). An unweathered mantle-derived end-member typically shows $^{206}Pb/^{204}Pb$ ratios of 18.5. Weathering of these rocks causes an increase of $^{206}Pb/^{204}Pb$ in solution, depending on the magnitude of deep-water mixing. In the North Atlantic for example, the weathering product (solute) of the aforementioned rocks displays $^{206}Pb/^{204}Pb$ ratios of ~19.3 (Frank, 2002). The deep-water isotope composition is then recorded in authigenic chemical precipitates in the ocean. Foster and Vance (2006) applied this proxy to ferromanganese crusts, which precipitate directly from seawater. Results demonstrated how the seawater Pb isotope composition, and therefore weathering on continents varied over the past. The Pb isotope data showed that during early stages of interglacial periods, where fresh soil-parent material was exposed after the retreat of continental ice sheets, chemical weathering rates were high. However, the Pb isotope proxy has some limiting factors. For instance, Pb isotope compositions are a function of source and may possibly reflect only localised weathering signals. Furthermore, the Pb isotope composition is not homogeneous in all oceans and since this proxy is dependent on deep ocean circulation, a mixing between two oceans through an open seaway would cause great variations in the radiogenic isotopes of Pb to non-radiogenic ^{204}Pb (Frank,

2002). Willenbring and von Blanckenburg (2010) proposed that the Pb isotope composition in ocean sediments does not reflect the silicate weathering flux but rather denudation style and source-rock isotope composition.

Beryllium isotopes

The ratio of cosmogenic ^{10}Be to ^{9}Be can be used as a tracer of the overall supply of terrigenous material entering in the ocean (von Blanckenburg et al., 1996; von Blanckenburg and O'Nions, 1999). The stable ^{9}Be isotope concentration in the continental crust is a few parts per million and gets transported to the ocean via erosion, where it has an average residence time of 200 – 1000 years (Frank, 2002). The cosmogenic isotope ^{10}Be on the other hand is produced in the atmosphere through the spallation of oxygen and nitrogen. ^{10}Be enters the ocean mainly through rainfall and has been shown to be spatially relatively constant over several thousands of years (von Blanckenburg et al., 1996). Because ^{9}Be derives only from the erosion of continents, a decrease in the ^{10}Be/^{9}Be ratio can be interpreted as an enhanced supply of terrigenous material (von Blanckenburg and O'Nions, 1999). The application of this proxy on marine sediments has shown that over the past 12 Ma, continental weathering remained relatively stable and neither an increase of erosion nor any pulse in weathering material occurred (Willenbring and von Blanckenburg, 2010). This finding challenges the idea that an increase in silicate weathering and associated atmospheric CO_2 consumption was the cause for Cenozoic global cooling. However, ^{10}Be/^{9}Be also changes as a function of geomagnetic field cycles, which makes it a complex weathering proxy to be applied on geological long timescales (Willenbring and Jerolmack, 2016). Similar to Pb isotopes, the Be isotope composition in the ocean is not homogeneous and is spatially variable. For example, the Atlantic and Arctic ocean basins show lower ^{10}Be/^{9}Be ratios compared to the Pacific Ocean, owing to the difference in coast length and ^{9}Be input through continents (Willenbring and von Blanckenburg, 2010). Furthermore, ^{9}Be does not directly reflect erosion rates and it is not sensitive to basalt or carbonate weathering.

^{87}Sr/^{86}Sr isotopes in the ocean: a long-term proxy

The strontium isotope proxy is the most commonly used isotope tracer to reconstruct changes in weathering reactions. Strontium has four stable isotopes: ^{84}Sr, ^{86}Sr, ^{87}Sr, and ^{88}Sr. The Sr isotope composition varies due to the formation of ^{87}Sr by the decay of ^{87}Rb, with a half-life of 4.88 x 10^{10} years (Faure, 1986). Studies have shown that individual minerals such as mica or feldspar have specific ^{87}Sr/^{86}Sr ratios due to different initial

Rb/Sr and the decay of ^{87}Rb. When these minerals are weathered, the dissolved and suspended loads carry this specific Sr isotope signal. Therefore, the $^{87}Sr/^{86}Sr$ ratio may be used to trace weathering reactions of specific mineral phases. For instance, this characteristic can be used to differentiate between carbonate and silicate weathering sources, as both exhibit very different Sr isotope ratios (Jacobson et al., 2002; Chamberlain et al., 2005; Jin et al., 2012). High $^{87}Sr/^{86}Sr$ ratios derive from weathering of continental crust i.e. fluvial inputs, whereas low ratios are indicative of mantle-derived high-temperature hydrothermal inputs at the mid-ocean ridges (Frank, 2002). Because the incorporation of strontium in carbonates does not involve any isotope fractionation, marine carbonate records, that reflect the seawater isotope composition, can be used to reconstruct palaeo weathering sources. A strontium isotope record in marine limestones revealed that continental weathering responded to the Himalayan orogeny, where silicate weathering dominated over carbonate weathering (Edmond, 1992) (Figure 6). However, other studies proposed that an increase in $^{87}Sr/^{86}Sr$ could simply reflect the weathering of Himalayan carbonate sediments that were enriched in ^{87}Sr during Himalayan metamorphism (Galy et al., 1999).

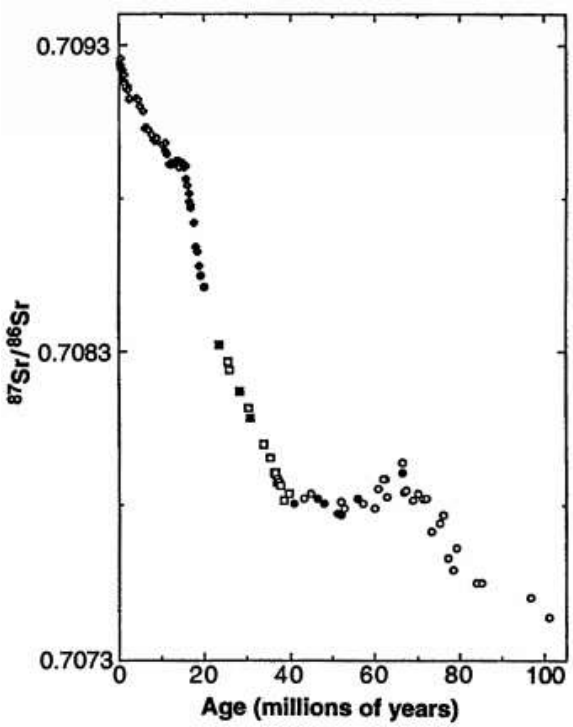

Figure 6: $^{87}Sr/^{86}Sr$ of marine limestones as a function of time. Source: Edmond (1992).

The reliability of this proxy is questionable, because the strontium isotope composition only reflects the relative contribution of silicate versus carbonate reservoirs. If, for

example, silicate weathering rates remain constant while carbonate weathering rates decrease, the ratio $^{87}Sr/^{86}Sr$ would increase. Similarly, changes in hydrothermal fluxes greatly affect the $^{87}Sr/^{86}Sr$. Furthermore, minerals weather at different rates and the Sr isotope signature is dominated by minerals with high dissolution kinetics (Sharp et al., 2002). Therefore, the $^{87}Sr/^{86}Sr$ record is dependent on the mineral assemblage and its dissolution kinetics of the source rock.

2.4 A critical reflection on chemical weathering proxies

Chemical weathering proxies that rely on the mobility of elements in the weathering environment (V, R, WIP, CIA) give a good indication of incipient and moderate stages of weathering within a weathering profile (Middelburg et al., 1988). However, these proxies are strongly dependent on the rock type and chemical composition. Moreover, at extreme weathering conditions, or in highly organic environments, phases that are considered immobile can be readily leached, which makes these proxies inapplicable. Furthermore, selective leaching of rocks, where minerals dissolve at individual rates depending on dissolution kinetics, limits the application of these weathering indices. Post-depositional leaching of a weathering product may modify its chemical composition. The clay mineralogy, which is essentially the weathering end-product, may indicate under which weathering condition a clay was formed. However, too many variables govern the formation of clays. For example, soil topography, vegetation, source rock and local climate variability may significantly affect the clay mineralogy (Kantor and Schwertmann, 1974). Also, clay may not form even though all thermodynamic conditions are fulfilled (Chadwick et al., 2003). Isotope proxies such as Nd ($^{143}Nd/^{144}Nd$) and Hf ($^{176}Hf/^{177}Hf$) are excellent tracers for weathering sources. However, these isotope systems may not quantify the degree of weathering. If, for example, the weathering source remains constant, no change in weathering regime can be observed with Nd and Hf isotopes. Pb isotopes ($^{206}Pb/^{204}Pb$), $^{10}Be/^{9}Be$ and $^{87}Sr/^{86}Sr$ have the advantage that diagenetic alteration or post-depositional exchange with fluids does not significantly affect the isotope ratio of the weathering product (Frank, 2002). But because of the short residence time of Pb and Be isotopes in oceans, and because these isotope systems are affected by deep-water circulation in the ocean, the observed weathering signal in ocean records cannot be globalised and is therefore only reflecting the weathering flux of local/regional catchments. A more global weathering signal can be derived from Sr isotopes in marine carbonates, where the $^{87}Sr/^{86}Sr$ ratio mirrors the weathering of silicates relative to

carbonates. However, the weathering-derived Sr is difficult to define because of differences in Sr dissolved flux, which is controlled by the source rock isotopic composition, the differences in mineralogy along flow paths and mineral dissolution characteristics (Åberg et al., 1989).

Given the limitations of these chemical weathering proxies, a more reliable weathering proxy is crucial. In the last two decades, several novel isotope proxies have been suggested that may better explain weathering reactions. Among these are B, Mg, Ca, and Li isotopes. While B, Mg, and Ca isotope signatures have shown to be influenced by vegetation, Li isotopes is primarily affected by chemical weathering reactions. During weathering, the lighter isotope ^{6}Li is preferentially incorporated into secondary mineral phases (Huh et al., 1998; Pistiner and Henderson, 2003; Vigier et al., 2008) and secondary mineral formation. In comparison to other weathering tracers, the Li isotope proxy allows for the reconstruction of solely silicate weathering conditions, because Li is highly enriched in silicates relative to carbonates (Kısakűrek et al., 2005). Li is not influenced by redox reactions, is not part of atmospheric, biological or hydrological cycles and is not affected by mineral sorting (Burton and Vigier, 2012). Also, the Li isotope composition of seawater is globally homogeneous, which implies that the proxy may reflect the average global weathering flux over geologic time scales. Because the Li isotope proxy (especially in continental archives) is still in its infancy, more data are necessary to evaluate its potential use as a continental chemical weathering tracer.

References

Åberg, G., Jacks, G. & Hamilton, P. J. 1989. Weathering rates and $^{87}Sr/^{86}Sr$ ratios: an isotopic approach. *Journal of Hydrology,* 109**,** 65-78.

Andersson, P. S., Dahlqvist, R., Ingri, J. & Gustafsson, Ö. 2001. The isotopic composition of Nd in a boreal river: a reflection of selective weathering and colloidal transport. *Geochimica et Cosmochimica Acta,* 65**,** 521-527.

Asikainen, C. A., Francus, P. & Brigham-Grette, J. 2007. Sedimentology, clay mineralogy and grain-size as indicators of 65 ka of climate change from El'gygytgyn Crater Lake, Northeastern Siberia. *Journal of Paleolimnology,* 37**,** 105-122.

Bayon, G., Burton, K., Soulet, G., Vigier, N., Dennielou, B., Etoubleau, J., Ponzevera, E., German, C. & Nesbitt, R. 2009. Hf and Nd isotopes in marine sediments: Constraints on global silicate weathering. *Earth and Planetary Science Letters,* 277**,** 318-326.

Bayon, G., Skonieczny, C., Delvigne, C., Toucanne, S., Bermell, S., Ponzevera, E. & Andre, L. 2016. Environmental Hf–Nd isotopic decoupling in world river clays. *Earth and Planetary Science Letters,* 438**,** 25-36.

Bayon, G., De Deckker, P., Magee, J. W., Germain, Y., Bermell, S., Tachikawa, K. & Norman, M. D. 2017. Extensive wet episodes in Late Glacial Australia resulting from high-latitude forcings. *Scientific Reports,* 7**,** 44054.

Berner, R. A., Lasaga, A. C. & Garrels, R. M. 1983. The carbonate-silicate geochemical cycle and its effect on atmospheric carbon dioxide over the past 100 million years. *American Journal of Science,* 283**,** 641-683.

Berner, R. A. & Kothavala, Z. 2001. GEOCARB III: a revised model of atmospheric CO_2 over Phanerozoic time. *American Journal of Science,* 301**,** 182-204.

Blaxland, A. B. 1974. Geochemistry and geochronology of chemical weathering, Butler Hill Granite, Missouri. *Geochimica et Cosmochimica Acta,* 38**,** 843-852.

Bluth, G. J. & Kump, L. R. 1994. Lithologic and climatologic controls of river chemistry. *Geochimica et Cosmochimica Acta,* 58**,** 2341-2359.

Broecker, W. S. & Sanyal, A. 1998. Does atmospheric CO_2 police the rate of chemical weathering? *Global Biogeochemical Cycles,* 12**,** 403-408.

Burke, B. C., Heimsath, A. M. & White, A. F. 2007. Coupling chemical weathering with soil production across soil-mantled landscapes. *Earth Surface Processes and Landforms,* 32**,** 853-873.

Burton, K. W. & Vance, D. 2000. Glacial–interglacial variations in the neodymium isotope composition of seawater in the Bay of Bengal recorded by planktonic foraminifera. *Earth and Planetary Science Letters,* 176**,** 425-441.

Burton, K. W. & Vigier, N. 2012. Lithium Isotopes as Tracers in Marine and Terrestrial Environments. *In:* Baskaran, M. (ed.) *Handbook of Environmental Isotope Geochemistry: Vol I.* Berlin, Heidelberg: Springer Berlin Heidelberg, 41-59.

Chadwick, O. A., Gavenda, R. T., Kelly, E. F., Ziegler, K., Olson, C. G., Elliott, W. C. & Hendricks, D. M. 2003. The impact of climate on the biogeochemical functioning of volcanic soils. *Chemical Geology,* 202**,** 195-223.

Chamberlain, C. P., Waldbauer, J. R. & Jacobson, A. D. 2005. Strontium, hydrothermal systems and steady-state chemical weathering in active mountain belts. *Earth and Planetary Science Letters,* 238**,** 351-366.

Chamley, H. 2013. *Clay Sedimentology,* Springer Science & Business Media, pp.

Chow, T. J. & Patterson, C. 1962. The occurrence and significance of lead isotopes in pelagic sediments. *Geochimica et Cosmochimica Acta,* 26**,** 263-308.

Cividini, D., Lemarchand, D., Chabaux, F., Boutin, R. & Pierret, M.-C. 2010. From biological to lithological control of the B geochemical cycle in a forest watershed (Strengbach, Vosges). *Geochimica et Cosmochimica Acta,* 74**,** 3143-3163.

Clift, P. D., Wan, S. & Blusztajn, J. 2014. Reconstructing chemical weathering, physical erosion and monsoon intensity since 25 Ma in the northern South China Sea: a review of competing proxies. *Earth-Science Reviews,* 130**,** 86-102.

Dausmann, V., Frank, M., Siebert, C., Christl, M. & Hein, J. R. 2015. The evolution of climatically driven weathering inputs into the western Arctic Ocean since the late Miocene: Radiogenic isotope evidence. *Earth and Planetary Science Letters,* 419**,** 111-124.

Dou, Y., Yang, S., Shi, X., Clift, P. D., Liu, S., Liu, J., Li, C., Bi, L. & Zhao, Y. 2016. Provenance weathering and erosion records in southern Okinawa Trough sediments since 28ka: geochemical and Sr–Nd–Pb isotopic evidences. *Chemical Geology,* 425**,** 93-109.

Dupré, B., Gaillardet, J., Rousseau, D. & Allègre, C. J. 1996. Major and trace elements of river-borne material: the Congo Basin. *Geochimica et Cosmochimica Acta,* 60**,** 1301-1321.

Edmond, J. 1992. Himalayan tectonics, weathering processes, and the strontium isotope record in marine limestones. *Science,* 258**,** 1594-1594.

Erel, Y., Harlavan, Y. & Blum, J. D. 1994. Lead isotope systematics of granitoid weathering. *Geochimica et Cosmochimica Acta,* 58**,** 5299-5306.

Eswaran, H., Stoops, G. & De Paepe, R. 1973. A contribution to the study of soil formation on Isla Santa Cruz, Galapagos. *Pedologie,* 23**,** 100-122.

Faure, G. 1986. *Principles of Isotope Geology,* John Wiley and Sons Ltd, New York, 589 pp.

Fedo, C. M., Nesbitt, H. W. & Young, G. M. 1995. Unraveling the effects of potassium metasomatism in sedimentary rocks and paleosols, with implications for paleoweathering conditions and provenance. *Geology,* 23**,** 921-924.

Foster, G. L. & Vance, D. 2006. Negligible glacial-interglacial variation in continental chemical weathering rates. *Nature,* 444**,** 918.

Frank, M. 2002. Radiogenic isotopes: tracers of past ocean circulation and erosional input. *Reviews of geophysics,* 40**,** 1-38.

Gaillardet, J., Dupré, B., Louvat, P. & Allègre, C. 1999. Global silicate weathering and CO_2 consumption rates deduced from the chemistry of large rivers. *Chemical Geology,* 159**,** 3-30.

Galy, A., France-Lanord, C. & Derry, L. A. 1999. The strontium isotopic budget of Himalayan rivers in Nepal and Bangladesh. *Geochimica et Cosmochimica Acta,* 63**,** 1905-1925.

Goldberg, K. & Humayun, M. 2010. The applicability of the Chemical Index of Alteration as a paleoclimatic indicator: An example from the Permian of the Paraná Basin, Brazil. *Palaeogeography, Palaeoclimatology, Palaeoecology,* 293**,** 175-183.

Goldstein, S. L., O'nions, R. K. & Hamilton, P. J. 1984. A Sm-Nd isotopic study of atmospheric dusts and particulates from major river systems. *Earth and Planetary Science Letters,* 70**,** 221-236.

Grantham, J. H. & Velbel, M. A. 1988. The influence of climate and topography on rock-fragment abundance in modern fluvial sands of the southern Blue Ridge Mountains, North Carolina. *Journal of Sedimentary Research,* 58**,** 219-227.

Hilley, G., Chamberlain, C., Moon, S., Porder, S. & Willett, S. 2010. Competition between erosion and reaction kinetics in controlling silicate-weathering rates. *Earth and Planetary Science Letters,* 293**,** 191-199.

Huh, Y., Chan, L.-H., Zhang, L. & Edmond, J. M. 1998. Lithium and its isotopes in major world rivers: implications for weathering and the oceanic budget. *Geochimica et Cosmochimica Acta,* 62**,** 2039-2051.

Jacobson, A. D., Blum, J. D., Chamberlain, C. P., Poage, M. A. & Sloan, V. F. 2002. Ca/Sr and Sr isotope systematics of a Himalayan glacial chronosequence: carbonate versus silicate weathering rates as a function of landscape surface age. *Geochimica et Cosmochimica Acta,* 66**,** 13-27.

Jeandel, C. 1993. Concentration and isotopic composition of Nd in the South Atlantic Ocean. *Earth and Planetary Science Letters,* 117**,** 581-591.

Jeandel, C., Bishop, J. & Zindler, A. 1995. Exchange of neodymium and its isotopes between seawater and small and large particles in the Sargasso Sea. *Geochimica et Cosmochimica Acta,* 59**,** 535-547.

Jin, L., Mukasa, S. B., Hamilton, S. K. & Walter, L. M. 2012. Impacts of glacial/interglacial cycles on continental rock weathering inferred using Sr/Ca and $^{87}Sr/^{86}Sr$ ratios in Michigan watersheds. *Chemical Geology,* 300**,** 97-108.

Jin, Z., Cao, J., Wu, J. & Wang, S. 2006. A Rb/Sr record of catchment weathering response to Holocene climate change in Inner Mongolia. *Earth Surface Processes and Landforms,* 31**,** 285-291.

Jones, C. E., Halliday, A. N., Rea, D. K. & Owen, R. M. 2000. Eolian inputs of lead to the North Pacific. *Geochimica et Cosmochimica Acta,* 64**,** 1405-1416.

Kantor, W. & Schwertmann, U. 1974. Mineralogy and genesis of clays in red-black soil toposequences on basic igneous rocks in Kenya. *European Journal of Soil Science,* 25**,** 67-78.

Kim, S. & Park, H.-D. 2003. The relationship between physical and chemical weathering indices of granites around Seoul, Korea. *Bulletin of Engineering Geology and the Environment,* 62**,** 207-212.

Kısakűrek, B., James, R. H. & Harris, N. B. 2005. Li and δ^7Li in Himalayan rivers: proxies for silicate weathering? *Earth and Planetary Science Letters,* 237**,** 387-401.

Kronberg, B., Fyfe, W., Leonardos, O. & Santos, A. 1979. The chemistry of some Brazilian soils: element mobility during intense weathering. *Chemical Geology,* 24**,** 211-229.

Lemarchand, D. & Gaillardet, J. 2006. Transient features of the erosion of shales in the Mackenzie basin (Canada), evidences from boron isotopes. *Earth and Planetary Science Letters,* 245**,** 174-189.

Li, C. & Yang, S. 2010. Is chemical index of alteration (CIA) a reliable proxy for chemical weathering in global drainage basins? *American Journal of Science,* 310**,** 111-127.

Louvat, P. & Allègre, C. J. 1997. Present denudation rates on the island of Réunion determined by river geochemistry: basalt weathering and mass budget between chemical and mechanical erosions. *Geochimica et Cosmochimica Acta,* 61**,** 3645-3669.

Ludwig, W. & Probst, J.-L. 1998. River sediment discharge to the oceans; present-day controls and global budgets. *American Journal of Science,* 298**,** 265-295.

Lupker, M., France-Lanord, C., Galy, V., Lavé, J. & Kudrass, H. 2013. Increasing chemical weathering in the Himalayan system since the Last Glacial Maximum. *Earth and Planetary Science Letters,* 365**,** 243-252.

Maher, K. & Chamberlain, C. 2014. Hydrologic regulation of chemical weathering and the geologic carbon cycle. *Science,* 343**,** 1502-1504.

Middelburg, J. J., Van Der Weijden, C. H. & Woittiez, J. R. 1988. Chemical processes affecting the mobility of major, minor and trace elements during weathering of granitic rocks. *Chemical Geology,* 68**,** 253-273.

Molnar, P. & England, P. 1990. Late Cenozoic uplift of mountain ranges and global climate change: chicken or egg? *Nature,* 346**,** 29-34.

Moon, S., Chamberlain, C. & Hilley, G. 2014. New estimates of silicate weathering rates and their uncertainties in global rivers. *Geochimica et Cosmochimica Acta,* 134**,** 257-274.

Munhoven, G. 2002. Glacial–interglacial changes of continental weathering: estimates of the related CO_2 and HCO_3^- flux variations and their uncertainties. *Global and Planetary Change,* 33**,** 155-176.

Nesbitt, H. & Young, G. 1982. Early Proterozoic climates and plate motions inferred from major element chemistry of lutites. *Nature,* 299**,** 715-717.

Nesbitt, H. W., Fedo, C. M. & Young, G. M. 1997. Quartz and feldspar stability, steady and non-steady-state weathering, and petrogenesis of siliciclastic sands and muds. *The Journal of Geology,* 105**,** 173-192.

Öhlander, B., Ingri, J., Land, M. & Schöberg, H. 2000. Change of Sm-Nd isotope composition during weathering of till. *Geochimica et Cosmochimica Acta,* 64**,** 813-820.

Parker, A. 1970. An index of weathering for silicate rocks. *Geological Magazine,* 107**,** 501-504.

Pinet, P. & Souriau, M. 1988. Continental erosion and large-scale relief. *Tectonics,* 7**,** 563-582.

Pistiner, J. S. & Henderson, G. M. 2003. Lithium-isotope fractionation during continental weathering processes. *Earth and Planetary Science Letters,* 214**,** 327-339.

Price, J. R. & Velbel, M. A. 2003. Chemical weathering indices applied to weathering profiles developed on heterogeneous felsic metamorphic parent rocks. *Chemical Geology,* 202**,** 397-416.

Randall, S. & Anderson, S. 2005. Soils Genesis and Geomorphology. *Cambridge University Press, UK, ISBN,* 521812011**,** 832.

Raymo, M. & Ruddiman, W. F. 1992. Tectonic forcing of late Cenozoic climate. *Nature,* 359**,** 117-122.

Raymo, M. E., Ruddiman, W. F. & Froelich, P. N. 1988. Influence of late Cenozoic mountain building on ocean geochemical cycles. *Geology,* 16**,** 649-653.

Roaldset, E. 1972. Mineralogy and geochemistry of Quaternary clays in the Numedal area, southern Norway. *Norsk Geologisk Tidsskrift,* 52**,** 335-369.

Ruxton, B. P. 1968. Measures of the degree of chemical weathering of rocks. *The Journal of Geology,* 76**,** 518-527.

Schmitt, A.-D., Vigier, N., Lemarchand, D., Millot, R., Stille, P. & Chabaux, F. 2012. Processes controlling the stable isotope compositions of Li, B, Mg and Ca in plants, soils and waters: A review. *Comptes Rendus Geoscience,* 344**,** 704-722.

Shao, J., Yang, S. & Li, C. 2012. Chemical indices (CIA and WIP) as proxies for integrated chemical weathering in China: inferences from analysis of fluvial sediments. *Sedimentary Geology,* 265**,** 110-120.

Sharp, M., Creaser, R. A. & Skidmore, M. 2002. Strontium isotope composition of runoff from a glaciated carbonate terrain. *Geochimica et Cosmochimica Acta,* 66**,** 595-614.

Singer, A. 1980. The paleoclimatic interpretation of clay minerals in soils and weathering profiles. *Earth-Science Reviews,* 15**,** 303-326.

Singh, S. K., Rai, S. K. & Krishnaswami, S. 2008. Sr and Nd isotopes in river sediments from the Ganga Basin: sediment provenance and spatial variability in physical erosion. *Journal of Geophysical Research: Earth Surface,* 113.

Summerfield, M. & Hulton, N. 1994. Natural controls of fluvial denudation rates in major world drainage basins. *Journal of Geophysical Research: Solid Earth,* 99**,** 13,871-13,871.

Sun, J. 2005. Nd and Sr isotopic variations in Chinese eolian deposits during the past 8 Ma: Implications for provenance change. *Earth and Planetary Science Letters,* 240**,** 454-466.

Tachikawa, K., Jeandel, C. & Roy-Barman, M. 1999. A new approach to the Nd residence time in the ocean: the role of atmospheric inputs. *Earth and Planetary Science Letters,* 170**,** 433-446.

Thamban, M. & Rao, V. P. 2005. Clay minerals as palaeomonsoon proxies: Evaluation and relevance to the late Quaternary records from SE Arabian Sea. *In:* S. Rajan, P. C. P. (ed.) *Antarctic Geoscience: Ocean–atmosphere Interaction and Paleoclimatology.* Goa, India: National Centre for Antarctic & Ocean Research, 198-215.

Thiry, M. 2000. Palaeoclimatic interpretation of clay minerals in marine deposits: an outlook from the continental origin. *Earth-Science Reviews,* 49**,** 201-221.

Tipper, E., Galy, A. & Bickle, M. 2006. Riverine evidence for a fractionated reservoir of Ca and Mg on the continents: implications for the oceanic Ca cycle. *Earth and Planetary Science Letters,* 247**,** 267-279.

Tipper, E. T., Galy, A. & Bickle, M. J. 2008. Calcium and magnesium isotope systematics in rivers draining the Himalaya-Tibetan-Plateau region: Lithological or fractionation control? *Geochimica et Cosmochimica Acta,* 72**,** 1057-1075.

Tipper, E. T., Gaillardet, J., Louvat, P., Capmas, F. & White, A. F. 2010. Mg isotope constraints on soil pore-fluid chemistry: evidence from Santa Cruz, California. *Geochimica et Cosmochimica Acta,* 74**,** 3883-3896.

Urey, H. C. & Korff, S. A. 1952. The planets: their origin and development. *Physics Today,* 5**,** 12-12.

Van Daele, M., Moernaut, J., Silversmit, G., Schmidt, S., Fontijn, K., Heirman, K., Vandoorne, W., De Clercq, M., Van Acker, J. & Wolff, C. 2014. The 600 yr eruptive history of Villarrica Volcano (Chile) revealed by annually laminated lake sediments. *Bulletin,* 126**,** 481-498.

Van De Flierdt, T., Frank, M., Lee, D.-C. & Halliday, A. N. 2002. Glacial weathering and the hafnium isotope composition of seawater. *Earth and Planetary Science Letters,* 201**,** 639-647.

Vance, D., Teagle, D. A. & Foster, G. L. 2009. Variable Quaternary chemical weathering fluxes and imbalances in marine geochemical budgets. *Nature,* 458**,** 493-496.

Vigier, N., Decarreau, A., Millot, R., Carignan, J., Petit, S. & France-Lanord, C. 2008. Quantifying Li isotope fractionation during smectite formation and implications for the Li cycle. *Geochimica et Cosmochimica Acta,* 72**,** 780-792.

Vogt, T. 1927. *Sulitjelmafeltets geologi og petrografi,* Norges Geologiske Undersokelse, 560 pp.

Von Blanckenburg, F., O'nions, R. K., Belshaw, N. S., Gibb, A. & Hein, J. R. 1996. Global distribution of beryllium isotopes in deep ocean water as derived from Fe-Mn crusts. *Earth and Planetary Science Letters,* 141**,** 213-226.

Von Blanckenburg, F. & O'nions, R. K. 1999. Response of beryllium and radiogenic isotope ratios in Northern Atlantic Deep Water to the onset of northern hemisphere glaciation. *Earth and Planetary Science Letters,* 167**,** 175-182.

Von Blanckenburg, F. & Nägler, T. F. 2001. Weathering versus circulation-controlled changes in radiogenic isotope tracer composition of the Labrador Sea and North Atlantic Deep Water. *Paleoceanography,* 16**,** 424-434.

Von Blanckenburg, F., Bouchez, J., Ibarra, D. E. & Maher, K. 2015. Stable runoff and weathering fluxes into the oceans over Quaternary climate cycles. *Nature Geoscience,* 8**,** 538.

Von Strandmann, P. a. P., Burton, K. W., James, R. H., Van Calsteren, P., Gislason, S. R. & Sigfússon, B. 2008. The influence of weathering processes on riverine magnesium isotopes in a basaltic terrain. *Earth and Planetary Science Letters,* 276**,** 187-197.

Walker, J. C., Hays, P. & Kasting, J. F. 1981. A negative feedback mechanism for the long-term stabilization of Earth's surface temperature. *Journal of Geophysical Research: Oceans,* 86**,** 9776-9782.

West, A. J., Galy, A. & Bickle, M. 2005. Tectonic and climatic controls on silicate weathering. *Earth and Planetary Science Letters,* 235**,** 211-228.

Willenbring, J. K. & Von Blanckenburg, F. 2010. Long-term stability of global erosion rates and weathering during late-Cenozoic cooling. *Nature,* 465**,** 211.

Willenbring, J. K. & Jerolmack, D. J. 2016. The null hypothesis: globally steady rates of erosion, weathering fluxes and shelf sediment accumulation during Late Cenozoic mountain uplift and glaciation. *Terra Nova,* 28**,** 11-18.

3 Lithium isotopes – a chemical weathering proxy

3.1 Stable isotope fractionation

Isotope fractionation occurs because of so-called 'equilibrium' and 'kinetic' effects. Equilibrium effects are the basis of most isotope fractionation and are associated with differences in atomic mass and bond strength. Mass dependent effects arise mainly from vibrational motions of molecules in gases, liquids and atoms in crystals (White, 2013). For example, if a light isotope in a molecular site is replaced by a heavier isotope, the nuclear charge or electronic distribution of the molecule is not affected, however the bond strength is. More energy is required to break the bond between heavier isotopes compared to lighter isotopes. The difference in bond strengths allows a predictable isotope fractionation between two phases. The degree of isotope fractionation can be expressed with the fractionation factor α. It is defined as the ratio of two isotopes in one chemical compound (A) divided by the corresponding ratio for another chemical compound (B) (Hoefs, 2015):

$$\alpha_{A-B} = R_A/R_B \tag{8}$$

The enrichment of an isotope in one phase relative to a coexisting phase in isotopic equilibrium is a function of temperature (Sharp, 2017). In terms of equilibrium thermodynamics, an isotope exchange reaction is considered complete when isotopes of a single element are exchanged between two phases until equilibrium is reached. An example of such an isotope exchange reaction between two phases is given by

$$^{7}Li(s) + {}^{6}LiF(s) = {}^{6}Li(s) + {}^{7}LiF(s) \tag{9}$$

where Li = lithium and F = fluoride. The equilibrium constant (K) for the above reaction can be written as

$$K = \frac{(^{6}Li(s))*(^{7}LiF(s))}{(^{7}Li(s))*(^{6}LiF(s))} = \frac{(^{6}Li(s))/(^{7}Li(s))}{(^{6}LiF(s))/(^{7}LiF(s))} \tag{10}$$

In this example, the isotopic composition of F is fixed. Hence, because F has the same value in the numerator and denominator, equation (10) becomes

$$K = \frac{(^6Li/^7Li)}{(^6Li/^7Li)_F} \quad (11)$$

which is directly related to the fractionation factor α for isotope exchange reactions following

$$\alpha = K^{1/n} \quad (12)$$

where n is the number of atoms that are exchanged during equilibrium isotope fractionation. Generally, equilibrium isotope fractionation is inversely correlated with temperature, where isotope fractionation decreases with increasing temperature, proportional to $1/T^2$. For Li isotopes, the majority of observed fractionation processes at the Earth surface are associated with chemical weathering reactions at low temperatures (<50°C) (Burton and Vigier, 2012).

Kinetic effects are the second major component causing fractionation between stable isotopes. These effects are irreversible, incomplete, or unidirectional e.g. diffusion, dissociation reactions or evaporation. They occur fast and often result in larger isotope fractionation compared to equilibrium effects. Reaction products for unidirectional chemical reactions have shown to preferentially incorporate the lighter isotope. This is due to the difference in kinetic energies for given molecules (Sharp, 2017). For example, according to

$$E_k = {}^1/_2\, mv^2 \quad (13)$$

where E_k is the kinetic energy, m is the mass, and v is the velocity, the velocity of $^{12}C^{16}O$ (mol weight = 28) is greater than of $^{12}C^{18}O$ (mol weight = 30) because of the differences in molecular weights:

$$K.E.(^{12}C^{16}O) = K.E.(^{12}C^{18}O) \quad (14)$$

$${}^1/_2\,(28)(v_{28})^2 = {}^1/_2\,(30)(v_{30})^2 \quad (15)$$

$$v_{28} = \sqrt{\frac{30}{28v_{30}}} = 1.035v_{30} \quad (16)$$

This means that at any given temperature, the average velocity of the lighter molecule $^{12}C^{16}O$ will be 3.5 % greater than for $^{12}C^{18}O$. A classic example in nature where this effect plays a role is during photosynthesis. Plants do not convert all carbon dioxide to organic carbon and are therefore enriched in ^{12}C relative to atmospheric CO_2 (White, 2013). For Li, a diffusion driven isotope fractionation factor was identified in silicate melts and solids, where minerals interact with fluids (Richter et al., 2003; Richter et al., 2006). Extreme fractionation, relative to that produced by equilibrium effects, was observed at moderate temperatures (≤340°C), which was accounted to the large differences in diffusion coefficients between ^{6}Li and ^{7}Li (Teng et al., 2006).

Some apparent isotope fractionation can be described via Rayleigh distillation or condensation, or by batch fractionation (Dellinger et al., 2015). An example would be the fractionation of oxygen isotopes between water (l) and water vapor (v). The Rayleigh equation governing this process is:

$$R_v = R_v^0 f^{\alpha-1} \quad (17)$$

where Rv is the isotope ratio of the remaining vapor, R_v^0 is the isotope ratio of the initial vapor, f is the fraction of vapor remaining, and

$$\alpha = \frac{R_l}{R_v} \quad (18)$$

This type of fractionation effect was observed for Li isotopes during alteration experiments (Ryu et al., 2014) and during progressive weathering of saprolite in North American soils (Rudnick et al., 2004).

For most stable isotope systems, the ratio between two isotopes is reported with the delta (δ) notation:

$$\delta = \left(\frac{R_y - R_{std}}{R_{std}}\right) x\ 1000 \tag{19}$$

where R is the ratio of the heavy and light isotope, y is the measured sample, and std is the value of the international isotopic standard. Delta values are reported in per mil (‰) deviation from a reference standard. For Li isotopes, equation (19) can be re-written as

$$\delta^7 Li = \left(\frac{\left(\frac{^7Li}{^6Li}\right)_{sample} - \left(\frac{^7Li}{^6Li}\right)_{L-SVEC}}{\left(\frac{^7Li}{^6Li}\right)_{L-SVEC}} \right) x\ 1000 \tag{20}$$

where the commonly used standard is L-SVEC, a Li carbonate material, which is defined with $^7Li/^6Li = 12.1725$.

3.2 Lithium isotopes – a novel chemical weathering proxy

Li has two stable isotopes: ^7Li and ^6Li, which have a mass difference of 16 %. Only a few studies exist that investigated the role of Li in the biosphere, but it is thought to not be particularly involved in vegetation or atmospheric cycles (Lemarchand et al., 2010). Silicate minerals are highly enriched in Li (1 – 4,000 ppm) and largely depleted in carbonates (<1 ppm). During chemical weathering, Li isotopes fractionate significantly, where the lighter ^6Li preferentially incorporates into clay minerals (Huh et al., 1998; Pistiner and Henderson, 2003; Vigier et al., 2008). The main evidence of Li isotope fractionation during chemical weathering includes that the δ^7Li composition measured for continental waters is systematically higher than that for drained rocks and the transported sediments (Figure 7).

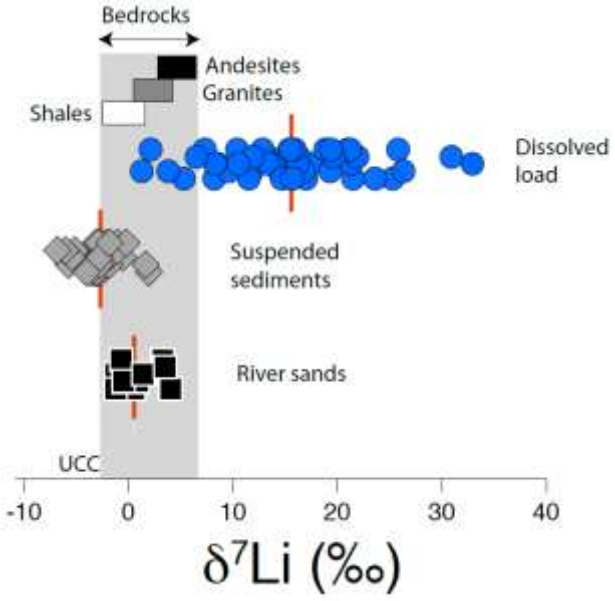

Figure 7: The Li isotope composition of various reservoirs from the Amazon River Basin. The red bar represents the mean isotope composition of each reservoir. UCC stands for upper continental crust. Source: Dellinger et al. (2015).

The δ^7Li value of the ocean (31.2 ‰ relative to L-SVEC e.g. ((Lui-Heung and Edmond, 1988; Millot et al., 2004)) is significantly higher than published values for Li ocean sources: 23.4 ‰ for river waters and 9 ‰ for hydrothermal flux (Lui-Heung et al., 1994; Huh et al., 1998).

In contrast to most 'traditional' weathering proxies, Li provides several advantages:

- ^{6}Li and ^{7}Li have a larger relative mass difference (~16 %) than any isotope pair (aside from hydrogen and deuterium) and therefore cover a large range of isotopic values
- Li is not particularly involved in biological or atmospheric cycles, therefore isotope fractionation processes are purely related to weathering reactions (Lemarchand et al., 2010; Burton and Vigier, 2012)
- Li is highly enriched in silicate minerals relative to carbonates which allows the reconstruction of silicate weathering conditions (Huh et al., 2001; Huh et al., 2004; Millot et al., 2010)

3.3 Lithium isotope fractionation – state of the art

The first ever reported Li isotope fractionation involving clay minerals was reported in 1938 by Taylor and Urey (1938). They conducted experiments with several zeolite-packed columns through which they passed Li chloride solutions. The solution after

column pass had a lower concentration of ^{6}Li than the initial Li chloride solution, which meant that ^{6}Li, relative to ^{7}Li, was preferentially taken up by the zeolites. With the advancements of instrumentation to precisely measure the ratio $^{7}Li/^{6}Li$, more experiments were conducted to determine the exact mechanics of Li isotope fractionation in the natural environment. The main processes that may cause Li isotope fractionation are: primary mineral dissolution, secondary mineral formation and adsorption onto minerals (Vigier et al., 2008). Experimental work has shown that primary mineral dissolution only causes minor fractionation and hence does not contribute significantly to the Li isotope composition of waters (Pistiner and Henderson, 2003; Wimpenny et al., 2010a; Verney-Carron et al., 2011). The largest Li isotope fractionation occurs during secondary mineral (e.g. clays or Mn-Fe oxides-oxyhydroxides) and soil formation, where ^{6}Li retains in the weathered residue and ^{7}Li is released into the hydrosphere. Huh et al. (1998) also found that the Li behaviour is closely linked to that of magnesium in major rivers. Experiments on synthetic clays showed that the incorporation of Li takes place in interlayer or octahedral sites in substitution for Mg^{2+} (Figure 8) (Vigier et al., 2008).

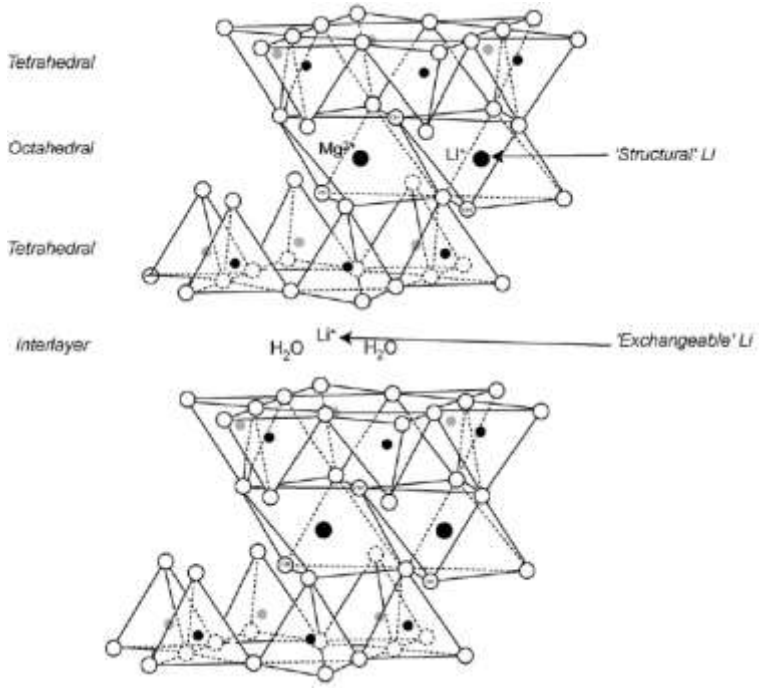

Figure 8: Schematic representation of a hectorite mineral structure. In substitution for Mg^{2+}, one Li^{+} occupies an octahedral site (structural Li), and another enters the interlayer position (exchangeable Li). Black and grey circles represent Si^{4+} cations. White circles are positions of oxygen. Modified after Vigier et al. (2008).

3.3.1 Reaction time effect and flow rate

The duration at which water-rock interactions take place may alter the Li isotope signature of water bodies (Wimpenny et al., 2010b). Wimpenny et al. (2010b) showed that during fluid-mineral interactions ^{6}Li is preferentially incorporated into neo-formed secondary phases, in turn resulting in the fluid to be enriched in ^{7}Li. This was tested by a dissolution-precipitation experiment where forsterite reacted with a Li-free fluid. The Li isotope composition of the forsterite was measured prior to the experiment and yielded a $\delta^{7}Li$ value of 1.57 ‰. After 50 hours, the the fluid shifted towards a $\delta^{7}Li$ value of 4.41 ‰ (Figure 9).

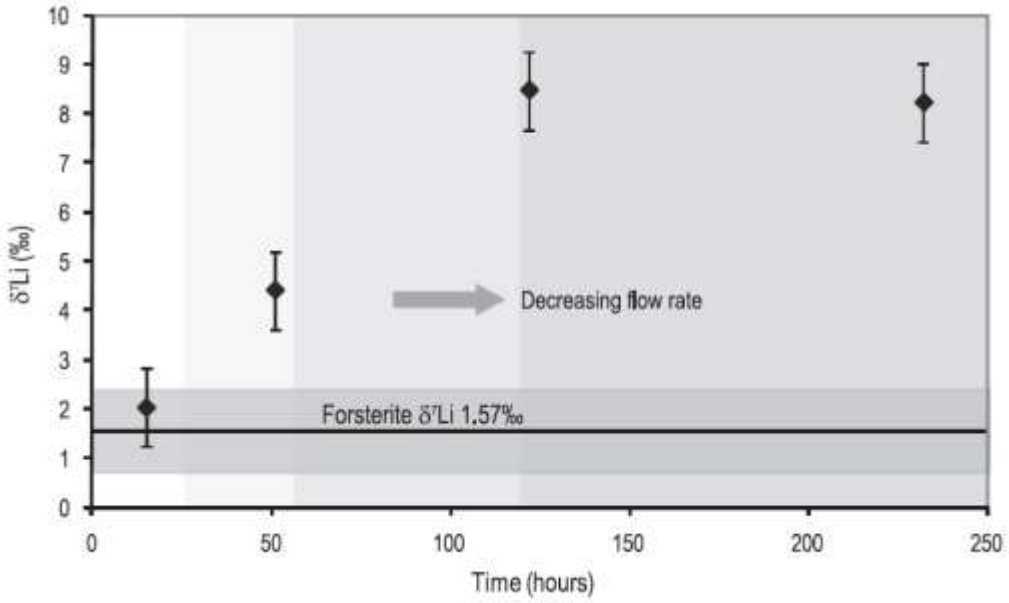

Figure 9: The $\delta^{7}Li$ composition of forsterite (FO_3) and an experimental fluid. Diamonds are the Li isotope compositions of the fluid. The experiment was conducted at 25°C and pH 10. Error bars show the external reproducibility (2σ). Source: Wimpenny et al. (2010b).

After ~120h, the $\delta^{7}Li$ composition of the fluid increased to 8.46 ‰ and remained constant until 232h of reaction. This experiment also demonstrates is how the flow rate affects the Li isotope composition of the fluid. Figure 9 shows that the rate of isotope fractionation is highest during high flow rates at early stages of the dissolution-precipitation experiment (grey arrow). These findings imply that the duration at which minerals and waters react affects the Li composition in fluid phases: fast flow rates result in positive $\delta^{7}Li$ values of waters (Wimpenny et al., 2010b).

3.3.2 Temperature dependency

An experimental approach by Decarreau et al. (2012) showed that the uptake of Li by clay minerals varies with temperature. At 90°C, Li concentrations reach a steady state after 60 days, whereas at 150°C, steady state is already reached after two weeks (Figure 10).

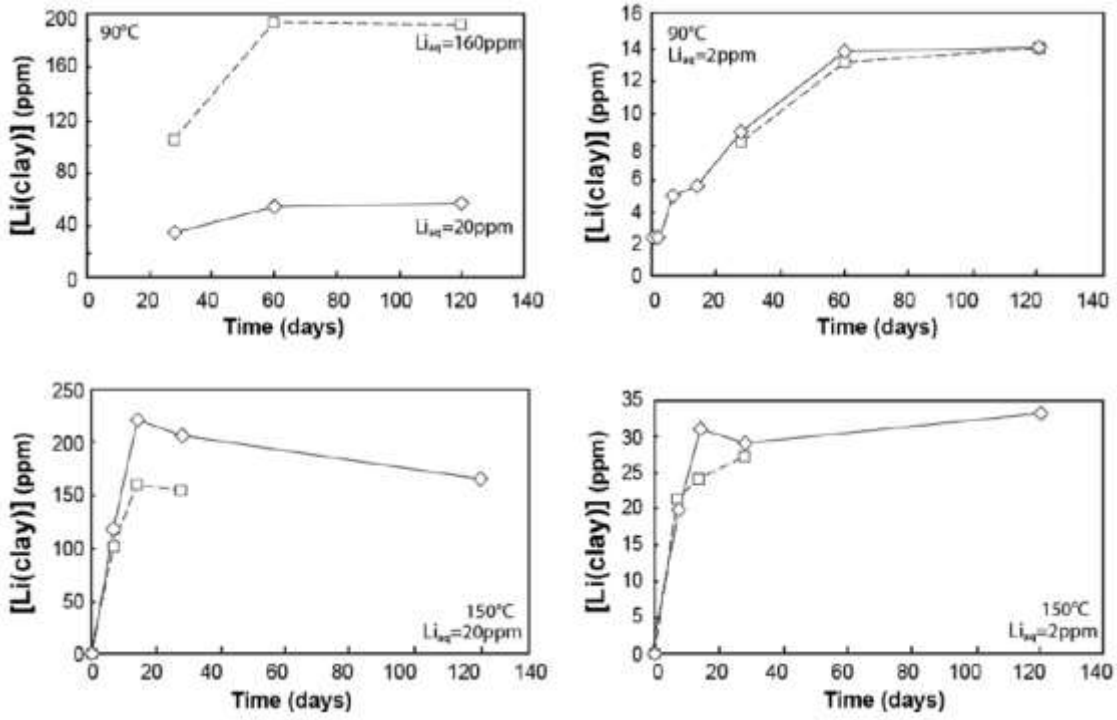

Figure 10: Partitioning of Li between clays (smectites) and Li-rich solutions at variable temperatures and Li concentrations. Source: Decarreau et al. (2012).

This experiment also shows how the Li concentration of the aqueous phase affects the rate at which Li partitions into clays. Solutions with 160, 20 and 2 ppm of Li show the same temporal trend of Li partitioning, implying that the Li concentration of the aqueous phase does not control the rate at which clays incorporate Li.

The effect different reaction temperatures have on Li isotope fractionation was shown by Vigier et al. (2008). Experiments were conducted with synthesised clays in contact with solutions at various temperatures. Results are shown in Table 1.

Table 1: Li isotope fractionation between solution and clays during various temperatures. Source: Vigier et al. (2008).

	$\delta^7Li_{solution}$		δ^7Li_{clay}		$\Delta^7Li_{clay\text{-}solution}$	
T (°C)	**(‰)**	**2σ**	**(‰)**	**2σ**	**(‰)**	**2σ**
25	12.2	0.8	3.4	1.7	-8.8	1.9
25	14.7	1.4	4.6	1.0	-10.1	1.7
60	12.2	0.8	1.3	0.5	-10.9	0.9
90	9.5	0.6	-0.9	1.1	-10.4	1.3
90	9.5	0.6	-0.5	1.2	-10.0	1.3
90	14.7	1.4	4.3	1.0	-10.4	1.8
90	14.7	1.4	4.3	0.5	-10.4	1.7
150	12.2	0.8	5.1	1.0	-7.1	1.9
200	9.5	0.6	6.1	0.4	-3.4	1.2
200	9.5	0.6	6.4	0.7	-3.1	0.7
200	14.7	1.4	10.8	0.2	-3.9	1.4
250	12.2	0.8	10.6	0.8	-1.6	1.3
250	12.2	0.8	10.5	1.0	-1.7	1.3
250	14.7	1.4	12.0	1.3	-2.7	1.9

$\delta^7Li_{solution}$ is the initial solution (LiCl) used for clay syntheses experiments and $\Delta^7Li_{clay\text{-}solution}$ is $\delta^7Li_{clay} - \delta^7Li_{solution}$.

The difference between the δ^7Li composition of clay and solution ($\Delta^7Li_{clay\text{-}solution}$) demonstrates that isotope fractionation during the interaction between clay and solution inversely correlates with temperature (Figure 11).

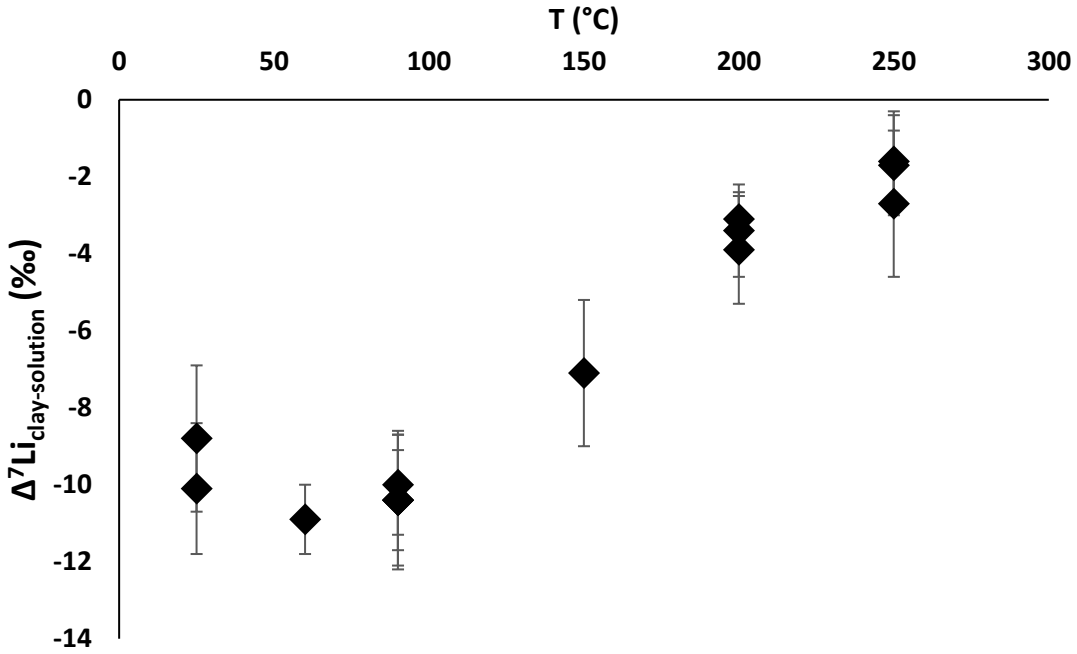

Figure 11: Relationship between temperature and Li isotope fractionation during clay-solution interaction. $\Delta^7Li_{clay\text{-}solution}$ is $\delta^7Li_{clay} - \delta^7Li_{solution}$. Uncertainties are given at the 2σ level. Modified after Vigier et al. (2008).

High temperatures (250°C) cause only minor fractionation between solution and clay, relative to the initial Li isotope composition. In contrast, below 90°C, isotopic fractionation remains constant around a δ^7Li composition of -10 ‰ (within errors) (Vigier et al., 2008). This implies that the highest degree of isotope fractionation during dissolution/precipitation reactions occurs at relatively low temperatures between 90 and 25°C.

In the natural environment, Lui-Heung et al. (1994) studied the Li isotope composition of hydrothermal fluids of the Gaymas Basin to identify the role of temperature on isotope fractionation. The aim was to investigate Li concentration and isotope redistribution during hydrothermal alteration of a sediment covered spreading centre. A shallow sill intrusion and the underlying spreading centre with magmatic activity was tested for Li concentration and Li isotopes and results showed that that Li is leached from the sediments by heated fluids. The alteration products showed a preferential retention of ^{6}Li. The isotopic composition of the contact zone above the sill was slightly isotopically lighter. In contrast, the hydrothermally altered zone below displayed large deviations in its Li isotope values. This verifies the findings from Vigier et al. (2008) that temperature

plays a significant role on fractionation of Li isotopes. However, as stated above, at very high temperatures (>250°C) Li retention in weathering products is reduced. Another example of the temperature dependence of Li isotope fractionation was shown by Li and West (2014), who suggested that Li isotope fractionation, that is accompanied by the uptake into marine clays at ambient temperatures, is much higher than for the uptake by altered oceanic basalts.

The above described temperature-dependent isotope fractionation factors were all in the presence of a secondary phase, which retains the lighter ^{6}Li. But isotope fractionation associated with weathering reactions can also occur without the precipitation of secondary minerals. Basaltic glass alteration experiments performed under saturation have shown a diffusion driven isotope fractionation (as opposed to equilibrium fractionation), independent of secondary mineral precipitation. During non-equilibrium conditions with various elevated temperatures (50 and 90°C), pH (3 and 9), and mineral surface area/volume of solution ratios (0.7 and 7 cm^{-1}), the produced solutions has a lighter Li isotopic composition than the starting material (Verney-Carron et al., 2011). This means that in natural systems, where water rock interactions take place at temperatures between 50 and 100°C, without the precipitation of secondary phases, the released solution may be enriched in ^{6}Li (Verney-Carron et al., 2011). This phenomenon was observed in a traverse of pegmatites of the Tin Mountain (South Dakota, USA), where a ~30 ‰ Li isotopic change was recorded, which was linked to diffusion-driven isotope fractionation (Teng et al., 2006).

3.3.3 Type of clay

The type of clay mineral and the crystal size may also play an important role to which degree Li isotopes fractionate (Williams and Hervig, 2005). During illitisation, where smectite minerals react to illite minerals, Li concentration and isotopic composition of the products change. Li substitutes into octahedral sites of the silicate structure during crystallisation. Illitisation of smectite is a crystal growth process, which encompasses a change/increase in crystal size. The experiment was conducted in the presence of a fluid with a δ^{7}Li composition of -65.7 ‰. Before isotope analyses, the different size fractions were treated with NH_4 to remove interlayer-Li. A large difference in δ^{7}Li values of up to 9 ‰ was observed when comparing the three crystal size fractions (<0.2, 0.2 – 2.0, and >2.0 µm) (Figure 12).

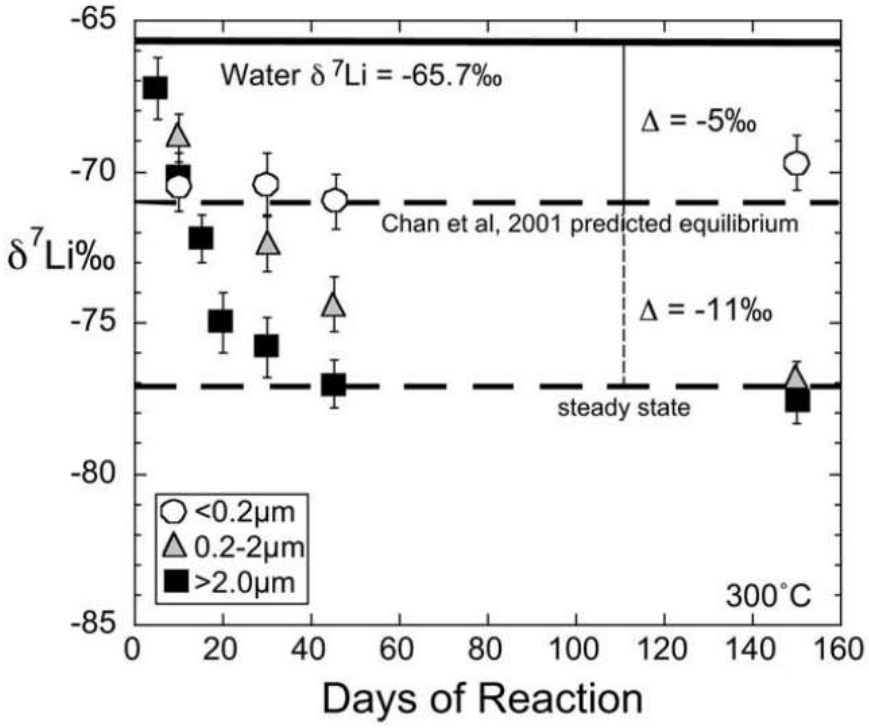

Figure 12: Li isotope composition of different crystal size fractions during illitisation. The difference between the Li isotope composition of the present fluid and the δ^7Li value of the crystal size fractions is indicated by Δ. Source: Williams and Hervig (2005).

The fine-grained fraction (<0.2 µm) was isotopically lighter compared to the medium size (0.2 – 2.0 µm) and coarse-grained fraction (>2.0 µm). Furthermore, after approximately 40 days of reaction, a steady state was reached for all crystal size fractions, where isotopic values remained constant. The authors concluded that crystal growth mechanisms and surface energy effects of nanoscale crystals potentially play an important role during weathering processes and formation of clays, where larger crystal may encompass a greater degree of Li isotope fractionation (Williams and Hervig, 2005).

Another experiment by Wimpenny et al. (2015) targeted the specific Li isotope fractionation associated with the mineral gibbsite, which is often found between silicate sheets of clay mineral groups. The Li isotope behaviour during the synthesis of gibbsite showed that ^{6}Li is favoured during intercalation (structural incorporation into the crystal). At low Li concentrations of the solution (1M LiCl), little to no isotopic fractionation was observed in the gibbsite crystals. With increasing Li concentration of the solution (4M LiCl), the fractionation of Li isotopes can be described in two stages: First, during the initial Li loading, the gibbsite structure expands and Li fills octahedral sites. Because of

the preferential uptake of ^{6}Li over ^{7}Li, this step decreases the $\delta^{7}Li$ composition of the gibbsite (Figure 13).

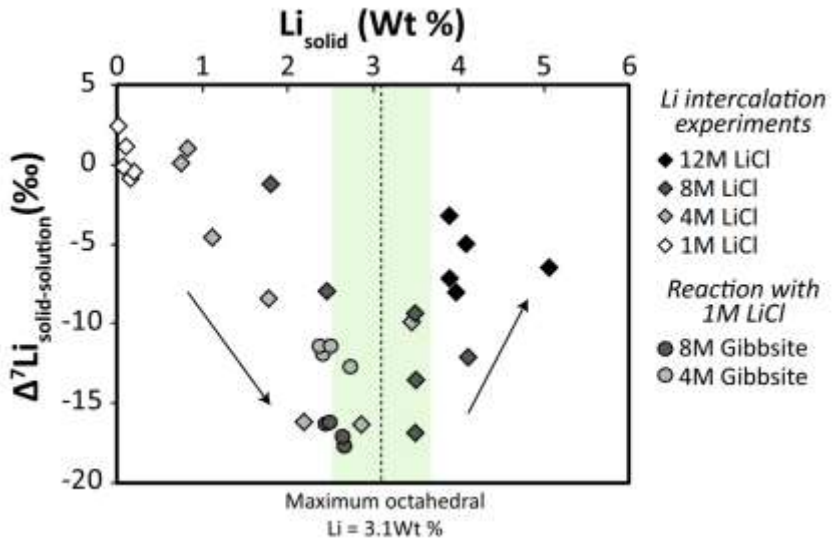

Figure 13: Li isotopic fractionation during incorporation into gibbsite relative to the Li concentration (in mol) of the solution. Source: Wimpenny et al. (2015).

A maximum octahedral load was observed at 3.1 wt % Li, where the solution had a concentration of 4M LiCl. Increasing the concentration of the solution resulted in further Li loading and the uptake of Li into surface and interlayer of the gibbsite without any isotopic fractionation, which increased $\delta^{7}Li$ values. Continued loading therefore resulted in $\delta^{7}Li$ values close to parent solution (Wimpenny et al., 2015). Furthermore, solid-solution fractionation depends on counter ion identity (e.g. Cl^{-}, NO^{3-}, ClO^{4-}) of the fluid. The largest isotopic fractionation between solid and solution of up to ~-13 ‰ was observed where gibbsite was formed in a 4M LiCl solution at 25°C. At the same temperature, a 4M $LiNO_3$ solution resulted in a maximum isotope fractionation of ~-4 ‰. On the other hand, Vigier et al. (2008) found no difference related to the chemical composition of the solution. So far, no other experiments have been conducted that target clay mineral-specific Li isotope fractionation effects of e.g. smectite, kaolinite, or illite. This will be discussed in Chapter 7 of this thesis.

3.3.4 Mineral surface exchange effects

Adsorption onto mineral surfaces may also induce Li isotope fractionation. Depending on both mineral surface chemistry and composition of the solution, aqueous Li ions may undergo adsorption onto minerals with preferential retention of the lighter ^{6}Li isotope. For example, Fe-oxyhydroxides are known to adsorb Li^{+} ions from solution (Chan and

Hein, 2007). To determine the amplitude of this isotope fractionation effect, Wimpenny et al. (2010a) performed leaching experiments on fine-grained suspended particles submerged in a fluid with a δ^7Li composition of 25 ‰. After removing loosely-bound Li with an acetate buffer solution, the Li concentration of the solid phase decreased by ~2 % relative to the initial concentration, and the leaching solution displayed δ^7Li values of ~15 ‰. After treating suspended particles with 2M HCl (to release Fe-oxyhydroxide phases), 60 % of the Li from the particles was lost to the leaching reagent. The latter showed δ^7Li values of ~5 ‰ (Figure 14):

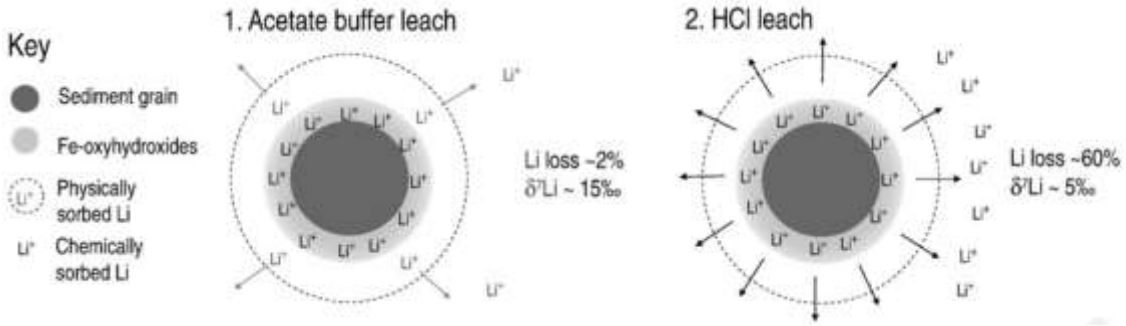

Figure 14: Schematic two-step leaching experiment to remove Li associated with Fe-oxyhydroxides for determining the Li isotope composition of loosely bound Li. 1.: loosely bound Li was leached from mineral surfaces with an acetate buffer solution. 2.: Release of Fe-oxyhydroxide phases with 2M HCl. Source: Wimpenny et al. (2010a).

These experiments showed that loosely-bound Li may have a lower δ^7Li composition (i.e. 15 ‰) compared to the dissolved load, which in this experiment was 25 ‰. This is somewhat surprising as Li that is bonded to mineral surfaces by electrostatic attractions are thought to not encompass any isotopic fractionation (Pistiner and Henderson, 2003; Chan and Hein, 2007). A possible explanation for the observed low δ^7Li composition of the leached fraction is that the acetate buffer may have released 'structural' Li which was incorporated during mineral formation, rather than during surface adsorption. The Li isotope composition of structural Li is much lower than that of dissolved loads (Vigier et al., 2008). Nevertheless, under natural conditions, the adsorbed Li secondary mineral surfaces (e.g. MnO_2) seems to play a minor role at low temperature. Chan and Hein (2007) identified significant amounts of Li adsorbed to mineral surfaces (relative to structural Li) of ferromanganese deposits formed at high temperature in the ocean. They found that the Li bound on mineral surfaces reflected seawater-like isotopic compositions (δ^7Li value of ~32 ‰). In contrast, the more tightly bound Li in MnO_2 or FeOOH minerals

displayed lower δ^7Li values than that of seawater. This implies that under some specific conditions, surface-exchange effects on Li isotope fractionation may play an insignificant role.

3.4 Lithium isotopes in the Earth's surface environment at present

Several studies have been conducted to constrain the global Li geochemical cycle. The majority of Li on the Earth's surface derives from silicates of the continental crust. The latter contains about 7 % of the global Li budget, whereas the oceanic crust only holds ~1 % (Teng et al., 2004). Inorganic and biogenic carbonates are particularly depleted in Li. The Li isotope variations in major reservoirs is illustrated in Figure 15.

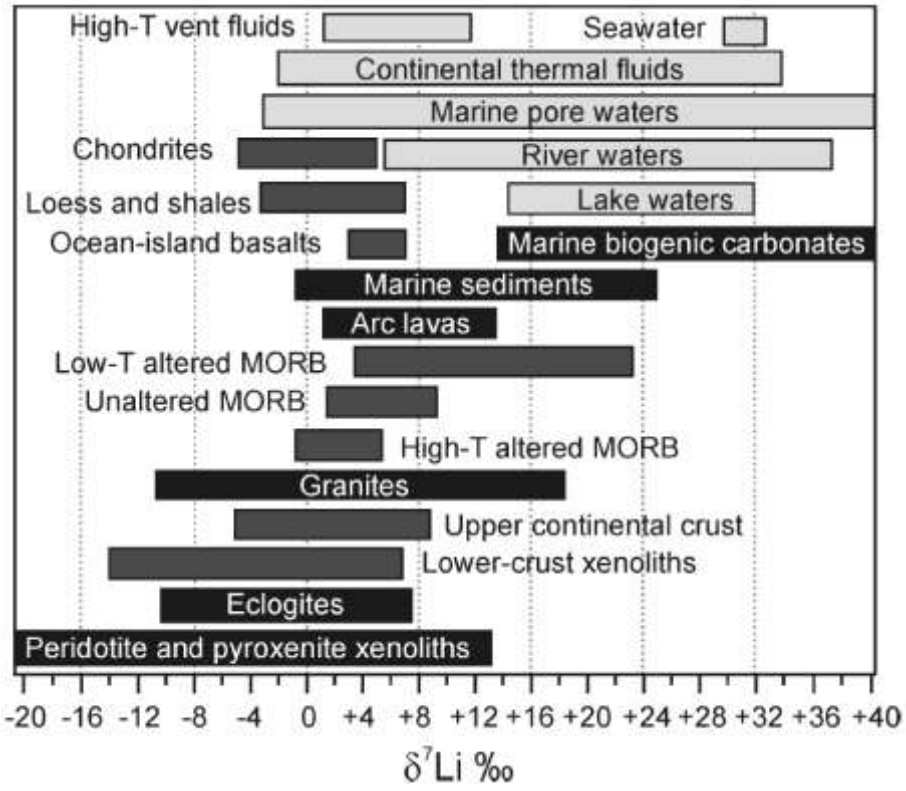

Figure 15: Li isotope variations (given in δ^7Li relative to L-SVEC) in major reservoirs. Data: seawater (Lui-Heung and Edmond, 1988; You and Chan, 1996; Moriguti and Nakamura, 1998b; Tomascak et al., 1999; James and Palmer, 2000; Rudnick et al., 2004); river water (Huh et al., 1998; Huh et al., 2001); high-temperature vent fluids (Lui-Heung et al., 1994; Foustoukos et al., 2004; Kısakürek et al., 2004); arc lavas (Moriguti and Nakamura, 1998a; Tomascak et al., 2000; Tomascak et al., 2002; Chan et al., 2002b); oceanic island basalts (Tomascak et al., 1999; Chan and Frey, 2003); fresh mid-ocean ridge basalts (MORB) (Chan et al., 1992; Moriguti and Nakamura, 1998a;

Tomascak and Langmuir, 1999; Chan et al., 2002a); altered MORB (Chan et al., 1992; Chan et al., 2002b); marine sediments (Lui-Heung et al., 1994; Zhang et al., 1998; James et al., 1999; Chan and Kastner, 2000; Bouman et al., 2004); loess, shales, and upper continental crust (Teng et al., 2004); eclogite data (Zack et al., 2003); peridotite and pyroxenite xenoliths (Tomascak, 2004; Tang et al., 2007a). Source: Tang et al. (2007b).

The following sections explore natural Li isotope fractionation processes in various surface environments.

3.4.1 River waters and sediments

Rivers represent one of the two most important sources of Li to the ocean. During low temperature weathering, the lighter ^{6}Li preferentially incorporates into clay minerals, which causes the ratio $^{7}Li/^{6}Li$ of river waters to increase (higher $\delta^{7}Li$ values).

One of the first conducted studies that looked at Li isotopes in major world rivers as an implication for weathering and oceanic budget was done by Huh et al. (1998)**.** At the time, the isotopic mass balance of Li in the ocean was poorly constrained and data for Li input from river waters into the ocean was rare. To better quantify the global Li isotope budget, especially that of the ocean, and isotope fractionation processes that occur during continental weathering. Huh et al. (1998) showed that major world rivers (Amazon, Orinoco, Ganges-Brahmaputra, Siberian rivers, Chinese rivers, and Baikal rivers) displayed $\delta^{7}Li$ values from -0.6 to 30.1 ‰. The authors were not able to link specific $\delta^{7}Li$ values to individual lithologies, but found that in general, rivers draining marine evaporates displayed values from 13 to 15 ‰, carbonates from 19.5 to 26 ‰, black shales ~19.5 ‰, shields from -0.6 to 15.5 ‰, and mixed siliceous terrains from -1 to 21.5 ‰. Since the ocean displays significantly higher $\delta^{7}Li$ values of 26 ‰ (note that this value is not representative anymore), rivers cannot solely be accounted for the ocean's Li isotope budget. Clays were known to be enriched in Li and have shown to preferentially incorporate the lighter ^{6}Li. Therefore, Huh et al. (1998) proposed that authigenic clays may be a major control of Li isotope fractionation in the ocean.

The possible effect of different 'weathering regimes' on the magnitude of Li isotope fractionation was investigated by Huh et al. (2001). The authors evaluated the relationship between suspended and dissolved load on a basin-wide scale for the Orinoco Basin, in which one of the longest rivers in South America are found. Due to its size and variation in elevation and slope, the Orinoco Basin is a suitable system to study the behaviour of Li isotopes during weathering for 'transport-limited' and 'reaction-limited'

environments. When erosion processes are slow relative to chemical weathering rates, the chemical weathering regime can be described as ‘transport-limited. In contrast, ‘reaction-limited’ or ‘weathering-limited’ weathering environments describe higher erosion rates, where silicate chemical weathering is incomplete (West et al., 2005). It was found that the dissolved load in shield regions (transport-limited), displays relatively low values from -0.5 to 15.5 ‰, compared to Andean rivers (reaction-limited) which range from 15.3 to 30.1 ‰) (Figure 16).

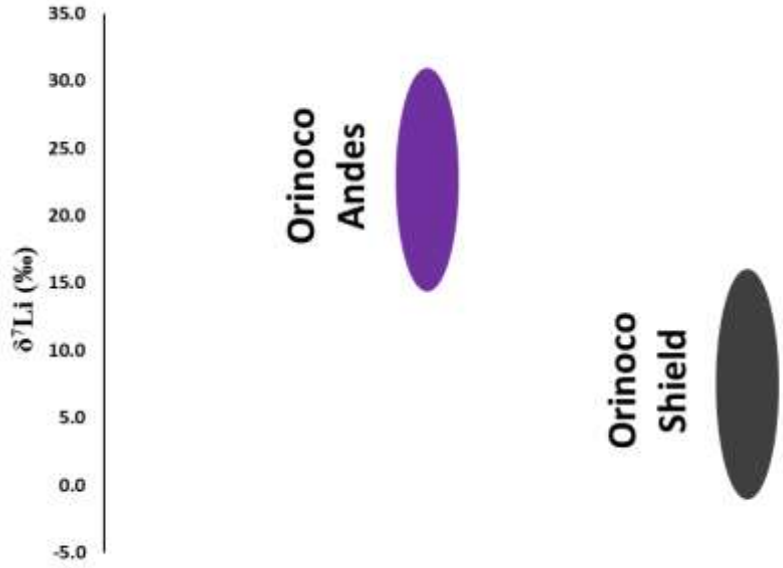

Figure 16: The δ^7Li composition of river dissolved loads from the Orinoco Basin. The purple ellipse covers the range of δ^7Li values from Andean rivers, which drainage area experiences a ‘reaction-limited’ weathering regime. The grey ellipse covers the range of δ^7Li values of rivers from stable shield regions, which experience a ‘transport-limited’ weathering regime. Modified after Huh et al. (2001).

Suspended loads from both shield and Andean regions were found to be almost identical and homogeneously lower in their Li isotope signature. The authors suggested that there are two different isotope fractionation processes occurring in the Orinoco Basin. In reaction-limited regions, kinetic isotope fractionation causes the dissolved load to be isotopically heavy. In contrast, in transport-limited regions, Rayleigh-type extraction of ^{7}Li from a reservoir and a more intense weathering reaction causes the δ^7Li composition of the dissolved load to reach low values (Huh et al., 2001).

Kısakűrek et al. (2005) aimed to identify the effects of lithology, relief and seasonality on Li isotope fractionation in Himalayan river systems. They investigated several

tributaries of the Ganges in central and eastern Nepal. Carbonate catchments were compared to silicate catchments and it was found that the latter are the major source for the dissolved Li load, even in carbonate-dominated catchments. Furthermore, the varying lithology seems to only affect Li concentration. Li isotope composition overlapped between the two catchments which suggests that isotope fractionation is not driven by varying lithologies but by weathering processes only. In terms of relief, catchments at high altitude show the highest degree of fractionation between dissolved and suspended load. This supports the conclusion of Huh et al. (2001) that at fast discharge rates, which are characteristic of high altitude catchments, kinetic isotope fractionation causes the dissolved river loads to be isotopically heavier than the suspended loads. Furthermore, seasonality influences the δ^7Li values of the dissolved loads. After the monsoon, when runoff is promoted due to elevated temperatures and more frequent rainfall, tributaries draining silicate catchments show lower δ^7Li values in dissolved loads compared to suspended loads (Kısakűrek et al., 2005). This is in contrast to findings by Huh et al. (2001), which suggests that river discharge is not the only control on Li isotope fractionation of dissolved loads.

To further investigate the role of individual weathering regimes on Li isotope fractionation in mixed lithology basins, rivers within the Mackenzie Basin were thoroughly studied by Millot et al. (2010). Suspended loads from the Mackenzie River show δ^7Li values from -1.7 ‰ to +3.2 ‰, relatively close to values measured for bedrocks. Dissolved loads range between +9.3 ‰ and +29.0 ‰ and are hence isotopically much heavier than suspended loads and bedload. The large variability of δ^7Li values in the Mackenzie Basin confirms that silicate weathering conditions can be variable over a large catchment. Millot et al. (2010) identified individual weathering regimes that uniquely control the Li isotope signature (Figure 17). Weathering regime #1 was characterised by weak (surficial) weathering, whereas weathering regime #2 was described by more intense water-rock interactions with significant formation of secondary phases. Considering the significant overlap between silicate weathering loads of the two individual weathering regimes, Millot et al. (2010) suggested that weathering fluxes are not solely responsible for Li isotopic signals in dissolved loads, but are rather a function of specific weathering regimes.

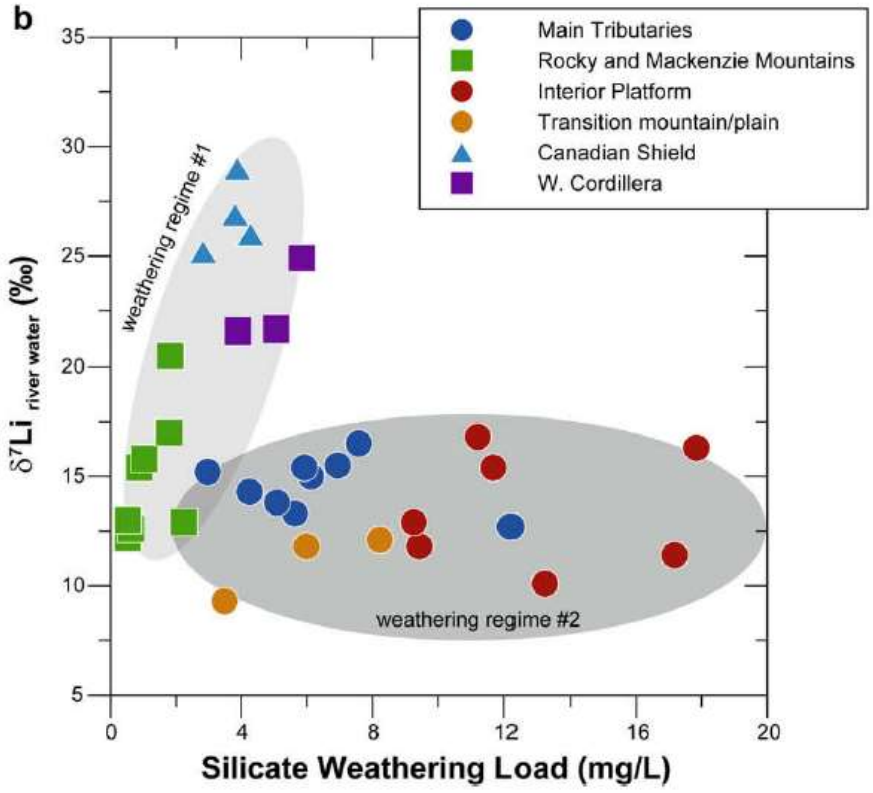

Figure 17: The δ^7Li composition of river dissolved loads as a function of silicate weathering load (total dissolved solids derived from silicate weathering). Source: Millot et al. (2010).

The Li isotope behaviour in the Changjiang River and its main tributaries were studied by Wang et al. (2015). They found that headwaters have relatively high Li concentrations compared to lower reaches, which they linked to the dissolution of evaporates in the upper headwater region. The δ^7Li composition of the dissolved load increased from upper to lower reaches, which was linked to the transition from reaction-limited to transport-limited weathering regimes. Similarly to the low δ^7Li values of Andean headwaters (e.g. Dellinger et al. (2015)), weathering reactions at higher altitudes were limited and less Li was incorporated into secondary phases. In the lower reaches, erosion rates are lower which leaves more time for water-rock interactions to take place.

Dellinger et al. (2015) studied the role of different weathering regimes on the Li isotope composition in the Amazon Basin. The δ^7Li composition of river dissolved loads correlated with Li/Na and Li/Mg. This was used as evidence that the main control of Amazon's river water Li isotope composition is associated with the incorporation of Li into secondary minerals. Furthermore, it was found that dissolved loads of Andean

headwaters and lowland rivers cover a similar range of δ^7Li values (+1.2 ‰ to +18 ‰) (Figure 18). This is surprising as these two locations are characterised with very different weathering and erosion regimes.

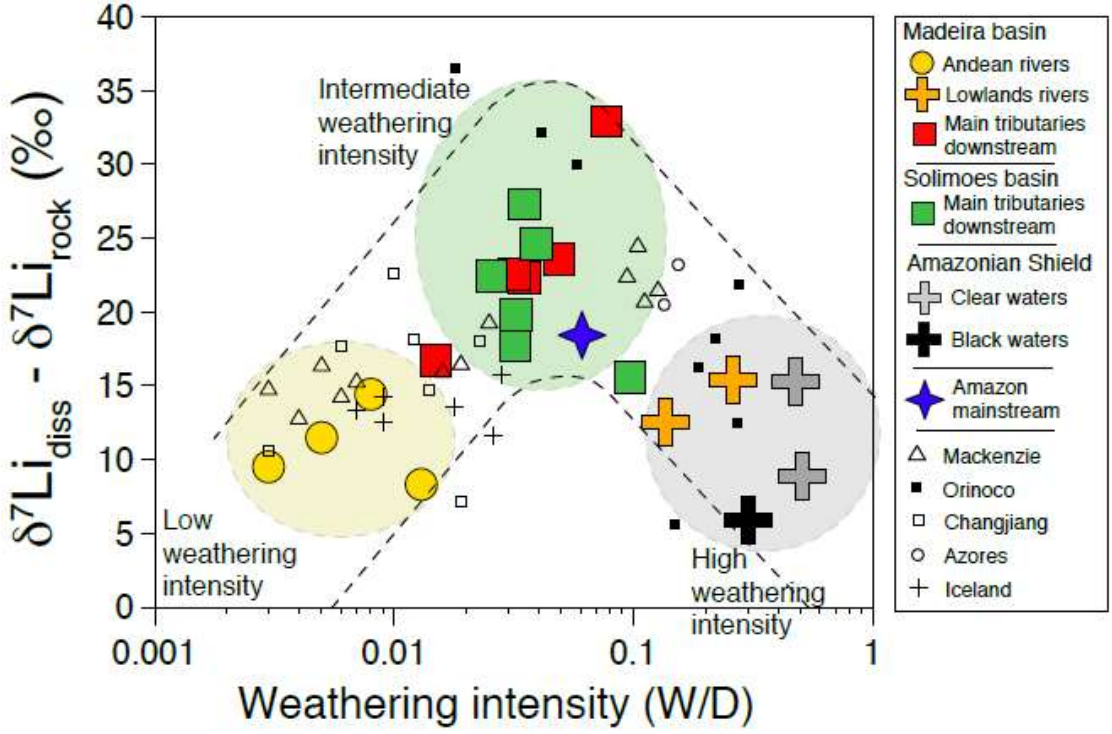

Figure 18: Li isotope composition of dissolved loads from world rivers (focus on Amazon Basin), corrected for the δ^7Li composition of the bedrock, against weathering intensity (W/D), where W is the silicate weathering rate and D the total denudation. Source: Dellinger et al. (2015).

Andean rivers for example are characterised as being reaction-limited, where little water-rock interactions are taken place. In theory, this should result in relatively high δ^7Li values (Huh et al., 2001). However, δ^7Li values of this weathering environment were relatively low. Dellinger et al. (2015) linked this to be the result of 'too' high discharge rates, where the Li flux through mineral dissolution outweighs that of secondary mineral precipitation. Lowland rivers of the Amazonian shield and Madeira Basin cover an identical range of δ^7Li values as Andean rivers. Low δ^7Li values were explained by possible oversaturation and re-dissolution of secondary minerals via organic matter (c.f. (Pogge von Strandmann et al., 2006)). These results are important findings for interpreting the Li isotope composition of dissolved loads as two completely different weathering regimes (Andean rivers and shield rivers) can display identical δ^7Li values.

Bagard et al. (2015) investigated the dissolved fluxes of rivers draining the Ganges-Brahmaputra floodplain. Similarly to findings by Wang et al. (2015), they showed that the δ^7Li composition of the riverine flux increases downstream across the floodplain. This was explained by the reaction between waters and floodplain sediments, where ^{6}Li is preferentially removed from the water and incorporated into clays. Interestingly, the Li isotope composition of deep ground waters (>40 m) has δ^7Li values close to that of the bedrock, which was linked to the dissolution of floodplain sediments, possibly as a result of long residence times. These results imply that the Li isotope composition in an aquifer may undergo stratification, where surface waters can have different δ^7Li values compared to groundwaters.

Pogge von Strandmann et al. (2006) investigated Icelandic rivers draining predominantly basaltic catchments in a glaciated terrain. Besides suspended and dissolved river loads, river bedload sediments were also examined. As expected, δ^7Li values of the suspended load were systematically lower than those of bedload due to the incorporation of the lighter ^{6}Li into secondary phases. Dissolved loads on the other hand were isotopically heavier than bedload. The Li isotope evolution in dissolved loads was linked to the amount of dissolved silicon, which is an indicator of the silicate weathering intensity when vegetation is scarce (Figure 19). High Si concentrations in the dissolved load, unless overprinted by biological activity, generally reflect high silicate weathering intensities.

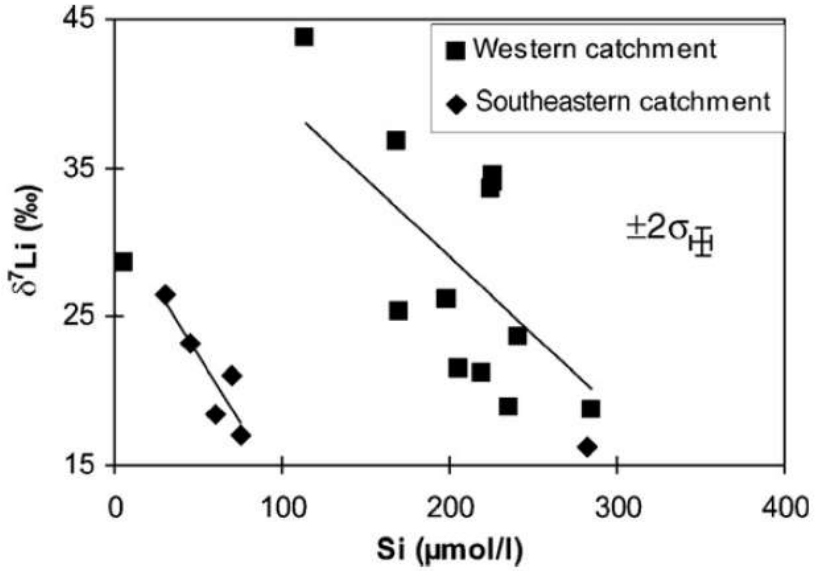

Figure 19: The δ^7Li composition as a function of Si concentration for dissolved river loads (western and south-eastern catchments) of Icelandic rivers. Source: Pogge von Strandmann et al. (2006)

In this case, Figure 19 shows that when the silicate weathering intensity is high, the δ^7Li composition of the dissolved load is low. Therefore, Pogge von Strandmann et al. (2006) propose that δ^7Li values in river water evolves as a function of chemical weathering intensity, which is inversely related to the physical weathering rate. However, an alternative scenario was proposed that when river water is oversaturated with secondary mineral phases, δ^7Li values of the dissolved load may also decrease. This effect is associated with rapid secondary mineral precipitation where isotope fractionation between Li in the secondary minerals and Li in solution is reduced (Pogge von Strandmann et al., 2006).

Vigier et al. (2009) studied the riverine Li isotope composition of Icelandic rivers. They specifically investigated the compositional relationship between dissolved phase, suspended and bedload sediments of major Icelandic rivers. Dissolved loads ranged between 10.1 ‰ and 23.8 ‰, while bedload and suspended sediments displayed δ^7Li values close to that of unweathered Mid-Ocean Ridge Basalts (MORB) (3.1 ‰ – 4.8 ‰). Waters draining old and weathered basalts display high δ^7Li values and are associated with high K/Li, Na/Li and Mg/Li ratios. Low δ^7Li values for river waters were found in the geologically younger parts of the island. Vigier et al. (2009) showed that in these younger areas, chemical erosion rates are higher and more congruent weathering occurs, due to the higher susceptibility to weathering of glassy hyaloclastites. It was suggested that the δ^7Li composition of dissolved loads reflect silicate weathering rates, where δ^7Li values correlate inversely with silicate weathering rates and that significant glass weathering in younger or volcanically active terranes covered by ice explains the lowest δ^7Li values (Figure 20).

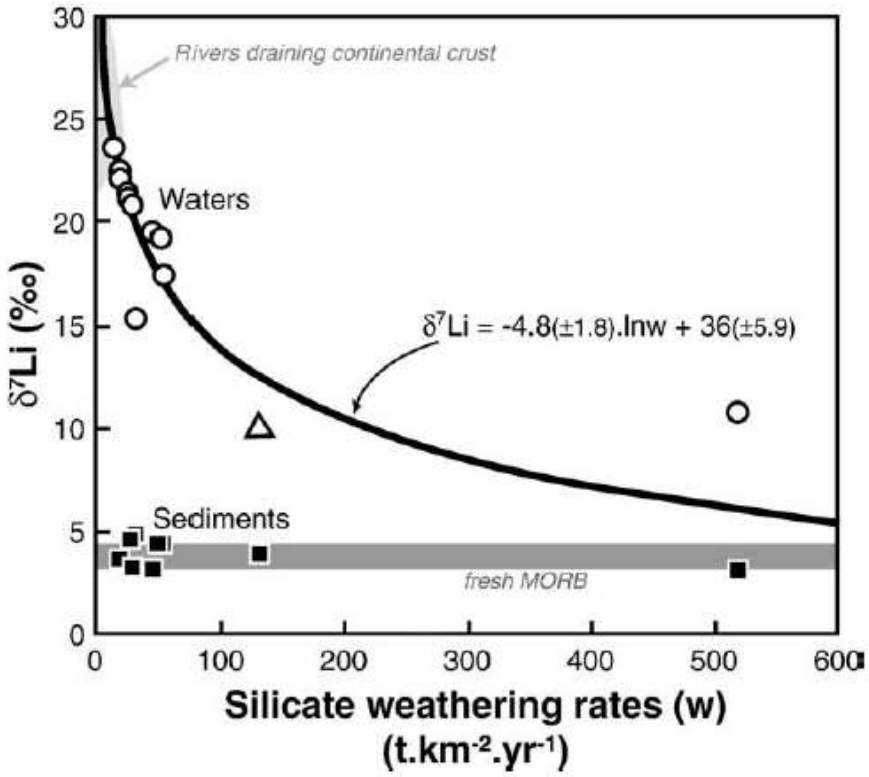

Figure 20: Silicate weathering rates, calculated from major element compositions, inversely correlate with δ^7Li values of river waters. MORB stands for Mid-Ocean Ridge Basalt. Source: Vigier et al. (2009).

In Greenland, glacial river waters show a slight difference in their Li isotope composition compared to non-glacial rivers (Wimpenny et al., 2010a). The average δ^7Li value of glacial rivers is slightly lower (~26 ‰) than non-glacial rivers (~30 ‰). In this specific climatic setting on West Greenland, the main Li isotope fractionation was linked to Fe-oxyhydroxide phases (rather than clay minerals), which are supersaturated in non-glacial rivers. For glacial rivers, it was found that initial fractionation of Li isotopes occurs under the ice via formation of Fe-oxyhydroxides, which is a by-product of sulphide oxidation. Fe-oxyhydroxides are known for Li^+ sorption onto surfaces and to preferentially incorporate ^{6}Li over ^{7}Li, which leaves the dissolved load with relatively high δ^7Li compositions (Wimpenny et al., 2010a).

Small catchments and minor water bodies

Lemarchand et al. (2010) investigated mechanisms that drive the behaviour of Li isotopes of water bodies in relatively small catchments. Li concentrations and isotopic compositions were analysed in various surface reservoirs such as soils, rocks, waters and

plants. The studied forested catchment area is underlain by a granitic lithology and is situated in the Vosges Mountains in France. Li isotope compositions of dissolved loads vary strongly, even at the scale of minor catchments. In contrast to studies in Hawaii (e.g. (Pistiner and Henderson, 2003; Huh et al., 2004)), it was found that at this locality, atmospheric inputs represented a minor contribution to the Li isotope signature. Vegetation did not affect the Li isotope composition and instead, Li concentration and isotopic composition are mainly controlled by water-rock interactions and the precipitation of secondary minerals. Huge Li isotope variations were found in soil waters, ranging a δ^7Li composition from -17.3 to +31.1 ‰, which the authors explained to be the result of another secondary phase i.e. iron oxides, which may incorporate Li with a higher isotope fractionation (Lemarchand et al., 2010). Similar observations were also made by Wimpenny et al. (2010a) in West Greenland.

The behaviour of Li isotopes in rivers draining a basaltic terrain on the small island of Sao Miguel in the Azores Archipelago was conducted by Pogge von Strandmann et al. (2010). River waters that were oversaturated with secondary minerals showed lower δ^7Li values (closer to parent material), which the authors explained by rapid secondary mineral precipitation and therefore reduced Li isotope fractionation between Li in secondary phases and solution (c.f. Pogge von Strandmann et al. (2006)). Furthermore, the authors suggested that the Li isotope composition of river waters is not only a function of initial input and dilution, but is instead associated with weathering regimes relative to climatic factors. For example, a difference in local climatic variability may impact the isotopic ratio of dissolved loads of individual water bodies (Pogge von Strandmann et al., 2010).

Liu et al. (2015) investigated the Li isotope concentration and composition of river waters draining a monolithologic terrain, the Columbia River Basalts, in the Cascades Mountains. A single continental lithology has the advantage that the observed Li isotope composition is not related to a change in bedrock source. In response to the conclusions of Pogge von Strandmann et al. (2010), the objective of this study was to demonstrate how different climate zones control the Li isotope composition of river waters. Streams were sampled from two climatic zones: east of the Cascades Mountains where it is mostly dry, and west of the mountain range, where it is dominantly wet. Furthermore, samples were taken during two different seasons (summer and late winter). River waters from both climatic zones displayed highly variable δ^7Li values (>20 ‰), which means that a difference in climate cannot be the only control of the Li isotope composition of river

waters. Instead, other controls were identified, such as the interaction between water and suspended and/or bed loads. It was proposed that the duration of water-rock interaction plays a major role on Li isotope fractionation in river systems. A transport simulation showed the possible effect of the subsurface residence time on the δ^7Li composition of both dissolved load and secondary minerals (Figure 21). The model predicts that, with a constant Li composition of the bulk rock, the dissolved load and secondary mineral phases evolve as a function of residence time (duration of water-rock interactions) where isotope compositions become heavier with increasing residence time.

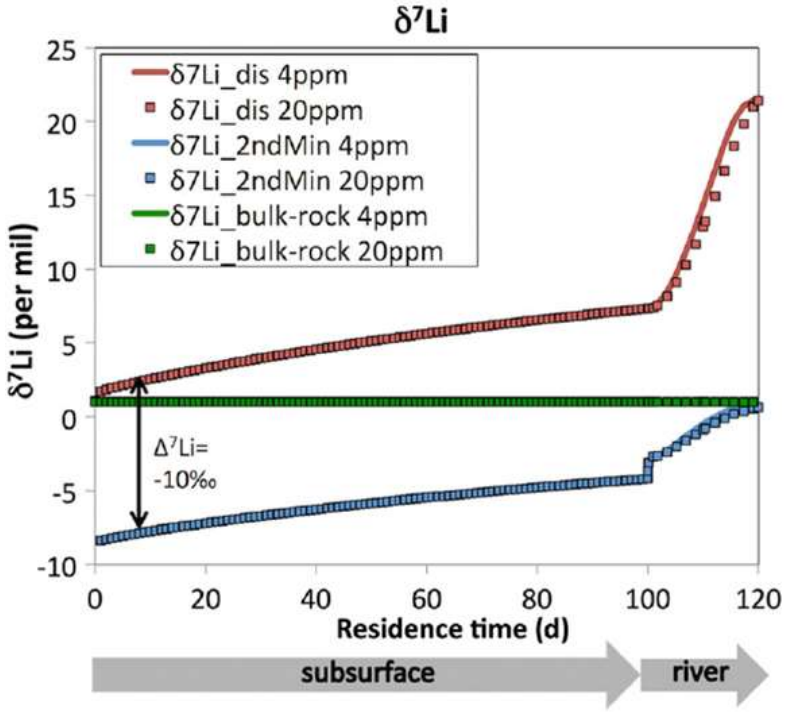

Figure 21: Model results of the effect of residence time on Li isotope fractionation during water-rock interactions. Red data points: δ^7Li values of dissolved loads. Blue: δ^7Li values of secondary minerals (clay phases and oxyhydroxides). Green: δ^7Li values of bulk rock. Modified after Liu et al. (2015).

The relation between uplift and the Li isotope ratio of river waters was shown by Pogge von Strandmann and Henderson (2015). Samples were taken from South Island, New Zealand, from rivers with relatively small catchment areas. Rivers that drain area of rapid uplift showed lower δ^7Li values than rivers draining areas characterised by a slow uplift. This suggests that rivers in rapidly uplifting areas are characterised by a reaction-limited environment, producing relatively low δ^7Li values due to the deficiency of secondary

mineral formation (c.f. δ^7Li values of Andean rivers studied by Dellinger et al. (2015). This highlights how tectonics may influence Li isotopic ratios of river water bodies.

3.4.2 Lithium isotope signature of sediments

Interpreting Li isotope ratios of river sediments can be challenging. Li isotopes fractionate during secondary mineral formation and mainly clay minerals are considered to reflect the isotopic fractionated signal and therefore represent chemical weathering conditions. However, unless a specific mineral is targeted, a mixture between several mineral phases is to be expected. This mixture may include mineral phases that have not participated in weathering reactions and therefore interpreting the Li isotope signature of these sediments may be difficult. This was shown by Dellinger et al. (2014) who analysed the Li content and isotope composition of suspended sediments along river depth profiles and respective bedload sediments in three of the largest river systems on Earth: the Amazon, the Mackenzie River and the Ganga-Brahmaputra River. The δ^7Li composition of river sediments revealed a relationship with Al/Si ratios, a proxy for grain size (Figure 22).

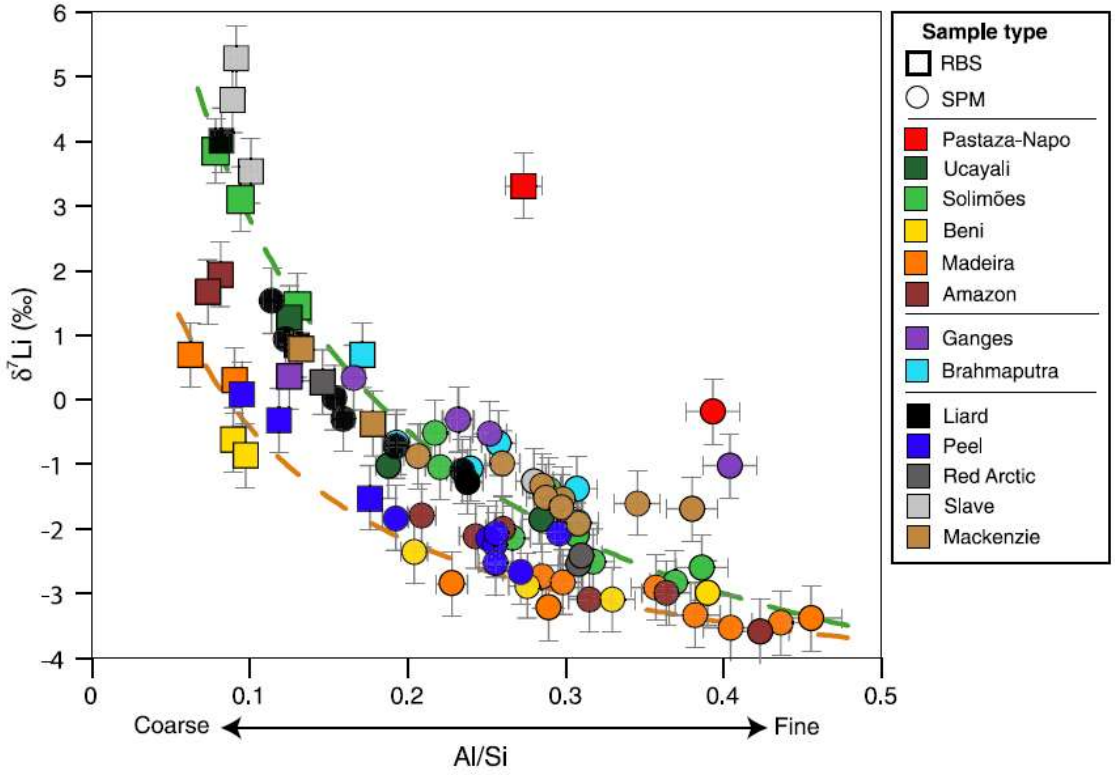

Figure 22: The δ^7Li composition of river sediments as a function their (Al/Si). Squares: river bed sands (RBS). Circles: suspended sediments (SPM). The orange and green dotted

curves represent a mixing hyperbola between fine and coarse sediments for the Madeira and Solimões rivers, respectively. Source: Dellinger et al. (2014).

River and suspended sediments show δ^7Li values from -3.6 to +5.3 ‰ and decrease with sediment grain size (Al/Si). It was proposed that a mixture between coarse unweathered sediments and weathered rock fragments could be an explanation for this. Similar observations were made for lake floor and river terrace sediments by Weynell et al. (2017), where δ^7Li values of sediments correlated inversely with Al/Si ratios. The authors suggest that only the finest surface sediments contain the complementary reservoir of Li solubilised by water-rock interactions within watersheds.

The lithological effect on the δ^7Li composition of sediments

While studies suggest that Li isotopes fractionate during weathering and the degree of fractionation is mainly associated with chemical weathering conditions, the Li isotope composition of the source rock prior to weathering may be an important control. The 'lithological' effect has shown to slightly influence the δ^7Li composition of the fine-grained fraction of large river sediments (Dellinger et al., 2017). Therefore, in order to better constrain the weathering signal derived from fine sediments, the bedrock variability must be corrected for. In particular, in a mixed lithology weathering regime, the relative Li contribution from each rock unit must be evaluated and the δ^7Li composition of the source accounted for. Sedimentary rocks are generally contributing the most to the Li budget (Holland, 1984). Igneous and metamorphic rocks have Li concentrations close to the average upper continental crust, which is much lower than that of sedimentary rocks. The latter are generally characterised with lower δ^7Li values compared to igneous and metamorphic rocks (Dellinger et al., 2017). Rocks originating from tectonic settings may also possess unique Li signatures. For example, Teng et al. (2006) showed that the Li concentration and δ^7Li composition of country rocks of the Tin Mountain pegmatite exceed large variations of δ^7Li values as a function of distance from a tectonic contact zone. They explain that this variation is the cause of Li diffusion from the Li-rich pegmatite into amphibolites. In this setting, differences in Li concentrations and δ^7Li composition may vary from ~1 wt. % to ~70 ppm and +10.8 to -18.6 ‰, respectively (for more details, see Section 3.3.2). Therefore, local bedrock variability must be carefully investigated before assessing the weathering signal of sediments via Li isotopes.

On a more global scale, the average Li composition and concentration of the continental crust must be identified in order to understand large scale continental weathering records,

such as the Cenozoic seawater record by Misra and Froelich (2012). One approach is to investigate windblown dust deposits from several parts of the world. Sauzéat et al. (2015) showed that desert loess has a homogenous δ^7Li signature and may therefore serve as an excellent proxy for identifying the average Li composition of the upper continental crust. They found that the average Li concentration of the upper crust is 30.5 ± 3.6 (2σ) ppm and a δ^7Li value of 0.6 ± 0.6 ‰ (2σ). However, windblown dust consists of a mixture between fine-grained weathered material and coarse-grained relatively unweathered material (Teng et al., 2004; Sauzéat et al., 2015). Depending on the source of dust, either from weathered or unweathered endmembers of the upper continental crust, the determination of the global average Li concentration and isotopic composition of the continental crust remains challenging.

3.4.3 Weathering profiles

To understand the Li isotope signature of sediments that derive from the weathering of soil profiles, the evolution of Li during soil development have been investigated. Only a few studies exist that explored the Li isotope behaviour in soil profiles. Basalt profiles in Laki, Iceland show that the top is isotopically light compared to the bottom of the profile. This is the result from preferential incorporation of ^{6}Li into secondary minerals such as clays or oxide-rich phases (Pistiner and Henderson, 2003). The authors postulate that isotopic fractionation associated with chemical weathering occurs on a <300-year time scale. However, a soil profile from Kilauea, Hawaii gave contrasting results. Li isotope compositions did not show any significant evolution throughout the soil profile and surface samples and, surprisingly, top soil horizons were not isotopically lighter than samples further down the profile (Figure 23). This was explained by trapped dust in these wet top soils and the influence of isotopically heavy rainwater infiltrating deep parts of the soil profile (Pistiner and Henderson, 2003).

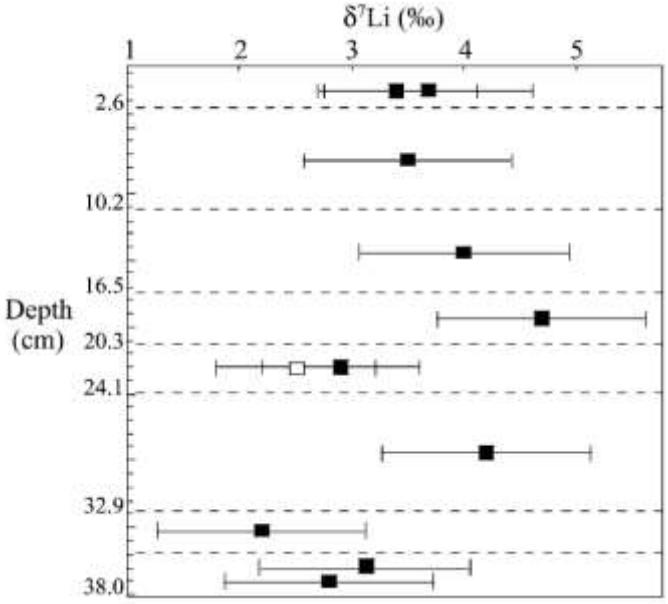

Figure 23: The δ^7Li composition of a Hawaiian soil profile (Thurston). Source Pistiner and Henderson (2003).

Liu et al. (2013) used the same explanation for the two weathering profiles that showed extremely high δ^7Li values at the surface compared to lower parts of the profile. Rudnick et al. (2004) studied two saprolites (chemically weathered rocks) from South Carolina, USA for their Li concentration and isotopic composition. These weathered rocks had consistently lower δ^7Li values compared to the unweathered igneous rock on which they formed. Furthermore, they show that δ^7Li values correlate inversely with the CIA, confirming that the Li isotope composition in soils may reflect the degree of chemical weathering. The sample with the lowest δ^7Li value (-6.8 ‰) of the first saprolite profile was taken adjacent to a soil horizon. The second saprolite profile was developed on a diabase dike. The most negative δ^7Li values were not observed at the surface but at 6 m depth at an inferred palaeo-water table (Rudnick et al., 2004; Teng et al., 2010) (Figure 24).

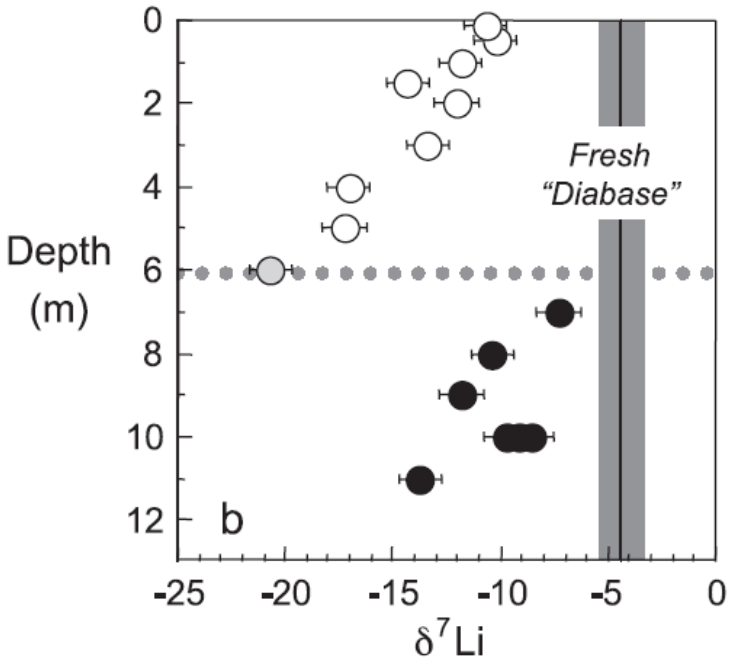

Figure 24: The δ^7Li (‰) composition as a function of depth in a diabase weathering profile from South Carolina, USA. The dashed grey horizontal line represents a palaeo-water table. Modified after Rudnick et al. (2004).

This means that Li isotope fractionation in soil profiles is the highest where in contact with water i.e. where most water-rock interactions take place. A similar observation was made for a basalt-laterite weathering profile in India (Kısakürek et al., 2004). Lowest δ^7Li values were associated with a palaeo-water table, where ^{7}Li was preferentially mobilised during water-rock interactions. Furthermore, surface samples at this profile were isotopically lighter compared to the unweathered bedrock, which is consistent with a more weathered top soil horizon (Kısakürek et al., 2004). However, as mentioned above, soil surface samples may be subject to weathered or unweathered aeolian deposition, which could cause an inconsistency of δ^7Li values over the depth of a soil profile (Liu et al., 2013). A distinct trend of δ^7Li values over a soil profile is not always given. For example, soil samples from a forested granitic catchment in Strengbach (France) show little variation of the δ^7Li composition along the profile, instead the Li isotope composition remains close to parent rock (Lemarchand et al., 2010). Similarly, Ryu et al. (2014) reported Li isotope data of Hawaiian soils the youngest soil profile, 300 years old, showed similar δ^7Li values as fresh basalt, regardless of depth (Figure 25).

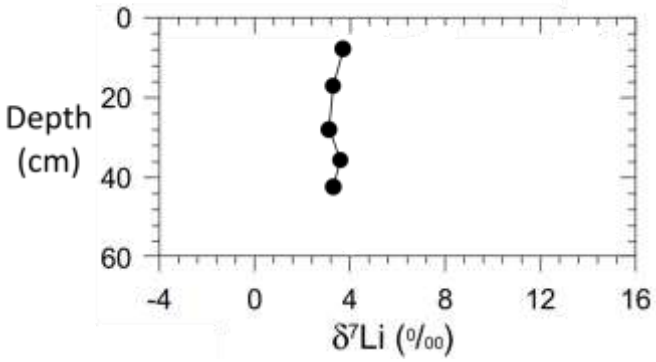

Figure 25: The δ^7Li composition of a soil profile developed in a humid-environment chronosequence in the Hawaiian Islands. Modified after Ryu et al. (2014).

In a soil climo-sequence in Hawaii, both Li concentrations and isotope ratios suggest that under arid and sub-humid conditions, isotopic fractionation in soils is at a minimum and marine aerosol (isotopically heavy) may overprint the weathering signature and driving δ^7Li to positive values (Huh et al., 2004). In contrast, under wet conditions with heavy rainfalls, soils are isotopically lighter, which means that ^{6}Li is increasingly adsorbed and sequestered by secondary minerals. The effectivity of ^{6}Li retention in clays is also depending on the cation exchange capacity of the soil (Huh et al., 2004).

3.4.4 Quaternary variations of the δ^7Li composition

Ryu et al. (2014) reported Li isotope data for soils developed along a four million year humid-environment chrono-sequence on Hawaii. The youngest soil profile, 300 years old, showed similar δ^7Li values as fresh basalt, regardless of depth. Older soils (>20,000 years) cover a large range of δ^7Li values and vary non-linearly as a function of time (Figure 26).

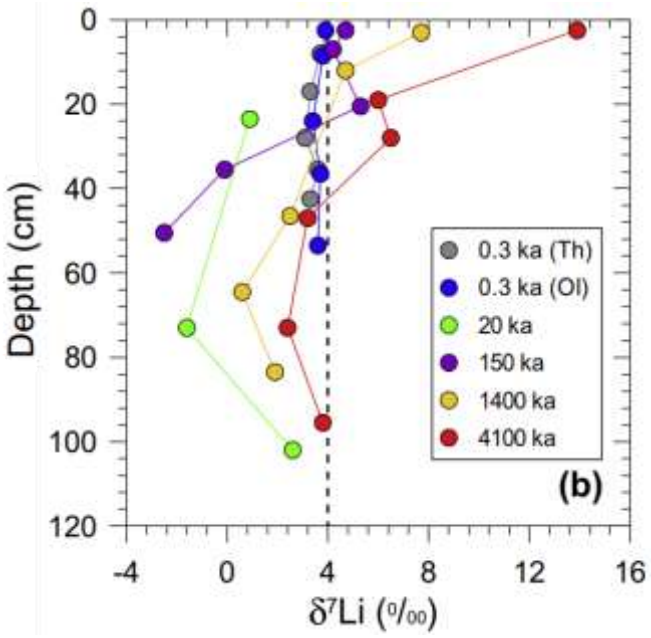

Figure 26: The δ^7Li composition of differently aged soil profiles on the Hawaiian Islands. Modified after Ryu et al. (2014).

The authors suggest that progressive mineral transformations, especially that of kaolinite, is the main control of Li isotope fractionation of Hawaiian soils. Furthermore, the evolution the δ^7Li composition of regolith over the past four million years co-varies with climatic variations, where a more congruent release of Li isotopes occurs during warm and wet periods (Ryu et al., 2014).

Clay-sized fractions (<2 µm) of sediments of fluvial terraces in the Himalayan Range were analysed to reconstruct chemical weathering conditions in a mountainous area over the past 40,000 years (Dosseto et al., 2015). The clay-sized fraction was chosen because it should record the most accurate weathering signature (see Section 3.4.2). Clays of fluvial terraces in the Himalaya range became isotopically heavier between 25,000 and 10,000 years ago (Figure 27).

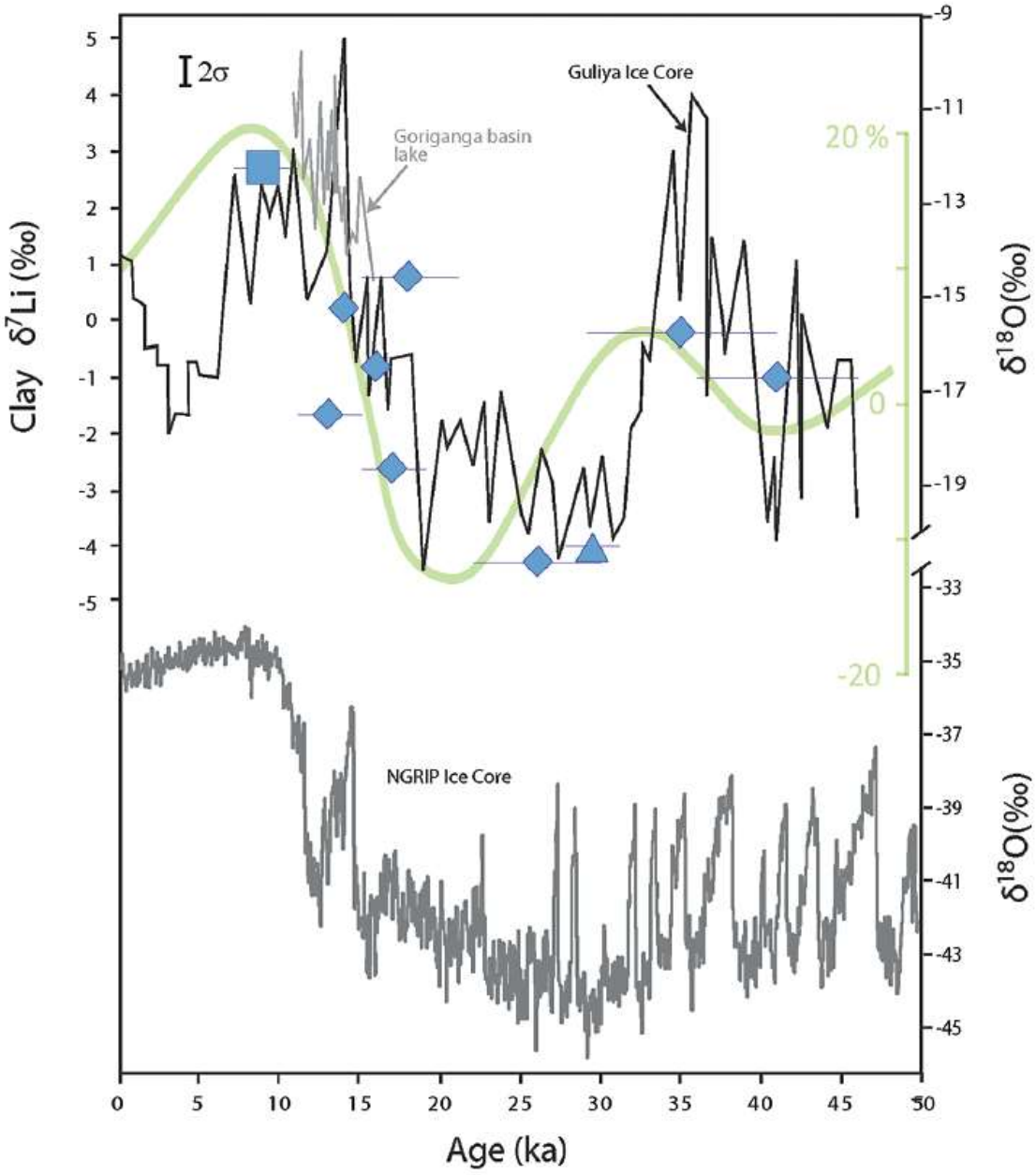

Figure 27: The δ^7Li composition of clays as a function of deposition age. Squares: Yamuna, triangle: Donga Fan, diamonds: Alaknanda. The green curve is the change in precipitation in the SW Indian Monsoon for South Asia (Sanyal and Sinha, 2010). The black curve (top panel) is the $\delta^{18}O_{SMOW}$ record from the Guliya ice core (Thompson et al., 1997). The grey curve (top panel) is the $\delta^{18}O_{VDPB}$ lacustrine sediment record from Goriganga Basin (Beukema et al., 2011). The grey curve (bottom panel) is the NGRIP ice core $\delta^{18}O$ record from Greenland (Andersen et al., 2004). Source: Dosseto et al. (2015).

During this period, monsoon intensified and precipitation increased substantially (Goodbred and Kuehl, 2000; Sanyal and Sinha, 2010; Beukema et al., 2011).

Consequently, runoff and physical erosion were enhanced, which inhibited water-rock interactions. This is reflected by increasing δ^7Li values of clays towards values close to unweathered bedrock, which suggests that weathering intensities must have decreased in response to enhanced fluvial activity. These results demonstrate how past climate variations, especially a shift in precipitation, may affect chemical weathering reactions in mountainous settings (Dosseto et al., 2015).

Bastian et al. (2017) investigated how chemical weathering conditions varied in the Nile Basin in northeast Africa over the past 32,000 years. Li isotope ratios were measured on the clay-sized fraction of samples obtained from a marine sediment core from the Eastern Mediterranean Sea, in the Nile delta. The δ^7Li values of clays co-varied with monsoon reconstructions, suggesting that silicate weathering may respond rapidly to hydroclimate variations. However, in contrast to findings by Dosseto et al. (2015), the δ^7Li composition of clays is lower and more homogeneous during humid periods and higher and more variable during arid phases (Figure 28). This is modelled as variations of the dissolution/neoformation ratio, which increases to an equilibrium state during wetter periods (Bastian et al., 2017).

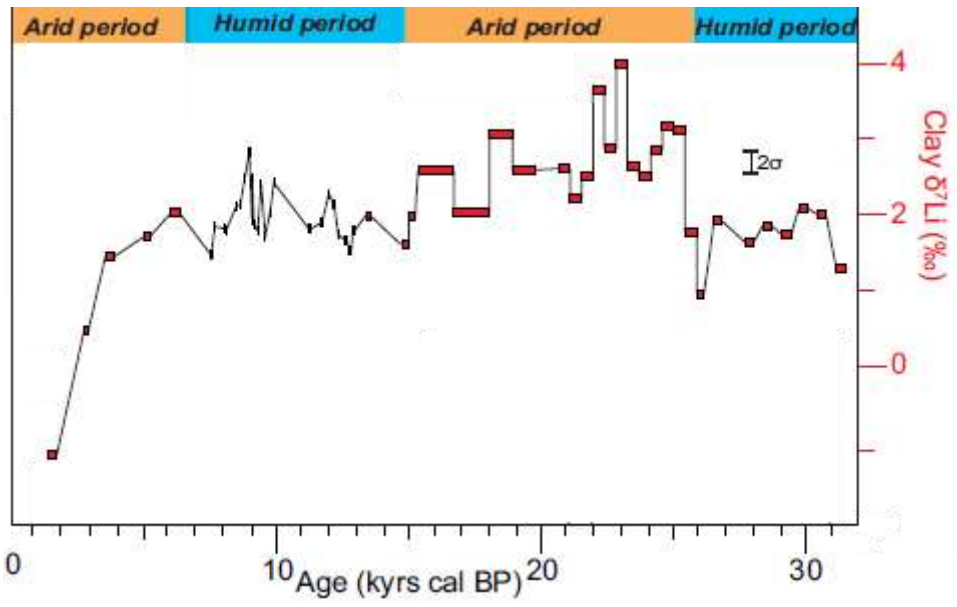

Figure 28: The δ^7Li composition of clay-sized fractions from a marine sediment core from the Eastern Mediterranean Sea (Nile delta) as a function of deposition age. Modified after Bastian et al. (2017).

Recently, Pogge von Strandmann et al. (2017b) analysed Li concentrations and isotope compositions in calcite from speleothems that formed during the past 200,000 years in two Israeli caves: Soreq and Tzavoa. The speleothem chemistry is controlled by the drip water chemistry which records the chemical weathering processes immediately above the cave and Pogge von Strandmann et al. (2017b) found that the Li isotope composition in these speleothems is controlled by weathering of the overlying aeolian silicate soils. The δ^7Li composition of speleothem was high during glacial periods and low during interglacials (Figure 29).

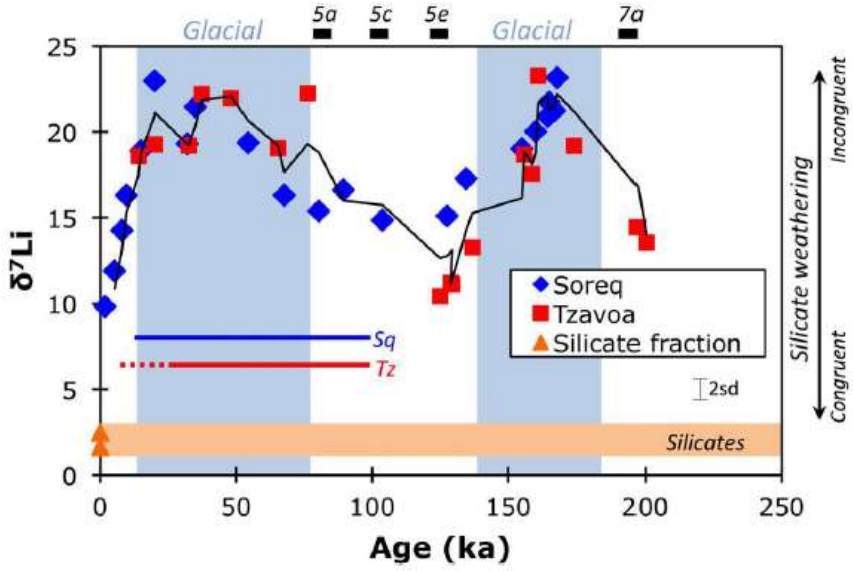

Figure 29: The δ^7Li composition (‰) of speleothems in Soreq and Tzvoa caves (Israel). Black line represents a 2-point running average of both data sets. Blue and red lines represent periods where soil was deposited at both Soreq (Sq) and Tzavoa (Tz). Dotted red line represents the time period where soil was eroded and valleys incised. Modified after Pogge von Strandmann et al. (2017b).

This shows that over the past 200,000 years, climate variability is directly associated with the congruency of silicate weathering, where congruent weathering is observed during interglacial periods, and incongruent weathering during glacial phases. This suggests a strong relationship between climate and silicate weathering as seen in Li isotopes (Pogge von Strandmann et al., 2017b).

3.4.5 Variations of the δ^7Li composition over the past 100 million years

Because the Li isotope proxy is still in its infancy, not many studies exist that utilised Li isotope ratios to infer palaeo chemical weathering conditions over the Cenozoic Era.

Hathorne and James (2006) presented a δ^7Li record of planktonic foraminifera from the Pacific and Atlantic oceans for the past 18 Ma. Li in seawater is well-mixed and its concentration and isotope composition vertically and laterally homogenous. The residence time of Li in seawater is ~1.2 million years and therefore much longer than ocean mixing time (~1,000 years) (Misra and Froelich, 2012). During the formation of foraminifera shells of some species (e.g. O. universa), Li is incorporated from the surrounding seawater without encompassing any isotopic fractionation (Hathorne and James, 2006). Hence, the Li isotope composition of certain foraminifera shells should represent the seawater δ^7Li composition at the time their growth. Changes in δ^7Li values of planktonic foraminifera is interpreted to reflect the variability of Li isotope compositions of the source i.e. the global average river fluxes. Even though, some have challenged this hypothesis and consider that vital effects may alter this record (Vigier and Godderis, 2015). Over the past 18 Ma, the δ^7Li composition of foraminifera shells ranged from 25 to 31 ‰ (Figure 30). From 16 to 8 Ma, δ^7Li values increased, suggesting that silicate weathering rates decreased during this time interval. The following 8 Ma, δ^7Li values remained relatively constant, suggesting no significant change in silicate weathering rates during this time.

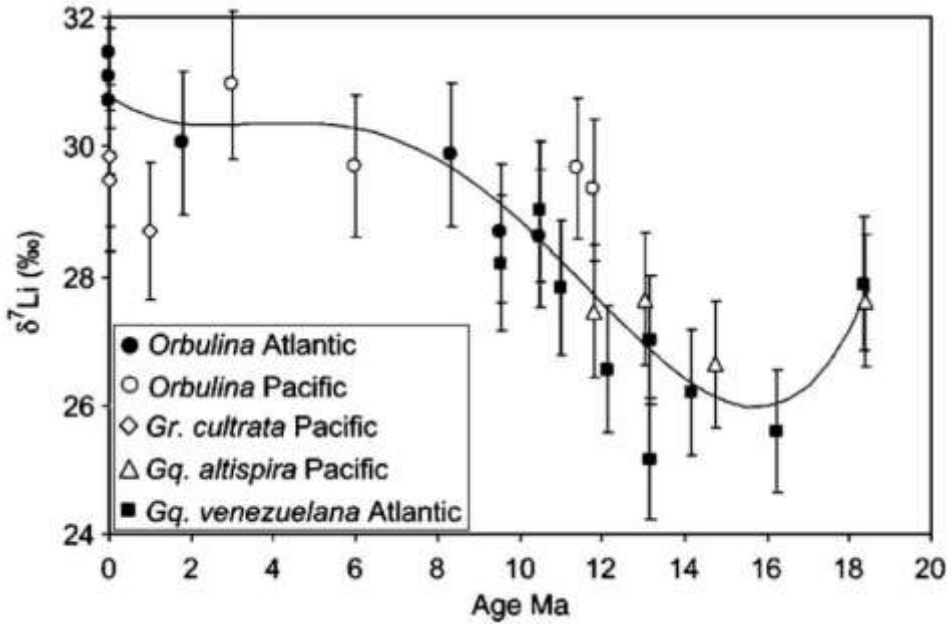

Figure 30: The δ^7Li record of planktonic foraminifera from the Pacific and Atlantic oceans for the past 18 Ma. Error bars are the external error (2σ). Source: Hathorne and James (2006).

Misra and Froelich (2012) presented the first a high-resolution marine Li isotope record, obtained from foraminifera, covering the past 68 Ma. Li isotope ratios are low at ~60 million years and show a constant increase from 60 Ma until present (Figure 31).

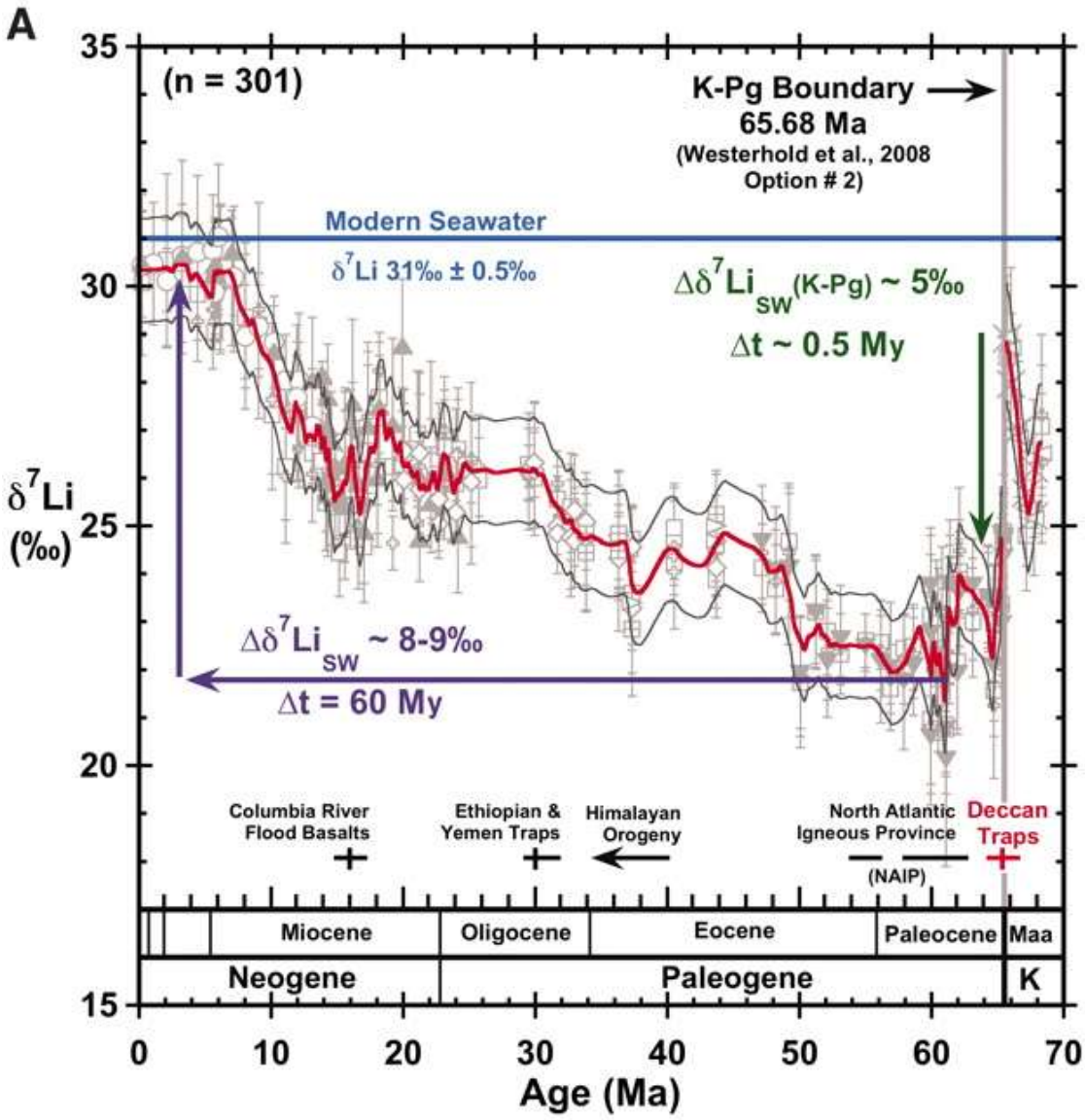

Figure 31: The δ^7Li record of foraminifera over the past 68 million years. Modified after Misra and Froelich (2012).

The authors explained that low δ^7Li values at 60 Ma is associated with the Himalaya orogeny, which is thought to have significantly impacted the continental weathering regime. Incongruent weathering conditions must have increasingly prevailed as a consequence of the tectonic uplift. Water-rock interactions became limited due to accelerated continental denudation, which must have increased riverine dissolved δ^7Li values. The marine Li isotope record is consistent with other weathering proxies such as

$^{87}Sr/^{86}Sr$ (Hess et al., 1986) and $^{187}Os/^{186}Os$ (Peucker-Ehrenbrink and Ravizza, 2000), which reflect enhanced continental weathering at the time of the Himalaya orogeny. These results represent an important finding on how tectonic uplift and orogenesis may have altered the Li isotope distribution in the oceans by shifting the continental weathering regime. However, this interpretation has been challenged by various modelling studies, which claim that the Li isotope record does not provide direct evidence for changes in weathering rates in response to the Cenozoic tectonic uplift (Li and West, 2014; Vigier and Godderis, 2015).

Enhanced weathering during Oceanic Anoxic Event 2 (OAE2), 93.5 million years ago, was identified with the use of Li isotopes. Pogge von Strandmann et al. (2013) showed that δ^7Li values from carbonates at the timing of OAE2 exhibited the lowest values, which is interpreted as an extreme pulse of continental weathering, with subsequent atmospheric CO_2 removal. Causes for accelerated weathering were linked to the eruption of a large igneous province, which increased atmospheric CO_2 concentrations, accompanied with rapid global warming. This in turn was followed by an enhanced hydrological cycle, which increased continental weathering rates and inhibited water-rock interactions (low chemical weathering intensities). It was suggested that this pulse of silicate weathering, as seen in Li isotopes, and the subsequent atmospheric CO_2 draw-down allowed the climate to rapidly recover.

3.4.6 Palaeozoic variations of the δ^7Li composition

Pogge von Strandmann et al. (2017c) linked the global climate recovery after the end-Ordovician Hirnantian glaciation (~445 Ma) to lower silicate weathering rates. Li isotope ratios of bulk carbonates and brachiopods from Anticosti Island, Canada and the UK were analysed. A positive excursion of δ^7Li values was observed during the glaciation phase, which the authors interpret as low weathering rates. The latter would imply that atmospheric CO_2 must have increased because less atmospheric CO_2 was drawn down via silicate weathering. Pogge von Strandmann et al. (2017c) therefore argued that the temperature-dependent feedback with silicate weathering was the reason for the climate to stabilise.

3.5 Conclusions

The Li isotope proxy is a potentially excellent tool to trace past and present chemical weathering conditions. During low temperature chemical weathering, Li isotopes fractionate significantly, where the lighter ^6Li preferentially incorporates into clay

minerals (Huh et al., 1998; Pistiner and Henderson, 2003; Vigier et al., 2008). Consequently, dissolved loads show consistently higher $^{7}Li/^{6}Li$ ratios than solid weathering products. The magnitude of Li isotope fractionation during weathering is mostly controlled by chemical weathering conditions in the catchment area. It is suggested that $\delta^{7}Li$ values of river waters represent the weathering 'intensity' for a given catchment. Furthermore, studies have shown that the dissolved load in transport-limited regions display relatively low $\delta^{7}Li$ values compared to reaction-limited environments (Huh et al., 2001). This implies that the Li isotope composition of dissolved loads directly reflect the catchment-specific weathering regime. In contrast to silicate rocks, carbonates are depleted in Li, and therefore the main source for the dissolved Li load are silicates. Hence, the Li isotope composition of dissolved loads reflects silicate weathering conditions. A similar approach was applied in ocean records, where $\delta^{7}Li$ values of planktonic foraminifera are interpreted to reflect the variability of Li isotope compositions of the source i.e. the global average river fluxes (Hathorne and James, 2006). Not many studies exist that have applied the Li isotope proxy on solid weathering products i.e. clay-sized fractions. Thus far, it is suggested that $\delta^{7}Li$ values of clays follow hydrologic activity in response to climate variations (Dosseto et al., 2015; Bastian et al., 2017).

References

Andersen, K. K., Azuma, N., Barnola, J.-M., Bigler, M., Biscaye, P., Caillon, N., Chappellaz, J., Clausen, H. B., Dahl-Jensen, D. & Fischer, H. 2004. High-resolution record of Northern Hemisphere climate extending into the last interglacial period. *Nature,* 431**,** 147.

Bagard, M.-L., West, A. J., Newman, K. & Basu, A. R. 2015. Lithium isotope fractionation in the Ganges–Brahmaputra floodplain and implications for groundwater impact on seawater isotopic composition. *Earth and Planetary Science Letters,* 432**,** 404-414.

Bastian, L., Revel, M., Bayon, G., Dufour, A. & Vigier, N. 2017. Abrupt response of chemical weathering to Late Quaternary hydroclimate changes in northeast Africa. *Scientific Reports,* 7**,** 44231.

Beukema, S. P., Krishnamurthy, R., Juyal, N., Basavaiah, N. & Singhvi, A. 2011. Monsoon variability and chemical weathering during the late Pleistocene in the Goriganga basin, higher central Himalaya, India. *Quaternary Research,* 75**,** 597-604.

Bouman, C., Elliott, T. & Vroon, P. Z. 2004. Lithium inputs to subduction zones. *Chemical Geology,* 212**,** 59-79.

Burton, K. W. & Vigier, N. 2012. Lithium Isotopes as Tracers in Marine and Terrestrial Environments. *In:* Baskaran, M. (ed.) *Handbook of Environmental Isotope Geochemistry: Vol I.* Berlin, Heidelberg: Springer Berlin Heidelberg, 41-59.

Chan, L.-H. & Kastner, M. 2000. Lithium isotopic compositions of pore fluids and sediments in the Costa Rica subduction zone: implications for fluid processes and sediment contribution to the arc volcanoes. *Earth and Planetary Science Letters,* 183**,** 275-290.

Chan, L.-H., Alt, J. C. & Teagle, D. A. 2002a. Lithium and lithium isotope profiles through the upper oceanic crust: a study of seawater–basalt exchange at ODP Sites 504B and 896A. *Earth and Planetary Science Letters,* 201**,** 187-201.

Chan, L.-H. & Hein, J. R. 2007. Lithium contents and isotopic compositions of ferromanganese deposits from the global ocean. *Deep Sea Research Part II: Topical Studies in Oceanography,* 54**,** 1147-1162.

Chan, L., Edmond, J., Thompson, G. & Gillis, K. 1992. Lithium isotopic composition of submarine basalts: implications for the lithium cycle in the oceans. *Earth and Planetary Science Letters,* 108**,** 151-160.

Chan, L. H., Leeman, W. & You, C.-F. 2002b. Lithium isotopic composition of Central American volcanic arc lavas: implications for modification of subarc mantle by slab-derived fluids: correction. *Chemical Geology,* 182**,** 293-300.

Chan, L. H. & Frey, F. A. 2003. Lithium isotope geochemistry of the Hawaiian plume: results from the Hawaii Scientific Drilling Project and Koolau volcano. *Geochemistry, Geophysics, Geosystems,* 4.

Decarreau, A., Vigier, N., Pálková, H., Petit, S., Vieillard, P. & Fontaine, C. 2012. Partitioning of lithium between smectite and solution: An experimental approach. *Geochimica et Cosmochimica Acta,* 85**,** 314-325.

Dellinger, M., Gaillardet, J., Bouchez, J., Calmels, D., Galy, V., Hilton, R. G., Louvat, P. & France-Lanord, C. 2014. Lithium isotopes in large rivers reveal the cannibalistic nature of modern continental weathering and erosion. *Earth and Planetary Science Letters,* 401**,** 359-372.

Dellinger, M., Gaillardet, J., Bouchez, J., Calmels, D., Louvat, P., Dosseto, A., Gorge, C., Alanoca, L. & Maurice, L. 2015. Riverine Li isotope fractionation in the Amazon River basin controlled by the weathering regimes. *Geochimica et Cosmochimica Acta,* 164**,** 71-93.

Dellinger, M., Bouchez, J., Gaillardet, J., Faure, L. & Moureau, J. 2017. Tracing weathering regimes using the lithium isotope composition of detrital sediments. *Geology,* 45**,** 411-414.

Dosseto, A., Vigier, N., Joannes-Boyau, R. C., Moffat, I., Singh, T. & Srivastava, P. 2015. Rapid response of silicate weathering rates to climate change in the Himalaya. *Geochemical Perspectives Letters,* 1**,** 10-19.

Foustoukos, D., James, R., Berndt, M. & Seyfried, W. 2004. Lithium isotopic systematics of hydrothermal vent fluids at the Main Endeavour Field, Northern Juan de Fuca Ridge. *Chemical Geology,* 212**,** 17-26.

Goodbred, S. L. & Kuehl, S. A. 2000. Enormous Ganges-Brahmaputra sediment discharge during strengthened early Holocene monsoon. *Geology,* 28**,** 1083-1086.

Hathorne, E. C. & James, R. H. 2006. Temporal record of lithium in seawater: A tracer for silicate weathering? *Earth and Planetary Science Letters,* 246**,** 393-406.

Hess, J., Bender, M. L. & Schilling, J.-G. 1986. Evolution of the ratio of strontium-87 to strontium-86 in seawater fromm Cretaceous to present. *Science,* 231**,** 979-985.

Hoefs, J. 2015. Isotope fractionation processes of selected elements. *Stable Isotope Geochemistry.* Springer, 47-190.

Holland, H. D. 1984. *The chemical evolution of the atmosphere and oceans,* Princeton University Press, pp.

Huh, Y., Chan, L.-H., Zhang, L. & Edmond, J. M. 1998. Lithium and its isotopes in major world rivers: implications for weathering and the oceanic budget. *Geochimica et Cosmochimica Acta,* 62**,** 2039-2051.

Huh, Y., Chan, L.-H. & Edmond, J. M. 2001. Lithium isotopes as a probe of weathering processes: Orinoco River. *Earth and Planetary Science Letters,* 194**,** 189-199.

Huh, Y., Chan, L. H. & Chadwick, O. A. 2004. Behavior of lithium and its isotopes during weathering of Hawaiian basalt. *Geochemistry, Geophysics, Geosystems,* 5.

James, R. H., Rudnicki, M. D. & Palmer, M. R. 1999. The alkali element and boron geochemistry of the Escanaba Trough sediment-hosted hydrothermal system. *Earth and Planetary Science Letters,* 171**,** 157-169.

James, R. H. & Palmer, M. R. 2000. The lithium isotope composition of international rock standards. *Chemical Geology,* 166**,** 319-326.

Kısakürek, B., Widdowson, M. & James, R. H. 2004. Behaviour of Li isotopes during continental weathering: the Bidar laterite profile, India. *Chemical Geology,* 212**,** 27-44.

Kısakűrek, B., James, R. H. & Harris, N. B. 2005. Li and δ^7Li in Himalayan rivers: proxies for silicate weathering? *Earth and Planetary Science Letters,* 237**,** 387-401.

Lemarchand, E., Chabaux, F., Vigier, N., Millot, R. & Pierret, M.-C. 2010. Lithium isotope systematics in a forested granitic catchment (Strengbach, Vosges Mountains, France). *Geochimica et Cosmochimica Acta,* 74**,** 4612-4628.

Li, G. & West, A. J. 2014. Evolution of Cenozoic seawater lithium isotopes: Coupling of global denudation regime and shifting seawater sinks. *Earth and Planetary Science Letters,* 401**,** 284-293.

Liu, X.-M., Rudnick, R. L., Mcdonough, W. F. & Cummings, M. L. 2013. Influence of chemical weathering on the composition of the continental crust: Insights from Li and Nd isotopes in bauxite profiles developed on Columbia River Basalts. *Geochimica et Cosmochimica Acta,* 115**,** 73-91.

Liu, X.-M., Wanner, C., Rudnick, R. L. & Mcdonough, W. F. 2015. Processes controlling δ 7 Li in rivers illuminated by study of streams and groundwaters draining basalts. *Earth and Planetary Science Letters,* 409**,** 212-224.

Lui-Heung, C. & Edmond, J. M. 1988. Variation of lithium isotope composition in the marine environment: A preliminary report. *Geochimica et Cosmochimica Acta,* 52**,** 1711-1717.

Lui-Heung, C., Gieskes, J. M., Chen-Feng, Y. & Edmond, J. M. 1994. Lithium isotope geochemistry of sediments and hydrothermal fluids of the Guaymas Basin, Gulf of California. *Geochimica et Cosmochimica Acta,* 58**,** 4443-4454.

Millot, R., Guerrot, C. & Vigier, N. 2004. Accurate and High-Precision Measurement of Lithium Isotopes in Two Reference Materials by MC-ICP-MS. *Geostandards and Geoanalytical Research,* 28**,** 153-159.

Millot, R., Vigier, N. & Gaillardet, J. 2010. Behaviour of lithium and its isotopes during weathering in the Mackenzie Basin, Canada. *Geochimica et Cosmochimica Acta,* 74**,** 3897-3912.

Misra, S. & Froelich, P. N. 2012. Lithium isotope history of Cenozoic seawater: changes in silicate weathering and reverse weathering. *Science,* 335**,** 818-823.

Moriguti, T. & Nakamura, E. 1998a. High-yield lithium separation and the precise isotopic analysis for natural rock and aqueous samples. *Chemical Geology,* 145**,** 91-104.

Moriguti, T. & Nakamura, E. 1998b. Across-arc variation of Li isotopes in lavas and implications for crust/mantle recycling at subduction zones. *Earth and planetary science letters,* 163**,** 167-174.

Peucker-Ehrenbrink, B. & Ravizza, G. 2000. The marine osmium isotope record. *Terra Nova,* 12**,** 205-219.

Pistiner, J. S. & Henderson, G. M. 2003. Lithium-isotope fractionation during continental weathering processes. *Earth and Planetary Science Letters,* 214**,** 327-339.

Pogge Von Strandmann, P. A., Burton, K. W., James, R. H., Van Calsteren, P., Gíslason, S. R. & Mokadem, F. 2006. Riverine behaviour of uranium and lithium isotopes in an actively glaciated basaltic terrain. *Earth and Planetary Science Letters,* 251**,** 134-147.

Pogge Von Strandmann, P. A., Burton, K. W., James, R. H., Van Calsteren, P. & Gislason, S. R. 2010. Assessing the role of climate on uranium and lithium isotope behaviour in rivers draining a basaltic terrain. *Chemical Geology,* 270**,** 227-239.

Pogge Von Strandmann, P. A., Jenkyns, H. C. & Woodfine, R. G. 2013. Lithium isotope evidence for enhanced weathering during Oceanic Anoxic Event 2. *Nature Geoscience,* 6**,** 668-672.

Pogge Von Strandmann, P. A. & Henderson, G. M. 2015. The Li isotope response to mountain uplift. *Geology,* 43**,** 67-70.

Pogge Von Strandmann, P. A., Desrochers, A., Murphy, M., Finlay, A., Selby, D. & Lenton, T. 2017a. Global climate stabilisation by chemical weathering during the Hirnantian glaciation. *Geophysical Research Letters.*, 3**,** 230-237.

Pogge Von Strandmann, P. A., Vaks, A., Bar-Matthews, M., Ayalon, A., Jacob, E. & Henderson, G. M. 2017b. Lithium isotopes in speleothems: Temperature-controlled variation in silicate weathering during glacial cycles. *Earth and Planetary Science Letters,* 469**,** 64-74.

Richter, F. M., Davis, A. M., Depaolo, D. J. & Watson, E. B. 2003. Isotope fractionation by chemical diffusion between molten basalt and rhyolite. *Geochimica et Cosmochimica Acta,* 67**,** 3905-3923.

Richter, F. M., Mendybaev, R. A., Christensen, J. N., Hutcheon, I. D., Williams, R. W., Sturchio, N. C. & Beloso Jr, A. D. 2006. Kinetic isotopic fractionation during diffusion of ionic species in water. *Geochimica et Cosmochimica Acta,* 70**,** 277-289.

Rudnick, R. L., Tomascak, P. B., Njo, H. B. & Gardner, L. R. 2004. Extreme lithium isotopic fractionation during continental weathering revealed in saprolites from South Carolina. *Chemical Geology,* 212**,** 45-57.

Ryu, J.-S., Vigier, N., Lee, S.-W., Lee, K.-S. & Chadwick, O. A. 2014. Variation of lithium isotope geochemistry during basalt weathering and secondary mineral transformations in Hawaii. *Geochimica et Cosmochimica Acta,* 145**,** 103-115.

Sanyal, P. & Sinha, R. 2010. Evolution of the Indian summer monsoon: synthesis of continental records. *Geological Society, London, Special Publications,* 342**,** 153-183.

Sauzéat, L., Rudnick, R. L., Chauvel, C., Garçon, M. & Tang, M. 2015. New perspectives on the Li isotopic composition of the upper continental crust and its weathering signature. *Earth and Planetary Science Letters,* 428**,** 181-192.

Sharp, Z. 2017. Principles of stable isotope geochemistry.

Tang, Y.-J., Zhang, H.-F., Nakamura, E., Moriguti, T., Kobayashi, K. & Ying, J.-F. 2007a. Lithium isotopic systematics of peridotite xenoliths from Hannuoba, North

China Craton: implications for melt–rock interaction in the considerably thinned lithospheric mantle. *Geochimica et Cosmochimica Acta,* 71**,** 4327-4341.

Tang, Y.-J., Zhang, H.-F. & Ying, J.-F. 2007b. Review of the lithium isotope system as a geochemical tracer. *International Geology Review,* 49**,** 374-388.

Taylor, T. I. & Urey, H. C. 1938. Fractionation of the lithium and potassium isotopes by chemical exchange with zeolites. *The Journal of Chemical Physics,* 6**,** 429-438.

Teng, F.-Z., Mcdonough, W. F., Rudnick, R., Dalpé, C., Tomascak, P., Chappell, B. W. & Gao, S. 2004. Lithium isotopic composition and concentration of the upper continental crust. *Geochimica et Cosmochimica Acta,* 68**,** 4167-4178.

Teng, F.-Z., Mcdonough, W. F., Rudnick, R. L. & Walker, R. J. 2006. Diffusion-driven extreme lithium isotopic fractionation in country rocks of the Tin Mountain pegmatite. *Earth and Planetary Science Letters,* 243**,** 701-710.

Teng, F.-Z., Li, W.-Y., Rudnick, R. L. & Gardner, L. R. 2010. Contrasting lithium and magnesium isotope fractionation during continental weathering. *Earth and Planetary Science Letters,* 300**,** 63-71.

Thompson, L. O., Yao, T., Davis, M., Henderson, K., Mosley-Thompson, E., Lin, P.-N., Beer, J., Synal, H.-A., Cole-Dai, J. & Bolzan, J. 1997. Tropical climate instability: The last glacial cycle from a Qinghai-Tibetan ice core. *Science,* 276**,** 1821-1825.

Tomascak, P. & Langmuir, C. 1999. Lithium isotope variability in MORB. *Eos,* 80**,** F1086-F1087.

Tomascak, P. B., Tera, F., Helz, R. T. & Walker, R. J. 1999. The absence of lithium isotope fractionation during basalt differentiation: new measurements by multicollector sector ICP-MS. *Geochimica et Cosmochimica Acta,* 63**,** 907-910.

Tomascak, P. B., Ryan, J. G. & Defant, M. J. 2000. Lithium isotope evidence for light element decoupling in the Panama subarc mantle. *Geology,* 28**,** 507-510.

Tomascak, P. B., Widom, E., Benton, L. D., Goldstein, S. L. & Ryan, J. G. 2002. The control of lithium budgets in island arcs. *Earth and Planetary Science Letters,* 196**,** 227-238.

Tomascak, P. B. 2004. Developments in the understanding and application of lithium isotopes in the earth and planetary sciences. *Reviews in Mineralogy and Geochemistry,* 55**,** 153-195.

Verney-Carron, A., Vigier, N. & Millot, R. 2011. Experimental determination of the role of diffusion on Li isotope fractionation during basaltic glass weathering. *Geochimica et Cosmochimica Acta,* 75**,** 3452-3468.

Vigier, N., Decarreau, A., Millot, R., Carignan, J., Petit, S. & France-Lanord, C. 2008. Quantifying Li isotope fractionation during smectite formation and implications for the Li cycle. *Geochimica et Cosmochimica Acta,* 72**,** 780-792.

Vigier, N., Gislason, S. R., Burton, K., Millot, R. & Mokadem, F. 2009. The relationship between riverine lithium isotope composition and silicate weathering rates in Iceland. *Earth and Planetary Science Letters,* 287**,** 434-441.

Vigier, N. & Godderis, Y. 2015. A new approach for modeling Cenozoic oceanic lithium isotope paleo-variations: the key role of climate. *Climate of the Past Discussions,* 11**,** 635-645.

Wang, Q.-L., Chetelat, B., Zhao, Z.-Q., Ding, H., Li, S.-L., Wang, B.-L., Li, J. & Liu, X.-L. 2015. Behavior of lithium isotopes in the Changjiang River system: sources effects and response to weathering and erosion. *Geochimica et Cosmochimica Acta,* 151**,** 117-132.

Weynell, M., Wiechert, U. & Schuessler, J. A. 2017. Lithium isotopes and implications on chemical weathering in the catchment of Lake Donggi Cona, northeastern Tibetan Plateau. *Geochimica et Cosmochimica Acta*.

White, W. M. 2013. *Geochemistry,* John Wiley & Sons, pp.

Williams, L. B. & Hervig, R. L. 2005. Lithium and boron isotopes in illite-smectite: the importance of crystal size. *Geochimica et Cosmochimica Acta,* 69**,** 5705-5716.

Wimpenny, J., James, R. H., Burton, K. W., Gannoun, A., Mokadem, F. & Gíslason, S. R. 2010a. Glacial effects on weathering processes: new insights from the elemental

and lithium isotopic composition of West Greenland rivers. *Earth and Planetary Science Letters,* 290**,** 427-437.

Wimpenny, J., Gíslason, S. R., James, R. H., Gannoun, A., Pogge Von Strandmann, P. A. & Burton, K. W. 2010b. The behaviour of Li and Mg isotopes during primary phase dissolution and secondary mineral formation in basalt. *Geochimica et Cosmochimica Acta,* 74**,** 5259-5279.

Wimpenny, J., Colla, C. A., Yu, P., Yin, Q.-Z., Rustad, J. R. & Casey, W. H. 2015. Lithium isotope fractionation during uptake by gibbsite. *Geochimica et Cosmochimica Acta,* 168**,** 133-150.

You, C.-F. & Chan, L.-H. 1996. Precise determination of lithium isotopic composition in low concentration natural samples. *Geochimica et Cosmochimica Acta,* 60**,** 909-915.

Zack, T., Tomascak, P. B., Rudnick, R. L., Dalpé, C. & Mcdonough, W. F. 2003. Extremely light Li in orogenic eclogites: the role of isotope fractionation during dehydration in subducted oceanic crust. *Earth and Planetary Science Letters,* 208**,** 279-290.

Zhang, L., Chan, L.-H. & Gieskes, J. M. 1998. Lithium isotope geochemistry of pore waters from Ocean Drilling Program Sites 918 and 919, Irminger Basin. *Geochimica et Cosmochimica Acta,* 62**,** 2437-2450.

4 Climate of Australia

In the following sections, a brief description of the climate drivers of Australia is given. Furthermore, climate change in Australia over the last glacial cycle, with emphasis on south-east Australia, is discussed.

4.1 Climate drivers of Australia

Australia spans from latitude 10 °S to 43 °S. It is bordered by Indonesia and New Guinea to the North, the Pacific Ocean to the East, the Southern Ocean to the South and the Indian Ocean to the West. Two opposing climate engines drive the climate of Australia: the Antarctic cold waters from the Southern Ocean, and the heat of the equatorial tropics, the Indo-Pacific Warm Pool (IPWP) (Figure 32). Other oceanographic features affecting the Australian climate are also shown in Figure 32. The main controls of the continental climate are the prevailing westerlies in the South, the South-East Trade winds from the E-SE, the Sub-tropical High Pressure Belt and the summer monsoon in the North (Reeves et al., 2013). Because of Australia's large size, the centre exhibits hot and dry conditions, with wetter conditions towards the coast (Reeves et al., 2013). Australia's climate responds to seasonal zonal circulation caused by continental heating and cooling and the land-sea temperature contrast (Gimeno et al., 2010). In northern and eastern Australia, anomalies in summer and winter rainfall can be attributed to a strengthening of the Southern Oscillation-Walker circulation, which enhances the Australian monsoon and causes increased precipitation (Pittock, 1975; Rognon and Williams, 1977; McBride and Nicholls, 1983; Allan, 1985; Harrison, 1993). The coastal-near environment from mid-East to South Australia encompasses a large range of different rainfall regimes (Petherick et al., 2013). Southern Australia exhibits high rainfall during winter, which is associated with the westerly winds and water-saturated cold fronts that arrive when the high-pressure systems move towards northern Australia. The area in between these two opposing climate regimes is characterised with uniform rainfall rates throughout the year (Petherick et al., 2013) (Figure 33).

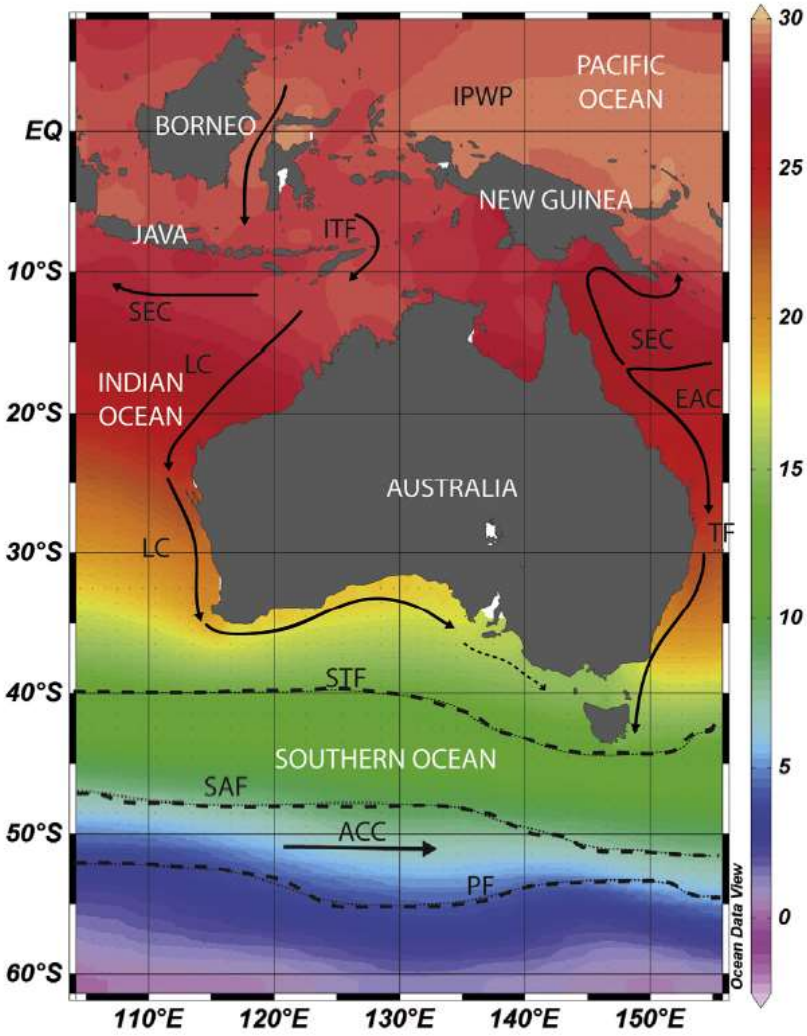

Figure 32: Major oceanographic features surrounding and influencing the climate of Australia. Colours indicate the average modern sea surface temperature. Solid lines are major currents. IPWP = Indo-Pacific Warm Pool, ITF = Indonesian Throughflow, SEC = South Equatorial Current, LC = Leeuwin Current (dashed line represents extent during La Niña), EAC = East Australian Current, ACC = Antarctic Circumpolar Current. Dotted lines are the mean positions of major fronts: TF = Tasman Front, STF = Subtropical Front, SAF = Subantarctic Front, PF = Polar Front. Source: Reeves et al. (2013).

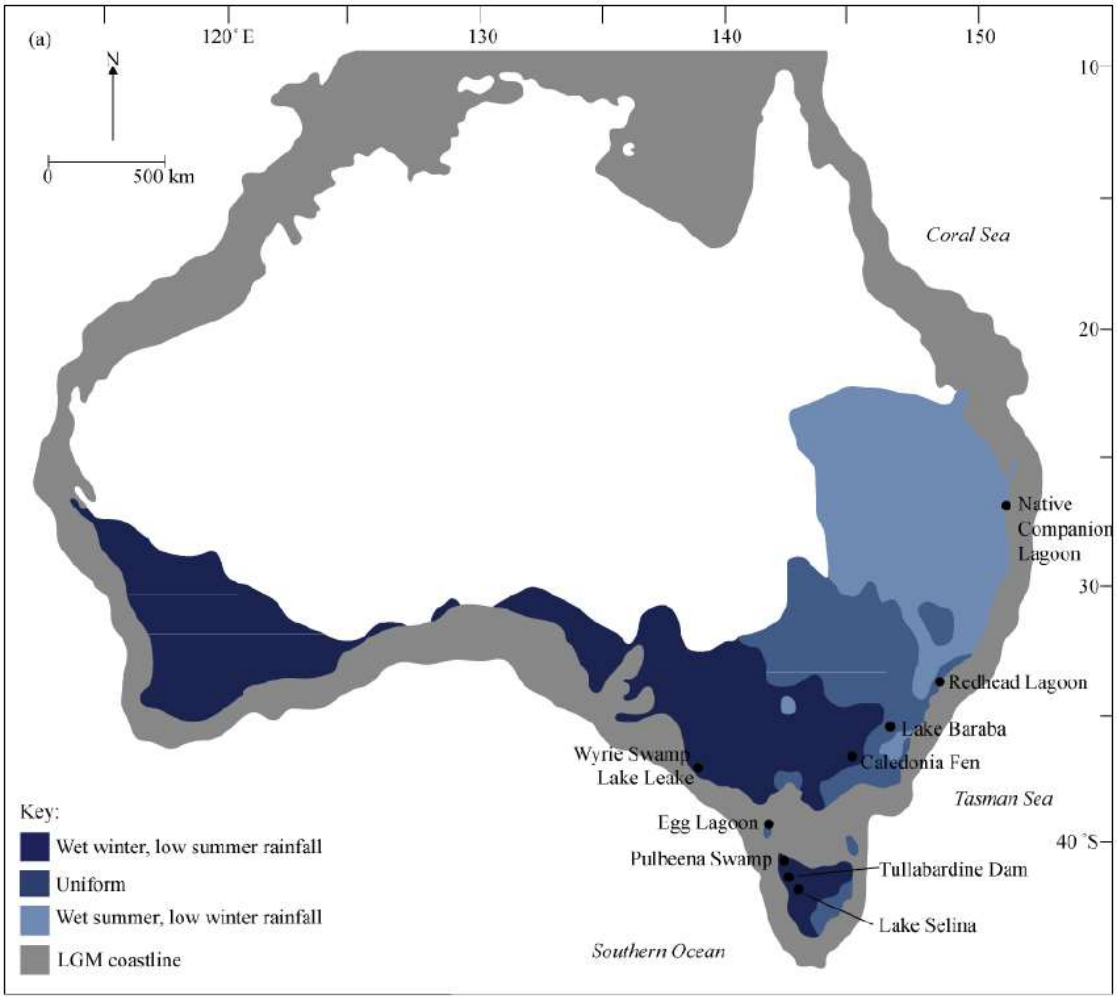

Figure 33: Map of temperate Australia, defined by Petherick et al. (2013). Coloured areas highlight contrasting climate regimes. Source: Petherick et al. (2013).

Climate drivers of south-east Australia

Recent hydroclimatic variations in south-east Australia have been associated with:

1. El Niño-Southern Oscillation (ENSO) e.g. McBride and Nicholls (1983); Jones and Trewin (2000)
2. Tropical and extratropical Pacific and Indian Ocean sea surface temperature variability e.g. Nicholls (1989); Drosdowsky and Chambers (2001)
3. Latitude of the sub-tropical ridge (STR) e.g. Pittock (1975); Drosdowsky (2005)
4. Southern Annular Mode (SAM) e.g. Hendon et al. (2007); Meneghini et al. (2007)
5. Madden-Julian Oscillation (MJO) e.g. Donald et al. (2006)

The El Niño-Southern Oscillation (ENSO) has been associated with modulating rainfall over most parts of Australia (Nicholls, 1989). Variations of sea surface temperature (SST)

in the equatorial Pacific are the direct cause of rainfall variability in central and eastern parts of Australia. However, south-east Australia is only minorly affected by monsoon (Ummenhofer et al., 2009). Instead, Ummenhofer et al. (2009) show that the Indian Ocean SST variability is the key driver of hydro-climatic change in south-east Australia since the past 120 years. The STR mostly influences seasonal climate where the position and strength of the STR affects the mid-latitude storm track, which regulates rainfall in southern parts of Australia (Drosdowsky, 2005). Similarly to the Indian Ocean SST variability, the STR has shown to correlate with rainfall variability in south-east Australia (Pittock, 1975; Drosdowsky, 2005). The SAM is associated with large-scale variability of extratropical circulation in the southern hemisphere. The zonally symmetric exchange of mass between mid-latitudes and polar regions govern Australian rainfall variability (Thompson and Wallace, 2000). During high phases of SAM, winter rainfall in south-east Australia declines and summer rainfall increases (Hendon et al., 2007). The Madden-Julian Oscillation, also known as the 30-60-day wave, is an eastward propagating area of increased tropical convection, which has shown to affect rainfall over Australia (Murphy and Timbal, 2008). However, its effect on rainfall in south-east Australia is minor and only occurs in selected areas and some seasons (Murphy and Timbal, 2008).

4.2 Present climate of the Riverina and Murrumbidgee River catchment

Climate of the Riverina and Murrumbidgee River catchment lies within 1) the seasonally uniform climate zone, where rainfall rates do not vary significantly throughout the year and 2) the climate zone characterised with higher rainfall during winter. The upper Murrumbidgee River catchment is encompassing alpine climate in the Snowy Mountains, where cool to cold weather prevails all year, with snowfall during winter. In contrast, the lower catchment exhibits warm temperatures during summer, mild temperatures during winter and relatively constant rainfall throughout the year. Seasonal temperature variations are only little across the Riverina (Eardley, 2001). Figure 34 shows the average annual temperature for the Murrumbidgee River catchment and the Riverina (NSW) over the time period 1961-1990.

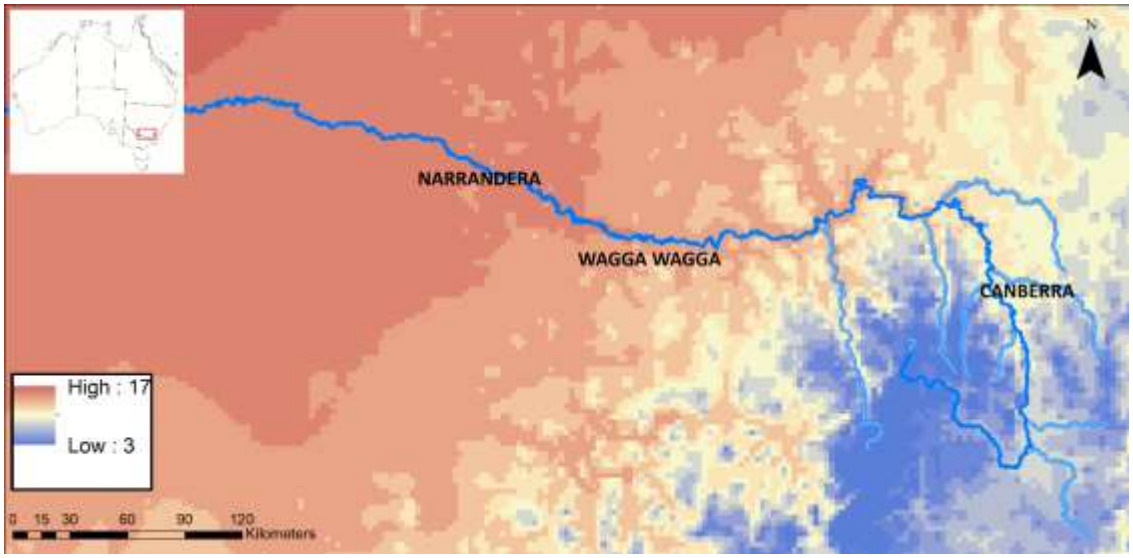

Figure 34: Average annual temperature for the Murrumbidgee River catchment and the Riverina (NSW) based on a standard 30-year climatology (1961-1990). Source: (BOM, 2017). Temperatures are given in degrees Celsius. Insert top left: map of Australia, red rectangle marks the Murrumbidgee River catchment and Riverine Plain.

The upper catchment of the Murrumbidgee River, south-west of Canberra, reaches an annual average of 3-6°C, whereas the Riverina, west of Wagga Wagga is with an annual average of 15-17°C much warmer. Highest annual rainfall is observed in the upper catchment, with a maximum average of 2,000 mm per year (Figure 35). The lower catchment and the Riverina receives the least rainfall between 600 and 400 mm per year.

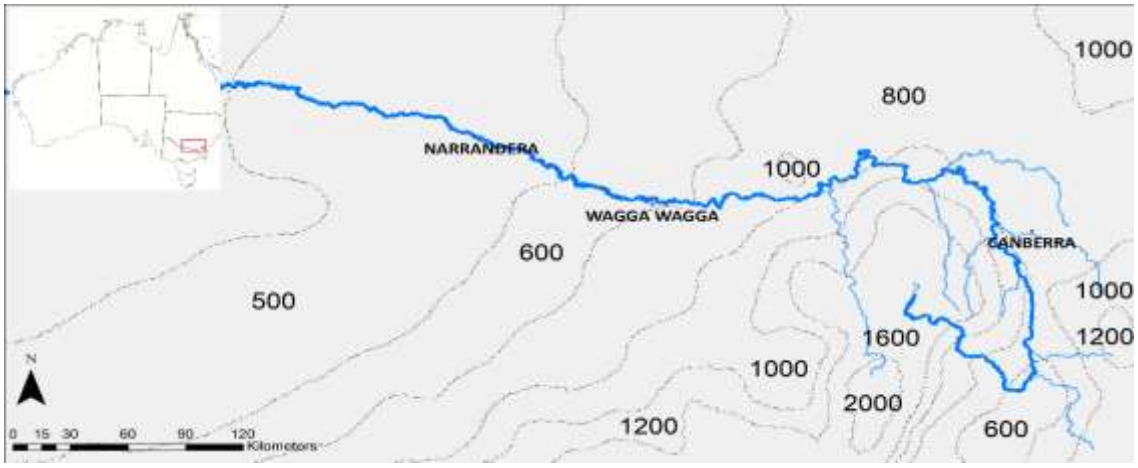

Figure 35: Average annual rainfall for the Murrumbidgee River catchment and the Riverina (NSW) based on a standard 30-year climatology (1961-1990). Source: (BOM, 2017). Rainfall rates are given in millimetres per year. Insert top left: map of Australia, red rectangle marks the Murrumbidgee River catchment and Riverine Plain.

4.3 Australian climate over the last glacial cycle

First attempts to reconstruct the Australian climate over the last glacial cycle began in the mid 1920's. Taylor (1926) proposed that the mean temperature in south-east Australia during the last glacial must have been 4°C lower than today's. Other sources suggested it was ~7 to 9°C colder during the maximum glaciation (Keble, 1947; Browne, 1957; Galloway, 1965). Evidence for these past lower temperature estimates were based on qualitative landscape observations, such as periglacial deposits. Most of the Australian continent is not affected by periglaciation associated with past colder climates. However, at high altitudes in south-east Australia, e.g. the Snowy Mountains, frost action and periglacial movements take place today. The occurrence of widespread periglacial deposits all around south-eastern Australia has therefore led to infer that temperatures during the last glaciation were much colder than today (Galloway, 1965). However, because these historical palaeo-climate reconstructions were solely based on landscape observations, they are only qualitative and subject to significant uncertainties.

Only with the emergence of more quantitative climate proxies such as oxygen isotopes ($\delta^{18}O$), a picture of the past climate could be reconstructed. Oxygen isotope composition is typically reported as deviation from an isotopic standard following the δ-notation:

$$\delta^{18}O = \left(\frac{\left(\frac{^{18}O}{^{16}O}\right)_{sample}}{\left(\frac{^{18}O}{^{16}O}\right)_{standard}} - 1 \right) * 1000 \qquad (21)$$

The oxygen isotope composition of marine carbonates reflects changes in temperature. Most of the oxygen-isotope based climate reconstructions were undertaken in the Northern Hemisphere. This is mainly because of the larger landmass in the Northern hemisphere, the availability of suitable study sites (Jones et al., 2001), but also because less research has been undertaken in the southern hemisphere. Therefore, only few climate archives exist that mirror the past climate of the southern Hemisphere. The geographically closest deep-sea oxygen isotope record to Australia was taken several hundred kilometres south of the Solomon Islands, at equatorial latitudes (Shackleton and Opdyke, 1973). The climate of the Southern Hemisphere over the last glacial cycle can

be subdivided into five major phases, which are commonly referred to as oxygen isotope stages (OIS) (Figure 36).

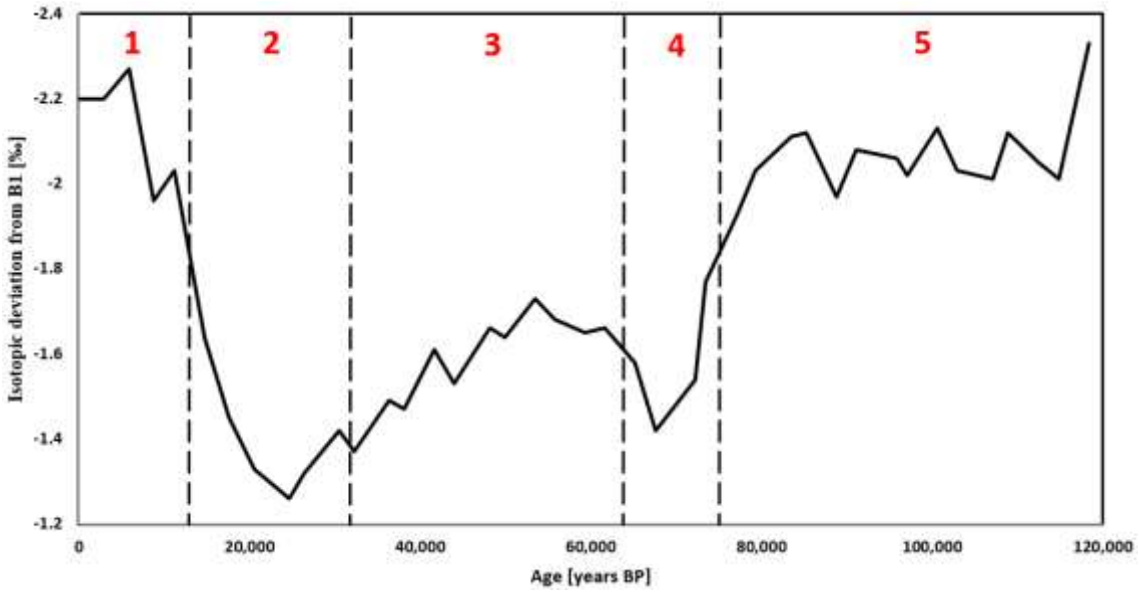

Figure 36: Oxygen isotope composition of G. sacculifera from deep-sea sediment core V28-238 (Shackleton and Opdyke, 1973). Isotope data are reported as deviation from Emiliani B1 standard in ‰. Dashed lines mark the borders between oxygen isotope stages (red font). For more details see Shackleton and Opdyke (1973). Uncertainty of measurements is oxygen isotope measurements 0.14 ‰ (2σ).

OIS 1 and 5 show similar oxygen isotope compositions, implying that mean annual temperatures 120,000 – 75,000 years ago, were close to that of the present. Temperatures during interglacial OIS 3 were lower than during OIS 1 and 5, but higher than during glacial phases OIS 2 and 4. While oxygen isotope data give a good indication of the general climate trend over the last glacial cycle in the southern Hemisphere, the climate evolution on continents is extremely complex and does not necessarily mirror that what is recorded in the oceans. Therefore, terrestrial climate archives are necessary as a complementary palaeo climate reconstruction.

An example for such an archive is the pollen record from Lynch's crater in north Queensland, Australia (Kershaw, 1986), which shows that rainfall patterns in north-east Australia over the last glacial cycle co-vary with the oxygen isotope curve from Shackleton and Opdyke (1973) (Figure 37).

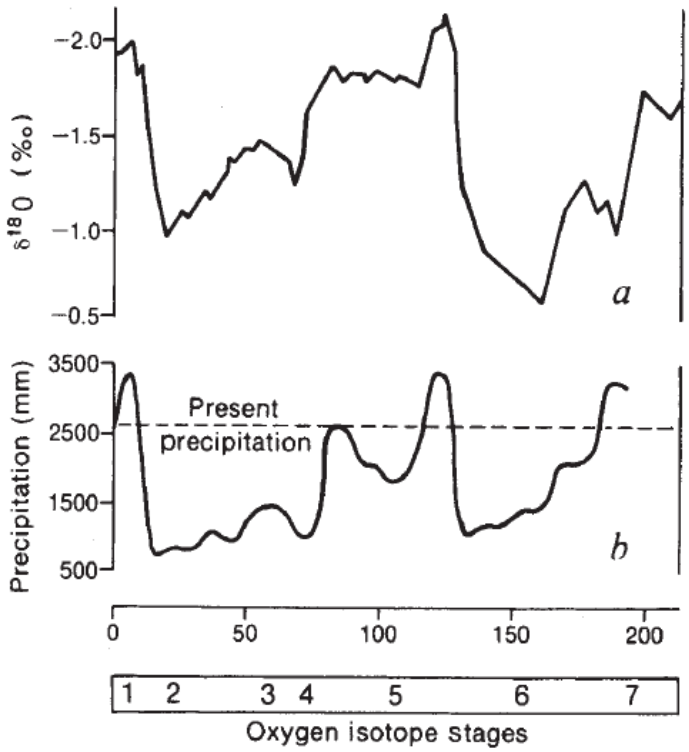

Figure 37: a) Oxygen isotope record from deep-sea core V28-238 (Shackleton and Opdyke, 1973) compared to b) pollen-based annual rainfall reconstruction for Lynch's Crater (Kershaw, 1986). X-axis is the age in kilo years.

In detail, the pollen record provides evidence for high levels of rainfall at present (2,600 mm), relatively low annual rainfall throughout oxygen isotope stages 2 to 4 (600-1,500 mm), and variable but high rainfall during stage 5 (1,800-2,500 mm). OIS 2 displays the lowest precipitation rates, followed by OIS 3 and 4 (Figure 37). These results demonstrate that the terrestrial climate of north-eastern Australian is linked to that of the equatorial region.

However, because the climate of north-eastern Australia is mainly controlled by monsoon (see Section 0), these findings may not reflect the climate conditions of south-east Australia, where the study site of this PhD project is located. Therefore, the local climate variability with emphasis on past fluvial activity in the Murrumbidgee River catchment is discussed in the following sections.

4.3.1 South-east Australian climate over the last glacial cycle

Page et al. (1996) investigated the Murrumbidgee catchment and the Riverine Plain (south-east Australia) in detail and showed how palaeo rivers responded to climate

variability over the last glacial cycle. Based on stratigraphic data, palaeo river dynamics during individual oxygen isotope stages, as defined by Shackleton and Opdyke (1973), were estimated and flow conditions were reconstructed. The authors identified four major palaeochannel episodes, which they could link to the proposed oxygen isotope stages: The Coleambally phase (105-80 ka), Kerarbury (55-35 ka), Gum Creek (35-25 ka), and Yanco (20-13 ka). The Coleambally phase was active during the mid- to later part of OIS 5, Kerarbury during OIS 3, Gum Creek during late OIS 3 to early OIS 2, and Yanco during late OIS 2 (Figure 38).

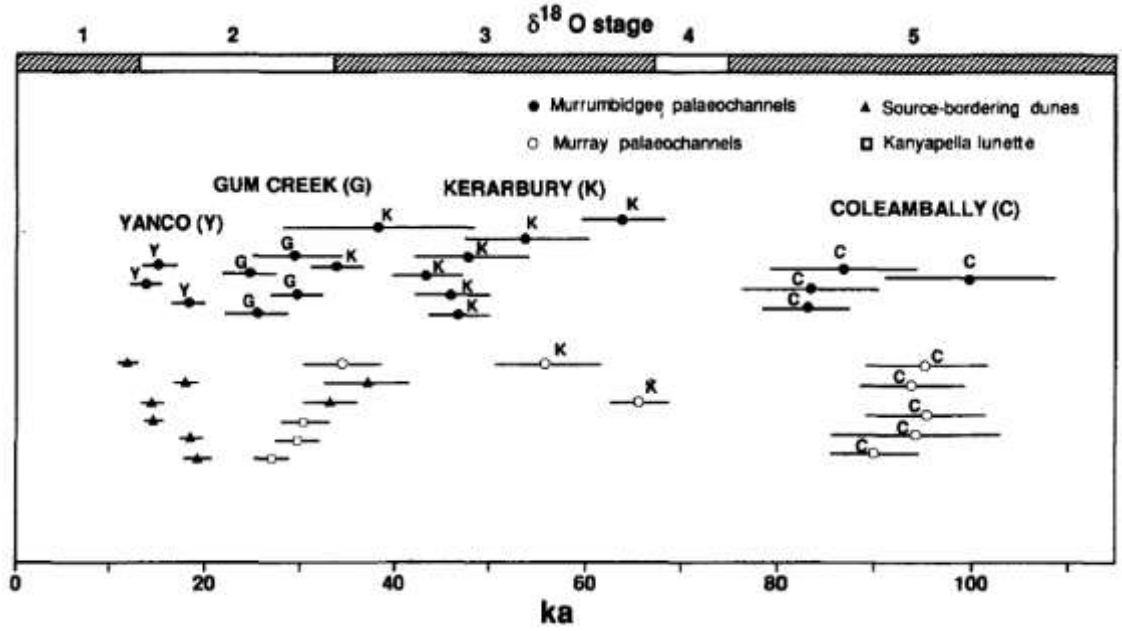

Figure 38: Palaeo channel systems and their activity in the Riverine Plain, south-east Australia (Page et al., 1996). Data derived from Page et al. (1991); Page et al. (1994). Oxygen isotope stages defined by Shackleton and Opdyke (1973) and revised by Martinson et al. (1987).

Climate conditions in south-east Australia, with focus on the Murrumbidgee River catchment, during individual oxygen isotope stages are characterised in the following sections.

OIS 5

Palaeo rivers from the Murrumbidgee showed enhanced fluvial activity during OIS 5. The palaeo discharge ratio was estimated to be between 4.8-5.6 when compared to present (Schumm, 1968; Page and Nanson, 1996). Similar results were obtained from a lacustrine record from Lake Frome and Lake Eyre, in the southern latitudes of central Australia,

where during mid-late OIS 5, the lake level was significantly high (Magee et al., 2004; Cohen et al., 2011). Both accelerated fluvial activity and high lake level stands suggest a much wetter climate during OIS 5 than at present. This is also evident through a precipitation from Naracoorte caves (south eastern Australia), which shows that annual rainfall was high during OIS 5, possibly linked to the strengthening of the Walker circulation (Ayliffe et al., 1998).

OIS 4

None of the investigated palaeo-channel deposits by Page et al. (1996) covered the timing of the relatively short-lived OIS 4. The authors explain the absence of stage 4 in the sedimentary record by a considerably reduced fluvial activity. This would suggest arid conditions in the Riverine Plain between 80-55 ka. The Vostok ice core from Antarctica (Petit et al., 1990) displays a major dust peak between ~80-55 ka, confirming widespread dry conditions during OIS 4. Interestingly, lacustrine records indicate high lake levels during stage 4, similar to that of OIS 5 (Magee et al., 2004; Cohen et al., 2011), which is contradictory to the theory of a dry OIS 4. At the onset of stage 4, pollen data from the Caledonia Fen in the south-eastern highlands of Australia show a slight increase in Chenopodiaceae, which is generally indicative of dry conditions (Kershaw et al., 2007). Nevertheless, this pollen assemblage is variable throughout stage 4, which could imply that aridity in south-east Australia was not a consistent feature of this glacial period. Studies have shown that In the alpine areas of Victoria and NSW, lower temperatures allowed the accumulation of ice and the expansion of periglacial zone at altitudes above 1,000 m (Barrows et al., 2001; Barrows et al., 2004).

OIS 3

Similar to OIS 5, stage 3 was characterised with more than eight times the bankfull discharges on the Riverine Plain compared to present (Schumm, 1968; Page and Nanson, 1996). This was due to high rainfall and reduced evaporation under cool conditions (Galloway, 1965; Bowler and Wasson, 1984). Pollen records agree with this climate interpretation and show that during OIS 3, continental Australia exhibited cool and moist conditions with widespread woodland and forest vegetation (Kershaw and Nanson, 1993). Large permanent lakes existed in inland Australia and in southern latitudes (Bowler and Wasson, 1984; Cohen et al., 2011; Bowler et al., 2012; Cohen et al., 2012). During late OIS 3, fluvial activity reached its maximum over the past 100 ka, both in the northern (Nanson et al., 2008; Veth et al., 2009) and southern parts of the Australian continent,

particularly in south-east Australia (Bowler and Wasson, 1984; Page et al., 1996; Page and Nanson, 1996; Kemp and Rhodes, 2010). Snow occurrence in the Snowy Mountains during OIS 3 grew significantly larger and the presence of enlarged snow mass in the upper Murrumbidgee catchment suggests a strong seasonal flow regime with flood peaks during spring, caused by snow melting. These floods caused accelerated erosion, evident through an increased production of coarse bedload sediments as a result of more intense physical weathering in the upper Murrumbidgee catchment (Galloway, 1965; Davies, 1969).

OIS 2

While most climate models for Australia suggest generally arid conditions during OIS 2 (Shackleton and Opdyke, 1973; Kershaw, 1986; Petit et al., 1990). Murrumbidgee palaeo-rivers during the Gum Creek and Yanco phase show enhanced fluvial activity, with an intermittent dry phase between 25 and 20 ka (Page et al., 1996). Water level reconstructions at lakes Urana and Cullivel (in the Riverine Plain) support this finding, where high water levels were found between 20 and 12 ka, and 30 and 25 ka (Page et al., 1994). OIS 2 includes the last glacial maximum (LGM), which in Australia was proposed to have been around 18.5 ka or 22k a (Petit et al., 1990; Colhoun, 1991; Kershaw and Nanson, 1993). Palaeo-river deposits covering the LGM were not found and Page et al. (1996) suggest that this is due to a significantly reduced fluvial activity associated with a brief period of aridity. A relatively wet OIS 2 was also recorded in a palynological record from the Caledonia Fan (SE Australia), which showed only little evidence for aridity between 30 and 11 ka (Kershaw et al., 2007).

OIS 1 (Holocene)

While the early Holocene in most parts of coastal Australia is marked by warmer and wetter conditions, fluvial activity in the Riverine Plain reached its minimum over the last glacial cycle (Schumm, 1968; Page et al., 1996; Page and Nanson, 1996). This is likely to have been the cause of a southerly migration of the westerly wind belt, which restricted moisture availability west of the Great Dividing Range (Reeves et al., 2013). During the Holocene, the last remnants of glaciers in the highlands of south-east Australia disappeared and the alpine environment was once again covered by vegetation (Martin, 1986; Page et al., 1996). Interestingly, the pollen record of the Caledonia Fan (Kershaw, 1986) shows that annual precipitation during OIS 1 was comparable to that of OIS 5. Lacustrine records of southern inland Australia showed occasional lake-filling episodes,

but lake water volumes were significantly smaller when compared to previous oxygen isotope stages (Magee et al., 2004; Cohen et al., 2011).

Summary

For most of the last glacial cycle, rivers of the Riverine Plain were significantly more active with bankfull discharges up to 11-fold than at present (Schumm, 1968; Page and Nanson, 1996; Kemp and Rhodes, 2010), implying generally wetter conditions. Lacustrine records from northern and southern latitudes of Australia show a gradual decrease in lake level stands from OIS 5 to OIS 1, suggesting that southern Australia became progressively more arid over the last glacial cycle (Magee et al., 2004; Cohen et al., 2011). There is strong indication for a much wetter climate in south-east Australia during OIS 5 and 3, evident by significantly larger and more active river channel systems (Schumm, 1968; Page et al., 1996; Page and Nanson, 1996). Climate conditions during OIS 4 are somewhat contradictory. Page et al. (1996) propose that during OIS 4, fluvial activity in the Riverine Plain was limited due to dry conditions. In other regions of south-east Australia, studies report substantial water-supply, comparable to OIS 5 (Magee et al., 2004; Cohen et al., 2011). In contrast to climate reconstructions for most parts of Australia, south-east Australia experienced mostly wet conditions during OIS 2, evident through enhanced fluvial activity in the Murrumbidgee area. Briefly reduced fluvial activity must have persisted during the LGM, where dry conditions prevailed between 18.5 – 22 ka (Page et al., 1996). While temperature and precipitation increased in most parts of Australia during OIS 1, fluvial activity in the Murrumbidgee was significantly lower than during previous oxygen isotope stages, indicating that in the Riverine Plain, dry conditions persisted throughout OIS 1 (Page et al., 1996).

References

Allan, R. J. 1985. *The Australasian summer monsoon, teleconnections, and flooding in the Lake Eyre basin*, Royal Geographical Society of Australasia, SA Branch, pp.

Ayliffe, L. K., Marianelli, P. C., Moriarty, K. C., Wells, R. T., Mcculloch, M. T., Mortimer, G. E. & Hellstrom, J. C. 1998. 500 ka precipitation record from southeastern Australia: evidence for interglacial relative aridity. *Geology,* 26**,** 147-150.

Barrows, T. T., Stone, J. O., Fifield, L. K. & Cresswell, R. G. 2001. Late Pleistocene glaciation of the Kosciuszko massif, snowy mountains, Australia. *Quaternary Research,* 55**,** 179-189.

Barrows, T. T., Stone, J. O. & Fifield, L. K. 2004. Exposure ages for Pleistocene periglacial deposits in Australia. *Quaternary Science Reviews,* 23**,** 697-708.

Bom. 2017. *Average daily mean temperature Annual* [Online]. Available: http://www.bom.gov.au/jsp/ncc/climate_averages/temperature/index.jsp?maptype=6&period=an#maps [Accessed 31. August 2017].

Bowler, J. & Wasson, R. 1984. Glacial age environments of inland Australia. *Late Cainozoic palaeoclimates of the southern hemisphere***,** 183-208.

Bowler, J. M., Gillespie, R., Johnston, H. & Boljkovac, K. 2012. Wind v water: Glacial maximum records from the Willandra Lakes. *Peopled Landscapes: Archaeological and Biogeographic Approaches to Landscapes. Terra Australis,* 34**,** 271e296.

Browne, W. 1957. Pleistocene glaciation in the Commonwealth of Australia. *Journal of Glaciology,* 3**,** 111-115.

Cohen, T., Nanson, G., Jansen, J. D., Jones, B., Jacobs, Z., Larsen, J., May, J.-H., Treble, P., Price, D. & Smith, A. 2012. Late Quaternary mega-lakes fed by the northern and southern river systems of central Australia: varying moisture sources and increased continental aridity. *Palaeogeography, Palaeoclimatology, Palaeoecology,* 356**,** 89-108.

Cohen, T. J., Nanson, G. C., Jansen, J. D., Jones, B. G., Jacobs, Z., Treble, P., Price, D. M., May, J.-H., Smith, A. M. & Ayliffe, L. K. 2011. Continental aridification and the vanishing of Australia's megalakes. *Geology,* 39**,** 167-170.

Colhoun, E. A. 1991. *Climate During the Last Glacial Maximum in Australia and New Guinea: evidence inferred from biogeographical and geomorphological data,* Australian and New Zealand Geomorphology Group, pp.

Davies, J. L. 1969. Landforms of cold climates.

Donald, A., Meinke, H., Power, B., Maia, A. D. H., Wheeler, M. C., White, N., Stone, R. C. & Ribbe, J. 2006. Near-global impact of the Madden-Julian Oscillation on rainfall. *Geophysical Research Letters,* 33.

Drosdowsky, W. & Chambers, L. E. 2001. Near-global sea surface temperature anomalies as predictors of Australian seasonal rainfall. *Journal of Climate,* 14**,** 1677-1687.

Drosdowsky, W. 2005. The latitude of the subtropical ridge over eastern Australia: The L index revisited. *International Journal of Climatology,* 25**,** 1291-1299.

Eardley, K. A. 2001. *A foundation for conservation in the Riverina Bioregion,* NSW National Parks and Wildlife Service, pp.

Galloway, R. 1965. Late quaternary climates in Australia. *The Journal of Geology,* 73**,** 603-618.

Gimeno, L., Drumond, A., Nieto, R., Trigo, R. M. & Stohl, A. 2010. On the origin of continental precipitation. *Geophysical Research Letters,* 37.

Harrison, S. P. 1993. Late Quaternary lake-level changes and climates of Australia. *Quaternary Science Reviews,* 12**,** 211-231.

Hendon, H. H., Thompson, D. W. & Wheeler, M. C. 2007. Australian rainfall and surface temperature variations associated with the Southern Hemisphere annular mode. *Journal of Climate,* 20**,** 2452-2467.

Jones, D. A. & Trewin, B. C. 2000. On the relationships between the El Niño–Southern Oscillation and Australian land surface temperature. *International Journal of Climatology,* 20**,** 697-719.

Jones, P., Osborn, T. & Briffa, K. 2001. The evolution of climate over the last millennium. *Science,* 292**,** 662-667.

Keble, R. 1947. *Notes on Australian Quaternary climates and migration,* National Museum, pp.

Kemp, J. & Rhodes, E. 2010. Episodic fluvial activity of inland rivers in southeastern Australia: palaeochannel systems and terraces of the Lachlan River. *Quaternary Science Reviews,* 29**,** 732-752.

Kershaw, A. P. 1986. Climatic change and Aboriginal burning in north-east Australia during the last two glacial/interglacial cycles. *Nature,* 322**,** 47-49.

Kershaw, A. P. & Nanson, G. 1993. The last full glacial cycle in the Australian region. *Global and Planetary Change,* 7**,** 1-9.

Kershaw, A. P., Mckenzie, G., Porch, N., Roberts, R., Brown, J., Heijnis, H., Orr, M., Jacobsen, G. & Newall, P. 2007. A high-resolution record of vegetation and climate through the last glacial cycle from Caledonia Fen, southeastern highlands of Australia. *Journal of Quaternary Science,* 22**,** 481-500.

Magee, J. W., Miller, G. H., Spooner, N. A. & Questiaux, D. 2004. Continuous 150 ky monsoon record from Lake Eyre, Australia: insolation-forcing implications and unexpected Holocene failure. *Geology,* 32**,** 885-888.

Martin, A. 1986. Late glacial and early Holocene vegetation of the alpine zone, Kosciusko National Park. *Flora and fauna of alpine Australasia, ages and origins***,** 161-172.

Martinson, D. G., Pisias, N. G., Hays, J. D., Imbrie, J., Moore, T. C. & Shackleton, N. J. 1987. Age dating and the orbital theory of the ice ages: development of a high-resolution 0 to 300,000-year chronostratigraphy. *Quaternary research,* 27**,** 1-29.

Mcbride, J. L. & Nicholls, N. 1983. Seasonal relationships between Australian rainfall and the Southern Oscillation. *Monthly Weather Review,* 111**,** 1998-2004.

Meneghini, B., Simmonds, I. & Smith, I. N. 2007. Association between Australian rainfall and the southern annular mode. *International Journal of Climatology,* 27**,** 109-121.

Murphy, B. F. & Timbal, B. 2008. A review of recent climate variability and climate change in southeastern Australia. *International journal of Climatology,* 28**,** 859-879.

Nanson, G. C., Price, D. M., Jones, B. G., Maroulis, J. C., Coleman, M., Bowman, H., Cohen, T. J., Pietsch, T. J. & Larsen, J. R. 2008. Alluvial evidence for major climate and flow regime changes during the middle and late Quaternary in eastern central Australia. *Geomorphology,* 101**,** 109-129.

Nicholls, N. 1989. Sea surface temperatures and Australian winter rainfall. *Journal of Climate,* 2**,** 965-973.

Page, K., Nanson, G. & Price, D. 1991. Thermoluminescence chronology of late quaternary deposition on the riverine plain of South-Eastern Australia. *The Australian Geographer,* 22**,** 14-23.

Page, K., Dare-Edwards, A., Nanson, G. & Price, D. 1994. Late Quaternary evolution of Lake Urana, New South Wales, Australia. *Journal of Quaternary Science,* 9**,** 47-57.

Page, K., Nanson, G. & Price, D. 1996. Chronology of Murrumbidgee river palaeochannels on the Riverine Plain, southeastern Australia. *Journal of Quaternary Science,* 11**,** 311-326.

Page, K. & Nanson, G. 1996. Stratigraphic architecture resulting from Late Quaternary evolution of the Riverine Plain, south-eastern Australia. *Sedimentology,* 43**,** 927-945.

Petherick, L., Bostock, H., Cohen, T. J., Fitzsimmons, K., Tibby, J., Fletcher, M.-S., Moss, P., Reeves, J., Mooney, S. & Barrows, T. 2013. Climatic records over the past 30 ka from temperate Australia–a synthesis from the Oz-INTIMATE workgroup. *Quaternary Science Reviews,* 74**,** 58-77.

Petit, J.-R., Mounier, L., Jouzel, J., Korotkevich, Y. S., Kotlyakov, V. & Lorius, C. 1990. Palaeoclimatological and chronological implications of the Vostok core dust record. *Nature,* 343**,** 56.

Pittock, A. 1975. Climatic change and the patterns of variation in Australian rainfall.

Reeves, J. M., Barrows, T. T., Cohen, T. J., Kiem, A. S., Bostock, H. C., Fitzsimmons, K. E., Jansen, J. D., Kemp, J., Krause, C. & Petherick, L. 2013. Climate variability over the last 35,000 years recorded in marine and terrestrial archives in the Australian region: an OZ-INTIMATE compilation. *Quaternary Science Reviews,* 74**,** 21-34.

Rognon, P. & Williams, M. 1977. Late Quaternary climatic changes in Australia and North Africa: a preliminary interpretation. *Palaeogeography, Palaeoclimatology, Palaeoecology,* 21**,** 285-327.

Schumm, S. A. 1968. *River adjustment to altered hydrologic regimen, Murrumbidgee River and paleochannels, Australia,* US Government Printing Office, 598 pp.

Shackleton, N. J. & Opdyke, N. D. 1973. Oxygen isotope and palaeomagnetic stratigraphy of Equatorial Pacific core V28-238: Oxygen isotope temperatures

and ice volumes on a 105 year and 106 year scale. *Quaternary research,* 3**,** 39-55.

Taylor, G. Glaciation in the southwest Pacific. Proceedings of the Third Pan-Pacific Science Congress, 1926. 1819-1825.

Thompson, D. W. & Wallace, J. M. 2000. Annular modes in the extratropical circulation. Part I: Month-to-month variability. *Journal of climate,* 13**,** 1000-1016.

Ummenhofer, C. C., England, M. H., Mcintosh, P. C., Meyers, G. A., Pook, M. J., Risbey, J. S., Gupta, A. S. & Taschetto, A. S. 2009. What causes southeast Australia's worst droughts? *Geophysical Research Letters,* 36.

Veth, P., Smith, M., Bowler, J., Fitzsimmons, K., Williams, A. & Hiscock, P. 2009. Excavations at Parnkupirti, Lake Gregory, great sandy desert: OSL ages for occupation before the last glacial maximum. *Australian Archaeology,* 69**,** 1-10.

5 The Murrumbidgee River Basin & Riverine Plain

The main study area of this PhD project is the Murrumbidgee River Basin. It lies within the Murray-Darling Basin in east south-east Australia. The topographical and geological features of the Murray Darling Basin, with emphasis on the Murrumbidgee River catchment and the Riverine Plain, are described in the following sections.

5.1 Murray Darling Basin

The Murray Darling Basin is located in east south-east Australia and covers 75 % of New South Wales, more than 50 % of Victoria, 15 % of Queensland, 8 % of South Australia and 100 % of the Australian Capital Territory. With an area of over one million km^2, equivalent to 14 % of Australia's total surface area, the basin is considered the 20^{th} largest in the world. It can be divided into a northern and a southern basin (Figure 39) (Geoscience Australia, 2013). Besides the subdivision into northern and southern basin, the Murray Darling Basin can be further divided into individual catchments (Figure 40). In the southern part of the Murray-Darling Basin, west of Canberra, lies the Murrumbidgee River catchment, which is the study area of this PhD project.

Figure 39: The Murray Darling Basin, divided in northern and southern basin. Source: https://www.mdba.gov.au/discover-basin/landscape/geography. Accessed 17th Oct 2017.

Figure 40: Individual catchments within the Murray Darling Basin. Source: https://www.mdba.gov.au/discover-basin/catchments. Accessed 17th Oct 2017.

5.1.1 Geological setting

The Murrumbidgee River Basin and the Riverine Plain are part of the Murray Basin, which formed from tectonism during the separation of Australia from Antarctica (Brown and Stephenson, 1991). Proterozoic and Palaeozoic rocks describe a saucer-shaped intra-cratonic structure and build the basin's margins, which are flanked by low mountain ranges (Page et al., 2009). The eastern border of the Murray Basin is the New England Fold Belt to the north and the Lachlan Fold Belt to the south (Figure 41).

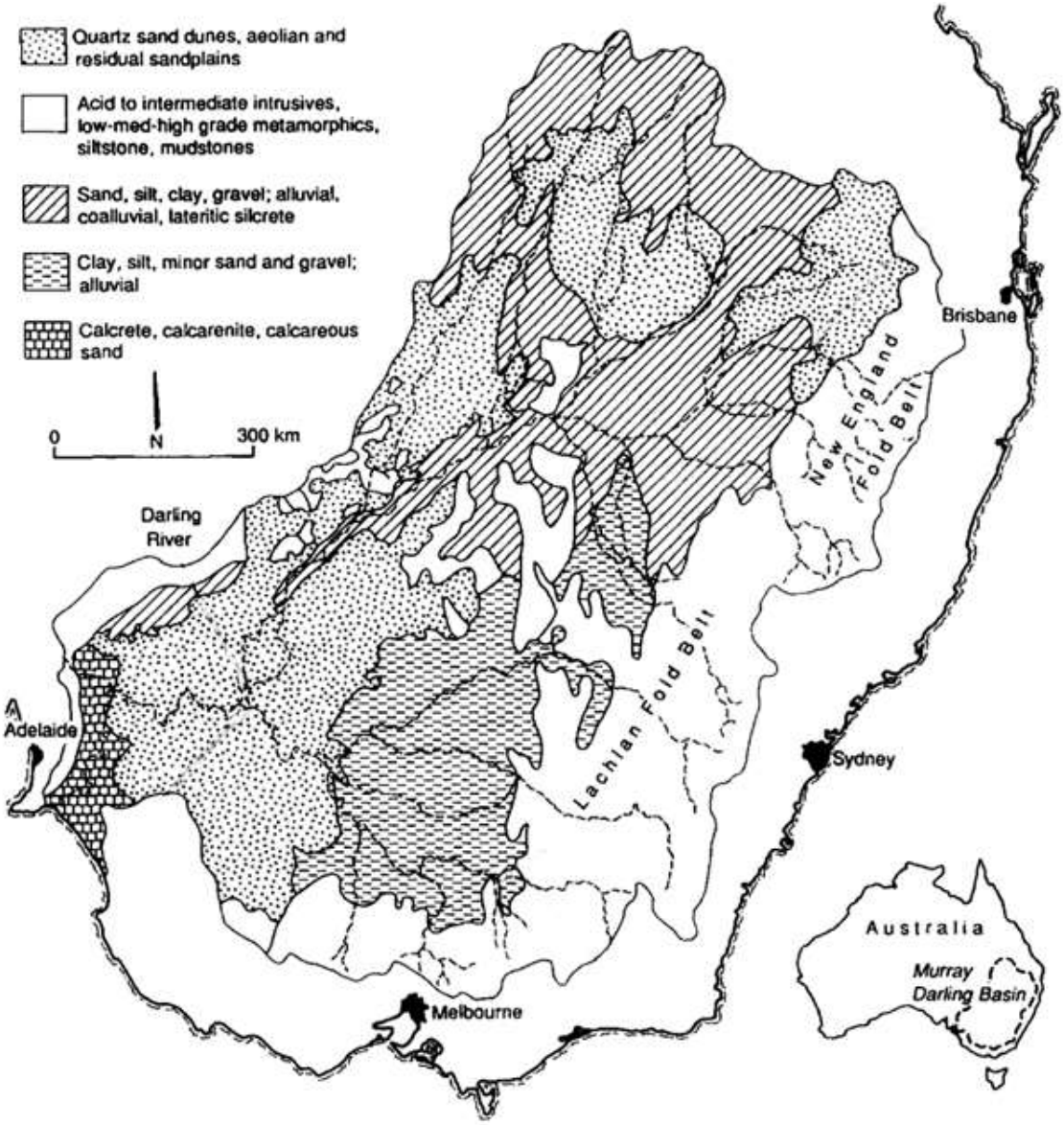

Figure 41: The Murray Darling Basin with simplified geological units. Modified after Douglas et al. (1995).

The basin was formed ~60 million years ago and its sediment fill, with an average of 200 m thickness, is relatively thin (Brown and Stephenson, 1991). Maximum sediment thickness of 500 m is observed in the central western parts of the basin.

5.1.2 Rivers of the Murray Darling Basin

The main rivers of the Murray Darling Basin are the Lachlan, the Murrumbidgee, the Murray, and the Darling River. The Murray, Murrumbidgee, and Lachlan River originate in the highlands of the Australian Alps, also known as the Great Dividing Range (GDR), southwest of Australia's capital Canberra, and flow westwards. The Darling River emerges from the northern part of the Murray Darling Basin (Figure 42).

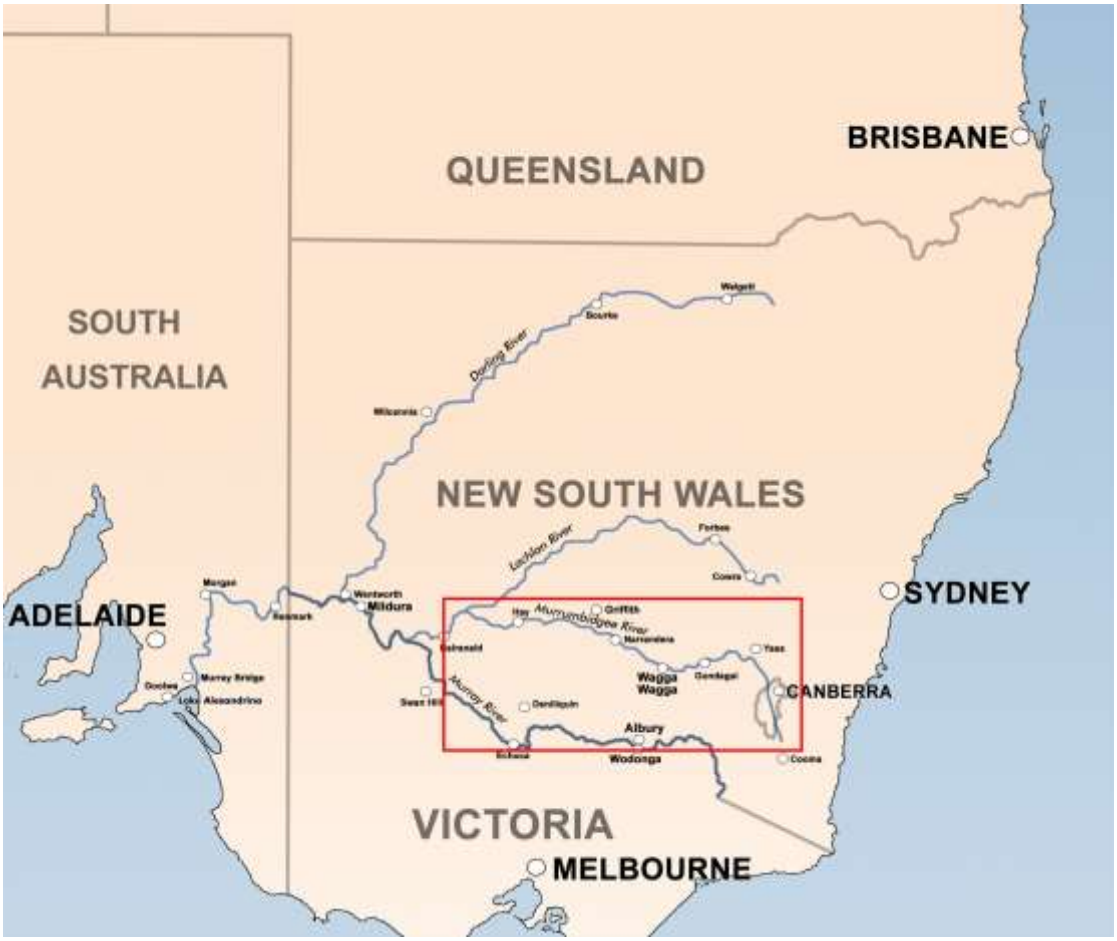

Figure 42: The four main rivers in the Murray Basin. Red rectangle outlines the extent of the study area of this project: The Murrumbidgee River catchment with its upper catchment south-west of Canberra and the Riverine Plain in the west. Source: https://commons.wikimedia.org/wiki/File:Darling_Lachlan_Murrumbidgee_Murray_Rivers.png (accessed 9th Oct 2017)

5.2 Murrumbidgee River

The Murrumbidgee River is with 1,485 km the second longest river in Australia (Geoscience Australia, 2013). It originates in the Australian alps at an elevation of 1,560 m and flows westward and merges with the Lachlan River, a few kilometres west of the town Hay. Further downstream, the Lachlan and Murrumbidgee River confluence with the Murray River. The Murrumbidgee River is bordered by the GDR to the east, the Murray catchment to the south and the Lachlan catchment to the north (Green et al., 2011). The river undergoes diverse climatic environments, from alpine settings in the Snowy Mountains to the east and to semi-arid conditions in the Riverine Plains to the west. Since 1852 and 2010, nine major floods have been recorded. In 1907, a damn was

constructed about 60 km south-west of Yass, which significantly reduced the frequency of flood events (Butcher, 2002). The Murrumbidgee River has close to 100 tributaries, from which 24 can be characterised as rivers and many smaller water bodies such as creeks and gullies. The main tributaries are: Molonglo River, Lachlan River, Gudgenby River, Goodradigbee River, Cotter River, Bredbo River, Yass River, Tumut River, and Numeralla River. Figure 43 shows the present-day flow path of the Murrumbidgee River and its main tributaries (Lachlan River is not shown).

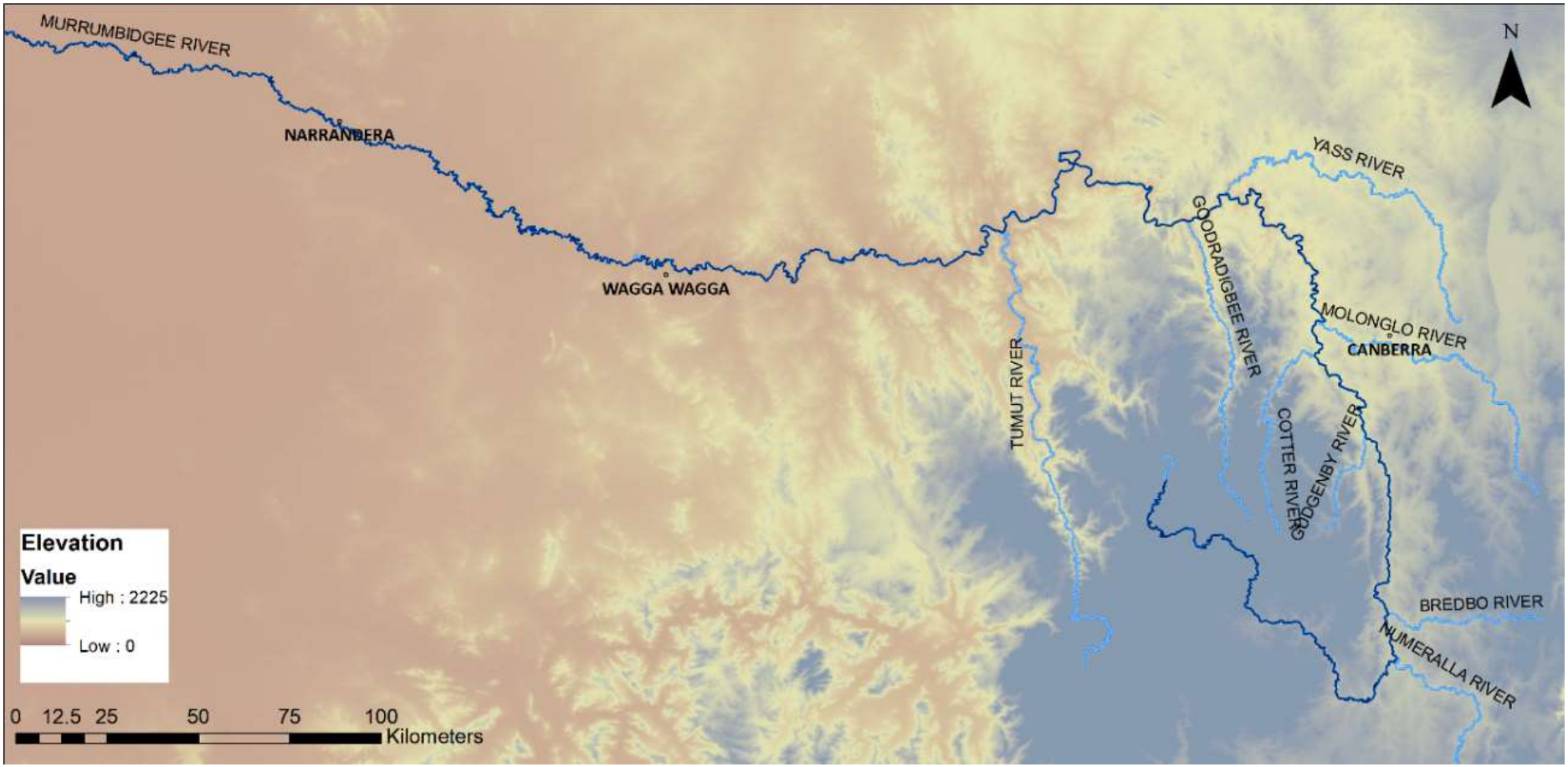

Figure 43: Digital elevation model of the Murrumbidgee River catchment. Murrumbidgee River is shown in dark blue and main tributaries in light blue. This map was created with ArcGIS Desktop Advanced 10.4 software.

5.2.1 Geology of the Murrumbidgee River catchment and Riverine Plain

The Murrumbidgee River catchment and Riverine Plain are geologically part of the Murray Darling Basin (see Section 5.1.1). The upper catchment of the Murrumbidgee River is composed of several distinct lithologies, which includes sandstones, mudstones, slates, felsic and basic volcanics, and granites (Olley and Wasson 2003). Volcanic rocks are concentrated in the northern and eastern parts of the upper Murrumbidgee River catchment, which are intermittent by granodiorite and sedimentary siliclastic rocks. The lower catchment of the Murrumbidgee River, east of Wagga Wagga, is almost entirely dominated by regolith. Regolith are loose layers of heterogenous material covering the solid rock that are composed of broken rocks, dust, and soil. Figure 44 shows a simplified geological map of the Murrumbidgee catchment and the Riverine Plain.

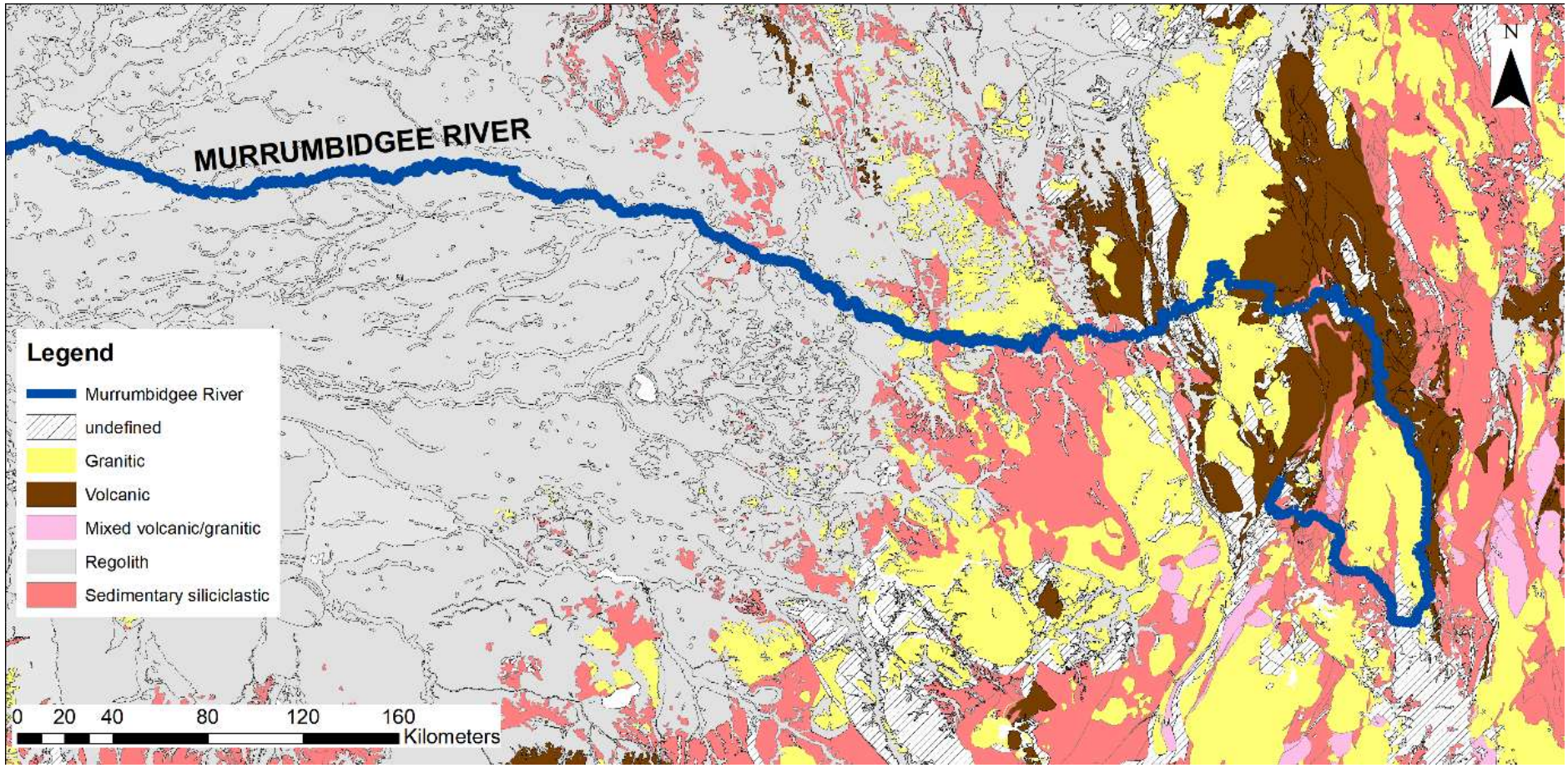

Figure 44: Simplified geological units of the Murrumbidgee River catchment and the Riverine Plain. This map was created with ArcGIS Desktop Advanced 10.4 software.

Another common geological feature of this study area is the presence of Parna, an aeolian clay, which is associated with arid climatic phases during the Quaternary. In contrast to loess, Parna is the erosion product of soils by wind. It's clay content varies from 35 to 70 % (Butler and Hutton, 1956).

5.3 Riverine Plain

The Riverine Plain is located in south-east Australia and is a medium sized alluvial plain, covering an area of 76,800 km^2. It is fed by sediments carried by westward flowing rivers originating in the GDR (Schumm, 1968). Apart from minor tributaries, the main rivers that have formed these fluvial plains are the Murray, Murrumbidgee, Goulburn, and Lachlan River (Butler, 1950). The Riverine plain includes a series of alluvial fans with very gentle slopes and floodplains onto which they merge (Schumm, 1968). About 36 km west of the highlands, few isolated hills exist in the Riverine Plain: Mt Wycherproof (46 m above the Plain), Pyramid Hill (101 m), Mt Terrick Terrick (95 m), Mt Boomanooma (143 m), the Darnick Range (24 m), and Manara Hills (122 m). Over the past 60 million years, the Riverine Plain has accumulated sediments from several different fluvial phases. Unlike the western part of the Murray Darling Basin, the Riverine Plain has not been affected by seawater fluctuations and has only been influenced by terrestrial fluvial activity (Page and Nanson, 1996).

5.3.1 Murrumbidgee palaeo-channels

Aerial photography of the Murrumbidgee River area from the 1940s and 1950s revealed many traces of old, once active, river channels. These palaeo-channels were formed by Pleistocene and Holocene fluvial deposition. Rivers in this region were not significantly affected by tectonic activities and are therefore well preserved. Page et al. (1996) studied the evolution of these palaeo-channels on the Riverine Plain using thermo-luminescence dating techniques (TL). They identified four individual palaeo-channel systems: Coleambally (105-80 ka), Kerarbury (65-35 ka), Gum Creek (35-25 ka), and Yanco (20-13 ka) (Figure 45). It is worth keeping in mind that the dated palaeo-channel infills represent the terminal phase of these ancient rivers.

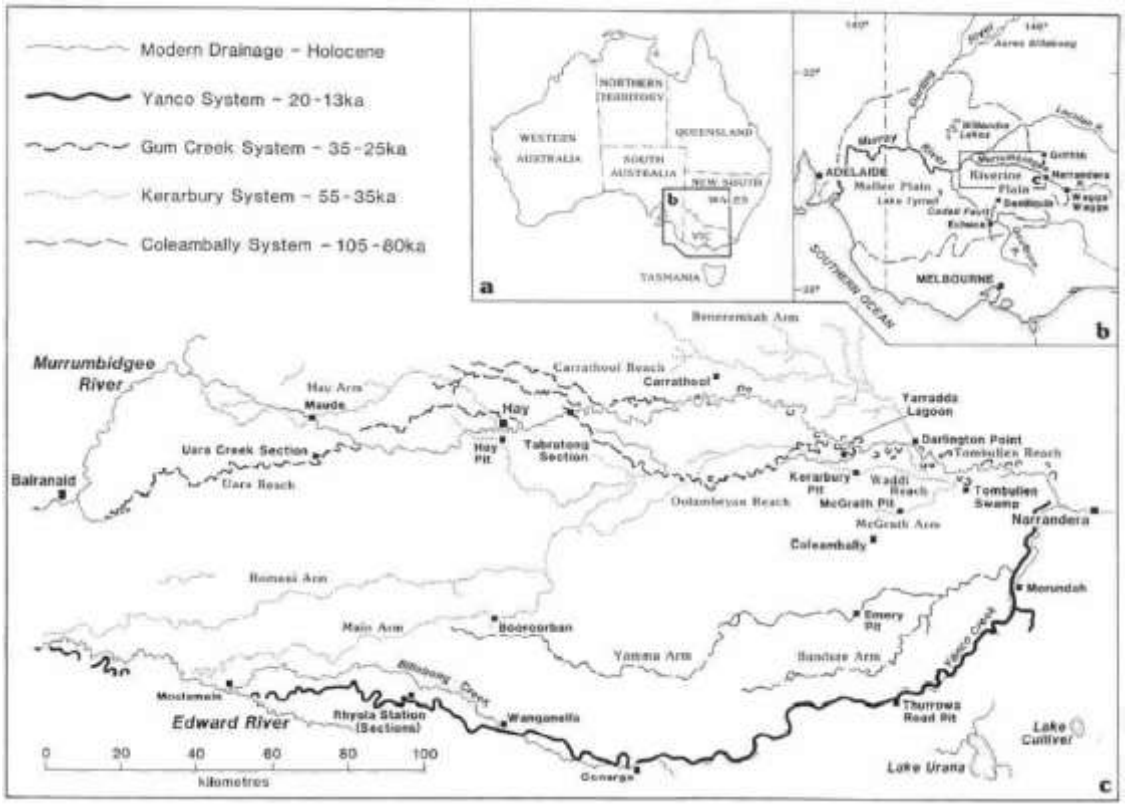

Figure 45: An overview of the Murrumbidgee palaeo-channels. a: map of Australia b: southern extent of the Murray Darling Basin. c: Murrumbidgee palaeo-channel systems and modern drainage. Source: Page and Nanson (1996).

Coleambally palaeo-channel

The oldest palaeo-channel system, Coleambally, was active between 105-80 ka. In the western part, near Morundah, the channel divides itself into two main subsets: Yamma Arm and Bundure Arm (Figure 45). Both flow almost parallel to Yanco Creek, which is located ~10-20 km further south. The Yamma Arm is traceable downstream until Booroorban, whereas Bundure Arm peters out at about half the length of Yamma Arm. Pels (1971) described the surface morphology of these two palaeo-channel arms to have low sinuosity and slightly elevated levee-bordered depressions in the landscape. The east and north of Yamma Arm is characterised with marginal dunes. This feature is missing at Bundure Arm, which suggests that they were not active at the same time. Page et al. (1996) assumed that Bundure Arm is slightly older than Yamma Arm, because the latter is better preserved. They confirmed this by dating at four spatially variable locations using TL techniques. Their results revealed deposition ages from 100.0 ± 9.0 ka to 83.0 ± 4.5 ka. Sediments from the Bundure Arm were among the oldest. Youngest deposition ages were obtained from sediments deposits further downstream, which were extracted by

auger from deposits beneath the overlying Kerarbury palaeo-channel, southwest of Booroorban (Page et al., 1996). Previous studies from the Murray-Goulburn sectors of the Riverine Plain (Page et al., 1991; Page et al., 1994) yielded similar dates for the Coleambally system. It can therefore be assumed that the Coleambally river system was active during OIS 5. The palaeo river discharge was estimated to have been around five-fold compared to present (Schumm, 1968; Page and Nanson, 1996).

Kerarbury palaeo-channel

The Kerarbury system is the second oldest in the Murrumbidgee area that dates back to 55-35 ka. Compared to the Coleambally system, the pathway of Kerarbury is much more complex. It is cut in several places by the overlying deposits of the younger Gum Creek system and the modern Murrumbidgee River. However, the flow direction appears to have maintained a general westward trend. Main distributaries of the Kerarbury system are the Benerembah, Hay, McGrath, and Romani Arms (Figure 45). They bifurcate from the main channel at Tombullen Swap, southeast of Darlington Point. The Benerembah Arm flows to the northwest and is traceable until Carrathool. McGrath is the shortest arm, which branches off to the southwest and peters out a few km north of the town Coleambally. The Hay Arm follows a similar westward trend as the Murrumbidgee River and is found further downstream in the Lowbidgee region. The Romani Arm flows to the southwest where it cuts through the Coleambally system near Booroorban. From there it follows the same general course west, similar to the Coleambally system. Page et al. (1996) suggest that the Kerarbury must have exited the Riverine Plain as the most significant river since the last glacial cycle, with more than eight times the discharge compared to present. The Kerarbury palaeo-channels were TL dated at eight different locations, yielding ages from 63.7 ± 4.1 ka to 33.6 ± 2.5 ka. The oldest age estimations were obtained from sediment deposits near Booroorban, whereas sediments from McGrath Arm yielded younger ages. Since the dated samples, i.e. sandy infills, represent the final activity of the palaeo-channel, it is suggested that the Kerarbury system must have been active between 60 to 55 ka which corresponds to OIS 3 (Page et al., 1996).

Gum Creek palaeo-channel

Large meanders define the shape of the Gum Creek system. It originates at Yarradda Lagoon, west of Darlington Point, and flows westward following the course of the present drainage of the Murrumbidgee River. The meander wavelengths decrease in size further down the floodplain. Channel morphology at the upstream of Yarradda Lagoon indicate

that the Gum Creek's discharge rate must have been four times higher than that of the modern Murrumbidgee River (Page and Nanson, 1996). The Gum Creek system is divided into several sub-channels: Tombullen Reach, Oolambeyan Reach, Carrathool Reach, and Uara Creek Reach. The flow path of the Tombullen Reach was almost parallel to the present drainage. Large meander features can be identified between Wagga and Carrathool. The meander wavelengths are with an average of 2,920 m over 23 palaeo-channel meanders significantly higher than those of the present Murrumbidgee River, which averages only around 750 m. The channel width of Gum Creek was estimated to have been up to four-fold larger compared to present (Page et al., 1996). At the southern margin of the Murrumbidgee floodplain, the Oolambeyan Reach occurs as a large sinuous channel. Its flow direction was south-west and it cuts through channels of the Kerarbury system at several locations, before flowing north-west towards the Murrumbidgee floodplain. The Carrathool Reach is a sinuous channel with low meander wavelengths, which reduce further downstream. Page et al. (1996) proposed that the Oolabeyan and Carrathool Reach might have been active simultaneously, dividing the water discharge from the Tombullen Reach. Uara Creek is the distributary further west, which is characterised by highly variable meander wavelengths, however comparable to the upper stream reaches. Similar to the present Murrumbidgee River, meander wavelengths decline further downstream, where flood peaks must have been infrequent. Sediment deposits from the Gum Creek palaeo-channel system revealed ages from 24.7 ± 2.8 ka to 29.8 ± 2.9 ka. The Gum Creek system can therefore be accounted to parts of OIS 3 & 2. Overall, the preserved physical features of this palaeo-channel system indicate enhanced fluvial activity during its active phase compared to the present Murrumbidgee River.

Yanco palaeo-channel

The Yanco palaeo-channel originates several kilometres west of Narrandera, where it branches south from the modern Murrumbidgee River. Its flow path follows a general south-west to west trend across the plain until Moulamein, where it abruptly disappears. Large meanders can be identified along both higher and upper reaches of the Yanco System. However, the most significant meanders have left their traces in the south-western reaches. Page et al. (1996) estimated the average channel width to have been around 225 m and a meander wavelength of ~3,000 m. The present Murrumbidgee further downstream of Hay is characterised with a channel width of 60 m and 550 m meander wavelength. This indicates that the Yanco phase must have been a significantly more

active river than the present Murrumbidgee River. Page and Nanson (1996) calculated the discharge rate of Yanco to have been 4.5 times that at present. Sediments of the Yanco system were dated from 13.6 ± 1.6 ka to 18.2 ± 1.5 ka. Considering that the dated sediments represent the final phase of the Yanco system, it is likely that this palaeo-channel system was active following the last glacial maximum at ~22 ka (Page et al., 1996).

5.4 Palaeo-channel sedimentation processes

In order to apply chemical weathering proxies on sediment deposits of palaeo-channels, it is crucial to recognise the origin of these sediments and the exact mechanisms that led to the termination of each palaeo-channel. While TL dating of the Murrumbidgee palaeo-channel deposits allows to estimate the time of the final fluvial activity of a palaeo-channel system, the full duration of individual palaeo-rivers remains unclear (Page et al., 1996). Palaeo-channels form when a river channel aggrades and sediment accumulates on its bed. These sediments are typically dominated by coarse sands, which are fining upward (Page and Nanson, 1996). The top of a palaeo-channel consists of a clay layer and an aeolian deposit. The latter can generally be identified through a high concentration of lime (Kemp and Rhodes, 2010). Two types of palaeo-channel deposition mechanics were identified in the Riverine Plain: migrational and an aggradational palaeo-channel depositions (Figure 46).

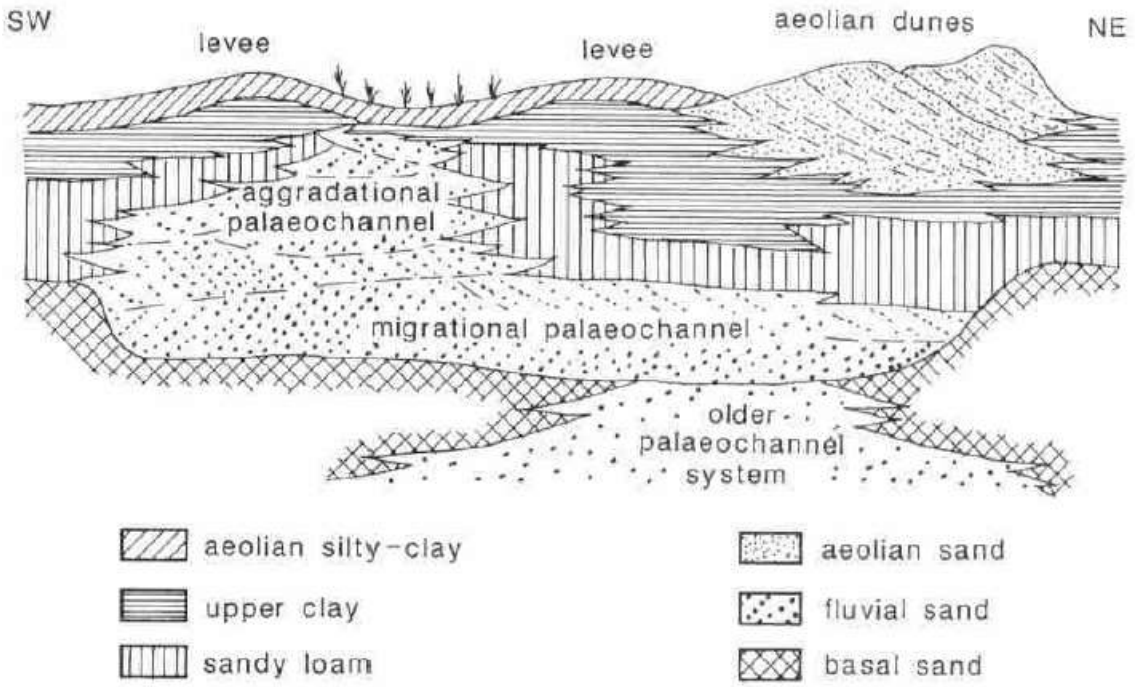

Figure 46: Simplified stratigraphy of Murrumbidgee palaeo-channels. Palaeo-channels may have developed migrational or aggradational. Source: Page and Nanson (1996)

A migrational palaeo-channel is the result of the formation of a sinuous, laterally migrating, mixed-load channel, which exhibits occasional bedload accretion events (Page and Nanson, 1996). Over time and in response to varying fluvial activity, a change in sediment delivery from headwaters causes an accretion of sediments on the plain, which eventually results in the abandonment of a river channel. During flood events or a sequence of floods, where large volumes of coarse sediments erode from the upper catchments, a mixed-load channel may transition into a bedload channel, which forms an aggradational palaeo-channel (Page et al., 1994). Despite the different mechanics of the migrational and aggradational palaeo-channels, both systems can coeval. In terms of age-profile of a palaeo-channel system, channel and floodplain deposits become progressively younger towards the active channel (Kemp and Rhodes, 2010). This means that these sediments are more likely to reflect the later phase of a palaeo-channel.

In summary, sediments of the Murrumbidgee palaeo-channels record the last fluvial activity of a river system. The exact duration of a palaeo-river system is speculative. Because the termination of a palaeo-channel system may be triggered by large flood events, the transported sediment may have originated from an exceptionally large area of the upper stream catchment, which integrated a variety of different weathering regimes.

Therefore, palaeo-channel sediments are likely to derive from a mixed source of the upper catchment.

References

Brown, C. M. & Stephenson, A. E. 1991. *Geology of the Murray Basin, southeastern Australia,* Australian Govt. Pub. Service, pp.

Butcher, A. C. 2002. *Gundagai, a Track Winding Back,* AC Butcher, pp.

Butler, B. 1950. A theory of prior streams as a casual factor of soil occurrence in the Riverine Plain of south-eastern Australia. *Australian Journal of Agricultural Research,* 1**,** 231-252.

Butler, B. & Hutton, J. 1956. Parna in the Riverine Plain of south-eastern Australia and the soils thereon. *Australian Journal of Agricultural Research,* 7**,** 536-553.

Douglas, G., Gray, C., Hart, B. & Beckett, R. 1995. A strontium isotopic investigation of the origin of suspended particulate matter (SPM) in the Murray-Darling River system, Australia. *Geochimica et Cosmochimica Acta,* 59**,** 3799-3815.

Geoscience_Australia. 2013. *Longest Rivers* [Online]. Geoscience Australia: Geoscience Australia. Available: http://www.ga.gov.au/scientific-topics/national-location-information/landforms/longest-rivers#heading-1 [Accessed 6 Oct 2017].

Green, D., Petrovic, J., Moss, P. & Burrell, M. 2011. Water resources and management overview: Murrumbidgee catchment. *NSW Office of Water, Sydney*.

Kemp, J. & Rhodes, E. 2010. Episodic fluvial activity of inland rivers in southeastern Australia: palaeochannel systems and terraces of the Lachlan River. *Quaternary Science Reviews,* 29**,** 732-752.

Page, K., Nanson, G. & Price, D. 1991. Thermoluminescence chronology of late quaternary deposition on the riverine plain of South-Eastern Australia. *The Australian Geographer,* 22**,** 14-23.

Page, K., Dare-Edwards, A., Nanson, G. & Price, D. 1994. Late Quaternary evolution of Lake Urana, New South Wales, Australia. *Journal of Quaternary Science,* 9**,** 47-57.

Page, K. & Nanson, G. 1996. Stratigraphic architecture resulting from Late Quaternary evolution of the Riverine Plain, south-eastern Australia. *Sedimentology,* 43**,** 927-945.

Page, K., Nanson, G. & Price, D. 1996. Chronology of Murrumbidgee river palaeochannels on the Riverine Plain, southeastern Australia. *Journal of Quaternary Science,* 11**,** 311-326.

Page, K., Kemp, J. & Nanson, G. C. 2009. Late Quaternary evolution of riverine plain paleochannels, southeastern Australia. *Australian Journal of Earth Sciences,* 56**,** S19-S33.

Pels, S. 1971. River systems and climatic changes in southeastern Australia. *Aboriginal man and environment in Australia***,** 38-46.

Schumm, S. A. 1968. *River adjustment to altered hydrologic regimen, Murrumbidgee River and paleochannels, Australia,* US Government Printing Office, 598 pp.

6 Methods and study sites

This chapter outlines the different methods applied for the three studies conducted during this PhD project: present weathering conditions in the Murrumbidgee River Basin, palaeo-weathering conditions in the Murrumbidgee Basin, and soil development during the Holocene at Lake Dojran (Greece/FYROM) in response to climate change and human impact. Samples for the Murrumbidgee River project were collected during three field campaigns: December 2014, March 2016, and September 2016. Palaeo-channel sediments were sampled in August 2015. Samples for the Lake Dojran project were provided by Alexander Francke (University of Cologne) in 2015.

6.1 Murrumbidgee River

In order to construct an accurate representation of the present weathering regime of the Murrumbidgee River catchment, a large quantity of samples was collected from upper and lower catchments and from monolithologic catchments. Three types of samples were collected: bedrock, river sediments, and river waters. Sediments and waters were collected from the Murrumbidgee River, main tributaries, and from rivers draining through monolithologic catchments. One bedrock sample was collected from each main lithology (granodiorite, volcanic, sedimentary siliclastic). Photographs of each sample site can be found in Section 6.4.

6.1.1 Sediments

Sediments were collected from river banks of the Murrumbidgee River, main tributaries, and monolithologic catchments. Table 2 shows the GPS locations of individual samples. Figure 47 and Figure 48 show an overview of sample positions in the Murrumbidgee River Basin relative to a digital elevation model and bedrock lithology, respectively.

Table 2: GPS locations of sediment samples collected in the Murrumbidgee River Basin.

Sample ID	GPS position (decimal degrees WGS84)
Murrumbidgee #01	-35.627320° 148.581300°
Murrumbidgee #03 Tantangara	-35.797672° 148.668375°
Murrumbidgee #05	-35.980572° 148.840150°
Murrumbidgee #06	-36.170375° 149.091106°
Murrumbidgee #08	-36.085131° 149.134064°
Murrumbidgee #10 Spring Valley Creek	-35.047870° 148.144400°
Murrumbidgee #12	-35.582942° 149.108956°
Murrumbidgee #13 at Tharwa	-35.508539° 149.070758°
Murrumbidgee after Cotter River	-35.323092° 148.950130°
Murrumbidgee before Tumut (9A/B, 2014)	-34.991310° 148.223590°
Murrumbidgee #20 at Jugiong	-34.824707° 148.332066°
Murrumbidgee at Gundagai	-35.074339° 148.105496°
Murrumbidgee #22 (before Yass)	-35.004330° 148.849210°
Murrumbidgee at Wagga	-35.099282° 147.367875°
Murrumbidgee at Narrandera	-34.759465° 146.536123°
Murrumbidgee before Hay	-34.466981° 145.441435°
Granodiorite catchment A at Cunningham creek	-34.688068° 148.430413°
Granodiorite catchment C Adjungbilly creek	-35.021750° 148.230690°
Granodiorite catchment F	-35.428520° 147.927890°
Granodiorite Back creek near Adaminaby	-35.977255° 148.901353°
Granodiorite/Volcanic Jourama creek	-35.565702° 148.331938°
Granite catchment Gocup creek	-35.266646° 148.186432°
Volcanic catchment A	-34.695200° 148.521590°
Volcanic catchment B	-35.595040° 149.144332°

Volcanic catchment D Gomindena Creek	-35.199390° 148.979620°
Volcanic catchment E	-35.019297° 148.951230°
Volcanic catchment F	-35.254026° 148.972963°
Volcanic catchment Rockflat Creek	-36.346749° 149.210341°
Volcanic catchment upper Goodmans Gully	-35.693192° 148.495646°
Sedimentary catchment B	-35.088490° 149.316280°
Sedimentary catchment C Umbango creek	-35.380870° 147.773480°
Sedimentary catchment E Jellingro creek	-35.088770° 147.871920°
Sedimentary catchment F Alac creek	-35.800078° 148.674241°
Yass River lower catchment	-34.862500° 148.801990°
Yass River middle catchment	-34.867540° 148.955950°
Yass River upper catchment	-34.926320° 149.101980°
Tumut River lower catchment	-35.121630° 148.206020°

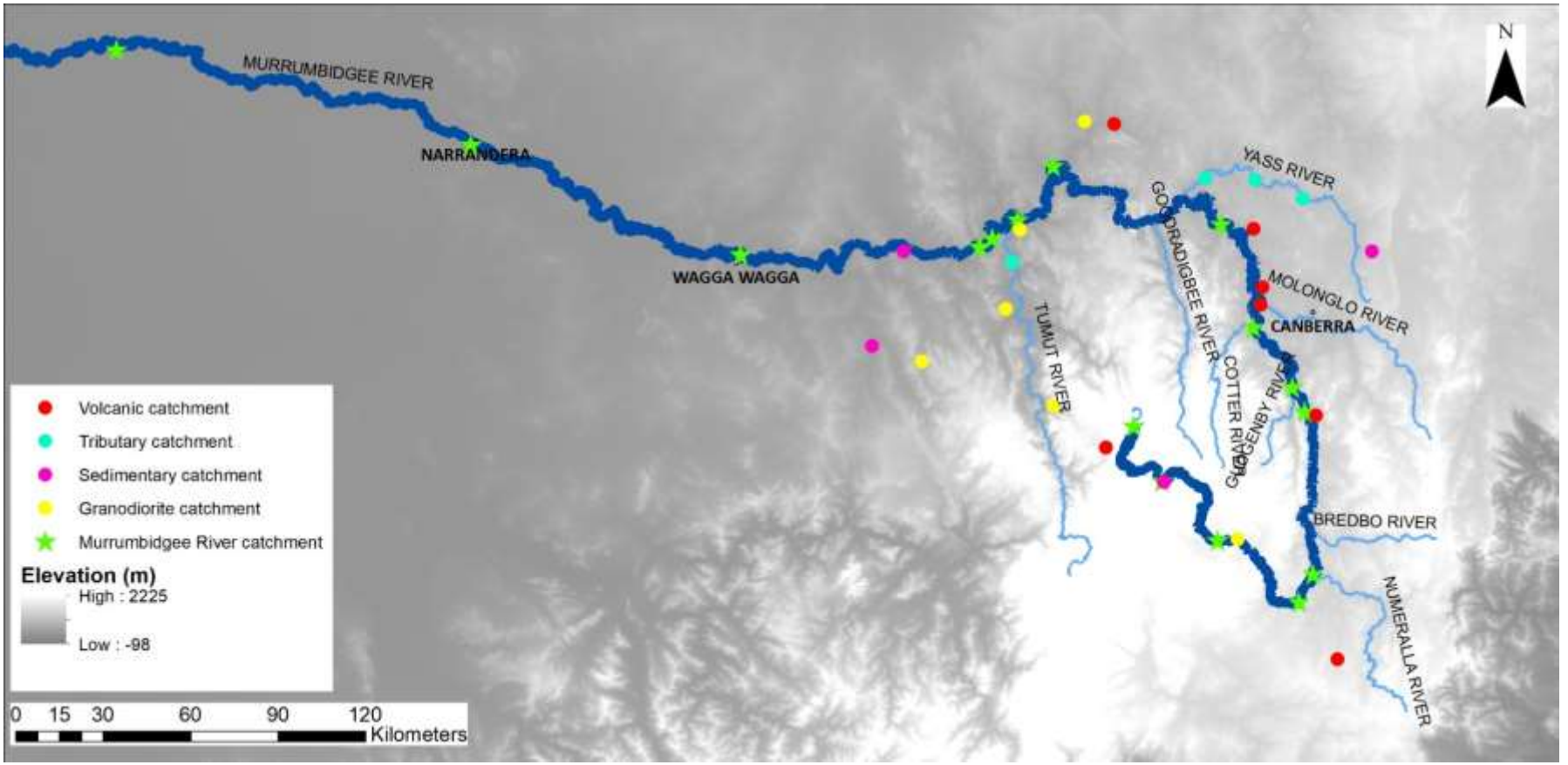

Figure 47: Sediment samples obtained in the Murrumbidgee River Basin. This map was created using a digital elevation model (DEM), calculated with with ArcGIS 10.3.1.

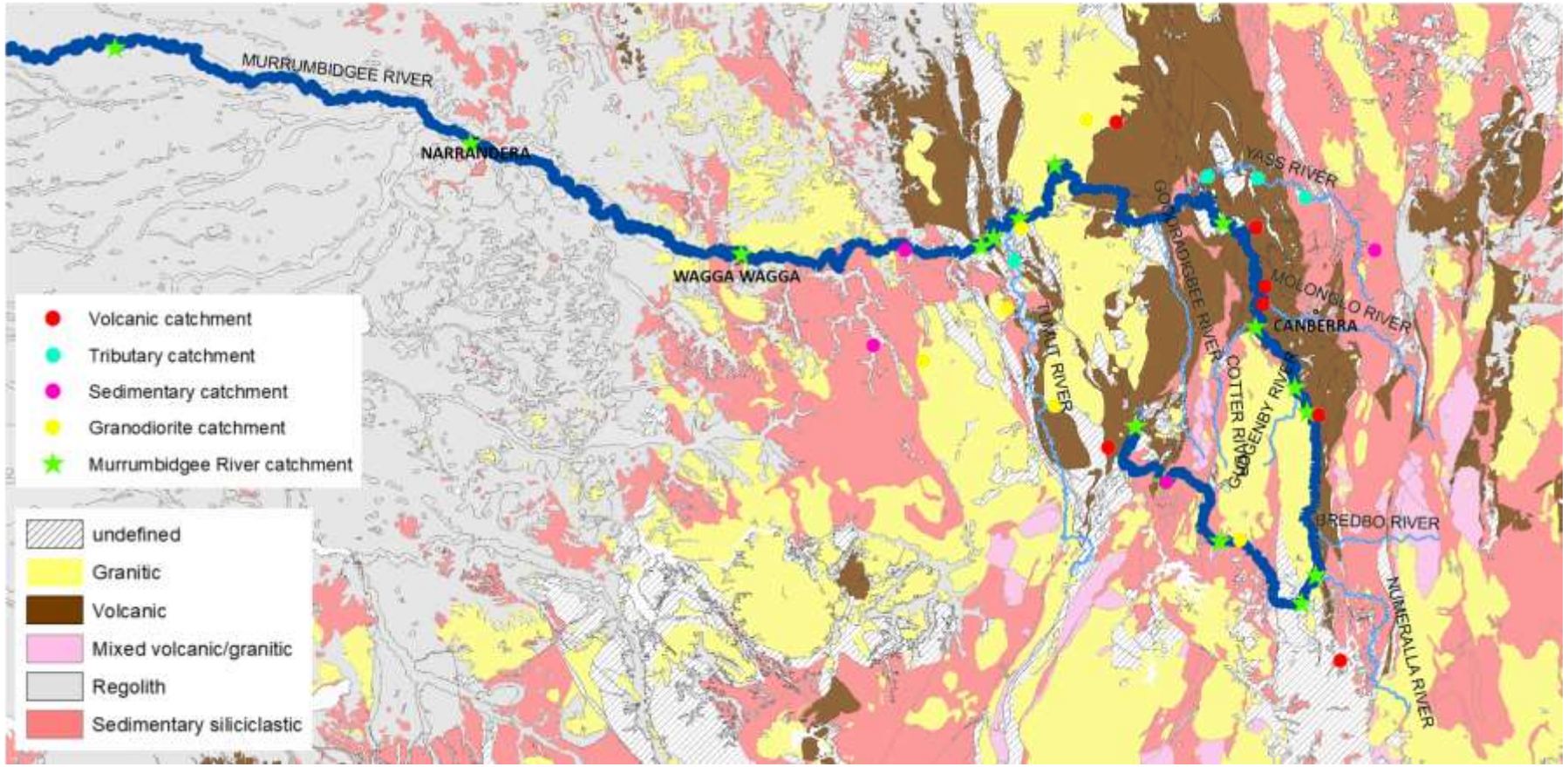

Figure 48: Sediment samples obtained in the Murrumbidgee River Basin relative to bedrock lithology. This map was created with with ArcGIS 10.3.1.

Where possible, samples were obtained from river point bars, which are areas of deposition (Figure 49). These sediments are generally well-sorted and the elevation is very close to the water level. To avoid sampling soil-derived clays from alluvium, only coarse (sand) sediments were collected and sampling next to hills was avoided. Up to four samples at ~2-metre intervals were collected at each sample location. This was done to ensure that the chemical signature of sediments from individual point bars are homogenous. An example is shown in Figure 50.

Figure 49: Sediment sample location from a river point bar. In this example, the location of sample Murrumbidgee #22 (before Yass) is displayed. Source: GoogleEarth.

Figure 50: Example of how sediments were collected from river banks. Red circles indicate the different sample aliquots. Sample site shown is Granodiorite catchment A at Cunningham Creek.

A total of ~three kilogram per sample was collected in separate plastic bags and labelled accordingly e.g. 'Granodiorite catchment A at Cunningham Creek, aliquot A'. After sample collection, samples were air-dried at the University of Wollongong for ~5 days. Following this, sediment samples were wet-sieved with distilled water to <63 µm using a sieve stack with mesh sizes 2 mm, 500 µm, and 63 µm. This combination of sieves was used to prevent the finest mesh from clogging. The grain size fraction smaller 63 µm was transferred into 50 mL centrifuge tubes and approximately 0.25 g (1 % of the sediment's weight) of $(NaPO_3)_6$ was added, which acts as a dispersing agent. The clay-sized fraction was then separated via centrifuging. This method resulted in an almost pure (>90 %) <2 µm size fraction. After crushing clays with mortar and pestle, a selection of samples was mounted on thin slides for X-ray diffraction (XRD) analyses (see Chapter 9). Another aliquot of the crushed clay samples was chemically dissolved and analysed for major and trace element concentrations, Li isotopes, and Nd isotopes (see Chapter 9).

6.1.2 River water

River waters were collected in 500 mL LDPE bottles. These were pre-cleaned with acetone for 30 seconds to remove traces of organic matter in the bottles and rinsed with 18.2 MΩ water. After that, bottles were filled with 0.015M HNO_3 and left for 24h. Finally, after discarding the HNO_3, bottles were rinsed several times with 18.2 MΩ water. GPS locations of each sample site are shown in Table 3. Figure 51 and Figure 52 show an overview of sample locations in the Murrumbidgee River Basin relative to a digital elevation model and bedrock lithology. Where possible, samples were collected from a bridge (Figure 53) or as close to the centre of the channel as possible (Figure 54). All river water samples were collected during a single season in September 2016.

Table 3: GPS locations of waters collected in the Murrumbidgee River Basin.

Sample ID	GPS position (decimal degrees WGS84)
Murrumbidgee #03 Tantangara	-35.797672° 148.668375°
Murrumbidgee #05	-35.980572° 148.840150°
Murrumbidgee #06	-36.170375° 149.091106°
Murrumbidgee #08	-36.085131° 149.134064°
Murrumbidgee #10 Spring Valley Creek	-35.047870° 148.144400°
Murrumbidgee #12	-35.582942° 149.108956°
Murrumbidgee #13 at Tharwa	-35.508539° 149.070758°
Murrumbidgee before Tumut (9A/B, 2014)	-34.991310° 148.223590°
Murrumbidgee #20 at Jugiong	-34.824707° 148.332066°
Murrumbidgee at Gundagai	-35.074339° 148.105496°
Murrumbidgee #22 (before Yass)	-35.004330° 148.849210°
Murrumbidgee at Wagga	-35.099282° 147.367875°
Granodiorite catchment A at Cunningham creek	-34.688068° 148.430413°
Granodiorite catchment C Adjungbilly creek	-35.021750° 148.230690°
Granodiorite catchment F	-35.428520° 147.927890°
Granodiorite Back creek near Adaminaby	-35.977255° 148.901353°
Granodiorite/Volcanic Jourama creek	-35.565702° 148.331938°
Granite catchment Gocup creek	-35.266646° 148.186432°
Volcanic catchment A	-34.695200° 148.521590°
Volcanic catchment B	-35.595040° 149.144332°
Volcanic catchment D Gomindena Creek	-35.199390° 148.979620°
Volcanic catchment E	-35.019297° 148.951230°
Volcanic catchment F	-35.254026° 148.972963°
Volcanic catchment Rockflat Creek	-36.346749° 149.210341°
Volcanic catchment upper Goodmans Gully	-35.693192° 148.495646°
Sedimentary catchment C Umbango creek	-35.380870° 147.773480°
Sedimentary catchment E Jellingro creek	-35.088770° 147.871920°
Sedimentary catchment F Alac creek	-35.800078° 148.674241°

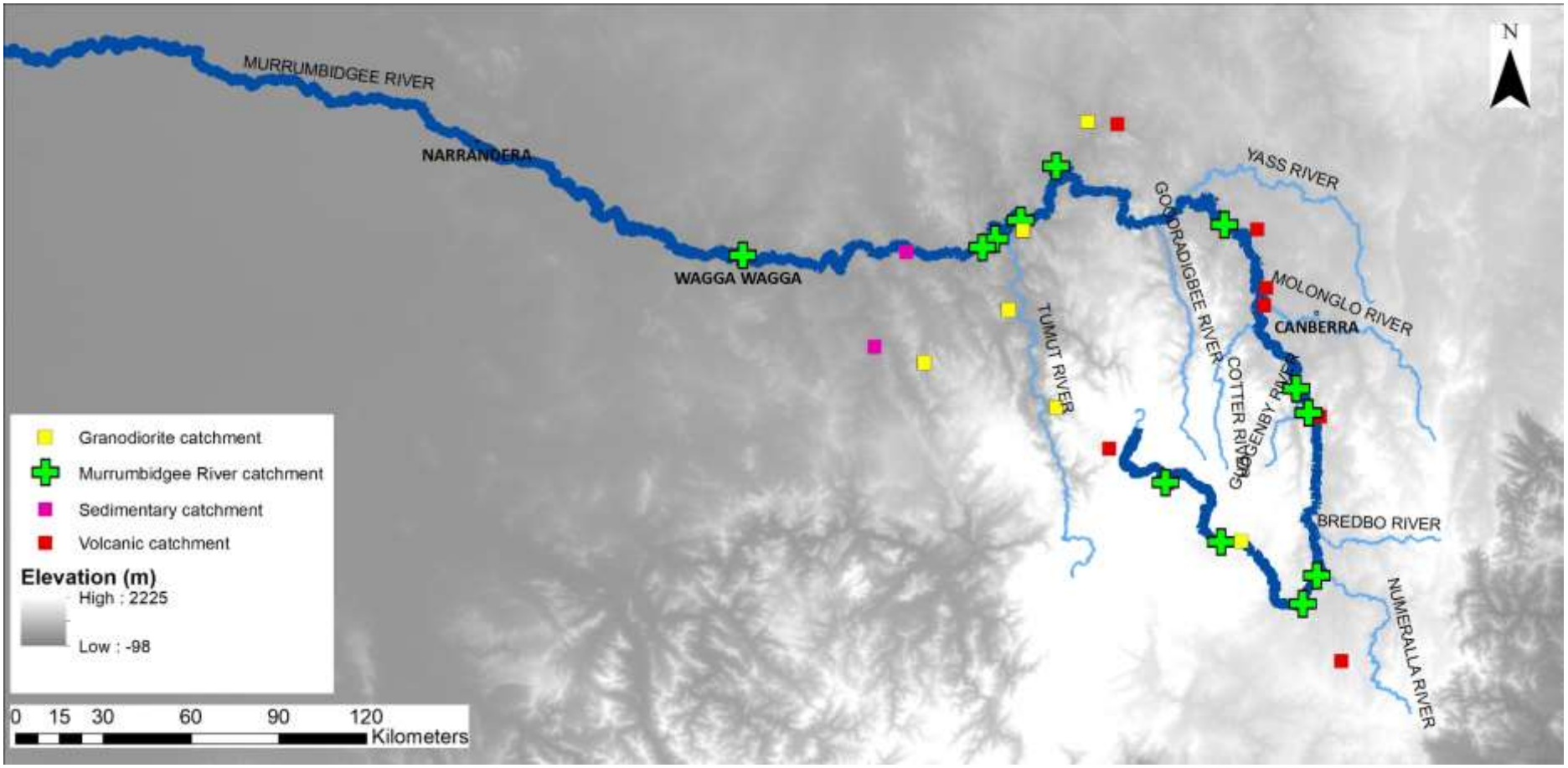

Figure 51: Water samples obtained in the Murrumbidgee River Basin. This map was created using a digital elevation model (DEM), calculated with with ArcGIS 10.3.1.

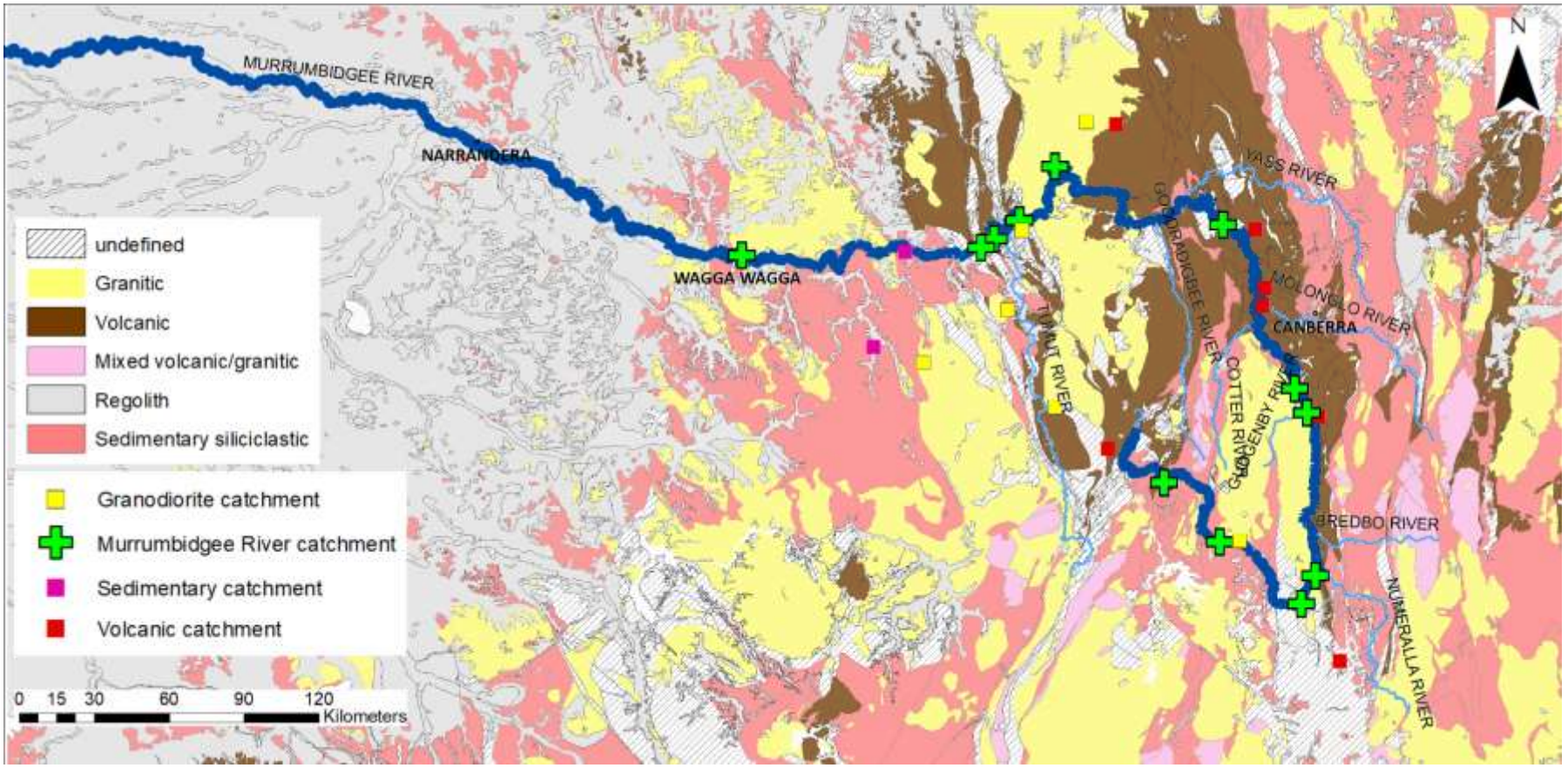

Figure 52: Water samples obtained in the Murrumbidgee River Basin relative to bedrock lithology. This map was created with with ArcGIS 10.3.1.

Figure 53: River water sample collection at Wagga Wagga. Sample bottle is hanging on a string to collect water from the centre of the channel.

Figure 54: River water sample collection at Granodiorite catchment at Jourama Creek.

Empty sample bottles were rinsed twice with river water before obtaining the sample. A total of 34 water samples were collected in the Murrumbidgee River Basin, which include Murrumbidgee River waters, and waters draining through monolithologic catchments. Sample localities are shown in Table 3, Figure 51 and Figure 52. Samples were collected during the day and filtered in the evening with MCE (mixed cellulose ester) membrane filters (particle retention of 0.2 µm) using a portable water filtration system. Filtered water samples were tested for pH following the method of Barnes (1964). After pH measurements, all samples were acidified with HNO_3 to 0.3M for storage. An aliquot was then measured on a Q ICP-MS to determine major and trace element concentrations (see

Chapter 9). Another aliquot, equivalent to 60 ng of Li, was evaporated and taken up in 1M HCl for ion exchange chromatography (see Chapter 9).

6.1.3 Bedrock

Three bedrock samples were collected in the Murrumbidgee River Basin, one from each main lithology, which includes a sedimentary siliclastic unit, a volcanic unit, and a granite unit. The sedimentary rock is a late Ordovician metamorphosed siltstone (in this study classified as graywacke). The granite unit is a Silurian (Ludlow group) igneous felsic intrusive rock, classified as granodiorite, and the volcanic rock is a Silurian (Pridoli epoch) igneous felsic volcanic rock, classified as ignimbrite (Australia, 2015). GPS coordinates of the collected bedrock samples are shown in Table 4 and an overview relative to a digital elevation is shown in Figure 55.

Table 4: GPS coordinates of bedrock samples collected in the Murrumbidgee River Basin.

Sample ID	GPS position (decimal degrees WGS84)
Bedrock sedimentary catchment (graywacke)	-35.428520° 147.927890°
Bedrock volcanic catchment	-34.695200° 148.521590°
Bedrock granodiorite catchment	-34.695200° 148.521590°

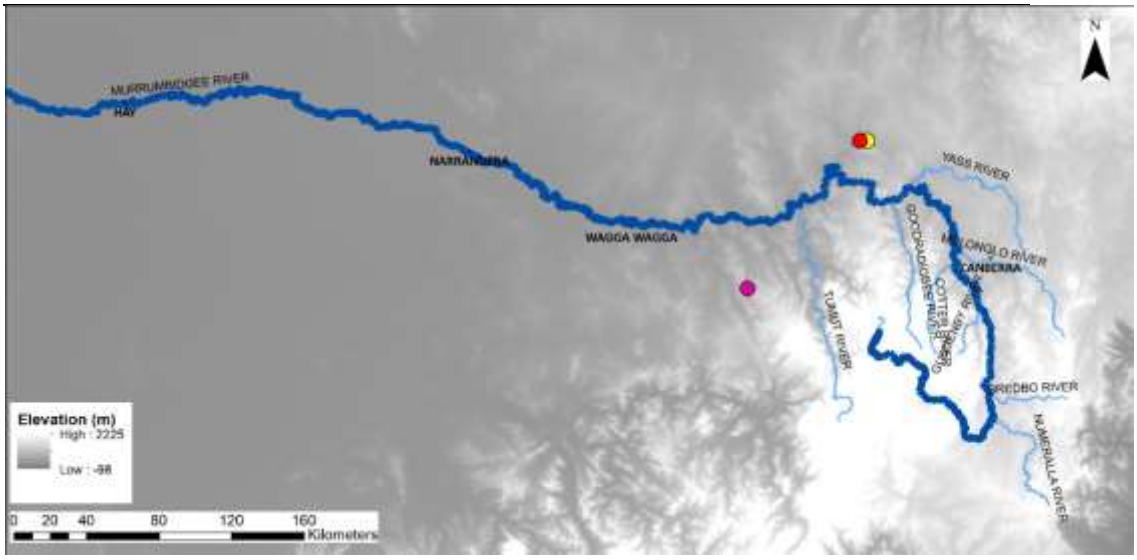

Figure 55: Collected bedrock samples from the main three lithology units in the Murrumbidgee River Basin. Pink: sedimentary siliclastic (graywacke). Red: volcanic rock. Yellow: granodiorite rock. This map was created using a digital elevation model (DEM), calculated with with ArcGIS 10.3.1.

Rocks were obtained from outcrops and a hammer was used to break off surface layers. At the University of Wollongong, weathered edges of rock samples were cut off with a diamond saw and the remaining core was crushed using a laboratory disc mill (TEMA). Photographs of each bedrock sample can be found in Section 6.4. Roughly 100 mg of sample was weighed in and chemically dissolved (see Chapter 9). An aliquot of the dissolved samples was analysed for major and trace elements, Li isotopes, and Nd isotopes.

6.1.4 Dust

One dust sample was collected in the alpine mire in the Snowy Mountains near Cabramurra (35.9370°S, 148.3846°E) in 2009, using a high-volume polycarbonate filter. Dust was accumulated over a period of two weeks. This sample was kindly provided by Sam Marx (University of Wollongong) and Nicola Stromsoe (University of Queensland). More details on sample collection and location can be found in (Stromsoe et al., 2013).

6.2 Murrumbidgee palaeo-channels

Palaeo-channel deposits are located at the lower reaches of the Murrumbidgee River, between Hay and Narrandera. Detailed information on the formation and geomorphology of Murrumbidgee palaeo-channel deposits can be found in Chapter 5. Table 5 shows GPS coordinates of each sample site, the respective channel system, and their position in the profile (i.e. depth below surface) and Figure 56 displays an overview of the sample sites in the Murrumbidgee River Basin. All palaeo-channel samples were collected in August 2015.

Table 5: Sample locations and descriptions of sediments collected from palaeo-channels.

Sample ID	Position in profile	Channel system	Comment	GPS position (decimal degrees WGS85)
Gala Vale 'south' 3	0.72 m / inside	Coleambally	exposed	-34.949261° 145.786096°
Gala Vale 'south' 3*	*0.72 m / inside*	*Coleambally*	*exposed*	-34.949261° 145.786096°
Gala Vale 'south' 2	1.57 m / outside	Coleambally	exposed	-34.949261° 145.786096°
Gala Vale 'south' 2	1.57 m / inside	Coleambally	exposed	-34.949261° 145.786096°
Gala Vale 'south' 1	2.27 m / outside	Coleambally	exposed	-34.949261° 145.786096°
Gala Vale 'south' 1	2.27 m / inside	Coleambally	exposed	-34.949261° 145.786096°
Gala Vale 3	0.30 m / outside	Coleambally	exposed	-34.892487° 145.932456°
Gala Vale 3	0.30 m / inside	Coleambally	exposed	-34.892487° 145.932456°
Gala Vale 2	0.80 m / inside	Coleambally	exposed	-34.892487° 145.932456°
Gala Vale 1	1.25 m / outside	Coleambally	exposed	-34.892487° 145.932456°
Gala Vale 1	1.25 m / inside	Coleambally	exposed	-34.892487° 145.932456°
Bundure 1	0.50 m	Coleambally	shovel sample	-35.085057° 145.800168°
Bundure 2	1.90 m	Coleambally	shovel sample	-35.085057° 145.800168°
N. Booroorban 1	0.55 - 0.65 m	Kerarbury	ground surface coring	-34.844744° 144.774799°
N. Booroorban 2	0.65 - 0.75 m	Kerarbury	ground surface coring	-34.878355° 144.758676°

Headless Horseman 3	0.15 m / inside & outside	Kerarbury	exposed	-34.906733° 144.759557°
Headless Horseman 2	0.60 m / inside & outside	Kerarbury	exposed	-34.906733° 144.759557°
Headless Horseman 1	1.00 m / inside & outside	Kerarbury	exposed	-34.906733° 144.759557°
Kerarbury 3	0.50 m / inside & outside	Kerarbury	exposed	-34.628817° 145.842109°
Kerarbury 2	3.00 m / inside	Kerarbury	exposed	-34.628817° 145.842109°
Kerarbury 1	4.00 m / outside	Kerarbury	exposed	-34.628817° 145.842109°
Kerarbury 1	4.00 m / inside	Kerarbury	exposed	-34.628817° 145.842109°
MGCY-5#4 uow 1315**	13.81 m	Gum Creek	auger core	-34.561068° 145.781019°
MGC 8-3#5 40cm uow 1390**	4.65 m	Gum Creek	auger core	-34.472034° 145.024333°
MGC 4-4#5 uow 1322**	5.85 m	Gum Creek	auger core	-34.578983° 145.831491°
MGC 2-1 clay uow 1306**	4.55 m	Gum Creek	auger core	-34.614353° 146.022324°
Tabratong 3	0.30 m / inside & outside	Gum Creek	exposed	-34.471994° 145.024783°
Tabratong 2	0.80 m / inside & outside	Gum Creek	exposed	-34.471994° 145.024783°
Tabratong 1	1.35 m / inside & outside	Gum Creek	exposed	-34.471994° 145.024783°
MYA-2#4 uow 1523**	3.77 m	Yanco	auger core	-35.151396° 145.936984°
MYA 1#6 uow 1521**	6.72 m	Yanco	auger core	-34.978238° 146.239382°

Wanganella 3	0.30 m / inside & outside	Yanco	exposed	-35.215989° 144.831814°
Wanganella 2	0.55 m / inside	Yanco	exposed	-35.215989° 144.831814°
Wanganella 1	0.90 m / outside	Yanco	exposed	-35.215989° 144.831814°
Wanganella 1	0.90 m / inside	Yanco	exposed	-35.215989° 144.831814°
Thurrowa Road 3	0.65 m	Yanco	exposed	-35.152106° 145.937379°
Thurrowa Road 3*	*0.65 m*	*Yanco*	*exposed*	-35.152106° 145.937379°
Thurrowa Road 2	2.93 m / inside & outside	Yanco	exposed	-35.152106° 145.937379°
Thurrowa Road 1	3.60 m / inside & outside	Yanco	exposed	-35.152106° 145.937379°
Yanco 'a' 4	0.25 m / inside & outside	Yanco	exposed	-35.149598° 145.767846°
Yanco 'a' 3	1.10 m	Yanco	exposed (white layer)	-35.149598° 145.767846°
Yanco 'a' 2	1.18 m / inside & outside	Yanco	exposed	-35.149598° 145.767846°
Yanco 'a' 2*	*1.18 m / inside & outside*	*Yanco*	*exposed*	-35.149598° 145.767846°
Yanco 'a' 1	2.00 m / inside & outside	Yanco	exposed	-35.149598° 145.767846°

**Sample replicate*

***Sample supplied by Daniela Mueller and Timothy Cohen (University of Wollongong)*

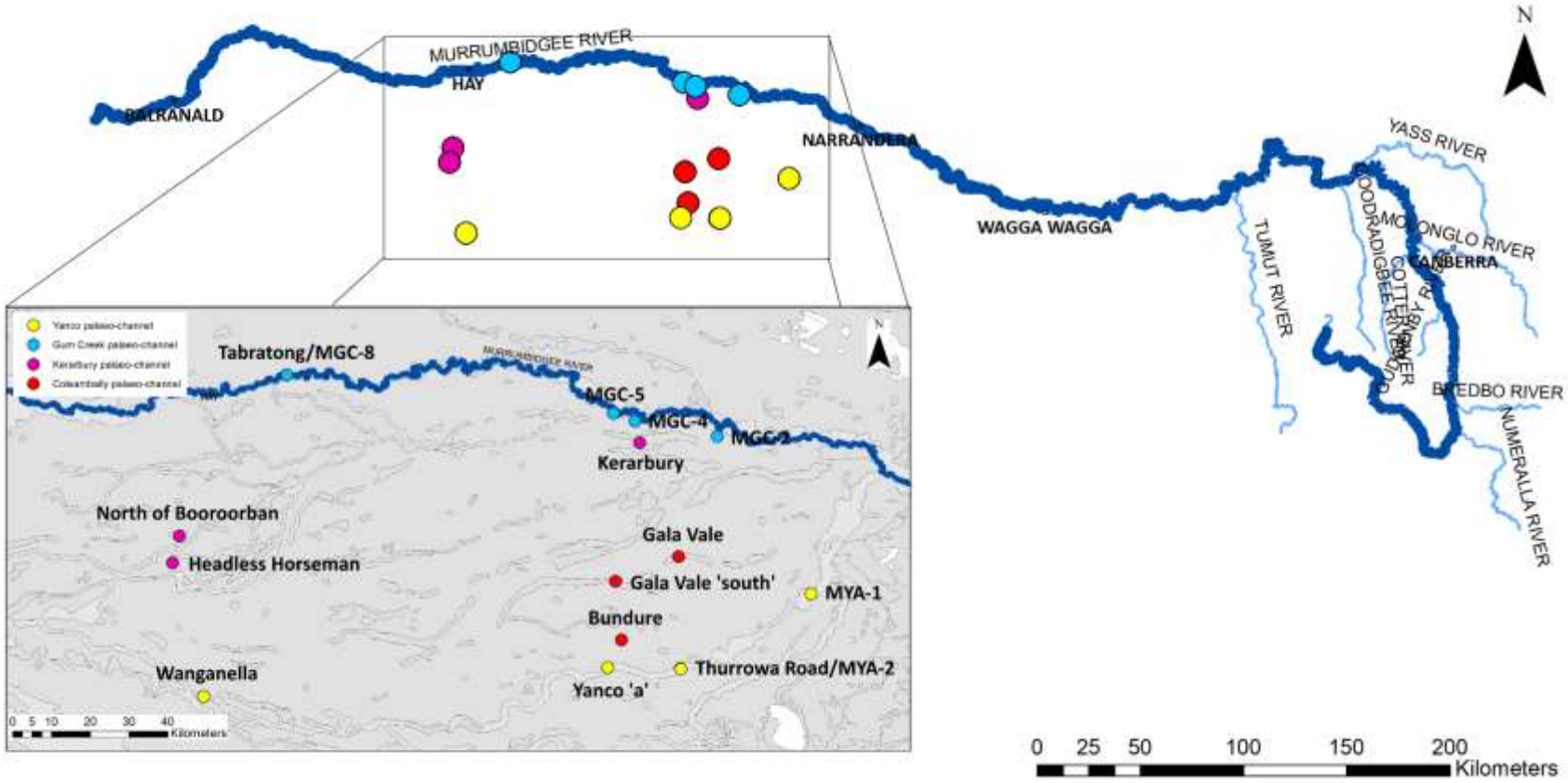

Figure 56: Overview of samples obtained from Murrumbidgee palaeo-channels. Grey elongated features in the insert outline palaeo-channels.

Palaeo-channel sediments were collected with several techniques, which depended on the sediment exposure at each sample site. Before sample collection, sediment layers that were exposed to the surface were removed with a shovel. At sample sites, where sediments were vertically exposed, several aluminium pipes (6 cm diameter) were hammered into the sediment wall. The objective was to obtain material from as deep inside the sediment succession as possible to avoid collecting sediment that had frequently been exposed to rainwater. Aluminium core sediments were separated into 'inside' and 'outside', where 'inside' refers to the sediment coming from the deepest part of aluminium pipe and 'outside' to the sediment closer to the surface. At study sites, where natural vertical sediment faces were not present, an aluminium pipe was drilled vertically through the ground to retrieve sediments from where sediment is more likely to be associated with palaeo-channel deposits. At sample sites, where sediments were too compact to hammer aluminium pipes through, pits were dug with a shovel and samples were taken from deep sediment layers. Additional samples, retrieved via auger cores, were provided by Daniela Mueller and Timothy Cohen (University of Wollongong). Method descriptions, sample locations and characteristics, are described in detail in Mueller et al. (under review).

After sample collection, samples were air-dried at the University of Wollongong for several days. Following this, sediment samples were wet-sieved with distilled water to <63 µm using a sieve stack with mesh sizes 2 mm, 500 µm, and 63 µm. The grain size fraction smaller 63 µm was transferred into 50 mL centrifuge tubes and approximately 0.25 g (1 % of the sediment's weight) of $(NaPO_3)_6$ was added, which acts as a dispersing agent. The clay-sized fraction was then separated via centrifuging. Clay samples were crushed with mortar and pestle and afterwards chemically dissolved and analysed for major and trace element concentrations, Li isotopes, and Nd isotopes (see Chapter 9).

6.2.1 Coleambally

Sediments from the Coleambally palaeo-channel were collected at three different locations: Gala Vale, Gala Vale 'south', and Bundure (Figure 56, Table 5). At Gala Vale, three core samples were retrieved from different depths using 60 mm diameter aluminium pipes (Figure 57). An overview of the sample site is displayed in Figure 58. At Gala Vale 'south', the same sampling technique as for Gala Vale was applied i.e. samples were obtained from different depths using aluminium pipes (Figure 59). Figure 60 shows an overview over the sample site.

Figure 57: Gala Vale sample profile. Bottom hole: Gala Vale 1. Centre: Gala Vale 2. Top: Gala Vale 3.

Figure 58: Overview of sample site Gala Vale.

Figure 59: Gala Vale 'south' sample profile. Bottom hole: Gala Vale 'south' 1. Centre: Gala Vale 'south' 2. Top: Gala Vale 'south' 3.

Figure 60: Overview of sample site Gala Vale 'south'.

Sample site Bundure is located on a cattle farm. An overview is displayed in Figure 61. The sediment at this sample site was too compact to push an aluminium pipe through. Instead, the weathered surface was removed with a shovel and samples were taken from an upper and lower sediment layers, about 1.40 m vertically apart (Figure 62, Figure 63).

Figure 61: Overview of sample site Bundure.

Figure 62: Bundure shovel sample (Bundure 1). Sediment was taken from the 'cleaned' patch in the centre of the image.

Figure 63: Bundure shovel sample. The white/grey layer below the red horizon (190 cm from surface, marked by red circle) was sampled (Bundure 2).

6.2.2 Kerarbury

Sediments from the Kerarbury palaeo-channel system were obtained from four sample sites: Kerarbury, Headless Horseman, N. of Booroorban 1, and N. of Booroorban 2 (Table 5, Figure 56). At sample site Kerarbury, three samples were retrieved with aluminium pipes. An overview over the entire sample site is shown in Figure 64. Two samples were collected from 4.00 m and 3.00 m below the surface (Figure 65), and a third at 0.50 m below the surface (Figure 66).

Figure 64: Overview of sample site Kerarbury.

Figure 65: Kerarbury sample site. Red arrows mark the position where cores were retrieved. Bottom hole: Kerarbury 1. Top hole: Kerarbury 2.

Figure 66: Kerarbury sample site (Kerarbury 3), above Kerarbury 1 & 2.

Another sediment succession was sampled at Headless Horseman (named after the nearby hotel/pub). Figure 67 shows an overview over the exposed sediment at this sample site. Sediments were taken from three different depths (Figure 68).

Figure 67: Overview of sample site Headless Horseman.

Figure 68: Kerarbury palaeo-channel, sample site Headless Horseman. Bottom hole is Headless Horseman 3, centre hole is Headless Horseman 2, and top hole is Headless Horseman 1.

At N. of Booroorban 1 and 2, no exposed sediment was available. Figure 69 and Figure 70 show an overview of sample sites N. of Booroorban 1 and 2, respectively. At both sample sites, an aluminium pipe was forced vertically into the ground to obtain samples from deep/unexposed sediment layers (Figure 71, Figure 72).

Figure 69: Overview of sample site N. of Booroorban 1.

Figure 70: Overview of sample site N. of Booroorban 2.

Figure 71: Kerarbury palaeo-channel system, sample N. of Booroorban 1. Aluminium pipe was hammered ~0.55-0.65 m into the ground. Sediments that surrounded the aluminium pipe were removed after hammering.

Figure 72: Kerarbury palaeo-channel system, sample N. of Booroorban 2. Aluminium pipe was hammered ~0.65-0.75 m into the ground.

6.2.3 Gum Creek

In this study, the Gum Creek palaeo-channel was only sampled at one location, at Tabratong. However, additional samples were provided by Daniela Mueller and Timothy Cohen (University of Wollongong) (Figure 56, Table 5). At Tabratong, sediments were retrieved from three different depths with aluminium pipes (Figure 73). Unfortunately, no overview picture was taken at this sample site. Additional samples for the Gum Creek palaeo-channel system MGCY and MGC were obtained via auger cores. Sample locations and depths are in detail described in Mueller et al. (under review).

Figure 73: Gum Creek palaeo-channel system, sample Tabratong. Bottom hole (with pipe inside) is Tabratong 1, Centre hole (indicated by red circle) is Tabratong 2, and top hole (indicated by red circle) is Tabratong 3.

6.2.4 Yanco

The geologically youngest palaeo-channel, Yanco, was sampled at three locations (Wanganella, Thurrowa Road, Yanco ‘a’), and two additional samples were provided by Daniela Mueller and Timothy Cohen (University of Wollongong) (Figure 56, Table 5). At Wanganella, sediments were obtained from three different depths using aluminium pipes (Figure 74). An overview over the sample site is displayed in Figure 75.

Figure 74: Yanco palaeo-channel, Wanganella sample site. Bottom hole (below aluminium pipe) is Wanganella 1, centre hole (with aluminium pipe inside) is Wanganella 2, top hole (indicated by red circle) is Wanganella 3.

Figure 75: Overview of sample site Wanganella.

At Thurrowa Road, samples were obtained from three different depths, using aluminium pipes (Figure 76). An overview of the sample site is shown in Figure 77.

Figure 76: Yanco palaeo-channel system, sample site Thurrowa Road. Bottom hole is Thurrowa Road 1, centre hole (above) is Thurrowa Road 2, top hole (indicated by red circle) is Thurrowa Road 3.

Figure 77: Overview of sample site Thurrowa Road.

Sample site Yanco ‘a’ appear to be a relatively young pit, dug by an excavator. An overview of the sample site is shown in Figure 78. A total of four samples from different depths were taken: three using aluminium pipes and an additional white layer was sampled with a shovel, because the sediment at this spot was too compact (Figure 79). Additional samples for the Yanco palaeo-channel system, MYA, were retrieved via auger cores Detailed sample location and descriptions can be found in Mueller et al. (under review).

Figure 78: Overview of sample site Yanco A.

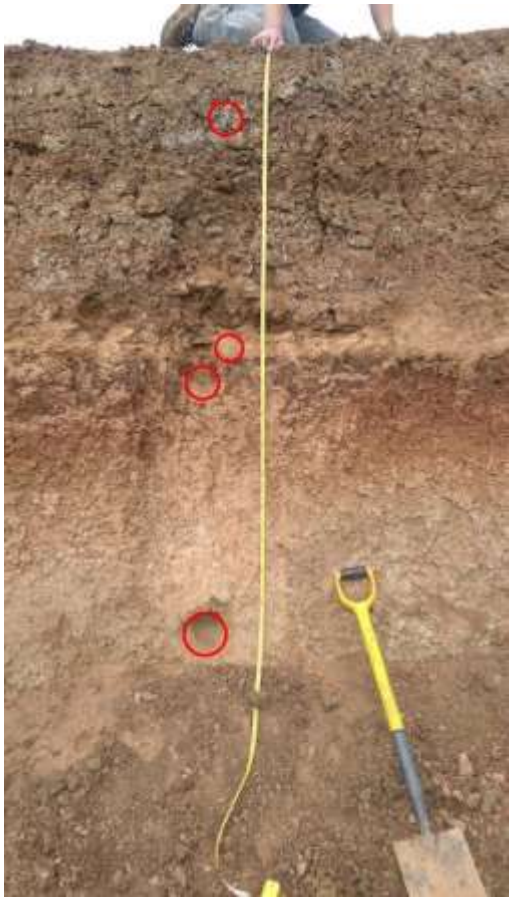

Figure 79: Yanco palaeo-channel system, sample site Yanco 'a'. Bottom hole is Yanco 'a' 1, second hole from bottom is Yanco 'a' 2, third hole from bottom is Yanco 'a' 3 (white layer), and top hole is Yanco 'a' 4. Red circles mark the location, where sediment was retrieved via coring.

6.3 Lake Dojran

The third major project during this PhD is built on the sediment record of Lake Dojran (Francke et al., 2013). Sediment samples were provided by Alexander Francke (University of Cologne/University of Wollongong). Several geochemical proxies, including major and trace element concentrations, XRD, Li and U isotopes, were applied to this record to reconstruct how soils developed in response to climatic oscillations and human activity over the past 12,300 years.

6.3.1 Lake sediments

The sediment core was drilled in June 2011 using a gravity corer for undisturbed surface sediments and a percussion piston corer for deeper sediment layers. The drilling location is shown in Figure 80.

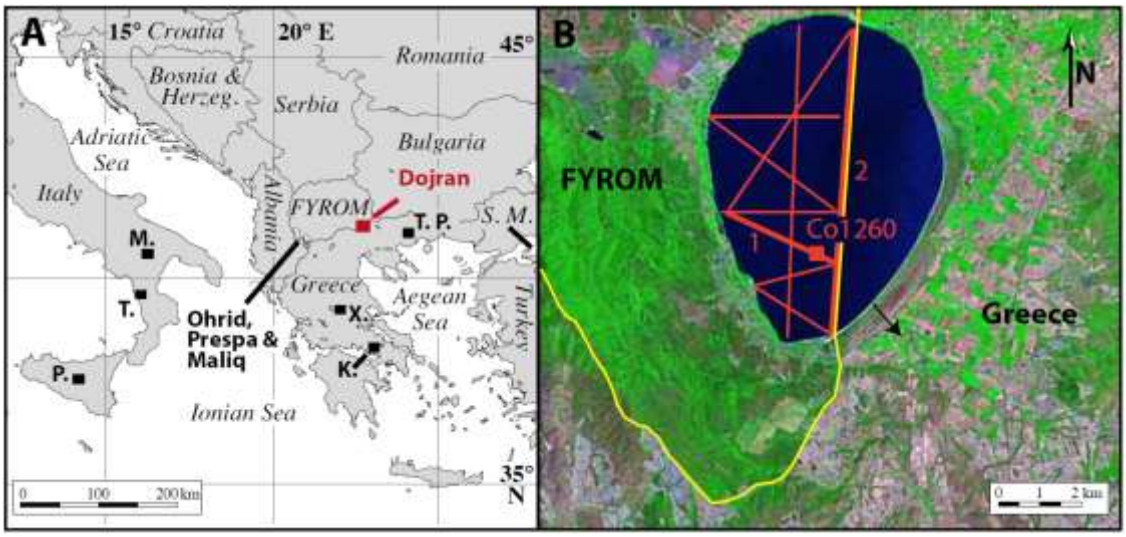

Figure 80: A: Location of Lake Dojran in south-eastern Europe. Also shown are other palaeo-climate records (Lake Ohrid, Lake Prespa, Lake Maliq, Lake Xinias (X.), Lake Kopais (K.), Lago Grande di Monticchio (M.), Lago di Trifoglietti (T.), Lago di Pergusa (P.), Tenaghi Philippon (T.P., and the Sea of Marmara (S.M.). B: satellite image of Lake Dojran with core location marked as red square. Red lines mark hydro-acoustic profiles, and black arrow indicated former outlet. Yellow line indicates the border between FYROM and Greece. Source: (Francke et al., 2013).

More details regarding the applied drilling techniques and core descriptions are given in (Francke et al., 2013). The following sample preparation procedures were performed by Alexander Francke (University of Cologne/University of Wollongong). Sediments were treated with 30 % H_2O_2, 10 % HCl, and NaOH to remove organic matter, endogenic calcite and biogenic silica, respectively. Samples were then sieved to 63 µm and grain size analyses were carried out on the <63 µm fraction at the University of Cologne using a Beckman LS^{TM} 13 320 particle size analyser. Further sample preparation was done by Leo Rothacker at the University of Wollongong. One aliquot of the <63 µm fraction was mounted onto thin slides for XRD analyses. Another aliquot was crushed with pestle and mortar and afterwards chemically dissolved and prepared for major and trace element concentrations analyses, Li isotopes, and U isotopes.

6.3.2 Stream sediments

To study the present weathering environment, sediments from ten streams draining into Lake Dojran were collected. Sampling was undertaken in December 2015 by Alexander

Francke. An overview of stream sample locations is shown in Figure 81. GPS coordinates of each sample point are shown in Table 6.

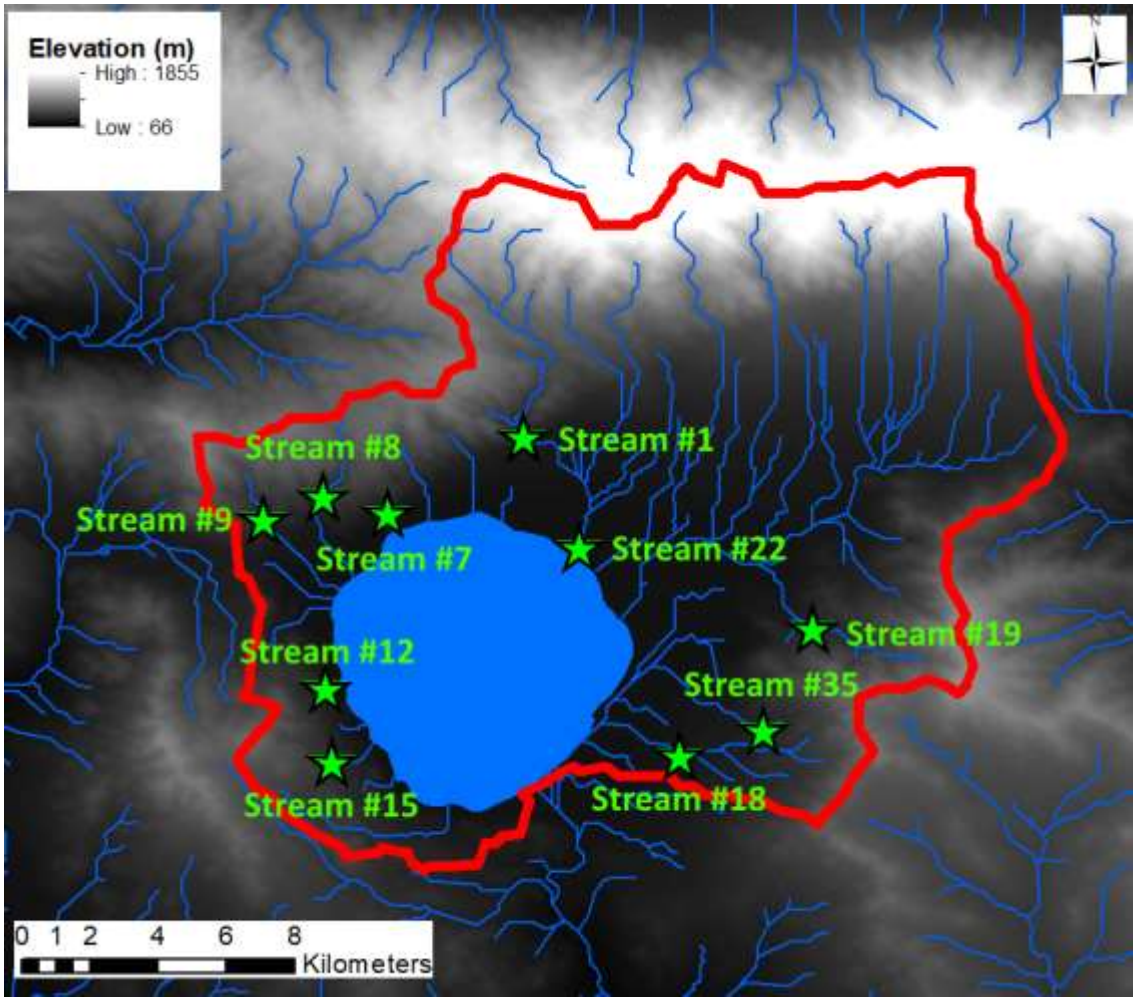

Figure 81: Stream samples taken at the Lake Dojran catchment. Stars show sample locations for stream sediments. Red line is the catchment boundary. Blue lines are representing the modern stream system. Stream network was calculated with ArcGIS Desktop Advanced 10.4 software (https://esriaustralia.com.au/arcgis-desktop) using a 1-arc second digital elevation model (DEM).

Table 6: GPS coordinates of stream samples taken at the Lake Dojran catchment.

Sample ID	GPS position (decimal degrees WGS84)
Dojran stream #1	41.271083° 22.758400°
Dojran stream #7	41.251067° 22.722600°
Dojran stream #8	41.255633° 22.705700°
Dojran stream #9	41.249367° 22.689867°
Dojran stream #12	41.205017° 22.706317°
Dojran stream #15	41.185650° 22.707833°
Dojran stream #18	41.187317° 22.799650°
Dojran stream #19	41.220814° 22.834656°
Dojran stream #22	41.242150° 22.773233°
Dojran stream #35	41.194008° 22.821453°

Most streams were smaller than 2 m in width and had little to no water present at the time of sampling (Figure 82). The sampling objective was to obtain material that was actively transported into Lake Dojran. Therefore, sediments were taken from river beds, which in some cases were under water. Similar to lake sediments, stream samples were sieved to 63 µm, crushed with pestle and mortar, and chemically dissolved to be analysed for Li isotope compositions. From stream sample #22, biotite grains were hand-picked by Alexander Francke and chemically dissolved and analysed for Li isotopes. Photographs of each sample site can be found in Section 6.4.

Figure 82: Examples of typical streams flowing into Lake Dojran during winter 2015. Left: stream sample #4. Right: stream sample #1. Channel width on right picture was approximately 2 m. Photos were taken by Alexander Francke.

6.3.3 Bedrock

A total of 11 bedrock samples were sampled from the catchment of Lake Dojran. In the eastern part of the catchment, the bedrock lithology is composed of gneiss, mica schist, granite, Quaternary alluvial sediment, and amphibolite. South of the lake is a small area with volcanoclastic sedimentary rocks. In the western part of the catchment, the lithology consists mostly of muscovite gneiss, gabbro, green schist, serpentinite, granite, biotite gneiss, and marble. A selection of these bedrock units was collected in the catchment, including gneiss, granite, phyllite, greenschist, marble, volcanoclastic sedimentary rocks, peridotite, and gabbro (Table 7, Figure 83). Photographs of each sample site are shown in Section 6.4.

Table 7: Bedrock samples collected at Lake Dojran catchment.

Sample name	Rock type	GPS position (decimal degrees WGS84)
#1	Gneiss	41.274033° 22.755600°
#2	Phyllite	41.268217° 22.752300°
#3	Greenschist	41.263300° 22.737833°
#4	Marble	41.235900° 22.690417°
#5	Phyllite	41.212650° 22.709033°
#6	Volcanoclastic sedimentary rock	41.167967° 22.762733°
#7	Peridotite	41.187133° 22.822200°
#8	Gneiss	41.183600° 22.840583°
#9	Granite	41.221233° 22.835667°
#10	Gneiss	41.329600° 22.861550°
#11	Gabbro	41.328033° 22.872361°

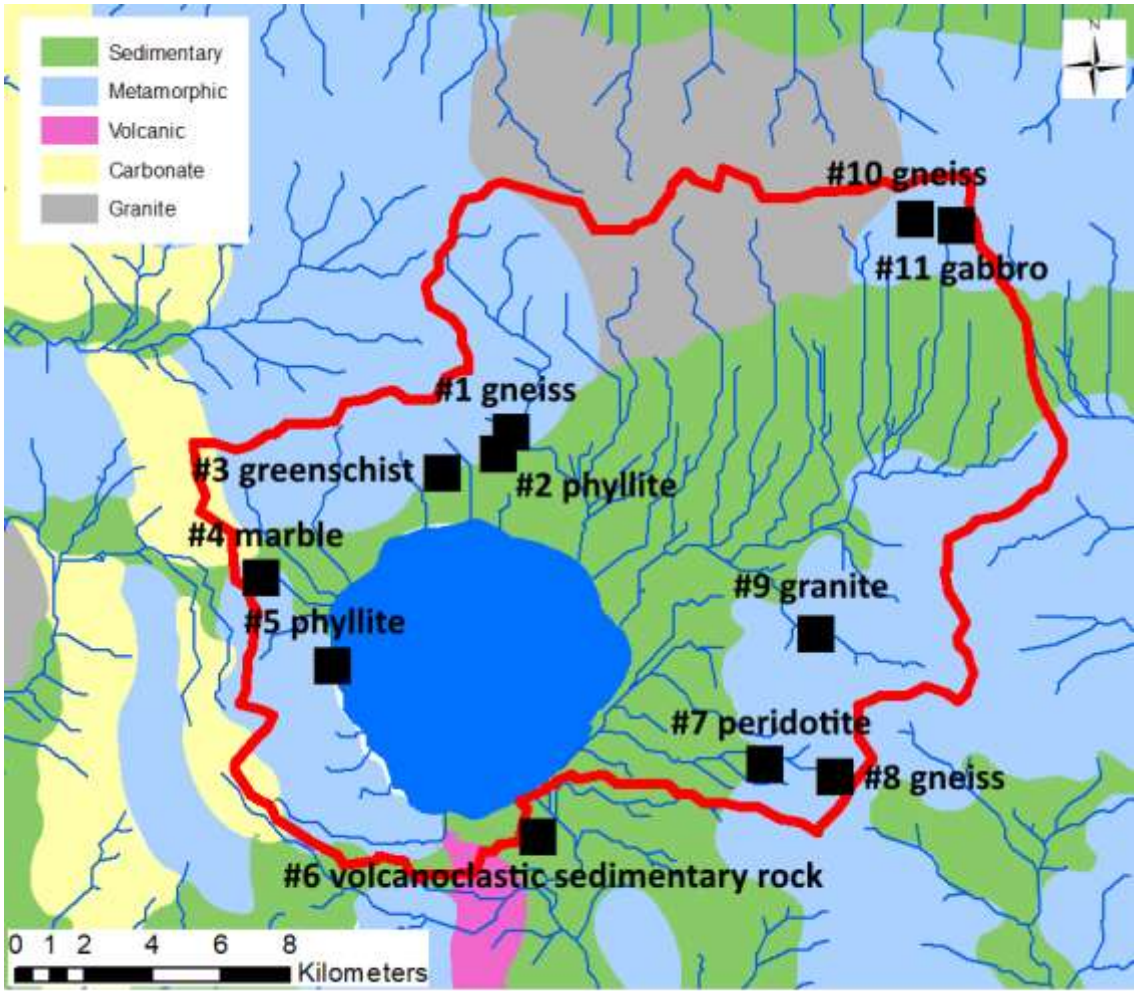

Figure 83: Bedrock samples (black squares) obtained from different lithologies at the Lake Dojran catchment. Individual lithology areas were estimated and manually drawn. Red curve: catchment boundary, blue lines: stream network. Stream network and catchment area was calculated with ArcGIS Desktop Advanced 10.4 software (https://esriaustralia.com.au/arcgis-desktop) using a 1-arc second digital elevation model (DEM).

Weathered edges of rock samples were cut off with a diamond saw and the remaining core was crushed using a laboratory disc mill (TEMA). The rock powder was chemically dissolved (see Chapter 9) and analysed for U isotopes by Davide Menozzi (University of Wollongong).

6.4 Appendix

Murrumbidgee #01

Very coarse sand, pebbles. Small river flow at this upper-most location.

Murrumbidgee #03 Tantangara

Sediment is very coarse, pebbles. Sample taken after dam.

Murrumbidgee #05

Poorly sorted sediment. Lots of organic material and roots, almost like soil.

Murrumbidgee #06

Fine-grained muds, little sand present.

Murrumbidgee #08

Coarse sands.

Murrumbidgee #10 Spring Valley Creek

Poorly sorted sediment.

Murrumbidgee #12

Poorly sorted sands from river deposits on a large sand bank.

Murrumbidgee #13 at Tharwa

Well-sorted coarse-grained sand.

Murrumbidgee before Tumut (9A/B, 2014)

Sediment well-sorted. Coarse alluvial sands.

Murrumbidgee #20 at Jugiong

Coarse-grained sands. Not well-sorted. Some trees near bank of the river.

Murrumbidgee after Cotter River

Coarse-grained sands.

Murrumbidgee at Gundagai

Poorly sorted sediment from large pebbles to clays.

Murrumbidgee #22 (before Yass)

Sediment well-sorted (sand). Vegetation scarce.

Murrumbidgee at Wagga

Muddy, fine-grained sand with abundant clay.

Murrumbidgee before Hay

Muddy, fine-grained sand with abundant clay.

Murrumbidgee at Narrandera

Muddy, fine-grained sand with abundant clay.

Granodiorite catchment A at Cunningham creek

Coarse sediment, almost gravel. Poorly sorted. Stream very clear.

Granodiorite catchment C Adjungbilly creek

Coarse sands and only little clay. Not well-sorted.

Granodiorite catchment F

Narrow, sandy channel in a grassy valley. Sediment rich in muscovite. Very well-sorted.

Granodiorite Back creek near Adaminaby

Took water, sediment and bedrock sample.

Granodiorite/Volcanic Jourama creek

Next to public campsite. Took water, bedrock and sediment sample.

Volcanic catchment A

Coarse sands, well-sorted. Relatively steep sediment banks. Clear water.

Volcanic catchment B

Took sediment sample and water sample.

Volcanic catchment D Gomindena creek

Only water sample taken here. Private property.

Volcanic catchment E

Reddish-brown sediment. Not well-sorted. Mostly sandy.

Volcanic catchment F

Red sandy sediment. Sediment sample and water sample taken.

Volcanic catchment Rockflat Creek

Muddy sediment with lots of clay.

Volcanic catchment upper Goodmans Gully

Very minor stream, almost no water present. Took water and sediment sample.

Sedimentary catchment B

Organic rich sediment. Coarse-grained, poorly sorted. Lots of edgy/sharp rocks.

Sedimentary catchment C Umbango creek

High water level. Water very muddy. Took water and bedrock sample.

Sedimentary catchment E Jellingro creek

Water sample taken.

Sedimentary catchment F Alac creek

Clear waters, little suspended load. Took water, sediment, and rock sample. Sediment sample taken from river bed.

Yass River lower catchment

Coarse-grained sand. Fairly well-sorted.

Yass River middle catchment

Silt-clay sediment. Relatively high water level.

Yass River upper catchment

Coarse sediment. Relatively fast river flow.

Tumut River lower catchment

Coarse sediment. Muddy sand and lots of organics.

Bedrock sedimentary catchment (graywacke)

Bedrock volcanic catchment

Bedrock granodiorite catchment

Dojran stream #1

Dojran stream #7

Dojran stream #8

Dojran stream #9

Dojran stream #12

Dojran stream #15

Dojran stream #18

Dojran stream #19

Dojran stream #22

Dojran stream #35

Dojran bedrock #1 gneiss

Dojran bedrock #2 phyllite

Dojran bedrock #3 greenschist

Dojran bedrock#4 marble

Dojran bedrock #5 phyllite

Dojran bedrock #6 volcanoclastic sedimentary rock

Dojran bedrock #7 peridotite

Dojran bedrock #8 gneiss

Dojran bedrock #9 granite

Dojran bedrock #10 gneiss

N/A

Dojran bedrock #11 gabbro

N/A

References

Australia, G. 2015. Australian stratigraphic units database. *Australian Government. Website:* http://www. *ga. gov. au/data-pubs/data-standards/reference-databases/stratigraphic-units*.

Barnes, I. 1964. Field measurement of alkalinity and pH. USGPO.

Francke, A., Wagner, B., Leng, M. J. & Rethemeyer, J. 2013. A Late Glacial to Holocene record of environmental change from Lake Dojran (Macedonia, Greece). *Climate of the Past,* 9**,** 481-498.

Mueller, D., Jacobs, Z., Cohen, T., Price, D., Reinfelds, I. & Shulmeister, J. under review. Revisiting an arid LGM using fluvial archives: a luminescence chronology for palaeochannels of the Murrumbidgee River, southeastern Australia. *Journal of Quaternary Science*.

Stromsoe, N., Callow, J. N., Mcgowan, H. A. & Marx, S. K. 2013. Attribution of sources to metal accumulation in an alpine tarn, the Snowy Mountains, Australia. *Environmental pollution,* 181**,** 133-143.

7 Past and present weathering conditions in the Murrumbidgee River Basin

The chemical decomposition of rocks is complex and may be controlled by many factors such as bedrock type, climate, topographic/tectonic settings, soil development, vegetation, and human activity (Raymo and Ruddiman, 1992; Gaillardet et al., 1999; West et al., 2005; Koppes and Montgomery, 2009; Bayon et al., 2012). One major difficulty of assessing weathering reactions and identifying their controls is the lack of a reliable proxy. The main aim of this PhD project is to test the novel weathering proxy Li isotopes on samples from the Murrumbidgee River Basin. The Murrumbidgee River is the second longest river in Australia and its basin covers a variety of climatic and topographic environments, as described in Chapter 5. The Li isotope proxy is applied to a variety of samples including sediments (clay-sized fraction), waters, and bedrock, which are representative of the different lithologies and weathering environments of the Murrumbidgee River Basin. Besides Li isotope measurements, pH, major and trace element concentrations, clay mineralogy, particle size distribution, and neodymium isotope compositions are used as complementary data to characterise water-rock interactions of the various parts of the Murrumbidgee River catchment. The second part of this chapter aims at reconstructing temporal variations of chemical weathering conditions in the Murrumbidgee River Basin. Over the last glacial cycle, several palaeo-channel systems had been active in the Murrumbidgee River Basin. Sediments from these palaeo-channels were sampled and the clay-sized fraction was analysed for Li and Nd isotopes, clay mineralogy, and major- and trace element concentrations. The objective is to show if and how the weathering conditions in the Murrumbidgee River Basin changed during the past 100,000 years in response to climatic and hydrological variations during this period of time.

All field methods and analytical methods used in this chapter are reported in Chapter 6 and Chapter 9, respectively. For details on sample locations, please see Chapter 6.

7.1 River dissolved loads

The Li isotope composition of river dissolved loads is assumed to reflect weathering reactions submitted to silicate minerals and rocks, occurring in the catchment area (Huh et al., 1998; Huh et al., 2001; Pistiner and Henderson, 2003; Kısakűrek et al., 2005). Indeed, Li isotopes fractionate during silicate weathering, where waters become enriched

in ^{7}Li relative to the weathering product (Pistiner and Henderson, 2003; Vigier et al., 2008). As shown by several articles published within the last 20 year, the degree of fractionation may be a function of the weathering intensity of water-rock interactions (Huh et al., 1998; Huh et al., 2001; Kısakűrek et al., 2005; Pogge von Strandmann et al., 2006; Pogge von Strandmann et al., 2008; Pogge von Strandmann et al., 2010; Millot et al., 2010), silicate weathering fluxes (Vigier et al., 2009), fluid residence time (Liu et al., 2015), or water-sediment interactions (Wimpenny et al., 2010a; Tipper et al., 2012; Pogge von Strandmann et al., 2012). Hence, the Li isotope signature of river dissolved loads ($\delta^{7}Li_{diss}$) of individual catchments within the Murrumbidgee River Basin may reveal chemical weathering reactions. Samples were taken from various parts of the Murrumbidgee River, including upper-, mid-, and lower reaches. To evaluate the effect of lithology on Li isotope fractionation in dissolved loads, samples from monolithologic catchments were obtained. Besides Li isotopes, each water sample was tested for pH and major and trace element concentrations. The sampling strategy is discussed in detail in Chapter 6.

7.1.1 Results: major and trace element composition of dissolved loads

The concentration of a large range of chemical elements was measured for dissolved loads from the Murrumbidgee River and waters flowing through monolithologic catchments. Only a small selection of major and trace element concentrations is used to describe the weathering derived chemical signature of the Murrumbidgee River and the lithological effect. These include: Na, K, Mg, Ca, Al, Ti, and Li. Results for major and trace element concentrations for river dissolved loads are shown in Table 8. The poor external reproducibility of major elements Na (46.3 %), K (11.8 %), Mg (24.5 %), Ca (36.3 %), and Al (21.2 %) is most likely related to the high and extremely variable total procedure blanks. Concentration measurements on blanks, calculated into mass, showed values of 126 ng – 3.59 µg, 404 ng – 4.3 µg, 187 ng – 3.0 µg, 579 ng – 109 µg, 755 ng – 29.5 µg, for Na, K, Mg, Ca, and Al, respectively. The blank contribution and its effect on element concentrations is in detail discussed in Chapter 9.

Table 8: Major and trace element concentrations of dissolved loads of Murrumbidgee River samples.

Sample	Distance downstream (km)	Li (ppb)	Ti (ppb)	Na (ppm)	Mg (ppm)	Al (ppm)	K (ppm)	Ca (ppm)
Murrumbidgee #3 Tantangara	20	0.8	6.2	2.0	1.1	0.26	0.8	3.8
Murrumbidgee #5	44	1.9	8.1	2.9	1.2	0.41	1.2	5.1
Murrumbidgee #6	80	1.9	13.5	9.8	5.2	0.49	2.1	7.3
Murrumbidgee #8	90	1.9	12.7	7.7	4.5	0.44	1.3	8.9
Murrumbidgee #10 Spring Valley Creek	105	2.8	27.1	14.6	7.1	0.71	3.0	12.9
Murrumbidgee #12	145	2.3	13.9	11.1	6.1	0.29	1.7	9.6
Murrumbidgee #13 @ Tharwa	154	3.2	22.0	10.3	4.4	0.70	2.2	13.6
Murrumbidgee #20 at Jugiong	264	3.2	16.6	14.3	6.2	0.20	2.8	14.3
Murrumbidgee #22	213	3.4	16.2	13.7	6.7	0.44	2.5	12.3
Murrumbidgee #9 before Tumut	284	3.3	18.2	14.2	6.3	0.31	2.6	14.2
Murrumbidgee @ Gundagai	298	2.8	107.3	17.9	8.3	1.31	3.4	14.8
Murrumbidgee @ Wagga Eunony bridge	364	4.4	19.5	15.1	6.4	0.50	3.5	13.6
Volcanic catchment A		4.7	16.4	31.1	13.4	0.26	2.5	16.5
Volcanic catchment B		2.8	14.0	7.9	4.2	0.53	2.9	9.4
Volcanic D Gomindena creek		3.0	25.9	24.5	15.5	0.29	3.8	25.9
Volcanic E		5.0	34.7	35.2	18.2	0.23	5.6	34.0
Volcanic catchment F		3.3	25.5	22.2	10.4	0.59	4.1	22.3
Volcanic catchment Rockflat creek		1.3	37.6	14.4	19.2	0.74	3.6	21.7
Volcanic catchment upper Goodmans Gully		3.4	10.2	4.7	0.9	0.22	1.6	7.9
Sedimentary C Umbango creek		11.0	13.0	17.4	6.7	0.74	2.9	7.6
Sedimentary E Jellingro creek		6.0	13.0	17.5	8.9	0.45	3.8	10.7
Sedimentary F Alac Creek		1.2	5.9	1.5	1.8	0.06	0.4	3.5

Granodiorite A at Cunningham creek	7.4	43.5	0.0	31.0	0.33	8.1	41.9
Granodiorite C Adjungbilly creek	2.4	11.7	8.0	6.7	0.47	1.6	9.9
Granodiorite F	17.4	21.1	13.5	5.1	0.51	3.3	11.0
Granodiorite Back creek near Adaminaby	2.1	27.8	6.3	0.9	2.85	1.3	3.5
Granodiorite/Volcanic Jourama creek	1.5	9.2	2.4	1.0	0.27	0.9	6.4
Granite catchment Gocup creek	6.7	8.4	8.4	1.5	0.39	1.3	5.4

Distance downstream refers to the distance from the river source or headwater.

External reproducibility (2RSE) of Na, K, Mg, Ca, Al, Ti, Li, Nb, and Ta is estimated at 46.3 %, 11.8 %, 24.5 %, 36.3 %, 21.2 %, 11.6 %, 6.6 %, 6.3 %, and 5.8 %, respectively.

Dissolved Li, Ti, Na, Mg, Al, K, and Ca of all river dissolved loads range from 0.8 to 17.4 ppb, 5.9 to 107.3 ppm, < 0.5 to 35.2 ppm, 0.9 to 31 ppm, 0.1 to 2.8 ppm, 0.4 to 8.1 ppm, and 3.5 to 41.9 ppm, respectively. Upper reaches of the Murrumbidgee River show the lowest concentrations of all analysed elements, which increases further downstream until ~145 km distance from the headwaters where concentrations remain relatively stable until the last sample point at Wagga Wagga (~364 km distance from headwaters). Major and trace element concentrations of dissolved loads of monolithologic catchments display large variations between and within the three lithology groups (volcanic, sedimentary siliclastic, granitic).

7.1.2 Results: lithium isotope composition and pH of dissolved loads

A total of eight samples of the Murrumbidgee River and several minor water bodies that flow through monolithologic catchments were analysed for Li isotopes and pH. Results are shown in Table 9, Figure 84, and Figure 85.

Table 9: Li isotope compositions of river dissolved loads (δ^7Li_{diss}) and pH.

Sample	pH	δ^7Li_{diss}	distance downstream (km)
Murrumbidgee #03 Tantangara	7.0	18.5	20
Murrumbidgee #05*	6.6	17.7	44
Murrumbidgee #08	7.5	23.8	90
Murrumbidgee #10	7.8	14.0	105
Murrumbidgee #12	7.8	24.5	145
Murrumbidgee #22 (before Yass)	7.6	18.3	213
Murrumbidgee before Tumut (9A/B, 2014)	7.5	23.6	284
Murrumbidgee at Wagga	7.3	18.0	364
Granodiorite catchment A (Cunningham Creek)	8.2	26.0	
Granodiorite catchment C	7.5	24.1	
Volcanic catchment A	7.9	23.6	
Volcanic catchment B*	7.7	10.0	
Volcanic catchment E	8.2	19.8	
Volcanic catchment F	7.7	21.7	
Sedimentary catchment F	6.8	23.4	
Sedimentary catchment C (Umbango Creek)	7.0	15.4	
Sedimentary catchment E (Jellingro Creek)	7.4	17.5	

Distance downstream refers to the distance from the river source or headwater.

**δ^7Li value is the average over two measured aliquots. External reproducibility (2SE) of δ^7Li values is 0.5 ‰.*

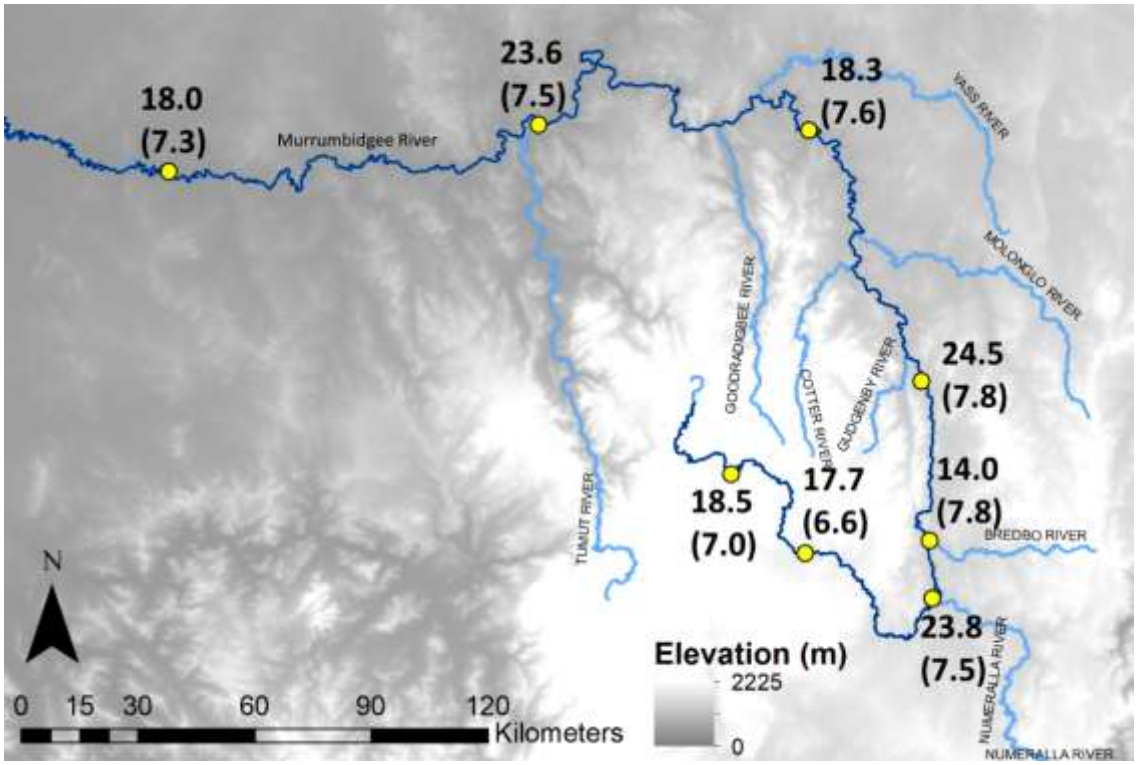

Figure 84: The δ^7Li composition and pH (in parentheses) of dissolved loads from the Murrumbidgee River. External uncertainty (2SE) of δ^7Li values is 0.5 ‰.

The Li isotope composition of river dissolved loads is highly variable with no obvious systematic evolution downstream (Figure 84). The uppermost sample at Tantangara shows 18.5 ‰. About 24 km further downstream, the Li isotope ratio declines to 17.7 ‰ (Table 9, Figure 84). Before the confluence with the Numeralla River, the uppermost tributary of the Murrumbidgee River, the δ^7Li value increases to 23.8 ‰, and decreases just after to 14.0 ‰, which is the lowest isotopic composition observed for all investigated samples. Before the confluence with the Gudgenby River, the δ^7Li value reaches the highest value of 24.5 ‰. At about mid-catchment, Li isotope ratios decrease to 18.3 ‰, followed by an increase to 23.6 ‰. The lower catchment shows a δ^7Li composition of 18.0 ‰, which is about the same range observed for river dissolved loads from the upper catchment. The three uppermost samples display pH values from 6.6 to 7.5 (Table 9, Figure 84). At the confluence with Bredbo River, the water pH is 7.8 and decreases continuously downstream until pH 7.3 at Wagga Wagga.

Li isotope ratios in waters from volcanic catchments range from 10.0 to 23.6 ‰ (Table 9, Figure 85). Two granodiorite catchments show δ^7Li_{diss} of 24.1 and 26.0 ‰. A large range of Li isotope compositions is observed for river dissolved loads from sedimentary catchments, where δ^7Li values range from 15.4 to 23.4 ‰. The pH of waters from volcanic, granodiorite, and sedimentary catchments varies between 7.7 to 8.2, 7.5 to 8.2, and 6.8 to 7.4, respectively.

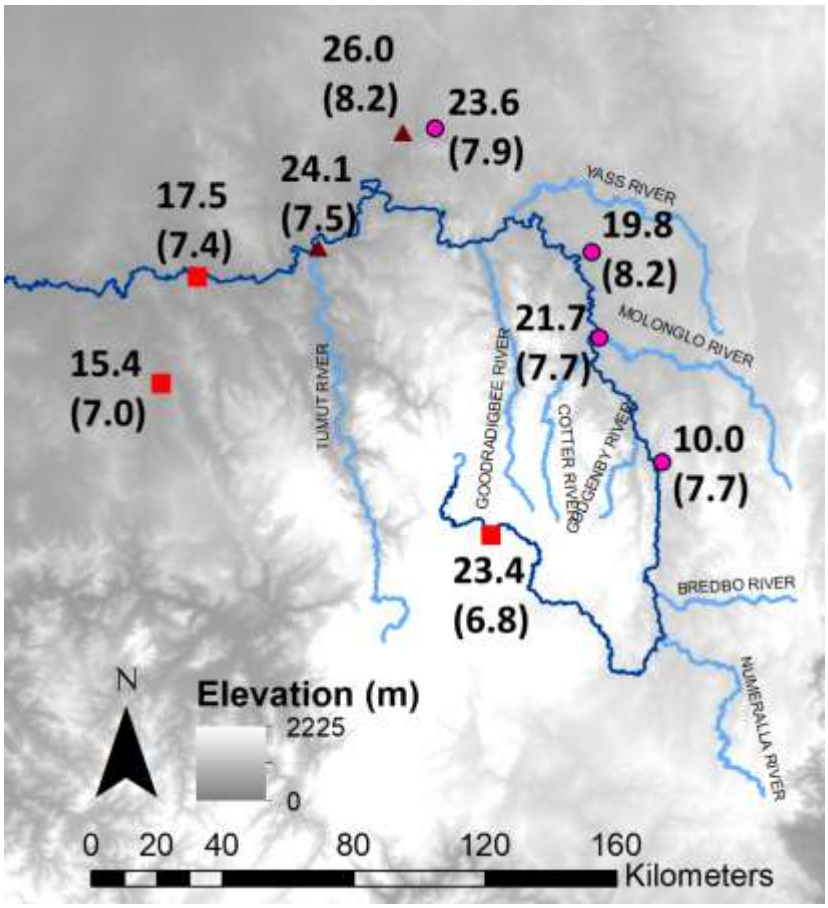

Figure 85: The δ^7Li composition and pH (in parentheses) of dissolved loads from monolithologic catchments. Red squares; sedimentary siliclastic bedrock; brown triangles: granodiorite bedrock; pink circles: volcanic bedrock. External uncertainty of δ^7Li values is 0.5 ‰.

7.2 River sediments and source rocks

Sediments were collected from exposed sandy point bars of the Murrumbidgee River catchment and of minor creeks that flow through monolithologic catchments. After grain size analysis of sediments, the clay-sized fraction was separated and the Li isotope composition, and major and trace element concentrations were determined. Bedrock

samples were collected from each lithology unit (sedimentary, volcanic, and granodiorite) and the Li isotope composition was measured. See Chapter 6, for a detailed sampling strategy.

7.2.1 Results: grain size distribution of river sediments

All river sediments consist mostly of sand (63 µm – 2 mm) and silt (63 µm – 2 µm), with very little particles in the clay-sized fraction (<2 µm) (Table 10). Samples from the Murrumbidgee River catchment vary between 57 to 100 % sand, 0 – 41 % silt, and up to 2 % clay (Figure 86). Sediments from sedimentary catchments show sand proportions between 69 to 92 %, 82 to 92 % silt, and 1 to 4 % clay. Grain size distributions of samples from volcanic catchments range from 84 to 91 % sand, 8 to 15 % silt, and 0 to 1 % clay. Sediments from granodiorite catchments vary between 85 to 97 % sand, 3 to 14 % silt, and 0 to 1 % clay. The mean grain size is somewhat variable within each catchment. Granodiorite catchments seem to produce the coarsest sediment, followed by volcanic catchments. Sediments from sedimentary catchments show the smallest mean particle size and Murrumbidgee River sediments show the highest variability of mean particle size.

Table 10: Grain size distribution of river sediments from the Murrumbidgee River and monolithologic catchments.

Sample	Aliquot	Sand (%)	Silt (%)	Clay (%)	Mean (µm)
Murrumbidgee before Tumut (9A/B, 2014)	A	99	1	0	535
Murrumbidgee before Tumut (9A/B, 2014)	B	100	0	0	643
Murrumbidgee #10	A	57	41	2	69
Murrumbidgee #10	B	87	12	1	287
*Murrumbidgee #10 (replicate)**	*B*	*87*	*12*	*1*	*287*
Murrumbidgee #22	B	95	5	0	274
Sedimentary catchment B	A	87	12	1	308
Sedimentary catchment B	B	83	15	1	252
Sedimentary catchment C	A	69	28	4	114
Sedimentary catchment C	B	92	8	1	461
Sedimentary catchment E	B	83	16	1	284
Sedimentary catchment E	A	82	16	1	325
Volcanic catchment A	B	84	15	1	324
Volcanic catchment A	A	88	11	1	334
Volcanic catchment D	B	91	8	1	370
Volcanic catchment D	A	89	10	1	356
Granodiorite catchment A	B	85	14	1	385
Granodiorite catchment A	A	94	5	0	821
Granodiorite catchment C	N/A	88	11	1	379
Granodiorite catchment F	B	94	6	0	552
Granodiorite catchment F	A	97	3	0	475

Uncertainty of grain size measurements was not determined because replicate samples yielded the same results. See Chapter 9 for details.

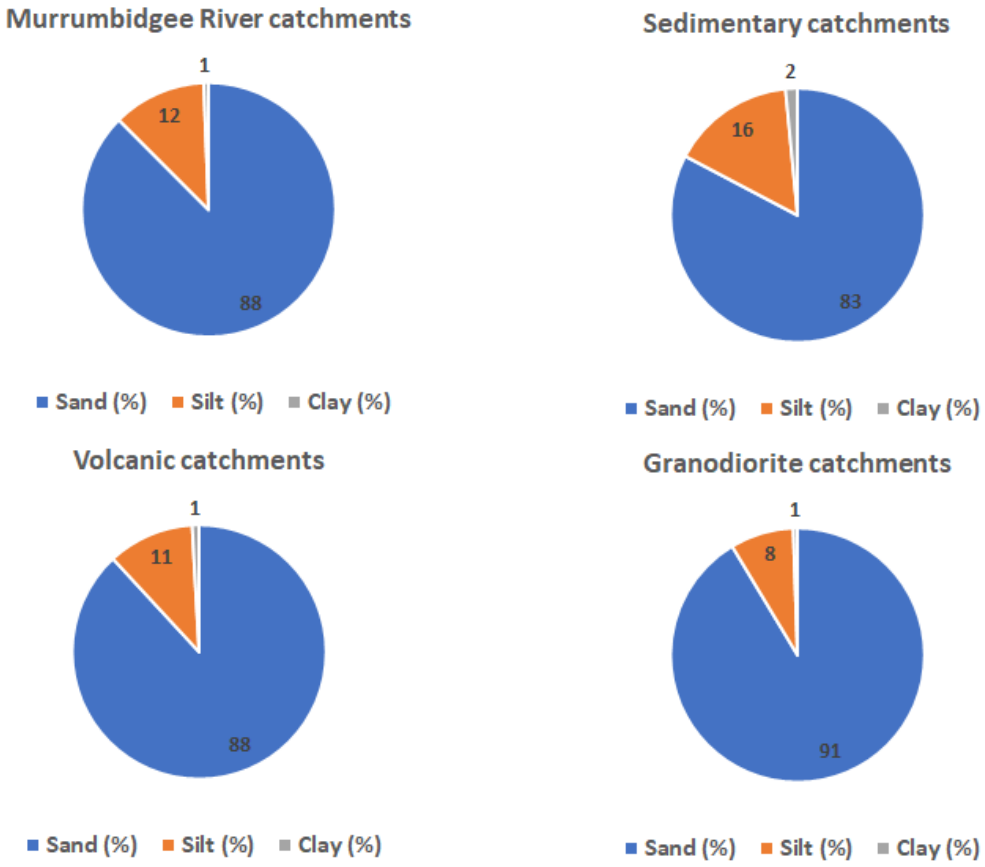

Figure 86: Mean grain size distribution of catchments from the Murrumbidgee River (n = 6), sedimentary (n = 6), volcanic (n = 4), and granodiorite catchments (n = 5).

7.2.2 Results: mineral composition of clays

Using X-ray diffraction techniques (XRD), the mineralogy of clay samples was estimated. This was performed on a selection of samples from the Murrumbidgee River, monolithologic catchments, and several tributaries of the Murrumbidgee River. Besides quartz, four clay mineral groups were quantified: kaolinite, illite, smectite (expandable clay), and mixed layer clay. The latter consists of clays that alternate from one type to another by a stacking sequence. The presence of smectites (expandable clays) is based on a very rough estimation, indicating whether the expendable clay fraction is significant (=1) or insignificant (=0) (see Chapter 9 for details). Quartz contents range from 3 to 19 wt %, mixed layer clays from 1 to 31 wt %, kaolinite from 18 to 86 wt %, and Illite from 3 to 56 wt % (Table 11). The overall clay mineral assemblage for each catchment group (Murrumbidgee River, tributaries, and individual monolithologic catchments) appears very similar. Clays from granodiorite catchments show on average the lowest content of mixed layer clays.

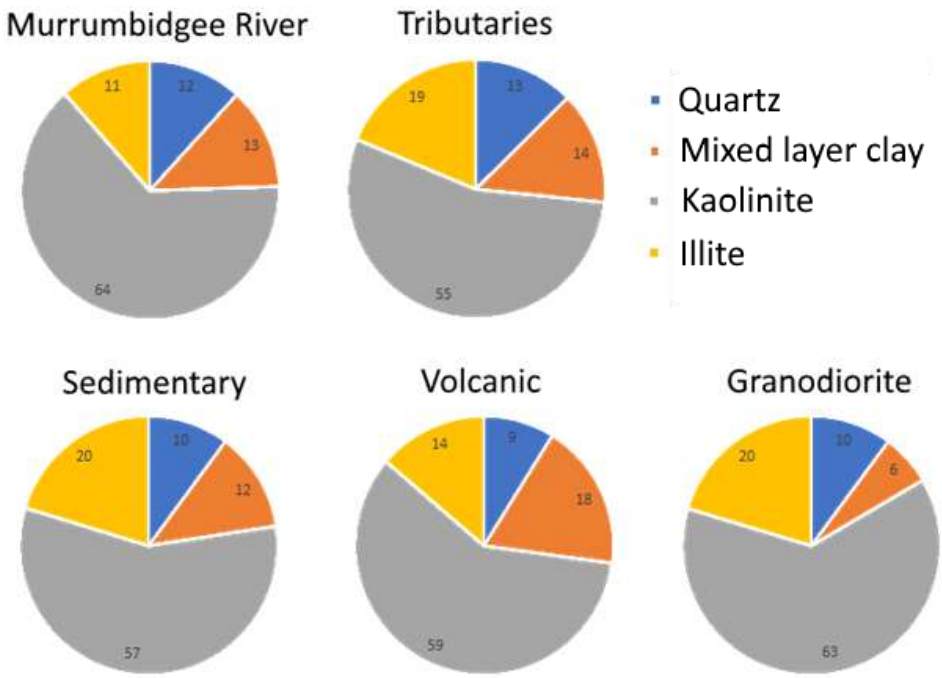

Figure 87: Mean clay mineral distribution of the different catchments determined via XRD technique. Murrumbidgee River (n = 6), tributaries (n = 7), sedimentary (n = 6), volcanic (n = 5), granodiorite (n = 4). Relative errors on mineral contents are less than 5 % (2σ).

Table 11: Clay mineral composition of clay-sized fractions of sediment collected in the Murrumbidgee River Basin.

Sample	Aliquot	Quartz (%)	Mixed layer clay (%)	Kaolinite (%)	Illite (%)	Expandable clays (1= yes, 0= negligible)
MR#06	N/A	5	19	72	3	1
Murrumbidgee after Tumut	A	10	1	72	16	1
Murrumbidgee after Tumut	B	9	2	74	15	1
Murrumbidgee before Tumut (9A/B, 2014)	A	19	24	48	9	0
Murrumbidgee before Tumut (9A/B, 2014)	B	18	25	51	6	0
Murrumbidgee before Yass	A	11	3	67	19	1
Murrumbidgee before Yass	B	10	15	63	12	1
Tumut River lower catchment	A	7	4	75	15	0
Yass River lower catchment	A	14	11	65	11	0
Yass River lower catchment	B	16	10	18	56	0
Yass River lower catchment	C	18	30	31	21	0
Yass River lower catchment	D	7	31	55	7	1
Yass River middle catchment	N/A	12	8	69	12	1
Yass River upper catchment	N/A	15	6	71	9	1
Sedimentary catchment B	A	9	2	45	45	0
Sedimentary catchment B	B	11	21	63	5	0
Sedimentary catchment C Umbango Creek	A	13	11	65	11	1
Sedimentary catchment C Umbango Creek	B	8	22	64	6	0
Sedimentary catchment E Jellingro Creek	A	10	2	47	41	0
Sedimentary catchment E	B	10	17	60	13	0
Volcanic catchment A	A	10	12	57	21	0
Volcanic catchment A	B	6	19	64	11	0
Volcanic catchment B	N/A	13	34			0

Volcanic catchment D	A	6	24	58	12	0
Volcanic catchment D	B	8	2	72	18	1
Granodiorite catchment A at Cunningham Creek	A	13	5	44	38	1
Granodiorite catchment A at Cunningham Creek	B	13	12	55	20	1
Granodiorite catchment C	N/A	3	3	86	8	1
Granodiorite catchment F	A	11	6	67	16	0

The external reproducibility (2SE) for quartz, mixed layer clay, illite and kaolinite is estimated at 4.6 %, 11.1 %, 4.3 %, and 10.6 %, respectively.

7.2.3 Results: major and trace element composition of clays and bedrock

The major and trace element concentrations were measured on the clay-sized fraction of river sediments of the Murrumbidgee River. Likewise, one bedrock sample of each major lithology unit in the Murrumbidgee River Basin (i.e. sedimentary, volcanic, and granodiorite) were crushed and analysed. Li concentrations of clays from different parts of the Murrumbidgee River catchment vary from 97 to 351 ppm. Major element concentrations range from 2,744 to 32,420 ppm, 6,170 to 13,422 ppm, 72,090 to 129,947 ppm, 16,485 to 30,765 ppm, 1,356 to 24,898 ppm, and 1,826 to 7,320 ppm for Na, Mg, Al, K, Ca, and Ti, respectively (Table 12). The sedimentary bedrock (graywacke) showed the lowest Li concentration of 85 ppm, compared to the volcanic and granodiorite bedrock which displayed concentrations of 118 and 192 ppm, respectively. Similarly, the K concentration of the sedimentary bedrock was measured the lowest at 9,208 ppm, compared to 27,022 ppm and 27,501 ppm for the volcanic and granite bedrock sample, respectively. In contrast, the Ca concentration of the sedimentary bedrock sample is the highest with 20,748 ppm compared to the volcanic and granitic bedrock sample which showed Ca concentrations of 11,116 ppm and 9,323 ppm, respectively.

Table 12: Major and trace element composition of selected Murrumbidgee River clays and bedrock samples.

Sample	distance downstream (km)	Li (ppm)	Na (ppm)	Mg (ppm)	Al (ppm)	K (ppm)	Ca (ppm)	Ti (ppm)
Murrumbidgee #01	0	115	2,988	7,759	94,376	20,891	8,584	1,826
Murrumbidgee #03 Tantangara	20	130	2,744	10,348	113,141	30,765	12,842	2,808
Murrumbidgee #05	44	112	3,465	7,805	72,090	19,576	1,657	1,982
Murrumbidgee #6	80	101	4,394	13,422	105,747	12,603	24,898	6,855
Murrumbidgee #08	90	130	8,524	13,286	93,935	24,361	21,737	5,011
Murrumbidgee #10	105	97	8,575	9,614	82,319	27,165	16,639	3,218
Murrumbidgee #12	145	283	5,707	12,599	94,678	25,369	1,880	4,162
Murrumbidgee #13	154	100	32,420	6,170	70,940	16,485	17,092	2,321
Murrumbidgee after Cotter River	202	164	11,753	10,708	129,947	22,863	24,419	5,265
Murrumbidgee #20 at Jugiong	264	280	10,458	11,089	109,271	24,251	1,934	5,785
Murrumbidgee at Gundagai	298	180	8,237	10,165	110,748	23,677	13,651	5,247
Murrumbidgee at Wagga	364	318	7,011	9,888	122,109	21,138	1,356	5,454
Murrumbidgee at Narrandera	450	351	3,071	9,195	107,090	18,696	2,322	4,594
Murrumbidgee before Hay	555	214	5,160	8,837	108,580	24,636	1,930	7,320
Bedrock sedimentary catchment (graywacke)		85	13,561	8,552	67,815	9,208	20,748	4,327
Bedrock volcanic catchment		118	17,735	8,558	71,770	27,022	11,116	3,801
Bedrock granodiorite catchment		192	14,820	8,556	64,694	27,501	9,323	2,644

External reproducibility (2RSE) of Na, K, Mg, Ca, Al, Ti, and Li, is estimated at 46.3 %, 11.8 %, 24.5 %, 36.3 %, 21.2 %, 11.6 %, and 6.6 %, respectively.

7.2.4 Results: lithium isotope composition of clays and source rocks

The Li isotope composition was measured on the clay-sized fraction of sediments collected in the Murrumbidgee River Basin. The δ^7Li values of clays from the Murrumbidgee River catchment vary between -2.3 and 0.6 ‰ (Table 13). Clays formed in granodiorite and sedimentary catchments show a large range of δ^7Li values from -3.8 to 1.9 ‰ and from -3.9 to 0.9 ‰, respectively. In contrast, the range of Li isotope ratios of clays from volcanic catchments is more restricted with δ^7Li values ranging between -1.4 to 0.3 ‰. A total of three bedrock samples were measured for Li isotopes, one for each major lithology unit in the Murrumbidgee River catchment. These show δ^7Li values of 6.4, 2.1, and 1.6 ‰ for sedimentary, volcanic and granodiorite rocks, respectively. A histogram of the δ^7Li values of clays from each catchment group is shown in Figure 88. A dust sample collected in the Snowy Mountains near Cabramurra, provided by Sam Marx (University of Wollongong) and Nicola Stromsoe (University of Queensland), was also processed and yielded a δ^7Li value of 1.7 ‰. See Chapter 6 for details on how samples were processed.

Table 13: Li isotope composition of clay-sized fractions (δ^7Li_{clay}) from sediments in the Murrumbidgee River catchment.

Sample	Aliquot	δ^7Li_{clay}	distance downstream (km)
Murrumbidgee #10	N/A	-0.4	105
Murrumbidgee #12	N/A	0.6	145
Murrumbidgee #22 (before Yass)	A	-0.5	213
Murrumbidgee #22 (before Yass)	B	-1.0	213
Murrumbidgee before Tumut (9A/B, 2014)	A	-0.3	284
Murrumbidgee before Tumut (9A/B, 2014)	B	-1.0	284
Murrumbidgee after Tumut	N/A	-1.6	290
Murrumbidgee at Wagga	N/A	-2.3	364
Murrumbidgee at Narrandera	N/A	-2.1	450
Murrumbidgee before Hay	N/A	-1.4	555
Granodiorite Catchment A at Cunningham Creek	A	1.0	
Granodiorite Catchment A at Cunningham Creek (replicate)	*A*	*1.9*	
Granodiorite Catchment A at Cunningham Creek	B	0.5	
Granodiorite C	N/A	-0.3	
Granodiorite F	B	-3.8	
Granodiorite F (replicate)	*B*	*-2.3*	
Granodiorite F	A	-3.1	
Volcanic Catchment A	B	0.3	
Volcanic Catchment A	A	-1.4	
Volcanic catchment D	A	-0.3	
Volcanic catchment D	B	-1.3	
Sedimentary B	B	0.9	
Sedimentary B	A	-0.1	
Sedimentary catchment C Umbango Creek	A	-3.9	
Sedimentary catchment C Umbango Creek	B	-3.9	
Sedimentary E Jellingro Creek	B	-1.3	
Sedimentary E Jellingro Creek	A	-1.4	
Bedrock sedimentary catchment (graywacke)	N/A	6.4	
Bedrock volcanic catchment	N/A	2.1	
Bedrock granodiorite catchment	N/A	1.6	
Snowy Mountain dust	N/A	1.7	

Distance downstream refers to the distance from the river source or headwater.

External uncertainty (2SE) of δ^7Li values is 0.5 ‰.

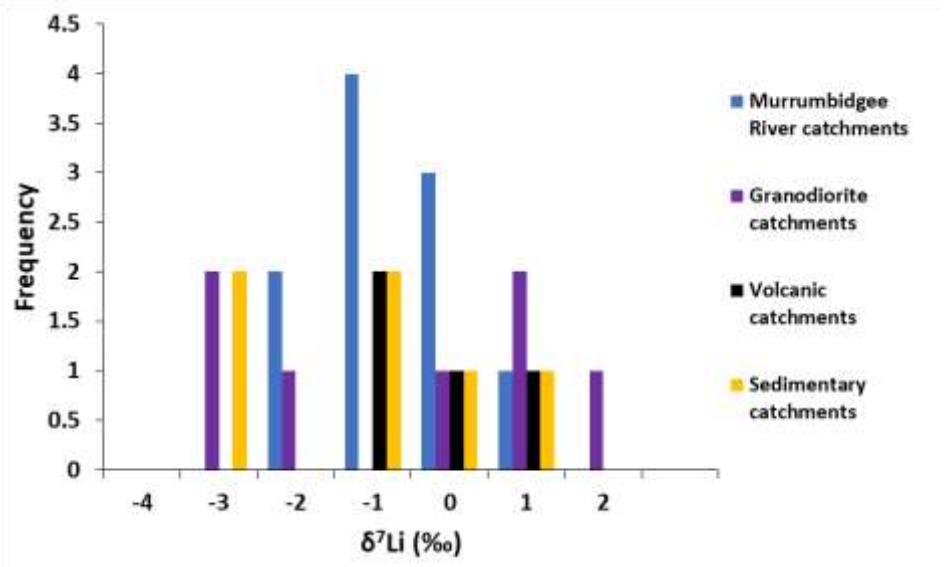

Figure 88: Comparison of Li isotope compositions of clays between the different catchments. Murrumbidgee River catchments (n = 10), granodiorite catchments (n = 7) volcanic catchments (n = 4), sedimentary catchments (n = 4). External uncertainty (2SE) of δ^7Li values is 0.5 ‰.

7.2.5 Results: neodymium isotope composition of Murrumbidgee clays and source rocks

The Nd isotope ratio $^{143}Nd/^{144}Nd$, here expressed as εNd, is calculated via

$$\varepsilon Nd = \left(\frac{\left(\frac{^{143}Nd}{^{144}Nd}_{sample} - \frac{^{143}Nd}{^{144}Nd}_{CHUR} \right)}{\frac{^{143}Nd}{^{144}Nd}_{CHUR}} \right) * 10{,}000 \quad (22)$$

where $^{143}Nd/^{144}Nd_{CHUR}$ = 0.511836 (Jacobsen and Wasserburg, 1980). Clay-sized fractions from the Murrumbidgee River, monolithologic catchments and three bedrock samples (sedimentary, volcanic, and granodiorite) were analysed for Nd isotopes. Murrumbidgee clay samples cover a relatively large range of εNd values from -13.5 to -7.5 (Table 14). Clay-sized fractions from sediments from sedimentary catchments display εNd values of -14.7 and -10.1. Granodiorite catchments show only little variance with εNd values of -10.8 and -8.7. Similarly, εNd values of clays from volcanic catchments vary between -10.7 and -8.8. The three source rocks collected in the Murrumbidgee River Basin displayed εNd values of -16.4, -4.1, and -11.2 for a sedimentary-siliclastic bedrock, a granodiorite (I-type), and a volcanic rock, respectively. Typical bedrock $^{143}Nd/^{144}Nd$ from the literature are compiled for sedimentary siliclastic rocks, granite (S-type), granite (I-type) and volcanic rocks (Table 14). The highest εNd values are observed for I-type granites (-8.9 to 0.4), intermediate for S-type granites (-10.1 to -8.0), and lowest for volcanic (-17.2 to -11.6) and sedimentary rocks (-10.5 to -9.5). The εNd values of bedrock samples from the Murrumbidgee River Basin fall within the range of what is reported elsewhere.

Table 14: The Nd isotope composition (εNd) of clay-sized fraction of sediments from the Murrumbidgee River and monolithologic catchments and various source rocks.

Sample	Aliquot	Type	$^{143}Nd/^{144}Nd$	εNd	Reference
Murrumbidgee #03	N/A	clay	0.511958	-13.5	this study
Murrumbidgee #06 clay	N/A	clay	0.512266	-7.5	this study
Murrumbidgee #12 clay	N/A	clay	0.512067	-11.3	this study
Murrumbidgee at Wagga	N/A	clay	0.512185	-9.0	this study
Sedimentary catchment F	N/A	clay	0.511894	-14.7	this study
Sedimentary catchment E	B	clay	0.512129	-10.1	this study
Granodiorite catchment C	N/A	clay	0.512202	-8.7	this study
Granodiorite catchment F	B	clay	0.512092	-10.8	this study
Volcanic catchment B	N/A	clay	0.512188	-9.0	this study
Volcanic catchment D	A	clay	0.512101	-10.7	this study
Bedrock sedimentary siliclastic	N/A	sedimentary siliclastic	0.511809	-16.4	this study
Bedrock granodiorite	N/A	granite (S-type)	0.512438	-4.1	this study
Bedrock volcanic	N/A	volcanic	0.512073	-11.2	this study
wa1	N/A	granite (S-type)	0.512149	-9.7	(Elburg, 1996)
wa3	N/A	granite (S-type)	0.512141	-9.9	(Elburg, 1996)
wa16h	N/A	granite (S-type)	0.512131	-10.1	(Elburg, 1996)
BB19	N/A	granite (S-type)	0.512217	-8.4	(McCulloch and Woodhead, 1993)
BB2	N/A	granite (S-type)	0.512238	-8.0	(McCulloch and Woodhead, 1993)
wa23	N/A	granite (I-type)	0.512343	-5.9	(Elburg, 1996)
wa37	N/A	granite (I-type)	0.512397	-4.9	(Elburg, 1996)
wa43	N/A	granite (I-type)	0.512413	-4.6	(Elburg, 1996)

BB61	N/A	granite (I-type)	0.512192	-8.9	(McCulloch and Woodhead, 1993)
BB10	N/A	granite (I-type)	0.512515	-2.6	(McCulloch and Woodhead, 1993)
BB48	N/A	granite (I-type)	0.512376	-5.3	(McCulloch and Woodhead, 1993)
BB104	N/A	granite (I-type)	0.512535	-2.2	(McCulloch and Woodhead, 1993)
BB62	N/A	granite (I-type)	0.512669	0.4	(McCulloch and Woodhead, 1993)
BB60	N/A	granite (I-type)	0.512479	-3.3	(McCulloch and Woodhead, 1993)
KB22	N/A	granite (I-type)	0.512392	-5.0	(McCulloch and Woodhead, 1993)
wa16e	N/A	granite (I-type)	0.512209	-8.6	(Elburg, 1996)
IWS1	N/A	sedimentary siliclastic	0.512110	-10.5	(McCulloch and Woodhead, 1993)
IWS2	N/A	sedimentary siliclastic	0.512151	-9.7	(McCulloch and Woodhead, 1993)
IWS3	N/A	sedimentary siliclastic	0.512161	-9.5	(McCulloch and Woodhead, 1993)
IWS4	N/A	sedimentary siliclastic	0.512140	-9.9	(McCulloch and Woodhead, 1993)
69-1013	N/A	volcanic	0.512004	-12.6	(McDonough et al., 1985)
2154	N/A	volcanic	0.512030	-12.1	(McDonough et al., 1985)
2183	N/A	volcanic	0.511984	-13.0	(McDonough et al., 1985)
2178	N/A	volcanic	0.512007	-12.5	(McDonough et al., 1985)
2101	N/A	volcanic	0.512006	-12.5	(McDonough et al., 1985)
2102	N/A	volcanic	0.512004	-12.6	(McDonough et al., 1985)
2209	N/A	volcanic	0.512053	-11.6	(McDonough et al., 1985)
2177	N/A	volcanic	0.511765	-17.2	(McDonough et al., 1985)
2125	N/A	volcanic	0.511945	-13.7	(McDonough et al., 1985)
69-1018	N/A	volcanic	0.511990	-12.8	(McDonough et al., 1985)
2152	N/A	volcanic	0.511865	-15.3	(McDonough et al., 1985)
69-1006	N/A	volcanic	0.512008	-12.5	(McDonough et al., 1985)
69-1026	N/A	volcanic	0.511775	-17.0	(McDonough et al., 1985)
69-1020	N/A	volcanic	0.511925	-14.1	(McDonough et al., 1985)
69-1033	N/A	volcanic	0.511970	-13.2	(McDonough et al., 1985)

2201	N/A	volcanic	0.512018	-12.3	(McDonough et al., 1985)
2149	N/A	volcanic	0.512025	-12.2	(McDonough et al., 1985)
69-1036	N/A	volcanic	0.511992	-12.8	(McDonough et al., 1985)
2156	N/A	volcanic	0.512007	-12.5	(McDonough et al., 1985)
2164	N/A	volcanic	0.512021	-12.2	(McDonough et al., 1985)
2679	N/A	volcanic	0.512031	-12.0	(McDonough et al., 1985)
2128	N/A	volcanic	0.512000	-12.6	(McDonough et al., 1985)
2650	N/A	volcanic	0.511997	-12.7	(McDonough et al., 1985)
71-10	N/A	volcanic	0.511930	-14.0	(McDonough et al., 1985)
71-8	N/A	volcanic	0.511971	-13.2	(McDonough et al., 1985)

Literature data for volcanic rocks are from the southern border of the Murray-Darling Basin, granite and sedimentary rocks from the Lachlan fold belt. External uncertainty (2SE) for εNd values in this study is 0.3.

7.3 Palaeo-channel sediments

A total of four palaeo-channel systems were investigated. Where available, palaeo-channel sediments were collected from exposed deposits, where cores were retrieved. If no exposed deposit was available or the sediment was too tough, pits were dug with a shovel. Additional samples were obtained via drill cores. The latter were provided by Daniela Mueller and Timothy Cohen (University of Wollongong). See Chapter 6 for a detailed sample strategy and how samples were processed. Clay-sized fractions of palaeo-channel deposits were analysed for Li and Nd isotopes, major and trace element concentrations, and clay mineralogy. See Chapter 9 for details. At least four different samples from each palaeo-channel system were analysed for Nd isotopes. Most deposition ages displayed in Table 15 are based on literature data by Page et al. (1996). Samples provided by Daniela Mueller and Timothy Cohen were dated with OSL (Mueller et al., under review). No age determination was performed on sediments collected in this study. Instead, all sample locations in this study were chosen based on the established palaeo-channel maps found in Page et al. (1996) and should therefore roughly fit within the proposed deposition timeframe.

7.3.1 Results: Li and Nd isotopes and major and trace elements

Two out of three sample sites (Gala Vale & Gala Vale 'south') for the Coleambally palaeo-channel system were exposed deposits, where samples were taken from different depths of the sediment succession using aluminium pipes. The third sample site, Bundure, is an exposed pit where samples were taken with a shovel. See chapter 6 for a detailed sample strategy. Li isotope ratios of the Coleambally palaeo-channel system range from -2.4 to 1.9 ‰ (Table 15). From this system, three samples were analysed for their εNd composition, which range from -12.4 to -7.2. Li concentrations are 165 to 291 ppm, Nb 9 to 21 ppm, Ta 1 to 2 ppm, and K from 1.8 to 3 %. The second oldest palaeo-channel system, Kerarbury, was sampled at three different sites: N. Booroorban, Headless Horseman, and Kerarbury. Samples from N. Booroorban were retrieved through ground surface coring, while samples from Headless Horseman and Kerarbury were obtained from exposed deposits. The Li isotope composition of sediments from the Kerarbury system varies between -0.9 and 2.0 ‰, εNd values range from -9 to -2.5 (n = 6), Li concentrations from 156 to 237 ppm, Nb concentrations from 10 and 18 ppm, Ta from 1 to 2 ppm, and K from 1.9 to 2.8 %. For the Gum Creek system, two sample sites were investigated: Tabratong and MGC. The former is an exposed deposit, where several

aliquots from different depths were obtained. At MGC, sediments were retrieved from 4.55 – 13.81 m depth. Note that these samples were obtained by Daniela Mueller (University of Wollongong). The δ^7Li values from the Gum Creek system range from -1.7 to 1.0 ‰. Nd isotope ratios were measured on four samples, which show εNd values from -11.3 to -7.8. Li, Nb, Ta, and K concentrations vary from 167 to 343 ppm, 12 to 31 ppm, 1 to 3 ppm, and 2.1 to 2.8 %, respectively. The Yanco palaeo-channel system was sampled at four different locations: Yanco, Yanco 'a', Thurrowa Road, and MYA. All samples except for MYA were obtained from exposed deposits. At MYA, sediments were retrieved from 3.77 – 6.72 m and kindly provided by Daniela Mueller (University of Wollongong). Li isotope compositions from the Yanco system range from -3.3 to 1.2 ‰. A total of seven samples were analysed for Nd isotopes which yielded εNd values from -11.1 to -8.9. Li, Nb, Ta, and K concentrations display values from 135 to 305 ppm, 9 to 21 ppm, 1 to 2 ppm, and 1.7 to 3.1 %, respectively.

Table 15: Results for palaeo-channel sediments (clay-sized fractions) from the Murrumbidgee River Basin.

Sample	Position in profile	Channel system	Deposition age (ka)	δ^7Li (‰)	εNd	Li (ppm)	Nb (ppm)	Ta (ppm)	K (%)	Comment
Gala Vale 'south' 3	0.72 m / inside	Coleambally	100 ± 9	-0.7		233	15	1	2.9	exposed
*Gala Vale 'south' 3**	*0.72 m / inside*	*Coleambally*	*100 ± 9*	*-0.1*		*203*	*13*	*1*	*2.3*	*exposed*
Gala Vale 'south' 2	1.57 m / outside	Coleambally	100 ± 9	0.3		169	10	1	2.3	exposed
Gala Vale 'south' 2	1.57 m / inside	Coleambally	100 ± 9	-1.3		200	12	1	2.8	exposed
Gala Vale 'south' 1	2.27 m / outside	Coleambally	100 ± 9	-0.4	-8.8	186	13	1	3.0	exposed
Gala Vale 'south' 1	2.27 m / inside	Coleambally	100 ± 9	-0.7		176	13	1	2.8	exposed
Gala Vale 3	0.30 m / outside	Coleambally	100 ± 9	1.2		244	13	1	1.8	exposed
Gala Vale 3	0.30 m / inside	Coleambally	100 ± 9	1.6	-7.2	215	11	1	2.0	exposed
Gala Vale 2	0.80 m / inside	Coleambally	100 ± 9	1.5	-12.4	208	10	1	2.3	exposed
Gala Vale 1	1.25 m / outside	Coleambally	100 ± 9	0.1		291	10	1	2.0	exposed
Gala Vale 1	1.25 m / inside	Coleambally	100 ± 9	1.9		235	9	1	2.1	exposed
Bundure 1	0.50 m	Coleambally	100 ± 9	-1.5	-8.7	165	21	2	2.7	shovel sample
Bundure 2	1.90 m	Coleambally	100 ± 9	-2.4	-10.1	174	12	1	2.1	shovel sample
N. Booroorban 1	0.55 - 0.65 m	Kerarbury	46 ± 4	2.0	-8.8	156	18	2	2.8	ground surface coring
N. Booroorban 2	0.65 - 0.75 m	Kerarbury	46 ± 4	-0.4	-8.8	163	11	1	2.4	ground surface coring
Headless Horseman 3	0.15 m / inside & outside	Kerarbury	46 ± 4	1.1		167	12	1	2.1	exposed
Headless Horseman 2	0.60 m / inside & outside	Kerarbury	46 ± 4	0.3	-6.5	177	11	1	2.1	exposed

Headless Horseman 1	1.00 m / inside & outside	Kerarbury	46 ± 4	0.4	-7.6	157	10	1	1.9	exposed
Kerarbury 3	0.50 m / inside & outside	Kerarbury	46 ± 4	1.2		202	15	2	2.8	exposed
Kerarbury 2	3.00 m / inside	Kerarbury	46 ± 4	0.1	-9.0	210	13	1	2.5	exposed
Kerarbury 1	4.00 m / outside	Kerarbury	46 ± 4	-0.9	-2.5	228	13	1	2.4	exposed
Kerarbury 1	4.00 m / inside	Kerarbury	46 ± 4	1.2		237	12	1	2.4	exposed
MGCY-5#4 uow 1315**	13.81 m	Gum Creek	33.0 ± 1.8	0.7	-9.4	342	31	3	2.8	auger core
MGC 8-3#5 uow 1390**	4.65 m	Gum Creek	33.1 ± 1.7	-1.1	-11.3	287	20	2	2.2	auger core
MGC 4-4#5 uow 1322**	5.85 m	Gum Creek	33.7 ± 2.0	-0.9		343	22	2	2.1	auger core
MGC 2-1 clay uow 1306**	4.55 m	Gum Creek	36.7 ± 2.1	-1.7		263	26	2	2.3	auger core
Tabratong 3	0.30 m / inside & outside	Gum Creek	25 ± 3	1.0		201	16	2	N/A	exposed
Tabratong 2	0.80 m / inside & outside	Gum Creek	25 ± 3	-0.2	-7.8	192	12	1	2.3	exposed
Tabratong 1	1.35 m / inside & outside	Gum Creek	25 ± 3	-1.2	-8.8	167	12	1	2.1	exposed
MYA-2#4 uow 1523**	3.77 m	Yanco	32.4 ± 1.7	0.7		297	21	2	2.5	auger core
MYA 1#6 uow 1521**	6.72 m	Yanco	20.0 ± 1.2	1.2	-10.1	305	16	2	2.7	auger core
Wanganella 3	0.30 m / inside & outside	Yanco	15 ± 2	-2.9	-11.1	146	21	2	3.1	exposed
Wanganella 2	0.55 m / inside	Yanco	15 ± 2	-3.1	-9.7	174	20	2	2.8	exposed

Wanganella 1	0.90 m / outside	Yanco	15 ± 2	-3.3		171	15	1	2.2	exposed
Wanganella 1	0.90 m / inside	Yanco	15 ± 2	-1.7		135	13	1	2.1	exposed
Thurrowa Road 3	0.65 m	Yanco	15 ± 2	-1.8	-10.0	177	17	2	2.7	exposed
Thurrowa Road 3*	*0.65 m*	*Yanco*	*15 ± 2*	*-1.7*		*168*	*17*	*2*	*2.8*	*exposed*
Thurrowa Road 2	2.93 m / inside & outside	Yanco	15 ± 2	-1.4	-9.9	164	10	1	1.8	exposed
Thurrowa Road 1	3.60 m / inside & outside	Yanco	15 ± 2	-1.3		185	9	1	1.7	exposed
Yanco 'a' 4	0.25 m / inside & outside	Yanco	15 ± 2	-0.1		173	16	2	2.8	exposed
Yanco 'a' 3	1.10 m	Yanco	15 ± 2	0.2		143	21	2	2.6	exposed (white layer)
Yanco 'a' 2	1.18 m / inside & outside	Yanco	15 ± 2	-0.3	-9.1	207	17	2	2.7	exposed
Yanco 'a' 2*	*1.18 m / inside & outside*	*Yanco*	*15 ± 2*	*-0.6*		*203*	*16*	*2*	*2.5*	*exposed*
Yanco 'a' 1	2.00 m / inside & outside	Yanco	15 ± 2	-0.2	-8.9	185	12	1	2.6	exposed

**replicate samples*

***samples provided by Daniela Mueller and Timothy Cohen (University of Wollongong)*

Inside and outside refers to the lateral distance (outside: closest from the surface; inside: deepest part of the sediment core)

Deposition age estimates derived from TL dating (Page et al., 1996). Auger core samples were dated by Daniela Mueller (University of Wollongong) via optically-stimulated luminescence technique (Mueller et al., under review). External reproducibility (2SE) of δ^7Li values, εNd values, Li, Nb, Ta, and K is 0.5 ‰, 0.3, 6.6 %, 6.3 %, 5.8 %, and 11.8 %, respectively.

7.3.2 Results: mineral composition of palaeo-channel clays

The mineralogy of palaeo-channel clays was determined using XRD techniques. Quartz contents range from 4 to 31 %, mixed layer clays from 1 to 52 %, kaolinite from 31 to 73 %, and illite from 1 to 11 % (Table 16). The presence of expandable clays (e.g. smectite) is based on a very rough estimation (see Chapter 9 for details), indicating whether the expandable clay fraction is significant (=1) or insignificant (=0). Palaeo-channel sediments show no systematic enrichment or depletion in any clay mineral group relative to the sample depth.

Table 16: Mineralogy of clay-sized fractions of palaeo-channel sediments determined via XRD techniques.

Sample	Aliquot	Quartz (%)	Mixed layer clay (%)	Kaolinite (%)	Illite (%)	Expandable clays (1= yes, 0= negligible)
Yanco 'a' 1	2.00 m / inside & outside	9	21	65	5	1
N. Booroorban 2	0.65 – 0.75 m	4	19	66	11	0
Tabratong 2	0.80 m / inside & outside	10	6	75	8	1
Gala Vale 'south' 2	0.80 m / inside	7	26	61	6	0
Thurrowa Road 3	0.65 m	16	1	73	10	1
Gala Vale 2	0.80 m / inside	5	19	69	7	0
Bundure 1	0.50 m	31	20	46	3	0
MGC 4-4#5	5.85 m	20	41	36	3	1
MGCY 5#4	13.81 m	13	31	52	4	0
MYA 1#6	6.72 m	16	41	35	9	0
Headless Horseman 2	0.60 m / inside & outside	17	52	31	1	1
*N. Booroorban 2**	*0.65 - 0.75 m*	*22*	*26*	*49*	*3*	*0*
Wanganella 2	0.55 m / inside	20	22	52	5	0
Kerarbury 1	4.00 m / inside	12	25	56	8	1

**Replicate sample.*

The external reproducibility (2SE) for quartz, mixed layer, illite and kaolinite is estimated at 4.6 %, 11.1 %, 4.3 %, and 10.6 %, respectively.

7.4 Discussion – present weathering conditions

In this section, the main controls on the Li isotope composition of dissolved loads and clay-sized fractions from the Murrumbidgee River are being discussed. It is shown how river pH evolves from upper to lower reaches, how it differs for various monolithologic catchments and how it affects the Li isotope fractionation. Data of waters and clays obtained from various monolithologic catchments help explain how the underlying lithology may control the Li isotope composition in this mixed lithology basin. The annual chemical weathering flux is estimated, and the weathering regime of the Murrumbidgee River is characterised. Furthermore, the implication of the Li isotope composition of sedimentary deposits, especially that of the clay-sized fraction, in terms of chemical weathering conditions, is elucidated.

7.4.1 Murrumbidgee River: upper to lower reaches

The Murrumbidgee River exhibits a large range of pH values, varying from 6.6 to 7.8. A distinct evolution of water pH as a function of distance downstream can be identified

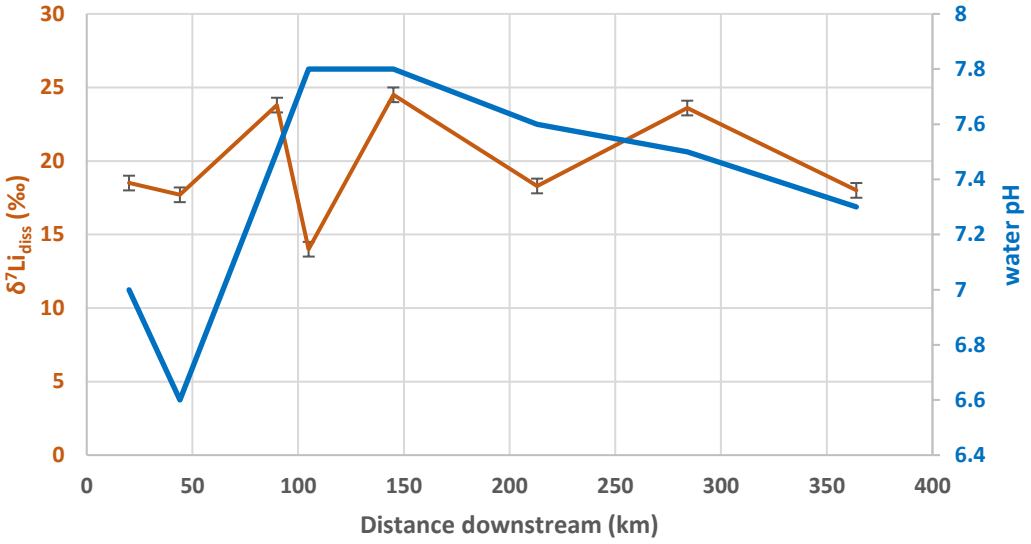

Figure 89).

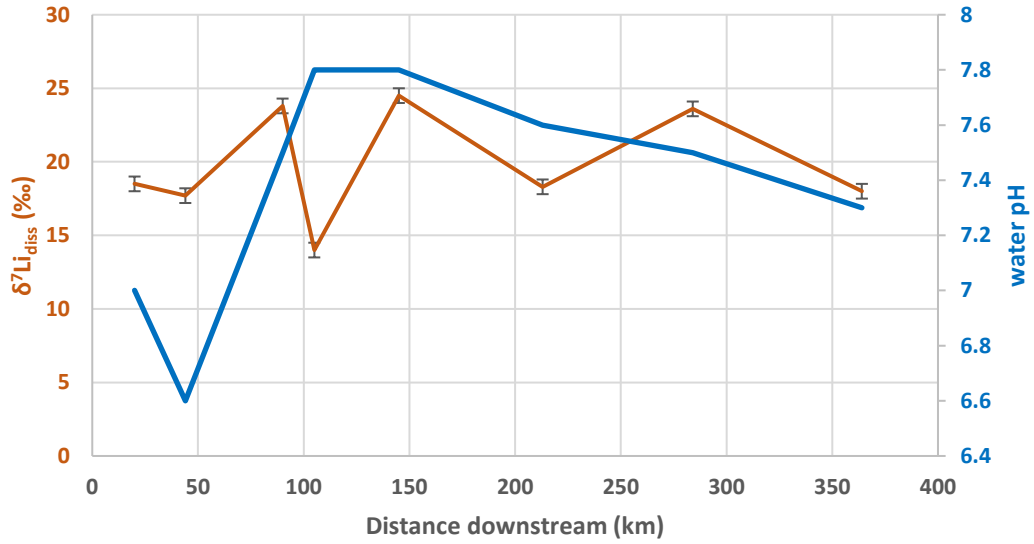

Figure 89: The δ^7Li composition and pH of dissolved loads from the Murrumbidgee River as a function of distance downstream. Orange curve is δ^7Li of the river dissolved load (δ^7Li_{diss}). Blue curve is water pH. External uncertainty (2SE) of δ^7Li values is 0.5 ‰.

The pH of waters from the upper parts of the catchment (the first 100 km) appears to be significantly lower compared to waters at lower reaches. This might be related to the short reaction time between rainwater and rocks/sediments in the upper catchment. This is because rainwater is typically acidic due to the presence of carbonic acid (H_2CO_3). From

50 to 100 km distance downstream, the water pH increases to 7.8, which is the maximum pH observed along the Murrumbidgee River. This could imply that the relatively low pH of rainwater is completely buffered by water-rock interactions at this part of the catchment. From 140 km distance from headwaters and onwards, the pH continuously decreases (Figure 89). A decrease in pH of dissolved loads in the lower reaches of the Murrumbidgee River may be attributed to several factors. For example, the relative abundance of limestone in the watershed may buffer the water pH (Wurts and Durborow, 1992). Furthermore, biological activity, i.e. decay of organic matter, can acidify river waters. This implies that the amount of vegetation in the vicinity of the river body may contribute to lowering the water pH. Similarly, an increasing contribution of acidic groundwaters, associated with soil respiration processes, to surface waters may lower the pH (Hem, 1985; Drever, 1997). However, the former has not been reported anywhere and therefore remains speculative. The relationship between biological activity in river waters and pH is widely recognised and it was found that an inverse correlation exists between organic matter concentrations and river pH (Viers et al., 1997; Viers et al., 2000; Deberdt et al., 2002). A direct control of the evolution of the water pH from upper to lower reaches of the Murrumbidgee River could not be identified with the data obtained in this study. More importantly for this project was to identify the link between water pH and the Li isotope composition of dissolved loads. Unlike water pH, the Li isotope composition of the dissolved load does not evolve as a function of distance downstream (Figure 89). No obvious trend between the Li isotope composition of the river dissolved load from upper and lower reaches can be recognised. This is somewhat surprising as studies of other large river systems (e.g. Yangtze River) report an increase of δ^7Li values from upper to lower reaches (Wang et al., 2015). This is thought to be associated with the spatial evolution of different weathering regimes, where upper reaches were described as reaction-limited and lower reaches were characterised as transport-limited (Wang et al., 2015). Similarly, an increase of the δ^7Li_{diss} was observed along the course of Andean rivers (Dellinger et al., 2015). Here the authors proposed that this was due to the re-incorporation of dissolved Li in sediments during transport. A comparison between the Murrumbidgee and the Yangtze or Andean rivers is difficult, as the Murrumbidgee River is with a catchment area of less than 30,000 km^2 significantly smaller. Unfortunately, no other river system of a similar size has been studied in that detail for Li isotopes and therefore, a comparison with an equally sized drainage basin cannot be drawn. The absence of a downstream evolution of

δ^7Li_{diss} of the Murrumbidgee River may suggest that not a single but a variety of distinct weathering regimes control the water chemistry from upper to lower reaches. Unlike other rivers such as lowland rivers of the Amazon (Dellinger et al., 2015), the δ^7Li_{diss} of the Murrumbidgee River does not evolve as a function of pH (Figure 90).

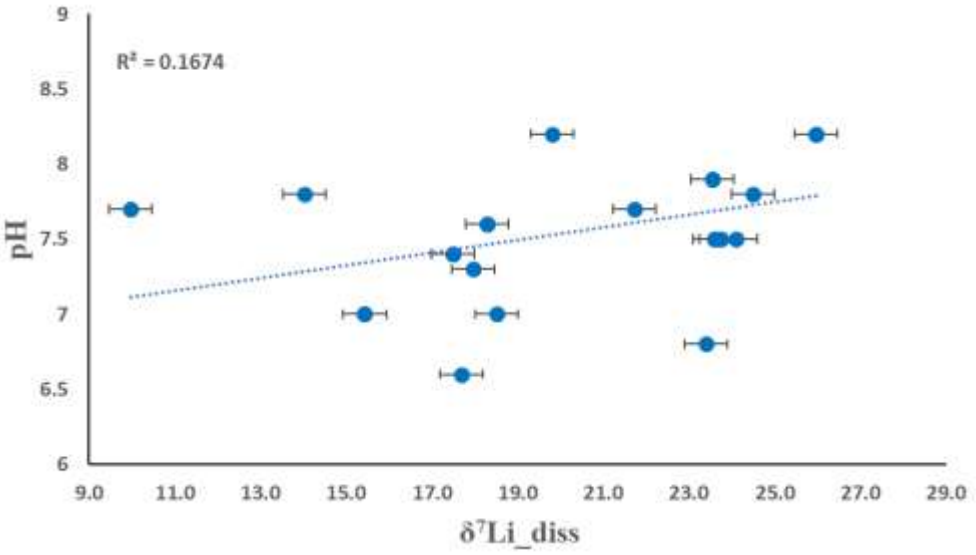

Figure 90: Correlation between pH and respective δ^7Li values of dissolved loads (δ^7Li_{diss}) from rivers in the Murrumbidgee River Basin (n = 17). External reproducibility (2SE) of δ^7Li values is 0.5 ‰. Error on pH was not determined.

A pH dependency on δ^7Li_{diss} was previously linked to the amount of dissolved organic carbon, which enhances dissolution rates and silicate weathering intensities (Dellinger et al., 2015). The absence of such correlation between δ^7Li_{diss} and pH in the Murrumbidgee River Basin may therefore be linked to the relatively scarce vegetation cover compared to other large river systems. Also, the Murrumbidgee River is much smaller than most investigated river systems, which could imply that the isotopic signal of the main channel may be significantly influenced by mixing with tributary waters with varying isotopic signatures. This suggests that the δ^7Li_{diss} value of each individual water sample along the Murrumbidgee River reflects a mixing of local weathering regimes, which uniquely control the Li isotope signature of the dissolved load. This is in agreement with findings by Millot et al. (2010) in the Mackenzie Basin, where individual weathering regimes were accounted for an equally large variability of δ^7Li_{diss} (9.3 – 29.0 ‰).

Total dissolved ions (Li, Ti, Na, Mg, K, and Ca) show a gradual increase from the upper to lower reaches of the Murrumbidgee River (Figure 91). The steepest increase is

observed in the first 100 km from headwaters. Further downstream, Li, Ti, Na, Mg, K, and Ca concentrations increase only slightly.

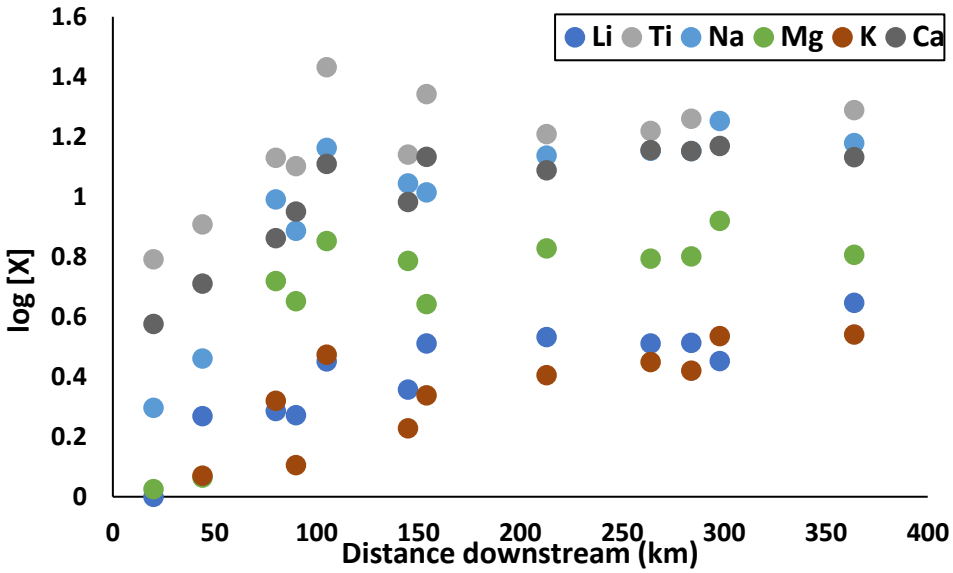

Figure 91: Chemical evolution of Li, Ti, Na, Mg, K, and Ca Li of dissolved loads from the Murrumbidgee River as a function of distance downstream. Element concentrations are displayed as log[X]. External reproducibility (2RSE) of Na, K, Mg, Ca, Al, Ti, and Li is estimated at 46.3 %, 11.8 %, 24.5 %, 36.3 %, 21.2 %, 11.6 %, and 6.6 %, respectively.

A major control that affects the dissolved ion concentration is the underlying lithology. For example, an increase in dissolved Ca and Mg may be linked to the dissolution of sedimentary rocks (Singh and Hasnain, 1998). Considering that the Murrumbidgee River flows through a mixed bedrock terrain with no single dominant rock type (see Chapter 5), it is more likely that the observed increase in dissolved ion concentration may be attributed to an increase in basin area from upper to lower reaches, where a large number of tributaries contribute to the dissolved ion concentration of the Murrumbidgee River. This observation was made for other rivers worldwide. For example, the Bow River (Canada), which has a similar catchment as the Murrumbidgee River, also shows an increase in total dissolved solids (TDS) along the course of the river with the lowest concentrations in the headwaters (Grasby et al., 1999). Similarly, the Yamuna River (India), which is equally long as the Murrumbidgee River but with a much larger catchment area, shows low major ion concentrations at upper reaches compared to lower catchments (Dalai et al., 2002). Larger river systems, such as the Yellow River, also show a downward increase in major ion concentration (Chen et al., 2005). Only few rivers show

a decrease in total dissolved solid concentrations from upper to lower reaches. One example is the Yangtze River, where significantly higher major ion concentrations in the upper catchment was linked to the severe erosion areas in the mountainous regions (Chen et al., 2002).

Furthermore, evaporation processes may have concentrating effects of the total ion concentration of the Murrumbidgee River. Daily evaporation rates in the Murrumbidgee River Basin vary between 1.5 mm in the upper catchment and up to 5 mm in the lower catchment (Figure 92). The steep increase of major element concentrations from upper to mid reaches may therefore also be linked to increasing evaporation rates downstream. A similar observation was made for the Murray River, which is also draining through the Murray-Darling Basin, which was classified as aa evaporation dominated river (Gaillardet et al., 1999).

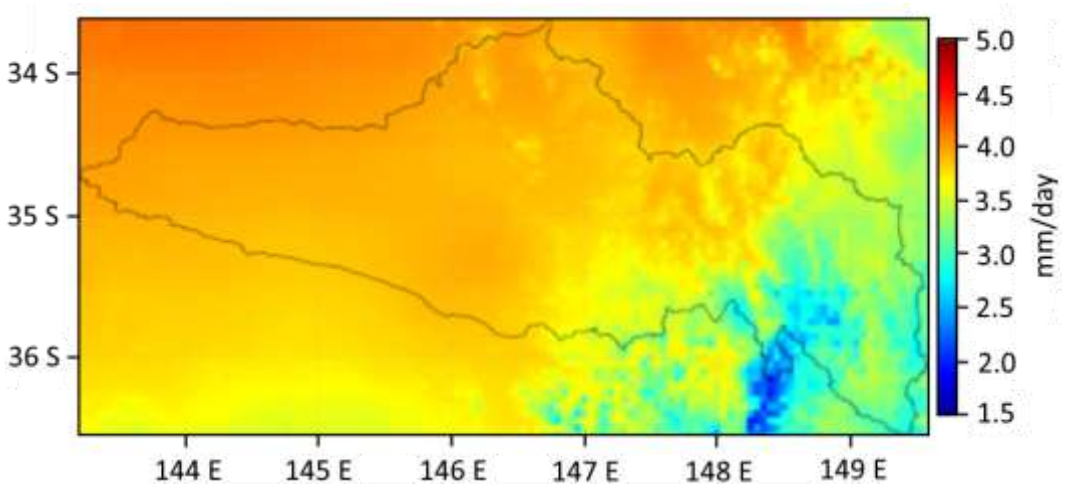

Figure 92: Daily evaporation rates in the Murrumbidgee River Basin. Modified after Weiland et al. (2015).

While total major ion concentrations of dissolved loads reflect changes in catchment area and possibly evaporation effects, Na-normalised molar ratios (e.g. Ca/Na, Mg/Na) can be used to trace weathering reactions (Gaillardet et al., 1999). Unlike absolute elemental concentrations, elemental ratios are not affected by dilution or evaporation processes and therefore allow the differentiation of various weathering sources relative to different lithologies (Negrel et al., 1993; Gaillardet et al., 1997; Gaillardet et al., 1999). Figure 93 shows a mixing diagram of Mg/Na vs. Ca/Na for all investigated waters, in the Murrumbidgee River Basin against published values for endmembers (waters draining through various monolithologic basins: evaporate, silicate, volcanic, carbonate).

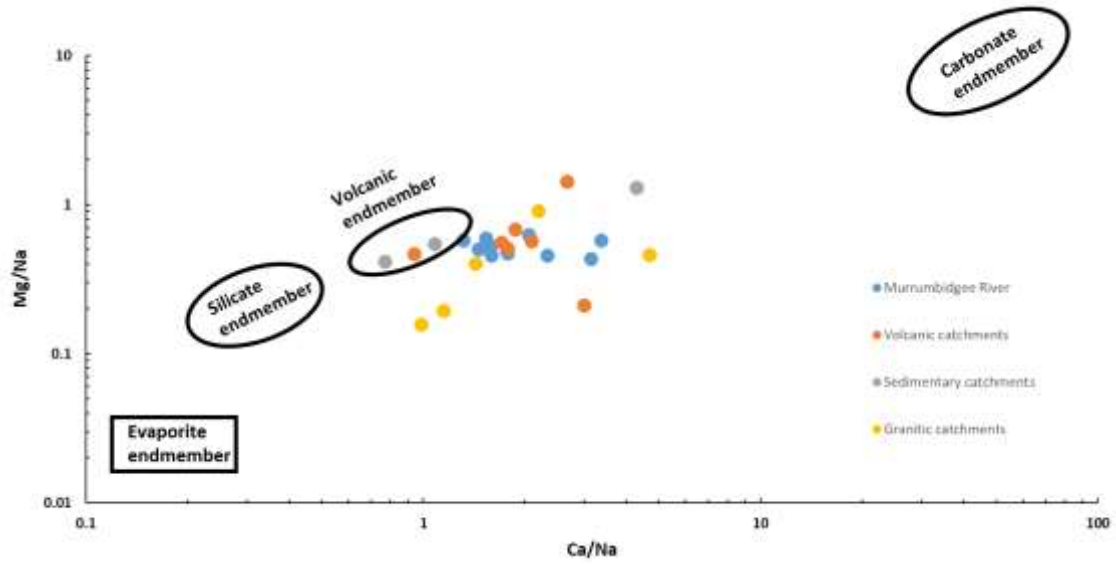

Figure 93: Mixing diagram using Na-normalised molar ratios in dissolved loads waters from the Murrumbidgee River Basin (blue: Murrumbidgee River, orange: volcanic catchments, grey: sedimentary catchments, yellow: granitic catchments). Endmembers for evaporite, volcanic, silicate and carbonate are taken from Gaillardet et al. (1999) and references within.

As discussed in Chapter 5, the three main bedrock units found in the Murrumbidgee River Basin are of granitic, volcanic, or sedimentary composition. Note, that sedimentary bedrocks are mostly sandstone and shale. Only few parts show traces of carbonate bearing rocks. However, Murrumbidgee waters clearly show higher Ca/Na values, indicating the presence of a carbonate rock weathering source (Figure 93). The same is observed for waters from monolithologic catchments (volcanic, granitic, sedimentary), which shows that these catchments are not purely monolithologic. These findings are not surprising as only very little carbonate needs to be present in the catchment to dominate the TDS concentration (Jacobson and Blum, 2003). Another reservoir, which is not shown in Figure 93, is rainwater which may contain a seawater-like chemical composition. Its contribution to the TDS is commonly corrected via the Cl concentration of the dissolved load. Most rocks are generally depleted in Cl and if there is no evaporate source in the river catchment, Cl is derived entirely from the atmosphere. A high abundance of Cl in river waters may therefore indicate a large atmospheric input of sea salts. Using elemental ratios of seawater such as Cl/Na, Ca/Na, Mg/Na, and HCO_3/Na can then be applied to calculate the atmospheric input to the river water (Gaillardet et al., 1999). Unfortunately,

the Cl concentration was not determined, and therefore no correction via Cl was applied. Instead, a less conventional method, similar to that found in Mortatti and Probst (2003), was applied to correct for atmospheric input. The correction factor for each major ion is in detail discussed in Section 7.4.3. In summary, the chemical signature (Mg/Na, Ca/Na) of dissolved loads from the Murrumbidgee River and rivers flowing through monolithologic catchments show that the weathering sources are dominated by silicate and carbonate rocks.

7.4.2 Main controls of the lithium isotope composition of dissolved loads

Data obtained from waters of monolithologic catchments may explain the observed variability in δ^7Li_{diss}. The pH could be a major control on Li isotope fractionation as it directly controls mineral dissolution rates and clay neo-formation. The latter is the process which may encompass large isotope fractionation (Pistiner and Henderson, 2003). Even though only a small selection of water samples from monolithologic catchments were analysed (total of nine), the results reveal that the pH is lowest for sedimentary siliclastic bedrock (pH 6.8 to 7.4), followed by granodiorite bedrock (pH 7.5 and 8.2) and highest for volcanic source rocks (pH 7.7 to 8.2) (Figure 85). Bearing in mind that the sample size may be statistically insignificant, these results point towards a bedrock-dependent control on river pH, where sedimentary rocks produce more acidic waters compared to volcanic and granodiorite rocks. This was previously shown by Abdalla and bin Yahya Al-Abri (2014), who linked river pH to specific bedrock type. Mineral dissolution experiments by Malmström and Banwart (1997) have shown that, under various CO_2 conditions/environments, dissolution rates of biotite are directly controlled by pH. In detail, their experiment shows that dissolution rates of biotite are lowest between near-neutral pH (6 and 9), and increasing towards lower and higher pH. If the pH dependency on dissolution rates holds true for other minerals, then this implies that sedimentary catchments potentially produce waters with a lower pH compared to other catchments, which in turn increases the mineral dissolution rate. However, no correlation was found between water pH and the Li isotope composition of waters, which indicates that differences in mineral dissolution rates have an insignificant effect on δ^7Li_{diss}. The Li isotope composition of dissolved loads from individual monolithologic catchments is highly variable and despite the large differences of δ^7Li values between each source rock (sedimentary: 6.4 ‰, volcanic: 2.1 ‰, granodiorite: 1.6 ‰), the underlying lithology does not appear to govern the δ^7Li composition of dissolved loads (Figure 94).

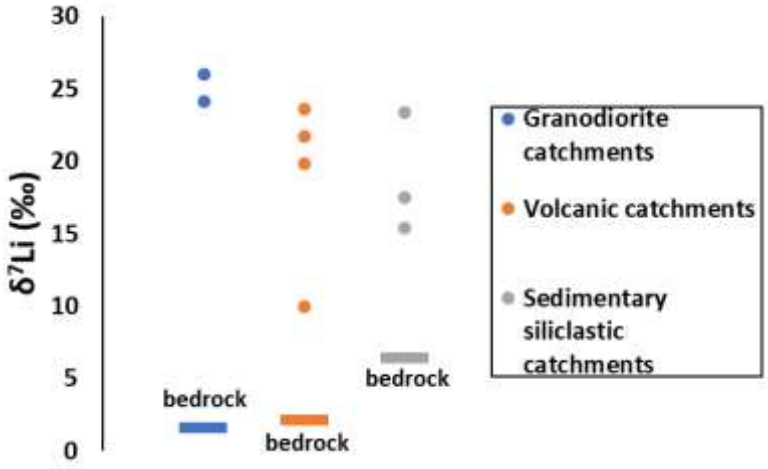

Figure 94: The δ^7Li composition of dissolved loads from monolithologic catchments relative to δ^7Li of the source rock. Error on δ^7Li values (2SE) is 0.5 ‰.

In summary, it can be concluded that while the underlying lithology may affect water pH which controls mineral dissolution rates, but its effect on the Li isotope composition of dissolved loads is negligible. Furthermore, while the three main bedrock units in the Murrumbidgee River Basin show distinct differences in their Li isotope composition, δ^7Li values of dissolved loads over all investigated monolithologic catchments cover a large range, implying that the underlying lithology does not control δ^7Li_{diss}.

7.4.3 Chemical weathering conditions of the Murrumbidgee River

The annual chemical weathering rate (silicate + carbonate) (W) in tons/km^2/yr of the Murrumbidgee River can be calculated via the flux of major dissolved elements (Na, Ca, Mg, and K in µmol/L), the annual discharge, and the total catchment area:

$$W = \phi(Na) + \phi(K) + \phi(Mg) + \phi(Ca) \quad (23)$$

where ϕ is the surface specific flux of each element derived from silicate and carbonate weathering (Millot et al., 2002; Bouchez and Gaillardet, 2014). Silicon concentrations are excluded in the calculation of chemical weathering rates, due to the fact that mineral phases controlling silicon in river water are poorly understood (Millot et al., 2002), and silicon may be significantly taken up by plants (Oliva et al., 1999). Based on equation (23), the W for the Murrumbidgee River (at Wagga Wagga) was calculated to be 4.9

t/km^2/yr, using a catchment area of 29,057 km^2 (Green et al., 2011), a mean discharge of 120 m^3/s (Green et al., 2011), and a TDS of 39 mg/L. As discussed in Section 7.4.2, the major ion concentration of dissolved loads must be corrected for the atmospheric input. This was done following the method by Mortatti and Probst (2003): based on the entire catchment area of the Murrumbidgee River, i.e. 29,057 km^2 (Green et al., 2011), and the mean annual precipitation of ~539 mm (BOM, 2017), the total deposition rate of each major ion in t/km^2/yr by rainfall over the entire Murrumbidgee River catchment could be calculated (Table 17).

Table 17: Deposition rate of major ions by rainwater (at Wagga Wagga) over the entire Murrumbidgee River.

Reservoir	Na (t/km^2/yr)	K (t/km^2/yr)	Mg (t/km^2/yr)	Ca (t/km^2/yr)	Reference
Rainwater	0.3	0.1	0.1	0.2	(Crosbie et al., 2012)

The above calculated W of the Murrumbidgee River at Wagga Wagga can therefore be corrected by subtracting the sum of deposition rates of all major ions (0.7 t/km^2/yr) from W. The resulting W for the Murrumbidgee River, corrected for atmospheric inputs, is 4.3 t/km^2/yr. This means that ~14 % of the annual TDS (i.e. 5.6 mg/L) is derived from rainwater. For simplification, no differentiation was made between silicate and carbonate derived weathering fluxes. Studies have shown that only little carbonate bedrock is required in the catchment to dominate the overall chemical weathering budget because carbonates dissolve up to 350 times faster than silicates (Jacobson and Blum, 2003). This seems to be also the case for the Murrumbidgee as, even though the most dominant bedrock type in the Murrumbidgee River is silicate based (granite, volcanic, sedimentary siliclastic), carbonates contribute significantly to the TDS. This was demonstrated in Section 7.4.1 with a mixing diagram between Mg/Na and Ca/Na, which shows that all investigated waters deviate from the silicate endmember towards the carbonate endmember. Therefore, the calculated W for the Murrumbidgee River is a mixture between silicate and carbonate weathering. Total chemical weathering rates (silicate + carbonate) based on equation (23) were also calculated for other river systems (Table 18).

Table 18: Weathering rates and Li isotope compositions for various rivers world-wide.

River	Na (µmol/L)	K (µmol/L)	Mg (µmol/L)	Ca (µmol/L)	TDS (mg/L)	Catchment area (km^2)	Discharge (m^3/s)	δ^7Li (‰)	W ($t/km^2/yr$)	E ($t/km^2/yr$)	D ($t/km^2/yr$)	W/D
Murrumbidgee River Basin												
Murrumbidgee @ Wagga						29,057				19		
Eunony bridge	657	89	263	339	33		120	18.0	4.3		23	0.188
Madeira Basin												
AM01-04	62	12	78	55	6	5,353	260	7.3	9.2	1,500	1,509	0.006
AM01-07	44	16	75	119	8	10,900	400	8.5	9.5	3,900	3,910	0.002
AM01-08	282	57	359	416	34	21,197	750	13.4	38.1	3,800	3,838	0.010
AM01-14	138	38	199	328	23	69,980	2,153	10.5	22.0	3,140	3,162	0.007
AM07-04	164	25	204	286	21	69,980	2,153	10.5	20.6	3,140	3,161	0.007
AM01-16	119	48	212	290	21	114,379	3,772	15.7	22.3	1,020	1,042	0.021
AM07-09	87	33	125	197	14	114,379	3,772	15.7	14.8	1,020	1,035	0.014
AM01-15	72	30	61	171	11	124,231	5,602	21.3	15.9	570	586	0.027
AM07-14	77	28	63	190	12	124,231	5,602	21.3	17.1	570	587	0.029
AM01-17	66	41	39	62	7	33,485	475	11.5	2.9	55	58	0.051
AM01-18	22	15	18	12	2	20,770	222	14.4	0.7	10	11	0.064
AM01-19	155	48	146	202	17	618,220	7,916	31.9	6.9	96	103	0.067
AM07-19	137	71	122	162	15	618,220	7,916	31.9	6.2	96	102	0.061
AM01-21	99	38	106	173	13	954,400	18,300	21.5	8.0	276	284	0.028
AM06-35	58	32	58	101	8	1,325,000	31,250	22.6	6.0	184	190	0.031
AM05-16	90	29	68	115	9	1,325,000	31,250	22.6	7.0	184	191	0.037

Solimoes Basin												
AM08-33	185	25	100	455	26	114,237	4,975	21.9	35.6	890	926	0.038
AM08-38	1,660	32	96	653	68	85,000	3,042	26.3	76.7	710	787	0.098
AM08-05	397	36	97	607	37	722,089	30,148	18.8	49.0	560	609	0.081
AM08-24	477	29	82	502	34	357,255	16,885	23.6	51.0	470	521	0.098
AM08-13	308	40	114	683	39	352,593	12,090	16.7	42.0	570	612	0.069
AM05-4	125	25	48	213	14	2,148,000	103,000	14.5	20.5	188	208	0.099
AM06-15	101	20	50	188	12	2,148,000	103,000	14.5	17.9	188	205	0.087
Amazon river mainstream												
AM06-63	105	21	39	165	11	4,618,750	182,200	18.1	13.4	231	244	0.055
AM05-37	81	20	36	131	9	4,618,750	182,200	18.1	10.9	231	242	0.045
AM05-35	86	21	38	138	9	4,618,750	182,200	18.1	11.5	231	243	0.047
AM05-39	85	23	48	158	10	4,618,750	182,200	18.1	12.9	231	244	0.053
Amazonian shield rivers												
AM6/1-20	33	22	18	24	3	490,000	13,500	15.3	2.6	11	14	0.192
Trombetas	31	23	9	11	2	250,000	6,200	8.9	1.8	6	8	0.229
AM6/1-2	12	6	3	4	1	691,000	29,000	5.9	1.0	14	15	0.066
AM01-22	14	5	3	5	1	691,000	29,000	5.9	1.0	14	15	0.069
Changjiang												
CJ14	554	57	379	949	62	867,000	8,602	10.5	19.5	488	508	0.038

CJ60	351	55	243	762	47	1,250,000	16,719	17.2	19.7	296	316	0.062
CJ52	409	56	305	864	54	1,488,000	19,761	18.2	22.5	271	293	0.077
CJ36	308	60	241	774	46	1,705,000	27,429	22.1	23.5	249	272	0.086
CJ5	496	66	343	916	59	133,000	2,596	7.7	36.4	358	394	0.092
CJ33	140	60	146	765	40	947,000	2,591	12.6	3.4	122	126	0.027
CJ34	147	69	96	351	22	809,000	2,236	15.4	2.0	138	140	0.014
Mackenzie												
Mackenzie @ Tsiigehtchic	282	21	418	919	54	1,680,000	8,996	15.0	9.2	64	73	0.126
Peel @ Fort McPherson	167	13	673	1,142	66	70,600	687	13.3	20.4	295	315	0.065
Red Arctic @ Tsiigehtchic	134	18	845	1,418	81	18,600	159	13.8	21.9	392	414	0.053
Slave @ Fort Smith	227	24	265	694	40	616,400	3,202	15.5	6.6	57	64	0.104
Peace @ Peace Point	168	20	302	806	44	305,500	927	15.4	4.2	122	126	0.034
Liard @ Fort Simpson	106	16	483	1,062	57	275,000	2,452	14.3	16.1	167	183	0.088
Liard @ Liard River	60	16	404	869	47	33,400	371	18.3	16.4	30	47	0.351
Fort Nelson @ Fort Nelson	141	17	507	1,146	62	43,500	334	11.8	15.1	281	296	0.051
Yellowknife River (CAN96-31)	62	21	64	99	8	16,300	37	26.9	0.6	2	3	0.188
Wecho River (CAN99-84)	75	24	61	101	8	3,400	10	26.0	0.7	2	3	0.235
Yellowknife (CAN99-90)	74	23	67	104	8	16,300	37	29.0	0.6	2	3	0.200

Iceland

E7: Skaftá river	136	13	110	347	20	1,500	139	16.3	59.1	8,138	8,197	0.007
Hvita-S	290	14	52	102	13	2,200	118	19.5	21.3	1,180	1,201	0.018
Hvita-W	272	10	39	72	11	2,200	118	17.4	17.8	1,893	1,911	0.009
Jökulsa a Fjöllum	479	15	67	105	17	7,100	177	18.1	13.7	3,219	3,233	0.004
Jökulsa a Dal	142	5	32	97	8	3,300	157	17.1	12.2	2,911	2,923	0.004

Catchment area and discharge for the Murrumbidgee River are from Green et al. (2011). Total dissolved solids (TDS) is the sum of Na, K, Ca, and Mg (corrected for atmospheric input; for Murrumbidgee River, see text). Data for dissolved ion concentrations, catchment area, and river discharge for Madeira Basin, Solimoes Basin, Amazon river mainstream, and Amazonian shield rivers are from Dellinger et al. (2015). TDS, catchment area, and river discharge for Changijang (Yangtze) are from Chetelat et al. (2008) and data for Mackenzie and Iceland are from Millot et al. (2003) and Vigier et al. (2006), respectively. W (chemical weathering rate) is calculated via TDS/(catchment area x discharge). W for the Murrumbidgee River was corrected for atmospheric input by subtracting 0.7 t/km^2/yr (see text for details). E (erosion rate) is derived from sediment gauging experiments. Data for E for the Murrumbidgee River are from Olley and Wasson (2003). E for the Madeira Basin, the Solimoes Basin, the Amazon river mainstream, and the Amazonian shield rivers are from Dellinger et al. (2015). E for Changjiang (Yangtze) are from Wang et al. (2015). E for Mackenzie are from Church et al. (1989); Carson et al. (1998); Millot et al. (2002). E for Iceland are from Vigier et al. (2006). Denudation (D) is W + E. External reproducibility (2SE) of δ^7Li values measured in this study is 0.5 ‰.

While W informs us of the total flux of major ions in the dissolved load derived from weathering of rocks, it does not reflect the weathering regime and the 'intensity' of water-rock interactions. The W/D ratio (W= weathering rate; D= total denudation rate, where D= chemical weathering rate + physical weathering rate), as defined by Riebe et al. (2003), is a metric for weathering intensity, which is similar to the chemical depletion factor (Brimhall and Dietrich, 1987; Riebe et al., 2001), or the CIA (Nesbitt and Young, 1982) (see Chapter 2 for more details). Unlike the weathering rate or physical erosion rate, the weathering intensity is not bound to discharge and drainage area (Bouchez et al., 2014), which makes it an excellent tool to characterise weathering regimes. Likewise, the Li isotope composition of the dissolved load has been suggested to reflect the weathering intensity (Huh et al., 1998; Huh et al., 2001; Kısakűrek et al., 2005; Pogge von Strandmann et al., 2006; Pogge von Strandmann et al., 2008; Pogge von Strandmann et al., 2010; Millot et al., 2010; Dellinger et al., 2015). A combined approach between the δ^7Li composition and W/D to characterise weathering regimes was proposed by Dellinger et al. (2015). They found that positive δ^7Li values are generally associated with intermediate weathering intensities, while lower δ^7Li values may be indicative of either low or high weathering intensities (see more details in Chapter 3). Note that Dellinger et al. (2015) calculated W of silicate weathering only and corrected for the Li isotope composition of the source rock. Here, W is calculated for silicate + carbonate weathering (corrected for atmospheric inputs) and the δ^7Li composition of source rocks was not used to correct δ^7Li_{diss}. The latter was not done because in the Murrumbidgee River Basin, clays formed from source rocks with different Li isotope composition yielded a similar range of δ^7Li values (see Section 7.4.2 for details). The weathering intensity was calculated for other river systems and δ^7Li values were taken from the literature (Table

18). Figure 95 shows that the Murrumbidgee River falls under the 'high weathering intensity' regime.

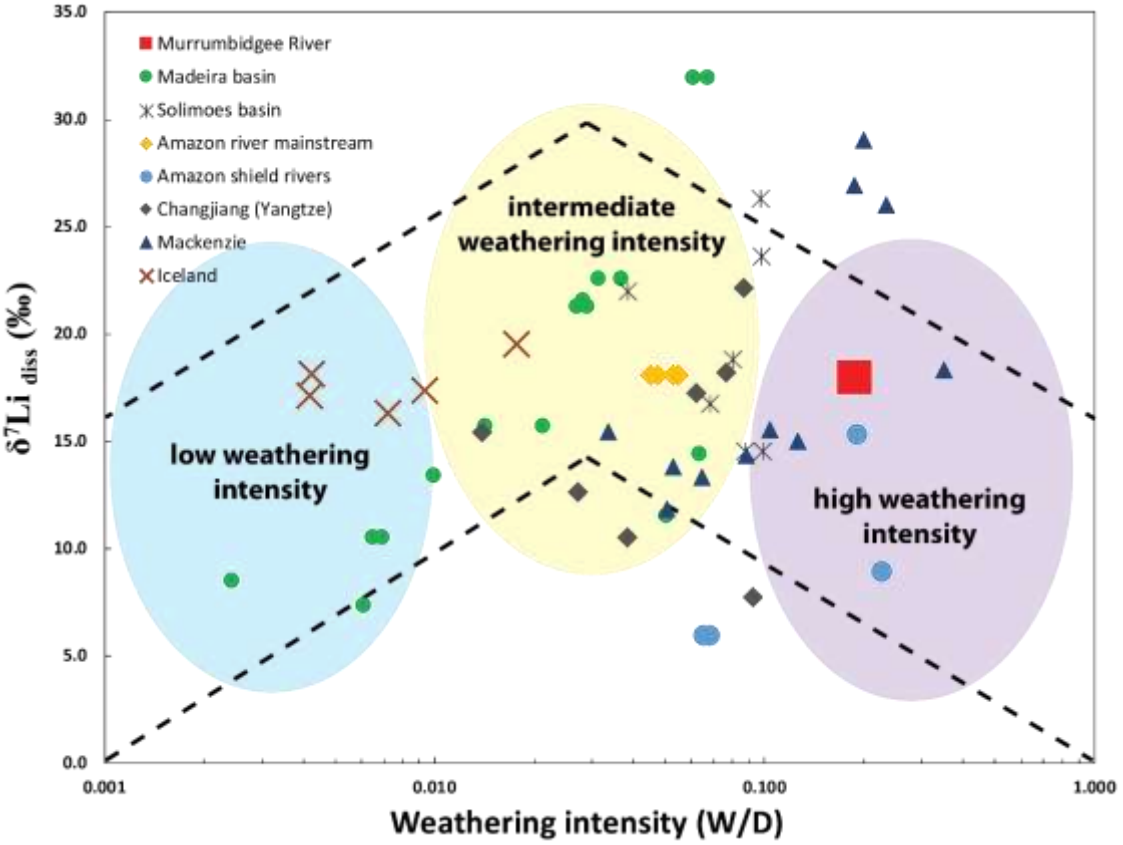

Figure 95: The δ^7Li composition of dissolved loads (δ^7Li_{diss}) as a function of weathering intensity W/D (Bouchez et al., 2014). Calculation of W/D is given in Table 18. External reproducibility (2SE) of δ^7Li values measured in this study is 0.5 ‰.

7.4.4 Lithium isotope composition of clay-sized fractions

Most studies that apply Li isotopes as a proxy for chemical weathering conditions on continents have focused on the dissolved load of rivers, e.g. Huh et al. (1998); Huh et al. (2001); Vigier et al. (2009); Millot et al. (2010); Dellinger et al. (2014). While the interpretation of δ^7Li_{diss} is not entirely agreed upon (Dellinger et al., 2014), in the majority of cases, high δ^7Li_{diss} is associated with low chemical weathering rates (Vigier et al., 2009; Millot et al., 2010; Dellinger et al., 2014). So far only few studies, e.g. Dellinger et al. (2017), explored how the δ^7Li composition of sediments, especially clay minerals, are related to the Li isotope composition of the dissolved load and how δ^7Li values of clays evolve as a function of chemical weathering rates. The basic assumption of the relationship between the δ^7Li composition of dissolved loads and clays is that clay minerals are in isotopic equilibrium with the solution from which they are formed:

$$\delta^7Li_{clay} = \delta^7Li_{diss} + \Delta^7Li_{clay-diss} \quad (24)$$

Therefore, in theory, the Li isotope composition is determined by isotopic fractionation between solution and secondary mineral phases, which is driven by specific chemical weathering conditions (Kısakűrek et al., 2005). Dosseto et al. (2015) proposed that δ^7Li_{clay} is directly related to δ^7Li_{diss}, and both parameters correlate inversely with chemical weathering rates (Figure 96).

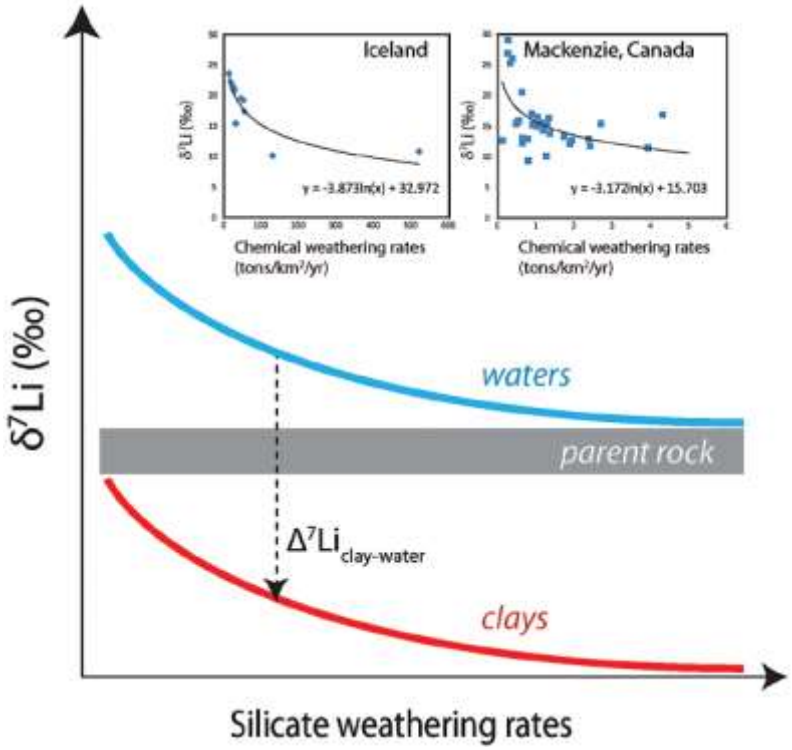

Figure 96: Relationship between Li isotope composition of waters and clays as a function of silicate weathering rates. Insets show data from Vigier et al. (2009) in Iceland and Millot et al. (2010) in Canada. Curves in the insets present a logarithmic regression through the data. Source: Dosseto et al. (2015).

Based on this model, at high chemical weathering rates, both δ^7Li values of dissolved loads and clays, if both in isotopic equilibrium, shift in parallel towards low values. However, this model cannot be true for all weathering environments. For instance, dissolved loads from the Amazonian shield, where silicate weathering rates are relatively low (1 to 10 t/km^2/yr) (Gaillardet et al., 1997; Bouchez et al., 2014), show low δ^7Li values

similar to those observed for Andean rivers, where silicate weathering rates are with a mean value of 22 t/km^2/yr (Moquet et al., 2011) much higher. If the clay-sized fraction evolved in isotopic equilibrium with the dissolved load, then these two contrasting weathering environments would yield δ^7Li values of a similar range. Therefore, Dellinger et al. (2017) argued that fine-grained sediments do not reflect silicate weathering rates as proposed by Dosseto et al. (2015), but rather weathering intensities. Sediments from large rivers (< 63 µm) inversely correlate with the weathering intensity (W/D) (Figure 97). Note that Dellinger et al. (2017) corrected the Li isotope composition of fine sediments from the isotopic composition of the source rock. This was not done here (see explanation below). Also shown in Figure 97 is the clay sample of the Murrumbidgee River (at Wagga Wagga).

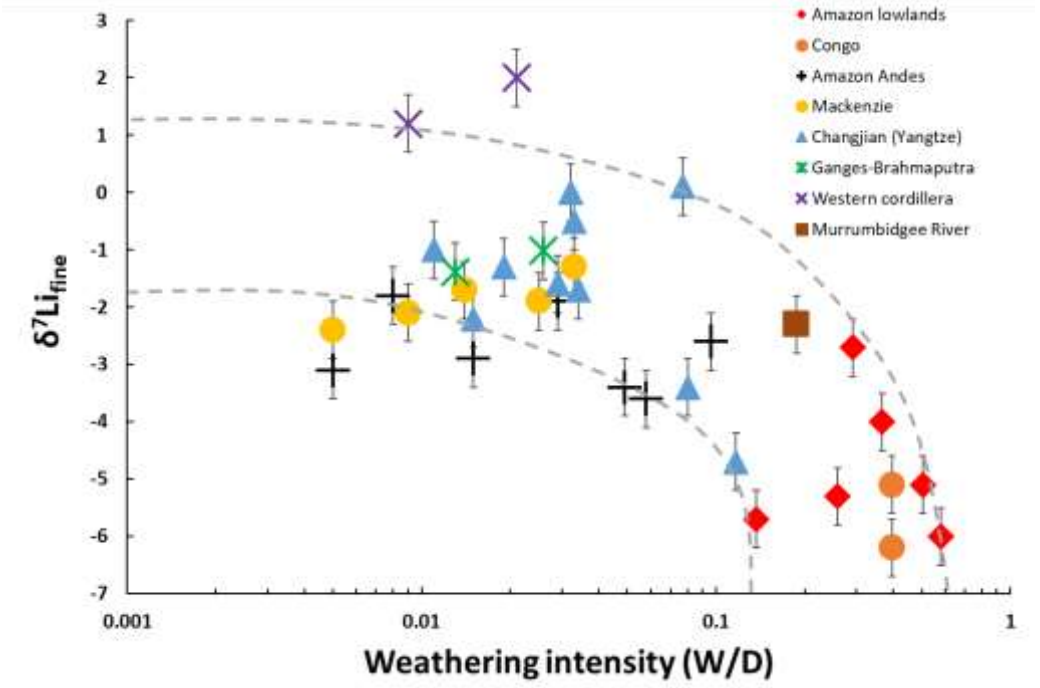

Figure 97: The Li isotope composition of fine-grained sediments (δ^7Li_{fine}; < 63 µm) from rivers as a function of weathering intensity W/D (Bouchez et al., 2014). The Murrumbidgee River sample was taken from Wagga Wagga and the clay-sized fraction was analysed. See Table 18 for details on how W/D was calculated. Modified after Dellinger et al. (2017).

These findings imply that low δ^7Li values of fine-grained detrital sediments reflect high weathering intensity regimes, which characterise a supply-limited weathering environment. An example for such weathering environments are lowland rivers of the

Amazon. In contrast, at low weathering intensities i.e. high discharge environments (e.g. Andean rivers), where weathering reactions are limited, δ^7Li values are more positive. The clay sample of the Murrumbidgee River (at Wagga Wagga) is well within the observed range of Li isotope compositions of fine sediments relative to weathering intensities (W/D) of other river systems.

Dellinger et al. (2017) found that the Li isotope composition of the source rock (before chemical alteration), has a great influence on the δ^7Li composition of fine-grained sediments. They proposed that, in order to compare δ^7Li values of fine-grained detrital sediments from different catchments world-wide, the initial Li isotope composition of the catchment-specific source rock must be subtracted from the sediment following:

$$\Delta^7 Li_{fine-source} = \delta^7 Li_{fine} - \delta^7 Li_{source} \quad (25)$$

This 'lithological effect' was investigated in the Murrumbidgee River Basin, to see (i) whether the observed δ^7Li values for clay-sized fractions are a function of the underlying lithology, and (ii) to evaluate if the Li isotope composition of sediments for each catchment must be corrected from the source rock. One bedrock sample for each lithology was collected from monolithologic catchments and the Li isotope composition was measured. While the δ^7Li composition of the granodiorite and volcanic rock cover a similar range (~2 ‰), the sedimentary siliclastic bedrock sample is isotopically much heavier (~6 ‰). Nevertheless, the produced weathering product (clays) of each lithological unit (granodiorite, volcanic, sedimentary siliclastic) covers an identical range of δ^7Li values (Figure 98).

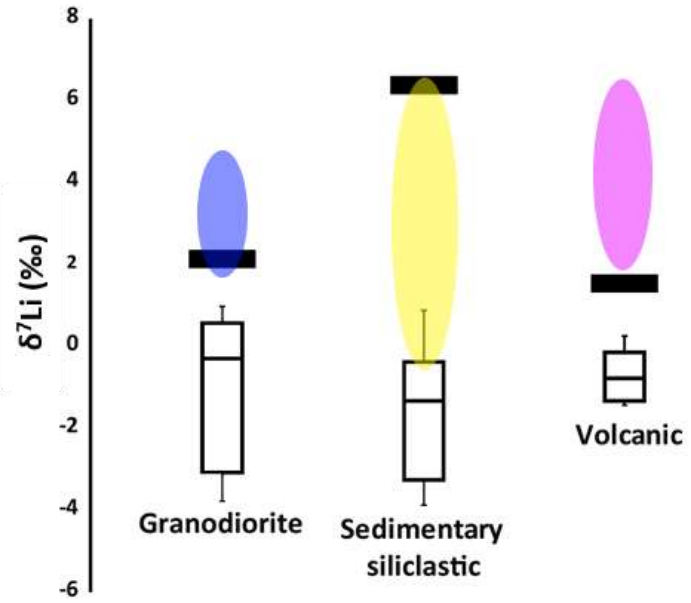

Figure 98: Range of δ^7Li_{clay} for individual source rocks. Black bars represent the isotope composition of the 'fresh' bedrock collected in the Murrumbidgee River Basin (n = 1 for each lithological unit). The ellipses show the observed global range of δ^7Li values for each lithology from the literature (Dellinger et al., 2015). Box plots show median values (solid horizontal line), 50th percentile (box), and min./max. values (whiskers). External uncertainty (2SE) of δ^7Li values measurements is 0.5 ‰.

Volcanic rocks seem to produce the narrowest range of δ^7Li_{clay}. Considering the much higher δ^7Li value of the sedimentary siliclastic bedrock sample, the produced clays from these catchments are within range of clays produced in granodiorite and volcanic bedrock catchments. This suggests that, in the Murrumbidgee River Basin, the underlying lithology does not, at least not directly, control the Li isotope composition of the weathering product.

One of the major aims of this study is to evaluate the relationship between the Li isotope composition of dissolved loads and the respective solid weathering products in the Murrumbidgee River Basin. Due to the limitations of the suggested model by Dosseto et al. (2015) (Figure 96), this study focuses on using the Li isotope ratio of clays to describe the weathering regime relative to weathering intensities, as suggested by Dellinger et al. (2017).

To test if dissolved loads and clays in the Murrumbidgee River Basin have formed in isotopic equilibrium, water and sediment samples were collected from various parts of

the Murrumbidgee River and monolithologic catchments. Indeed, a linear correlation between the Li isotope composition of dissolved loads and the respective clay-sized fraction shows that δ^7Li_{clay} evolves as a function of the Li isotope composition of the solution (Figure 99).

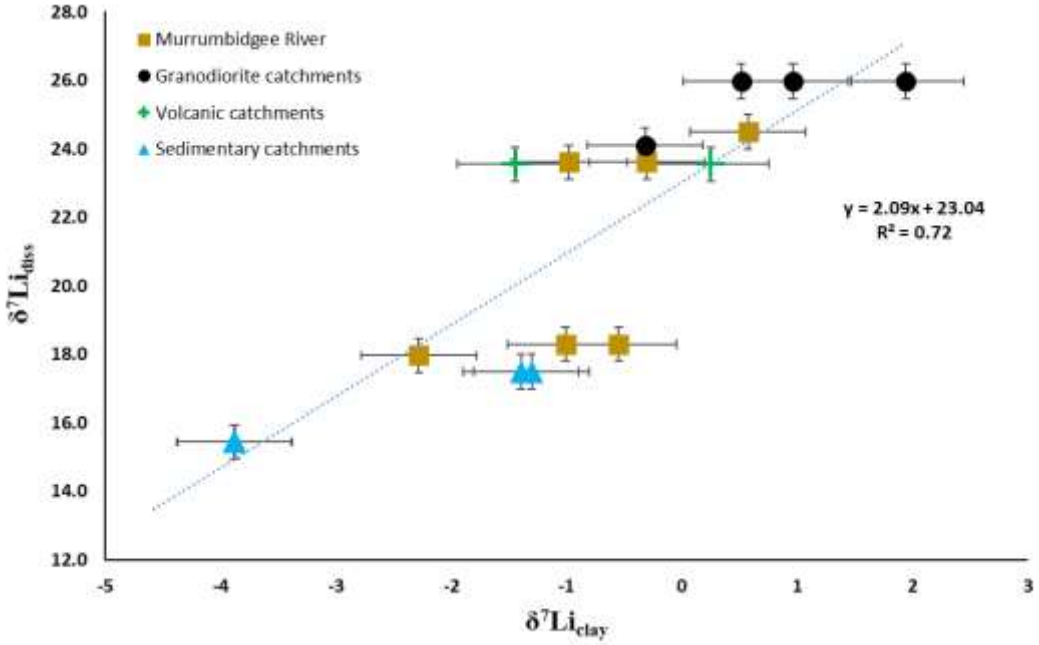

Figure 99: Relationship between the δ^7Li composition of dissolved loads (δ^7Li_{diss}) and clay-sized fractions (δ^7Li_{clay}). Sample pairs (n=17) were obtained from various parts of the Murrumbidgee River and monolithologic catchments. External uncertainty (2SE) of δ^7Li values is 0.5 ‰.

The positive correlation (R^2=0.72) between δ^7Li_{clay} and δ^7Li_{diss} suggests a significant dependency between the two parameters. The slope of the linear regression line is ~2x, meaning that δ^7Li_{diss} increases twice as fast as δ^7Li_{clay}. The statistical relevance of the relationship between the Li isotope composition of dissolved loads and clays was verified with a Spearman's rank correlation calculation, which can be used to assess the dependency between two variables using a monotonic function. In contrast to the R^2 coefficient of determination, the Spearman correlation coefficient, denoted by ρ, does not assume a linear dependency between the two analysed parameters and is therefore considered nonparametric. The Spearman correlation revealed ρ of > 0.90, indicating a strong positive relationship between δ^7Li values of dissolved loads and clays. However, the small sample size of this study (n=17) may negatively affect the likelihood of a nominally statistical significance. Also, water samples and sediment samples were taken

during different times of the year. Waters were sampled during spring, while sediments were collected during spring and summer. The difference in seasonality, e.g. change in rainfall or snow melt, might affect the Li isotope composition of dissolved loads, where waters could have derived from different parts of the catchment with unique weathering regimes. This was shown in Himalayan river systems, where the δ^7Li_{diss} composition was lower during monsoon season, where runoff is higher (Kısakűrek et al., 2005). The effect of seasonality on the Li isotope signature of clays in the Murrumbidgee River Basin has not been investigated. Another factor that could cause an offset between δ^7Li_{clay} and δ^7Li_{diss} is that sediments were taken from river point bars rather than from within the water. Therefore, while clays could have potentially been formed at isotopic equilibrium with solution, the latter could have been different to what was analysed in this study (i.e. the river channel). In this case, the δ^7Li_{clay} would reflect a very local weathering signal, unrelated with the Li isotope composition of the investigated river water. In summary, the δ^7Li composition of waters and sediments collected from the Murrumbidgee River Basin show a strong dependency, indicating that clays have formed in isotopic equilibrium with the dissolved load. Therefore, similar to previous studies that use the Li isotope composition of dissolved loads to reconstruct weathering conditions (e.g. Huh et al. (1998); Huh et al. (2001); Vigier et al. (2009); Millot et al. (2010); Dellinger et al. (2014)), clays may serve as the complementary Li isotope record, which can be used to reconstruct both present and past weathering conditions at a given watershed.

The role of water pH on Li isotope fractionation is another factor that was targeted in this study. A correlation between δ^7Li_{clay} and pH shows that most negative Li isotope ratios are associated with low pH, while at high pH, δ^7Li_{clay} reaches maximum values (Figure 100).

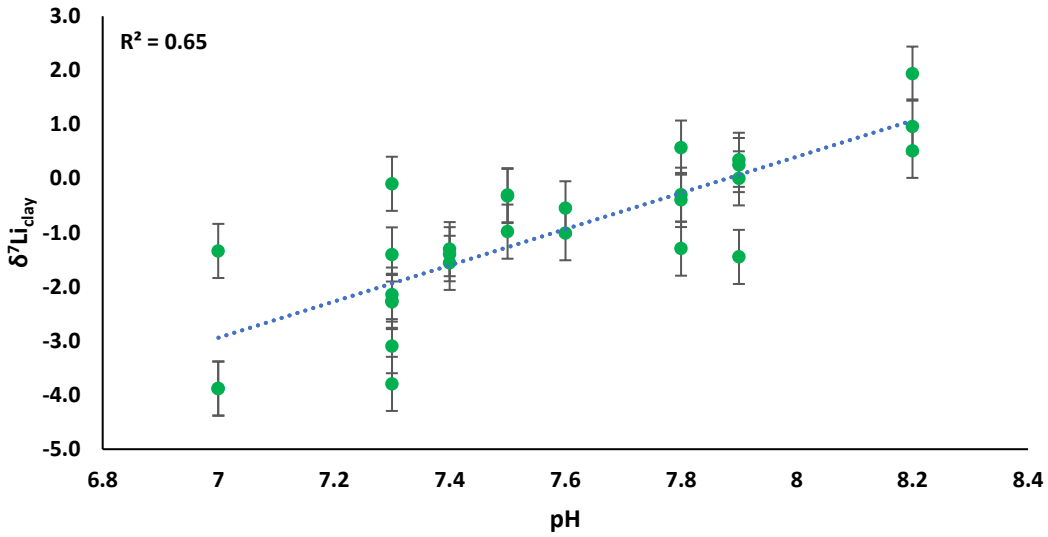

Figure 100: Relationship between δ^7Li_{clay} with the corresponding pH of dissolved loads. Total number of sample pairs is 29. External uncertainty (2SE) of δ^7Li values is 0.5 ‰.

The correlation coefficient R^2 is relatively high (0.65), indicating a clear relationship between water pH and Li isotope composition of clays. This is also confirmed by the high Spearman coefficient ($\rho = 0.81$). A possible explanation for this relationship could be that the specific catchment weathering regime controls the water pH, which in turn controls the type of clay mineral that is being formed. Experiments have shown that pH plays an important role on illitisation, the smectite-to-illite reaction (Small, 1994). These reactions are known to affect the degree at which Li isotopes fractionate (Williams and Hervig, 2005). However, no significant correlation between pH, δ^7Li_{clay}, and any clay mineral group could be identified. Furthermore, based on the mineral composition of clays from various monolithologic catchments, tributaries, and the Murrumbidgee River, it appears that the clay type does not vary significantly across the Murrumbidgee River Basin (Figure 87). The non-quantitative assessment of the expandable clay fraction (see Chapter 9) yielded no relationship with δ^7Li_{clay}. The clay concentration of the sediment is not playing a factor either as no relationship could be found between particle size distribution and Li isotope composition. Because low water pH can be attributed to the oxidation of organic matter, a change in the Li isotope composition of clay minerals could be linked to higher levels of vegetation cover present during weathering reactions. A similar observation was made for lowland rivers of the Amazon basin, where an oversaturation and re-dissolution of secondary minerals via organic matter resulted in low Li isotope ratios (Dellinger et al., 2015). Similarly, on Hawaii, the δ^7Li composition of topsoils

samples, where organic matter is abundant, displayed higher values than the bottom of profiles (Ryu et al., 2014). Unfortunately, the presence of organic matter during weathering reactions for each investigated catchment was not quantified and therefore the control of vegetation cover on Li isotope fractionation processes remains speculative.

7.4.5 The source of sediments

The ratio $^{143}Nd/^{144}Nd$, here expressed as εNd, may be used to trace the origin, i.e. the source rock, of sediments. Figure 101 shows how εNd values of clays reflects the isotopic composition of the source rock.

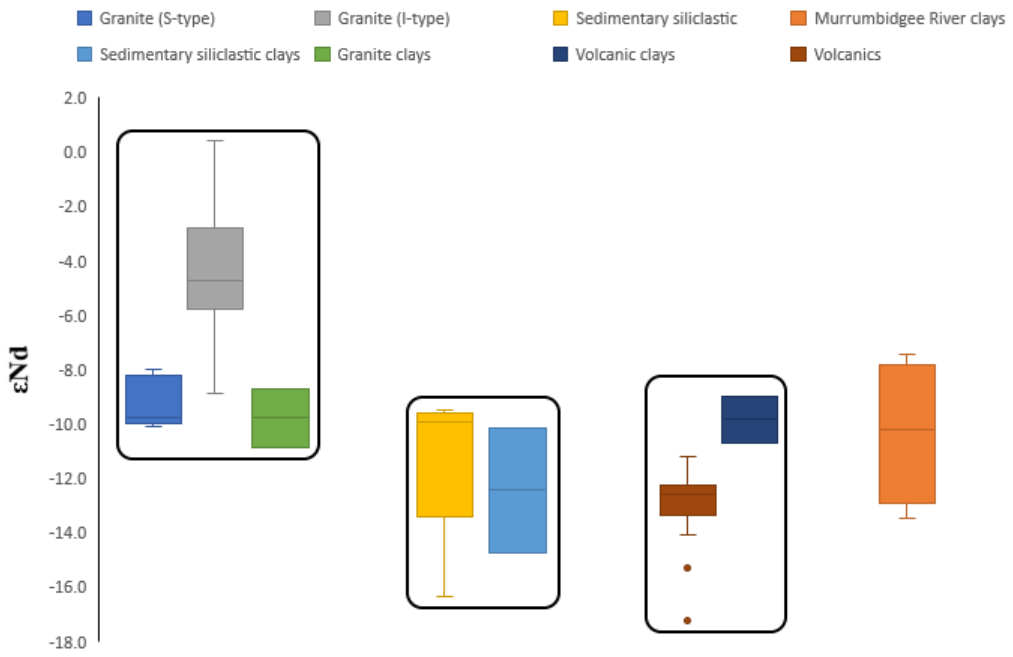

Figure 101: The εNd composition for individual rock types from the Murray-Darling Basin, SE Australia, displayed as box plots. Horizontal bar is the mean, box is the 50th percentile, whiskers are the 90th percentile and single dots are outliers. The left rectangle displays typical Nd isotope compositions in S-type and I-type granites compiled from the literature (McCulloch and Woodhead, 1993; Elburg, 1996) and clays processed in this study from granitic catchments. The second rectangle from the left shows εNd values of sedimentary rocks (McCulloch and Woodhead, 1993) and clays processed in this study from sedimentary catchments. The third rectangle from the left displays typical εNd values for volcanic rocks (McDonough et al., 1985) and clays processed in this study from volcanic catchments. External error on εNd values is 0.3 epsilon units (2SE).

The I-type granite is a less common feature of the Murrumbidgee River Basin and is only occurring at the southern extreme of the Lachlan Fold Belt in south-eastern Australia (Healy et al., 2004). The I-type granites display a wide range of εNd values and are particularly more positive than all other source rocks. S-type granites on the other hand are with εNd values between -8.0 and -10.1 significantly lower. Clays that derive from weathering of these granitic catchments resemble the Nd isotope ratio of the S-type granite, rather than the I-type. This is not surprising as I-type granites are less abundant in the Murrumbidgee River catchment and are only present in small catchments of the upper Murrumbidgee River (Healy et al., 2004). Clays from sedimentary catchments cover an almost identical range of εNd_{values} compared to the source rock, implying that the Nd isotope composition of sedimentary rocks may control the εNd composition of the weathering products. Nd isotope ratios of clays from volcanic catchments do not overlap with the εNd composition of corresponding source rock. Only one aliquot of volcanic bedrock was analysed for this study, which shows a slightly lower εNd value of -11.2 compared to the corresponding clays. All other εNd compositions of volcanic rocks are compiled from the literature, which have εNd values significantly more negative than the volcanic rock collected in the Murrumbidgee River Basin. The compiled data for volcanic rocks derive from the southern margin of the Murray-Darling Basin and are therefore spatially very different from the volcanic rocks found in the Murrumbidgee Basin. Therefore, the difference between the εNd composition of volcanic rocks and analysed clays from volcanic catchments could be a function of spatial variability, where volcanic rocks from other parts of the Murray-Darling Basin exhibit lower εNd values. The Nd isotope composition of clay-sized fractions from the Murrumbidgee River should reflect a mixture between εNd values of granitic, volcanic, and sedimentary rocks. Indeed, the εNd composition of Murrumbidgee River clays cover a wide range of values and overlap with the εNd vlues of clays from each monolithologic catchment. These results prove that analysed clays in this study directly derive from weathering of the various source rocks found in the catchment area: S-type granites, sedimentary siliclastic rocks, and volcanic rocks.

7.4.6 Conclusions

The Murrumbidgee River exhibits a decrease in water pH from upper to lower reaches, which is possibly associated with the oxidisation of organic material due to increased biological activity in soil waters. The Li isotope composition of the dissolved load does

not evolve as a function of river pH. Furthermore, δ^7Li_{diss} of the Murrumbidgee River undergoes significant changes from upper to lower reaches as a result of mixing with various individual weathering regimes in the upper catchment.

The Li isotope signature of waters from granodiorite, volcanic, and sedimentary catchments cover a large but similar range, suggesting that the different weathering regimes are not directly controlled by individual bedrock types.

Unlike dissolved loads, clay-sized fractions show a significant correlation with water pH, implying that the degree of Li isotope fractionation during secondary mineral formation may be indirectly linked to levels of vegetation cover present during weathering reactions.

Despite large differences of the δ^7Li composition of source rocks, clays from monolithologic catchments show the same range of δ^7Li values, which suggests that the underlying bedrock does not affect the Li isotope composition of solid weathering products.

The annual chemical weathering flux of the Murrumbidgee River, corrected for the atmospheric input, was calculated to be 4.3 $t/km^2/yr$.

Both δ^7Li_{clay} and δ^7Li_{diss} of the Murrumbidgee River (at Wagga Wagga) fall within the 'high weathering intensity' zone, which is characterised as a supply-limited weathering regime

A strong correlation between the Li isotope composition of dissolved loads and the respective clay-sized fraction shows that δ^7Li values of clays evolves as a function of the Li isotope composition of the solution. This suggests that, compared to previous studies that use the Li isotope composition of dissolved loads to reconstruct chemical weathering conditions, the clay-sized fraction represents the complementary record. Therefore, the Li isotope composition of clays from sediment archives can be used to to reconstruct both present and past weathering conditions at a given watershed.

7.5 Discussion – palaeo-weathering conditions

A total of four different palaeo-channel systems were investigated:

- Coleambally: 92.5 ± 12.5 ka
- Kerarbury: 45 ± 10 ka
- Gum Creek: 30 ± 5 ka
- Yanco: 16.5 ± 3.5 ka

Each palaeo-channel system was sampled at upper and lower reaches, in order to test whether there is spatial variability in the depositional environment. A detailed sampling strategy is given in Chapter 5. The Li isotope composition of the clay-sized fraction of sediments from individual palaeo-channel systems is used to infer chemical weathering conditions during the time of clay formation. Main assumptions behind this are in detail described in Section 7.4.4. Palaeo-channel sites were strategically sampled to rule out weathering processes that might have affected the Li isotope composition post deposition (see Chapter 6) Furthermore, sediment provenance was determined via Nd isotopes on several sample aliquots to test if a change in sediment source occurred over the past 100,000 years in the Murrumbidgee River Basin.

Sediments from each palaeo-channel system show a large range of δ^7Li values, but overall, the Coleambally and Kerarbury system display higher δ^7Li compositions than the Gum Greek, Yanco, and the present Murrumbidgee River.

7.5.1 Post-depositional alteration processes

Post-depositional weathering processes of the investigated sediments could potentially cause a shift in the observed Li isotope composition. This could be associated with either the re-dissolution of weathering products due to fluid interactions (e.g. rainwater infiltration) or with neo-formation of secondary minerals after deposition. The former is known to only affect the ‘exchangeable’ Li through adsorption processes (Vigier et al., 2008). The effect of this was tested on clay samples from palaeo-channels, which is discussed below in this section. To ensure that the δ^7Li composition of clay-sized fractions is not a function of sample bias induced by post-depositional alteration processes, samples were obtained from different depths of palaeo-channel deposits. If post-depositional alteration processes through fluid interactions were to change the chemistry and the Li isotope composition of sediment deposits, then only samples at or

near the surface should be affected by this. To investigate this, samples were collected from shallow and deep parts of each palaeo-channel system (Figure 102).

Figure 102: Palaeo-channel samples taken from different depths. Top hole = shallow, centre hole = intermediate, bottom hole = deep. This sample site is Gala Vale.

Furthermore, for samples that were retrieved with aluminium pipes, sediments were divided into two parts: 'inside' (deepest part from a vertical surface) and 'outside' (closer to the point of entry). Details are given in Chapter 6. Where possible, 'inside' and 'outside' aliquots were processed individually. Theoretically, the 'outside' aliquot of the aluminium pipe, which is closer to the surface, may be subject to post-weathering processes via rainwater infiltration.

Post depositional weathering effects are identified by the comparison of element ratios of samples obtained from different parts of the sediment profiles. The ratio between a mobile element (e.g. potassium) and an immobile element (e.g. titanium) indicates losses or gains of the mobile element i.e. mineral leaching (Chesworth et al., 1981; Kurtz et al., 2000). For example, low ratios could imply that the sediment had undergone high degrees of post-depositional leaching processes. Therefore, the comparison of mobile vs. immobile element ratios between sample aliquots of a palaeo-channel deposit can be used to identify whether sediments had undergone extensive mineral leaching post deposition. Potassium (K) is used here as mobile, and niobium (Nb) as immobile element. Nb typically has a low aqueous solubility (Kurtz et al., 2000). The immobility of Nb in the investigated

samples can be tested by comparing it against another typical immobile element such as tantalum (Ta) (Figure 103).

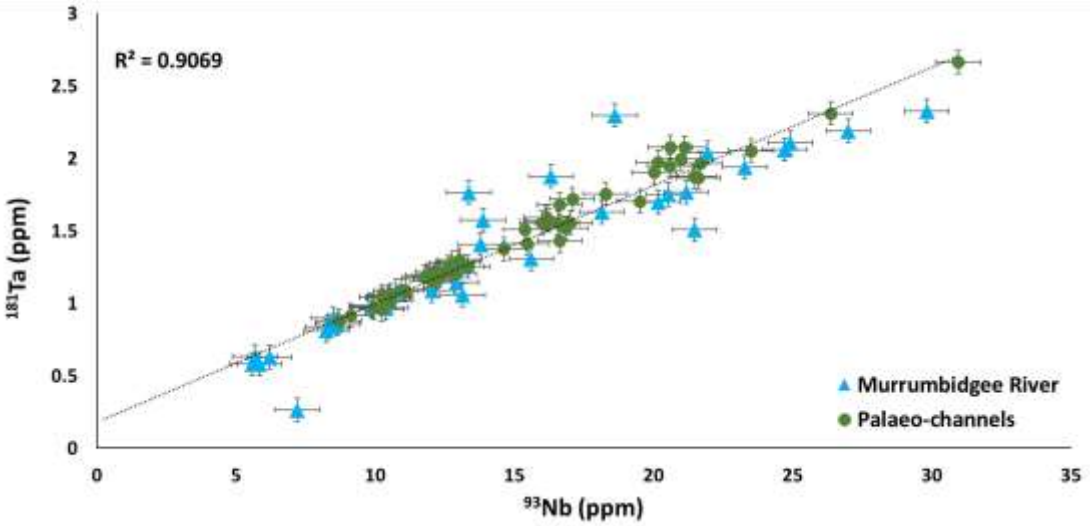

Figure 103: Correlation between tantalum (Ta) and Nb (niobium) concentrations. Murrumbidgee River samples include clays from the Murrumbidgee River, monolithologic catchments and main tributaries. Palaeo-channel data points include all investigated palaeo-channel systems.

The strong correlation between Nb and Ta (R^2 = 0.91) shows that either of the two elements are suitable to be applied as an immobile element index. Accordingly, to demonstrate the effect of mineral leaching on the clay-sized fraction of palaeo-channels, the ratio K/Nb was calculated for all sample aliquots taken from each palaeo-channel system. Figure 104 shows K/Nb ratios of samples from each palaeo-channel system relative to sample depth.

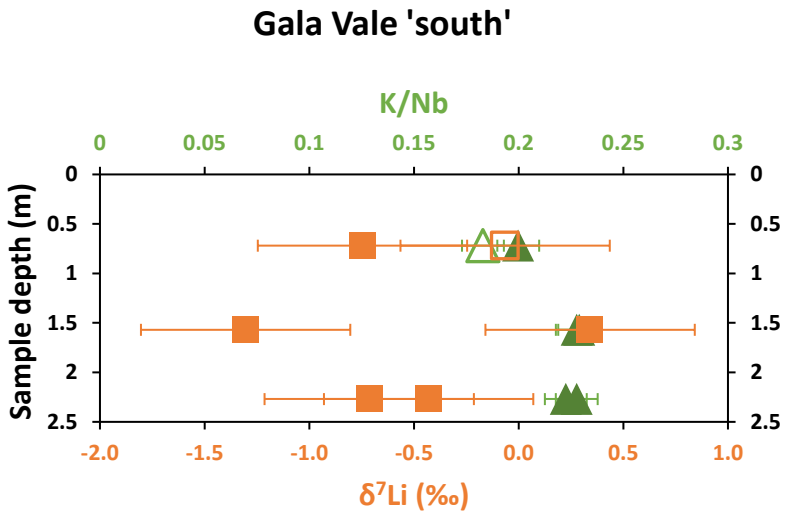
Gala Vale 'south'
K/Nb
0
0.05
0.1
0.15
0.2
0.25
0.3
Sample depth (m)
0
0.5
1
1.5
2
2.5
-2.0
-1.5
-1.0
-0.5
0.0
0.5
1.0
δ7Li (‰)

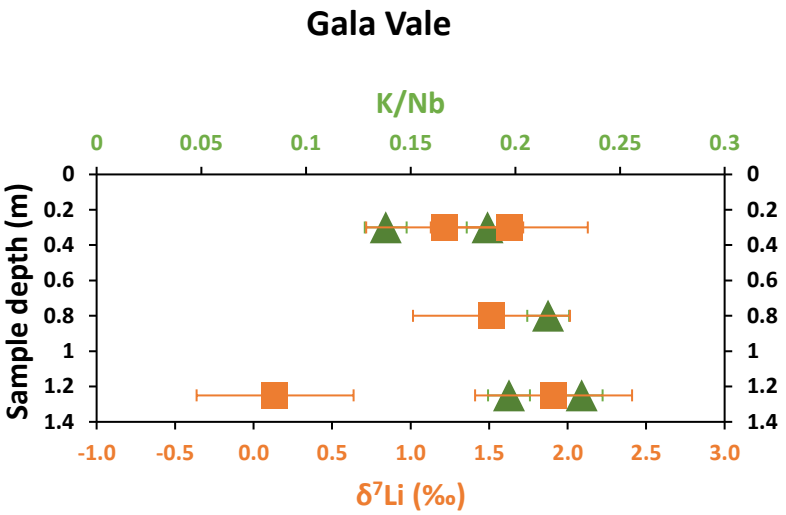
Gala Vale
K/Nb
0
0.05
0.1
0.15
0.2
0.25
0.3
Sample depth (m)
0
0.2
0.4
0.6
0.8
1
1.2
1.4
-1.0
-0.5
0.0
0.5
1.0
1.5
2.0
2.5
3.0
δ7Li (‰)

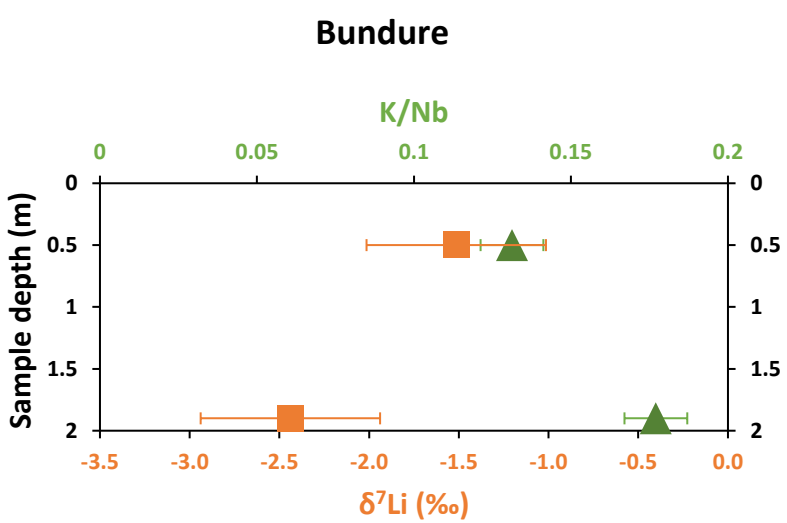
Bundure
K/Nb
0
0.05
0.1
0.15
0.2
Sample depth (m)
0
0.5
1
1.5
2
-3.5
-3.0
-2.5
-2.0
-1.5
-1.0
-0.5
0.0
δ7Li (‰)

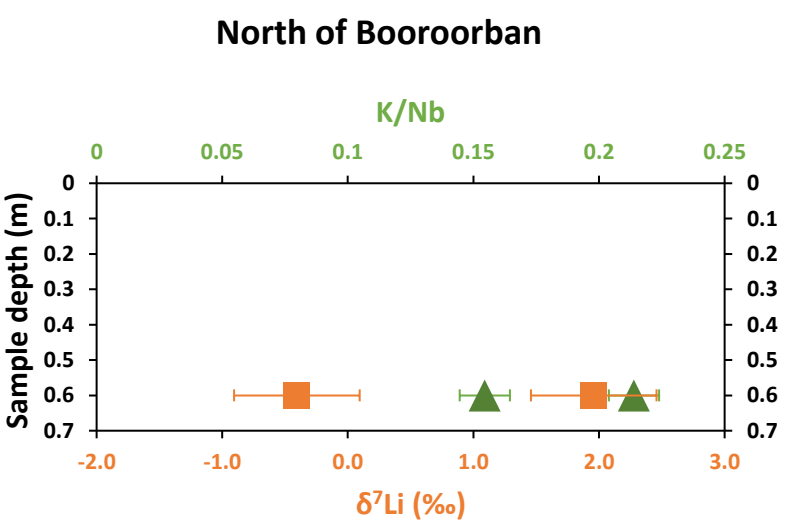
North of Booroorban
K/Nb
0
0.05
0.1
0.15
0.2
0.25
Sample depth (m)
0
0.1
0.2
0.3
0.4
0.5
0.6
0.7
-2.0
-1.0
0.0
1.0
2.0
3.0
δ7Li (‰)

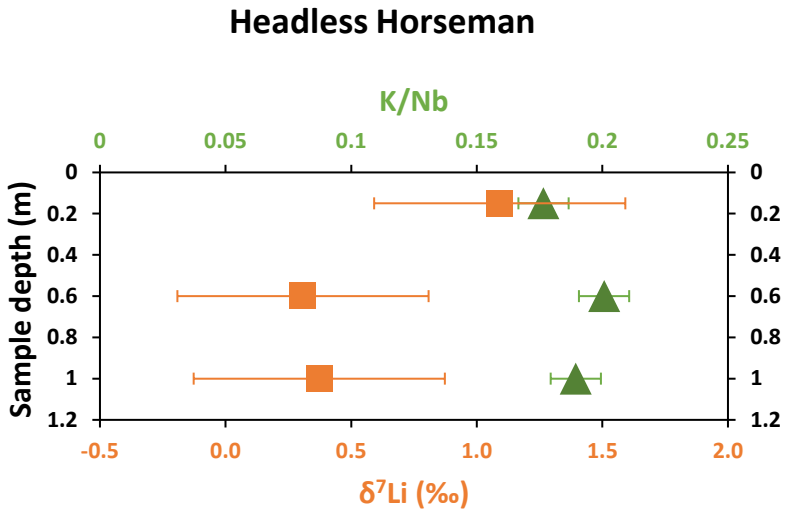
Headless Horseman
K/Nb
0
0.05
0.1
0.15
0.2
0.25
Sample depth (m)
0
0.2
0.4
0.6
0.8
1
1.2
-0.5
0.0
0.5
1.0
1.5
2.0
δ7Li (‰)

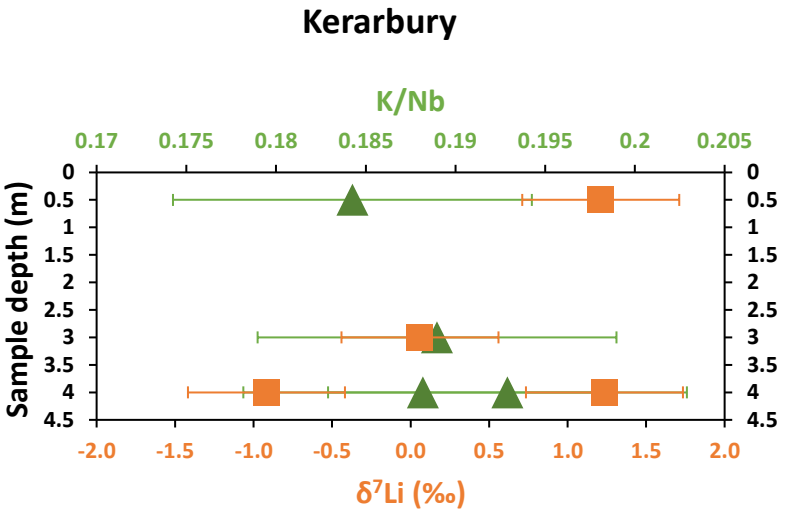
Kerarbury
K/Nb
0.17
0.175
0.18
0.185
0.19
0.195
0.2
0.205
Sample depth (m)
0
0.5
1
1.5
2
2.5
3
3.5
4
4.5
-2.0
-1.5
-1.0
-0.5
0.0
0.5
1.0
1.5
2.0
δ7Li (‰)

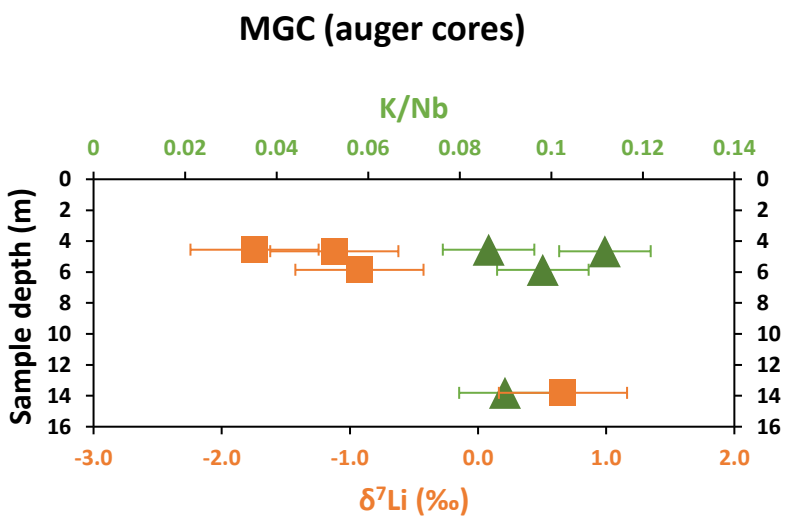
MGC (auger cores)
K/Nb
0
0.02
0.04
0.06
0.08
0.1
0.12
0.14
Sample depth (m)
0
2
4
6
8
10
12
14
16
-3.0
-2.0
-1.0
0.0
1.0
2.0
δ7Li (‰)

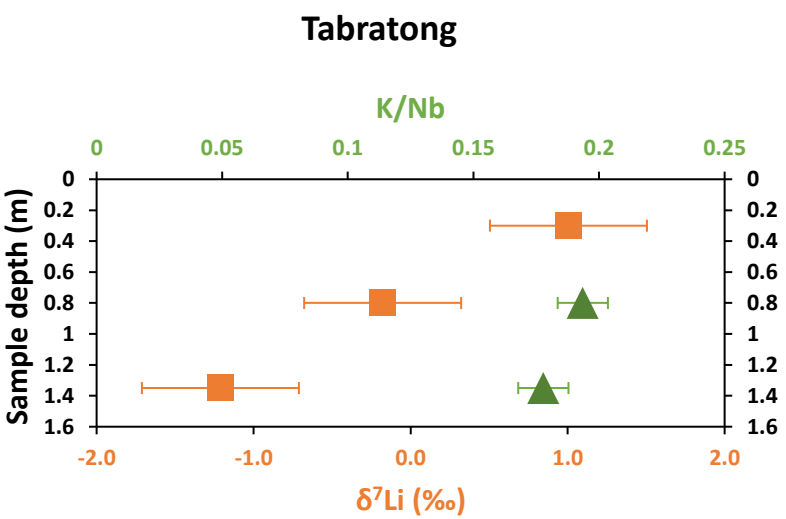
Tabratong
K/Nb
0
0.05
0.1
0.15
0.2
0.25
Sample depth (m)
0
0.2
0.4
0.6
0.8
1
1.2
1.4
1.6
-2.0
-1.0
0.0
1.0
2.0
δ7Li (‰)

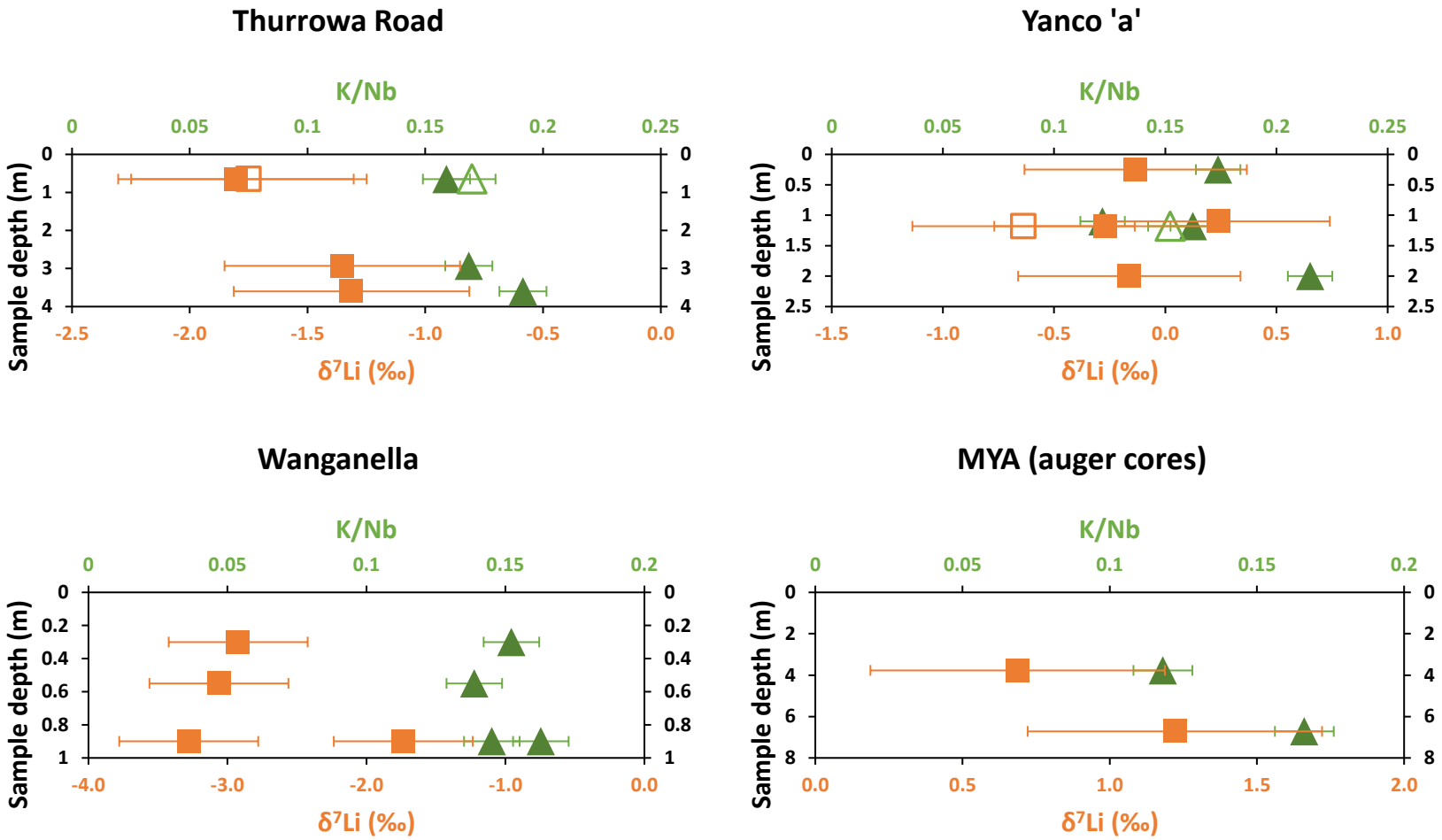

Figure 104: The δ^7Li composition (orange squares) and K/Nb (green triangles) of the clay-sized fraction relative to vertical sample depth of each palaeo-channel sample site. Open symbols are sample replicates. Error bars on K/Nb are the average of 2SE of sample replicates. External reproducibility (2SE) of δ^7Li values is 0.5 ‰.

In theory, sediments obtained from near the surface should display much lower K/Nb ratios associated with extensive mineral leaching due to more frequent fluid interactions via rainwater infiltration. This is true for most palaeo-channel sample profiles, where near surface samples display lower K/Nb ratios compared to deeper parts of the sediment succession (Figure 104). This proves that samples obtained from near-surface are indeed subject to post-depositional alteration via mineral leaching. However, in contrast, the Li isotope composition neither displays any systematic evolution in the sediment profile, nor co-varies with the degree of mineral leaching as seen in K/Nb ratios (Figure 104). Similarly, δ^7Li values of 'inside' and 'outside' sample aliquots of aluminium pipes cover an almost identical range of Li isotope values (Table 15), suggesting that post-depositional mineral leaching is not followed by a change in the Li isotope composition of the clay-sized fraction.

Mineral surface exchange reactions have shown to affect the Li isotope composition of bulk clay samples. Chan and Hein (2007) found that loosely-bound Li reflects the isotopic composition of the fluid (e.g. rainwater). Hence, depending on the amount of Li and isotope composition adsorbed onto mineral surfaces, this may impact the δ^7Li composition of clay-sized fractions. Mineral surface exchange reactions are especially high for certain clay minerals, such as expandable clays, which are known to 'swell' when exposed to solution. Using XRD techniques, it was possible to semi-quantify the presence of expandable clays in the analysed clay-sized fractions (see Chapter 9). Samples where no expandable clays were detected cover a large range of δ^7Li values (Figure 105).

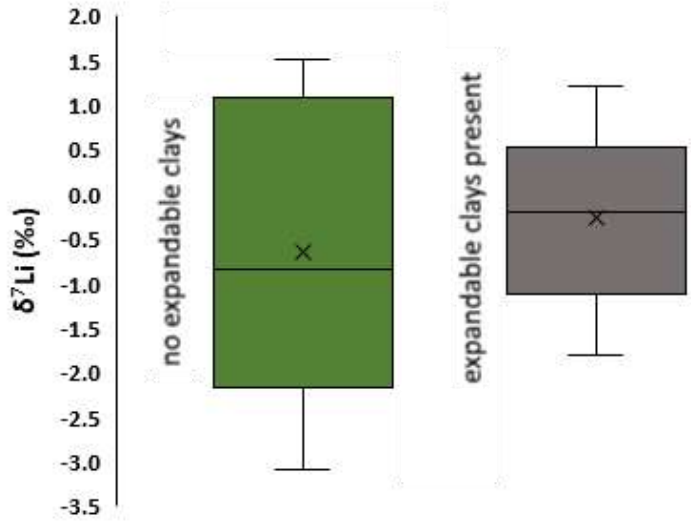

Figure 105: The δ^7Li distribution of palaeo-channel clay-sized fractions with significant amounts of expandable clays (n = 8) and insignificant amounts (n = 6). Horizontal bar is the mean, cross is the median, box is the 50th percentile, whiskers are min./max. values.

Clays where significant amounts of expandable clays were detected cover a similar but slightly smaller range of δ^7Li values. A possible explanation for this observation is that the adsorbed solution by the expandable clay fraction was isotopically heavier than the Li isotope composition of the structural clay. To further investigate this, a sequential extraction experiment was conducted. Two clay samples which showed significant amounts of expandable clays were treated with 8 mL NH_4Cl for one hour at room temperature to remove the exchangeable Li fraction (Tessier et al., 1979). Samples were then washed with 18.2 MΩ water for 5 minutes. Another two aliquots of the same samples were processed along but without any sequential leaching treatment. Clay samples where the exchangeable Li was removed (Clay_1_leached, Clay_2_leached) yielded δ^7Li values of -0.4 ‰ and -0.1 ‰ and the same samples where the exchangeable Li fraction was not removed (Clay_1, Clay_2) showed δ^7Li values of -1.0 ‰ and -0.4 ‰, respectively (Table 19).

Table 19: Li isotope composition of leached and un-leached samples

Sample name	δ^7Li (‰)
Clay_1	-1.0
Clay_1_leached	-0.4
Clay_2	-0.4
Clay_2_leached	-0.1

External uncertainty (2SE) for δ^7Li values is 0.5 ‰.

This is within the external reproducibility of δ^7Li values (± 0.5 ‰). These findings suggest that the presence of expandable clays and its associated mineral surface exchange reactions has no significant impact on the Li isotope composition of the clay-sized fraction.

Another factor that could account for post-depositional alteration of the Li isotope composition of the clay-sized fraction of palaeo-channel deposits is a change in clay mineral type during burial. Studies have shown that during burial and frequent interaction with groundwater, minerals may be altered via illitisation, the mineral transition reaction from smectite (which are included in mixed layer clays) to illite (Retallack, 1991). This process is known to follow a change in the Li isotope composition, which is mainly linked to crystal growth mechanisms and surface energy effects of nanoscale crystals (Williams and Hervig, 2005). To test if the observed δ^7Li values of palaeo-channel clays are a function of clay mineral composition, a selection of samples for each palaeo-channel system was analysed using XRD techniques (Figure 106).

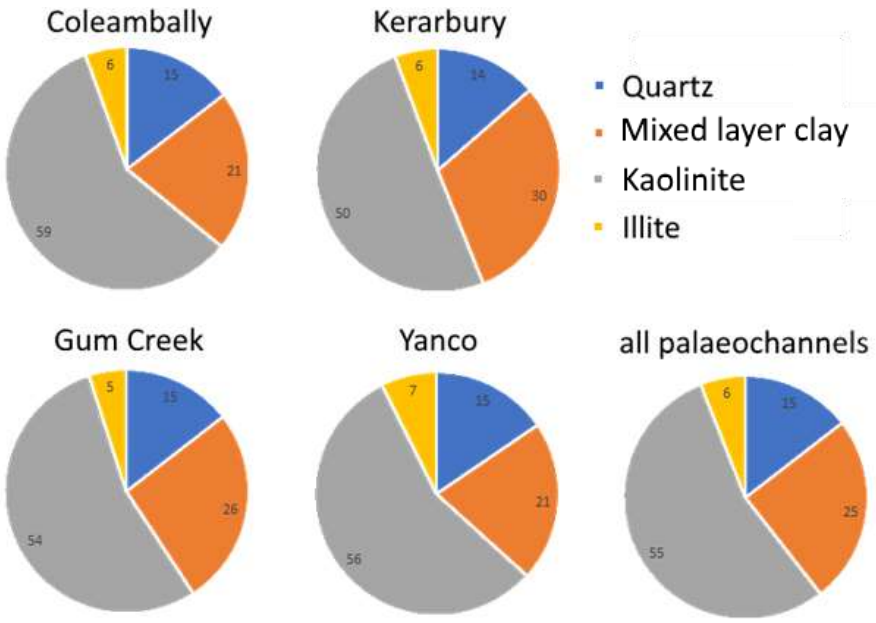

Figure 106: Average mineral composition of individual palaeo-channel clay samples (n=3-4), determined via XRD. Relative errors on mineral contents are less than 5 % (2σ).

The clay mineral composition is similar for all palaeo-channel deposits, implying that either mineral alteration during burial affected all palaeo-channel samples equally, or the type of clay mineral does not account for the observed variability of δ^7Li_{clay} within each palaeo-channel system. Compared to present-day clays from the Murrumbidgee River,

palaeo-channel clays show on average more mixed-layer clays (clays that alternate from one type to another by a stacking sequence), less illite and kaolinite, given the relative error of 5 % for mineral quantification via XRD (Figure 107).

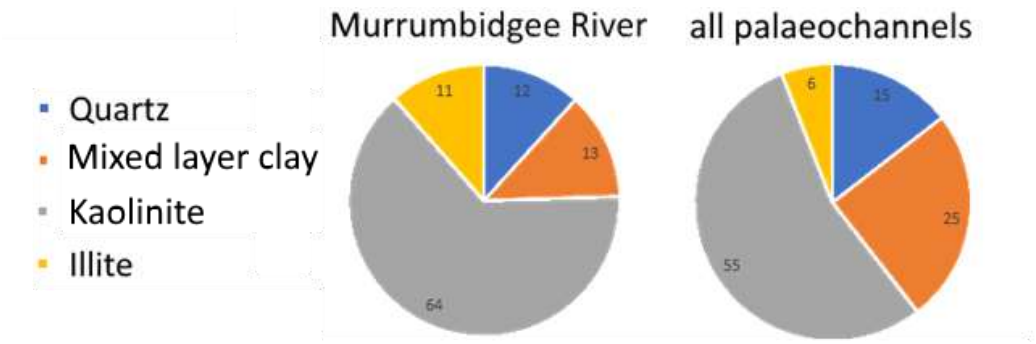

Figure 107: Mean mineral composition of clays from the Murrumbidgee River (n = 7) and palaeo-channels (n = 14). Mineral composition was determined via XRD. Relative errors on mineral contents are less than 5 % (2σ).

The slight difference between the present-day clay mineral composition of the Murrumbidgee River and palaeo-channel samples could be explained by a change in mineralogy i.e. illitisation. However, during illitisation, smectites react to illite and palaeo-channel clays display more mixed-layer clays compared to present-day clays. Therefore, clay mineral alteration associated with illitisation during burial is a less likely scenario for the observed difference between the clay composition of palaeo-channels and present-day clays.

7.5.2 Palaeo-channel weathering sources

The Nd isotope composition of present-day and palaeo-channel clays was measured to evaluate if the variation of clay mineral assemblage and the δ^7Li composition of each palaeo-channel system is a function of change in the weathering source. Present-day clays cover a fairly broad range of εNd values and overlap with most of the palaeo-channel systems (Figure 108).

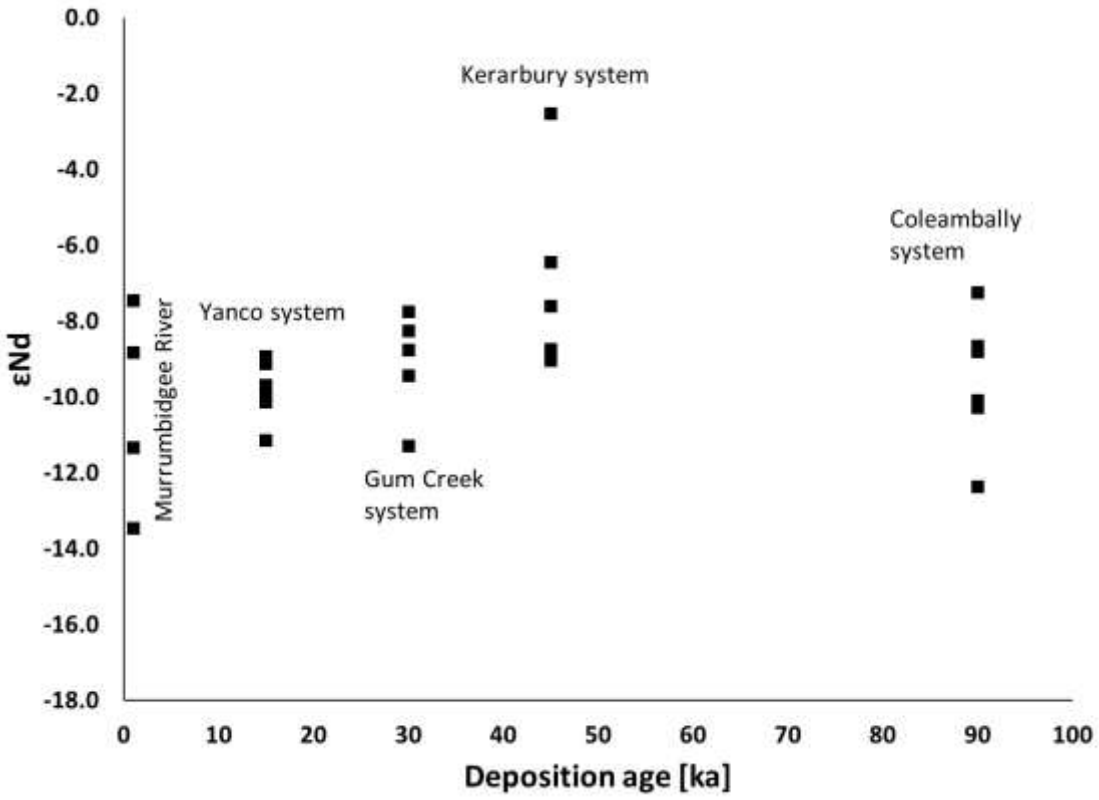

Figure 108: The εNd composition of clay-sized fractions of Murrumbidgee River samples and palaeo-channel samples. External error of εNd values is 0.3 epsilon units (2SE).

Over the past 100,000 years, the most significant difference of εNd compositions of clays can be seen during the Kerarbury palaeo-channel phase, where εNd values are slightly more positive compared to other palaeo-channel systems and present-day clays. Because Nd isotopes do not fractionate during weathering and dissolution, a change in the εNd composition is directly associated with a variation in weathering source (Frank, 2002). Therefore, during the Kearbury palaeo-channel phase, the data indicate that the weathering source was somewhat different. But considering the overall overlap between the Nd isotope composition of clays from the Murrumbidgee River and palaeo-channels, the sediment source must have remained relatively similar over most of the past 100,000 years. To test whether the δ^7Li variation over the past 100,000 years is a function of changes in chemical weathering conditions rather than weathering source, a mixing diagram between εNd and δ^7Li values can be applied. Figure 109 shows how δ^7Li and εNd values of the clay-sized fraction of all palaeo-channel and Murrumbidgee River samples compare to unweathered bedrock.

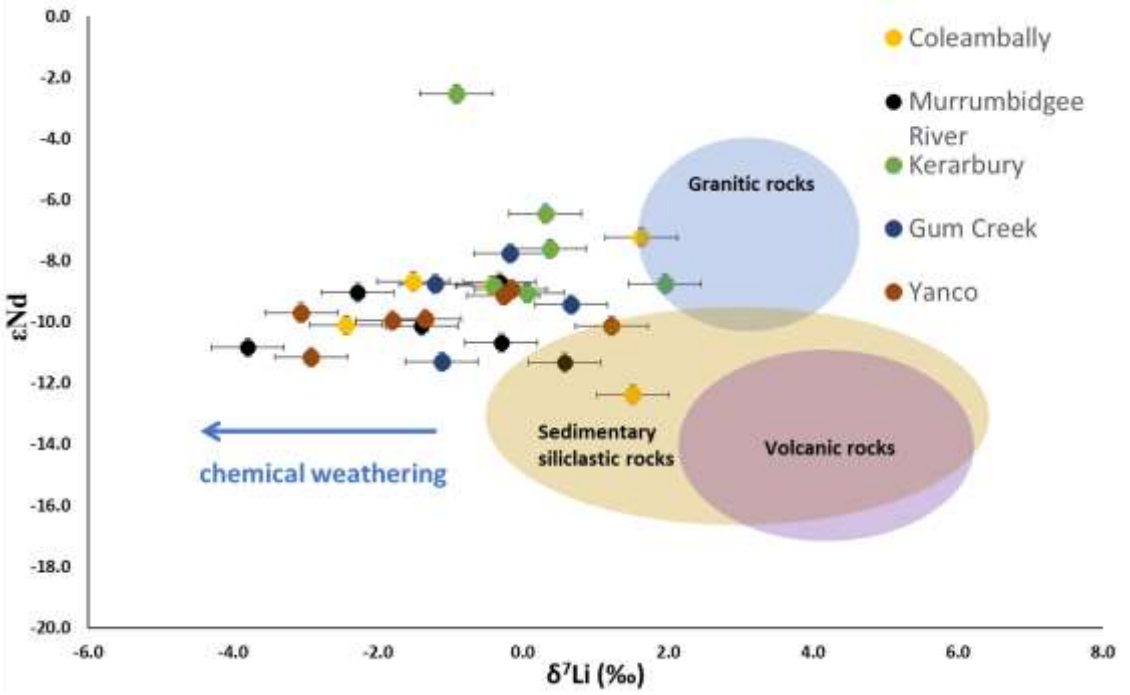

Figure 109: Li isotope composition of bedrock and clay-sized fractions of palaeo-channel samples and Murrumbidgee River samples as a function of the εNd composition. One bedrock sample of each lithology unit (granitic, volcanic, sedimentary siliclastic) in the Murrumbidgee River catchment was measured Li and Nd isotope. Other Li isotope data for bedrock (granite, volcanic, shales) are global mean values (Dellinger et al., 2015) and Nd isotope compositions of bedrock in SE Australia are taken from McDonough et al. (1985); McCulloch and Woodhead (1993); Elburg (1996).

As mentioned above, isotopic fractionation of Nd isotopes does not occur during weathering and dissolution and weathering products should exhibit identical εNd values as the source rock (Frank, 2002). For the majority of present-day and palaeo-clays this is indeed the case. However, one sample shows a εNd composition of -2.5, which indicates that there is one endmember missing in Figure 109. This endmember might be aeolian dust. Dust deposits at Lake Eyre have been measured for Nd isotopes which displayed εNd values of -3 to -4 (Revel-Rolland et al., 2006). Therefore, the sample with a εNd composition of -2.5 (Figure 109) might have derived from a dust. In contrast to Nd isotopes, Li isotopes fractionate during weathering processes with preferential retention of ^{6}Li in the weathering product. Therefore, clays with lower $\delta^{7}Li$ values than the source rock must have been altered by chemical weathering processes, which is true for the majority of samples from palaeo-channels and Murrumbidgee River samples (Figure

109). This implies that a change in weathering source over the past 100,000 years cannot account alone for the variation in the Li isotope composition.

7.5.3 Chemical weathering conditions over the past 100,000 years

Considering the discussion above (see Section 7.5.1), it is unlikely that post-depositional alteration of clays from palaeo-channel deposits via mineral leaching induced any systematic isotopic fractionation. Furthermore, the sample position in the sediment profile, clay mineral assemblage, and sediment source do not control the Li isotope composition of palaeo-channel samples. Therefore, the identification of outliers associated with any of the above-mentioned effects proves difficult and removing samples that showed high levels of mineral leaching did not significantly change the range and average δ^7Li value of each palaeo-channel system. As a result, no δ^7Li_{clay} data points are discriminated, and a box plot serves as a statistical aid to visualise the Li isotope evolution of clay minerals over the past 100,000 years (Figure 110).

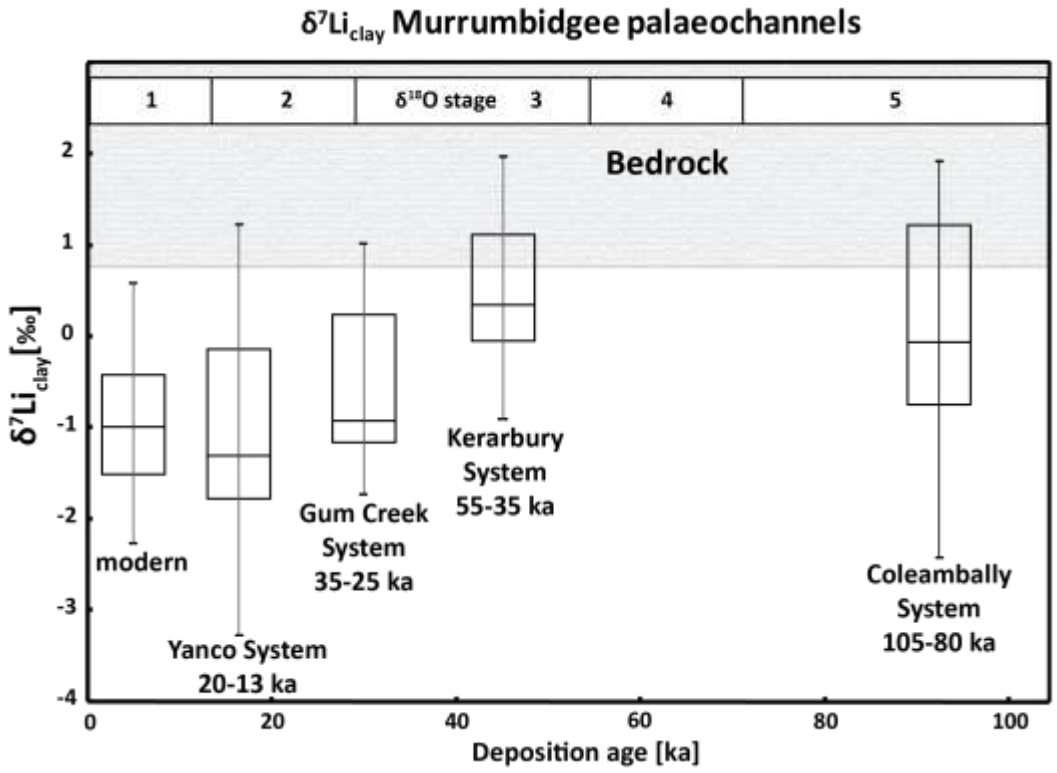

Figure 110: Li isotope composition of clays from four different palaeo-channel deposits. Clays from Murrumbidgee River deposits ('modern') are also included. Age estimates for palaeo-channel deposits are based on TL dating (Page et al., 1996). The top gray bar represents the δ^7Li range of bedrocks and dust from the catchment (n = 1 for each lithology and dust sample). Oxygen isotope stage intervals are defined by Shackleton and

Opdyke (1973). Horizontal bar is the mean, box is the 50th percentile, whiskers are min. and max. values. External reproducibility of δ^7Li values is 0.5 ‰.

Most age estimates for palaeo-channel sediments rely on TL dating done by Page et al. (1996). Some of these age estimates were re-confirmed by Banerjee et al. (2002) using optically-stimulated luminescence (OSL) techniques. Their results show that the Coleambally and Kerarbury system must have been active from 105 – 80 ka, and 55 – 35 ka. However, they proposed that the Yanco palaeo-channel could have been active as recently as 9 ka (Banerjee et al., 2002). A selection of sample aliquots of this study (provided by Daniela Mueller and Timothy Cohen, University of Wollongong) from the Gum Creek (n = 4) and Yanco system (n = 2) was dated using OSL by Mueller et al. (under review). Mueller et al. (under review) show that Gum Creek sediments were deposited between 36.7 ± 2.1 ka and 33.0 ± 1.8 ka, which is within error of the age estimates by Page et al. (1996): 35 – 25 ka. Two samples from the Yanco system by Mueller et al. (under review) revealed deposition ages of 32.4 ± 1.7 ka and 20.0 ± 1.2 ka, much older than the age estimate by Banerjee et al. (2002). The former deposition age is too old to be associated with the Yanco system and Mueller et al. (under review) proposed that the dated sediment was most likely re-deposited from a Gum Creek channel arm, which is known to have intersected the Yanco channel at the study site. The clay-sized fraction of the sample with deposition age 32.4 ± 1.7 ka showed δ^7Li values of 0.7 ± 0.5 ‰, which is similar to the Li isotope composition observed for both Yanco and Gum Creek systems. Because of the uncertainty of the source (and deposition age) of this sediment sample, this sample remains to be associated with the Yanco rather than the Gum Creek palaeo-channel system.

Clays from each palaeo-channel system cover a large range of δ^7Li values. This is not surprising, as a similar variability of δ^7Li values is observed for present-day clays of the Murrumbidgee River, which is a function of the different weathering regimes of the upper catchment (see Section 7.4.1). This implies that, similar to the present weathering environment, palaeo-channel deposits are made up of a mixture of clays which originated from various weathering regimes of the upper catchment. While the range of δ^7Li values within each palaeo-channel system remains relatively large, an overall shift towards more positive values can be observed for Coleambally, Kerarbury, and Gum Creek. This could imply that, while the weathering source remained relatively similar, the weathering

regime could have shifted over time. An important aspect when interpreting palaeo-channel sediments is the deposition history, because palaeo-channel sediments represent the terminal phase of individual river systems, which means that age estimates reflect the last stage where a river was active. Furthermore, sediment aggradation during final river phases was most likely triggered by a change in sediment delivery from headwaters, which may have been associated with a large flood event or a sequence of floods, where large volumes of coarse sediments eroded from the upper catchment (Page et al., 1994). Because flood events are generally associated with erosion peaks, it is possible that the final sediment deposit of a river system was stripped off the landscape, where deeper soil horizons were mobilised. Therefore, Li isotope compositions of clays similar to bedrock values could reflect either unweathered primary minerals or clays that formed during very low reaction times due to high discharge water flows. The same interpretation was applied in a lake sediment record from Lake Dojran, where positive δ^7Li values of fine sediments was interpreted as the erosion product of deep, unweathered soil horizons (Rothacker et al., 2018). Another explanation for positive δ^7Li values of palaeo-channel clays is the presence of parna, an aeolian clay, which is associated with arid climatic phases during the Quaternary (Butler and Hutton, 1956). In contrast to loess, parna is made of 35-70 % clay. A present-day dust sample collected in the Snowy Mountains was analysed for Li isotopes and showed a δ^7Li value of 1.7 ± 0.5 ‰. Unfortunately, only one sample was measured and therefore it is impossible to assess if the Li isotope composition of dust is homogenous. Also, the δ^7Li composition of dust could have varied in the past, making it difficult to evaluate the role of parna on palaeo-channel deposits.

Considering the discussion in Section 7.4.4, δ^7Li_{clay} should represent the equivalent to δ^7Li_{diss}, because clays form in isotopic equilibrium with solution. Higher Li isotope ratios generally indicate a decrease in chemical weathering intensity at the scale of the watershed (Kısakűrek et al., 2005; Vigier et al., 2009; Millot et al., 2010; Dosseto et al., 2015; Dellinger et al., 2015). For clay samples from palaeo-channel deposits, this means that positive δ^7Li values can be associated with low chemical weathering intensities, where water-rock interaction times are short and erosion rates are high. Based on this assumption, the following sections describe the chemical weathering conditions during each palaeo-river phase in response to climate and hydrological variability.

Coleambally phase (OIS 5)

The Coleambally phase was active between 105 and 80 ka, and therefore corresponds to oxygen isotope stage 5 (OIS 5) (Page et al., 1996). Based on channel width, the river discharge was estimated to have been around 5-fold compared to present (Schumm, 1968; Page and Nanson, 1996) (Figure 111).

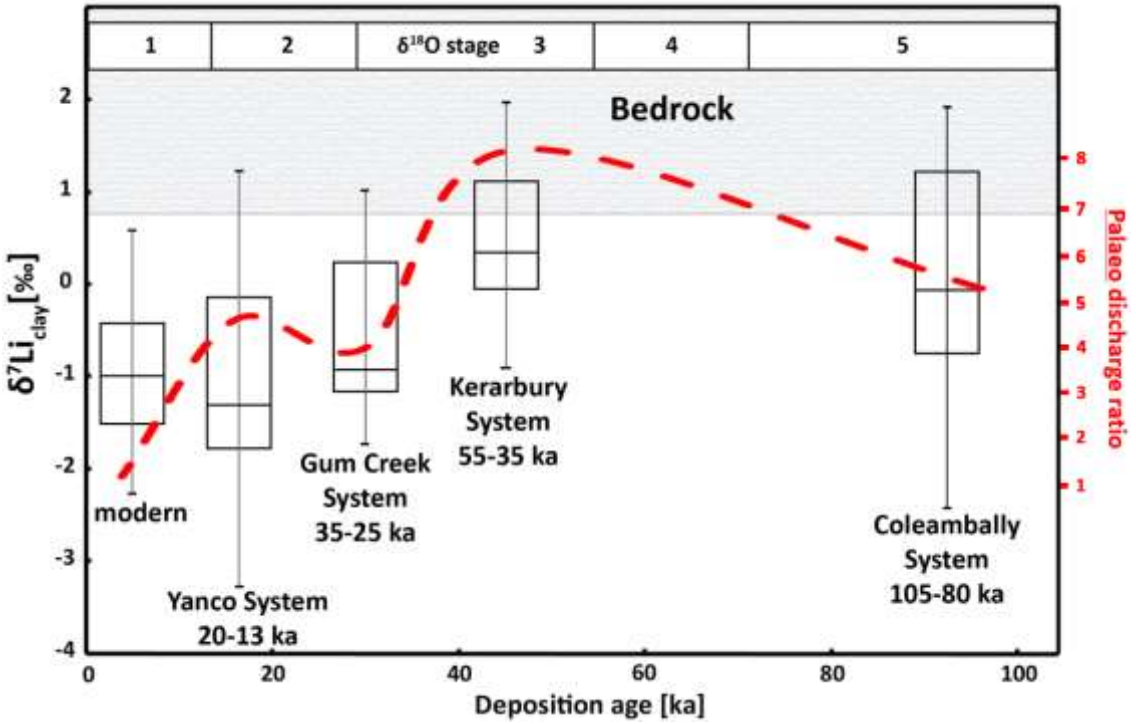

Figure 111: Li isotope composition of clays from four different palaeo-channel deposits relative to palaeo discharge estimates, shown as dashed red line (Schumm, 1968; Page and Nanson, 1996). Clays from Murrumbidgee River deposits ('modern') are also included. Age estimates for palaeo-channel deposits are based on TL dating (Page et al., 1996). The top gray bar represents the δ^7Li range of bedrocks and dust from the catchment (n = 1 for each lithology and dust sample). Oxygen isotope stage intervals are defined by Shackleton and Opdyke (1973). Horizontal bar is the mean, box is the 50th percentile, whiskers are min. and max. values. External reproducibility of δ^7Li values is 0.5 ‰.

A high hydrological activity is also shown in lacustrine records from Lake Frome and Lake Eyre, which display significantly high lake levels during OIS 5 (Magee et al., 2004; Cohen et al., 2011). Furthermore, a precipitation record from Naracoorte caves (SE Australia) shows evidence for high annual rainfall, possibly linked to the strengthening

of the Walker circulation (Ayliffe et al., 1998). All this suggests that the climate in the Murrumbidgee River Basin was much wetter during OIS 5 than at present. The overall positive distribution of δ^7Li_{clay} of the Coleambally palaeo-channel system points towards relatively low chemical weathering intensities as a consequence of high annual rainfall and increased runoff where weathering reactions were limited. A similar observation was made by Dosseto et al. (2015) in the Himalaya, where the most positive δ^7Li values of sediments (clay-sized fraction) were found during episodes of increased runoff associated with monsoon intensification.

Kerarbury phase (OIS 3)

Sediment deposits from the Kerarbury palaeo-channel indicate that the river was active between 60 and 55 ka, which corresponds to OIS 3 (Page et al., 1996). Page et al. (1996) suggest that the Kerarbury river must have exited the Riverine Plain as the most significant river since the last glacial cycle. Its palaeo-discharge was estimated to have been over eight times compared to present (Schumm, 1968; Page and Nanson, 1996) (Figure 111). Climatically, OIS 3 is characterised with high rainfall and reduced evaporation under cool conditions (Galloway, 1965; Bowler and Wasson, 1984; Kershaw and Nanson, 1993). Large permanent lakes existed in inland Australia and in southern latitudes during this time (Bowler and Wasson, 1984; Cohen et al., 2011; Bowler et al., 2012; Cohen et al., 2012). Overall, fluvial activity reached its maximum during late OIS 3, particularly in south-east Australia (Bowler and Wasson, 1984; Page and Nanson, 1996; Page et al., 1996; Kemp and Rhodes, 2010). In the Snowy Mountains, the upper catchment of the Murrumbidgee River, large snow masses caused a strong seasonal flow regime with flood peaks during spring. Li isotope ratios of clays from the Kerarbury system show the most positive δ^7Li_{clay} distribution, suggesting the lowest chemical weathering intensities throughout the past 100,000 years. Similar to OIS 5 (Coleambally system), weathering reactions were limited by the low residence time of soils and sediments. On average, δ^7Li_{clay} during OIS 3 are even higher than during OIS 5, which might have been a consequence of accelerated erosion associated with the strong seasonal flow regime (Bowler and Wasson, 1984; Page and Nanson, 1996; Page et al., 1996; Kemp and Rhodes, 2010). Interestingly, the Nd isotope composition of Kerarbury sediments indicate a slight change in sediment source during OIS 3, where εNd values are more positive (Figure 108). As discussed in Section 7.5.2, the sample with the highest εNd value (-2.5) possibly originated from a dust source and this particular sample showed a

δ^7Li value of -0.9 ± 0.5 ‰, which is lower than the average δ^7Li composition of all Kerarbury samples.

Gum Creek phase (OIS 3 & 2)

The Gum Creek palaeo-channel is estimated to have been active between 35 and 20 ka. This timeframe sets the river system's activity between OIS 3 and 2 (Page et al., 1996). The Gum Creek phase experienced similar climatic conditions to the Kerarbury phase and both channel systems might have temporarily overlapped. The Gum Creek's discharge rate was estimated to have been four times that at present (Schumm, 1968; Page and Nanson, 1996) (Figure 111). At the end of OIS 3 towards OIS 2, Gum Creek showed enhanced fluvial activity, with an intermittent dry phase between 25 and 20 ka, which may explain the lower palaeo-discharge rate compared to the Kerarbury phase (Page et al., 1996). The δ^7Li_{clay} range of Gum Creek samples are lower than that of the Kerarbury system, suggesting an increase in chemical weathering intensities, which might be linked to the drier phase between 25 and 20 ka (Page et al., 1996) with limited hydrological activity. During this phase, the residence time of soils and sediments could have been increased due to a lower flow regime, in turn explaining the observed distribution of δ^7Li_{clay} towards more negative values.

Yanco phase (OIS 2)

The deposition age of sediments of the Yanco system were dated to 20 to 13 ka (Page et al., 1996), which covers the time period of OIS 2. While most climate models show relatively dry conditions during OIS 2 (Shackleton and Opdyke, 1973; Kershaw, 1986; Petit et al., 1990), the Yanco palaeo-channel shows evidence for enhanced fluvial activity, with discharge rates of 4-5 times that of the present (Schumm, 1968; Page and Nanson, 1996) (Figure 111). Other climate records from the Riverine Plain confirm that climate conditions in the Murrumbidgee River Basin were relatively wet (Page et al., 1994). A palynological record from Caledonia Fan (SE Australia) shows little evidence for aridity during OIS 2, however climate conditions are considered to have been relatively dry between 30 and 11 ka (Kershaw et al., 2007). The range of δ^7Li_{clay} of the Yanco palaeo-channel system closely resembles that of the Gum Creek system and the present river channel. Therefore, a similar explanation as for the Gum Creek phase applies here: weathering reactions were enhanced by the increase in residence time of soil and sediment, and chemical weathering intensities were close to that of the Gum Creek phase.

7.5.4 Palaeo-weathering regimes

In Section 7.4.3, the chemical weathering regime of the modern Murrumbidgee River falls under the category 'high weathering intensity' with high W/D and low δ^7Li values of dissolved loads (Figure 95). This means that at present, the Murrumbidgee River falls under a supply-limited weathering regime, consistent with a low land area. During the past 100,000 years, fluvial activity in the Murrumbidgee River Basin was significantly stronger with palaeo-discharge estimates of up to eight-fold than at present (Schumm, 1968; Page and Nanson, 1996). Together with overall higher annual rainfall and accelerated erosion, mainly during OIS 5 and 3, weathering reactions in the catchment area could have been limited and as a consequence a different weathering regime may have prevailed. The Li isotope composition of palaeo-channel clays can be used to better characterise these past weathering environments.

As shown in Section 7.4.4, the δ^7Li composition of dissolved load and fine-grained sediments from the Murrumbidgee River Basin show a strong positive correlation, indicating that (at present) clays form in isotopic equilibrium with the dissolved load. Assuming this relationship also existed in the past, this implies that clays from palaeo-channel sediments in the Murrumbidgee River Basin may reflect the Li isotope composition of the dissolved load at the time of clay formation. For example, positive δ^7Li values in clays can be interpreted as higher δ^7Li values in palaeo-dissolved loads. Using the relationship between the δ^7Li composition of clays and dissolved loads in the modern system (Figure 99), the δ^7Li composition of the palaeo-dissolved load from that of the palaeo-channel clays can be derived with the following equation:

$$\delta^7 Li_{palaeo-diss} = 2.09\ x\ \delta^7 Li_{clay} + 23 \quad (26)$$

Note that this estimation is speculative as it is based on the assumption that the same relationship between present dissolved loads and fine-grained sediments existed in the past. Therefore, $\delta^7Li_{palaeo\text{-}diss}$ is simply a rough estimation of the Li isotope composition of palaeo-dissolved loads. Table 20 shows $\delta^7Li_{palaeo\text{-}diss}$ calculated following Equation 26 for all investigated palaeo-channel systems. The mean Li isotope composition of palaeo-dissolved loads for the Coleambally, Kerarbury, Gum Creek, and Yanco system is 23.0 ±

1.5 ‰ (2SE, n = 13), 24.2 ± 1.3 ‰ (2SE, n = 9), 22.0 ± 1.6 ‰ (2SE, n = 7), and 20.8 ± 1.5 ‰ (2SE, n = 15), respectively. Using the combined approach of the δ^7Li composition and W/D as proposed by Dellinger et al. (2015), the palaeo-weathering intensity and weathering regime can be characterised for each palaeo-channel system. Figure 112 shows how the weathering regime in the Murrumbidgee River Basin evolved over the past 100,000 years.

Table 20: The δ^7Li composition of clay-sized fractions from palaeo-channel deposits and calculated δ^7Li values of palaeo-dissolved loads.

Sample	Position in profile	Channel system	Deposition age (ka)	δ^7Li_{clay} (‰)	$\delta^7Li_{palaeo\_diss}$ (‰)
Gala Vale 'south' 3	0.72 m / inside	Coleambally	100 ± 9	-0.7	21.5
*Gala Vale 'south' 3**	*0.72 m / inside*	*Coleambally*	*100 ± 9*	*-0.1*	*22.9*
Gala Vale 'south' 2	1.57 m / outside	Coleambally	100 ± 9	0.3	23.8
Gala Vale 'south' 2	1.57 m / inside	Coleambally	100 ± 9	-1.3	20.3
Gala Vale 'south' 1	2.27 m / outside	Coleambally	100 ± 9	-0.4	22.1
Gala Vale 'south' 1	2.27 m / inside	Coleambally	100 ± 9	-0.7	21.5
Gala Vale 3	0.30 m / outside	Coleambally	100 ± 9	1.2	25.6
Gala Vale 3	0.30 m / inside	Coleambally	100 ± 9	1.6	26.4
Gala Vale 2	0.80 m / inside	Coleambally	100 ± 9	1.5	26.2
Gala Vale 1	1.25 m / outside	Coleambally	100 ± 9	0.1	23.3
Gala Vale 1	1.25 m / inside	Coleambally	100 ± 9	1.9	27.0
Bundure 1	0.50 m	Coleambally	100 ± 9	-1.5	19.9
Bundure 2	1.90 m	Coleambally	100 ± 9	-2.4	17.9
N. Booroorban 1	0.55 - 0.65 m	Kerarbury	46 ± 4	2.0	27.1
N. Booroorban 2	0.65 - 0.75 m	Kerarbury	46 ± 4	-0.4	22.2
Headless Horseman 3	0.15 m / inside & outside	Kerarbury	46 ± 4	1.1	25.3
Headless Horseman 2	0.60 m / inside & outside	Kerarbury	46 ± 4	0.3	23.7
Headless Horseman 1	1.00 m / inside & outside	Kerarbury	46 ± 4	0.4	23.8
Kerarbury 3	0.50 m / inside & outside	Kerarbury	46 ± 4	1.2	25.6
Kerarbury 2	3.00 m / inside	Kerarbury	46 ± 4	0.1	23.2
Kerarbury 1	4.00 m / outside	Kerarbury	46 ± 4	-0.9	21.1
Kerarbury 1	4.00 m / inside	Kerarbury	46 ± 4	1.2	25.6
MGCY-5#4 uow 1315**	13.81 m	Gum Creek	33.0 ± 1.8	0.7	24.4
MGC 8-3#5 40cm uow 1390**	4.65 m	Gum Creek	33.1 ± 1.7	-1.1	20.7
MGC 4-4#5 uow 1322**	5.85 m	Gum Creek	33.7 ± 2.0	-0.9	21.1
MGC 2-1 clay uow 1306**	4.55 m	Gum Creek	36.7 ± 2.1	-1.7	19.4
Tabratong 3	0.30 m / inside & outside	Gum Creek	25 ± 3	1.0	25.1

Tabratong 2	0.80 m / inside & outside	Gum Creek	25 ± 3	-0.2	22.7
Tabratong 1	1.35 m / inside & outside	Gum Creek	25 ± 3	-1.2	20.5
MYA-2#4 uow 1523**	3.77 m	Yanco	32.4 ± 1.7	0.7	24.5
MYA 1#6 uow 1521**	6.72 m	Yanco	20.0 ± 1.2	1.2	25.6
Wanganella 3	0.30 m / inside & outside	Yanco	15 ± 2	-2.9	16.9
Wanganella 2	0.55 m / inside	Yanco	15 ± 2	-3.1	16.6
Wanganella 1	0.90 m / outside	Yanco	15 ± 2	-3.3	16.2
Wanganella 1	0.90 m / inside	Yanco	15 ± 2	-1.7	19.4
Thurrowa Road 3	0.65 m	Yanco	15 ± 2	-1.8	19.3
*Thurrowa Road 3**	*0.65 m*	*Yanco*	*15 ± 2*	*-1.7*	*19.4*
Thurrowa Road 2	2.93 m / inside & outside	Yanco	15 ± 2	-1.4	20.2
Thurrowa Road 1	3.60 m / inside & outside	Yanco	15 ± 2	-1.3	20.3
Yanco 'a' 4	0.25 m / inside & outside	Yanco	15 ± 2	-0.1	22.8
Yanco 'a' 3	1.10 m	Yanco	15 ± 2	0.2	23.5
Yanco 'a' 2	1.18 m / inside & outside	Yanco	15 ± 2	-0.3	22.5
*Yanco 'a' 2**	*1.18 m / inside & outside*	*Yanco*	*15 ± 2*	*-0.6*	*21.7*
Yanco 'a' 1	2.00 m / inside & outside	Yanco	15 ± 2	-0.2	22.7

**replicate samples*

***samples provided by Daniela Mueller and Timothy Cohen (University of Wollongong).*

Inside and outside refers to the lateral distance (outside: closest from the surface; inside: deepest part of the sediment core).

$\delta^7Li_{palaeo\text{-}diss}$ was calculated with equation (26).

Deposition age estimates derived from TL dating (Page et al., 1996). Auger core samples were dated by Daniela Mueller (University of Wollongong) via optically-stimulated luminescence technique (Mueller et al., under review).

External reproducibility of δ^7Li values is 0.5 ‰.

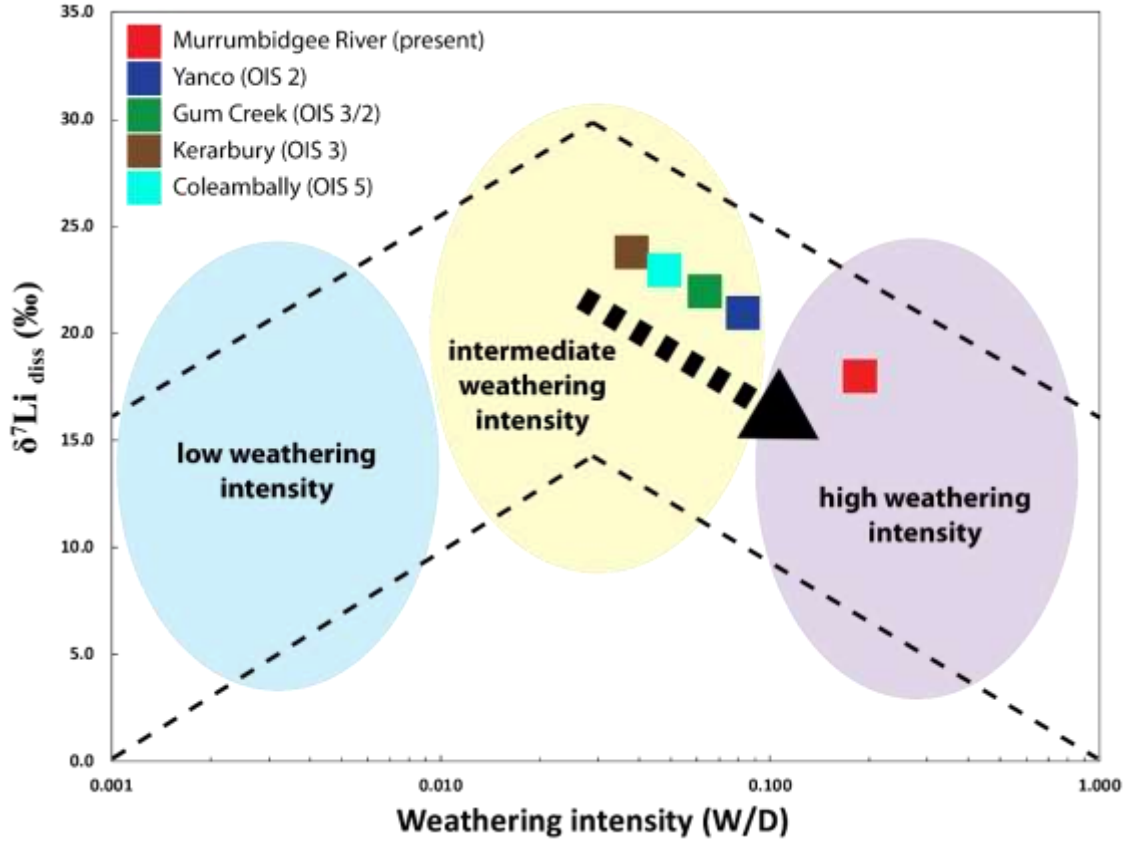

Figure 112: The δ^7Li composition of dissolved loads (δ^7Li_{diss}) as a function of weathering intensity W/D (Bouchez et al., 2014). For the Murrumbidgee River (denoted as 'present'), weathering rates (W) are based on total Na, K, Mg, and Ca concentrations and total denudation rates (D) are from Olley and Wasson (2003). The Li isotope composition of palaeo-dissolved loads is calculated using equation (26). Palaeo-weathering intensity (W/D) is extrapolated using $\delta^7Li_{palaeo\_diss}$ following the bell-shaped evolution of δ^7Li_{diss}. Based on the range of calculated $\delta^7Li_{palaeo\_diss}$ for each palaeo-channel system, the 2SE of δ^7Li_{diss} is 1.5 ‰, 1.3 ‰, 1.6 ‰, and 1.5 ‰ for Coleambally, Kerarbury, Gum Creek, and Yanco, respectively.

The estimation of palaeo-weathering intensity was done based on findings by Dellinger et al. (2017), as discussed in Section 7.4.3. Also, as discussed in Section 7.5.3, erosion rates for each palaeo-channel system must have been higher than at present, which limited weathering reactions, consequently lowering weathering intensities (W/D). Following this approach, the weathering regime of all palaeo-channel systems can be characterised as 'intermediate weathering intensity' (reaction-limited). The lowest weathering intensity could have persisted during the Coleambally (OIS 5) and Kerarbury system (OIS 3). The weathering intensity then steadily increased during the Gum Creek and Yanco palaeo-

channel phases, which correspond to the end of OIS 3 and OIS 2, until a complete shift of the weathering regime to 'high weathering intensity' (at present) occurred sometime between OIS 2 and 1 (Figure 113).

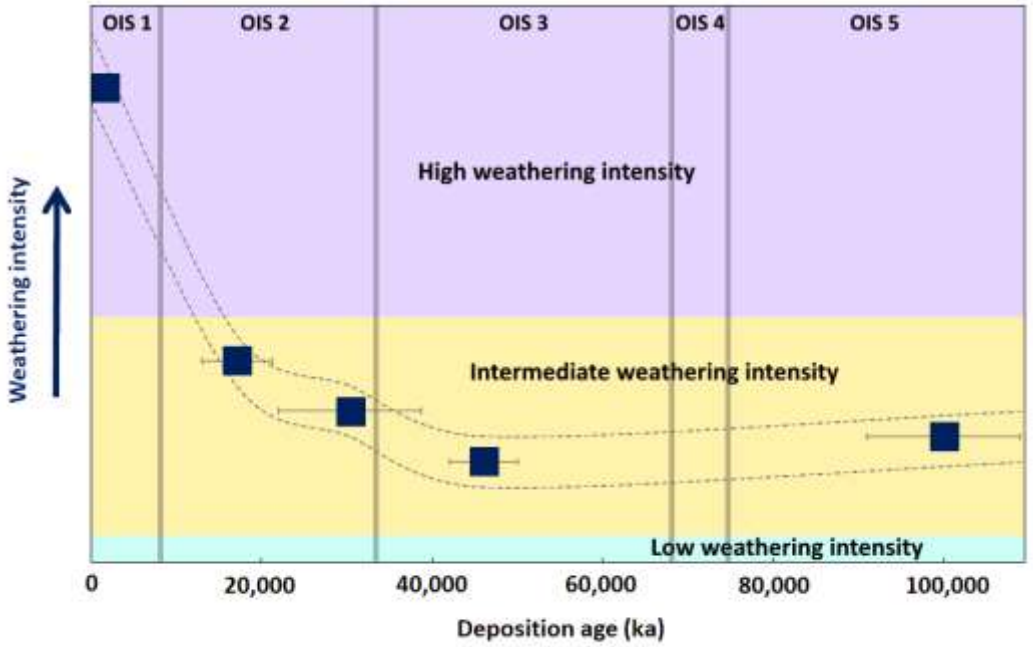

Figure 113: Conceptual representation of the evolution of weathering intensity in the Murrumbidgee River Basin over the past 100,000 years. Squares represent weathering intensities of each palaeo-channel system at a given time based on $\delta^7Li_{palaeo\_diss}$ *and W/D as shown in Figure 112. Dashed lines depict the evolution of weathering intensities over time, estimated by the range of* $\delta^7Li_{palaeo\_diss}$ *and respective weathering intensity (W/D). Values for W/D are not shown as this figure is a conceptual representation of palaeo-weathering intensity only. Vertical lines separate OIS intervals (Shackleton and Opdyke, 1973). Coloured areas highlight the extent of different weathering regimes (high, intermediate, and low weathering intensity). Deposition ages are from Page et al. (1996); Mueller et al. (under review).*

The semi-quantitative results shown in Figure 113 point towards a major change of the weathering regime in the Murrumbidgee River Basin over the past 100,000 years. If this hypothesis is valid, this must have been the consequence of a significant environmental change in this region. As discussed in Section 7.5.3, the river discharge was much higher for most of the last glacial cycle than at present. A change in weathering regime could have been triggered by an increase in temperature at ~20 ka, as indicated by a rapid

increase in atmospheric CO_2 (Petit et al., 1999). Figure 114 shows how the evolution of weathering intensities in the Murrumbidgee River Basin compare to atmospheric CO_2 concentrations as recorded in the Vostok ice core (Antarctica).

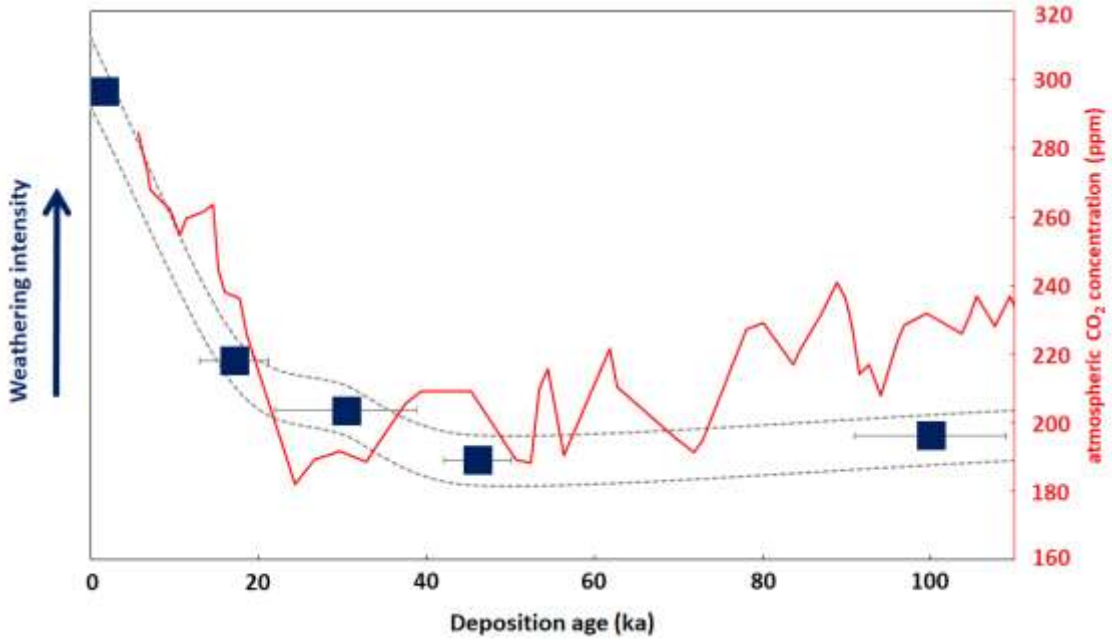

Figure 114: Conceptual representation of weathering intensities in the Murrumbidgee River Basin over the past 100,000 years relative to the atmospheric CO_2 reconstruction from the Vostok ice core (Petit et al., 1999). Squares represent weathering intensities of each palaeo-channel system at a given time. Dashed lines depict the evolution of weathering intensities over time. Deposition ages are from Page et al. (1996); Mueller et al. (under review).

Pollen records from NE Australia point towards an increase in annual rainfall since the beginning of OIS 1 (Kershaw, 1986). However, fluvial records from the Riverine Plain (SE Australia) suggest that during OIS 1, a southerly migration of the westerly wind belt restricted moisture availability west of the Great Dividing Range, which resulted in dry conditions in the Murrumbidgee River Basin (Reeves et al., 2013). As a consequence, erosion rates were reduced and chemical weathering reactions were enhanced by increasing water-rock reaction times. It is generally thought that warmer climates are associated with a more intense hydrologic cycle, which promotes sediment fluxes (von Blanckenburg et al., 2015b). However, in the Murrumbidgee River Basin, an increase in temperature at 20 ka was rather associated with arid conditions (Reeves et al., 2013). This implies that during geologically short timescales (10,000 to 20,000 years), temperature

plays a secondary role on weathering reactions compared to hydroclimatic variability. This is in agreement with findings by Dosseto et al. (2015), who showed that chemical weathering reactions in the Himalayan range are tightly coupled with monsoon intensities. Other studies show a contrasting evolution of chemical weathering rates during the last glacial cycle. Vance et al. (2009) suggested that since the last deglaciation (18 ka) and in response to increased melt water and wetter conditions, silicate weathering rates in the drainage basins of the two major Canadian Rivers, Mackenzie and St Lawrence, are three to four times higher than the long-term trend during the last glacial cycle. A similar observation was made in the European Alps between 17 and 11 ka, where a significant increase in sediment delivery to the Alpine valleys and lakes was recorded, which was linked to an increased amount of melt water and overall wetter conditions (Hinderer, 2001). This suggests that while chemical weathering may be directly affected by temperature fluctuations in some parts of the world, the specific catchment environment and hydroclimatic variation play a more significant role.

The originality of this study is the reconstruction of changes in weathering regimes (supply- vs. reaction-limited) during the last glacial cycle in SE Australia. Shifts in weathering regimes have been previously linked to tectonic-related geomorphological changes (Raymo and Ruddiman, 1992). For example, over long geological timescales, uplift has been proposed as the main driver of changes in continental weathering regimes (Raymo and Ruddiman, 1992; Misra and Froelich, 2012). However, the Murrumbidgee River Basin has been tectonically inactive over the past 100,000 years (Page et al., 1996) and therefore hydroclimatic factors may have been the main driver of the change in weathering regime. Hence, not only can the weathering regime of a tectonically inactive region shift in response to climate, but it can change during geologically short timescales of 10,000 – 20,000 years. Because these results on palaeo-channel sediments are the first of their kind, more work certainly needs to be done to evaluate the application of Li isotopes in these sediment archives as a proxy for chemical weathering intensities.

7.5.5 Conclusions

The Li isotope composition of the clay-sized fraction of sediments from four different palaeo-channel systems in the Murrumbidgee River Basin (SE Australia) was analysed to reconstruct changes in chemical weathering conditions in response to hydroclimatic variations during the last glacial cycle.

Post-depositional alteration of palaeo-channel sediments was identified for samples obtained from near-surface. These samples show low K/Nb ratios compared to deeper parts of the sediment succession, suggesting post-depositional mineral dissolution. However, the δ^7Li composition of clay-sized fractions neither displays any systematic evolution in the sediment profile, nor does the Li isotope composition co-vary with the degree of mineral dissolution. This suggests that the δ^7Li composition is not significantly affected by post-depositional alteration.

Changes in mineral abundances is unlikely to explain variations in δ^7Li values between palaeo-channel sediments as the mineralogy of all palaeo-channel samples is relatively similar. Furthermore, leaching experiments showed that surface exchange reactions, where Li is taken up from the solution and adsorbed onto expandable clays, cannot account for the observed Li isotope evolution of palaeo-channel systems.

Changes in sediment source are unlikely to be the main driver for the observed Li isotope evolution over the past 100,000 years. This was shown by comparing the Nd isotope composition of clays from individual palaeo-channels and present-day clays. During the Kerarbury phase (45 ± 10 ka), δ^7Li and εNd values were slightly more positive than at present, indicating, possibly indicating a change in weathering source. However, considering the large variability and the overall overlap of εNd and δ^7Li values from the Murrumbidgee River and palaeo-channels, the sediment sources must have remained relatively similar over most of the past 100,000 years.

Relatively low chemical weathering intensities (high δ^7Li_{clay}) have prevailed during the Coleambally system (OIS 5), a time associated with a warm and wet climate. Although climate conditions were similar during OIS 3, the lowest weathering intensities were observed during the Kerarbury palaeo-channel phase, possibly linked to accelerated erosion and a strong seasonal flow regime. From OIS 3 until present, the palaeo-channel records suggest an increase in weathering intensity (low $\delta^7Li_{clay)}$, as a possible response to an increasingly drier climate. As erosion rates decreased due to less rainfall, weathering reactions were enhanced as a consequence of longer water-rock interactions.

Over the last glacial cycle and in response to climate and hydrological variability, the overall weathering regime of the Murrumbidgee River catchment shifted from ‘intermediate weathering intensity’ (reaction-limited) to ‘high weathering intensity’ (supply-limited); the latter prevails today.

These results show that changes in chemical weathering in the Murrumbidgee River Basin during the last glacial cycle were controlled by hydroclimatic variations and the data indicate that a rapid shift in the weathering regime occurred at ~20 ka as a response to increasingly dry conditions.

References

Abdalla, O. & Bin Yahya Al-Abri, R. 2014. Factors affecting groundwater chemistry in regional arid basins of variable lithology: example of Wadi Umairy, Oman. *Arabian Journal of Geosciences,* 7**,** 2861-2870.

Ayliffe, L. K., Marianelli, P. C., Moriarty, K. C., Wells, R. T., Mcculloch, M. T., Mortimer, G. E. & Hellstrom, J. C. 1998. 500 ka precipitation record from southeastern Australia: evidence for interglacial relative aridity. *Geology,* 26**,** 147-150.

Banerjee, D., Page, K. & Lepper, K. 2002. Optical dating of paleochannel deposits in the Riverine Plain, southeastern Australia: testing the reliability of existing thermoluminescence dates. *Radiation protection dosimetry,* 101**,** 327-332.

Bayon, G., Dennielou, B., Etoubleau, J., Ponzevera, E., Toucanne, S. & Bermell, S. 2012. Intensifying weathering and land use in Iron Age Central Africa. *Science,* 335**,** 1219-1222.

Bom. 2017. *Average daily mean temperature Annual* [Online]. Available: http://www.bom.gov.au/jsp/ncc/climate_averages/temperature/index.jsp?maptype=6&period=an#maps [Accessed 31. August 2017].

Bouchez, J., Gaillardet, J. & Von Blanckenburg, F. 2014. Weathering intensity in lowland river basins: from the Andes to the Amazon mouth. *Procedia Earth and Planetary Science,* 10**,** 280-286.

Bowler, J. & Wasson, R. 1984. Glacial age environments of inland Australia. *Late Cainozoic palaeoclimates of the southern hemisphere***,** 183-208.

Bowler, J. M., Gillespie, R., Johnston, H. & Boljkovac, K. 2012. Wind v water: Glacial maximum records from the Willandra Lakes. *Peopled Landscapes: Archaeological and Biogeographic Approaches to Landscapes. Terra Australis,* 34**,** 271e296.

Brimhall, G. H. & Dietrich, W. E. 1987. Constitutive mass balance relations between chemical composition, volume, density, porosity, and strain in metasomatic hydrochemical systems: results on weathering and pedogenesis. *Geochimica et Cosmochimica Acta,* 51**,** 567-587.

Butler, B. & Hutton, J. 1956. Parna in the Riverine Plain of south-eastern Australia and the soils thereon. *Australian Journal of Agricultural Research,* 7**,** 536-553.

Carson, M., Jasper, J. & Conly, F. M. 1998. Magnitude and sources of sediment input to the Mackenzie Delta, Northwest Territories, 1974–94. *Arctic*, 116-124.

Chan, L.-H. & Hein, J. R. 2007. Lithium contents and isotopic compositions of ferromanganese deposits from the global ocean. *Deep Sea Research Part II: Topical Studies in Oceanography,* 54, 1147-1162.

Chen, J., Wang, F., Xia, X. & Zhang, L. 2002. Major element chemistry of the Changjiang (Yangtze River). *Chemical Geology,* 187, 231-255.

Chen, J., Wang, F., Meybeck, M., He, D., Xia, X. & Zhang, L. 2005. Spatial and temporal analysis of water chemistry records (1958–2000) in the Huanghe (Yellow River) basin. *Global biogeochemical cycles,* 19.

Chesworth, W., Dejou, J. & Larroque, P. 1981. The weathering of basalt and relative mobilities of the major elements at Belbex, France. *Geochimica et Cosmochimica Acta,* 45, 1235-1243.

Chetelat, B., Liu, C.-Q., Zhao, Z., Wang, Q., Li, S., Li, J. & Wang, B. 2008. Geochemistry of the dissolved load of the Changjiang Basin rivers: anthropogenic impacts and chemical weathering. *Geochimica et Cosmochimica Acta,* 72, 4254-4277.

Church, M., Kellerhals, R. & Day, T. J. 1989. Regional clastic sediment yield in British Columbia. *Canadian Journal of Earth Sciences,* 26, 31-45.

Cohen, T., Nanson, G., Jansen, J. D., Jones, B., Jacobs, Z., Larsen, J., May, J.-H., Treble, P., Price, D. & Smith, A. 2012. Late Quaternary mega-lakes fed by the northern and southern river systems of central Australia: varying moisture sources and increased continental aridity. *Palaeogeography, Palaeoclimatology, Palaeoecology,* 356, 89-108.

Cohen, T. J., Nanson, G. C., Jansen, J. D., Jones, B. G., Jacobs, Z., Treble, P., Price, D. M., May, J.-H., Smith, A. M. & Ayliffe, L. K. 2011. Continental aridification and the vanishing of Australia's megalakes. *Geology,* 39, 167-170.

Crosbie, R., Morrow, D., Cresswell, R., Leaney, F., Lamontagne, S. & Lefournour, M. 2012. New insights to the chemical and isotopic composition of rainfall across Australia.

Dalai, T., Krishnaswami, S. & Sarin, M. 2002. Major ion chemistry in the headwaters of the Yamuna river system:: Chemical weathering, its temperature dependence

and CO2 consumption in the Himalaya. *Geochimica et Cosmochimica Acta,* 66**,** 3397-3416.

Deberdt, S., Viers, J. & Dupré, B. 2002. New insights about the rare earth elements (REE) mobility in river waters. *Bulletin de la Société Géologique de France,* 173**,** 147-160.

Dellinger, M., Gaillardet, J., Bouchez, J., Calmels, D., Galy, V., Hilton, R. G., Louvat, P. & France-Lanord, C. 2014. Lithium isotopes in large rivers reveal the cannibalistic nature of modern continental weathering and erosion. *Earth and Planetary Science Letters,* 401**,** 359-372.

Dellinger, M., Gaillardet, J., Bouchez, J., Calmels, D., Louvat, P., Dosseto, A., Gorge, C., Alanoca, L. & Maurice, L. 2015. Riverine Li isotope fractionation in the Amazon River basin controlled by the weathering regimes. *Geochimica et Cosmochimica Acta,* 164**,** 71-93.

Dellinger, M., Bouchez, J., Gaillardet, J., Faure, L. & Moureau, J. 2017. Tracing weathering regimes using the lithium isotope composition of detrital sediments. *Geology,* 45**,** 411-414.

Dosseto, A., Vigier, N., Joannes-Boyau, R. C., Moffat, I., Singh, T. & Srivastava, P. 2015. Rapid response of silicate weathering rates to climate change in the Himalaya. *Geochemical Perspectives Letters,* 1**,** 10-19.

Drever, J. I. 1997. The geochemistry of natural waters: surface and groundwater environments. *Upper Saddle River*.

Elburg, M. A. 1996. Evidence of isotopic equilibration between microgranitoid enclaves and host granodiorite, Warburton Granodiorite, Lachlan Fold Belt, Australia. *Lithos,* 38**,** 1-22.

Frank, M. 2002. Radiogenic isotopes: tracers of past ocean circulation and erosional input. *Reviews of geophysics,* 40**,** 1-38.

Gaillardet, J., Dupre, B., Allegre, C. J. & Négrel, P. 1997. Chemical and physical denudation in the Amazon River Basin. *Chemical geology,* 142**,** 141-173.

Gaillardet, J., Dupré, B., Louvat, P. & Allègre, C. 1999. Global silicate weathering and CO_2 consumption rates deduced from the chemistry of large rivers. *Chemical Geology,* 159**,** 3-30.

Galloway, R. 1965. Late quaternary climates in Australia. *The Journal of Geology,* 73**,** 603-618.

Grasby, S. E., Hutcheon, I. & Mcfarland, L. 1999. Surface-water–groundwater interaction and the influence of ion exchange reactions on river chemistry. *Geology,* 27**,** 223-226.

Green, D., Petrovic, J., Moss, P. & Burrell, M. 2011. Water resources and management overview: Murrumbidgee catchment. *NSW Office of Water, Sydney*.

Healy, B., Collins, W. & Richards, S. 2004. A hybrid origin for Lachlan S-type granites: the Murrumbidgee Batholith example. *Lithos,* 78**,** 197-216.

Hem, J. D. 1985. *Study and interpretation of the chemical characteristics of natural water*, Department of the Interior, US Geological Survey, pp.

Hinderer, M. 2001. Late Quaternary denudation of the Alps, valley and lake fillings and modern river loads. *Geodinamica Acta,* 14**,** 231-263.

Huh, Y., Chan, L.-H., Zhang, L. & Edmond, J. M. 1998. Lithium and its isotopes in major world rivers: implications for weathering and the oceanic budget. *Geochimica et Cosmochimica Acta,* 62**,** 2039-2051.

Huh, Y., Chan, L.-H. & Edmond, J. M. 2001. Lithium isotopes as a probe of weathering processes: Orinoco River. *Earth and Planetary Science Letters,* 194**,** 189-199.

Jacobsen, S. B. & Wasserburg, G. 1980. Sm-Nd isotopic evolution of chondrites. *Earth and Planetary Science Letters,* 50**,** 139-155.

Jacobson, A. D. & Blum, J. D. 2003. Relationship between mechanical erosion and atmospheric CO2 consumption in the New Zealand Southern Alps. *Geology,* 31**,** 865-868.

Kemp, J. & Rhodes, E. 2010. Episodic fluvial activity of inland rivers in southeastern Australia: palaeochannel systems and terraces of the Lachlan River. *Quaternary Science Reviews,* 29**,** 732-752.

Kershaw, A. P. 1986. Climatic change and Aboriginal burning in north-east Australia during the last two glacial/interglacial cycles. *Nature,* 322**,** 47-49.

Kershaw, A. P. & Nanson, G. 1993. The last full glacial cycle in the Australian region. *Global and Planetary Change,* 7**,** 1-9.

Kershaw, A. P., Mckenzie, G., Porch, N., Roberts, R., Brown, J., Heijnis, H., Orr, M., Jacobsen, G. & Newall, P. 2007. A high‐resolution record of vegetation and climate through the last glacial cycle from Caledonia Fen, southeastern highlands of Australia. *Journal of Quaternary Science,* 22**,** 481-500.

Kısakűrek, B., James, R. H. & Harris, N. B. 2005. Li and δ^7Li in Himalayan rivers: proxies for silicate weathering? *Earth and Planetary Science Letters,* 237**,** 387-401.

Koppes, M. N. & Montgomery, D. R. 2009. The relative efficacy of fluvial and glacial erosion over modern to orogenic timescales. *Nature Geoscience,* 2**,** 644-647.

Kurtz, A. C., Derry, L. A., Chadwick, O. A. & Alfano, M. J. 2000. Refractory element mobility in volcanic soils. *Geology,* 28**,** 683-686.

Liu, X.-M., Wanner, C., Rudnick, R. L. & Mcdonough, W. F. 2015. Processes controlling δ 7 Li in rivers illuminated by study of streams and groundwaters draining basalts. *Earth and Planetary Science Letters,* 409**,** 212-224.

Magee, J. W., Miller, G. H., Spooner, N. A. & Questiaux, D. 2004. Continuous 150 ky monsoon record from Lake Eyre, Australia: insolation-forcing implications and unexpected Holocene failure. *Geology,* 32**,** 885-888.

Malmström, M. & Banwart, S. 1997. Biotite dissolution at 25 C: The pH dependence of dissolution rate and stoichiometry. *Geochimica et Cosmochimica Acta,* 61**,** 2779-2799.

Mcculloch, M. & Woodhead, J. 1993. Lead isotopic evidence for deep crustal-scale fluid transport during granite petrogenesis. *Geochimica et Cosmochimica Acta,* 57**,** 659-674.

Mcdonough, W., Mcculloch, M. & Sun, S. 1985. Isotopic and geochemical systematics in Tertiary-Recent basalts from southeastern Australia and implications for the evolution of the sub-continental lithosphere. *Geochimica et Cosmochimica Acta,* 49**,** 2051-2067.

Millot, R., Gaillardet, J., Dupré, B. & Allègre, C. J. 2002. The global control of silicate weathering rates and the coupling with physical erosion: new insights from rivers of the Canadian Shield. *Earth and Planetary Science Letters,* 196**,** 83-98.

Millot, R., Érôme Gaillardet, J., Dupré, B. & Allègre, C. J. 2003. Northern latitude chemical weathering rates: clues from the Mackenzie River Basin, Canada. *Geochimica et Cosmochimica Acta,* 67**,** 1305-1329.

Millot, R., Vigier, N. & Gaillardet, J. 2010. Behaviour of lithium and its isotopes during weathering in the Mackenzie Basin, Canada. *Geochimica et Cosmochimica Acta,* 74**,** 3897-3912.

Misra, S. & Froelich, P. N. 2012. Lithium isotope history of Cenozoic seawater: changes in silicate weathering and reverse weathering. *Science,* 335**,** 818-823.

Moquet, J.-S., Crave, A., Viers, J., Seyler, P., Armijos, E., Bourrel, L., Chavarri, E., Lagane, C., Laraque, A. & Casimiro, W. S. L. 2011. Chemical weathering and atmospheric/soil CO2 uptake in the Andean and Foreland Amazon basins. *Chemical Geology,* 287**,** 1-26.

Mortatti, J. & Probst, J.-L. 2003. Silicate rock weathering and atmospheric/soil CO2 uptake in the Amazon basin estimated from river water geochemistry: seasonal and spatial variations. *Chemical geology,* 197**,** 177-196.

Mueller, D., Jacobs, Z., Cohen, T., Price, D., Reinfelds, I. & Shulmeister, J. under review. Revisiting an arid LGM using fluvial archives: a luminescence chronology for palaeochannels of the Murrumbidgee River, southeastern Australia. *Journal of Quaternary Science*.

Negrel, P., Allègre, C. J., Dupré, B. & Lewin, E. 1993. Erosion sources determined by inversion of major and trace element ratios and strontium isotopic ratios in river water: the Congo Basin case. *Earth and Planetary Science Letters,* 120**,** 59-76.

Nesbitt, H. & Young, G. 1982. Early Proterozoic climates and plate motions inferred from major element chemistry of lutites. *Nature,* 299**,** 715-717.

Oliva, P., Viers, J., Dupré, B., Fortuné, J. P., Martin, F., Braun, J. J., Nahon, D. & Robain, H. 1999. The effect of organic matter on chemical weathering: Study of a small tropical watershed: Nsimi-Zoetele site, Cameroon. *Geochimica et Cosmochimica Acta,* 63**,** 4013-4035.

Olley, J. M. & Wasson, R. J. 2003. Changes in the flux of sediment in the Upper Murrumbidgee catchment, Southeastern Australia, since European settlement. *Hydrological processes,* 17**,** 3307-3320.

Page, K., Dare‐Edwards, A., Nanson, G. & Price, D. 1994. Late Quaternary evolution of Lake Urana, New South Wales, Australia. *Journal of Quaternary Science,* 9**,** 47-57.

Page, K., Nanson, G. & Price, D. 1996. Chronology of Murrumbidgee river palaeochannels on the Riverine Plain, southeastern Australia. *Journal of Quaternary Science,* 11**,** 311-326.

Page, K. & Nanson, G. 1996. Stratigraphic architecture resulting from Late Quaternary evolution of the Riverine Plain, south‐eastern Australia. *Sedimentology,* 43**,** 927-945.

Petit, J.-R., Mounier, L., Jouzel, J., Korotkevich, Y. S., Kotlyakov, V. & Lorius, C. 1990. Palaeoclimatological and chronological implications of the Vostok core dust record. *Nature,* 343**,** 56.

Petit, J.-R., Jouzel, J., Raynaud, D., Barkov, N. I., Barnola, J.-M., Basile, I., Bender, M., Chappellaz, J., Davis, M. & Delaygue, G. 1999. Climate and atmospheric history of the past 420,000 years from the Vostok ice core, Antarctica. *Nature,* 399**,** 429.

Pistiner, J. S. & Henderson, G. M. 2003. Lithium-isotope fractionation during continental weathering processes. *Earth and Planetary Science Letters,* 214**,** 327-339.

Pogge Von Strandmann, P. A., Burton, K. W., James, R. H., Van Calsteren, P., Gíslason, S. R. & Mokadem, F. 2006. Riverine behaviour of uranium and lithium isotopes in an actively glaciated basaltic terrain. *Earth and Planetary Science Letters,* 251**,** 134-147.

Pogge Von Strandmann, P. A., James, R. H., Van Calsteren, P., Gíslason, S. R. & Burton, K. W. 2008. Lithium, magnesium and uranium isotope behaviour in the estuarine environment of basaltic islands. *Earth and Planetary Science Letters,* 274**,** 462-471.

Pogge Von Strandmann, P. A., Burton, K. W., James, R. H., Van Calsteren, P. & Gislason, S. R. 2010. Assessing the role of climate on uranium and lithium isotope behaviour in rivers draining a basaltic terrain. *Chemical Geology,* 270**,** 227-239.

Pogge Von Strandmann, P. A., Opfergelt, S., Lai, Y.-J., Sigfússon, B., Gislason, S. R. & Burton, K. W. 2012. Lithium, magnesium and silicon isotope behaviour accompanying weathering in a basaltic soil and pore water profile in Iceland. *Earth and Planetary Science Letters,* 339**,** 11-23.

Raymo, M. & Ruddiman, W. F. 1992. Tectonic forcing of late Cenozoic climate. *Nature,* 359**,** 117-122.

Reeves, J. M., Barrows, T. T., Cohen, T. J., Kiem, A. S., Bostock, H. C., Fitzsimmons, K. E., Jansen, J. D., Kemp, J., Krause, C. & Petherick, L. 2013. Climate

variability over the last 35,000 years recorded in marine and terrestrial archives in the Australian region: an OZ-INTIMATE compilation. *Quaternary Science Reviews,* 74**,** 21-34.

Retallack, G. 1991. Untangling the effects of burial alteration and ancient soil formation. *Annual Review of Earth and Planetary Sciences,* 19**,** 183-206.

Revel-Rolland, M., De Deckker, P., Delmonte, B., Hesse, P., Magee, J., Basile-Doelsch, I., Grousset, F. & Bosch, D. 2006. Eastern Australia: a possible source of dust in East Antarctica interglacial ice. *Earth and Planetary Science Letters,* 249**,** 1-13.

Riebe, C. S., Kirchner, J. W., Granger, D. E. & Finkel, R. C. 2001. Strong tectonic and weak climatic control of long-term chemical weathering rates. *Geology,* 29**,** 511-514.

Riebe, C. S., Kirchner, J. W. & Finkel, R. C. 2003. Long-term rates of chemical weathering and physical erosion from cosmogenic nuclides and geochemical mass balance. *Geochimica et Cosmochimica Acta,* 67**,** 4411-4427.

Rothacker, L., Dosseto, A., Francke, A., Chivas, A. R., Vigier, N., Kotarba-Morley, A. M. & Menozzi, D. 2018. Impact of climate change and human activity on soil landscapes over the past 12,300 years. *Scientific reports,* 8**,** 247.

Ryu, J.-S., Vigier, N., Lee, S.-W., Lee, K.-S. & Chadwick, O. A. 2014. Variation of lithium isotope geochemistry during basalt weathering and secondary mineral transformations in Hawaii. *Geochimica et Cosmochimica Acta,* 145**,** 103-115.

Schumm, S. A. 1968. *River adjustment to altered hydrologic regimen, Murrumbidgee River and paleochannels, Australia,* US Government Printing Office, 598 pp.

Shackleton, N. J. & Opdyke, N. D. 1973. Oxygen isotope and palaeomagnetic stratigraphy of Equatorial Pacific core V28-238: Oxygen isotope temperatures and ice volumes on a 105 year and 106 year scale. *Quaternary research,* 3**,** 39-55.

Singh, A. K. & Hasnain, S. I. 1998. Major ion chemistry and weathering control in a high altitude basin: Alaknanda River, Garhwal Himalaya, India. *Hydrological sciences journal,* 43**,** 825-843.

Small, J. 1994. Fluid composition, mineralogy and morphological changes associated with the smectite-to-illite reaction: An experimental investigation of the effect of organic acid anions. *Clay Minerals,* 29**,** 539-554.

Tessier, A., Campbell, P. G. & Bisson, M. 1979. Sequential extraction procedure for the speciation of particulate trace metals. *Analytical chemistry,* 51**,** 844-851.

Tipper, E. T., Calmels, D., Gaillardet, J., Louvat, P., Capmas, F. & Dubacq, B. 2012. Positive correlation between Li and Mg isotope ratios in the river waters of the Mackenzie Basin challenges the interpretation of apparent isotopic fractionation during weathering. *Earth and Planetary Science Letters,* 333**,** 35-45.

Vance, D., Teagle, D. A. & Foster, G. L. 2009. Variable Quaternary chemical weathering fluxes and imbalances in marine geochemical budgets. *Nature,* 458**,** 493-496.

Viers, J., Dupré, B., Polvé, M., Schott, J., Dandurand, J.-L. & Braun, J.-J. 1997. Chemical weathering in the drainage basin of a tropical watershed (Nsimi-Zoetele site, Cameroon): comparison between organic-poor and organic-rich waters. *Chemical Geology,* 140**,** 181-206.

Viers, J., Dupré, B., Braun, J.-J., Deberdt, S., Angeletti, B., Ngoupayou, J. N. & Michard, A. 2000. Major and trace element abundances, and strontium isotopes in the Nyong basin rivers (Cameroon): constraints on chemical weathering processes and elements transport mechanisms in humid tropical environments. *Chemical Geology,* 169**,** 211-241.

Vigier, N., Burton, K., Gislason, S., Rogers, N., Duchene, S., Thomas, L., Hodge, E. & Schaefer, B. 2006. The relationship between riverine U-series disequilibria and erosion rates in a basaltic terrain. *Earth and Planetary Science Letters,* 249**,** 258-273.

Vigier, N., Decarreau, A., Millot, R., Carignan, J., Petit, S. & France-Lanord, C. 2008. Quantifying Li isotope fractionation during smectite formation and implications for the Li cycle. *Geochimica et Cosmochimica Acta,* 72**,** 780-792.

Vigier, N., Gislason, S. R., Burton, K., Millot, R. & Mokadem, F. 2009. The relationship between riverine lithium isotope composition and silicate weathering rates in Iceland. *Earth and Planetary Science Letters,* 287**,** 434-441.

Von Blanckenburg, F., Bouchez, J., Ibarra, D. E. & Maher, K. 2015. Stable runoff and weathering fluxes into the oceans over Quaternary climate cycles. *Nature Geoscience,* 8**,** 538-542.

Wang, Q.-L., Chetelat, B., Zhao, Z.-Q., Ding, H., Li, S.-L., Wang, B.-L., Li, J. & Liu, X.-L. 2015. Behavior of lithium isotopes in the Changjiang River system:

sources effects and response to weathering and erosion. *Geochimica et Cosmochimica Acta,* 151**,** 117-132.

Weiland, F. S., Lopez, P., Van Dijk, A. & Schellekens, J. Global high-resolution reference potential evaporation. MODSIM 2015, Conference Proceedings, Broadbeach, Queensland, Australia, 2015.

West, A. J., Galy, A. & Bickle, M. 2005. Tectonic and climatic controls on silicate weathering. *Earth and Planetary Science Letters,* 235**,** 211-228.

Williams, L. B. & Hervig, R. L. 2005. Lithium and boron isotopes in illite-smectite: the importance of crystal size. *Geochimica et Cosmochimica Acta,* 69**,** 5705-5716.

Wimpenny, J., James, R. H., Burton, K. W., Gannoun, A., Mokadem, F. & Gíslason, S. R. 2010. Glacial effects on weathering processes: new insights from the elemental and lithium isotopic composition of West Greenland rivers. *Earth and Planetary Science Letters,* 290**,** 427-437.

Wurts, W. A. & Durborow, R. M. 1992. Interactions of pH, carbon dioxide, alkalinity and hardness in fish ponds.

8 Impact of climate change and human activity on soil landscapes over the past 12,300 years

The short-term effect of climate on chemical weathering conditions is highly debated. While some studies show that chemical weathering may significantly respond to short-lived climate shifts (~500 years) (e.g. Jin et al. (2006), other studies suggest climate plays a negligible role on weathering reactions on such timescales (Bluth and Kump, 1994; Munhoven, 2002). Using a multi-proxy approach, Li and U isotopes, this study aims to identify the short-term response of climate variation and soil development and erosion over the past 12,300 years. Furthermore, the impact first humans had on the natural soil environment is poorly understood. This study shows the timing and gravity of how the landscape has responded to first agricultural practises by humans. Samples derived from the Lake Dojran (Greece/FYROM) sediment record, which spans the past 12,300 years.

This study is published online and can be found under: Rothacker, L., Dosseto, A., Francke, A., Chivas, A.R., Vigier, N., Kotarba-Morley, A.M. and Menozzi, D., 2018. Impact of climate change and human activity on soil landscapes over the past 12,300 years. *Scientific Reports*, *8*(1), p.247.

Please note that Anthony Dosseto (University of Wollongong) and Davide Menozzi (University of Wollongong) conducted the laboratory work for uranium isotopes. Leo Rothacker conducted all other laboratory work for this research project. The manuscript published in Scientific Reports was written by Anthony Dosseto and Leo Rothacker, with manuscript improvements by Alexander Francke, Allan R. Chivas, Nathalie Vigier, Anna M. Kotarba-Morley, and Davide Menozzi.

8.1 Introduction and study site

Soil systems are key components of a broad range of ecosystems. Their development via chemical weathering and mineral dissolution consumes carbon dioxide, and thus plays a substantial role in regulating the carbon cycle and Earth's climate (Walker et al., 1981; Berner et al., 1983; Broecker and Sanyal, 1998). Erosion plays a major role in chemical weathering, because it exposes unweathered minerals and thus promotes mineral dissolution and soil development. However, accelerated erosion due to deforestation or agricultural practices may inhibit this development, consequently limiting our soil resources in the future (Montgomery, 2007). Our understanding of the evolution of soil

systems is underpinned by our ability to ascertain how soil erosion and development respond to climatic variability and human activity. It is well known that soil erosion can respond rapidly to changes in rainfall and vegetation cover (anthropogenic or not) (Kosmas et al., 1997). Though, much less is known about the variability of soil development over time (Dearing et al., 2001; Vance et al., 2009; Arnaud et al., 2012; Brisset et al., 2013; Dosseto et al., 2015; Arnaud et al., 2016; Bastian et al., 2017; Bajard et al., 2017b; Bajard et al., 2017a). In this study, the relative impact of climate variability and human activity on soil systems during the Late Glacial and Holocene in south-eastern Europe was investigated. To achieve this, U and Li isotopes were measured in lacustrine sedimentary deposits which are used as proxies for soil erosion and development, respectively.

Both Li and U isotope proxies were applied to a sediment core from Lake Dojran at the Macedonian/Greek border. Lake Dojran is situated on the border between Macedonia and Greece (41°12'N, 22°44'E) (Figure 115).

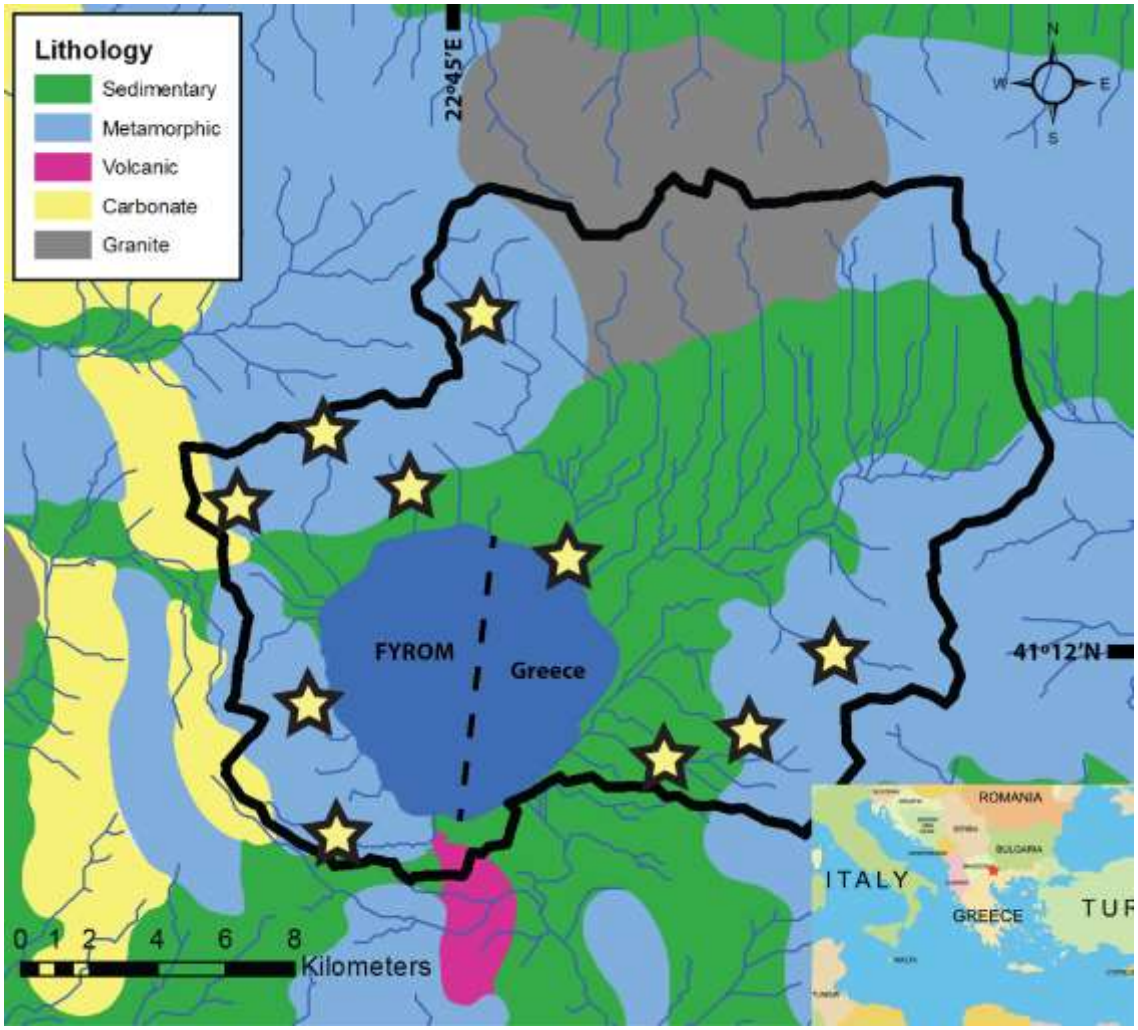

Figure 115: Simplified distribution of geological units for Lake Dojran catchment based on field mapping by A.F. and from ref. Ivanovski (1970); Andronopoulos (1990). Individual lithology areas were estimated and manually drawn by L.R. Black curve: catchment boundary, blue lines: stream network. Dashed line shows the border between FYROM and Greece. Stars show sample locations for stream sediments. Stream network and catchment area was calculated with ArcGIS Desktop Advanced 10.4 software (https://esriaustralia.com.au/arcgis-desktop) using a 1-arc second digital elevation model (DEM). Insert: South-east Europe, star marks location of Lake Dojran (open source: www.vectorworldmap.com Political World Map v. 2.2 (2009)).

Water surface area and average water depths were measured in 2004 at 40 km^2 and 3-4 m, respectively (Katsavouni and Petkovski, 2004). The catchment area (275 km^2) is drained by small rivers, creeks, and groundwater. The only outflow of Lake Dojran, located in the southern corner of the lake, was canalised in the 1950's. In the eastern part of the catchment, the lithology underlying the drainage area is composed of gneiss,

granite, mica schist, amphibolite, Quaternary alluvial sediment, and a small area of volcanic-sedimentary rock at the southern end of the lake (Figure 115). In the western part, the lithology consists of muscovite gneiss, green schist, gabbro, serpentinite, biotite gneiss, granite, and marble.

The sediment core is 7 m long and provides a record of palaeo-environmental change of the past 12,300 years, at the transition from the cold and arid Younger Dryas into the overall warmer and more humid Holocene (Francke et al., 2013). The lack of alluvial storage suggests a short sediment transfer time from hillslopes into the lake. Thus, no significant time lag between production and isotopic signal in soils and deposition in the lake is expected. Also, hydrodynamic sorting is expected to be minimal. A total of 26 samples were taken from the core and another 11 sediment samples were collected from modern streams draining into Lake Dojran. Furthermore, 11 bedrock samples were collected from the catchment of Lake Dojran. Mineral concentrations were determined, and U and Li isotopes analysed on size fractions <63 µm at the Wollongong Isotope Geochronology Laboratory, University of Wollongong. For details on field methods and analytical methods, see Chapter 6 and 9, respectively

The study area is climatically influenced by mid-latitude westerlies and the Subtropical High-pressure belt. The North Atlantic Oscillation (NAO) modulates winter precipitation and the migration of the Intertropical Convergence Zone (ITCZ) affects dry periods during summer (Lionello et al., 2006). Precipitation is highest during mild winters (612 mm/yr), and lowest during hot summers. Mean annual air temperature around the lake averaged 14.3°C between 1961 and 2000, whereas mean monthly summer and winter temperatures were 26.1°C and 3.7°C, respectively (Katsavouni and Petkovski, 2004).

8.2 Uranium isotopes as proxy for soil erosion

During chemical weathering, ^{234}U is preferentially lost from minerals compared to ^{238}U, as a result of recoil and preferential leaching (Dosseto, 2015). This depletion continues over time since the onset of weathering (*weathering age*; (Dosseto et al., 2014)), resulting in decreasing $\delta^{234}U$ values ($\delta^{234}U = (\lambda_{234}.N_{234}/\lambda_{238}.N_{238} - 1) \times 1000$; unit: parts per thousand, ‰. λ and N are the decay constant (in yr^{-1}) and number of atoms for each isotope, respectively; and subscripts 234 and 238 refer to ^{234}U and ^{238}U, respectively). In fine-grained soil/sediment, ^{234}U is lost at the mineral surface such that $^{234}U/^{238}U$ decreases over time. In weathering profiles, as the weathering front moves downward, soil age is

expected to increase with decreasing depth and as a result $\delta^{234}U$ values become more negative (Figure 116).

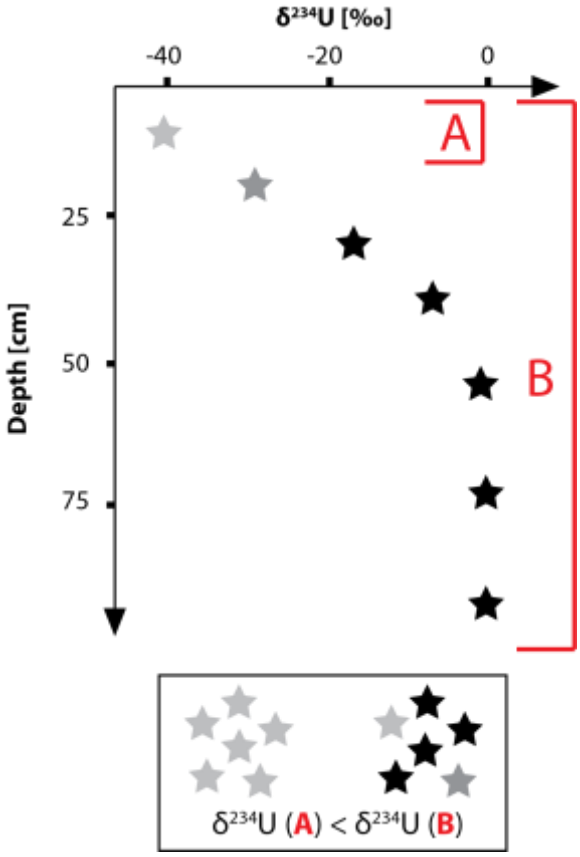

Figure 116: Conceptual representation of U isotope compositions in soil profiles. Deep soil horizons have $\delta^{234}U$ values close to secular equilibrium i.e. 0 ‰, whereas upper parts of a soil profile have been exposed to chemical weathering for longer, decreasing $\delta^{234}U$ values. If erosion is shallow (e.g. sediment A) and only the top soil is removed, sediments will exhibit a lower $\delta^{234}U$ than if erosion is deep and deeper soil material is mobilised (e.g. sediment B).

Decreasing $\delta^{234}U$ values with decreasing soil depth have been observed in the top meter of weathering profiles developed in temperate climate over a range of lithologies, from shale to granodiorite (Figure 117).

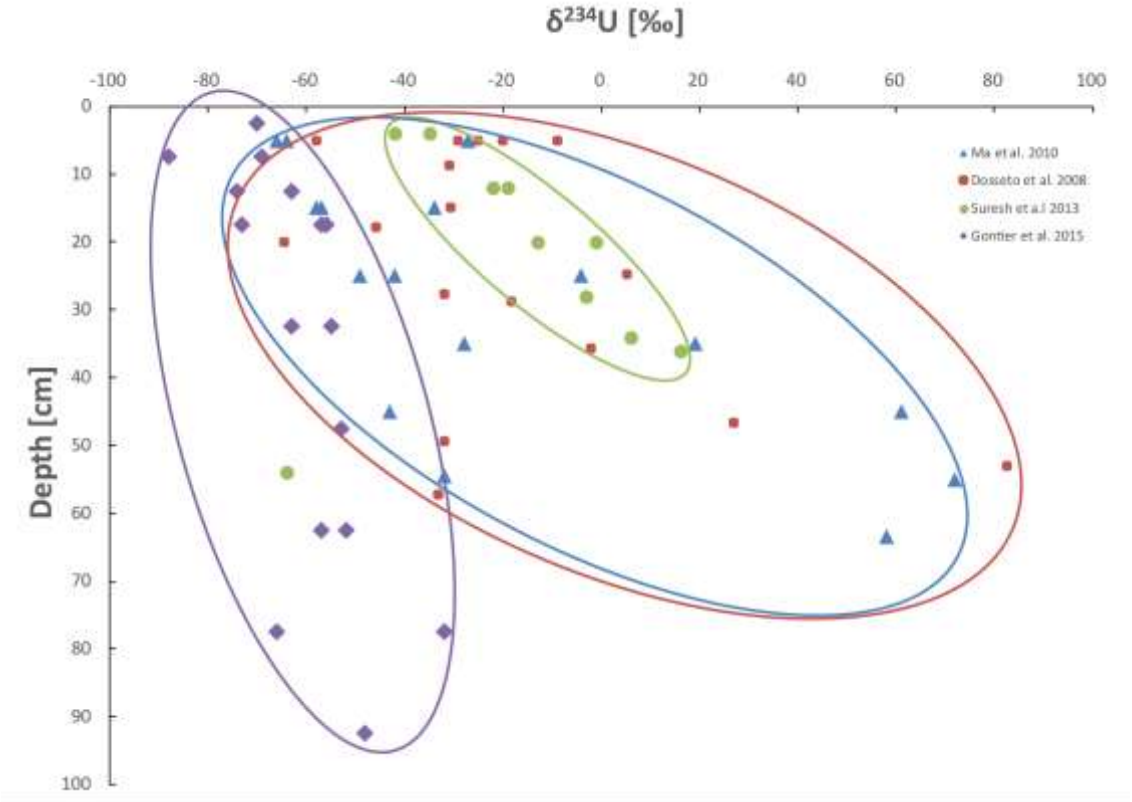

Figure 117: U isotope ratios (in ‰) as a function of depth (cm) in selected soil profiles from the literature (Dosseto et al., 2008; Ma et al., 2010; Suresh et al., 2013; Gontier et al., 2015), illustrating how $\delta^{234}U$ values decrease with soil depth.

Therefore, during shallow erosion, as only the top soil horizon is being mobilised, sediments are expected to display negative $\delta^{234}U$ values. In contrast, if erosion mobilises deeper parts of the soil profile, the resulting sediments are to display higher $\delta^{234}U$ values. Thus, in sedimentary records (e.g. lakes), the $\delta^{234}U$ values of the sediment could be used as a proxy for changes in soil erosion at the catchment scale.

8.3 Lithium isotopes as proxy for soil development

Li isotopes (^{7}Li and ^{6}Li) fractionate during clay formation, whereby ^{6}Li is preferentially enriched in clay minerals compared to ^{7}Li (Pistiner and Henderson, 2003; Vigier et al., 2008). Iron oxides show similar behaviour retaining ^{6}Li, however Li is generally depleted and therefore the Li contribution of Fe oxides to the overall Li pool in the analysed sediment is negligible (Verney-Carron et al., 2011). The Li isotope composition of weathering products, such as clays, therefore reflects weathering conditions shortly before the time of deposition. Clays usually have a $\delta^{7}Li$ composition lower than parent material, whereby $\delta^{7}Li = (^{7}Li/^{6}Li_{sample} / {}^{7}Li/^{6}Li_{L\text{-}SVEC} - 1) \times 1000$ (unit: parts per thousand,

‰). Experiments have shown that rock or mineral dissolution does not fractionate Li isotopes (Verney-Carron et al., 2011).

Sediments analysed in this study consist of a mixture between secondary phases and primary minerals. As soils develop, more clays, enriched in Li with relatively low δ^7Li values, are expected to be present in the sediment mixture. In turn, this drives the Li isotope ratio of the sediment to lower values. In a recent study, Dellinger et al. (2017) found a negative relationship between the Li isotope ratio of fine river sediments and the weathering intensity (ratio between silicate weathering rate and total denudation rate). They show that δ^7Li values of sediments are more negative for high weathering intensities. Therefore, the δ^7Li composition of sedimentary deposits could reflect changes in soil development at a given catchment over time. For large catchments with a mixed lithology, the Li isotope composition of sediments may vary depending on the δ^7Li composition of the source rock (Dellinger et al., 2017). In this study, considering the small catchment area of Lake Dojran (275 km^2) and the limited sediment pathways into the lake (Figure 115), it can be assumed that bedrock variability does not have a major influence on δ^7Li values of the lake sediments. Thus, in this context, the δ^7Li composition of the sedimentary record can be used to reconstruct palaeo-variations in soil development at the time of deposition. A conceptual illustration of the Li isotope behaviour during soil development is shown in Figure 118.

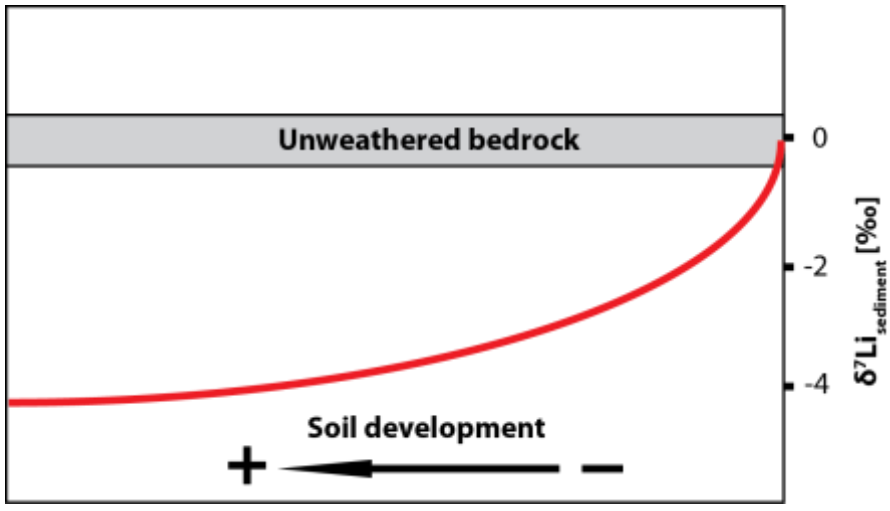

Figure 118: Conceptual representation of the evolution of Li isotope composition in sediments (red curve) as a result of increasing clay neo-formation and soil development. Sediments, i.e. a mixture of primary and secondary phases, exhibit low δ^7Li values where clays are more abundant relative to primary minerals. In contrast, sediments recording

more positive δ^7Li values are likely to consist dominantly of primary phases, as a result of little clay neo-formation.

In weathering profiles where primary minerals are continuously weathered into clays, soils are increasingly enriched in ^{6}Li, preferentially retained in clays over ^{7}Li. Thus, decreasing δ^7Li values reflect increasing clay formation, which can be used as a proxy for the extent of soil development (Figure 118) (Rudnick et al., 2004). Unlike U isotopes, the Li isotope composition is not expected to vary with soil depth (Rudnick et al., 2004; Lemarchand et al., 2010), because clay formation occurs pervasively through the weathering profile and is sensitive to hydrological conditions such as the depth of the water table (Rudnick et al., 2004). Recently, Dellinger et al. (2017) have shown that the Li isotope composition of river sediments inversely correlates with weathering intensity. This suggests that the δ^7Li composition of sediments records the conditions of soil development at the catchment scale. Thus, in this context, the measurement of Li and U isotopes in sedimentary archives such as lake sediments should allow us to determine how soil erosion and development have responded to climatic and/or anthropogenic perturbations over time.

8.4 Results

The δ^{234}U values of sediments from the Lake Dojran sediment record range from -42.3 ± 1.7 ‰ to 3.7 ± 1.7 ‰ with values increasing between 12,300 and 9,000 cal yr BP, followed by a rapid decrease to -39 ‰ at 8,100 cal yr BP (Table 21).

Table 21: Li and U isotope compositions in lake sediments.

Sample name	Depth (cm)	Age (cal yr BP)	δ^7Li (‰)	δ^{234}U (‰)
Dojran 1	1	0	-0.2	0
Dojran 65	73.3	500	0.1	-18
Dojran 94	131.3	1030	0.6	-12
Dojran 121	185.3	1610	-0.1	-5
Dojran 154	251.3	2550	0.3	-3
Dojran 159	261.3	2720	-0.6	-6
Dojran 163	269.3	2840	-1.0	-18
Dojran 189	278.9	3070	-1.9	-33

Dojran 199	298.9	3530	-2.8	-42
Dojran 204	308.9	3810	-2.4	-31
Dojran 208	316.9	4060	-2.6	-25
Dojran 215	330.9	4570	-2.0	-15
Dojran 223	346.9	5330	-1.7	-2
Dojran 229	358.9	6060	-1.9	-16
Dojran 229 replicate			-1.4	
Dojran 237	374.9	7070	-1.6	-24
Dojran 243	386.9	7690	-1.1	-18
Dojran 248	396.9	8110	-1.6	-39
Dojran 248 replicate			-1.6	
Dojran 255	410.9	8590	-0.6	-2
Dojran 261	422.9	8940	-0.8	4
Dojran 266	432.9	9190	-1.1	-16
Dojran 278	456.9	9700	-0.5	-11
Dojran 290	480.9	10120	-0.7	-22
Dojran 307	514.9	10620	0.4	-26
Dojran 348	546.9	11020	0.6	-26
Dojran 376	602.9	11610	0.3	-19
Dojran 460	682.1	12280	-0.2	-34

External uncertainty is 1.8 and 0.5 ‰ for $\delta^{234}U$ and $\delta^{7}Li$ values, respectively.

This decline is followed by a return to higher values until 5,300 cal yr BP when another negative trend occurs, reaching a minimum at 3,500 cal yr BP. Between 3,500 and 2,700 cal yr BP, values start increasing rapidly to culminate at 2,500 cal yr BP and then remain high throughout the Late Holocene except for a small negative excursion at 500 cal yr BP. Li isotope compositions decrease almost continuously between 12,300 and 3,500 cal yr BP, with δ^{7}Li values varying between -2.8 ± 0.4 ‰ to 0.6 ± 0.4 ‰. As with U isotope variations, δ^{7}Li values increase sharply between 3,500 and 2,500 cal yr BP and remain high for the remainder of the Late Holocene (Table 21).

The mean grain size shows large variability since 12,300 cal yr BP. Highest values are observed at 12,300 cal yr BP, 6,000 cal yr BP, and at present. The lowest mean grain size

distribution was recorded at 2,700 cal yr BP. K/Ti (an index for weathering reactions) shows an overall decrease since 11,000 cal yr BP, reaching a minimum beween 5,300 cal yr BP 4,000 cal yr BP. K/Ti ratios increase at 3,800 cal yr BP and stay high until present (Table 22).

Table 22: Grain size data and sediment K/Ti ratios of lake sediments. Sample depth is the mean over 2 cm thick sediment layers.

Sample name	Depth (cm)	Age (cal yr BP)	Mean grain size (µm)	K/Ti
Dojran 1	1	0	24	5.2
Dojran 65	73.3	500	18	5.2
Dojran 94	131.3	1030	18	4.9
Dojran 121	185.3	1610	16	5.6
Dojran 154	251.3	2550	16	4.9
Dojran 159	261.3	2720	15	4.8
Dojran 163	267.3	2840	18	4.7
Dojran 189	278.9	3070	19	4.4
Dojran 199	298.9	3530	19	5.6
Dojran 204	308.9	3810	18	4.4
Dojran 208	316.9	4060	22	3.9
Dojran 215	330.9	4570	23	3.8
Dojran 223	346.9	5330	22	3.7
Dojran 229	358.9	6060	24	3.9
Dojran 237	374.9	7070	20	4.0
Dojran 243	386.9	7690	21	4.2
Dojran 248	396.9	8110	20	4.6
Dojran 255	410.9	8590	19	4.3
Dojran 261	422.9	8940	21	4.1
Dojran 266	432.9	9190	17	4.6
Dojran 278	456.9	9700	19	4.7
Dojran 290	480.9	10120	21	4.6
Dojran 307	514.9	10620	22	5.1
Dojran 348	546.9	11020	19	5.6

Dojran 376	602.9	11610	17	6.0
Dojran 460	682.1	12280	23	4.4

Deposition ages were determined using radiocarbon. Uncertainty levels are in detail discussed in Francke et al. 2013 (Francke et al., 2013). External uncertainty for K/Ti ratios is 0.6, calculated from two replicate samples. Error on mean grain size data has not been determined.

Li isotope compositions of stream sediments show a large range of δ^7Li values: -4.8 to 0.8 ‰. The most positive δ^7Li value was measured in stream sample #22, which was analysed twice as a replicate (Table 23).

Table 23: Li isotope compositions of stream sediments.

Sample name	δ^7Li (‰)
Dojran stream #1	-0.4
Dojran stream #7	-0.7
Dojran stream #8	-1.4
Dojran stream #9	-4.1
Dojran stream #12	-4.8
Dojran stream #15	-4.4
Dojran stream #18	-0.0
Dojran stream #19	-0.3
Dojran stream #22	0.8
Dojran stream #22 replicate	0.5
Dojran stream #35	-0.4

External uncertainty of δ^7Li values is 0.5 ‰.

The Li isotope composition of hand-picked biotite grains was determined on two samples, derived from stream sample #22 (Table 23). The δ^7Li value varied from 2.0 and 2.4 ‰, with an external uncertainty (2SE) of 0.5 ‰.

The U isotope composition of the different bedrock units at Lake Dojran catchment show δ^{234}U values of -167 to 84 ‰ (Table 24).

Table 24: U isotope compositions of bedrock samples.

Sample name	δ^{234}U (‰)	Rock type
Lithology 1	-167	Gneiss
Lithology 2	-13	Phyllite
Lithology 3	-25	Greenschist
Lithology 4	55	Marble
Lithology 5	-58	Phyllite
Lithology 6	67	Volcanoclastic sedimentary rock
Lithology 7	-5	Peridotite
Lithology 8	84	Gneiss
Lithology 9	-40	Granite

Lithology 10	-8	Gneiss
Lithology 11	7	Gabbro

External uncertainty is 1.8 ‰ for $\delta^{234}U$ values.

Major minerals in the core sediments are calcite, quartz, muscovite, biotite and chlorite (Table 25).

Table 25: Mineralogy of lake sediments.

Sample name	Depth (cm)	Age (cal yr BP)	Augite (%)	Biotite (%)	Calcite (%)	Chlorite (%)	Dolomite (%)	Epidote (%)	Forsterite (%)	Muscovite (%)	Orthoclase (%)	Quartz (%)	Talc (%)
Dojran 1	1	0	3.7	13.6	5.4	7.9	0.3	0.3	0	40.3	11.3	13.2	3.9
Dojran 65	73.3	500	10.1	17.9	5.6	9	2.7	2.4	1.7	28.1	8.4	14.1	0.1
Dojran 94	131.3	1030	22.6	11.1	11.9	10.5	0.7	5.7	10.4	9.5	2.4	9.4	5.7
Dojran 121	185.3	1610	14.5	13.8	7.4	11.1	2.9	4.1	0	23.3	8.3	11.2	3.4
Dojran 154	251.3	2550	12	15.6	2.4	10.5	2.3	2.9	0	31.2	7.6	15.3	0.1
Dojran 159	261.3	2720	4.8	13.5	3	11.9	0.8	1	0	42.3	6.3	16.3	0
Dojran 163	267.3	2840	3.9	11.8	6	8.5	0.6	1.9	0	39.4	6.3	21.5	0
Dojran 189	278.9	3070	1.1	9.3	22.7	9.2	1.7	5	3.1	23.8	11.6	11.3	1.2
Dojran 199	298.9	3530	8.7	5.5	33.1	7.5	2.5	7.9	3	11.4	5	11.5	3.8
Dojran 204	308.9	3810	0	9.4	30.9	7.3	0	0	0	32.9	5.1	14.2	0
Dojran 208	316.9	4060	10.9	7	37.5	9.9	2.2	4.8	2.6	11.5	1.9	6.3	5.4
Dojran 215	330.9	4570	13.1	8.1	43.6	7.1	0.7	2.2	2.7	11.4	3.7	7.2	0.3
Dojran 223	346.9	5330	1.6	5	54.8	4.9	0.4	2.7	0	13.4	7	9.8	0.4
Dojran 229	358.9	6060	5.6	9.8	30.3	6.1	2	8.6	1.9	28.1	5.5	2.1	0.1
Dojran 237	374.9	7070	5.2	10.1	34.1	9.9	3.3	9.7	5.1	15.6	2.3	4.6	0.1
Dojran 243	386.9	7690	2.3	8.6	31.4	5.8	0	0	0	30.4	9.1	12.5	0
Dojran 248	396.9	8110	20.8	13.2	16.7	10.5	0.6	6.8	5.5	9	2.4	6.9	7.6
Dojran 255	410.9	8590	1.8	7.7	50.8	5.2	0.3	1.4	0.7	19	4.6	8.4	0.2

Dojran 261	422.9	8940	1.8	4.8	48.7	3.7	0.5	1.9	0	15.2	2.2	21.1	0
Dojran 266	432.9	9190	0.3	7.3	45.6	6.3	0.9	3.5	1.8	16.6	9.3	5.4	3
Dojran 278	456.9	9700	1.2	10.6	35.5	5.8	0.6	0	0	25.3	6.6	14.4	0
Dojran 290	480.9	10120	0	10.3	37.1	4.5	1.6	3.1	0	23.8	5.4	11.2	3
Dojran 307	514.9	10620	0	15.9	22.4	6.7	0.2	0	0	38.6	6	10.3	0
Dojran 348	546.9	11020	12.5	12.9	19.7	10	1.3	1.8	2.4	19.9	7.1	12.3	0.1
Dojran 376	602.9	11610	8.9	8.6	20.2	6.6	0.8	7.4	2.7	15.1	15.3	10.5	3.9
Dojran 460	682.1	12280	6.7	14	14	13.7	2	6.6	0	23.2	4.4	14.2	1

Relative errors on mineral contents are less than 5% (2σ).

8.5 Discussion

8.5.1 Sediment sources in the Lake Dojran catchment

To verify that the observed Holocene variations in both Li and U isotope proxies are not simply a function of varying sediment provenance, the present sediment sources of the lake, as well as the surrounding bedrock lithology were investigated. Lake Dojran is mostly fed by streams originating in the north-east east (NE-E) part of the catchment and transit through a small alluvial plain before reaching the lake (Figure 119). Streams in the northern, western and southwestern part of the catchment are ephemeral and have a low sediment transport capacity, therefore contribute little sediment to the lake. The only outlet is at the southeastern end of the lake and used to connect Lake Dojran with the Axios/Vardar River. Today this outlet is located several meters above lake level. Water loss is therefore only through evaporation and possibly groundwater outflow (Francke et al., 2013). Sediments were collected from streams feeding into Lake Dojran and analysed for Li isotopes; bedrock samples were collected from outcrops across the catchment and analysed for U isotopes. Stream sediments δ^7Li values range from -4.8 to +0.8 ‰. Streams with the most negative values are located in the western part of the catchment (Figure 119).

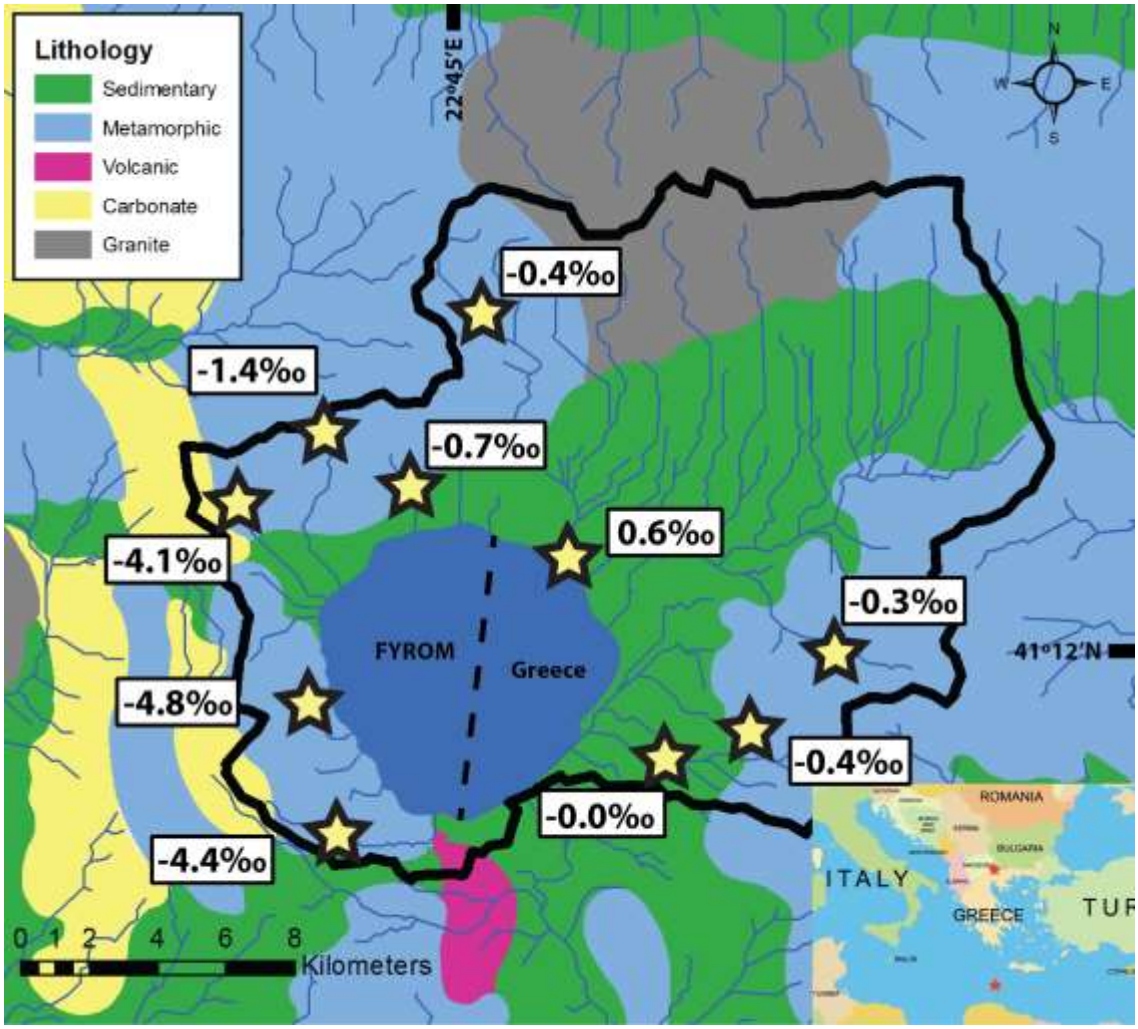

Figure 119: Simplified distribution of geological units for Lake Dojran catchment based on field mapping by A.F. and from ref. (Ivanovski, 1970; Andronopoulos, 1990). Individual lithology areas were estimated and manually drawn by L.R. This map was created with ArcGIS Desktop Advanced 10.4 software (https://esriaustralia.com.au/arcgis-desktop). Stars represent stream sample locations. Displayed values are δ^7Li compositions of stream sediments. External uncertainty of δ^7Li measurements is 0.5 ‰. A replicate was done for sample #22 for which the average δ^7Li value is displayed (0.6 ‰ n=2).

The Li isotope composition of lake sediments could potentially be controlled by changes in sediment provenance if, for instance, there was an increase contribution from western streams. However, the drainage area and channel length of these streams are small compared to those in the E-NE. Furthermore, western streams have narrow and shallow channels (<1 m^2) indicating a small sediment transport capacity. Consequently, these streams should have a very small contribution to the sediment budget of the lake.

Sediments are more likely to be derived from eastern and north-eastern streams. There, δ^7Li compositions are close to 0 ‰, similarly to the composition of the youngest lake sediments. Thus, sediment provenance alone cannot account for variations in δ^7Li compositions in lake sediments. Similarly, a change in the location of human activity around 3,500 cal yr BP from the western to the eastern parts of the catchment could not account for the increase in δ^7Li compositions in lake sediments, because of the minor role of western streams on the lake sediment budget.

Eleven bedrock samples were collected from outcrops around the catchment and measured for U isotope ratios (Figure 120).

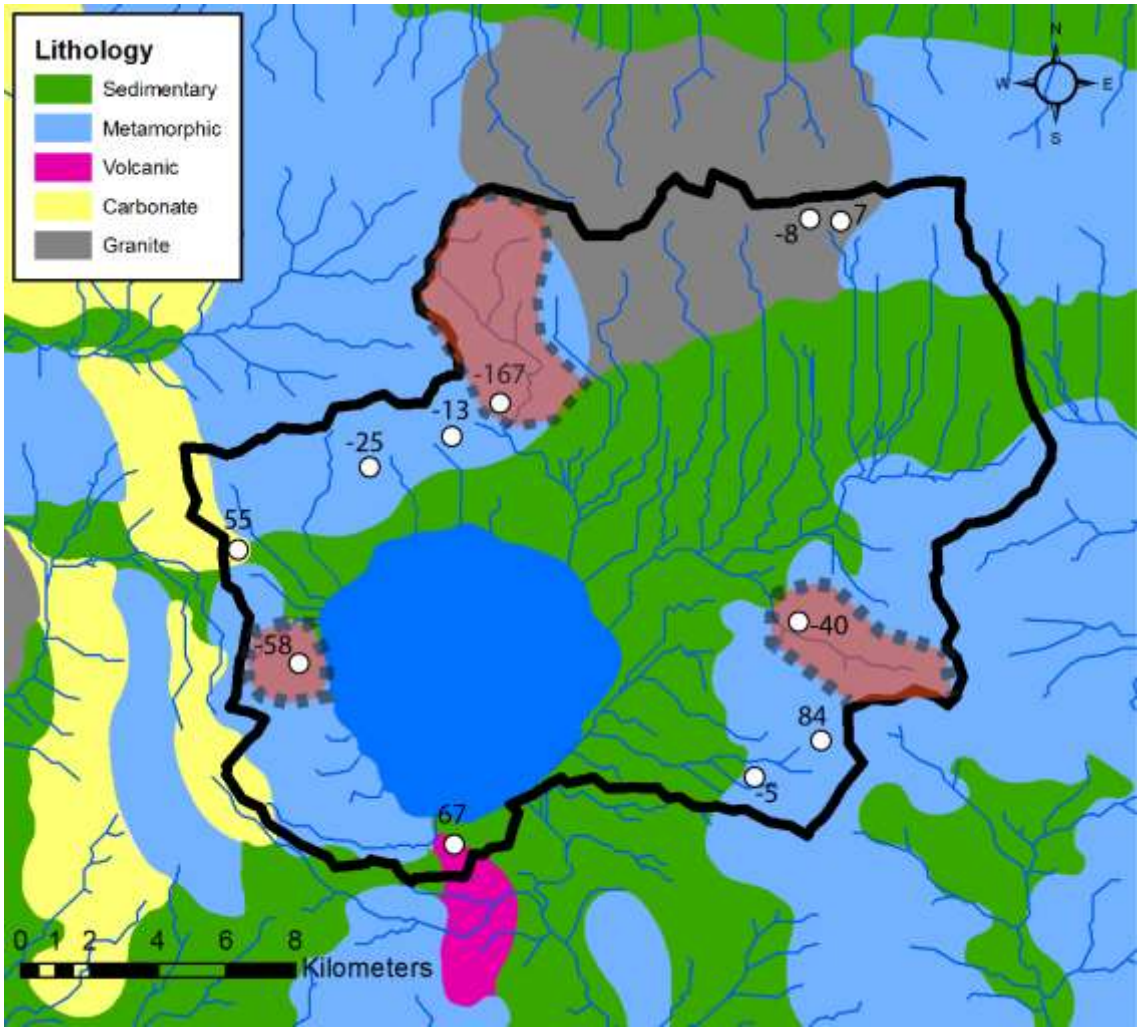

Figure 120: Simplified distribution of geological units for Lake Dojran catchment based on field mapping by A.F. and data from ref.(Ivanovski, 1970; Andronopoulos, 1990). This map was created with ArcGIS Desktop Advanced 10.4 software (https://esriaustralia.com.au/arcgis-desktop). White circles represent locations of

bedrock samples. Values are $\delta^{234}U$. Areas highlighted in red with dashed borders represent proposed areas that would need to be preferentially eroded to explain negative $\delta^{234}U$ excursions in the sediment record by a change in sediment provenance solely. External uncertainty for $\delta^{234}U$ values is 1.8 ‰.

Three samples (highlighted as red shaded areas) show $\delta^{234}U$ compositions lower than the lowest values observed in lake sediments. Thus, it could be tempting to explain negative $\delta^{234}U$ excursions in the lake sediment record by a greater contribution of sediments from areas draining these lithologies. However, the morphology of the streams draining these areas suggests that they would deliver only a small flux of sediments to the lake. Furthermore, because streams from these areas show overall low $\delta^{7}Li$ values, if these regions dominated for some reason the sediment budget, this would possibly result in low $\delta^{7}Li$ in lake sediments at the same time as low $\delta^{234}U$ values are observed. This is not the case. Nevertheless, the areas delimited in Figure 120 are restricted by the small number of bedrock samples, which does not allow a rigorous assessment of the variability of U isotope compositions to be conducted.

8.5.2 Post-depositional alteration

While it is possible that Li could be exchanged between sediments and lake water following deposition, it has been shown that clays release an insignificant amount of Li back into solution, which suggests a one-way transfer of Li from solution to clay (Pistiner and Henderson, 2003). Furthermore, given the relatively low Li concentration of natural waters (in the range of parts per billion; e.g. Liu et al. (2015)), compared to clays (in the range of parts per million; e.g. Dosseto et al. (2015)), post-depositional exchange of Li between clays and water is unlikely to impact the overall Li isotopic composition of sediments. Experiments have shown that for smectite, the exchangeable fraction of Li is negligible compared to structural Li (Decarreau et al., 2012). Nevertheless, in order to ensure that the exchange between clay and water represents an insignificant proportion of the sediment Li isotopic budget, we measured the Li isotope ratio of a clay sample for which two aliquots were prepared differently: one aliquot had the exchangeable Li was removed prior to analysis, while the exchangeable Li was not removed in the other aliquot. In each case, no pre-treatment for carbonate was performed as this mineral was not detected in the sample. Organic matter was removed using H_2O_2 before the experiment. The first aliquot was treated for one hour at room temperature with 8mL 1M

NH_4Cl for ~15 mg of sample (Tessier et al., 1979). The sample was then washed for 5 minutes with 18.2 MΩ water and processed for Li isotope analysis as described above. The aliquot where the exchangeable Li was removed (Clay_1_leached), yielded a δ^7Li value of -0.4 ± 0.2 ‰ (2σ). This is slightly higher than the δ^7Li value measured in the aliquot where the exchangeable Li was not removed (Clay_1): - 1.0 ± 0.2 ‰ (2σ). The experiment was repeated for another sample, and the δ^7Li value of the aliquot where the exchangeable Li was removed (Clay_2_leached), was -0.1 ± 0.2 ‰ (2σ). This is within error compared to the δ^7Li composition of the aliquot were the exchangeable Li was not removed (Clay_2): -0.40 ± 0.3 ‰ (2σ). These results suggest that the exchangeable Li plays a minor role on the sediment Li budget. Thus, post-depositional alteration is unlikely to significantly affect the Li isotope compositions of lake sediments, which is likely to record environmental conditions prior to deposition. Similarly, the pool of exchangeable U is negligible (Plater et al., 1992) thus any water-sediment interaction post-deposition would be unlikely to affect the $\delta^{234}U$ compositions.

The presence of authigenic carbonates within the lake could also contribute to the Li isotopic composition of sediment. They generally form in equilibrium with the lake water, which typically shows relatively positive δ^7Li values. However, carbonates are particularly depleted in Li (Li concentrations typically <1 ppm; (Burton and Vigier, 2012)), therefore their contribution to the isotopic composition of the sediment is likely to be negligible. Another possible process affecting δ^7Li values post deposition is mineral phase transformation: illitisation of smectites. Experiments have shown that Li isotope fractionation may occur during illitisation, where products are isotopically lighter (Williams and Hervig, 2005). If this were the case in our study, the δ^7Li composition of sediments would decline with increasing illitisation. So far, post-depositional illitisation of smectites has only been observed for lake deposits in highly saline environments (Singer and Stoffers, 1980). Therefore, considering the low salinity of Lake Dojran waters, this process is unlikely to take place.

8.5.3 Grain size distribution and mineralogical sorting

The mean grain size of the <63 µm fraction in the Lake Dojran sediment succession varies over the Holocene from 15 to 24 µm. From 12,300 to 6,000 cal yr BP, the mean grain size is variable and shows two minima at 11,600 and 9,200 cal yr BP. From 6,000 to 2,700 cal yr BP, values decrease followed by a gradual increase after 2,700 cal yr BP (Figure 121). Grain size distribution at the coring location is mainly affected by the size of Lake

Dojran, i.e. by a combination of wave action, lake-internal current systems, and the shoreline distance. The Li isotope data show no correlation with mean grain size of the sediment core succession (not shown). Similarly, the U isotope data do not significantly correlate with mean grain size (R^2 = 0.0094). Therefore, it can be concluded that hydrodynamic sorting does not play a role in Li and U isotope compositions of lake sediments.

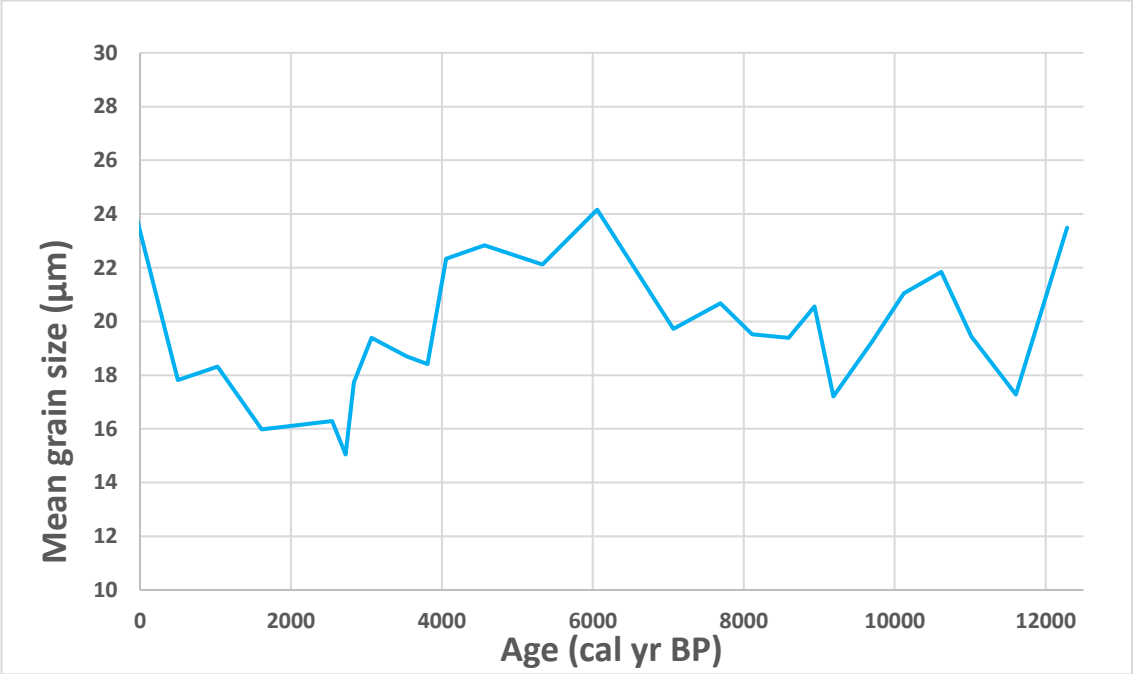

Figure 121: Mean grain size of Lake sediments (in µm) as a function of the deposition age (in cal yr BP).

Isotopic variations could also potentially be explained by variable mineral sorting over time, although small lake sediments are considerably less affected by these processes compared to deltaic sediments of large river basin. Major minerals in the core sediments are calcite, quartz, muscovite, biotite and chlorite. Between 12,000 and 3,000 cal yr BP, while calcite was a major phase, it almost completely disappeared after 3,000 cal yr BP (Figure 122). This is mainly the result of mutual dilution with clastic matter, caused by an increase in sediment flux. Other mineral phases show no obvious systematic changes. Considering the mineralogical composition of Lake Dojran sediments (Figure 122), biotite is likely to dominate the Li and U budgets. No relationship is observed between $\delta^{234}U$ values and biotite (or any other mineral) content (not shown), suggesting that

variable mineral content is not responsible for the observed $\delta^{234}U$ variations. Li isotope compositions show a broad positive relationship with biotite content (Figure 123).

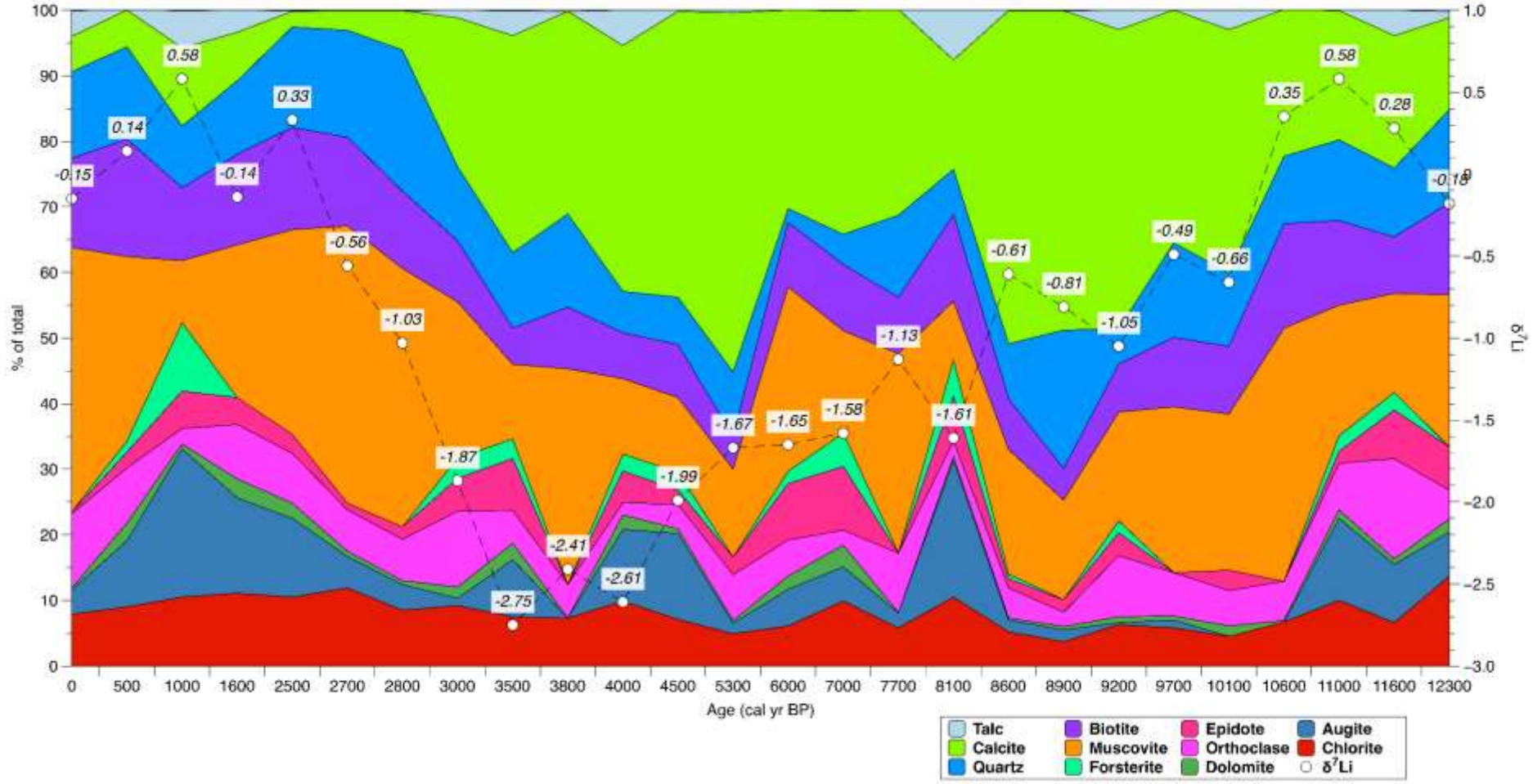

Figure 122: Cumulative mineralogical distribution (in wt %) in lake sediments as a function of depositional ages (in cal yr BP). Open circles: Li isotope compositions (right Y-axis) of lake sediments with an error of 0.5 ‰ (2SE

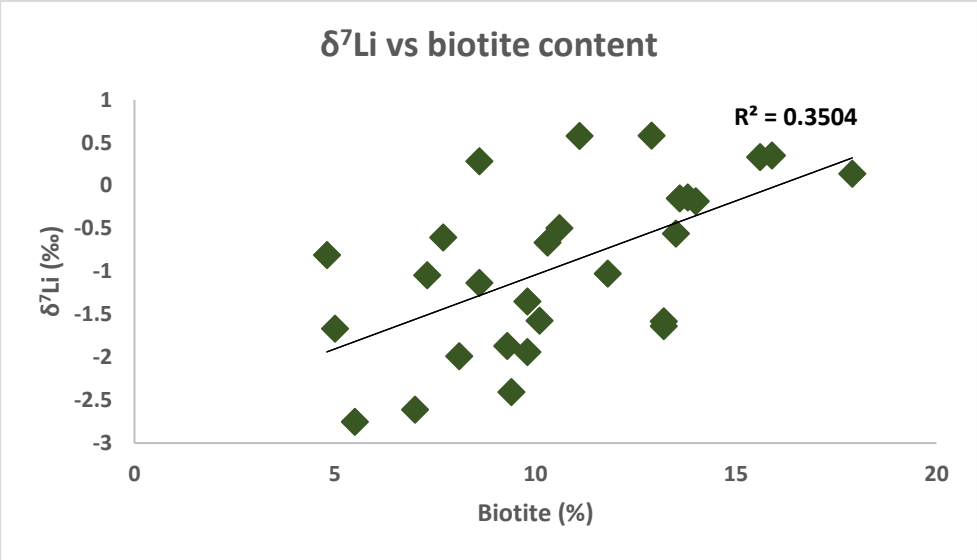

Figure 123: Li isotope ratios in lake sediments (in ‰) as a function of biotite content (in wt %).

This could suggest that higher δ^7Li values are explained by the higher abundance of biotite. This is confirmed by analysis of handpicked biotite grains from stream sediments, which display an average δ^7Li value of ~2.2 ± 0.2 ‰ (n=2). The role of biotite on the Li isotope composition of sediments is in agreement with Li isotopes recording the extent of soil development: poor soil development yields sediments enriched in primary minerals such as biotite, which then dominates the Li isotope composition of the sediment. More thorough soil development yields sediments enriched in secondary minerals such as clays, which dominate the δ^7Li composition of sediments with low values. Another possible contribution to the observed δ^7Li composition is the formation of Fe-Mn oxyhydroxides. Similarly to clay minerals, Fe-Mn oxyhydroxides formed during weathering at low temperatures preferentially take up ^{6}Li and an enrichment in Fe-Mn oxyhydroxides could therefore drive the Li isotope composition of a sediment mixture towards low δ^7Li values (Millot et al., 2010). Hence, negative δ^7Li values of sediments could reflect a combination of clay neo-formation and Fe-Mn oxide precipitation, both indicative of increasing soil formation. When comparing the Li isotope data with other weathering indices such as K/Ti, we observe a relatively good correlation (Figure 124, Figure 125).

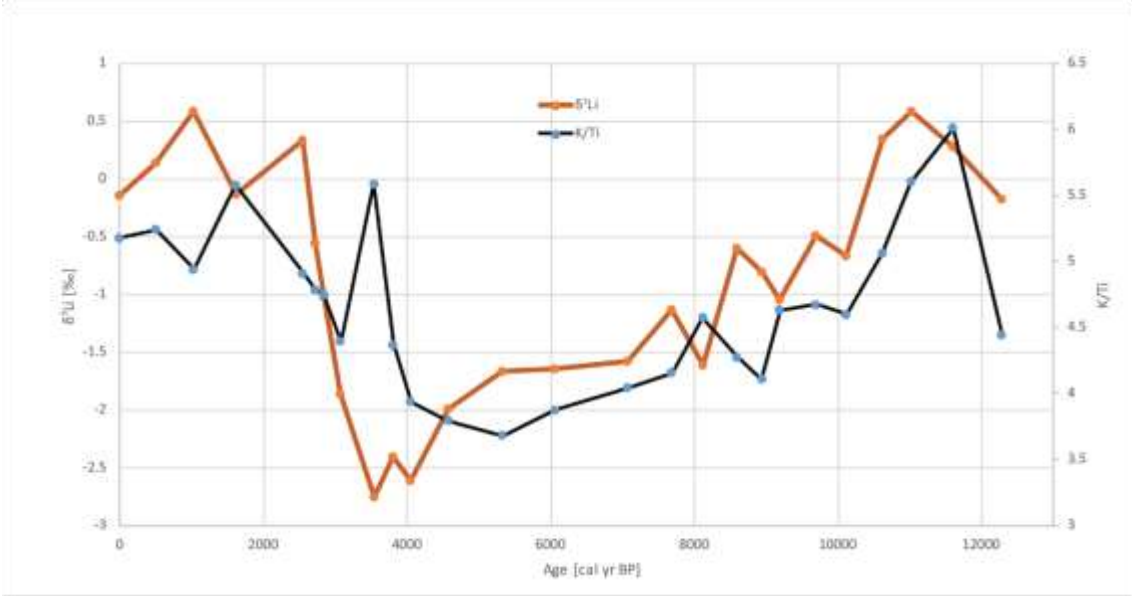

Figure 124: Li isotope compositions (in ‰, red line) and K/Ti ratios (unit less, black line) of lake sediments as a function of deposition age (in cal. yr BP). Both proxies indicate increasing chemical weathering associated with soil development until human impact ~3,000 cal. yr BP.

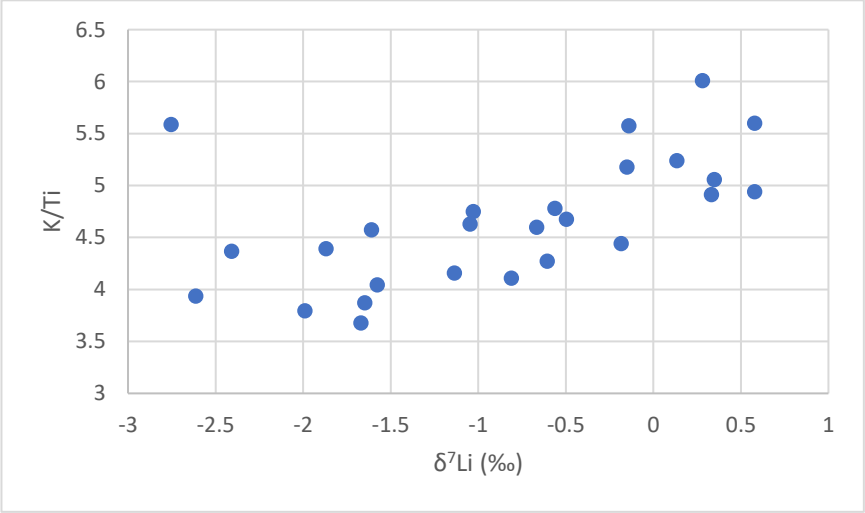

Figure 125: K/Ti ratios (unit less) as a function of δ^7Li compositions (in ‰) of lake sediments. The positive correlation between δ^7Li values and K/Ti ratios indicates that Li isotopes fractionate in concert with chemical weathering reactions. External uncertainty of δ^7Li values is 0.5 ‰.

Potassium is mobile during weathering, while titanium is in most cases immobile. In a sediment mixture of silt and clay, K/Ti ratios may be interpreted as i) reflecting chemical weathering reactions, where K is leached from soils or ii) being controlled by potassium-rich phases such as biotite. In both scenarios, low K/Ti ratios reflect increased chemical weathering and soil development. The sample at ~3,500 cal yr BP that shows an increase in K/Ti is most likely an outlier as it neither follows the general trend of K/Ti over time, nor does it correlate with other proxies such as Li isotopes.

8.5.4 Soil response to natural climate variations

Low $\delta^{234}U$ values are observed during the Younger Dryas (12,300 – 11,700 cal yr BP) and at around 8,100 and 4,000 cal yr BP. On the other hand, $\delta^{234}U$ displays high values during the Early Holocene (11,700 – 8,200 cal yr BP), Mid Holocene (4,200 – 7,800 cal yr BP) and Late Holocene (2,500 cal yr BP – present). This pattern co-varies with climate variability in the Eastern Mediterranean Region over the past 12,300 yr. Several archives show overall higher temperatures and humidity during the Holocene compared to the Late Glacial period, but with short-lived cool/dry events at 8,200 and 4,200 cal yr BP (Mayewski et al., 2004; Drysdale et al., 2006; Magny et al., 2009; Pross et al., 2009; Panagiotopoulos et al., 2013). This is consistent with variations in $CaCO_3$ concentrations in Lake Dojran sediments (Francke et al., 2013), used as a proxy for primary productivity (Figure 126).

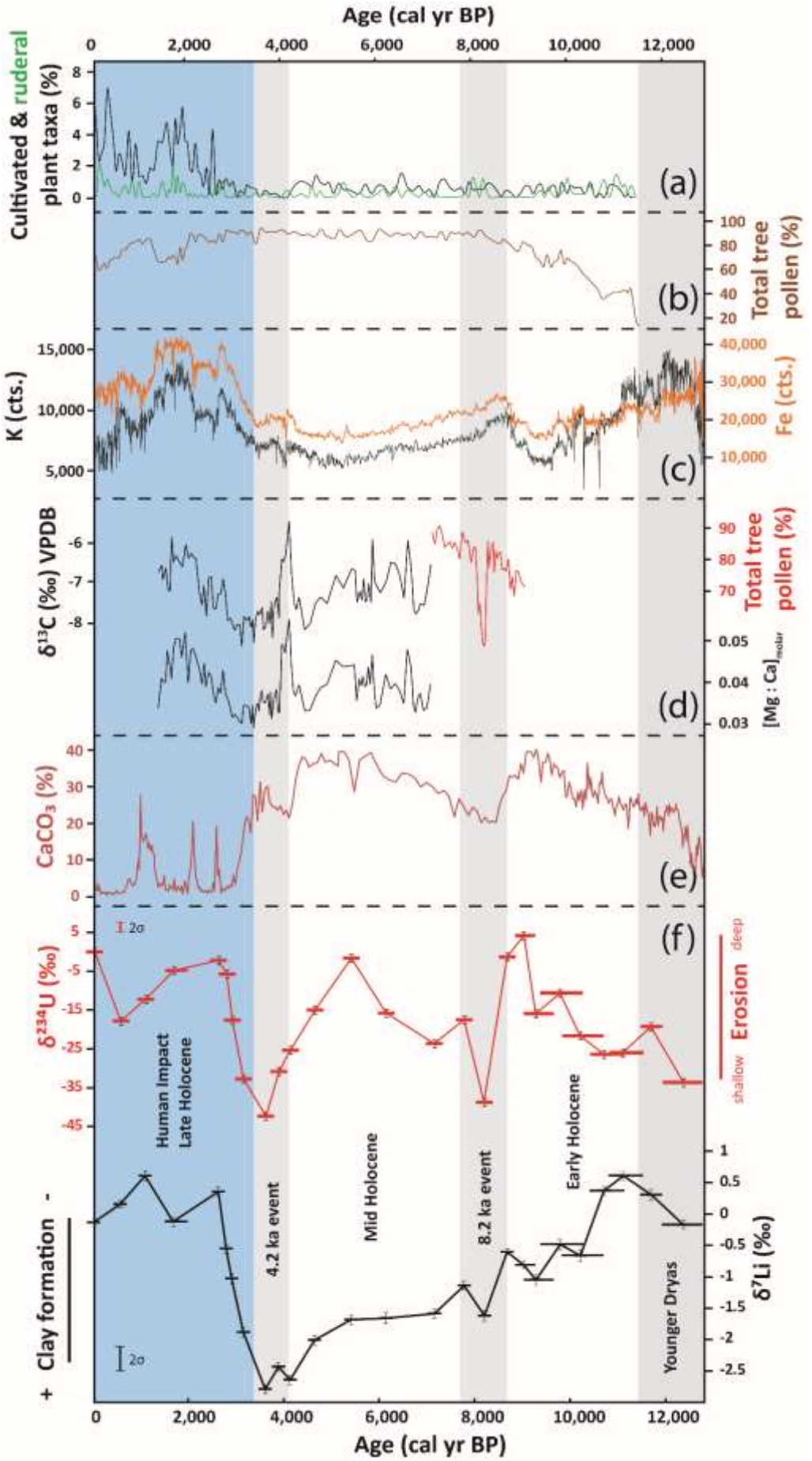
Age (cal yr BP)
0
2,000
4,000
6,000
8,000
10,000
12,000
Cultivated & ruderal plant taxa (%)
(a)
Total tree pollen (%)
(b)
K (cts.)
Fe (cts.)
(c)
δ13C (‰) VPDB
Total tree pollen (%)
[Mg : Ca]molar
(d)
CaCO3 (%)
(e)
δ234U (‰)
2σ
(f)
Erosion
shallow
deep
Human Impact
Late Holocene
4.2 ka event
Mid Holocene
8.2 ka event
Early Holocene
Younger Dryas
+ Clay formation -
δ7Li (‰)
2σ
Age (cal yr BP)

Figure 126: (a) Cultivated and ruderal plant taxa in % in Lake Dojran sediment succession. Data from (Thienemann et al., 2017). (b) Total tree pollen in Lake Dojran sediment succession. Data from (Thienemann et al., 2017). (c) K and Fe concentrations acquired by X-ray Fluorescence (XRF) scan using an ITRAX core scanner (Cox Analytical Systems, Sweden). Measured counts are a semi-quantitative estimate of the relative concentration. Data from (Francke et al., 2013). (d) Palaeo-climate proxies illustrating short-lived cold/dry events at 8.2 and 4.2 kyr BP: pollen data from N Greece (red curve (Pross et al., 2009)), carbon isotope values ($\delta^{13}C$) (black curve) and Mg/Ca ratios (black curve) in a flowstone from N Italy (Drysdale et al., 2006). (e) Calcium carbonate ($CaCO_3$) concentrations in the same core studied for U and Li isotopes. Data from (Francke et al., 2013). $CaCO_3$ concentrations show lake productivity, where high concentrations indicate warm temperatures and low concentrations colder temperatures. (f) Li and U isotope compositions of Holocene core sediment at Lake Dojran. Error bars are 2 standard error for both Li and U data. The external reproducibility for both $\delta^{234}U$ and $\delta^{7}Li$ values is displayed on the left side of the diagram. Error bars for deposition ages are displayed by the horizontal size of the symbol. Grey bands illustrate relatively cool and arid phases, while white bands show warm and wet phases (Drysdale et al., 2006; Pross et al., 2009; Lacey et al., 2015). The blue band shows the proposed period of anthropogenic overprint (Vogel et al., 2010; Panagiotopoulos et al., 2013; Francke et al., 2013).

High calcium carbonate concentrations during the Early- to Mid-Holocene between 11,700 and 2,500 cal yr BP indicate warm spring and summer temperatures, whereas low calcite concentrations during the Younger Dryas (13,000 and 11,700 cal yr BP) are consistent with a low primary productivity and low spring and summer temperatures. The low calcite concentrations during the Late Holocene (2,500 cal yr BP and present) are mainly a result of dilution with clastic matter, most likely caused by an increase in clastic sediment flux from the catchment. Two excursions towards low calcite concentration centred at 8,200 and 4,000 cal yr BP imply that the lake productivity decreased abruptly over a period of several hundred years. These two cold phases are commonly referred to as the *8.2* and *4.2 ka events*, which lasted for approximately 400 years (Drysdale et al., 2006; Pross et al., 2009; Lacey et al., 2015), and are associated with dry conditions at Lake Dojran (Francke et al., 2013), although not captured by the local pollen record (Thienemann et al., 2017). Independent climate data confirm the presence of these two

cool and arid phases in the Mediterranean region: tree pollen data obtained from northern Greece show an abrupt decline around 8,200 cal yr BP (Figure 126) (Pross et al., 2009). Flowstones from western Italy show a positive excursion of $\delta^{13}C$ values and Mg:Ca ratios at 4,000 cal yr BP (Figure 126), which is indicative of drier conditions (Drysdale et al., 2006).

Low $\delta^{234}U$ values during the two cold and dry periods, around 8,200 and 4,000 cal yr BP, are interpreted as reflecting shallow erosion of top soil horizons due to a decrease in annual rainfall. This contrasts with higher values during warmer and wetter periods (Early-, Mid-Holocene), when higher rainfall could have resulted in the mobilisation of deeper soil layers via gully or stream bank erosion. These results indicate that soil erosion is sensitive to abrupt climatic shifts and may respond on a relatively short timescale of 500-1,000-years.

By contrast, Li isotope values show a gradual decrease from the termination of the Younger Dryas until ~3,500 cal yr BP inclusive. This suggests a continuous production of neo-formed clays illustrating increasingly more developed soils. In this case, it seems that soil development was insensitive to shorter climatic shifts (at 8,200 and 4,200 cal yr BP). Instead, it responded steadily to the termination of the Younger Dryas, during which dry and cold conditions persisted for 1,200 years (Carlson, 2013). These results suggest that while soil erosion is sensitive to shorter climatic variations and responds over only a few hundreds of years, soil development requires longer-term climate shifts to be affected. Interestingly, even in periods where erosion was mobilising deeper soil material (high $\delta^{234}U$ values), the material exported still exhibited evidence for significant clay abundance in the deposited sediments (low $\delta^{7}Li$ values). This suggests that erosion was not deep enough to 'reset' the landscape and export poorly weathered material (i.e. thin to no soil cover).

8.5.5 Soil response to human activity

While Li and U isotopic records are decoupled for most of the past 12,300 years, both proxies show a sharp increase in $\delta^{7}Li$ and $\delta^{234}U$ values starting between 3,500 and 3,100 cal yr BP, and culminating at 2,500 cal yr BP (Figure 126). For U isotopes, this suggests a relatively rapid shift to deep sources of sediment. For Li isotopes, the increase of $\delta^{7}Li$ values indicates that sediments delivered to the lake are depleted in weathering products and are instead dominated by primary minerals. This suggests that soil cover was

diminished to the extent that sediments delivered to the lake consisted mostly of unweathered minerals derived from the bedrock. This is consistent with a sharp increase in iron and potassium concentrations in the same core from 3,500 to ~2,500 cal yr BP, interpreted as an increase in clastic flux to the lake (Figure 126). Furthermore, the sharp decrease in endogenic calcite abundance associated with an increase in primary minerals such as muscovite, biotite and augite also suggest an increase in clastic flux (Figure 122).

Along with geochemical and mineralogical data, both isotope proxies suggest unprecedented environmental changes initiated between 3,500 and 3,100 cal yr BP and peaking at 2,500 cal yr BP. Both Li and U data show that by 2,500 cal yr BP, deep erosion effectively 'reset' the landscape, exposing poorly developed soils. Biomarker records suggest a human impact/resettlement at 3,300 cal yr BP (Thienemann et al., 2017). At the same time, an increasing abundance of cultivated and ruderal plant taxa show first signs of agriculture around Lake Dojran (Figure 126) (Thienemann et al., 2017). These taxa peaked at 2,600 cal yr BP, implying a strong human impact associated with wide-spread land-use. A significant decrease in total tree pollen at 2,000 cal yr BP then indicates anthropogenic deforestation (Figure 126). These observations show that human impact at that time was so profound that it left a distinct trace in the geological record. Since 2,500 cal yr BP and the establishment of an *anthropogenic landscape*, there has been no return to the natural conditions experienced for most of Holocene. While the study area is relatively small (275 km^2) and observations may be of only local significance, the timing of the establishment of an anthropogenic landscape corresponds to the expansion of urban civilisations and the development of agricultural practises (Thienemann et al., 2017). Studies have shown that pastoralism may also play a role on soil erosion during this time period (Giguet-Covex et al., 2014; Bajard et al., 2017a). However, pollen data indicate that the most significant factor to induce the observed erosion event must have been the development of agricultural practises such as plant cultivation, and later widespread deforestation (Athanasiadis et al., 2000; Francke et al., 2013; Thienemann et al., 2017). The latter could have been triggered by the emergence of regional trade, when large amounts of high-quality Macedonian timber were required for shipbuilding and construction (Borza, 1987). Additionally, diversifying metal smelting, production of goods, heating and cooking, as well as warfare would have also caused a high demand for wood. Therefore, we suggest that the intensive large-scale land-use, first through plant cultivation at 3,300 cal yr BP and later through deforestation at 2,000 cal yr BP, is the direct cause of the observed erosion event in the Late Holocene (Figure 127).

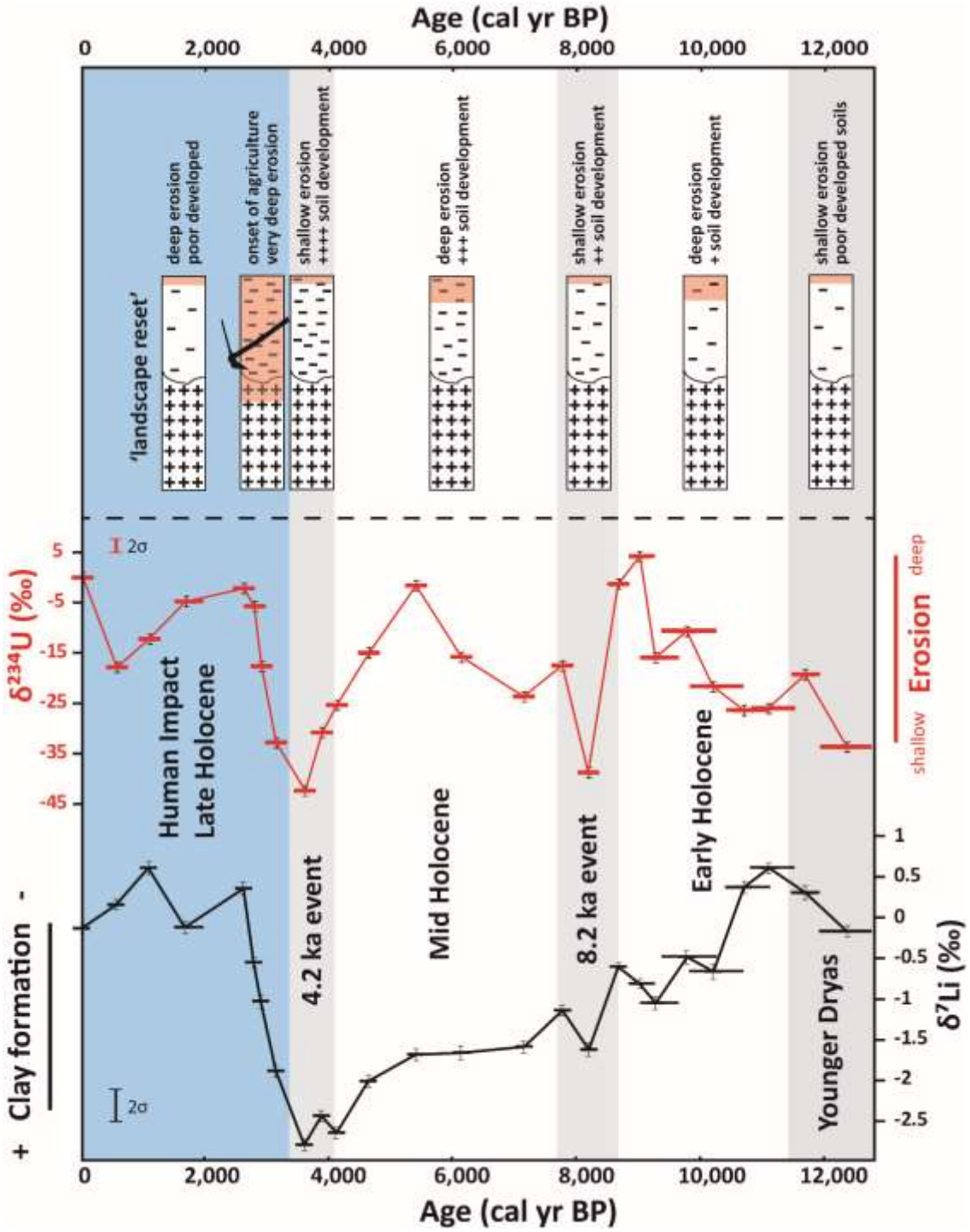

Figure 127: Top panel: Conceptual representation of the evolution of soil profiles at the Lake Dojran catchment throughout the Holocene. Areas highlighted in orange shade represent a schematic erosion depth of individual profiles. Hyphen density conceptualise clay abundances. Soil erosion depth varied over time and responded to short-lived (<1,000 years) climatic events, while clay concentrations increased continuously from 12,000 to 3,500 cal yr BP. Between 3,500 and 3,100 cal yr BP, anthropogenic agricultural practises caused the mobilisation of deeper soil horizons, effectively

'resetting' the landscape at ~2,500 cal yr BP to soil formation conditions unprecedented during Holocene. Bottom panel shows Li and U isotope compositions of Holocene core sediment at Lake Dojran. Error bars are 2 standard error for both Li and U data. The external reproducibility for both $\delta^{234}U$ and $\delta^{7}Li$ values is displayed on the left side of the diagram. Error bars for deposition ages are displayed by the horizontal size of the symbol. Grey bands illustrate relatively cool and arid phases, while white bands show warm and wet phases (Drysdale et al., 2006; Pross et al., 2009; Lacey et al., 2015). The blue band shows the proposed period of anthropogenic overprint (Vogel et al., 2010; Panagiotopoulos et al., 2013; Francke et al., 2013).

The erosion event occurred before or at the onset of the Greek 'Dark Ages' (~3,200 cal yr BP; (Pomeroy, 1999)). In this period, population declined, agriculture suffered, the metallurgy of bronze and the ability to write were forgotten (Pomeroy, 1999). Interestingly, the erosion peaked at the time (2,500 cal yr BP) when the Athenian Empire and other southern Greek *poleis* (city states) increased their demand for timber especially for naval construction. If the erosion event observed at Lake Dojran is of regional significance, the associated stress on natural resources could have triggered or at least contributed to a decline into 'Dark Ages'. Thus, while humans have impacted their environment since the onset of the Holocene, we show that the expansion of civilisation in this region resulted in environmental changes that in turn could have negatively impacted human societies.

8.6 Conclusions

The Li isotope ratio of sediments (<63 µm) may be used as a proxy for soil development and U isotope ratios reveal the depth of soil erosion. During the Holocene, soil erosion showed an almost immediate response to short-lived (500-1,000 years) climatic variations such as the 8.2 ka and 4.2 ka events. In contrast, soil formation was unaffected by these short-lived events and instead soils became more developed since the beginning of the Holocene until ~3,500 cal yr BP. While soil erosion and soil formation were decoupled through most of the Holocene, at 3,500 cal yr BP, both isotope proxies indicate a dramatic erosion event. The timing of this event coincides with intense human activity in the area. The emergence of agricultural practises could have dramatically disrupted the natural soil environment. This could have resulted in the depletion of soil resources, possibly triggering or at least contributing to the collapse of an ancient civilisation.

References

Andronopoulos, V. 1990. *Geological map of Greece. Herson Sheet.*, 1:50000. IGME.

Arnaud, F., Révillon, S., Debret, M., Revel, M., Chapron, E., Jacob, J., Giguet-Covex, C., Poulenard, J. & Magny, M. 2012. Lake Bourget regional erosion patterns reconstruction reveals Holocene NW European Alps soil evolution and paleohydrology. *Quaternary Science Reviews,* 51**,** 81-92.

Arnaud, F., Poulenard, J., Giguet-Covex, C., Wilhelm, B., Révillon, S., Jenny, J.-P., Revel, M., Enters, D., Bajard, M. & Fouinat, L. 2016. Erosion under climate and human pressures: An alpine lake sediment perspective. *Quaternary Science Reviews,* 152**,** 1-18.

Athanasiadis, N., Tonkov, S., Atanassova, J. & Bozilova, E. 2000. Palynological study of Holocene sediments from Lake Doirani in northern Greece. *Journal of Paleolimnology,* 24**,** 331-342.

Bajard, M., Poulenard, J., Sabatier, P., Develle, A.-L., Giguet-Covex, C., Jacob, J., Crouzet, C., David, F., Pignol, C. & Arnaud, F. 2017a. Progressive and regressive soil evolution phases in the Anthropocene. *Catena,* 150**,** 39-52.

Bajard, M., Poulenard, J., Sabatier, P., Etienne, D., Ficetola, F., Chen, W., Gielly, L., Taberlet, P., Develle, A.-L. & Rey, P.-J. 2017b. Long-term changes in alpine pedogenetic processes: Effect of millennial agro-pastoralism activities (French-Italian Alps). *Geoderma,* 306**,** 217-236.

Bastian, L., Revel, M., Bayon, G., Dufour, A. & Vigier, N. 2017. Abrupt response of chemical weathering to Late Quaternary hydroclimate changes in northeast Africa. *Scientific Reports,* 7**,** 44231.

Berner, R. A., Lasaga, A. C. & Garrels, R. M. 1983. The carbonate-silicate geochemical cycle and its effect on atmospheric carbon dioxide over the past 100 million years. *American Journal of Science,* 283**,** 641-683.

Bluth, G. J. & Kump, L. R. 1994. Lithologic and climatologic controls of river chemistry. *Geochimica et Cosmochimica Acta,* 58**,** 2341-2359.

Borza, E. N. 1987. Timber and politics in the ancient world: Macedon and the Greeks. *Proceedings of the American Philosophical Society,* 131**,** 32-52.

Brisset, E., Miramont, C., Guiter, F., Anthony, E. J., Tachikawa, K., Poulenard, J., Arnaud, F., Delhon, C., Meunier, J.-D. & Bard, E. 2013. Non-reversible

geosystem destabilisation at 4200 cal. BP: Sedimentological, geochemical and botanical markers of soil erosion recorded in a Mediterranean alpine lake. *The Holocene,* 23**,** 1863-1874.

Broecker, W. S. & Sanyal, A. 1998. Does atmospheric CO_2 police the rate of chemical weathering? *Global Biogeochemical Cycles,* 12**,** 403-408.

Burton, K. W. & Vigier, N. 2012. Lithium Isotopes as Tracers in Marine and Terrestrial Environments. *In:* Baskaran, M. (ed.) *Handbook of Environmental Isotope Geochemistry: Vol I.* Berlin, Heidelberg: Springer Berlin Heidelberg, 41-59.

Carlson, A. 2013. Paleoclimate | The Younger Dryas Climate Event. *Encyclopedia of Quaternary Science (Second Edition)***,** 126-134.

Dearing, J., Hu, Y., Doody, P., James, P. A. & Brauer, A. 2001. Preliminary reconstruction of sediment-source linkages for the past 6000 yr at the Petit Lac d'Annecy, France, based on mineral magnetic data. *Journal of Paleolimnology,* 25**,** 245-258.

Decarreau, A., Vigier, N., Pálková, H., Petit, S., Vieillard, P. & Fontaine, C. 2012. Partitioning of lithium between smectite and solution: An experimental approach. *Geochimica et Cosmochimica Acta,* 85**,** 314-325.

Dellinger, M., Bouchez, J., Gaillardet, J., Faure, L. & Moureau, J. 2017. Tracing weathering regimes using the lithium isotope composition of detrital sediments. *Geology,* 45**,** 411-414.

Dosseto, A., Turner, S. P. & Chappell, J. 2008. The evolution of weathering profiles through time: new insights from uranium-series isotopes. *Earth and Planetary Science Letters,* 274**,** 359-371.

Dosseto, A., Buss, H. L. & Chabaux, F. 2014. Age and weathering rate of sediments in small catchments: The role of hillslope erosion. *Geochimica et Cosmochimica Acta,* 132**,** 238-258.

Dosseto, A., Vigier, N., Joannes-Boyau, R. C., Moffat, I., Singh, T. & Srivastava, P. 2015. Rapid response of silicate weathering rates to climate change in the Himalaya. *Geochemical Perspectives Letters,* 1**,** 10-19.

Dosseto, A. 2015. Chemical Weathering (U-Series). *Encyclopedia of Scientific Dating Methods***,** 152-169.

Drysdale, R., Zanchetta, G., Hellstrom, J., Maas, R., Fallick, A., Pickett, M., Cartwright, I. & Piccini, L. 2006. Late Holocene drought responsible for the collapse of Old

World civilizations is recorded in an Italian cave flowstone. *Geology,* 34**,** 101-104.

Francke, A., Wagner, B., Leng, M. J. & Rethemeyer, J. 2013. A Late Glacial to Holocene record of environmental change from Lake Dojran (Macedonia, Greece). *Climate of the Past,* 9**,** 481-498.

Giguet-Covex, C., Pansu, J., Arnaud, F., Rey, P.-J., Griggo, C., Gielly, L., Domaizon, I., Coissac, E., David, F. & Choler, P. 2014. Long livestock farming history and human landscape shaping revealed by lake sediment DNA. *Nature communications,* 5**,** 3211.

Gontier, A., Rihs, S., Chabaux, F., Lemarchand, D., Pelt, E. & Turpault, M.-P. 2015. Lack of bedrock grain size influence on the soil production rate. *Geochimica et Cosmochimica Acta,* 166**,** 146-164.

Ivanovski, T. 1970. *Tumač za Osnovnu geološku kartu SFRJ 1:100000,* 1:100000. Savezni geološki institut.

Jin, Z., Cao, J., Wu, J. & Wang, S. 2006. A Rb/Sr record of catchment weathering response to Holocene climate change in Inner Mongolia. *Earth Surface Processes and Landforms,* 31**,** 285-291.

Katsavouni, S. & Petkovski, S. 2004. Lake Doiran-An overview of the current situation. *Greek Biotope/Wetland Center (EKBY), Society for the Investigation and Conservation of Biodiversity and the Sustainable Development of Natural Ecosystems (BIOECO).*

Kosmas, C., Danalatos, N., Cammeraat, L. H., Chabart, M., Diamantopoulos, J., Farand, R., Gutierrez, L., Jacob, A., Marques, H. & Martinez-Fernandez, J. 1997. The effect of land use on runoff and soil erosion rates under Mediterranean conditions. *Catena,* 29**,** 45-59.

Lacey, J. H., Francke, A., Leng, M. J., Vane, C. H. & Wagner, B. 2015. A high-resolution Late Glacial to Holocene record of environmental change in the Mediterranean from Lake Ohrid (Macedonia/Albania). *International Journal of Earth Sciences,* 104**,** 1623-1638.

Lemarchand, E., Chabaux, F., Vigier, N., Millot, R. & Pierret, M.-C. 2010. Lithium isotope systematics in a forested granitic catchment (Strengbach, Vosges Mountains, France). *Geochimica et Cosmochimica Acta,* 74**,** 4612-4628.

Lionello, P., Malanotte-Rizzoli, P., Boscolo, R., Alpert, P., Artale, V., Li, L., Luterbacher, J., May, W., Trigo, R. & Tsimplis, M. 2006. The Mediterranean climate: an overview of the main characteristics and issues. *Developments in earth and environmental sciences,* 4**,** 1-26.

Liu, X.-M., Wanner, C., Rudnick, R. L. & Mcdonough, W. F. 2015. Processes controlling δ 7 Li in rivers illuminated by study of streams and groundwaters draining basalts. *Earth and Planetary Science Letters,* 409**,** 212-224.

Ma, L., Chabaux, F., Pelt, E., Blaes, E., Jin, L. & Brantley, S. 2010. Regolith production rates calculated with uranium-series isotopes at Susquehanna/Shale Hills Critical Zone Observatory. *Earth and Planetary Science Letters,* 297**,** 211-225.

Magny, M., Vannière, B., Zanchetta, G., Fouache, E., Touchais, G., Petrika, L., Coussot, C., Walter-Simonnet, A.-V. & Arnaud, F. 2009. Possible complexity of the climatic event around 4300—3800 cal. BP in the central and western Mediterranean. *The Holocene,* 19**,** 823-833.

Mayewski, P. A., Rohling, E. E., Stager, J. C., Karlén, W., Maasch, K. A., Meeker, L. D., Meyerson, E. A., Gasse, F., Van Kreveld, S. & Holmgren, K. 2004. Holocene climate variability. *Quaternary research,* 62**,** 243-255.

Millot, R., Vigier, N. & Gaillardet, J. 2010. Behaviour of lithium and its isotopes during weathering in the Mackenzie Basin, Canada. *Geochimica et Cosmochimica Acta,* 74**,** 3897-3912.

Montgomery, D. R. 2007. Soil erosion and agricultural sustainability. *Proceedings of the National Academy of Sciences,* 104**,** 13268-13272.

Munhoven, G. 2002. Glacial–interglacial changes of continental weathering: estimates of the related CO_2 and HCO_3^- flux variations and their uncertainties. *Global and Planetary Change,* 33**,** 155-176.

Panagiotopoulos, K., Aufgebauer, A., Schäbitz, F. & Wagner, B. 2013. Vegetation and climate history of the Lake Prespa region since the Lateglacial. *Quaternary International,* 293**,** 157-169.

Pistiner, J. S. & Henderson, G. M. 2003. Lithium-isotope fractionation during continental weathering processes. *Earth and Planetary Science Letters,* 214**,** 327-339.

Plater, A., Ivanovich, M. & Dugdale, R. 1992. Uranium series disequilibrium in river sediments and waters: the significance of anomalous activity ratios. *Applied Geochemistry,* 7**,** 101-110.

Pomeroy, S. B. 1999. *Ancient Greece: a political, social, and cultural history,* Oxford University Press, USA, pp.

Pross, J., Kotthoff, U., Müller, U., Peyron, O., Dormoy, I., Schmiedl, G., Kalaitzidis, S. & Smith, A. 2009. Massive perturbation in terrestrial ecosystems of the Eastern Mediterranean region associated with the 8.2 kyr BP climatic event. *Geology,* 37**,** 887-890.

Rudnick, R. L., Tomascak, P. B., Njo, H. B. & Gardner, L. R. 2004. Extreme lithium isotopic fractionation during continental weathering revealed in saprolites from South Carolina. *Chemical Geology,* 212**,** 45-57.

Singer, A. & Stoffers, P. 1980. Clay mineral diagenesis in two East African lake sediments. *Clay Minerals,* 15**,** 291-307.

Suresh, P., Dosseto, A., Hesse, P. & Handley, H. 2013. Soil formation rates determined from Uranium-series isotope disequilibria in soil profiles from the southeastern Australian highlands. *Earth and Planetary Science Letters,* 379**,** 26-37.

Tessier, A., Campbell, P. G. & Bisson, M. 1979. Sequential extraction procedure for the speciation of particulate trace metals. *Analytical chemistry,* 51**,** 844-851.

Thienemann, M., Masi, A., Kusch, S., Sadori, L., John, S., Francke, A., Wagner, B. & Rethemeyer, J. 2017. Organic geochemical and palynological evidence for Holocene natural and anthropogenic environmental change at Lake Dojran (Macedonia/Greece). *The Holocene,* 0**,** 1-12.

Vance, D., Teagle, D. A. & Foster, G. L. 2009. Variable Quaternary chemical weathering fluxes and imbalances in marine geochemical budgets. *Nature,* 458**,** 493-496.

Verney-Carron, A., Vigier, N. & Millot, R. 2011. Experimental determination of the role of diffusion on Li isotope fractionation during basaltic glass weathering. *Geochimica et Cosmochimica Acta,* 75**,** 3452-3468.

Vigier, N., Decarreau, A., Millot, R., Carignan, J., Petit, S. & France-Lanord, C. 2008. Quantifying Li isotope fractionation during smectite formation and implications for the Li cycle. *Geochimica et Cosmochimica Acta,* 72**,** 780-792.

Vogel, H., Wagner, B., Zanchetta, G., Sulpizio, R. & Rosén, P. 2010. A paleoclimate record with tephrochronological age control for the last glacial-interglacial cycle from Lake Ohrid, Albania and Macedonia. *Journal of Paleolimnology,* 44**,** 295-310.

Walker, J. C., Hays, P. & Kasting, J. F. 1981. A negative feedback mechanism for the long-term stabilization of Earth's surface temperature. *Journal of Geophysical Research: Oceans,* 86**,** 9776-9782.

Williams, L. B. & Hervig, R. L. 2005. Lithium and boron isotopes in illite-smectite: the importance of crystal size. *Geochimica et Cosmochimica Acta,* 69**,** 5705-5716.

9 Analytical methods

9.1 Grain size distribution

Grain size measurements of samples collected from the Murrumbidgee River Basin were carried out at the University of Wollongong using a Malvern Mastersizer 2000 particle size analyser. Prior to sample introduction, the measurement accuracy was determined with a silt-size standard, which yielded 100 % silt over five measurements. Sediment samples for the Murrumbidgee were pre-sieved (dry) using a 2 mm mesh sieve. To determine external reproducibility on grain size distribution, two aliquots of the same sediment sample were processed, which showed identical results for both aliquots (87 % sand, 12 % silt, 1 % clay). Because only this one replicate was processed, the external reproducibility for grain size distribution could not be calculated.

Grain size distribution for sediments from Lake Dojran were measured by Alexander Francke at the University of Cologne. Prior to measurements, samples were treated with 30 % H_2O_2, 10 % HCl, and NaOH to remove organic matter, endogenic calcite and biogenic silica, respectively. This method is published in Francke et al. (2013). Samples were then sieved to <63 µm and grain size analyses were carried out on the <63 µm fraction at the University of Cologne using a Beckman LS^{TM} 13 320 particle size analyser.

9.2 Mineralogy

Mineralogical compositions were determined by X-ray diffraction (XRD) at the University of Wollongong. Ground clay fractions of the Murrumbidgee study and palaeo-channels, as well as >63 µm fractions of Lake Dojran sediments were dried at 50-60°C. The samples were then mounted on aluminium holders and placed in a Phillips 1130/90 diffractometer with Spellman DF3 generator set to 1 kW. The 1 kW energy is achieved by setting the diffractometer to 35 kV and 28.8 mA. Samples were analysed between 4 and 70° 2-theta at 2° per minute with a step size of 0.02. Traces were produced through a GBC 122 control system and analysed using softwares Traces, and SIROQUANT. Error on XRD spectrum was assessed by the chi-squared value (χ^2), where the observed spectrum was compared to the hypothetical spectrum based on user-selected mineral groups. The threshold for χ^2 was set to <8 for all spectra fits. The accuracy obtained by XRD routine analyses was not determined in this study but is reported to be about 3 % at the 95 % confidence interval (Hillier, 2000).

9.2.1 Clay mineral identification

Because of the platy structure of clay minerals, proper sample mounting is essential for the identification and quantification of clay mineral phases using XRD techniques. It is important to ensure a random orientation of clay minerals on the aluminium sample holder, which is achieved through a short suspension in acetone during sample mounting. XRD traces were calibrated using the quartz peak at 26.66° 2-theta. Regions between 3.5 to 5.7° 2-theta are subject to background radiation and were excluded. Similarly, traces between 44.4 and 44.9° 2-theta were excluded, because this region resembles the aluminium peak from the sample holder (Figure 128). Because natural clay minerals are often amorphous, and clays share similar 2-theta intervals, the quantification of mineral phases is difficult. Table 26 shows an example of a clay sample for which two individual aliquots (replicate) were analysed.

Table 26: XRD results of two replicate clay samples.

	N. Booroorban 2	***N. Booroorban 2 (replicate)***
Mineral phase	Wt (%)	Wt (%)
Quartz	4.3	8.9
Mixed layer	19	7.5
Illite	11	6.6
Kaolinite	66	77

Based on the results of these two replicate samples, the reproducibility of the quantification of quartz, mixed layer clay, illite, and kaolinite is 4.6 %, 11 %, 4.3 %, and 11 % (2SE; n=2), respectively.

To differentiate between expandable and non-expandable clays, each sample was measured twice. Before the second measurement, samples were placed in a desiccator with ethylene-glycol, which causes expandable clays to swell. Combining the results of these two preparation steps allows for the semi-quantification of expandable clays. Two examples of this quantification process are shown in Figure 128 & Figure 129.

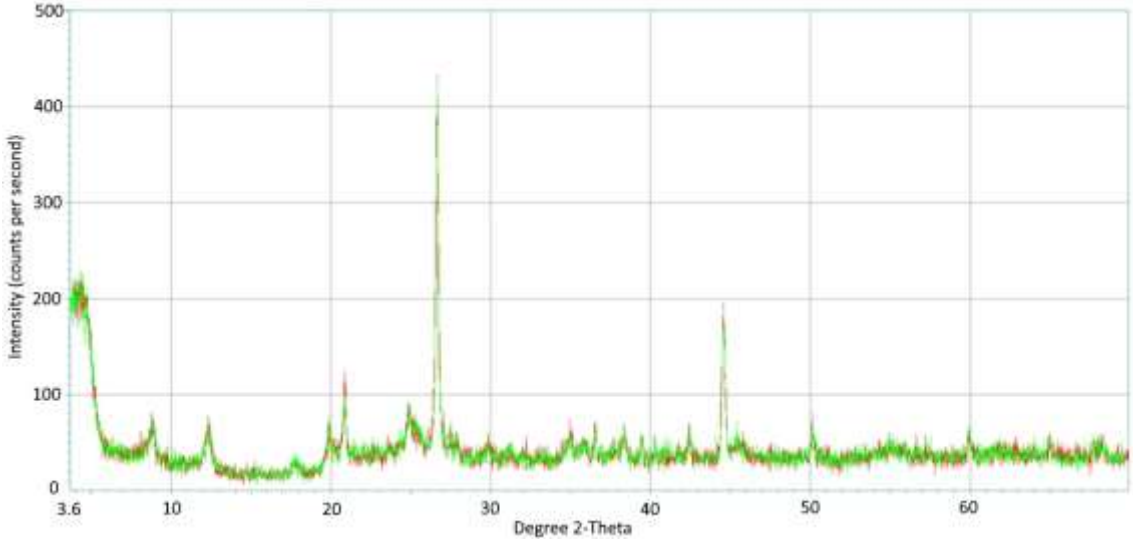

Figure 128: XRD traces of a clay sample A. Green line shows the sample without ethanol-glycol treatment. Red line (behind green) shows XRD traces after the sample was treated with ethylene-glycol.

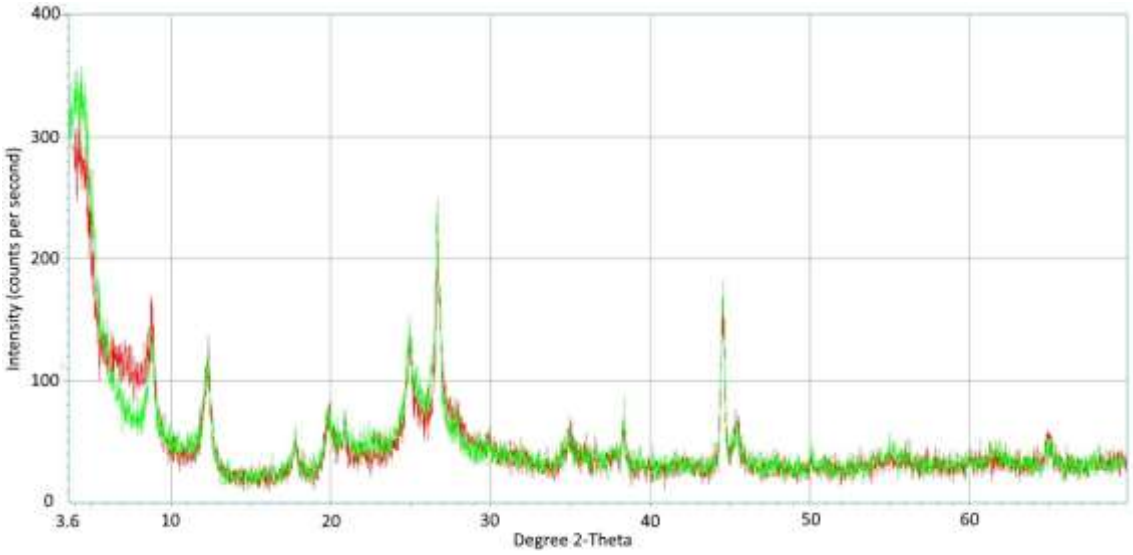

Figure 129: XRD traces of a clay sample B. Green line shows the sample without ethanol-glycol treatment. Red line (behind green) shows XRD traces after the sample was treated with ethylene-glycol.

Results of the clay sample A (Figure 128) shows that XRD traces of the ethylene-glycol treated aliquot match with that of the non-treated aliquot. This implies that no significant amount of expandable clays such as smectites are present in the clay sample. In contrast, clay sample B (Figure 129) shows a significant difference between XRD traces of the treated and non-treated aliquot. The elevated counts between 5-8° 2-theta suggest that

clays experienced swelling in response to the ethylene-glycol treatment and therefore indicate the presence of expandable clays. Hence, the difference between XRD traces between 5-8° 2-theta of treated and non-treated aliquots allows for the relative quantification of expandable clays present in a sample.

9.3 Quadrupole inductively-coupled-plasma mass spectrometry (Q ICP-MS)

Element concentration data were determined via measurements by an iCAP™ Q ICP-MS (Thermo Scientific, Bremen, Germany) at the University of Wollongong. Similar to the MC ICP-MS, samples were processed in liquid form with a 0.3M HNO_3 matrix. Sample solutions are introduced via a nebuliser with a flow rate of 200 µL/min and a cyclonic spray chamber. Ionisation of the nebulised sample is done with an inductively-coupled-plasma of argon (see Section 9.4). The ion beam is then passed through two sets of Ni cones (standard and skimmer), which allows the separation of the internal from the external vacuum. Based on the mass over charge ratio, a quadrupole mass analyser separates ions by alternating electrical fields. This is done via rods (hence quadrupole), which are positioned parallel to each other. Depending on the voltage and radiofrequency of the four rods, only specific ions with selected mass over charge ratios may pass through them. By changing the voltage and radiofrequency of the four rods (which can be done rapidly), ions with other mass over charge ratios can be allowed to pass through. Ion beam intensities are measured in a detector which translates the ion beam intensity into an electrical signal, commonly measured as counts per second (cps). With this approach, a Q ICP-MS can scan a wide range of masses from 2 – 260 amu and quantify the relative abundance of individual ions. Using a series of calibration standards (Inorganic Ventures-ICPMS-71A, Inorganic Ventures-ICPMS-71B, and IRMM016 SIGMA-ALDRICH) with known element concentrations, the measured counts per second for each element-specific ion beam can be converted into concentrations. Instrument drift over time was monitored through intermittent analysis of standard solutions with known concentration.

9.4 Multi-collector inductively-coupled-plasma mass spectrometry (MC ICP-MS)

High-precision isotopic analyses for Li, Nd, and U were performed on a Neptune Plus™ MC ICP-MS (Thermo Scientific, Bremen, Germany) at the University of Wollongong. All samples were analysed in a liquid form with a 0.3 M HNO_3 matrix. The sample inlet system comprises of a nebuliser, which creates a homogenous spray of the sample

solution. This is necessary in order to maximise the ionisation efficiency of the plasma. The nebulised sample travels through a cyclonic spray before being ionised in the torch. For samples with low signal sensitivity, the Apex IR desolvation device was used. It heats up the sample aerosol and passes it through a condenser cooled with air at room temperature. A second condenser at -5°C is then used to produce a dry aerosol. This aerosol is passed through an additional mixing chamber which enhances the signal stability. An inductively-coupled-plasma is created in the torch by a load coil, which is made of copper tubing on which a radio frequency power is applied. Inside the torch, which at this stage is at a temperature of ~8,000°C, the sample aerosol dehydrates, vaporises and atomises. Atoms then collide with the electrons and ionise. An ion transfer mechanism, composed of two Ni cones (sampler and skimmer) separates the internal vacuum from the external inlet system. The mass analyser controls the kinetic energy of the ion beam, shapes and focuses it. The ion beam is then accelerated through a magnetic field, which separates ions through their mass to charge ratio. For Li and Nd isotopes, a series of Faraday cups (detectors) receive the accelerated ion beams from individual masses (isotopes) and record the resulting intensity. For U isotopes, instead of Faraday cups, ion counters were used for detecting ion beams of low intensities.

9.5 Lithium isotopes

Sample preparation for Li isotope measurements was undertaken in a Class 10 cleanroom at the Wollongong Isotope Geochronology Laboratory, University of Wollongong. About 10 mg of the <63 µm fraction was dissolved in 48 % HF and 65 % HNO_3 at 100°C for >12 hours. After drying down, samples were redissolved in aqua regia at 130°C for >12 hr to break down any fluorides. After drying down, samples were redissolved in 1.5 mL 1M HCl. To separate Li from the sample matrix, cation exchange chromatography was applied. The method applied in this study was adapted after (Balter and Vigier, 2014). It is crucial to separate Li from other ions, especially Na, as they may suppress ionisation and cause additional isotopic fractionation during analysis (James and Palmer, 2000). Furthermore, it is essential to recover 100 % of Li, otherwise Li isotopes may fractionate by up to 200 ‰ during chromatography (Pistiner and Henderson, 2003). For this study, Savillex 30 mL micro columns (6.4 mm internal diameter, 9.6 cm outside diameter, capillary length of 25 cm) were used. Columns were vertically customised to have a capillary length of approximately 12 cm. Biorad AG50W-X8 resin (200-400 µm mesh) was used as cation exchange medium, with a volume of 3.06 cm^3 (9.5 cm length). Before

sample loading, columns were cleaned using 30 mL of 6M HCl, rinsed with 2-3 mL 18.2 MΩ water, and conditioned with 8 mL 1M HCl. The latter acid was titrated to 1 molar. Cation exchange columns were calibrated with seawater samples. On two individual columns, it was verified that over 99 % of the original Na was removed after two column passes, while maintaining ~ 100 % Li yield (Table 27, Figure 130). Li was collected from cut 4.5 to 8 mL.

Table 27: Cation exchange column calibration on two individual columns using seawater samples.

Seawater calibration (a)			**Seawater calibration (b)**		
Cut (mL)	Li (ng)	Na (ng)	**Cut (mL)**	Li (ng)	Na (ng)
0.5	0.1	8.4	0.5	0.0	3.5
1	0.0	3.3	1	0.0	2.8
1.5	0.1	2.5	1.5	0.1	1.8
2	0.1	1.9	2	0.1	1.4
2.5	0.1	1.1	2.5	0.1	0.7
3	0.1	0.9	3	0.0	4.6
3.5	0.1	0.8	3.5	0.0	0.4
4	0.1	0.7	4	0.1	0.3
4.5	1.8	0.8	4.5	1.5	0.2
5	17.6	1.1	5	11.6	2.0
5.5	55.1	1.0	5.5	47.7	1.2
6	111.1	8.4	6	105.6	7.2
6.5	92.4	456.2	6.5	84.5	221.9
7	0.2	6720.5	7	0.3	3908.9
7.5	0.1	108869.1	7.5	0.1	92543.3
8	0.1	194925.3	8	0.1	165324.5
8.5	0.1	545172.4	8.5	0.1	415229.9
9	0.1	898675.1	9	0.1	769585.7
9.5	0.1	1176802.7	9.5	0.1	1475550.6
10	0.1	695573.9	10	0.1	726241.0
10.5	0.1	254555.9	10.5	0.1	308806.2
11	0.1	88043.8	11	0.1	108373.3

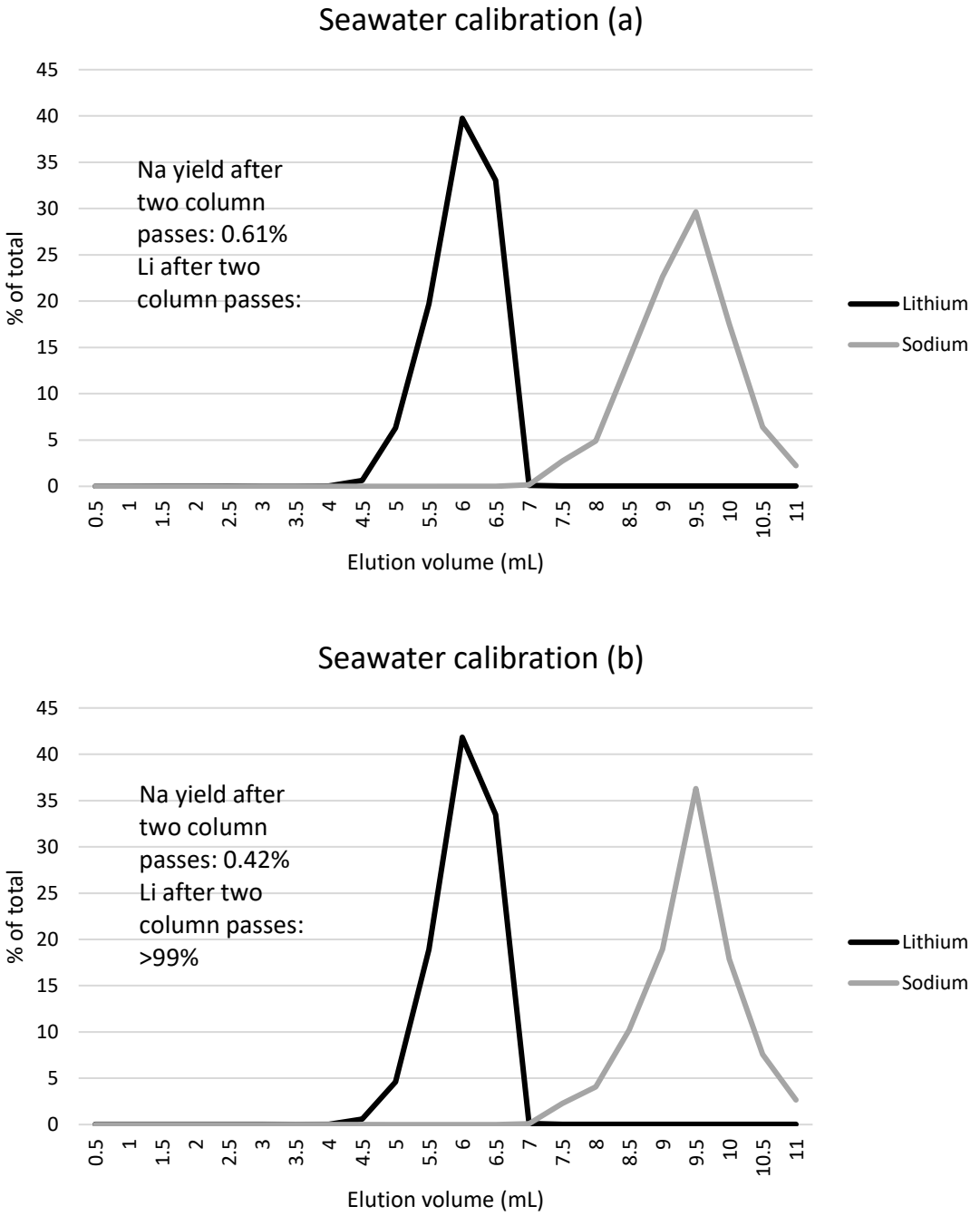

Figure 130: Elution of Li and Na from seawater on two individual columns. Both (a) and (b) show results from first pass through the cation exchange column. Elution reagent is 1M HCl. Li was collected from 4.5 – 8 mL.

The Li elution was dried down and taken up in 0.3M HNO_3 for isotopic analysis. Li isotope ratios were measured at the Wollongong Isotope Geochronology Laboratory, University of Wollongong, on a MC ICP-MS. Using wet plasma conditions, a 30 ppb single element Li tuning solution yielded a typical intensity of 1 V on ^{7}Li, while

background was of the order 5-50 mV on ^{7}Li. The cones setup consisted of a Ni Jet sampler and X-skimmer and a PFA-100 microflow nebuliser (ESI, Omaha, NE, USA) with a flow rate of 90 – 150 µL /min with a high sensitivity insert (Thermo Scientific). A standard bracketing technique was applied (Flesch et al., 1973) using IRMM16 as primary standard for $^{7}Li/^{6}Li$ ratios. Synthetic standards Li7-N and Li6-N (Carignan et al., 2007) were used to assess accuracy of isotopic ratio determination. Instrument blanks were measured between each standard and sample by introducing 0.3M HNO_3. Blank intensities were then subtracted from each isotope. Corrected $^{7}Li/^{6}Li$ were converted to $\delta^{7}Li$ values using L-SVEC as reference (Carignan et al., 2007). Results for Li7-N and Li6-N are: $\delta^{7}Li = 30.3 \pm 0.1$ ‰ (n=61, 2SE) and -7.9 ± 0.1 ‰ (n=63, 2SE), respectively (Table 28, Table 29, Figure 131, Figure 132)

Table 28: Li isotope composition of single element Li standard Li6-N (Carignan et al., 2007) measured on MC ICP-MS at University of Wollongong. Shown error is the analytical error.

Date	Sample description	δ^7Li rel. L-SVEC (‰)	2 std err δ^7Li abs (‰)
16/10/2015	Li6-N	-8.0	0.2
16/10/2015	Li6-N	-7.5	0.2
16/10/2015	Li6-N	-7.8	0.2
16/10/2015	Li6-N	-8.3	0.1
16/10/2015	Li6-N	-8.3	0.2
16/10/2015	Li6-N	-8.4	0.2
22/10/2015	Li6-N	-8.0	0.2
22/10/2015	Li6-N	-6.7	0.4
22/10/2015	Li6-N	-6.9	0.5
22/10/2015	Li6-N	-8.0	0.4
22/10/2015	Li6-N	-7.5	0.5
22/10/2015	Li6-N	-7.4	0.4
28/10/2015	Li6-N	-7.5	0.1
28/10/2015	Li6-N	-7.9	0.2
28/10/2015	Li6-N	-7.8	0.1
28/10/2015	Li6-N	-8.1	0.1
12/11/2015	Li6-N	-7.9	0.1
12/11/2015	Li6-N	-8.1	0.1
12/11/2015	Li6-N	-8.0	0.1
12/11/2015	Li6-N	-7.9	0.1
12/11/2015	Li6-N	-7.9	0.1
9/12/2015	Li6-N	-7.7	0.1
9/12/2015	Li6-N	-8.0	0.1
9/12/2015	Li6-N	-7.5	0.1
9/12/2015	Li6-N	-7.7	0.1
9/12/2015	Li6-N	-8.1	0.1
9/12/2015	Li6-N	-7.8	0.1
5/02/2016	Li6-N	-7.9	0.2
5/02/2016	Li6-N	-8.0	0.1
5/02/2016	Li6-N	-8.3	0.1

5/02/2016	Li6-N	-7.8	0.1
5/02/2016	Li6-N	-8.1	0.1
5/02/2016	Li6-N	-8.5	0.1
5/02/2016	Li6-N	-8.0	0.1
5/02/2016	Li6-N	-8.1	0.1
5/02/2016	Li6-N	-7.5	0.1
8/03/2016	Li6-N	-8.9	0.2
8/03/2016	Li6-N	-8.2	0.2
8/03/2016	Li6-N	-7.8	0.2
8/03/2016	Li6-N	-8.0	0.2
8/03/2016	Li6-N	-8.1	0.2
27/04/2016	Li6-N	-7.8	0.1
27/04/2016	Li6-N	-8.1	0.2
27/04/2016	Li6-N	-7.5	0.1
27/04/2016	Li6-N	-7.9	0.2
28/04/2016	Li6-N	-7.6	0.1
28/04/2016	Li6-N	-7.4	0.2
14/06/2016	Li6-N	-7.9	0.2
5/09/2016	Li6-N	-8.1	0.2
5/09/2016	Li6-N	-8.4	0.2
5/09/2016	Li6-N	-7.2	0.3
22/09/2016	Li6-N	-8.1	0.2
6/12/2016	Li6-N	-8.1	0.1
10/10/2017	Li6-N	-7.9	0.1
10/10/2017	Li6-N	-8.1	0.1
10/10/2017	Li6-N	-7.8	0.1
10/10/2017	Li6-N	-7.9	0.1
10/10/2017	Li6-N	-8.0	0.1
10/10/2017	Li6-N	-7.9	0.2
23/11/2017	Li6-N	-8.4	0.2
23/11/2017	Li6-N	-7.6	0.2
23/11/2017	Li6-N	-8.4	0.2
23/11/2017	Li6-N	-8.5	0.2

Table 29: Li isotope composition of single element Li standard Li7-N (Carignan et al., 2007) measured on MC ICP-MS at University of Wollongong. Shown error is the analytical error.

Date	Sample description	δ^7Li rel. L-SVEC (‰)	2 std err δ^7Li abs (‰)
16/10/2015	Li7-N	30.2	0.1
16/10/2015	Li7-N	30.7	0.2
16/10/2015	Li7-N	32.4	0.2
16/10/2015	Li7-N	30.2	0.1
16/10/2015	Li7-N	28.9	0.1
22/10/2015	Li7-N	30.2	0.2
22/10/2015	Li7-N	29.3	0.2
22/10/2015	Li7-N	30.3	0.2
22/10/2015	Li7-N	30.0	0.5
22/10/2015	Li7-N	30.7	0.5
28/10/2015	Li7-N	30.1	0.2
28/10/2015	Li7-N	30.3	0.2
28/10/2015	Li7-N	30.9	0.1
12/11/2015	Li7-N	30.6	0.1
12/11/2015	Li7-N	30.4	0.1
12/11/2015	Li7-N	30.4	0.1
12/11/2015	Li7-N	30.3	0.1
12/11/2015	Li7-N	30.6	0.1
9/12/2015	Li7-N	30.3	0.1
9/12/2015	Li7-N	30.4	0.1
9/12/2015	Li7-N	30.4	0.1
9/12/2015	Li7-N	30.6	0.1
9/12/2015	Li7-N	30.6	0.1
5/02/2016	Li7-N	30.4	0.1
5/02/2016	Li7-N	30.2	0.1
5/02/2016	Li7-N	30.5	0.2
5/02/2016	Li7-N	30.5	0.1
5/02/2016	Li7-N	30.2	0.2
5/02/2016	Li7-N	29.9	0.1
5/02/2016	Li7-N	30.5	0.2

5/02/2016	Li7-N	31.1	0.2
5/02/2016	Li7-N	30.1	0.1
8/03/2016	Li7-N	30.7	0.3
8/03/2016	Li7-N	30.8	0.3
8/03/2016	Li7-N	30.9	0.5
8/03/2016	Li7-N	30.5	0.2
28/04/2016	Li7-N	30.7	0.2
28/04/2016	Li7-N	30.8	0.2
28/04/2016	Li7-N	30.5	0.1
28/04/2016	Li7-N	30.1	0.2
29/07/2016	Li7-N	28.3	0.3
5/09/2016	Li7-N	30.7	0.2
5/09/2016	Li7-N	31.3	0.3
5/09/2016	Li7-N	30.1	0.2
5/09/2016	Li7-N	30.3	0.2
5/09/2016	Li7-N	30.4	0.2
6/12/2016	Li7-N	30.3	0.2
6/12/2016	Li7-N	30.4	0.2
6/12/2016	Li7-N	30.0	0.2
6/12/2016	Li7-N	30.2	0.2
6/12/2016	Li7-N	30.2	0.2
10/10/2017	Li7-N	30.3	0.2
10/10/2017	Li7-N	30.0	0.2
10/10/2017	Li7-N	30.3	0.2
10/10/2017	Li7-N	30.4	0.1
10/10/2017	Li7-N	30.3	0.2
10/10/2017	Li7-N	30.5	0.1
10/10/2017	Li7-N	30.3	0.2
13/10/2017	Li7-N	30.0	0.2
23/11/2017	Li7-N	29.7	0.4
23/11/2017	Li7-N	29.2	0.3

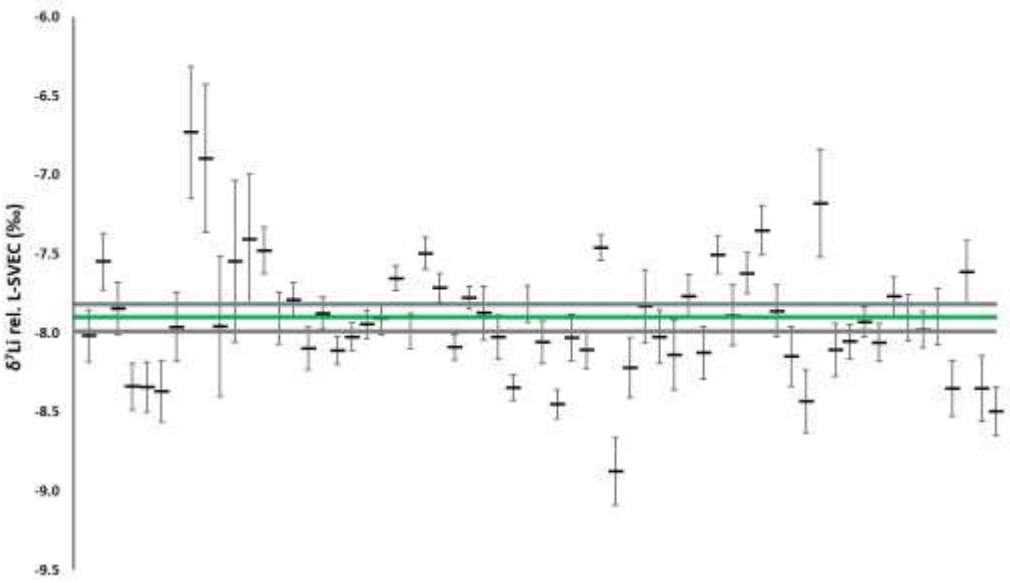

Figure 131: The Li isotope composition of Li6-N (Carignan et al., 2007) measured on the MC ICP-MS at the University of Wollongong. Green line represents the mean value over 63 measurements and grey line is the 2SE.

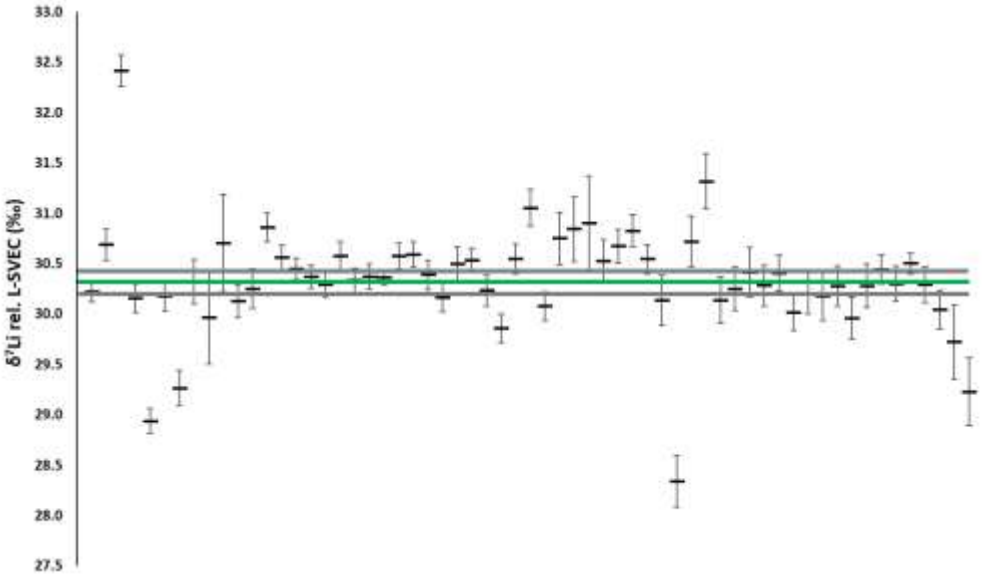

Figure 132: The Li isotope composition of Li7-N (Carignan et al., 2007) measured on the MC ICP-MS at the University of Wollongong. Green line represents the mean value over 61 measurements and grey line is the 2SE.

Each column (n = 20) was verified by passing seawater samples through, which typically yielded δ^7Li (rel. to L-SVEC) of 28.5 – 31.7 ‰ (Table 30).

Table 30: Seawater Li isotope composition tested on individual columns

Date	Column #	δ^7Li rel. L-SVEC (‰)	2 std err δ^7Li abs (‰)
29/06/2015	Column B	30.6	0.230
29/06/2015	Column A	30.8	0.232
29/06/2015	Column D	31.4	0.264
29/06/2015	Column L	29.2	0.250
29/06/2015	Column K	30.9	0.178
29/06/2015	Column J	31.4	0.191
29/06/2015	Column I	31.7	0.234
29/06/2015	Column E	28.8	0.262
29/06/2015	Column B	30.8	0.201
25/09/2015	Column C-1	30.0	0.154
25/09/2015	Column D-1	30.3	0.138
25/09/2015	Column Q	30.6	0.203
25/09/2015	Column P	29.5	0.215
25/09/2015	Column S	29.1	0.205
25/09/2015	Column O	29.3	0.160
25/09/2015	Column R	29.6	0.189
25/09/2015	Column H-1	30.0	0.178
25/09/2015	Column L-1	31.1	0.231
10/10/2017	Column F	25.9	0.137
10/10/2017	Column R	29.8	0.084
10/10/2017	Column B	29.3	0.087
10/10/2017	Column A	29.8	0.100
10/10/2017	Column Q	29.7	0.101
10/10/2017	Column C-1	28.5	0.120
10/10/2017	Column J	29.5	0.089

The average δ^7Li value of all 25 seawater samples is 29.9 ‰ with a 2SE of 0.5 ‰. Reported values for seawater vary between 28.0 and 32.5 ‰ (Pistiner and Henderson, 2003; Carignan et al., 2004). For columns where the Li isotope composition deviated from reported values for seawater were assorted, e.g. column F measured on 10/10/2017 (Table 30). To verify the sediment sample dissolution and ion exchange chromatography protocols for Li isotope measurements, a granitic geochemical reference material JG-2

(Imai et al., 1995) was processed along with all samples analysed during this PhD project's. Results of all measured JG-2 samples in this PhD project are shown in Table 31 and Figure 133. The average δ^7Li value obtained is 0.6 ± 0.2 ‰ (n=29, 2σ).

Table 31: The Li isotope composition of granitic geochemical reference material JG-2 (Imai et al., 1995).

Date	Sample description	δ^7Li rel. L-SVEC (‰)	2 std err δ^7Li abs (‰)
22/10/2015	JG-2	1.6	0.213
28/10/2015	JG-2	0.5	0.185
12/11/2015	JG-2	0.5	0.093
12/11/2015	JG-2	0.1	0.063
12/11/2015	JG-2	0.6	0.058
12/11/2015	JG-2	0.8	0.085
12/11/2015	JG-2	0.3	0.104
12/11/2015	JG-2	0.4	0.069
12/11/2015	JG-2	-0.2	0.073
9/12/2015	JG-2	0.3	0.073
9/12/2015	JG-2	0.5	0.065
9/12/2015	JG-2	0.7	0.057
9/12/2015	JG-2	0.5	0.088
9/12/2015	JG-2	0.9	0.076
9/12/2015	JG-2	0.7	0.069
9/12/2015	JG-2	0.5	0.082
9/12/2015	JG-2	0.6	0.062
9/12/2015	JG-2	0.6	0.084
9/12/2015	JG-2	0.8	0.064
9/12/2015	JG-2	0.5	0.072
9/12/2015	JG-2	0.5	0.071
5/02/2016	JG-2	0.6	0.176
5/02/2016	JG-2	0.5	0.154
5/02/2016	JG-2	0.0	0.149
8/03/2016	JG-2	0.7	0.229
5/09/2016	JG-2	0.5	0.215
5/09/2016	JG-2	1.4	0.295
6/12/2016	JG-2	1.0	0.181
23/11/2017	JG-2	-0.4	0.094

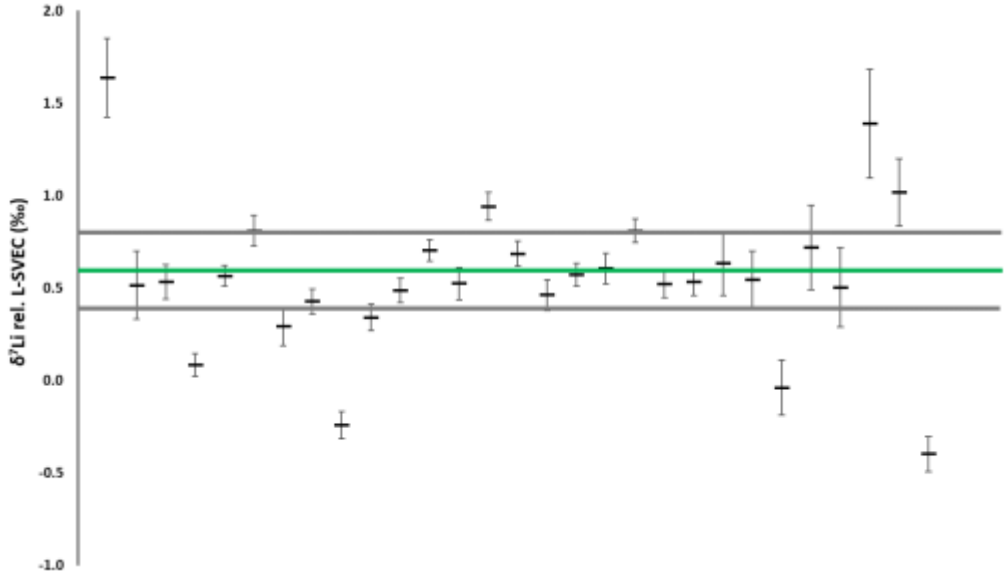

Figure 133: The Li isotope composition of JG-2 geochemical reference material (Imai et al., 1995) measured on the MC ICP-MS at the University of Wollongong. Green line represents the mean value over 29 measurements and grey line is the 2SE.

Measured Li isotope ratios for Li6-N, Li7-N, and JG-2 measured in this PhD project are well within reported values (Table 32).

Table 32: Li isotope measurements of reference materials.

Sample	**δ^7Li vs L-SVEC (‰)**	**Reference**
Li7-N (synthetic)	30.3 ± 1.1 (n=61)	this study
Li7-N	30.2 ± 0.3 (n=89)	(Carignan et al., 2007)
Li7-N	30.2 ± 0.3 (n=13)	(Vigier et al., 2008)
Li6-N (synthetic)	-7.9 ± 0.7 (n=63)	this study
Li6-N	-8.0 ± 0.3 (n=38)	(Carignan et al., 2007)
Li6-N	-8.9 ± 0.9 (n=9)	(Vigier et al., 2008)
JG-2 (granite)	0.6 ± 0.8 (n=29)	this study
JG-2 (granite)	0.4 ± 0.2 (n=3)	(James and Palmer, 2000)
JG-2 (granite)	0.2 ± 0.1	(Vigier et al., 2008)

Uncertainties are given at the 2σ level (2SD).

Total procedure blanks (n=8) yielded <1.2 ng of Li, with an average of 0.8 ng, which represents 0.003 – 0.462 % of the amount of Li processed for sample analysis (250-17,000 ng) (Table 33).

Table 33: Total procedure blanks for the Li isotope protocol in this study.

Sample ID	Li (ng)
1879	1.2
2481	0.6
2493	0.6
2510	0.6
2570	1.0
2580	1.0
1789	1.0
4127	0.5

Total procedure blanks were not measured on the MC ICP-MS because the signal sensitivity for Li was below detection limit, but based on the maximum blank contribution of 0.462 % and a difference in the δ^7Li composition of 30 ‰ relative to the sample, the blank can contribute a maximum of 0.1 ‰ to the sample. For all samples for Lake Dojran, Li elutions were measured twice yielding isotope compositions within analytical error of each other. The external reproducibility for Li isotope measurements of natural samples, calculated via the average of the 2-standard error (2SE) of eight replicate samples, is estimated at 0.5 ‰ (Table 34).

Table 34: Li isotope measurements on replicate samples

Sample name	**δ^7Li (‰)**
Granodiorite Catchment A at Cunningham Creek (A)	1.0
Granodiorite Catchment A at Cunningham Creek (A) replicate	*1.9*
Granodiorite F (B)	-3.8
Granodiorite F (B) replicate	*-2.3*
Dojran 229	-1.9
Dojran 229 replicate	-1.4
Dojran 248	-1.6
Dojran 248 replicate	-1.6
Dojran stream #22	0.8
Dojran stream #22 replicate	0.5
Gala Vale 'south' 3	-0.7
Gala Vale 'south' replicate	*-0.1*
Thurrowa Road 3	-1.8
Thurrowa Road 3 replicate	*-1.7*
Yanco 'a' 2	-0.3
Yanco 'a' 2 replicate	*-0.6*

9.5.1 Leaching experiments

Leaching experiments were conducted on clay-sized fractions of Murrumbidgee River samples in order to evaluate if the exchangeable fraction of Li that is adsorbed onto mineral surfaces needs to be removed prior to further sample processing. Two clay samples which showed significant amounts of expandable clays (see Section Clay mineral identification) were treated with 8 mL NH_4Cl for ~15 mg of sample for one hour at room temperature to remove the exchangeable Li fraction (Tessier et al., 1979). Samples were then washed with 18.2 MΩ water for 5 minutes. Another two aliquots of the same samples were processed along but without any sequential leaching treatment. Clay samples where the exchangeable Li was removed yielded δ^7Li values of -0.4 ‰ and -0.1 ‰ and the same samples where the exchangeable Li fraction was not removed showed δ^7Li values of -1.0 ‰ and -0.4 ‰, respectively (Table 35). This is within the external reproducibility of δ^7Li values (± 0.5 ‰). These findings suggest that no leaching procedure is necessary prior to

clay sample processing. Another leaching experiment was undertaken by Justin Meredith as an undergraduate project at the University of Wollongong under the supervision of Leo Rothacker. Methods and results of this experiment are shown in Section 9.9.2.

Table 35: Li isotope compositions of leached and un-leached samples

Sample name	δ^7Li (‰)
Clay_1	-1.0
Clay_1_leached	-0.4
Clay_2	-0.4
Clay_2_leached	-0.1

External uncertainty (2SE) for δ^7Li values is 0.5 ‰.

9.6 Uranium isotopes

U isotope measurements were not undertaken by Leo Rothacker, but because U data is used in the Lake Dojran study, the preparation protocol is described here. Sample processing for U isotopes, including data analyses, was undertaken by Anthony Dosseto, Davide Menozzi, and Lili Yu (University of Wollongong.) Following sample dissolution (see Section 9.5), a fraction of the 1M HCl solution, equivalent to 300-600 ng U, was dried down and re-dissolved in 1.5M HNO_3. U was separated by ion exchange chromatography following the protocol described in (Luo et al., 1997). U isotopes were analysed at the Wollongong Isotope Geochronology Laboratory using the same Thermo^{TM} Neptune Plus MC ICP-MS. U-234 was collected on a secondary electron multiplier (SEM) and ^{235}U and ^{238}U on Faraday cups. Measured isotope ratios were corrected for mass bias and Faraday/SEM yield by standard bracketing and using NBL U010 as primary standard (Richter et al., 2011). Total procedure blanks (n=3) yielded <40 pg U, which represents less than 0.01 % of the amount of U from the samples (300-600 ng). Accuracy and external reproducibility were assessed using USGS reference material QLO-1, a quartz latite in secular equilibrium (Flanagan and Flanagan, 1976; Sims et al., 2008). Two separate aliquots were processed separately and yielded (^{234}U/^{238}U) activity ratios of 1.002 ± 0.002 (2σ) and 1.003 ± 0.002 (2σ). Based on these two measurements, the external reproducibility (relative 2 standard deviation, n=2) was calculated to be 0.17 % of measured ^{234}U/^{238}U activity ratios.

9.7 Neodymium isotopes

Up to 100 mg of powdered samples, containing an equivalent of 1,600 ng Nd, were dissolved following the same dissolution protocol described in Section 9.5. After sample dissolution, samples were re-dissolved in 4 mL 1.5M HNO_3. Two separation protocols were necessary to purify the Nd fraction of the sample. These were developed on the prep*FAST*-MC™ (ESI, Omaha, NE, USA), a fully automated chromatography system. The first separation protocol included the segregation of rare earth elements (REE), using a 600 µL column filled with 100 µL of 100-150 µm Prefilter resin (Eichrom Technologies, USA) and 500 µL of 100-150 µm TRU resin (Eichron Technologies, USA). The Prefilter resin is used to prevent the TRU resin from leaking into the elution. Prior to sample loading, the column was cleaned with 6 mL 3M HCl, 6 mL 0.5M HCl, 6 mL 0.1M HCl + 0.3M HF, and conditioned with 4 mL 1.5M HNO_3. For the initial column calibration, the geochemical reference material JG-2 (Imai et al., 1995) was used. A volume of 2 mL of the dissolved JG-2 sample (~800 ng of Nd) was then loaded onto the column. To ensure that the entire sample solution was taken up, the sample vial was rinsed with 2 mL of 1.5M HNO_3, which was then loaded onto the column. The sample matrix was then washed out with 5 mL 1.5M HNO_3 (4 – 9 mL) and the REE fraction was eluted with 4.5 mL 3M HCl (9 – 13.5 mL). The entire elution volume from sample loading to REE elution was done in 0.5 mL steps to quantify the separation procedure. Each 0.5 mL elution was analysed on a Q ICP-MS at the University of Wollongong and Na, Mg, Al, K, Fe, Rb, Nd, Sm, and Yb concentrations were determined (Table 36, Figure 134).

Table 36: Element concentrations of the REE elution profile (Ercolani et al., (under review)).

Separation step	V in profile (mL)	Na (ng)	Mg (ng)	Al (ng)	K (ng)	Fe (ng)	Rb (ng)	Nd (ng)	Sm (ng)	Yb (ng)
L1 0.5	0.5	0.00	1	5463	0	2742	2	0	3	3
L1 1.0	1.0	26,897	27	83,540	15,645	75,130	60	0	0	1
L1 1.5	1.5	26,727	27	82,603	15,673	100,790	59	0	0	2
L1 2.0	2.0	23,766	25	75,506	13,484	96,274	52	0	0	3
R2 0.5	2.5	19,229	19	59,028	11,050	84,630	43	0	0	4
R2 1.0	3.0	0.00	1	2,438	0	20,134	0	0	0	2
R2 1.5	3.5	0.00	0	0	0	6,287	0	0	0	2
R2 2.0	4.0	0.00	0	0	0	4,645	0	0	0	1
W 0.5	4.5	0.00	0	0	0	3,464	0	0	0	1
W 1.0	5.0	0.00	0	0	0	1,496	0	0	0	1
W 1.5	5.5	0.00	0	0	0	659	0	0	0	1
W 2.0	6.0	0.00	0	0	0	294	0	0	0	1
W 2.5	6.5	0.00	0	0	0	0	0	0	0	0
W 3.0	7.0	0.00	0	0	0	0	0	0	0	0
W 3.5	7.5	0.00	0	0	0	0	0	0	0	0
W 4.0	8.0	0.00	0	0	0	0	0	0	0	0
W 4.5	8.5	0.00	0	0	0	0	0	0	0	0
W 5.0	9.0	0.00	0	0	0	0	0	0	0	0
REE 0.5	9.5	0.00	0	0	0	49	0	0	0	0
REE 1.0	10.0	0.00	0	0	0	13	0	77	19	0
REE 1.5	10.5	0.00	0	0	0	0	0	97	25	0
REE 2.0	11.0	0.00	0	0	0	0	0	12	3	0
REE 2.5	11.5	0.00	0	0	0	0	0	2	1	0
REE 3.0	12.0	0.00	0	0	0	0	0	1	0	0
REE 3.5	12.5	0.00	0	0	0	0	0	0	0	0
REE 4.0	13.0	0.00	0	0	0	0	0	0	0	0
REE 4.5	13.5	0.00	0	0	0	0	0	0	0	0

L= sample load, R = sample vial rinse and load, W = matrix wash, REE = rare earth element elution

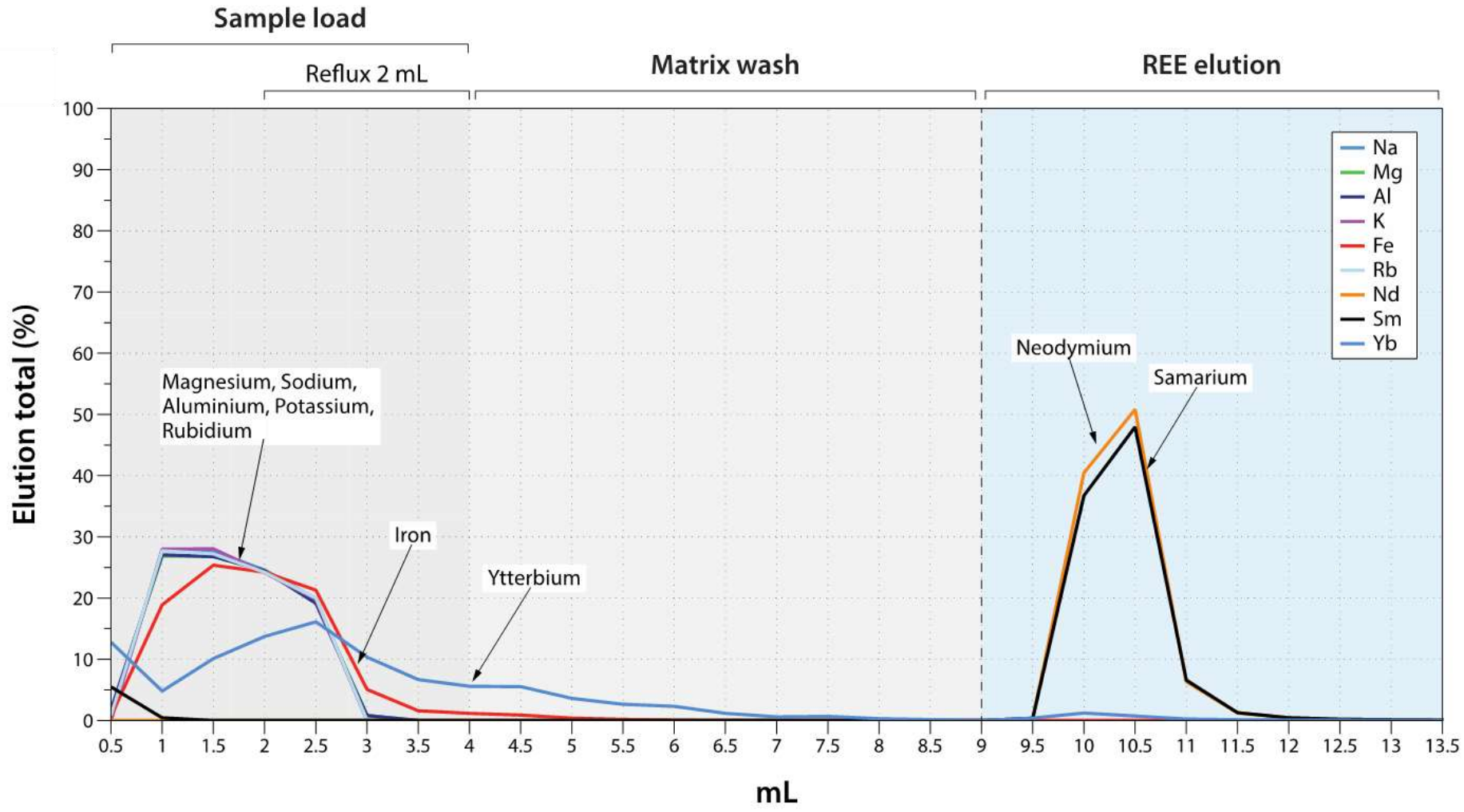

Figure 134: Elution profiles for separating rare earth elements (REE). Source: Ercolani et al. ((under review)).

For separating Nd from other REE, the REE elution from the first column procedure was dried down and re-dissolved in 500 µL 0.25M HCl. The chromatography column of the second separation protocol has a bed volume of 2000 µL and is filled with 50-100 µm Ln resin (Eichrom Technologies, USA). Prior to sample loading, the column was cleaned with 12 mL 6M HCl and 5 mL 18.2 MΩ water. Columns were then conditioned with 5 mL 0.25M HCl and afterwards the sample (500 µL 0.25M HCl) was loaded. A fraction of the sample matrix, mainly Eu, Ba, and Yb, was washed out by adding 5 mL 0.25M HCl. The Nd elution was then collected with 15 mL 0.25M HCl (Table 37, Figure 135).

Table 37: Element concentrations of the Nd elution profile (Ercolani et al., (under review)). (L= sample load, W = matrix wash, E = Nd elution, D = discarded)

Separation step	V in profile (mL)	La (ng)	Ce (ng)	Pr (ng)	Nd (ng)	Sm (ng)	Gd (ng)	Er (ng)	Yb (ng)
L/W1	1	0.048	0.310	0.017	0.094	0.072	0.134	0.114	0.042
W2	2	1.185	0.090	0.002	0.007	0.001	0.003	0.017	0.007
W3	3	8.823	0.547	0.010	0.018	0.001	0.006	0.008	0.005
W4	4	15.202	2.199	0.055	0.085	0.001	0.027	0.004	0.002
W5	5	9.385	5.843	0.182	0.333	0.001	0.065	0.003	0.001
E1	6	3.324	12.321	0.464	0.925	0.001	0.138	0.003	0.001
E2	7	0.623	17.325	0.810	1.750	0.000	0.175	0.003	0.001
E3	8	0.142	26.152	1.356	3.372	0.001	0.246	0.003	0.001
E4	9	0.060	18.501	1.631	4.462	0.001	0.212	0.005	0.000
E5	10	0.053	14.838	2.053	6.478	0.001	0.186	0.006	0.000
E6	11	0.044	9.198	1.896	7.006	0.002	0.123	0.005	0.001
E7	12	0.041	5.028	1.747	7.730	0.000	0.084	0.006	0.001
E8	13	0.038	2.549	1.392	7.401	0.001	0.055	0.005	0.000
E9	14	0.041	1.465	1.232	8.439	0.001	0.042	0.007	0.000
E10	15	0.034	0.591	0.716	5.984	0.000	0.021	0.004	0.000
E11	16	0.035	0.326	0.486	5.211	0.001	0.012	0.004	0.000
E12	17	0.032	0.191	0.306	3.860	0.000	0.008	0.003	0.000
E13	18	0.030	0.138	0.174	2.781	0.001	0.005	0.002	0.000
E14	19	0.034	0.128	0.108	2.033	0.002	0.005	0.002	0.000
E15	20	0.031	0.112	0.065	1.351	0.001	0.003	0.001	0.000
D1	21	0.040	0.134	0.046	1.007	0.001	0.003	0.001	0.000
D2	22	0.036	0.116	0.029	0.595	0.003	0.002	0.000	0.000
D3	23	0.041	0.134	0.027	0.457	0.005	0.002	0.001	0.000
D4	24	0.035	0.118	0.020	0.273	0.004	0.002	0.000	0.000
D5	25	0.035	0.111	0.018	0.179	0.005	0.002	0.000	0.000
D6	26	0.030	0.105	0.017	0.135	0.006	0.001	0.000	0.000
D7	27	0.035	0.111	0.018	0.111	0.007	0.001	0.000	0.000
D8	28	0.033	0.104	0.016	0.099	0.009	0.001	0.000	0.000
D9	29	0.031	0.095	0.015	0.085	0.008	0.001	0.000	0.000
D10	30	0.028	0.097	0.015	0.084	0.011	0.001	0.000	0.000

D11	31	0.030	0.099	0.016	0.084	0.014	0.001	0.000	0.000
D12	32	0.041	0.129	0.019	0.103	0.018	0.001	0.000	0.000
D13	33	0.036	0.115	0.017	0.091	0.021	0.001	0.000	0.000
D14	34	0.030	0.098	0.014	0.082	0.020	0.002	0.000	0.000
D15	35	0.034	0.112	0.018	0.091	0.028	0.001	0.000	0.000
D16	36	0.032	0.098	0.014	0.075	0.029	0.001	0.000	0.000
D17	37	0.034	0.108	0.015	0.083	0.037	0.001	0.000	0.000
D18	38	0.027	0.088	0.013	0.066	0.038	0.001	0.000	0.000
D19	39	0.028	0.093	0.014	0.077	0.044	0.001	0.000	0.000
D20	40	0.031	0.092	0.015	0.068	0.042	0.001	0.000	0.000
D21	45	0.000	0.000	0.000	0.000	3.525	0.005	0.000	0.000
D22	50	0.000	0.000	0.000	0.000	4.675	0.005	0.000	0.000
D23	55	0.000	0.000	0.000	0.000	5.850	0.005	0.000	0.000
D24	60	0.000	0.000	0.000	0.000	7.225	0.005	0.000	0.000
D25	65	0.000	0.000	0.000	0.000	8.575	0.005	0.000	0.000
D26	70	0.000	0.000	0.000	0.000	9.650	0.005	0.000	0.000
D27	75	0.000	0.000	0.000	0.000	9.950	0.005	0.000	0.000
D28	80	0.000	0.000	0.000	0.000	9.225	0.005	0.000	0.000
D29	85	0.000	0.000	0.000	0.000	8.900	0.005	0.000	0.000
D30	90	0.000	0.000	0.000	0.000	8.125	0.005	0.000	0.000
D31	95	0.000	0.000	0.000	0.000	7.275	0.005	0.000	0.000
D32	100	0.000	0.000	0.000	0.000	5.975	0.005	0.000	0.000
D33	105	0.000	0.000	0.000	0.000	5.100	0.005	0.000	0.000
D34	110	0.000	0.000	0.000	0.000	4.050	0.005	0.000	0.000
D35	115	0.000	0.000	0.000	0.000	3.175	0.005	0.000	0.000
D36	120	0.000	0.000	0.000	0.000	2.450	0.005	0.000	0.000
D37	125	0.000	0.000	0.000	0.000	1.875	0.005	0.000	0.000
D38	130	0.000	0.000	0.000	0.000	1.400	0.005	0.000	0.000
D39	135	0.000	0.000	0.000	0.000	1.025	0.005	0.000	0.000
D40	140	0.000	0.000	0.000	0.000	0.700	0.005	0.000	0.000

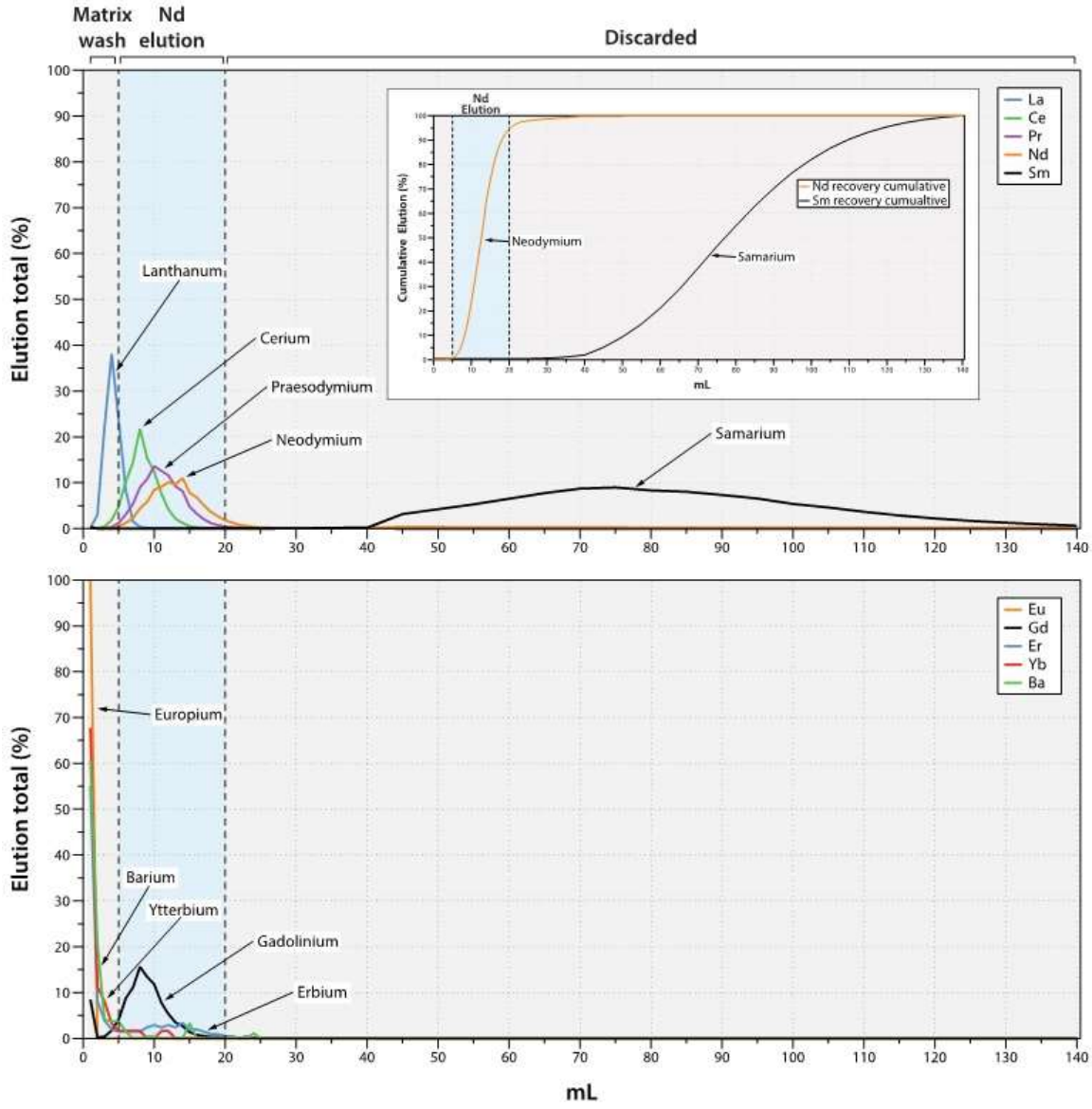

Figure 135: Elution profiles for separating Nd from Eu, Ba, Yb, and Sm. Source: (Ercolani et al., (under review)).

Neodymium isotope measurements were performed on a MC ICP-MS at the University of Wollongong. The static multi-collection in nine faraday cups allowed the monitoring of masses 140, 142, 143, 144, 145, 146, 148, and 150. The $^{143}Nd/^{144}Nd$ ratio was corrected for mass bias using Russell's exponential law (Baxter et al., 2006) and a $^{146}Nd/^{144}Nd$ ratio of 0.7219. Isobaric interference was corrected with ^{147}Sm, where $^{147}Sm/^{144}Nd$, $^{147}Sm/^{148}Nd$, and $^{147}Sm/^{150}Nd$ were corrected with values of 4.83870, 1.327400, and 2.027030, respectively. The cones setup consisted of a Ni standard sampler and skimmer and a PFA-100 microflow nebuliser (ESI, Omaha, NE, USA) with a flow rate of 90 – 150 µL /min with a high sensitivity insert (Thermo Scientific). Using wet plasma conditions,

a 200 ppb single element Nd solution (JNdi-1) yielded typically 0.6 V on ^{145}Nd, equivalent to 3 V ppm^{-1}, and $^{143}Nd/^{144}Nd = 0.512103 \pm 3$ (2SE; n = 54). This is in good agreement with other reported $^{143}Nd/^{144}Nd$ ratios (Figure 136, Table 38). Furthermore, three geochemical reference materials were processed, which showed $^{143}Nd/^{144}Nd$ ratios of 0.511364 ± 18 (n = 9), 0.512231 ± 31 (n = 8), and 0.512612 ± 20 (n = 7), for GSP-2, JG-2, and BCR-2, respectively.

Table 38: Compilation of Nd isotope composition of JNdi-1, GSP-2, BCR-2, and JG-2 (Ercolani et al., (under review)).

Material	**Study**	**Error type**	**N**	$^{143}Nd/^{144}Nd$	Reported error
JNdi-1	Miyazaki and Shuto, 1998	2SE	44	0.512106	0.000003
JNdi-1	Tanaka et al., 2000	2SE	133	0.512115	0.000007
JNdi-1	Valeriano et al., 2008	2SE	40	0.512092	0.000002
JNdi-1	Aciego et al., 2009	2SD	not reported	0.512102	0.000042
JNdi-1	Chu et al., 2009	2SD	13	0.512112	0.000028
JNdi-1	Ali and Srinivasan, 2011	2SE	15	0.512107	0.000013
JNdi-1	Huang et al., 2012	2SD	55	0.512116	0.000016
JNdi-1	Chu et al., 2014	2SD	12	0.512116	0.000016
JNdi-1	Chu et al., 2014a	2SE	8	0.512117	0.000010
JNdi-1	Crocket et al., 2014	2SD	44	0.512106	0.000006
JNdi-1	This study	2SE	54	0.512104	0.000003
GSP-2	Raczek et al., 2003	NA (mean)	2	0.511353	
GSP-2	Weis et al., 2006	2SD	5	0.511369	0.000003
GSP-2	Chu et al., 2009	2SE	not reported	0.511389	0.000012
GSP-2	Chu et al., 2014	2SD	5	0.511370	0.000017
GSP-2	Saji et al., 2016	NA (mean)	5	0.511376	
GSP-2	This study	2SE	9	0.511364	0.000018

BCR-2	Zhang et al., 2002	2SE	not reported	0.512638	0.000005
BCR-2	Raczek et al., 2003	2SE	5	0.512652	0.000016
BCR-2	Gao et al., 2004	2SE	not reported	0.512635	0.000004
BCR-2	Weis et al., 2006	2SD	11	0.512637	0.000012
BCR-2	She et al., 2006	2SE	2	0.512644	0.000015
BCR-2	Li et al., 2007	Not given	not reported	0.512632	0.000008
BCR-2	Chu et al., 2009	2SD	7	0.512641	0.000018
BCR-2	Aciego et al., 2009	2SD	11	0.512643	0.000037
BCR-2	Yang et al., 2010	2SE	not reported	0.512641	0.000004
BCR-2	Yang et al., 2010	2SE	not reported	0.512635	0.000006
BCR-2	Scher and Delaney, 2010	2SD	11	0.512639	0.000018
BCR-2	Ali and Srinivasan, 2011	2SE	9	0.512624	0.000015
BCR-2	Yang et al., 2011	2SE	not reported	0.512637	0.000007
BCR-2	Chu et al., 2014a	2SD	5	0.512641	0.000030
BCR-2	Crocket et al., 2014	2SD	14	0.512643	0.000008
BCR-2	Saji et al., 2016	NA (mean)	5	0.512636	
BCR-2	This study	2SE	7	0.512612	0.000020
JG-2	Arakawa, 1992	2SE	1	0.512232	0.000007
JG-2	Miyazaki and Shuto, 1998	2SE	5	0.512212	0.000015

JG-2	Shibata et al., 2003	2SE	not reported	0.512225	0.000008
JG-2	Li et al., 2007	Not given	not reported	0.51224	0.000010
JG-2	This study	2SE	8	0.512231	0.000031

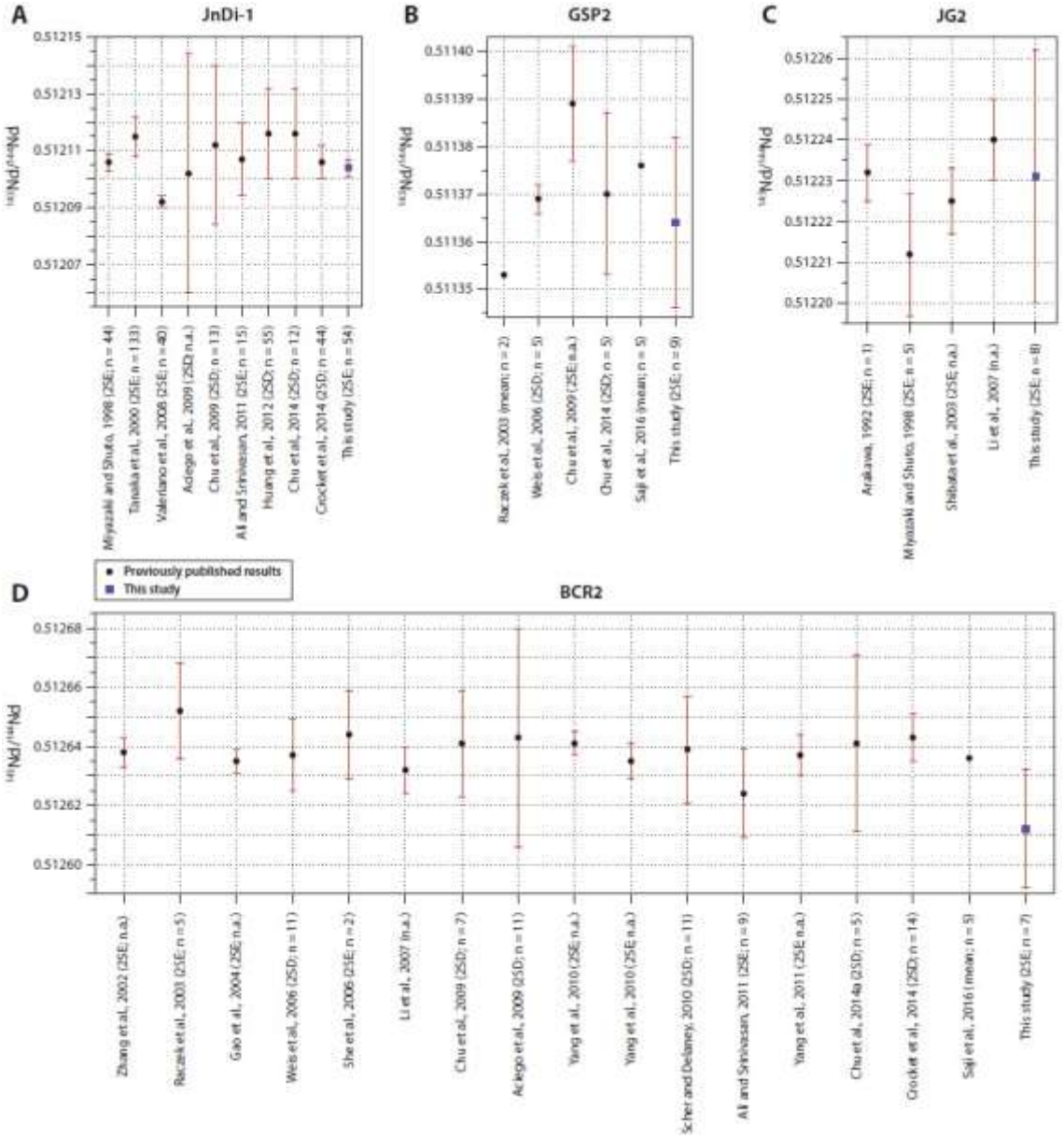

Figure 136: $^{143}Nd/^{144}Nd$ ratios of certified isotopic standard JNdi-1 (A) and geochemical reference materials GSP-2 (B), JG-2 (C), and BCR-2 (D). References: (Arakawa, 1992; Miyazaki and Shuto, 1998; Tanaka et al., 2000; Zhang et al., 2002; Raczek et al., 2003; Shibata et al., 2003; Gao et al., 2004; Weis et al., 2006; She et al., 2006; Li et al., 2007; Valeriano et al., 2008; Aciego et al., 2009; Chu et al., 2009; Yang et al., 2009; Scher and Delaney, 2010; Ali and Srinivasan, 2011; Yang et al., 2011; Huang et al., 2012; Chu et al., 2014b; Crocket et al., 2014; Chu et al., 2014a; Saji et al., 2016). Source: Ercolani et al. ((under review)).

Total procedure blanks for Nd showed an average of 136 ± 103 pg (2SE; n = 3), which corresponds to 0.0001% of the total amount of Nd processed for each sample and a

maximum contribution on the $^{143}Nd/^{144}Nd$ ratio of ± 0.000003, which is less than the average analytical precision of a typical session (± 0.000005) (Ercolani et al., (under review)). Based on the results of the processed rock standards, the external reproducibility was estimated at 0.000015 on $^{143}Nd/^{144}Nd$ ratios.

9.8 Major- and trace element concentrations

Following the same sample dissolution protocol, described in Section 9.5, dissolved samples were analysed for major elements (Na, K, Mg, Ca, Al, and Ti) and trace elements (Li, Nb, and Ta) using a Q ICP-MS at the Wollongong Isotope Geochronology Laboratory. Element concentrations were determined using a range (n=8) of calibration standards covering concentrations between 0.05 ppb and 200 ppb. Concentrations of all measured samples were diluted accordingly to fall within this range (typically 1:10,000 for major elements and 1:1,000 for trace elements). The blank intensity of a 0.3M HNO_3 was subtracted from each sample. For quality control, a standard solution with a known concentration of each analysed element was measured after every 10th sample. To verify the dissolution protocol and the accuracy for major and trace element analysis (see section 9.5), one JG-2 rock standard material was processed with every batch of 10-20 samples (Table 39).

Table 39: Major and trace element results for JG-2 rock standard material compared to reported concentrations

	Li (ppm)	**Nb (ppm)**	**Ta (ppm)**	**Na (%)**	**Mg (%)**	**Al (%)**	**K (%)**	**Ca (%)**	**Ti (%)**
	125.5	15.6	2.7	2.05	N/A	5.21	3.15	0.74	0.03
	167.8	10.5	1.1	2.59	N/A	6.57	3.96	0.80	0.04
	175.4	11.7	1.7	2.22	0.01	5.46	3.39	1.29	0.03
	160.1	9.0	1.1	0.91	0.64	7.19	N/A	1.51	N/A
	162.7	13.2	2.3	1.88	N/A	4.74	2.81	2.67	0.04
	223.7	16.4	2.7	2.41	0.15	6.47	3.86	0.32	0.07
	228.6	15.2	2.1	2.56	0.10	6.02	4.02	0.33	0.03
Reported	42.2	14.7	2.76	2.63	0.02	6.6	3.91	0.5	0.026

*Reported values are from Imai et al. (1995).*The average concentration of JG-2 (n = 7) for Li, Nb, Ta, Na, Mg, Al, K, Ca, and Ti was 177.7 ppm, 13.1 ppm, 2.0 ppm, 2.09 %, 0.23 %, 5.95 %, 3.53 %, 1.10 %, and 0.04 %, respectively. The 2RSE (relative 2 standard error) was 15.6 %, 16.2 %, 25.0 %, 21.0 %, 126.0 %, 10.9 %, 11.4 %, 56.9 %, and 33.8 % for Li, Nb, Ta, Na, Mg, Al, K, Ca, and Ti, respectively. Significantly higher Li concentrations were measured in this study compared to reported values. This is difficult

to explain as a high blank contribution cannot be accounted for this large increase in Li concentration (see Table 42). It is more likely that the Li concentration of this particular JG-2 reference batch is higher compared to previous batches. Besides Li, all other measured concentrations fall close within the range of reported values. The external reproducibility of each chemical element for natural samples was assessed via multiple sample replicates. Table 40 and Table 41 show the range 2RSE for each sample replicate pair. The 2RSE is calculated through the 2 standard error divided by the mean.

Table 40: External reproducibility of Na, K, Mg, Ca, Al, Ti, calculated via the 2RSE (2 standard error divided by the mean) of sample replicates.

Sample ID	Na (wt%)	2RSE (%)	K (wt%)	2RSE (%)	Mg (wt%)	2RSE (%)	Ca (wt%)	2RSE (%)	Al (wt%)	2RSE (%)	Ti (wt%)	2RSE (%)
Gala Vale 'south' 3	0.86		2.92		1.07		0.18		12.89		0.60	
*Gala Vale 'south' 3**	0.63	**31.9**	2.34	**22.3**	0.87	**21.5**	0.21	**13.8**	12.45	**3.5**	0.57	**5.9**
Thurrowa Road 3	0.81		2.72		0.94		0.23		11.60		0.61	
*Thurrowa Road 3**	0.84	**3.5**	2.82	**3.9**	0.97	**3.9**	0.26	**10.9**	11.89	**2.5**	0.64	**5.3**
Yanco 'a' 2	0.80		2.69		0.77		0.15		13.02		0.77	
*Yanco 'a' 2**	0.75	**6.4**	2.47	**8.3**	0.71	**8.3**	0.13	**10.5**	11.90	**9.0**	0.70	**9.9**
MGC 4-4#5 uow 1322	0.89		2.89		0.76		0.15		11.71		0.43	
*MGC 4-4#5 uow 1322**	0.82	**7.2**	2.13	**30.4**	0.49	**44.1**	0.05	**95.7**	8.02	**37.4**	0.28	**43.0**
thurrowa road top layer	0.84		2.82		0.97		0.26		11.89		0.64	
*thurrowa road top layer**	0.81	**3.5**	2.72	**3.9**	0.94	**3.9**	0.23	**10.9**	11.60	**2.5**	0.61	**5.3**
yanco 'a' core sample 2 inside and outside centre	0.75		2.47		0.71		0.13		11.90		0.70	
*yanco 'a' core sample 2 inside and outside centre**	0.80	**6.4**	2.69	**8.3**	0.77	**8.3**	0.15	**10.5**	13.02	**9.0**	0.77	**9.9**
CR#1	0.78		2.08		0.96		1.16		9.73		0.29	
*CR#1**	1.68	**72.9**	2.17	**4.4**	1.00	**3.7**	0.30	**117.3**	9.84	**1.1**	0.26	**8.6**
GDR#1	0.42		1.55		0.54		0.83		8.24		0.26	
*GDR#1**	0.76	**58.2**	1.74	**12.0**	0.66	**20.5**	3.07	**114.8**	9.84	**17.8**	0.29	**13.1**

GDR#4	0.97		2.28		0.86		2.61		9.40		0.29	
*GDR#4**	1.75	**57.6**	1.93	**16.7**	0.78	**9.8**	2.35	**10.4**	9.02	**4.1**	0.25	**16.1**
GR-mid	0.92		2.07		1.15		2.21		9.73		0.50	
*GR-mid**	1.76	**62.2**	1.88	**9.6**	1.06	**8.6**	2.75	**21.7**	9.49	**2.6**	0.46	**8.4**
MR#3	0.27		3.08		1.03		1.28		9.90		0.28	
*MR#3**	0.70	**86.8**	3.46	**11.9**	1.17	**12.6**	1.47	**13.8**	11.31	**13.4**	0.30	**6.5**
TR#1	0.54		1.54		0.82		1.72		9.26		0.38	
*TR#1**	0.86	**45.4**	1.45	**6.3**	0.77	**5.9**	1.49	**14.6**	9.52	**2.9**	0.34	**12.5**
TR#3	0.61		3.05		0.84		2.19		9.91		0.35	
*TR#3**	0.87	**34.2**	2.64	**14.4**	0.80	**5.8**	2.85	**26.4**	9.67	**2.5**	0.33	**4.8**
Dojran 248	1.21		3.48		2.39				10.92		0.76	
*Dojran 248**	0.03	**189.5**	3.82	**9.3**	0.07	**188.7**			0.32	**188.7**	0.85	**10.5**
Dojran 229	0.04		2.53		0.07				0.29		0.65	
*Dojran 229**	0.03	**28.7**	2.94	**14.9**	0.06	**22.3**			0.24	**21.0**	0.75	**13.7**

**replicate samples*

Table 41: External reproducibility of Li, Nb, and Ta calculated via the 2RSE (2 standard error divided by the mean) of sample replicates.

Sample ID	Li ppm	2RSE (%)	Nb ppm	2RSE (%)	Ta ppm	2RSE (%)
Gala Vale 'south' 3	232		15		1	
*Gala Vale 'south' 3**	203	**13.4**	13	**13.5**	1	**7.4**
Thurrowa Road 3	177		17		2	
*Thurrowa Road 3**	169	**4.9**	17	**2.7**	2	**2.2**
Yanco 'a' 2	207		17		2	
*Yanco 'a' 2**	203	**2.0**	16	**1.9**	2	**1.2**
MGC 4-4#5 uow 1322	321		21		2	
*MGC 4-4#5 uow 1322**	343	**6.5**	22	**2.6**	2	**5.4**
thurrowa road top layer	169		17		2	
*thurrowa road top layer**	177	**4.9**	17	**2.7**	2	**2.2**
yanco 'a' core sample 2 inside and outside centre	203		16		2	
*yanco 'a' core sample 2 inside and outside centre**	207	**2.0**	17	**1.9**	2	**1.2**
CR#1	161		14		2	
*CR#1**	168	**4.3**	13	**3.3**	2	**3.7**
GDR#1	143.8		5.8		0.6	
*GDR#1**	159.2	**10.2**	6.2	**5.9**	0.6	**7.9**
GDR#4	143.0		6.5		0.7	

*GDR#4**	137.4	**4.0**	5.6	**15.8**	0.6	**11.2**
GR-mid	257.2		15.3		1.8	
*GR-mid**	243.2	**5.6**	13.9	**9.9**	1.6	**11.9**
MR#3	130.2		8.2		0.8	
*MR#3**	139.1	**6.7**	8.3	**0.7**	0.8	**3.1**
TR#1	147.8		10.6		1.1	
*TR#1**	163.9	**10.3**	9.9	**7.5**	1.0	**7.5**
TR#3	140.9		9.9		1.0	
*TR#3**	126.4	**10.8**	8.6	**13.3**	0.9	**10.4**

**replicate samples*

The average 2RSE for Li, Nb, and Ta over all replicate samples in this study is 6.6 %, 6.3 %, and 5.8 %, respectively. In contrast, major elements show an average 2RSE of 46 %, 12 %, 25 %, 36 %, 21 %, and 12 % for Na, K, Mg, Ca, Al, and Ti, respectively.

Total procedure blanks for Na ranged from 126 ng to 3.59 µg (Table 42), which is between 0.01 % and 13 % of the total Na in a processed sample. Potassium blanks were of a similar magnitude with 404 ng to 4.3 µg, which is between 0.03 % and 2.5 % of the total K. For Mg, Ca, Al, and Ti, total procedure blanks ranged from 187 ng to 3.0 µg, 579 ng to 109 µg, 755 ng to 29.5 µg, and 76 ng to 894 ng, respectively. This represents a blank contribution of 0.02 % to 4.9 % for total Mg, 0.05 % to 807 % for total Ca, 0.01 % to 4.6 % for total Al, and 0.05 % to 0.5 % for total Ti. For trace elements, total procedure blanks showed concentrations of 0.5 to 1.2 ng, 0.005 to 0.071 ng, and 0.001 to 0.008 ng for Li, Nb, and Ta, respectively. This corresponds to a blank contribution of 0.003 – 0.5 % for Li, 0.0004 to 0.08 % for Nb, and 0.001 to 0.08 % for Ta.

Table 42: Total procedure blanks for major and trace elements.

Sample ID	Na (ng)	Mg (ng)	Al (ng)	K (ng)	Ca (ng)	Ti (ng)	Li (ng)	Nb (ng)	Ta (ng)
1789	383	0	10,288	2,157	12,677	319	1.22	0.005	0.005
1879	219	0	29,513	2,861	7,434	291	0.59	0.007	0.002
2481	2,613	0	13,767	1,017	109,378	894	0.57	0.009	0.002
2493	2,684	0	12,694	3,024	92,536	764	0.62	0.021	0.004
2510	3,589	0	11,982	0	102,532	811	1.02	0.007	0.001
2570	126	2,755	0	3,377	0	77	1.05	0.009	0.002
2580	1,107	3,024	0	4,278	6,020	117			
3088	1,199	187	755	404	579		1.04	0.071	0.008
4127							0.50		

The overall large blank contribution for most major elements is most likely associated with inferior equipment cleaning procedures. To improve total procedure blanks for major elements, different cleaning steps might be required. For example, Ahlers et al. (1990) suggested that all lab equipment that gets in contact with sample material needs to be soaked in hot 6M HNO_3 for several days or in 12M HNO_3 at room temperature for two weeks. This is then followed by a further leaching in 0.1M high-purity HNO_3 for at least two weeks. In this study, cleaning reagents used for cleaning PFA labware were mostly

analytical grade and could have therefore caused the relatively high levels of contamination of major elements.

9.9 Appendix

9.9.1 Automated Li isotope chromatography with the on the prep*FAST*-MC™ (ESI, Omaha, NE, USA)

During the course of this PhD, it was attempted to automate the Li isotope chromatography using the prepFAST-MC™. While some experiments were successful, results were inconsistent and this project was put on hold.

Equipment:

- 2 mL micro chromatography column
- Biorad AG50W-X8 (200 – 400 µm mesh size)
- HCl (6 M)
- HCl (1 M, precicely titrated)
- 18.2 MΩ water
- Sample in 1M HCl

Prepfast method setup for elution curve (Na and Li not separated):

1. Colum cleaning with 6 mL 6M HCl at 3 mL/min dispense speed
   ➔ Send to waste
2. Column cleaning with 2 mL 18.2 MΩ water at 3 mL/min dispense speed
   ➔ Send to waste
3. Column conditioning with 6 mL 1M HCl at 3 mL/min dispense speed
   ➔ Send to waste
4. Sample load (0.5 mL) at 0.1 mL/min dispense sped
   ➔ Collect in elution vial (destination 1)
5. Take up and deposit 0.5 mL 1M HCl at 3 mL/min dispense speed
   ➔ Collect in elution vial (destination 2)
6. Repeat step 5 until a total of 12 mL is collected over 24 elution vials

Elution volumes for Li were diluted 1:5 and for Na 1:10,000 using 0.3 M HNO_3. This resulted in the following separation efficiency using seawater (Table 43, Figure 137):

Table 43: Results for column calibration (separating Na from Li) with a seawater sample using the prepFAST-MC™.

elution in mL	Na (ppb)	Na (ng)	Na (%)	Na accum (%)	elution in mL	Li (ppb)	Li (ng)	Li (%)	Li accum (%)
0.5	0.0	0.0	0.0	0.0	0.5	0.0	0.0	0.0	0.0
1	0.0	0.0	0.0	0.0	1.0	0.0	0.1	0.0	0.0
1.5	0.0	0.0	0.0	0.0	1.5	0.0	0.0	0.0	0.0
2	0.0	0.0	0.0	0.0	2.0	0.0	0.0	0.0	0.0
2.5	0.0	0.0	0.0	0.0	2.5	0.0	0.0	0.0	0.0
3	0.0	0.0	0.0	0.0	3.0	0.0	0.1	0.0	0.0
3.5	0.0	0.0	0.0	0.0	3.5	0.2	0.9	0.1	0.1
4	0.0	0.0	0.0	0.0	4.0	1.5	6.2	0.6	0.8
4.5	0.0	0.0	0.0	0.0	4.5	0.0	0.1	0.0	0.8
5	0.0	0.0	0.0	0.0	5.0	20.7	82.7	8.7	9.5
5.5	0.0	0.0	0.0	0.0	5.5	43.3	173.2	18.2	27.6
6	0.0	0.0	0.0	0.0	6.0	60.1	240.2	25.2	52.9
6.5	0.0	0.0	0.0	0.0	6.5	57.5	229.8	24.1	77.0
7	0.0	0.0	0.0	0.0	7.0	35.2	140.9	14.8	91.8
7.5	4.7	69.9	1.2	1.2	7.5	14.6	58.3	6.1	97.9
8	11.8	176.3	3.1	4.3	8.0	4.0	16.1	1.7	99.6
8.5	32.2	482.7	8.4	12.7	8.5	0.8	3.2	0.3	100.0
9	57.8	866.4	15.1	27.7	9.0	0.1	0.5	0.0	100.0
9.5	71.8	1076.7	18.7	46.4	9.5	0.0	0.0	0.0	100.0

10	78.9	1183.6	20.6	67.0	10.0	0.0	0.0	0.0	100.0
10.5	60.0	900.1	15.6	82.6	10.5	0.0	0.0	0.0	100.0
11	36.1	541.8	9.4	92.0	11.0	0.0	0.0	0.0	100.0
11.5	23.9	357.8	6.2	98.3	11.5	0.0	0.0	0.0	100.0
12	6.7	99.9	1.7	100.0	12.0	0.0	0.0	0.0	100.0

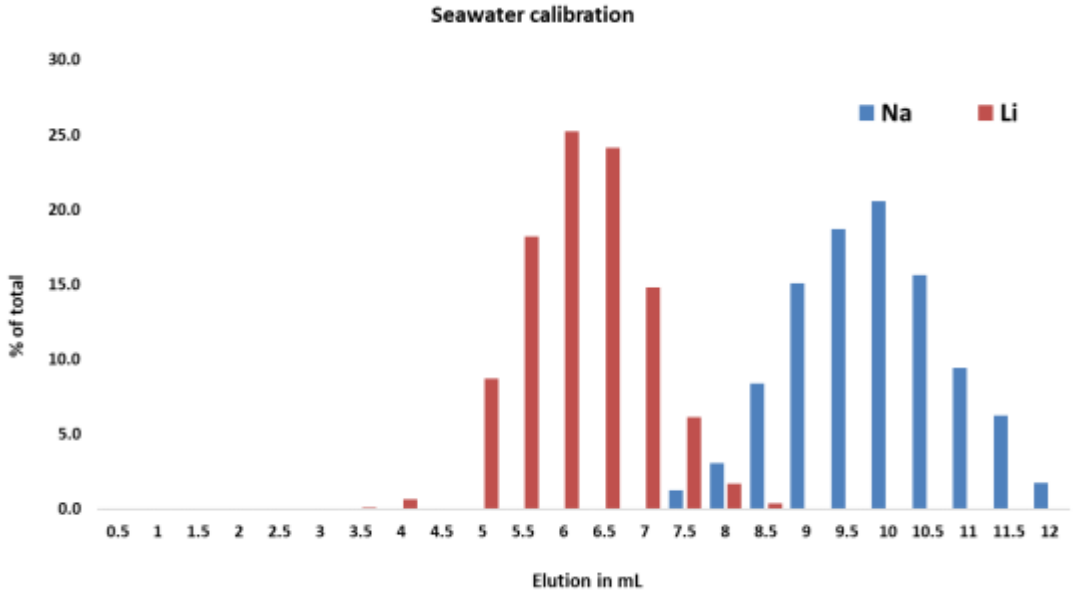

Figure 137: Separation of Na from Li of a seawater sample using the prepFAST-MC™.

Based on this elution curve and after a single column pass, samples collected from 4 to 8.5 mL have a yield of 99.8 % and 12.7 % for Li and Na, respectively. After the second column pass, the yield for Li and Na is 99.7 % and 1.6 %, respectively.

The next step was to test which elution volume is ideal for obtaining the correct Li isotope values for rock standards. The prepfast method was adapted so that after the sample load, all elution until 8.5 mL was collected in a sample vial (destination 1). Note that the entire elution volume was collected to ensure that all Li was collected. Another thing that had to be adjusted was the amount of Li loaded onto the column. Various experiments showed that a maximum of 30 ng Li can be loaded. Three different elution volumes were tested: 0 – 6.5 mL, 0 – 7.0 mL, and 0 – 7.5 mL. Below are the results for rock standards JG-2 and BCR-2 (Table 44).

Table 44: Test results of the Li isotope composition of JG-2 and BCR-2 rock standards after column chromatography with various elution volumes using the prepFAST-MC™.

Sample	δ^7Li vs L-SVEC (‰)
JG-2 (6.5 mL)	1.2 ± 0.2
JG-2 (7.0 mL)	0.1 ± 0.2
JG-2 (7.5 mL)	-0.2 ± 0.2
BCR-2 (6.5 mL)	3.3 ± 0.2
BCR-2 (7.0 mL)	1.5 ± 0.3
BCR-2 (7.5 mL)	1.5 ± 0.2

Reported δ^7Li values for JG-2 are between 0.2 – 0.4 ‰ (James and Palmer, 2000; Vigier et al., 2008). Reported δ^7Li values for BCR-2 are 2.87 ± 0.39 ‰ (Brand et al., 2014). Considering a typical reproducibility (2SE) of 0.5 ‰, the values produced with the prepfast are close to what is reported.

After this test, another two JG-2 samples were processed and 0 – 6.5 mL was collected. The δ^7Li composition of these two samples were -0.2 ± 0.4 ‰ and -0.1 ± 0.3 ‰, which is in good agreement with published δ^7Li values of JG-2 (Table 45).

Table 45: The Li isotope composition of two JG-2 rock standards after column chromatography (6.5 mL elution volume) using the prepFAST-MC™.

Sample	δ^7Li vs L-SVEC (‰)
JG-2 (6.5 mL)	-0.2 ± 0.4
JG-2 (6.5 mL)	0.1 ± 0.3

A final confirmation run was initiated after this with four JG-2 samples, where three samples yielded no Li and one sample was measured at δ^7Li of 2.7 ± 0.3 ‰ (Table 46).

Table 46: Final δ^7Li results of the automated Li chromatography method for JG-2 rock standard samples.

Sample	δ^7Li vs L-SVEC (‰)	Comment
JG-2 (6.5 mL)	2.7 ± 0.3	
JG-2 (6.5 mL)	n/a	No Li in elution (blank level)
JG-2 (6.5 mL)	n/a	No Li in elution (blank level)

The reason why this final test did not work out is unclear. It might have had something to do with either or a combination of 1) resin life, 2) blank contribution and carry-over, 3) resin capacity, or 4) software glitches. The latter is the most likely case as the prepfast would perform correctly ~30 % of the time. Unfortunately, it was decided not to pursue this project.

9.9.2 Removing exchangeable Li from clay minerals

This experiment was undertaken by Justin Meredith (UOW) as an undergraduate project under the supervision of Leo Rothacker.

To remove the exchangeable Li of clay-sized fractions (adsorbed onto mineral surfaces), a clay sample was agitated in leaching solutions (NH_4Cl) with a range of different molarities (0.25M, 0.5M, 1M, 1.25M, 1.5M, 1.75M, 2M). The aim of this experiment was to test how much Li is situated in the exchangeable site relative to structural Li and how removing this Li fraction affects the Li isotope composition of clays.

Equipment:

- NH_4Cl (0.25 M, 0.5 M, 1 M, 1.25 M, 1.5 M, 1.75 M, 2 M)
- 18.2 MΩ water
- Clay sample
- Shaker table
- Centrifuge

One clay sample (D: Thurrowa Road core sample 2 CENTRE (inside and outside)) was chosen for which several aliquots were taken for each leaching solution. The following procedure was done for each sample, except for one sample were the leaching solution was replaced by the equivalent volume of 18.2 MΩ water:

1. Weigh in ~15 mg of clay sample
2. Transfer clay sample into 50 mL centrifuge tube
3. Prepare leaching solutions (0.25 – 2 M NH_4Cl)
4. Add 8 mL of leaching solution into sample tube containing sample.
5. Shake sample tube and put on shaker table from step 4 for 1 hour
6. Centrifuge for 5 min at 4000 rpm and decant leaching solution into pre-cleaned centrifuge tubes

7. Analyse Li concentration of supernatant

The amount of Li in the supernatants varied from 39 to 49 ng. The highest Li content was measured in 1.00 M and 1.25 M NH_4Cl solutions (Table 47).

Table 47: Results for Li isotope composition and concentration of clay leaching experiments with NH_4Cl.

Sample	Description	Li (ng)	δ^7Li (‰)
0.00 M NH_4Cl	supernatant (MQ water)	39	
0.25 M NH_4Cl	supernatant	42	
0.50 M NH_4Cl	supernatant	47	-23.1 ± 0.8
0.75 M NH_4Cl	supernatant	46	
1.00 M NH_4Cl	supernatant	49	
1.25 M NH_4Cl	supernatant	49	
1.50 M NH_4Cl	supernatant	43	
1.75 M NH_4Cl	supernatant	45	
2.00 M NH_4Cl	supernatant	43	
Clay	original/not leached	2,500	-1.4 ± 0.2

The Li content of the clay sample used for this experiment was determined previously and yielded ~2,500 ng in 15 mg (170 ppm). Accordingly, a total of 1.5 to 2.0 % of Li is situated in the exchangeable sites of clay minerals.

The Li isotope composition was only determined for one leaching solution (0.5 M NH_4Cl) and the un-leached 'bulk' clay sample. The reason for this is that too many salts were present in the >0.5 M NH_4Cl supernatants and the 0.25M aliquot was accidently tipped over. The 0.5 M supernatant yielded a δ^7Li composition of -23.1 ± 0.8 ‰ and the un-treated clay sample -1.4 ± 0.2 ‰. The Li concentration of the supernatant was extremely low, which might have affected the measurement. The theoretical contribution of the Li isotope composition of the exchangeable fraction to the clay sample was then calculated to be 0.36 ‰, which is less than the external reproducibility (2SE) of natural clay samples. Hence, no more leaching experiments were conducted.

9.9.3 Li chromatography procedure

Column: Savillex 30 mL Microcolumn, 6.4 mm ID x 9.6 mm OD x 25 cm Capillary (incl. frits)

Resin: Biorad AG50W-X8

Resin height: 9.5c m (3.06 cm^3)

Reagents: A.R. 6M HCl, Milli-Q water, A.R. 1M HCl (titrated: needs to be exact), Ethanol/Acetone

Miscellaneous: Column rack, waste bins, clean PFA vials (15 mL), centrifuge tubes, ICP vials

Column preparations:

- Adjust/cut capillary height of column to ~12 cm
- Insert frit from the bottom and mark 9.5 cm
- Prepare resin by washing it with water several times to remove small particles
- Put resin into columns slowly, drop by drop. If you put it in too fast, you risk creating air bubbles, which in turn will affect the liquid flow
- When loading done, store columns in Milli-Q water

Sample preparations:

- Complete dissolution is vital
- Take up sample in 1.5 mL 1M HCl at the end of digestion
    - 180 ng Li
    - <1.5 meq
    - Load no more than 60 ng of Li
    - Load no more than 0.5 meq [mg x valence / molecular weight]

Cleaning:

- Put columns on a designated rack and place waste bins below. Waste bins volume should be at least 60mL and reasonably close to the bottom part of the column to avoid splashes.
- Fill full reservoir with A.R. 6M HCl. Do not fill it up too quickly to avoid creating air bubbles. This should take roughly 2.5 – 4 hours. Columns clog up easily when dry. Write down when you started and check frequently if all 6M HCl has gone through.
- Notice the resin will shrink. Observe for air bubbles or gaps within the resin.
- When all HCl went through, rinse with Milli-Q, ~2 mL

Conditioning:

- Add 8mL of 1M HCl. Remember, it has to be exactly 1M. Add it slowly to avoid air bubbles.

Sample loading:

1. Take up 0.5 mL of sample and put it into column, slowly drop by drop on top of the resin.
2. Discard the leftovers into a clean centrifuge tube.
3. Using a new/clean pipette tip, add 0.5 mL of 1M HCl into the (now empty) sample vial, move the vial to make sure everything is collected, then take it up again and put it slowly into column. Add 3 mL of 1M HCl (new pipette tip)
4. When columns stopped dripping, remove waste bins and replace them with clean PFA vials
5. Add 4 mL of 1M HCl (use same pipette tip as last step)
6. When done, evaporate what's inside the PFA vial at 100ºC
7. While vials are still hot, add 0.5 mL 1M HCl and ultrasonicate for 15 minutes at 60°C
8. Pass this through columns a second time and repeat step 1 – 6
9. After step 6, while vials are still hot, add 4mL suprapur 2 % HNO_3 and ultrasonicate for 15 minutes at 60°C
10. Transfer into pre-weighed ICP vials (weigh before and after)

9.9.4 Li isotope analysis on Neptune Plus:

Equipment:

- Primary standards (L-SVEC, IRMM16)
    - 30 ppb solutions
- Secondary standards (Li-6N, Li-7N)
    - 30 ppb solutions
- 2% HNO_3 (suprapur)
- Milli-Q water
- Appropriate cones (x-skimmer and jet sampler for ~30 ppb concentrations)
- Cyclonic spray chamber
- Nebuliser

Procedure:

- In Detector calibration, click on Gain
- After ~20 minutes, check if the right amplifiers are being used
- H4 (measures ^{7}Li) should have a gainfactor of ~1, L4 (measures ^{6}Li) should be at ~0.1
- In the cup configuration tab (Figure 138), load 'Lithium' and click on 'set collection' (if necessary)

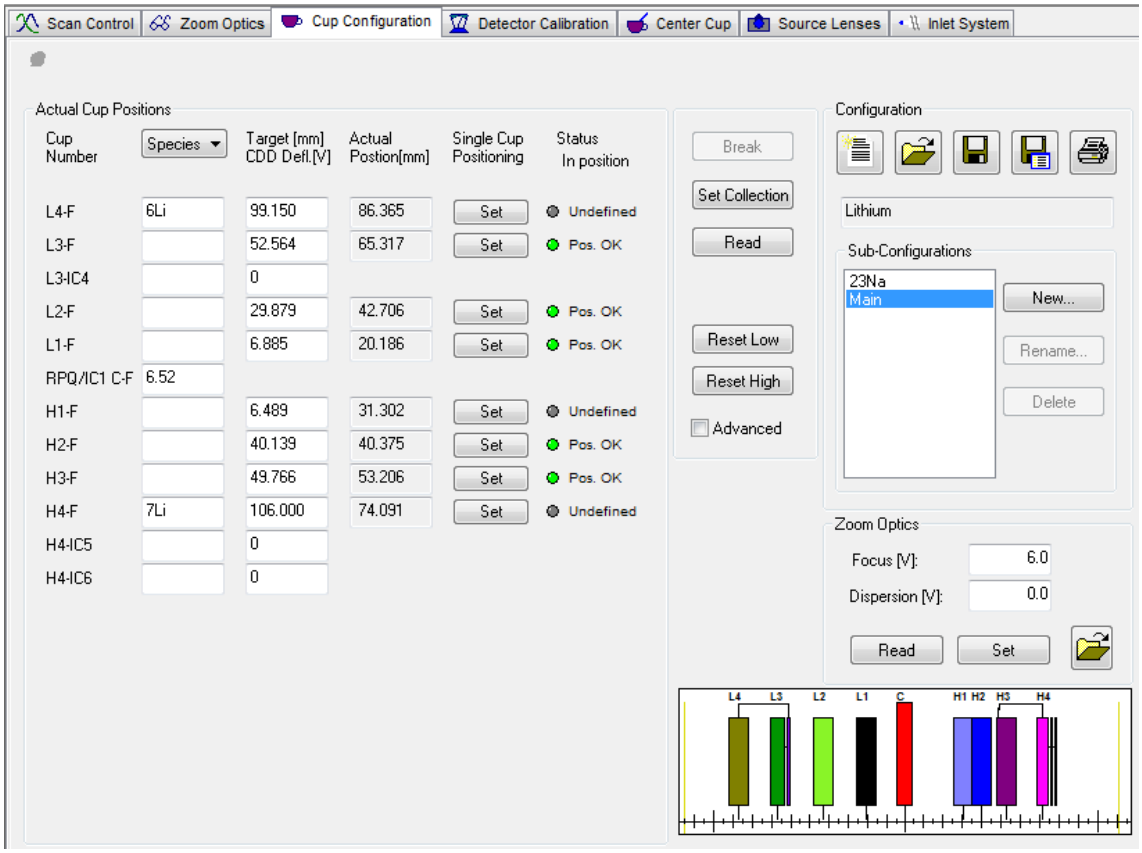

Figure 138: Cup configuration for measuring Li isotopes on the Neptune Plus MC ICP-MS.

- Load previous tuning settings (sort by date)
- Send autosampler probe into tuning solution (30 ppb IRMM16)
- Open Analyser gate in Inlet system
- Tuning settings for Inlet System and Sources Lenses should be similar to what is shown in Figure 139.

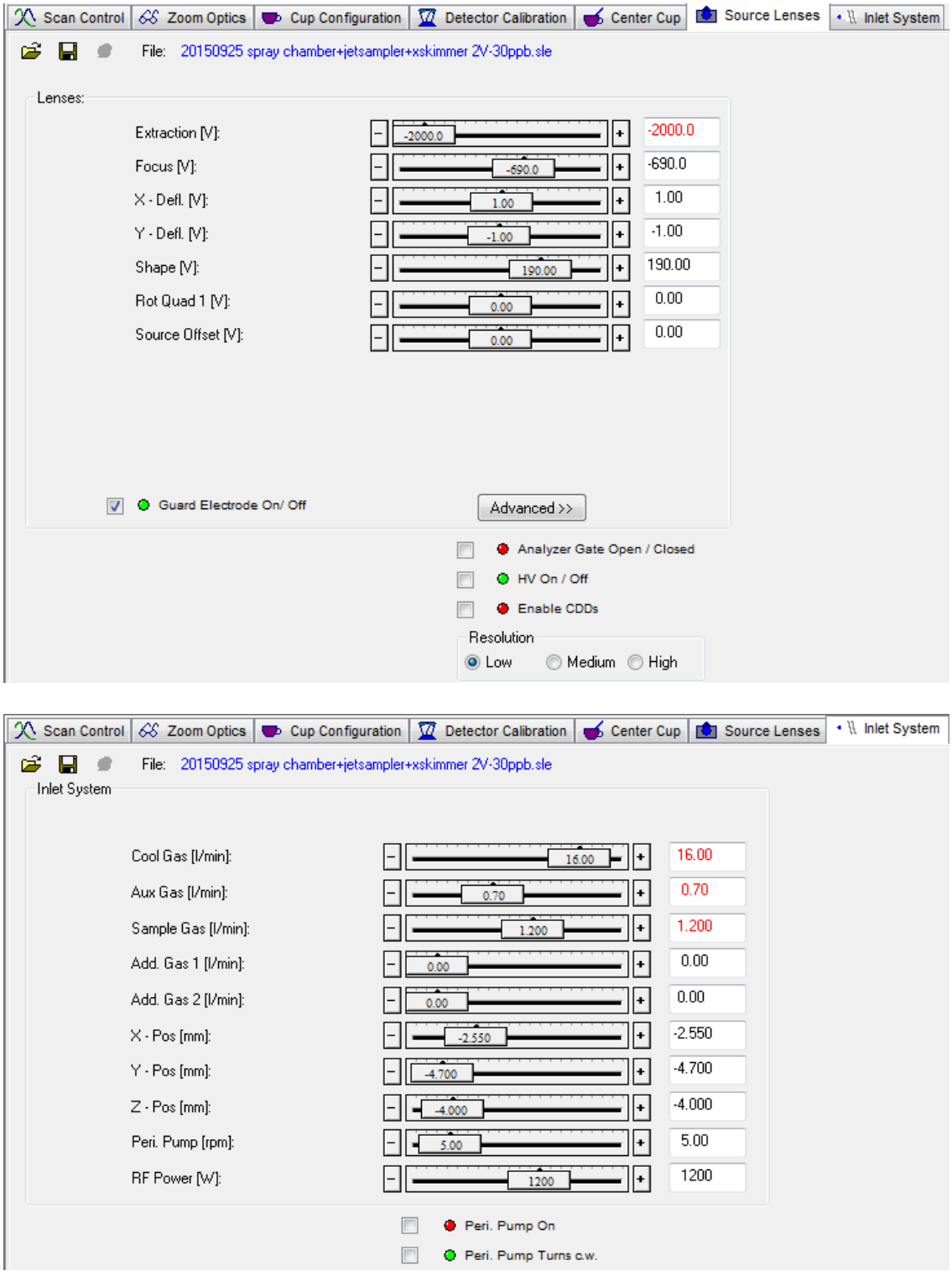

Figure 139: Source Lenses and Inlet System configuration for measuring Li isotopes on the Neptune Plus MC ICP-MS.

- Adjust tuning by playing with sample gas first
    - Do not go above 1.4 L/min

- When you maximise your signal (and it's stable), adjust torch positions (X, Y, Z)
    - Torch position parameters only need to be changed when the torch was taken out and reinstalled
- Move to Source Lenses tab and adjust Focus, X-Defl., Y-Defl., and shape
- An ideal tuning with X-skimmer and Jet sampler cones should result in about 2 V/30 ppb
- After optimising the signal, do a mass scan in continuous mode and adjust Zoom optics (Figure 140)

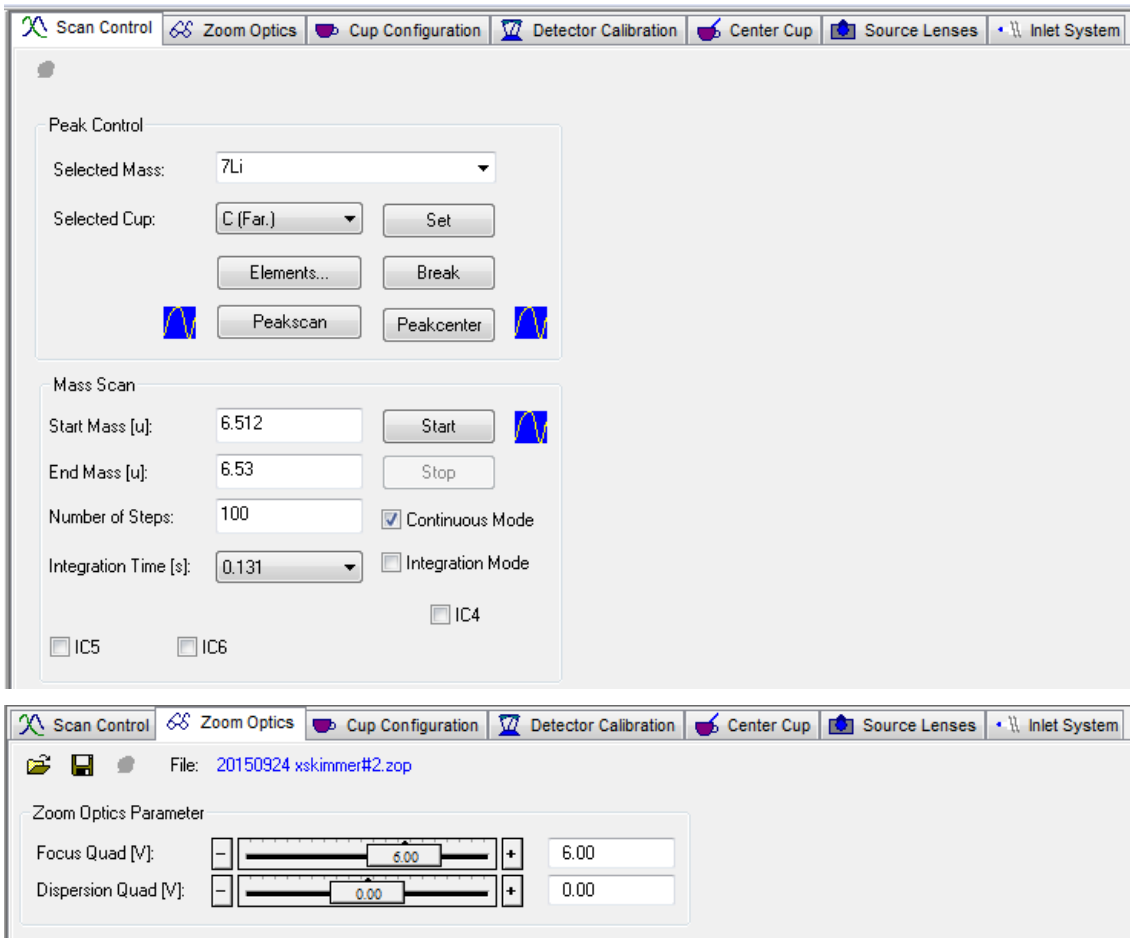

Figure 140: Scan Control and Zoom Optics tab on the Neptune Plus MC ICP-MS software.

- Usually the focus quad should be between 6 and 10
- A good peak shape looks something like this Figure 141:

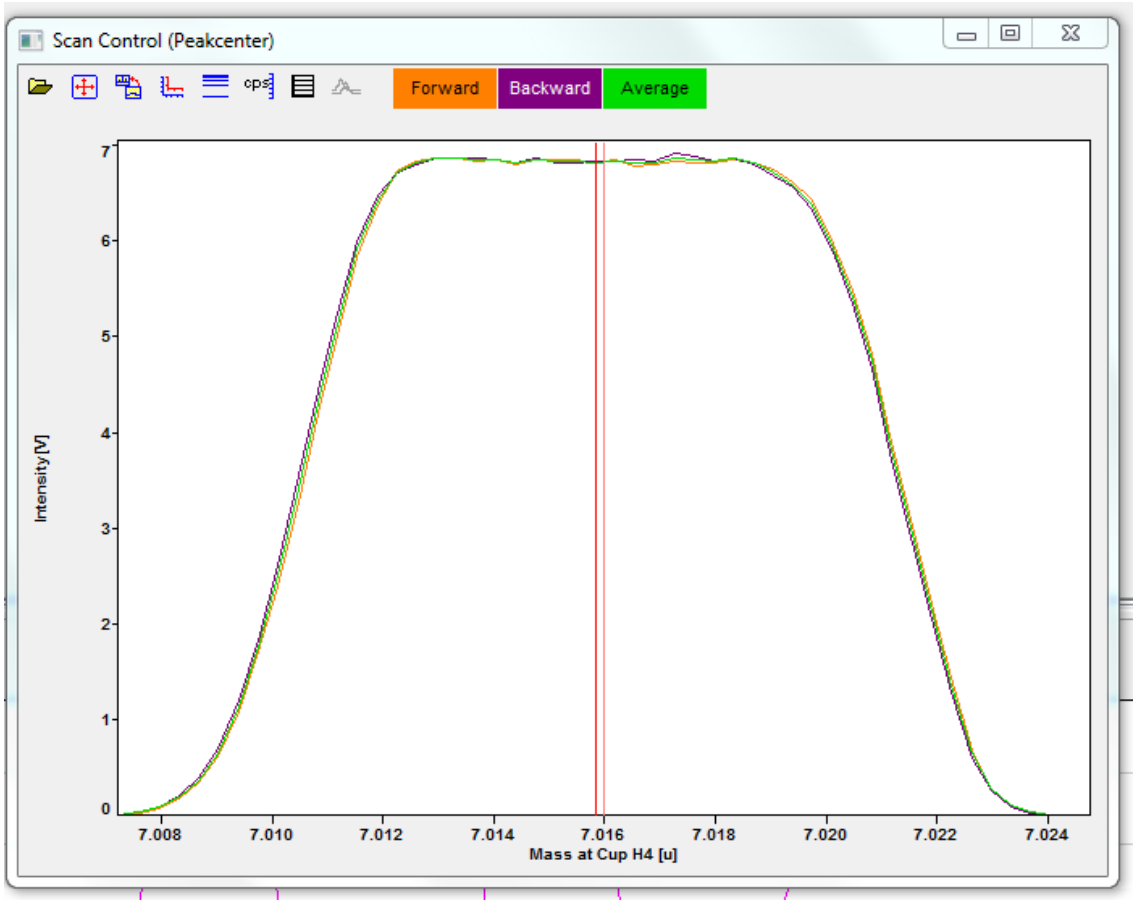

Figure 141: Example of a good peak shape for measuring Li isotopes on the Neptune Plus MC ICP-MS.

- When all this is satisfying, send probe to wash, then into 2% HNO_3 to check for background noise
- Background should be around 1-2 mV on ^{7}Li

Sequence:

- For Li isotope analysis we use standard bracketing (Figure 142):

Run Number	ampl Type	Sample ID	Filename	Blank 1 Line	Blank 2 Line	Standard 1 Line	Standard 2 Line
1	BLK	2% HNO3	001-2% HNO3	0	0	0	0
2	STD	IRMM16	002-IRMM16	1	3	0	0
3	BLK	2% HNO3	003-2% HNO3	0	0	0	0
4	SMP	Li-7N	004-Li-7N	3	5	2	6
5	BLK	2% HNO3	005-2% HNO3	0	0	0	0
6	STD	IRMM16	006-IRMM16	5	7	0	0
7	BLK	2% HNO3	007-2% HNO3	0	0	0	0
8	SMP	Li-6N	008-Li-6N	7	9	6	10
9	BLK	2% HNO3	009-2% HNO3	0	0	0	0
10	STD	IRMM16	010-IRMM16	9	11	0	0
11	BLK	2% HNO3	011-2% HNO3	0	0	0	0
12	SMP	Li-6N	012-Li-6N	11	13	10	14
13	BLK	2% HNO3	013-2% HNO3	0	0	0	0
14	STD	IRMM16	014-IRMM16	13	15	0	0
15	BLK	2% HNO3	015-2% HNO3	0	0	0	0
16	SMP	Li-6N	016-Li-6N	15	17	14	18
17	BLK	2% HNO3	017-2% HNO3	0	0	0	0
18	STD	IRMM16	018-IRMM16	17	19	0	0
19	BLK	2% HNO3	019-2% HNO3	0	0	0	0
20	SMP	Li-6N	020-Li-6N	19	21	18	22
21	BLK	2% HNO3	021-2% HNO3	0	0	0	0
22	STD	IRMM16	022-IRMM16	21	23	0	0
23	BLK	2% HNO3	023-2% HNO3	0	0	0	0
24	SMP	Li-7N	024-Li-7N	23	25	22	26
25	BLK	2% HNO3	025-2% HNO3	0	0	0	0
26	STD	IRMM16	026-IRMM16	25	27	0	0
27	BLK	2% HNO3	027-2% HNO3	0	0	0	0
28	SMP	Li-7N	028-Li-7N	27	29	26	30
29	BLK	2% HNO3	029-2% HNO3	0	0	0	0

Figure 142: Standard bracketing sequence for measuring Li isotopes on the Neptune Plus MC ICP-MS.

Method settings:

- Values are shown in Figure 143
- Be sure to have an idle time of 3s

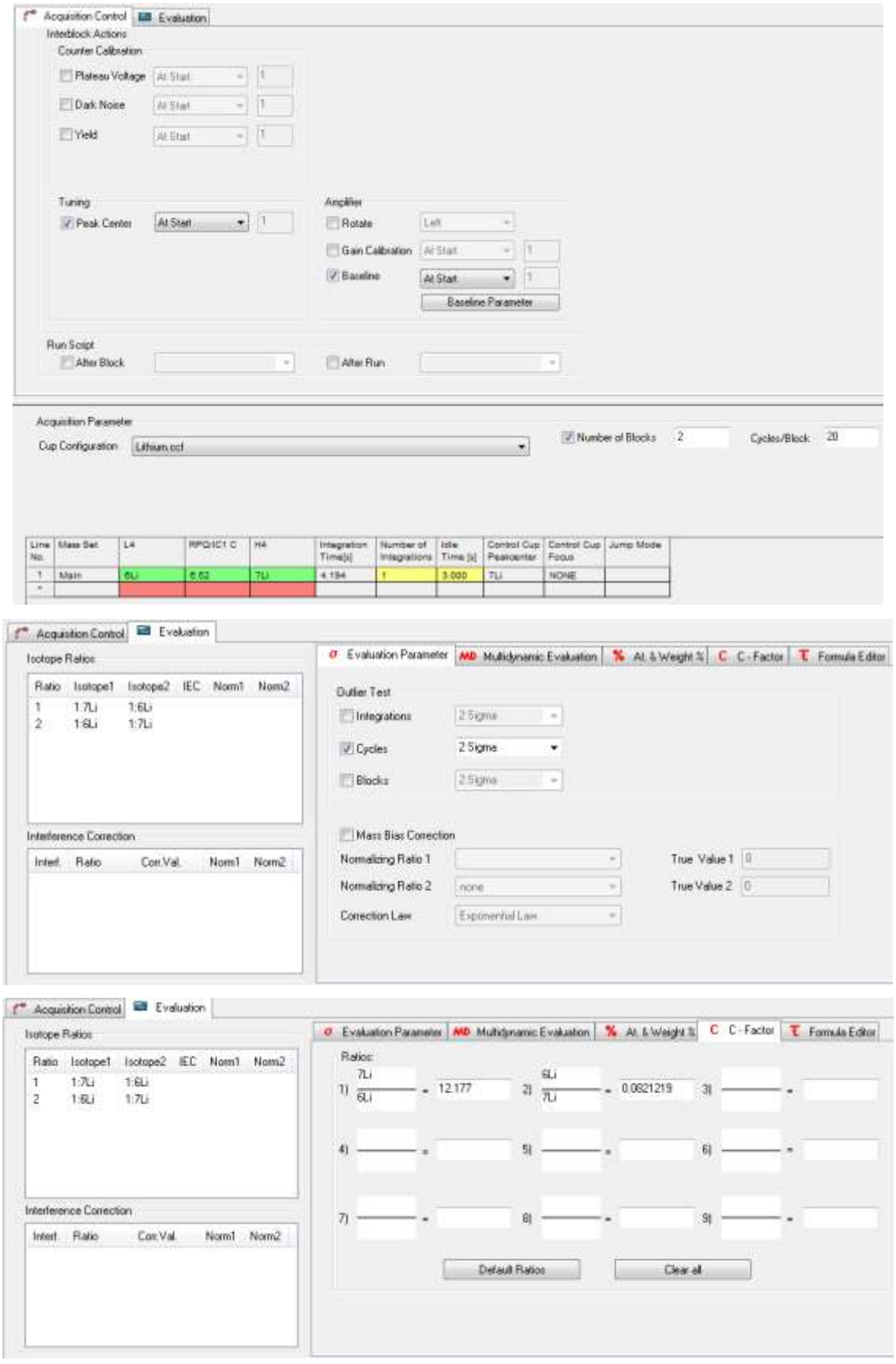

Figure 143: Method parameters for measuring Li isotopes on the Neptune Plus MC ICP-MS.

9.9.5 Clay separation procedure

Equipment:

- Centrifuge
- Meter scale
- Centrifuge tubes (50 mL)
- Milli-Q water
- (NaPO3)6
- stopwatch

Preparation:

- Wet-sieve sediment to <63 µm
- Milli-Q water has to be at room temperature ~20°C
- Measure distance between bottom of centrifuge tube and centre of centrifuge
- Measure distance between 50mL line of centrifuge tube and centre of centrifuge
- Be sure that the swing-bucket is installed/in use
- Set RPM to: 1000
- Set acceleration to: 9
- Set deceleration to: 5
- Without any vials inside, press start and note down the time it takes to accelerate to 1000 rpm (here: 11 seconds)
- Press stop and note down how long it takes to decelerate to a full stop (here: 31 seconds)

The above parameters can then be used to calculate the time it takes to separate <2 µm from >2 µm (Table 48).

Table 48: Swing bucket centrifuge configuration for clay (<2 µm) separation.

Swing Bucket Centrifuge in Distillery	
@23°C	
t (seconds)	176
n	0.00935
R	18
S	9.5
N	1000
Diameter	0.0001
density clay	2.65
density water	1
rev/sec	16.67
Pi	3.14
acceleration	11
deceleration	31
Hit stop after (s):	145.6

t = time; n = viscosity; R = distance bottom tube to centre; S = distance liquid surface to centre; N = rounds per minute

Procedure:

1. Weigh in ~25 g of sediment (depends on clay content)
    - If this yields too little clay, take a second aliquot
2. Add 0.25 g of (NaPO3)6 into each vial (label as sample # BULK)
3. Fill up each vial until the 50mL mark and shake them
4. Put vials into centrifuge (remember to have the same amount and weight of vials on the opposite side)
5. Press start on centrifuge and on stopwatch
6. After 2 minutes and 25 seconds, press stop (try to be as precise as possible)
7. The supernatant is now your clay fraction. Discard it into another clean centrifuge tube (label sample # CLAY)
8. Put the sample from step 7 (sample # CLAY) into the centrifuge, adjust the centrifuge to 4000 rpm and let it run for 15 minutes

9. After 15 minutes, discard the supernatant. The bottom sediment is now pure clay sized (<2 µm)
10. After step 7 you still have the remaining sample # BULK vial. Fill it up with Milli-Q, shake it, and put it inside the centrifuge.
11. Re-adjust the centrifuge to 1000 rpm, press start and stop again after 2 minutes and 25 seconds.
12. The supernatant is again your clay size fraction. Add it into the previous clay vial from step 7.

Repeat step 8 – 12 three to four times until the supernatant after step 11 is more or less clear.

This procedure yields a separation of >94 % clay.

9.9.6 Procedure for making a precise 1 molar HCl solution for Li column chromatography

Equipment:

- Titration agent (NaOH (s) or already titrated NaOH 1 M or 0.5 M (l))
- Milli-Q water
- Distilled water (Ellix)
- Scale
- Burette (at least 50 mL)
- Magnetic stirrer (only if titration agent comes as a solid)
- Hydrochloric acid
- 2x 1 L Erlenmeyer flasks
- Indicator (Methyl orange or equivalent)

Procedure:

Step 1:

- Make up a 1 M NaOH solution (this is the standard solution)
- Weigh in the calculated amount of NaOH (s) needed (use a precise scale for that) and dilute it with distilled water to get a final volume of 100 mL
- Use a magnetic stirrer to better dissolve the NaOH (s)
- Do the same thing with the hydrochloric acid → this is your solution of UNKNOWN concentration which should be at least close to 1 molar @ 100 mL

Step 2:

- Now you have precisely 1 M NaOH standard solution, 100 mL
- Your 1 M hydrochloric acid, 100 mL, is not accurate yet
- Add a few drops of indicator into the HCl flask
- Put the HCl solution below a burette
- Fill up the burette with your 1 M NaOH solution
- Take note on the amount of NaOH that is inside the burette
- If your burette is only 50 mL, fill it up once again after you added the NaOH solution into the HCl
- After adding about 80 % of the NaOH, keep adding it slowly drop by drop and shake the HCl flask
- At the end of titration the indicator should change colour. Remember to add the NaOH drop by drop as the endpoint of the titration is very sensitive.

Step 3:

- Take a note at what volume of NaOH the HCl changed colour (or lost colour, depending on which indicator you used)
- The idea is to have the endpoint reached after adding 100 mL of NaOH into 100 mL HCl
    - Ideally you want >95 mL of NaOH to reach the endpoint so that you have a precision of about 5 %

Step 4:

- If your UNKNOWN HCl solution changed color before 95 mL of your NaOH standard solution, that means your UNKOWN HCl was less than 1 molar
    - Go back to step 1 and increase molarity of your UNKNOWN 1 M HCl (by a few percent only)
- If your UNKNOWN HCl solution did not change color after 100 mL NaOH standard solution was added, that means your UNKOWN HCl was too high in molarity
    - Go back to step 1 and decrease molarity of your UNKNOWN 1 M HCl

References

Aciego, S. M., Bourdon, B., Lupker, M. & Rickli, J. 2009. A new procedure for separating and measuring radiogenic isotopes (U, Th, Pa, Ra, Sr, Nd, Hf) in ice cores. *Chemical Geology,* 266**,** 194-204.

Ahlers, W. W., Reid, M. R., Kim, J. P. & Hunter, K. A. 1990. Contamination-free sample collection and handling protocols for trace elements in natural fresh waters. *Marine and Freshwater Research,* 41**,** 713-720.

Ali, A. & Srinivasan, G. 2011. Precise thermal ionization mass spectrometric measurements of 142 Nd/144 Nd and 143 Nd/144 Nd isotopic ratios of Nd separated from geological standards by chromatographic methods. *International Journal of Mass Spectrometry,* 299**,** 27-34.

Arakawa, Y. 1992. 143Nd/144Nd ratios of twelve GSJ rock reference samples and reproducibility of the data. *Geochemical Journal,* 26**,** 105-109.

Balter, V. & Vigier, N. 2014. Natural variations of lithium isotopes in a mammalian model. *Metallomics,* 6**,** 582-586.

Baxter, D. C., Rodushkin, I., Engström, E. & Malinovsky, D. 2006. Revised exponential model for mass bias correction using an internal standard for isotope abundance ratio measurements by multi-collector inductively coupled plasma mass spectrometry. *Journal of Analytical Atomic Spectrometry,* 21**,** 427-430.

Brand, W. A., Coplen, T. B., Vogl, J., Rosner, M. & Prohaska, T. 2014. Assessment of international reference materials for isotope-ratio analysis (IUPAC Technical Report). *Pure and Applied Chemistry,* 86**,** 425-467.

Carignan, J., Cardinal, D., Eisenhauer, A., Galy, A., Rehkamper, M., Wombacher, F. & Vigier, N. 2004. A reflection on Mg, Cd, Ca, Li and Si isotopic measurements and related reference materials. *Geostandards and Geoanalytical Research,* 28**,** 139-148.

Carignan, J., Vigier, N. & Millot, R. 2007. Three Secondary Reference Materials for Lithium Isotope Measurements: Li7-N, Li6-N and LiCl-N Solutions. *Geostandards and Geoanalytical Research,* 31**,** 7-12.

Chu, Z.-Y., Li, C.-F., Hegner, E., Chen, Z., Yan, Y. & Guo, J.-H. 2014a. High-Precision 143Nd/144Nd Ratios from NdO+ Data Corrected with in-Run Measured Oxygen Isotope Ratios. *Analytical chemistry,* 86**,** 11141-11150.

Chu, Z., Chen, F., Yang, Y. & Guo, J. 2009. Precise determination of Sm, Nd concentrations and Nd isotopic compositions at the nanogram level in geological samples by thermal ionization mass spectrometry. *Journal of Analytical Atomic Spectrometry,* 24**,** 1534-1544.

Chu, Z., Guo, J., Yang, Y., Qi, L. & Li, C. 2014b. Precise determination of Sm and Nd concentrations and Nd isotopic compositions in highly depleted ultramafic reference materials. *Geostandards and Geoanalytical Research,* 38**,** 61-72.

Crocket, K. C., Lambelet, M., Van De Flierdt, T., Rehkämper, M. & Robinson, L. F. 2014. Measurement of fossil deep-sea coral Nd isotopic compositions and concentrations by TIMS as NdO+, with evaluation of cleaning protocols. *Chemical Geology,* 374**,** 128-140.

Ercolani, C. P., Enge, T. G., Rothacker, L., Field, M. P. & Dosseto, A. (under review). An automated chromatography procedure for the analysis of 143Nd/144Nd isotope ratios in geological materials.

Flanagan, F. J. & Flanagan, F. J. 1976. *Descriptions and analyses of eight new USGS rock standards,* US Government Printing Office, pp.

Flesch, G., Anderson, A. & Svec, H. 1973. A secondary isotopic standard for 6Li/7Li determinations. *International Journal of Mass Spectrometry and Ion Physics,* 12**,** 265-272.

Francke, A., Wagner, B., Leng, M. J. & Rethemeyer, J. 2013. A Late Glacial to Holocene record of environmental change from Lake Dojran (Macedonia, Greece). *Climate of the Past,* 9**,** 481-498.

Gao, S., Rudnick, R. L., Yuan, H.-L., Liu, X.-M., Liu, Y.-S., Xu, W.-L., Ling, W.-L., Ayers, J., Wang, X.-C. & Wang, Q.-H. 2004. Recycling lower continental crust in the North China craton. *Nature,* 432**,** 892-897.

Hillier, S. 2000. Accurate quantitative analysis of clay and other minerals in sandstones by XRD: comparison of a Rietveld and a reference intensity ratio (RIR) method and the importance of sample preparation. *Clay Minerals,* 35**,** 291-302.

Huang, K.-F., Blusztajn, J., Oppo, D. W., Curry, W. B. & Peucker-Ehrenbrink, B. 2012. High-precision and accurate determinations of neodymium isotopic compositions at nanogram levels in natural materials by MC-ICP-MS. *Journal of Analytical Atomic Spectrometry,* 27**,** 1560-1567.

Imai, N., Terashima, S., Itoh, S. & Ando, A. 1995. Compilation of analytical data for minor and trace elements in seventeen GSJ geochemical reference samples,"igneous rock series". *Geostandards Newsletter,* 19**,** 135-213.

James, R. H. & Palmer, M. R. 2000. The lithium isotope composition of international rock standards. *Chemical Geology,* 166**,** 319-326.

Li, C.-F., Chen, F. & Li, X.-H. 2007. Precise isotopic measurements of sub-nanogram Nd of standard reference material by thermal ionization mass spectrometry using the NdO+ technique. *International Journal of Mass Spectrometry,* 266**,** 34-41.

Luo, X., Rehkämper, M., Lee, D.-C. & Halliday, A. N. 1997. High precision 230 Th/232 Th and 234 U/238 U measurements using energyfiltered ICP magnetic sector multiple collector mass spectrometry. *International Journal of Mass Spectrometry and Ion Processes,* 171**,** 105-117.

Miyazaki, T. & Shuto, K. 1998. Sr and Nd isotope ratios of twelve GSJ rock reference samples. *Geochemical Journal,* 32**,** 345-350.

Pistiner, J. S. & Henderson, G. M. 2003. Lithium-isotope fractionation during continental weathering processes. *Earth and Planetary Science Letters,* 214**,** 327-339.

Raczek, I., Jochum, K. P. & Hofmann, A. W. 2003. Neodymium and strontium isotope data for USGS reference materials BCR-1, BCR-2, BHVO-1, BHVO-2, AGV-1, AGV-2, GSP-1, GSP-2 and eight MPI-DING reference glasses. *Geostandards and Geoanalytical Research,* 27**,** 173-179.

Richter, S., Kuhn, H., Aregbe, Y., Hedberg, M., Horta-Domenech, J., Mayer, K., Zuleger, E., Burger, S., Boulyga, S., Kopf, A., Poths, J. & Mathew, K. 2011. Improvements in routine uranium isotope ratio measurements using the modified total evaporation method for multi-collector thermal ionization mass spectrometry. *Journal of Analytical Atomic Spectrometry,* 26**,** 550-564.

Saji, N. S., Wielandt, D., Paton, C. & Bizzarro, M. 2016. Ultra-high-precision Nd-isotope measurements of geological materials by MC-ICPMS. *Journal of analytical atomic spectrometry,* 31**,** 1490-1504.

Scher, H. D. & Delaney, M. L. 2010. Breaking the glass ceiling for high resolution Nd isotope records in early Cenozoic paleoceanography. *Chemical Geology,* 269**,** 329-338.

She, Z., Ma, C., Mason, R., Li, J., Wang, G. & Lei, Y. 2006. Provenance of the Triassic Songpan–Ganzi flysch, west China. *Chemical Geology,* 231**,** 159-175.

Shibata, T., Yoshikawa, M. & Tatsumi, Y. 2003. An analytical method for determining precise Sr and Nd isotopic compositions and results for thirteen rock standard materials. *Frontier Research on Earth Evolution,* 1**,** 363-367.

Sims, K. W., Gill, J. B., Dosseto, A., Hoffmann, D. L., Lundstrom, C. C., Williams, R. W., Ball, L., Tollstrup, D., Turner, S. & Prytulak, J. 2008. An inter-laboratory assessment of the thorium isotopic composition of synthetic and rock reference materials. *Geostandards and Geoanalytical Research,* 32**,** 65-91.

Tanaka, T., Togashi, S., Kamioka, H., Amakawa, H., Kagami, H., Hamamoto, T., Yuhara, M., Orihashi, Y., Yoneda, S. & Shimizu, H. 2000. JNdi-1: a neodymium isotopic reference in consistency with LaJolla neodymium. *Chemical Geology,* 168**,** 279-281.

Tessier, A., Campbell, P. G. & Bisson, M. 1979. Sequential extraction procedure for the speciation of particulate trace metals. *Analytical chemistry,* 51**,** 844-851.

Valeriano, C., Vaz, G., Medeiros, S., Neto, C., Ragatky, C. & Geraldes, M. The Neodymium isotope composition of the JNdi-1 oxide reference material: results from the LAGIR Laboratory, Rio de Janeiro. VI South American Symposium on Isotope Geology, 2008. 1-2.

Vigier, N., Decarreau, A., Millot, R., Carignan, J., Petit, S. & France-Lanord, C. 2008. Quantifying Li isotope fractionation during smectite formation and implications for the Li cycle. *Geochimica et Cosmochimica Acta,* 72**,** 780-792.

Weis, D., Kieffer, B., Maerschalk, C., Barling, J., De Jong, J., Williams, G. A., Hanano, D., Pretorius, W., Mattielli, N. & Scoates, J. S. 2006. High-precision isotopic characterization of USGS reference materials by TIMS and MC-ICP-MS. *Geochemistry, Geophysics, Geosystems,* 7.

Yang, Y.-H., Chu, Z.-Y., Wu, F.-Y., Xie, L.-W. & Yang, J.-H. 2011. Precise and accurate determination of Sm, Nd concentrations and Nd isotopic compositions in geological samples by MC-ICP-MS. *Journal of Analytical Atomic Spectrometry,* 26**,** 1237-1244.

Yang, Y., Wu, F., Xie, L. & Zhang, Y. 2009. High-precision measurements of the 143Nd/144Nd isotope ratio in certified reference materials without Nd and Sm

separation by multiple collector inductively coupled plasma mass spectrometry. *Analytical Letters,* 43**,** 142-150.

Zhang, H., Gao, S., Zhong, Z., Zhang, B., Zhang, L. & Hu, S. 2002. Geochemical and Sr–Nd–Pb isotopic compositions of Cretaceous granitoids: constraints on tectonic framework and crustal structure of the Dabieshan ultrahigh-pressure metamorphic belt, China. *Chemical Geology,* 186**,** 281-299.

10 Conclusions

Over geologic time scales, chemical weathering is a major control of the carbon cycle, where continental silicate weathering consumes atmospheric CO_2 during weathering reactions (Walker et al., 1981). The coupling between CO_2 consumption via silicate weathering and climate, as well as the timescale at which chemical weathering interacts with climate is still poorly understood. An increase of the chemical weathering flux is generally observed when the hydrological cycle becomes enhanced as a result of increased rainfall (Bayon et al., 2012; von Blanckenburg et al., 2015a). However, evidence for this influence over short timescales (<10,000 years) is scarce and studies usually suggest that only a long-term change of climate or tectonic activity can significantly affect continental weathering at a large scale (Bluth and Kump, 1994; Munhoven, 2002). The currently active debates concerning the feedback between weathering and global climate over large and short timescales are in detail discussed in section 2.1 and 2.2, respectively. The main focus of this thesis was to investigate short-term changes (<100,000 years) in chemical weathering in response to climatic fluctuations.

The Li isotope proxy was applied as a tracer for chemical weathering reactions to evaluate present weathering reactions in the mixed-lithology Murrumbidgee River Basin. Furthermore, fine-grained sediments from palaeo-river systems in the Murrumbidgee River Basin were investigated to reconstruct changes in chemical weathering conditions in response to hydroclimatic variability over the last glacial cycle (100,000 years). Finally, through the analyses of Li isotopes in fine-grained sediments from the Lake Dojran sediment record (Francke et al., 2013), the temporal variation of soil development in ancient Greece/Macedonia (FYROM) throughout the Holocene was evaluated.

10.1 Present weathering conditions in the Murrumbidgee River Basin

The δ^7Li composition of Murrumbidgee River dissolved loads undergoes significant changes from upper to lower reaches which suggests that the Murrumbidgee River obtains its isotopic signature from various individual weathering regimes in the upper catchment. Despite large differences of the δ^7Li composition of the source rocks, Li isotope values of waters and fine-grained sediments (<2 µm) from monolithologic catchments (volcanic, granitic, sedimentary siliclastic) cover a large but similar range, suggesting that the different weathering regimes are not directly controlled by the underlying bedrock. The

δ^7Li composition of clay-sized fractions shows a significant correlation with river water pH, which suggests that the degree of Li isotope fractionation during secondary mineral formation may be indirectly governed by levels of vegetation cover present during weathering reactions. A strong correlation exists between the Li isotope composition of river dissolved loads and respective clay-sized fraction, suggesting that sediments and waters are in isotopic equilibrium, and δ^7Li values of clay-sized fractions evolve as a function of the δ^7Li composition of the solution. This suggests that the clay-sized fraction of sediment archives may be used to reconstruct the δ^7Li composition of palaeo dissolved loads, which in turn can be used to characterise palaeo weathering environments. Based on the Li isotope composition of the dissolved load, the annual chemical weathering flux (4.3 t/km^2/yr), erosion and denudation rates, the weathering regime of the Murrumbidgee River can be categorised as supply-limited, which is associated with high weathering intensities.

10.2 Weathering conditions in the Murrumbidgee River Basin over the last glacial cycle

Based on the δ^7Li composition of clay-sized fractions of four palaeo-channel river systems in the Murrumbidgee River Basin, the weathering conditions in SE Australia over the past 100,000 years were reconstructed. Low weathering intensities prevailed during OIS 5 and 3, which may be linked to enhanced erosion rates associated with a warm and wet climate. From the late OIS 3 until present, the Li isotope composition of the sediment record suggests higher weathering intensities as a possible response to an increasingly drier climate, which decreased erosion rates in the Murrumbidgee River Basin and allowed longer water-rock reaction times. This suggests that over the last glacial cycle, the weathering regime of the Murrumbidgee River Basin has shifted from an 'intermediate weathering intensity' to a 'high weathering intensity' (at present), as a consequence of a weaker hydrological activity (based on independent data). In conclusion, these results show that chemical weathering reactions in the Murrumbidgee River Basin are tightly coupled with hydroclimatic variations.

10.3 Soil development at Lake Dojran over the Holocene

Another aspect investigated in this thesis is the temporal variation of soil development in ancient Greece/Macedonia (FYROM) throughout the Holocene. Here, variations of the Li isotope ratio of fine-grained sediments (<63 µm) from the Lake Dojran sediment

record were interpreted as reflecting the degree of soil development and U isotope ratios were used to reconstruct the depth of soil erosion. While soil erosion responded almost immediately to short-lived climatic events, such as the 8.2 ka and 4.2 ka events, soil development was not affected by these events. Instead, soil formation responded steadily to the end of the Younger Dryas and the warming at the beginning of the Holocene and became more developed from 12,300 to 3,500 cal yr BP. At 3,500 cal yr BP, the data indicate a dramatic erosion event, triggered by intense human activity, which negatively affected the natural soil development. This was linked to the emergence of agricultural practices in ancient Greece/Macedonia. The depletion of soil resources could have triggered, or at least contributed, to the collapse of an ancient civilisation also known as the Greek 'Dark Ages'.

10.4 Final conclusions

The Li isotope data obtained this PhD show that chemical weathering reactions in the Murrumbidgee River Basin are tightly coupled with hydroclimatic variations and significant changes in the weathering regime can occur over geologically short timescales (<20,000 years). This is in agreement with previous findings by Dosseto et al. (2015), who applied the Li isotope proxy to sediment archives in the Himalaya range and proposed that chemical weathering reactions evolve as a function of monsoon intensities. Data from the Lake Dojran sediment record show that over shorter timescales (500 – 1,000 years) and under natural conditions, weathering (and associated soil formation) is not sensitive to hydroclimatic variations. However, with the emergence of agricultural practices in ancient Greece/Macedonia (FYROM) between 3,500 and 3,100 cal yr BP, the natural soil environment was disrupted rapidly, which may have resulted in the depletion of soil resources, possibly triggering or at least contributing to the collapse of an ancient civilisation.

Findings of this thesis show that the Li isotope proxy can be applied to sediment archives to reconstruct past and present continental weathering conditions. The application of this proxy to other sediment records will improve our understanding of weathering and climate interactions.

10.5 Limitations and future perspectives

In this thesis, the Li isotope proxy was applied to sediment archives (and river dissolved loads) to reconstruct past and present changes in chemical weathering conditions. Few

studies exist that have applied this palaeo-proxy to clays or fine-grained detrital sediments (e.g. (Dosseto et al., 2015; Bastian et al., 2017)), and the interpretation of δ^7Li values of such sediments in terms of chemical weathering conditions is still under debate. Further data on present-day and past fine-grained sediments are certainly needed in order to identify, understand, and model the relationship between the δ^7Li composition and chemical weathering reactions.

In this study, the relationship between the δ^7Li composition of river dissolved loads and solid weathering products (clays) is evaluated. Results for the Murrumbidgee River Basin indicate that the δ^7Li composition of river dissolved load and the δ^7Li composition of the respective clay-sized fraction (δ^7Li_{clay}) of river sediments positively correlate. Thus, temporal changes in δ^7Li_{clay} have been used to infer the Li isotope variation of corresponding dissolved loads. However, this relationship needs to be further tested by increasing the amount of sample pairs and investigating samples from different climatic zones.

It was found that δ^7Li_{clay} may be linked to the pH of the corresponding dissolved load. Changes in water pH can be a function of oxidation of organic matter, as shown by Viers et al. (1997); Deberdt et al. (2002); Dellinger et al. (2015). This raises the question whether the presence of organic matter during weathering reactions has an indirect effect on the Li isotope composition of clay minerals.

Despite large differences in δ^7Li values of the three bedrock units (sedimentary siliclastic, volcanic, granite), the produced clay minerals of all monolithologic catchments show the same range of δ^7Li values. Unfortunately, only one bedrock sample of each lithology was measured for Li isotopes and therefore the effect of lithology on δ^7Li_{clay} in the Murrumbidgee River Basin will need to be further evaluated.

It is not clear whether the degree of Li isotope fractionation during secondary mineral formation depends on certain clay mineral types. While this was tested here and no relationship between the δ^7Li composition and any clay mineral type was found, the results are questionable due to the fact that the quantification using XRD techniques is difficult and comes with large uncertainties. Other clay mineral identification techniques, such as Fourier Transform Infrared (FTIR) Spectroscopy (Madejová, 2003), could be applied that are more suitable for identifying and distinguishing between different clay

mineral groups, which may allow for a better comparison between δ^7Li_{clay} and clay mineral type.

Despite large differences in the Li isotope composition of the three bedrock units in the Murrumbidgee River Basin (sedimentary siliclastic, volcanic, granite), the produced clay minerals of all monolithologic catchments show the same range of δ^7Li values. Unfortunately, only one bedrock of each lithology was measured for Li isotopes and therefore the effect of lithology on the δ^7Li_{clay} composition in the Murrumbidgee River Basin will need to be further evaluated.

River dissolved loads were collected in the Murrumbidgee River Basin in September 2016. Studies have shown that the Li isotope composition of dissolved loads may be affected by seasonal changes (Kısakűrek et al., 2005). This was not investigated in this study and needs to be considered in the future for refining the link between annual mean weathering rate and Li isotope compositions.

The evolution of Li isotopes in soil profiles is still poorly understood and existing studies show contrasting results. For instance, basalt profiles in Iceland are isotopically light at the surface compared to the base of the profile as a result of preferential incorporation of ^6Li into secondary minerals (Pistiner and Henderson, 2003). In contrast, in Hawaii, upper soil horizons are isotopically heavier than the base of the profile, which was explained by isotopically heavy dust inputs (Pistiner and Henderson, 2003). Other studies proposed that the Li isotope composition in soil profiles follows palaeo water tables, at which δ^7Li values are the lowest (Rudnick et al., 2004). In Chapter 8, the Li isotope composition of fine-grained lake sediments was used to infer changes in soil development in the lake catchment. It was assumed that low δ^7Li values are associated with more developed soils, whereas high δ^7Li values correspond to either undeveloped soils or the erosion of primary minerals from deeper parts of soil profiles. However, this hypothesis is based on the assumption that there is no spatial evolution of Li isotopes in soil profiles. Because of the contrasting findings described above, the evolution of the δ^7Li composition in soil profiles needs to be further tested in order to apply the Li isotope proxy in sediment deposits as a proxy for soil development at the catchment scale.

Concerning the precise use of Li isotopes as a quantitative proxy for continental weathering, more work is still required, in particular on soils and fine-grained sediments. However, sample preparation for Li isotope analyses is time consuming and thus far large

are rare in the literature. During the course of this PhD project, an automated chromatography procedure for separating Li from the sample matrix using a prepFAST-MC™ has been developed (see Chapter 9). However, this was only partly achieved and final tests of this method showed difficulties, which have not yet been resolved. Finalising this method is important as this would allow to investigate large scale systematics of Li isotopes in natural and superficial environments.

References

Abdalla, O. & Bin Yahya Al-Abri, R. 2014. Factors affecting groundwater chemistry in regional arid basins of variable lithology: example of Wadi Umairy, Oman. *Arabian Journal of Geosciences,* 7**,** 2861-2870.

Åberg, G., Jacks, G. & Hamilton, P. J. 1989. Weathering rates and $^{87}Sr/^{86}Sr$ ratios: an isotopic approach. *Journal of Hydrology,* 109**,** 65-78.

Aciego, S. M., Bourdon, B., Lupker, M. & Rickli, J. 2009. A new procedure for separating and measuring radiogenic isotopes (U, Th, Pa, Ra, Sr, Nd, Hf) in ice cores. *Chemical Geology,* 266**,** 194-204.

Ahlers, W. W., Reid, M. R., Kim, J. P. & Hunter, K. A. 1990. Contamination-free sample collection and handling protocols for trace elements in natural fresh waters. *Marine and Freshwater Research,* 41**,** 713-720.

Ali, A. & Srinivasan, G. 2011. Precise thermal ionization mass spectrometric measurements of $^{142}Nd/^{144}Nd$ and $^{143}Nd/^{144}Nd$ isotopic ratios of Nd separated from geological standards by chromatographic methods. *International Journal of Mass Spectrometry,* 299**,** 27-34.

Allan, R. J. 1985. *The Australasian summer monsoon, teleconnections, and flooding in the Lake Eyre basin,* Royal Geographical Society of Australasia, SA Branch, pp.

Andersen, K. K., Azuma, N., Barnola, J.-M., Bigler, M., Biscaye, P., Caillon, N., Chappellaz, J., Clausen, H. B., Dahl-Jensen, D. & Fischer, H. 2004. High-resolution record of Northern Hemisphere climate extending into the last interglacial period. *Nature,* 431**,** 147.

Andersson, P. S., Dahlqvist, R., Ingri, J. & Gustafsson, Ö. 2001. The isotopic composition of Nd in a boreal river: a reflection of selective weathering and colloidal transport. *Geochimica et Cosmochimica Acta,* 65**,** 521-527.

Andronopoulos, V. 1990. *Geological map of Greece. Herson Sheet.*, 1:50000. IGME.

Arakawa, Y. 1992. 143Nd/144Nd ratios of twelve GSJ rock reference samples and reproducibility of the data. *Geochemical Journal,* 26**,** 105-109.

Archer, D., Winguth, A., Lea, D. & Mahowald, N. 2000. What caused the glacial/interglacial atmosphericp CO_2 cycles? *Reviews of Geophysics,* 38**,** 159-189.

Arnaud, F., Révillon, S., Debret, M., Revel, M., Chapron, E., Jacob, J., Giguet-Covex, C., Poulenard, J. & Magny, M. 2012. Lake Bourget regional erosion patterns

reconstruction reveals Holocene NW European Alps soil evolution and paleohydrology. *Quaternary Science Reviews,* 51**,** 81-92.

Arnaud, F., Poulenard, J., Giguet-Covex, C., Wilhelm, B., Révillon, S., Jenny, J.-P., Revel, M., Enters, D., Bajard, M. & Fouinat, L. 2016. Erosion under climate and human pressures: An alpine lake sediment perspective. *Quaternary Science Reviews,* 152**,** 1-18.

Asikainen, C. A., Francus, P. & Brigham-Grette, J. 2007. Sedimentology, clay mineralogy and grain-size as indicators of 65 ka of climate change from El'gygytgyn Crater Lake, Northeastern Siberia. *Journal of Paleolimnology,* 37**,** 105-122.

Athanasiadis, N., Tonkov, S., Atanassova, J. & Bozilova, E. 2000. Palynological study of Holocene sediments from Lake Doirani in northern Greece. *Journal of Paleolimnology,* 24**,** 331-342.

Australia, G. 2015. Australian stratigraphic units database. *Australian Government. Website: http://www.ga.gov.au/data-pubs/data-standards/reference-databases/stratigraphic-units*.

Ayliffe, L. K., Marianelli, P. C., Moriarty, K. C., Wells, R. T., Mcculloch, M. T., Mortimer, G. E. & Hellstrom, J. C. 1998. 500 ka precipitation record from southeastern Australia: evidence for interglacial relative aridity. *Geology,* 26**,** 147-150.

Bagard, M.-L., West, A. J., Newman, K. & Basu, A. R. 2015. Lithium isotope fractionation in the Ganges–Brahmaputra floodplain and implications for groundwater impact on seawater isotopic composition. *Earth and Planetary Science Letters,* 432**,** 404-414.

Bajard, M., Poulenard, J., Sabatier, P., Etienne, D., Ficetola, F., Chen, W., Gielly, L., Taberlet, P., Develle, A.-L. & Rey, P.-J. 2017a. Long-term changes in alpine pedogenetic processes: Effect of millennial agro-pastoralism activities (French-Italian Alps). *Geoderma,* 306**,** 217-236.

Bajard, M., Poulenard, J., Sabatier, P., Develle, A.-L., Giguet-Covex, C., Jacob, J., Crouzet, C., David, F., Pignol, C. & Arnaud, F. 2017b. Progressive and regressive soil evolution phases in the Anthropocene. *Catena,* 150**,** 39-52.

Balter, V. & Vigier, N. 2014. Natural variations of lithium isotopes in a mammalian model. *Metallomics,* 6**,** 582-586.

Banerjee, D., Page, K. & Lepper, K. 2002. Optical dating of paleochannel deposits in the Riverine Plain, southeastern Australia: testing the reliability of existing thermoluminescence dates. *Radiation protection dosimetry,* 101**,** 327-332.

Barber, D. C., Dyke, A., Hillaire-Marcel, C., Jennings, A. E., Andrews, J. T., Kerwin, M. W., Bilodeau, G., Mcneely, R., Southon, J., Morehead, M. D. & Gagnon, J.-M. 1999. Forcing of the cold event of 8,200 years ago by catastrophic drainage. *Nature,* 400**,** 344-348.

Barnes, I. 1964. Field measurement of alkalinity and pH. USGPO.

Barrows, T. T., Stone, J. O., Fifield, L. K. & Cresswell, R. G. 2001. Late Pleistocene glaciation of the Kosciuszko massif, snowy mountains, Australia. *Quaternary Research,* 55**,** 179-189.

Barrows, T. T., Stone, J. O. & Fifield, L. K. 2004. Exposure ages for Pleistocene periglacial deposits in Australia. *Quaternary Science Reviews,* 23**,** 697-708.

Bastian, L., Revel, M., Bayon, G., Dufour, A. & Vigier, N. 2017. Abrupt response of chemical weathering to Late Quaternary hydroclimate changes in northeast Africa. *Scientific Reports,* 7**,** 44231.

Baxter, D. C., Rodushkin, I., Engström, E. & Malinovsky, D. 2006. Revised exponential model for mass bias correction using an internal standard for isotope abundance ratio measurements by multi-collector inductively coupled plasma mass spectrometry. *Journal of Analytical Atomic Spectrometry,* 21**,** 427-430.

Bayon, G., Burton, K., Soulet, G., Vigier, N., Dennielou, B., Etoubleau, J., Ponzevera, E., German, C. & Nesbitt, R. 2009. Hf and Nd isotopes in marine sediments: Constraints on global silicate weathering. *Earth and Planetary Science Letters,* 277**,** 318-326.

Bayon, G., Dennielou, B., Etoubleau, J., Ponzevera, E., Toucanne, S. & Bermell, S. 2012. Intensifying weathering and land use in Iron Age Central Africa. *Science,* 335**,** 1219-1222.

Bayon, G., Skonieczny, C., Delvigne, C., Toucanne, S., Bermell, S., Ponzevera, E. & Andre, L. 2016. Environmental Hf–Nd isotopic decoupling in world river clays. *Earth and Planetary Science Letters,* 438**,** 25-36.

Bayon, G., De Deckker, P., Magee, J. W., Germain, Y., Bermell, S., Tachikawa, K. & Norman, M. D. 2017. Extensive wet episodes in Late Glacial Australia resulting from high-latitude forcings. *Scientific Reports,* 7**,** 44054.

Beaulieu, E., Goddéris, Y., Donnadieu, Y., Labat, D. & Roelandt, C. 2012. High sensitivity of the continental-weathering carbon dioxide sink to future climate change. *Nature Climate Change,* 2**,** 346-349.

Berner, R. A., Lasaga, A. C. & Garrels, R. M. 1983. The carbonate-silicate geochemical cycle and its effect on atmospheric carbon dioxide over the past 100 million years. *American Journal of Science,* 283**,** 641-683.

Berner, R. A. & Kothavala, Z. 2001. GEOCARB III: a revised model of atmospheric CO_2 over Phanerozoic time. *American Journal of Science,* 301**,** 182-204.

Beukema, S. P., Krishnamurthy, R., Juyal, N., Basavaiah, N. & Singhvi, A. 2011. Monsoon variability and chemical weathering during the late Pleistocene in the Goriganga basin, higher central Himalaya, India. *Quaternary Research,* 75**,** 597-604.

Blaxland, A. B. 1974. Geochemistry and geochronology of chemical weathering, Butler Hill Granite, Missouri. *Geochimica et Cosmochimica Acta,* 38**,** 843-852.

Bluth, G. J. & Kump, L. R. 1994. Lithologic and climatologic controls of river chemistry. *Geochimica et Cosmochimica Acta,* 58**,** 2341-2359.

Bom. 2017. *Average daily mean temperature Annual* [Online]. Available: http://www.bom.gov.au/jsp/ncc/climate_averages/temperature/index.jsp?maptype=6&period=an#maps [Accessed 31. August 2017].

Borza, E. N. 1987. Timber and politics in the ancient world: Macedon and the Greeks. *Proceedings of the American Philosophical Society,* 131**,** 32-52.

Bouchez, J., Gaillardet, J. & Von Blanckenburg, F. 2014. Weathering intensity in lowland river basins: from the Andes to the Amazon mouth. *Procedia Earth and Planetary Science,* 10**,** 280-286.

Bouchez, J. & Gaillardet, J. 2014. How accurate are rivers as gauges of chemical denudation of the Earth surface? *Geology,* 42**,** 171-174.

Bouman, C., Elliott, T. & Vroon, P. Z. 2004. Lithium inputs to subduction zones. *Chemical Geology,* 212**,** 59-79.

Bowler, J. & Wasson, R. 1984. Glacial age environments of inland Australia. *Late Cainozoic palaeoclimates of the southern hemisphere***,** 183-208.

Bowler, J. M., Gillespie, R., Johnston, H. & Boljkovac, K. 2012. Wind v water: Glacial maximum records from the Willandra Lakes. *Peopled Landscapes:*

Archaeological and Biogeographic Approaches to Landscapes. Terra Australis, 34**,** 271e296.

Brand, W. A., Coplen, T. B., Vogl, J., Rosner, M. & Prohaska, T. 2014. Assessment of international reference materials for isotope-ratio analysis (IUPAC Technical Report). *Pure and Applied Chemistry,* 86**,** 425-467.

Brimhall, G. H. & Dietrich, W. E. 1987. Constitutive mass balance relations between chemical composition, volume, density, porosity, and strain in metasomatic hydrochemical systems: results on weathering and pedogenesis. *Geochimica et Cosmochimica Acta,* 51**,** 567-587.

Brisset, E., Miramont, C., Guiter, F., Anthony, E. J., Tachikawa, K., Poulenard, J., Arnaud, F., Delhon, C., Meunier, J.-D. & Bard, E. 2013. Non-reversible geosystem destabilisation at 4200 cal. BP: Sedimentological, geochemical and botanical markers of soil erosion recorded in a Mediterranean alpine lake. *The Holocene,* 23**,** 1863-1874.

Broecker, W. S. & Sanyal, A. 1998. Does atmospheric CO_2 police the rate of chemical weathering? *Global Biogeochemical Cycles,* 12**,** 403-408.

Brown, C. M. & Stephenson, A. E. 1991. *Geology of the Murray Basin, southeastern Australia,* Australian Govt. Pub. Service, pp.

Browne, W. 1957. Pleistocene glaciation in the Commonwealth of Australia. *Journal of Glaciology,* 3**,** 111-115.

Burke, B. C., Heimsath, A. M. & White, A. F. 2007. Coupling chemical weathering with soil production across soil-mantled landscapes. *Earth Surface Processes and Landforms,* 32**,** 853-873.

Burton, K. W. & Vance, D. 2000. Glacial–interglacial variations in the neodymium isotope composition of seawater in the Bay of Bengal recorded by planktonic foraminifera. *Earth and Planetary Science Letters,* 176**,** 425-441.

Burton, K. W. & Vigier, N. 2012. Lithium Isotopes as Tracers in Marine and Terrestrial Environments. *In:* Baskaran, M. (ed.) *Handbook of Environmental Isotope Geochemistry: Vol I.* Berlin, Heidelberg: Springer Berlin Heidelberg, 41-59.

Butcher, A. C. 2002. *Gundagai, a Track Winding Back,* AC Butcher, pp.

Butler, B. 1950. A theory of prior streams as a casual factor of soil occurrence in the Riverine Plain of south-eastern Australia. *Australian Journal of Agricultural Research,* 1**,** 231-252.

Butler, B. & Hutton, J. 1956. Parna in the Riverine Plain of south-eastern Australia and the soils thereon. *Australian Journal of Agricultural Research,* 7**,** 536-553.

Carignan, J., Cardinal, D., Eisenhauer, A., Galy, A., Rehkamper, M., Wombacher, F. & Vigier, N. 2004. A reflection on Mg, Cd, Ca, Li and Si isotopic measurements and related reference materials. *Geostandards and Geoanalytical Research,* 28**,** 139-148.

Carignan, J., Vigier, N. & Millot, R. 2007. Three Secondary Reference Materials for Lithium Isotope Measurements: Li7-N, Li6-N and LiCl-N Solutions. *Geostandards and Geoanalytical Research,* 31**,** 7-12.

Carlson, A. 2013. Paleoclimate | The Younger Dryas Climate Event. *Encyclopedia of Quaternary Science (Second Edition)***,** 126-134.

Carson, M., Jasper, J. & Conly, F. M. 1998. Magnitude and sources of sediment input to the Mackenzie Delta, Northwest Territories, 1974–94. *Arctic***,** 116-124.

Chadwick, O. A., Gavenda, R. T., Kelly, E. F., Ziegler, K., Olson, C. G., Elliott, W. C. & Hendricks, D. M. 2003. The impact of climate on the biogeochemical functioning of volcanic soils. *Chemical Geology,* 202**,** 195-223.

Chamberlain, C. P., Waldbauer, J. R. & Jacobson, A. D. 2005. Strontium, hydrothermal systems and steady-state chemical weathering in active mountain belts. *Earth and Planetary Science Letters,* 238**,** 351-366.

Chamley, H. 2013. *Clay Sedimentology,* Springer Science & Business Media, pp.

Chan, L.-H. & Kastner, M. 2000. Lithium isotopic compositions of pore fluids and sediments in the Costa Rica subduction zone: implications for fluid processes and sediment contribution to the arc volcanoes. *Earth and Planetary Science Letters,* 183**,** 275-290.

Chan, L.-H., Alt, J. C. & Teagle, D. A. 2002a. Lithium and lithium isotope profiles through the upper oceanic crust: a study of seawater–basalt exchange at ODP Sites 504B and 896A. *Earth and Planetary Science Letters,* 201**,** 187-201.

Chan, L.-H. & Hein, J. R. 2007. Lithium contents and isotopic compositions of ferromanganese deposits from the global ocean. *Deep Sea Research Part II: Topical Studies in Oceanography,* 54**,** 1147-1162.

Chan, L., Edmond, J., Thompson, G. & Gillis, K. 1992. Lithium isotopic composition of submarine basalts: implications for the lithium cycle in the oceans. *Earth and Planetary Science Letters,* 108**,** 151-160.

Chan, L. H., Leeman, W. & You, C.-F. 2002b. Lithium isotopic composition of Central American volcanic arc lavas: implications for modification of subarc mantle by slab-derived fluids: correction. *Chemical Geology,* 182**,** 293-300.

Chan, L. H. & Frey, F. A. 2003. Lithium isotope geochemistry of the Hawaiian plume: results from the Hawaii Scientific Drilling Project and Koolau volcano. *Geochemistry, Geophysics, Geosystems,* 4.

Chen, J., Wang, F., Xia, X. & Zhang, L. 2002. Major element chemistry of the Changjiang (Yangtze River). *Chemical Geology,* 187**,** 231-255.

Chen, J., Wang, F., Meybeck, M., He, D., Xia, X. & Zhang, L. 2005. Spatial and temporal analysis of water chemistry records (1958–2000) in the Huanghe (Yellow River) basin. *Global biogeochemical cycles,* 19.

Chesworth, W., Dejou, J. & Larroque, P. 1981. The weathering of basalt and relative mobilities of the major elements at Belbex, France. *Geochimica et Cosmochimica Acta,* 45**,** 1235-1243.

Chetelat, B., Liu, C.-Q., Zhao, Z., Wang, Q., Li, S., Li, J. & Wang, B. 2008. Geochemistry of the dissolved load of the Changjiang Basin rivers: anthropogenic impacts and chemical weathering. *Geochimica et Cosmochimica Acta,* 72**,** 4254-4277.

Chow, T. J. & Patterson, C. 1962. The occurrence and significance of lead isotopes in pelagic sediments. *Geochimica et Cosmochimica Acta,* 26**,** 263-308.

Chu, Z.-Y., Li, C.-F., Hegner, E., Chen, Z., Yan, Y. & Guo, J.-H. 2014a. High-Precision $^{143}Nd/^{144}Nd$ Ratios from NdO^+ Data Corrected with in-Run Measured Oxygen Isotope Ratios. *Analytical chemistry,* 86**,** 11141-11150.

Chu, Z., Chen, F., Yang, Y. & Guo, J. 2009. Precise determination of Sm, Nd concentrations and Nd isotopic compositions at the nanogram level in geological samples by thermal ionization mass spectrometry. *Journal of Analytical Atomic Spectrometry,* 24**,** 1534-1544.

Chu, Z., Guo, J., Yang, Y., Qi, L. & Li, C. 2014b. Precise determination of Sm and Nd concentrations and Nd isotopic compositions in highly depleted ultramafic reference materials. *Geostandards and Geoanalytical Research,* 38**,** 61-72.

Church, M., Kellerhals, R. & Day, T. J. 1989. Regional clastic sediment yield in British Columbia. *Canadian Journal of Earth Sciences,* 26**,** 31-45.

Cividini, D., Lemarchand, D., Chabaux, F., Boutin, R. & Pierret, M.-C. 2010. From biological to lithological control of the B geochemical cycle in a forest watershed (Strengbach, Vosges). *Geochimica et Cosmochimica Acta,* 74**,** 3143-3163.

Clift, P. D., Wan, S. & Blusztajn, J. 2014. Reconstructing chemical weathering, physical erosion and monsoon intensity since 25 Ma in the northern South China Sea: a review of competing proxies. *Earth-Science Reviews,* 130**,** 86-102.

Cohen, T., Nanson, G., Jansen, J. D., Jones, B., Jacobs, Z., Larsen, J., May, J.-H., Treble, P., Price, D. & Smith, A. 2012. Late Quaternary mega-lakes fed by the northern and southern river systems of central Australia: varying moisture sources and increased continental aridity. *Palaeogeography, Palaeoclimatology, Palaeoecology,* 356**,** 89-108.

Cohen, T. J., Nanson, G. C., Jansen, J. D., Jones, B. G., Jacobs, Z., Treble, P., Price, D. M., May, J.-H., Smith, A. M. & Ayliffe, L. K. 2011. Continental aridification and the vanishing of Australia's megalakes. *Geology,* 39**,** 167-170.

Colhoun, E. A. 1991. *Climate During the Last Glacial Maximum in Australia and New Guinea: evidence inferred from biogeographical and geomorphological data,* Australian and New Zealand Geomorphology Group, pp.

Crocket, K. C., Lambelet, M., Van De Flierdt, T., Rehkämper, M. & Robinson, L. F. 2014. Measurement of fossil deep-sea coral Nd isotopic compositions and concentrations by TIMS as NdO^+, with evaluation of cleaning protocols. *Chemical Geology,* 374**,** 128-140.

Crosbie, R., Morrow, D., Cresswell, R., Leaney, F., Lamontagne, S. & Lefournour, M. 2012. New insights to the chemical and isotopic composition of rainfall across Australia.

Dalai, T., Krishnaswami, S. & Sarin, M. 2002. Major ion chemistry in the headwaters of the Yamuna river system:: Chemical weathering, its temperature dependence and CO2 consumption in the Himalaya. *Geochimica et Cosmochimica Acta,* 66**,** 3397-3416.

Dausmann, V., Frank, M., Siebert, C., Christl, M. & Hein, J. R. 2015. The evolution of climatically driven weathering inputs into the western Arctic Ocean since the late Miocene: Radiogenic isotope evidence. *Earth and Planetary Science Letters,* 419**,** 111-124.

Davies, J. L. 1969. Landforms of cold climates.

Dearing, J., Hu, Y., Doody, P., James, P. A. & Brauer, A. 2001. Preliminary reconstruction of sediment-source linkages for the past 6000 yr at the Petit Lac d'Annecy, France, based on mineral magnetic data. *Journal of Paleolimnology,* 25**,** 245-258.

Deberdt, S., Viers, J. & Dupré, B. 2002. New insights about the rare earth elements (REE) mobility in river waters. *Bulletin de la Société Géologique de France,* 173**,** 147-160.

Decarreau, A., Vigier, N., Pálková, H., Petit, S., Vieillard, P. & Fontaine, C. 2012. Partitioning of lithium between smectite and solution: An experimental approach. *Geochimica et Cosmochimica Acta,* 85**,** 314-325.

Dellinger, M., Gaillardet, J., Bouchez, J., Calmels, D., Galy, V., Hilton, R. G., Louvat, P. & France-Lanord, C. 2014. Lithium isotopes in large rivers reveal the cannibalistic nature of modern continental weathering and erosion. *Earth and Planetary Science Letters,* 401**,** 359-372.

Dellinger, M., Gaillardet, J., Bouchez, J., Calmels, D., Louvat, P., Dosseto, A., Gorge, C., Alanoca, L. & Maurice, L. 2015. Riverine Li isotope fractionation in the Amazon River basin controlled by the weathering regimes. *Geochimica et Cosmochimica Acta,* 164**,** 71-93.

Dellinger, M., Bouchez, J., Gaillardet, J., Faure, L. & Moureau, J. 2017. Tracing weathering regimes using the lithium isotope composition of detrital sediments. *Geology,* 45**,** 411-414.

Donald, A., Meinke, H., Power, B., Maia, A. D. H., Wheeler, M. C., White, N., Stone, R. C. & Ribbe, J. 2006. Near-global impact of the Madden-Julian Oscillation on rainfall. *Geophysical Research Letters,* 33.

Dosseto, A., Turner, S. P. & Chappell, J. 2008. The evolution of weathering profiles through time: new insights from uranium-series isotopes. *Earth and Planetary Science Letters,* 274**,** 359-371.

Dosseto, A., Hesse, P., Maher, K., Fryirs, K. & Turner, S. 2010. Climatic and vegetation control on sediment dynamics during the last glacial cycle. *Geology,* 38**,** 395-398.

Dosseto, A., Buss, H. L. & Chabaux, F. 2014. Age and weathering rate of sediments in small catchments: The role of hillslope erosion. *Geochimica et Cosmochimica Acta,* 132**,** 238-258.

Dosseto, A. 2015. Chemical Weathering (U-Series). *Encyclopedia of Scientific Dating Methods***,** 152-169.

Dosseto, A., Vigier, N., Joannes-Boyau, R. C., Moffat, I., Singh, T. & Srivastava, P. 2015. Rapid response of silicate weathering rates to climate change in the Himalaya. *Geochemical Perspectives Letters,* 1**,** 10-19.

Dou, Y., Yang, S., Shi, X., Clift, P. D., Liu, S., Liu, J., Li, C., Bi, L. & Zhao, Y. 2016. Provenance weathering and erosion records in southern Okinawa Trough sediments since 28ka: geochemical and Sr–Nd–Pb isotopic evidences. *Chemical Geology,* 425**,** 93-109.

Douglas, G., Gray, C., Hart, B. & Beckett, R. 1995. A strontium isotopic investigation of the origin of suspended particulate matter (SPM) in the Murray-Darling River system, Australia. *Geochimica et Cosmochimica Acta,* 59**,** 3799-3815.

Drever, J. I. 1997. The geochemistry of natural waters: surface and groundwater environments. *Upper Saddle River*.

Drosdowsky, W. & Chambers, L. E. 2001. Near-global sea surface temperature anomalies as predictors of Australian seasonal rainfall. *Journal of Climate,* 14**,** 1677-1687.

Drosdowsky, W. 2005. The latitude of the subtropical ridge over eastern Australia: The L index revisited. *International Journal of Climatology,* 25**,** 1291-1299.

Drysdale, R., Zanchetta, G., Hellstrom, J., Maas, R., Fallick, A., Pickett, M., Cartwright, I. & Piccini, L. 2006. Late Holocene drought responsible for the collapse of Old World civilizations is recorded in an Italian cave flowstone. *Geology,* 34**,** 101-104.

Dupré, B., Gaillardet, J., Rousseau, D. & Allègre, C. J. 1996. Major and trace elements of river-borne material: the Congo Basin. *Geochimica et Cosmochimica Acta,* 60**,** 1301-1321.

Eardley, K. A. 2001. *A foundation for conservation in the Riverina Bioregion,* NSW National Parks and Wildlife Service, pp.

Edmond, J. 1992. Himalayan tectonics, weathering processes, and the strontium isotope record in marine limestones. *Science,* 258**,** 1594-1594.

Elburg, M. A. 1996. Evidence of isotopic equilibration between microgranitoid enclaves and host granodiorite, Warburton Granodiorite, Lachlan Fold Belt, Australia. *Lithos,* 38**,** 1-22.

Ercolani, C. P., Enge, T. G., Rothacker, L., Field, M. P. & Dosseto, A. (under review). An automated chromatography procedure for the analysis of 143Nd/144Nd isotope ratios in geological materials.

Erel, Y., Harlavan, Y. & Blum, J. D. 1994. Lead isotope systematics of granitoid weathering. *Geochimica et Cosmochimica Acta,* 58**,** 5299-5306.

Eswaran, H., Stoops, G. & De Paepe, R. 1973. A contribution to the study of soil formation on Isla Santa Cruz, Galapagos. *Pedologie,* 23**,** 100-122.

Faure, G. 1986. *Principles of Isotope Geology,* John Wiley and Sons Ltd, New York, 589 pp.

Fedo, C. M., Nesbitt, H. W. & Young, G. M. 1995. Unraveling the effects of potassium metasomatism in sedimentary rocks and paleosols, with implications for paleoweathering conditions and provenance. *Geology,* 23**,** 921-924.

Flanagan, F. J. & Flanagan, F. J. 1976. *Descriptions and analyses of eight new USGS rock standards,* US Government Printing Office, pp.

Flesch, G., Anderson, A. & Svec, H. 1973. A secondary isotopic standard for 6Li/7Li determinations. *International Journal of Mass Spectrometry and Ion Physics,* 12**,** 265-272.

Foster, G. L. & Vance, D. 2006. Negligible glacial-interglacial variation in continental chemical weathering rates. *Nature,* 444**,** 918.

Foustoukos, D., James, R., Berndt, M. & Seyfried, W. 2004. Lithium isotopic systematics of hydrothermal vent fluids at the Main Endeavour Field, Northern Juan de Fuca Ridge. *Chemical Geology,* 212**,** 17-26.

Francke, A., Wagner, B., Leng, M. J. & Rethemeyer, J. 2013. A Late Glacial to Holocene record of environmental change from Lake Dojran (Macedonia, Greece). *Climate of the Past,* 9**,** 481-498.

Frank, M. 2002. Radiogenic isotopes: tracers of past ocean circulation and erosional input. *Reviews of geophysics,* 40**,** 1-38.

Gaillardet, J., Dupre, B., Allegre, C. J. & Négrel, P. 1997. Chemical and physical denudation in the Amazon River Basin. *Chemical geology,* 142**,** 141-173.

Gaillardet, J., Dupré, B., Louvat, P. & Allègre, C. 1999. Global silicate weathering and CO_2 consumption rates deduced from the chemistry of large rivers. *Chemical Geology,* 159**,** 3-30.

Galloway, R. 1965. Late quaternary climates in Australia. *The Journal of Geology,* 73**,** 603-618.

Galy, A., France-Lanord, C. & Derry, L. A. 1999. The strontium isotopic budget of Himalayan rivers in Nepal and Bangladesh. *Geochimica et Cosmochimica Acta,* 63**,** 1905-1925.

Gao, S., Rudnick, R. L., Yuan, H.-L., Liu, X.-M., Liu, Y.-S., Xu, W.-L., Ling, W.-L., Ayers, J., Wang, X.-C. & Wang, Q.-H. 2004. Recycling lower continental crust in the North China craton. *Nature,* 432**,** 892-897.

Geoscience_Australia. 2013. *Longest Rivers* [Online]. Geoscience Australia: Geoscience Australia. Available: http://www.ga.gov.au/scientific-topics/national-location-information/landforms/longest-rivers#heading-1 [Accessed 6 Oct 2017].

Giguet-Covex, C., Pansu, J., Arnaud, F., Rey, P.-J., Griggo, C., Gielly, L., Domaizon, I., Coissac, E., David, F. & Choler, P. 2014. Long livestock farming history and human landscape shaping revealed by lake sediment DNA. *Nature communications,* 5**,** 3211.

Gimeno, L., Drumond, A., Nieto, R., Trigo, R. M. & Stohl, A. 2010. On the origin of continental precipitation. *Geophysical Research Letters,* 37.

Gislason, S. R., Oelkers, E. H., Eiriksdottir, E. S., Kardjilov, M. I., Gisladottir, G., Sigfusson, B., Snorrason, A., Elefsen, S., Hardardottir, J., Torssander, P. & Oskarsson, N. 2009. Direct evidence of the feedback between climate and weathering. *Earth and Planetary Science Letters,* 277**,** 213-222.

Goddéris, Y., Brantley, S. L., François, L. M., Schott, J., Pollard, D., Déqué, M. & Dury, M. 2013. Rates of consumption of atmospheric CO_2 through the weathering of loess during the next 100 yr of climate change. *Biogeosciences,* 10**,** 135-148.

Goldberg, K. & Humayun, M. 2010. The applicability of the Chemical Index of Alteration as a paleoclimatic indicator: An example from the Permian of the Paraná Basin, Brazil. *Palaeogeography, Palaeoclimatology, Palaeoecology,* 293**,** 175-183.

Goldstein, S. L., O'nions, R. K. & Hamilton, P. J. 1984. A Sm-Nd isotopic study of atmospheric dusts and particulates from major river systems. *Earth and Planetary Science Letters,* 70**,** 221-236.

Gontier, A., Rihs, S., Chabaux, F., Lemarchand, D., Pelt, E. & Turpault, M.-P. 2015. Lack of bedrock grain size influence on the soil production rate. *Geochimica et Cosmochimica Acta,* 166**,** 146-164.

Goodbred, S. L. & Kuehl, S. A. 2000. Enormous Ganges-Brahmaputra sediment discharge during strengthened early Holocene monsoon. *Geology,* 28**,** 1083-1086.

Grantham, J. H. & Velbel, M. A. 1988. The influence of climate and topography on rock-fragment abundance in modern fluvial sands of the southern Blue Ridge Mountains, North Carolina. *Journal of Sedimentary Research,* 58**,** 219-227.

Grasby, S. E., Hutcheon, I. & Mcfarland, L. 1999. Surface-water–groundwater interaction and the influence of ion exchange reactions on river chemistry. *Geology,* 27**,** 223-226.

Green, D., Petrovic, J., Moss, P. & Burrell, M. 2011. Water resources and management overview: Murrumbidgee catchment. *NSW Office of Water, Sydney*.

Harrison, S. P. 1993. Late Quaternary lake-level changes and climates of Australia. *Quaternary Science Reviews,* 12**,** 211-231.

Hathorne, E. C. & James, R. H. 2006. Temporal record of lithium in seawater: A tracer for silicate weathering? *Earth and Planetary Science Letters,* 246**,** 393-406.

Healy, B., Collins, W. & Richards, S. 2004. A hybrid origin for Lachlan S-type granites: the Murrumbidgee Batholith example. *Lithos,* 78**,** 197-216.

Hem, J. D. 1985. *Study and interpretation of the chemical characteristics of natural water*, Department of the Interior, US Geological Survey, pp.

Hendon, H. H., Thompson, D. W. & Wheeler, M. C. 2007. Australian rainfall and surface temperature variations associated with the Southern Hemisphere annular mode. *Journal of Climate,* 20**,** 2452-2467.

Hess, J., Bender, M. L. & Schilling, J.-G. 1986. Evolution of the ratio of strontium-87 to strontium-86 in seawater fromm Cretaceous to present. *Science,* 231**,** 979-985.

Hilley, G., Chamberlain, C., Moon, S., Porder, S. & Willett, S. 2010. Competition between erosion and reaction kinetics in controlling silicate-weathering rates. *Earth and Planetary Science Letters,* 293**,** 191-199.

Hillier, S. 2000. Accurate quantitative analysis of clay and other minerals in sandstones by XRD: comparison of a Rietveld and a reference intensity ratio (RIR) method and the importance of sample preparation. *Clay Minerals,* 35**,** 291-302.

Hinderer, M. 2001. Late Quaternary denudation of the Alps, valley and lake fillings and modern river loads. *Geodinamica Acta,* 14**,** 231-263.

Hoefs, J. 2015. Isotope fractionation processes of selected elements. *Stable Isotope Geochemistry.* Springer, 47-190.

Holland, H. D. 1984. *The chemical evolution of the atmosphere and oceans,* Princeton University Press, pp.

Hu, D., Clift, P. D., Böning, P., Hannigan, R., Hillier, S., Blusztajn, J., Wan, S. & Fuller, D. Q. 2013. Holocene evolution in weathering and erosion patterns in the Pearl River delta. *Geochemistry, Geophysics, Geosystems,* 14**,** 2349-2368.

Huang, K.-F., Blusztajn, J., Oppo, D. W., Curry, W. B. & Peucker-Ehrenbrink, B. 2012. High-precision and accurate determinations of neodymium isotopic compositions at nanogram levels in natural materials by MC-ICP-MS. *Journal of Analytical Atomic Spectrometry,* 27**,** 1560-1567.

Huh, Y., Chan, L.-H., Zhang, L. & Edmond, J. M. 1998. Lithium and its isotopes in major world rivers: implications for weathering and the oceanic budget. *Geochimica et Cosmochimica Acta,* 62**,** 2039-2051.

Huh, Y., Chan, L.-H. & Edmond, J. M. 2001. Lithium isotopes as a probe of weathering processes: Orinoco River. *Earth and Planetary Science Letters,* 194**,** 189-199.

Huh, Y., Chan, L. H. & Chadwick, O. A. 2004. Behavior of lithium and its isotopes during weathering of Hawaiian basalt. *Geochemistry, Geophysics, Geosystems,* 5.

Imai, N., Terashima, S., Itoh, S. & Ando, A. 1995. Compilation of analytical data for minor and trace elements in seventeen GSJ geochemical reference samples,"igneous rock series". *Geostandards Newsletter,* 19**,** 135-213.

Ivanovski, T. 1970. *Tumač za Osnovnu geološku kartu SFRJ 1:100000,* 1:100000. Savezni geološki institut.

Jacobsen, S. B. & Wasserburg, G. 1980. Sm-Nd isotopic evolution of chondrites. *Earth and Planetary Science Letters,* 50**,** 139-155.

Jacobson, A. D., Blum, J. D., Chamberlain, C. P., Poage, M. A. & Sloan, V. F. 2002. Ca/Sr and Sr isotope systematics of a Himalayan glacial chronosequence:

carbonate versus silicate weathering rates as a function of landscape surface age. *Geochimica et Cosmochimica Acta,* 66**,** 13-27.

Jacobson, A. D. & Blum, J. D. 2003. Relationship between mechanical erosion and atmospheric CO2 consumption in the New Zealand Southern Alps. *Geology,* 31**,** 865-868.

James, R. H., Rudnicki, M. D. & Palmer, M. R. 1999. The alkali element and boron geochemistry of the Escanaba Trough sediment-hosted hydrothermal system. *Earth and Planetary Science Letters,* 171**,** 157-169.

James, R. H. & Palmer, M. R. 2000. The lithium isotope composition of international rock standards. *Chemical Geology,* 166**,** 319-326.

Jeandel, C. 1993. Concentration and isotopic composition of Nd in the South Atlantic Ocean. *Earth and Planetary Science Letters,* 117**,** 581-591.

Jeandel, C., Bishop, J. & Zindler, A. 1995. Exchange of neodymium and its isotopes between seawater and small and large particles in the Sargasso Sea. *Geochimica et Cosmochimica Acta,* 59**,** 535-547.

Jin, L., Mukasa, S. B., Hamilton, S. K. & Walter, L. M. 2012. Impacts of glacial/interglacial cycles on continental rock weathering inferred using Sr/Ca and $^{87}Sr/^{86}Sr$ ratios in Michigan watersheds. *Chemical Geology,* 300**,** 97-108.

Jin, Z., Cao, J., Wu, J. & Wang, S. 2006. A Rb/Sr record of catchment weathering response to Holocene climate change in Inner Mongolia. *Earth Surface Processes and Landforms,* 31**,** 285-291.

Jones, C. E., Halliday, A. N., Rea, D. K. & Owen, R. M. 2000. Eolian inputs of lead to the North Pacific. *Geochimica et Cosmochimica Acta,* 64**,** 1405-1416.

Jones, D. A. & Trewin, B. C. 2000. On the relationships between the El Niño–Southern Oscillation and Australian land surface temperature. *International Journal of Climatology,* 20**,** 697-719.

Jones, P., Osborn, T. & Briffa, K. 2001. The evolution of climate over the last millennium. *Science,* 292**,** 662-667.

Kantor, W. & Schwertmann, U. 1974. Mineralogy and genesis of clays in red-black soil toposequences on basic igneous rocks in Kenya. *European Journal of Soil Science,* 25**,** 67-78.

Katsavouni, S. & Petkovski, S. 2004. Lake Doiran-An overview of the current situation. *Greek Biotope/Wetland Center (EKBY), Society for the Investigation and*

Conservation of Biodiversity and the Sustainable Development of Natural Ecosystems (BIOECO).

Keble, R. 1947. *Notes on Australian Quaternary climates and migration,* National Museum, pp.

Kemp, J. & Rhodes, E. 2010. Episodic fluvial activity of inland rivers in southeastern Australia: palaeochannel systems and terraces of the Lachlan River. *Quaternary Science Reviews,* 29**,** 732-752.

Kershaw, A. P. 1986. Climatic change and Aboriginal burning in north-east Australia during the last two glacial/interglacial cycles. *Nature,* 322**,** 47-49.

Kershaw, A. P. & Nanson, G. 1993. The last full glacial cycle in the Australian region. *Global and Planetary Change,* 7**,** 1-9.

Kershaw, A. P., Mckenzie, G., Porch, N., Roberts, R., Brown, J., Heijnis, H., Orr, M., Jacobsen, G. & Newall, P. 2007. A high-resolution record of vegetation and climate through the last glacial cycle from Caledonia Fen, southeastern highlands of Australia. *Journal of Quaternary Science,* 22**,** 481-500.

Kim, S. & Park, H.-D. 2003. The relationship between physical and chemical weathering indices of granites around Seoul, Korea. *Bulletin of Engineering Geology and the Environment,* 62**,** 207-212.

Kısakürek, B., Widdowson, M. & James, R. H. 2004. Behaviour of Li isotopes during continental weathering: the Bidar laterite profile, India. *Chemical Geology,* 212**,** 27-44.

Kısakűrek, B., James, R. H. & Harris, N. B. 2005. Li and δ^7Li in Himalayan rivers: proxies for silicate weathering? *Earth and Planetary Science Letters,* 237**,** 387-401.

Koppes, M. N. & Montgomery, D. R. 2009. The relative efficacy of fluvial and glacial erosion over modern to orogenic timescales. *Nature Geoscience,* 2**,** 644-647.

Kosmas, C., Danalatos, N., Cammeraat, L. H., Chabart, M., Diamantopoulos, J., Farand, R., Gutierrez, L., Jacob, A., Marques, H. & Martinez-Fernandez, J. 1997. The effect of land use on runoff and soil erosion rates under Mediterranean conditions. *Catena,* 29**,** 45-59.

Kronberg, B., Fyfe, W., Leonardos, O. & Santos, A. 1979. The chemistry of some Brazilian soils: element mobility during intense weathering. *Chemical Geology,* 24**,** 211-229.

Kurtz, A. C., Derry, L. A., Chadwick, O. A. & Alfano, M. J. 2000. Refractory element mobility in volcanic soils. *Geology,* 28**,** 683-686.

Lacey, J. H., Francke, A., Leng, M. J., Vane, C. H. & Wagner, B. 2015. A high-resolution Late Glacial to Holocene record of environmental change in the Mediterranean from Lake Ohrid (Macedonia/Albania). *International Journal of Earth Sciences,* 104**,** 1623-1638.

Lemarchand, D. & Gaillardet, J. 2006. Transient features of the erosion of shales in the Mackenzie basin (Canada), evidences from boron isotopes. *Earth and Planetary Science Letters,* 245**,** 174-189.

Lemarchand, E., Chabaux, F., Vigier, N., Millot, R. & Pierret, M.-C. 2010. Lithium isotope systematics in a forested granitic catchment (Strengbach, Vosges Mountains, France). *Geochimica et Cosmochimica Acta,* 74**,** 4612-4628.

Li, C.-F., Chen, F. & Li, X.-H. 2007. Precise isotopic measurements of sub-nanogram Nd of standard reference material by thermal ionization mass spectrometry using the NdO+ technique. *International Journal of Mass Spectrometry,* 266**,** 34-41.

Li, C. & Yang, S. 2010. Is chemical index of alteration (CIA) a reliable proxy for chemical weathering in global drainage basins? *American Journal of Science,* 310**,** 111-127.

Li, G. & West, A. J. 2014. Evolution of Cenozoic seawater lithium isotopes: Coupling of global denudation regime and shifting seawater sinks. *Earth and Planetary Science Letters,* 401**,** 284-293.

Lionello, P., Malanotte-Rizzoli, P., Boscolo, R., Alpert, P., Artale, V., Li, L., Luterbacher, J., May, W., Trigo, R. & Tsimplis, M. 2006. The Mediterranean climate: an overview of the main characteristics and issues. *Developments in earth and environmental sciences,* 4**,** 1-26.

Liu, X.-M., Rudnick, R. L., Mcdonough, W. F. & Cummings, M. L. 2013. Influence of chemical weathering on the composition of the continental crust: Insights from Li and Nd isotopes in bauxite profiles developed on Columbia River Basalts. *Geochimica et Cosmochimica Acta,* 115**,** 73-91.

Liu, X.-M., Wanner, C., Rudnick, R. L. & Mcdonough, W. F. 2015. Processes controlling δ^7Li in rivers illuminated by study of streams and groundwaters draining basalts. *Earth and Planetary Science Letters,* 409**,** 212-224.

Louvat, P. & Allègre, C. J. 1997. Present denudation rates on the island of Réunion determined by river geochemistry: basalt weathering and mass budget between chemical and mechanical erosions. *Geochimica et Cosmochimica Acta,* 61**,** 3645-3669.

Ludwig, W. & Probst, J.-L. 1998. River sediment discharge to the oceans; present-day controls and global budgets. *American Journal of Science,* 298**,** 265-295.

Lui-Heung, C. & Edmond, J. M. 1988. Variation of lithium isotope composition in the marine environment: A preliminary report. *Geochimica et Cosmochimica Acta,* 52**,** 1711-1717.

Lui-Heung, C., Gieskes, J. M., Chen-Feng, Y. & Edmond, J. M. 1994. Lithium isotope geochemistry of sediments and hydrothermal fluids of the Guaymas Basin, Gulf of California. *Geochimica et Cosmochimica Acta,* 58**,** 4443-4454.

Luo, X., Rehkämper, M., Lee, D.-C. & Halliday, A. N. 1997. High precision $^{230}Th/^{232}Th$ and $^{234}U/^{238}U$ measurements using energyfiltered ICP magnetic sector multiple collector mass spectrometry. *International Journal of Mass Spectrometry and Ion Processes,* 171**,** 105-117.

Lupker, M., France-Lanord, C., Galy, V., Lavé, J. & Kudrass, H. 2013. Increasing chemical weathering in the Himalayan system since the Last Glacial Maximum. *Earth and Planetary Science Letters,* 365**,** 243-252.

Ma, L., Chabaux, F., Pelt, E., Blaes, E., Jin, L. & Brantley, S. 2010. Regolith production rates calculated with uranium-series isotopes at Susquehanna/Shale Hills Critical Zone Observatory. *Earth and Planetary Science Letters,* 297**,** 211-225.

Madejová, J. 2003. FTIR techniques in clay mineral studies. *Vibrational spectroscopy,* 31**,** 1-10.

Magee, J. W., Miller, G. H., Spooner, N. A. & Questiaux, D. 2004. Continuous 150 ky monsoon record from Lake Eyre, Australia: insolation-forcing implications and unexpected Holocene failure. *Geology,* 32**,** 885-888.

Magny, M., Vannière, B., Zanchetta, G., Fouache, E., Touchais, G., Petrika, L., Coussot, C., Walter-Simonnet, A.-V. & Arnaud, F. 2009. Possible complexity of the climatic event around 4300—3800 cal. BP in the central and western Mediterranean. *The Holocene,* 19**,** 823-833.

Maher, K. & Chamberlain, C. 2014. Hydrologic regulation of chemical weathering and the geologic carbon cycle. *Science,* 343**,** 1502-1504.

Malmström, M. & Banwart, S. 1997. Biotite dissolution at 25 C: The pH dependence of dissolution rate and stoichiometry. *Geochimica et Cosmochimica Acta,* 61**,** 2779-2799.

Martin, A. 1986. Late glacial and early Holocene vegetation of the alpine zone, Kosciusko National Park. *Flora and fauna of alpine Australasia, ages and origins***,** 161-172.

Martinson, D. G., Pisias, N. G., Hays, J. D., Imbrie, J., Moore, T. C. & Shackleton, N. J. 1987. Age dating and the orbital theory of the ice ages: development of a high-resolution 0 to 300,000-year chronostratigraphy. *Quaternary research,* 27**,** 1-29.

Mayewski, P. A., Rohling, E. E., Stager, J. C., Karlén, W., Maasch, K. A., Meeker, L. D., Meyerson, E. A., Gasse, F., Van Kreveld, S. & Holmgren, K. 2004. Holocene climate variability. *Quaternary research,* 62**,** 243-255.

Mcbride, J. L. & Nicholls, N. 1983. Seasonal relationships between Australian rainfall and the Southern Oscillation. *Monthly Weather Review,* 111**,** 1998-2004.

Mcculloch, M. & Woodhead, J. 1993. Lead isotopic evidence for deep crustal-scale fluid transport during granite petrogenesis. *Geochimica et Cosmochimica Acta,* 57**,** 659-674.

Mcdonough, W., Mcculloch, M. & Sun, S. 1985. Isotopic and geochemical systematics in Tertiary-Recent basalts from southeastern Australia and implications for the evolution of the sub-continental lithosphere. *Geochimica et Cosmochimica Acta,* 49**,** 2051-2067.

Meneghini, B., Simmonds, I. & Smith, I. N. 2007. Association between Australian rainfall and the southern annular mode. *International Journal of Climatology,* 27**,** 109-121.

Middelburg, J. J., Van Der Weijden, C. H. & Woittiez, J. R. 1988. Chemical processes affecting the mobility of major, minor and trace elements during weathering of granitic rocks. *Chemical Geology,* 68**,** 253-273.

Millot, R., Gaillardet, J., Dupré, B. & Allègre, C. J. 2002. The global control of silicate weathering rates and the coupling with physical erosion: new insights from rivers of the Canadian Shield. *Earth and Planetary Science Letters,* 196**,** 83-98.

Millot, R., Érôme Gaillardet, J., Dupré, B. & Allègre, C. J. 2003. Northern latitude chemical weathering rates: clues from the Mackenzie River Basin, Canada. *Geochimica et Cosmochimica Acta,* 67**,** 1305-1329.

Millot, R., Guerrot, C. & Vigier, N. 2004. Accurate and High-Precision Measurement of Lithium Isotopes in Two Reference Materials by MC-ICP-MS. *Geostandards and Geoanalytical Research,* 28**,** 153-159.

Millot, R., Vigier, N. & Gaillardet, J. 2010. Behaviour of lithium and its isotopes during weathering in the Mackenzie Basin, Canada. *Geochimica et Cosmochimica Acta,* 74**,** 3897-3912.

Misra, S. & Froelich, P. N. 2012. Lithium isotope history of Cenozoic seawater: changes in silicate weathering and reverse weathering. *Science,* 335**,** 818-823.

Miyazaki, T. & Shuto, K. 1998. Sr and Nd isotope ratios of twelve GSJ rock reference samples. *Geochemical Journal,* 32**,** 345-350.

Molnar, P. & England, P. 1990. Late Cenozoic uplift of mountain ranges and global climate change: chicken or egg? *Nature,* 346**,** 29-34.

Montgomery, D. R. 2007. Soil erosion and agricultural sustainability. *Proceedings of the National Academy of Sciences,* 104**,** 13268-13272.

Moon, S., Chamberlain, C. & Hilley, G. 2014. New estimates of silicate weathering rates and their uncertainties in global rivers. *Geochimica et Cosmochimica Acta,* 134**,** 257-274.

Moquet, J.-S., Crave, A., Viers, J., Seyler, P., Armijos, E., Bourrel, L., Chavarri, E., Lagane, C., Laraque, A. & Casimiro, W. S. L. 2011. Chemical weathering and atmospheric/soil CO2 uptake in the Andean and Foreland Amazon basins. *Chemical Geology,* 287**,** 1-26.

Moriguti, T. & Nakamura, E. 1998a. Across-arc variation of Li isotopes in lavas and implications for crust/mantle recycling at subduction zones. *Earth and planetary science letters,* 163**,** 167-174.

Moriguti, T. & Nakamura, E. 1998b. High-yield lithium separation and the precise isotopic analysis for natural rock and aqueous samples. *Chemical Geology,* 145**,** 91-104.

Mortatti, J. & Probst, J.-L. 2003. Silicate rock weathering and atmospheric/soil CO2 uptake in the Amazon basin estimated from river water geochemistry: seasonal and spatial variations. *Chemical geology,* 197**,** 177-196.

Mueller, D., Jacobs, Z., Cohen, T., Price, D., Reinfelds, I. & Shulmeister, J. under review. Revisiting an arid LGM using fluvial archives: a luminescence

chronology for palaeochannels of the Murrumbidgee River, southeastern Australia. *Journal of Quaternary Science*.

Munhoven, G. 2002. Glacial–interglacial changes of continental weathering: estimates of the related CO_2 and HCO_3^- flux variations and their uncertainties. *Global and Planetary Change,* 33**,** 155-176.

Murphy, B. F. & Timbal, B. 2008. A review of recent climate variability and climate change in southeastern Australia. *International journal of Climatology,* 28**,** 859-879.

Nanson, G. C., Price, D. M., Jones, B. G., Maroulis, J. C., Coleman, M., Bowman, H., Cohen, T. J., Pietsch, T. J. & Larsen, J. R. 2008. Alluvial evidence for major climate and flow regime changes during the middle and late Quaternary in eastern central Australia. *Geomorphology,* 101**,** 109-129.

Negrel, P., Allègre, C. J., Dupré, B. & Lewin, E. 1993. Erosion sources determined by inversion of major and trace element ratios and strontium isotopic ratios in river water: the Congo Basin case. *Earth and Planetary Science Letters,* 120**,** 59-76.

Nesbitt, H. & Young, G. 1982. Early Proterozoic climates and plate motions inferred from major element chemistry of lutites. *Nature,* 299**,** 715-717.

Nesbitt, H. W. & Markovics, G. 1980. Chemical processes affecting alkalis and alkaline earths during continental weathering. *Geochimica et Cosmochimica Acta,* 44**,** 1659-1666.

Nesbitt, H. W., Fedo, C. M. & Young, G. M. 1997. Quartz and feldspar stability, steady and non-steady-state weathering, and petrogenesis of siliciclastic sands and muds. *The Journal of Geology,* 105**,** 173-192.

Nicholls, N. 1989. Sea surface temperatures and Australian winter rainfall. *Journal of Climate,* 2**,** 965-973.

Öhlander, B., Ingri, J., Land, M. & Schöberg, H. 2000. Change of Sm-Nd isotope composition during weathering of till. *Geochimica et Cosmochimica Acta,* 64**,** 813-820.

Oliva, P., Viers, J., Dupré, B., Fortuné, J. P., Martin, F., Braun, J. J., Nahon, D. & Robain, H. 1999. The effect of organic matter on chemical weathering: Study of a small tropical watershed: Nsimi-Zoetele site, Cameroon. *Geochimica et Cosmochimica Acta,* 63**,** 4013-4035.

Olley, J. M. & Wasson, R. J. 2003. Changes in the flux of sediment in the Upper Murrumbidgee catchment, Southeastern Australia, since European settlement. *Hydrological processes,* 17**,** 3307-3320.

Page, K., Nanson, G. & Price, D. 1991. Thermoluminescence chronology of late quaternary deposition on the riverine plain of South-Eastern Australia. *The Australian Geographer,* 22**,** 14-23.

Page, K., Dare-Edwards, A., Nanson, G. & Price, D. 1994. Late Quaternary evolution of Lake Urana, New South Wales, Australia. *Journal of Quaternary Science,* 9**,** 47-57.

Page, K., Nanson, G. & Price, D. 1996. Chronology of Murrumbidgee river palaeochannels on the Riverine Plain, southeastern Australia. *Journal of Quaternary Science,* 11**,** 311-326.

Page, K. & Nanson, G. 1996. Stratigraphic architecture resulting from Late Quaternary evolution of the Riverine Plain, south-eastern Australia. *Sedimentology,* 43**,** 927-945.

Page, K., Kemp, J. & Nanson, G. C. 2009. Late Quaternary evolution of riverine plain paleochannels, southeastern Australia. *Australian Journal of Earth Sciences,* 56**,** S19-S33.

Panagiotopoulos, K., Aufgebauer, A., Schäbitz, F. & Wagner, B. 2013. Vegetation and climate history of the Lake Prespa region since the Lateglacial. *Quaternary International,* 293**,** 157-169.

Parker, A. 1970. An index of weathering for silicate rocks. *Geological Magazine,* 107**,** 501-504.

Pels, S. 1971. River systems and climatic changes in southeastern Australia. *Aboriginal man and environment in Australia***,** 38-46.

Petherick, L., Bostock, H., Cohen, T. J., Fitzsimmons, K., Tibby, J., Fletcher, M.-S., Moss, P., Reeves, J., Mooney, S. & Barrows, T. 2013. Climatic records over the past 30 ka from temperate Australia–a synthesis from the Oz-INTIMATE workgroup. *Quaternary Science Reviews,* 74**,** 58-77.

Petit, J.-R., Mounier, L., Jouzel, J., Korotkevich, Y. S., Kotlyakov, V. & Lorius, C. 1990. Palaeoclimatological and chronological implications of the Vostok core dust record. *Nature,* 343**,** 56.

Petit, J.-R., Jouzel, J., Raynaud, D., Barkov, N. I., Barnola, J.-M., Basile, I., Bender, M., Chappellaz, J., Davis, M. & Delaygue, G. 1999. Climate and atmospheric history of the past 420,000 years from the Vostok ice core, Antarctica. *Nature,* 399**,** 429.

Peucker-Ehrenbrink, B. & Ravizza, G. 2000. The marine osmium isotope record. *Terra Nova,* 12**,** 205-219.

Pinet, P. & Souriau, M. 1988. Continental erosion and large-scale relief. *Tectonics,* 7**,** 563-582.

Pistiner, J. S. & Henderson, G. M. 2003. Lithium-isotope fractionation during continental weathering processes. *Earth and Planetary Science Letters,* 214**,** 327-339.

Pittock, A. 1975. Climatic change and the patterns of variation in Australian rainfall.

Plater, A., Ivanovich, M. & Dugdale, R. 1992. Uranium series disequilibrium in river sediments and waters: the significance of anomalous activity ratios. *Applied Geochemistry,* 7**,** 101-110.

Pogge Von Strandmann, P. A., Burton, K. W., James, R. H., Van Calsteren, P., Gíslason, S. R. & Mokadem, F. 2006. Riverine behaviour of uranium and lithium isotopes in an actively glaciated basaltic terrain. *Earth and Planetary Science Letters,* 251**,** 134-147.

Pogge Von Strandmann, P. A., James, R. H., Van Calsteren, P., Gíslason, S. R. & Burton, K. W. 2008. Lithium, magnesium and uranium isotope behaviour in the estuarine environment of basaltic islands. *Earth and Planetary Science Letters,* 274**,** 462-471.

Pogge Von Strandmann, P. A., Burton, K. W., James, R. H., Van Calsteren, P. & Gislason, S. R. 2010. Assessing the role of climate on uranium and lithium isotope behaviour in rivers draining a basaltic terrain. *Chemical Geology,* 270**,** 227-239.

Pogge Von Strandmann, P. A., Opfergelt, S., Lai, Y.-J., Sigfússon, B., Gislason, S. R. & Burton, K. W. 2012. Lithium, magnesium and silicon isotope behaviour accompanying weathering in a basaltic soil and pore water profile in Iceland. *Earth and Planetary Science Letters,* 339**,** 11-23.

Pogge Von Strandmann, P. A., Jenkyns, H. C. & Woodfine, R. G. 2013. Lithium isotope evidence for enhanced weathering during Oceanic Anoxic Event 2. *Nature Geoscience,* 6**,** 668-672.

Pogge Von Strandmann, P. A. & Henderson, G. M. 2015. The Li isotope response to mountain uplift. *Geology,* 43**,** 67-70.

Pogge Von Strandmann, P. A., Frings, P. J. & Murphy, M. J. 2017a. Lithium isotope behaviour during weathering in the Ganges Alluvial Plain. *Geochimica et Cosmochimica Acta,* 198**,** 17-31.

Pogge Von Strandmann, P. A., Vaks, A., Bar-Matthews, M., Ayalon, A., Jacob, E. & Henderson, G. M. 2017b. Lithium isotopes in speleothems: Temperature-controlled variation in silicate weathering during glacial cycles. *Earth and Planetary Science Letters,* 469**,** 64-74.

Pogge Von Strandmann, P. A., Desrochers, A., Murphy, M., Finlay, A., Selby, D. & Lenton, T. 2017c. Global climate stabilisation by chemical weathering during the Hirnantian glaciation. *Geophysical Research Letters.,* 3**,** 230-237.

Pomeroy, S. B. 1999. *Ancient Greece: a political, social, and cultural history,* Oxford University Press, USA, pp.

Price, J. R. & Velbel, M. A. 2003. Chemical weathering indices applied to weathering profiles developed on heterogeneous felsic metamorphic parent rocks. *Chemical Geology,* 202**,** 397-416.

Pross, J., Kotthoff, U., Müller, U., Peyron, O., Dormoy, I., Schmiedl, G., Kalaitzidis, S. & Smith, A. 2009. Massive perturbation in terrestrial ecosystems of the Eastern Mediterranean region associated with the 8.2 kyr BP climatic event. *Geology,* 37**,** 887-890.

Raczek, I., Jochum, K. P. & Hofmann, A. W. 2003. Neodymium and strontium isotope data for USGS reference materials BCR-1, BCR-2, BHVO-1, BHVO-2, AGV-1, AGV-2, GSP-1, GSP-2 and eight MPI-DING reference glasses. *Geostandards and Geoanalytical Research,* 27**,** 173-179.

Randall, S. & Anderson, S. 2005. Soils Genesis and Geomorphology. *Cambridge University Press, UK, ISBN,* 521812011**,** 832.

Raymo, M. & Ruddiman, W. F. 1992. Tectonic forcing of late Cenozoic climate. *Nature,* 359**,** 117-122.

Raymo, M. E., Ruddiman, W. F. & Froelich, P. N. 1988. Influence of late Cenozoic mountain building on ocean geochemical cycles. *Geology,* 16**,** 649-653.

Raymond, P. A., Oh, N. H., Turner, R. E. & Broussard, W. 2008. Anthropogenically enhanced fluxes of water and carbon from the Mississippi River. *Nature,* 451**,** 449-52.

Reeves, J. M., Barrows, T. T., Cohen, T. J., Kiem, A. S., Bostock, H. C., Fitzsimmons, K. E., Jansen, J. D., Kemp, J., Krause, C. & Petherick, L. 2013. Climate variability over the last 35,000 years recorded in marine and terrestrial archives in the Australian region: an OZ-INTIMATE compilation. *Quaternary Science Reviews,* 74**,** 21-34.

Retallack, G. 1991. Untangling the effects of burial alteration and ancient soil formation. *Annual Review of Earth and Planetary Sciences,* 19**,** 183-206.

Revel-Rolland, M., De Deckker, P., Delmonte, B., Hesse, P., Magee, J., Basile-Doelsch, I., Grousset, F. & Bosch, D. 2006. Eastern Australia: a possible source of dust in East Antarctica interglacial ice. *Earth and Planetary Science Letters,* 249**,** 1-13.

Richter, F. M., Davis, A. M., Depaolo, D. J. & Watson, E. B. 2003. Isotope fractionation by chemical diffusion between molten basalt and rhyolite. *Geochimica et Cosmochimica Acta,* 67**,** 3905-3923.

Richter, F. M., Mendybaev, R. A., Christensen, J. N., Hutcheon, I. D., Williams, R. W., Sturchio, N. C. & Beloso Jr, A. D. 2006. Kinetic isotopic fractionation during diffusion of ionic species in water. *Geochimica et Cosmochimica Acta,* 70**,** 277-289.

Richter, S., Kuhn, H., Aregbe, Y., Hedberg, M., Horta-Domenech, J., Mayer, K., Zuleger, E., Burger, S., Boulyga, S., Kopf, A., Poths, J. & Mathew, K. 2011. Improvements in routine uranium isotope ratio measurements using the modified total evaporation method for multi-collector thermal ionization mass spectrometry. *Journal of Analytical Atomic Spectrometry,* 26**,** 550-564.

Riebe, C. S., Kirchner, J. W., Granger, D. E. & Finkel, R. C. 2001. Strong tectonic and weak climatic control of long-term chemical weathering rates. *Geology,* 29**,** 511-514.

Riebe, C. S., Kirchner, J. W. & Finkel, R. C. 2003. Long-term rates of chemical weathering and physical erosion from cosmogenic nuclides and geochemical mass balance. *Geochimica et Cosmochimica Acta,* 67**,** 4411-4427.

Roaldset, E. 1972. Mineralogy and geochemistry of Quaternary clays in the Numedal area, southern Norway. *Norsk Geologisk Tidsskrift,* 52**,** 335-369.

Rognon, P. & Williams, M. 1977. Late Quaternary climatic changes in Australia and North Africa: a preliminary interpretation. *Palaeogeography, Palaeoclimatology, Palaeoecology,* 21**,** 285-327.

Rothacker, L., Dosseto, A., Francke, A., Chivas, A. R., Vigier, N., Kotarba-Morley, A. M. & Menozzi, D. 2018. Impact of climate change and human activity on soil landscapes over the past 12,300 years. *Scientific reports,* 8**,** 247.

Rudnick, R. L., Tomascak, P. B., Njo, H. B. & Gardner, L. R. 2004. Extreme lithium isotopic fractionation during continental weathering revealed in saprolites from South Carolina. *Chemical Geology,* 212**,** 45-57.

Ruxton, B. P. 1968. Measures of the degree of chemical weathering of rocks. *The Journal of Geology,* 76**,** 518-527.

Ryu, J.-S., Vigier, N., Lee, S.-W., Lee, K.-S. & Chadwick, O. A. 2014. Variation of lithium isotope geochemistry during basalt weathering and secondary mineral transformations in Hawaii. *Geochimica et Cosmochimica Acta,* 145**,** 103-115.

Saji, N. S., Wielandt, D., Paton, C. & Bizzarro, M. 2016. Ultra-high-precision Nd-isotope measurements of geological materials by MC-ICPMS. *Journal of analytical atomic spectrometry,* 31**,** 1490-1504.

Sanyal, P. & Sinha, R. 2010. Evolution of the Indian summer monsoon: synthesis of continental records. *Geological Society, London, Special Publications,* 342**,** 153-183.

Sauzéat, L., Rudnick, R. L., Chauvel, C., Garçon, M. & Tang, M. 2015. New perspectives on the Li isotopic composition of the upper continental crust and its weathering signature. *Earth and Planetary Science Letters,* 428**,** 181-192.

Scher, H. D. & Delaney, M. L. 2010. Breaking the glass ceiling for high resolution Nd isotope records in early Cenozoic paleoceanography. *Chemical Geology,* 269**,** 329-338.

Schmitt, A.-D., Vigier, N., Lemarchand, D., Millot, R., Stille, P. & Chabaux, F. 2012. Processes controlling the stable isotope compositions of Li, B, Mg and Ca in plants, soils and waters: A review. *Comptes Rendus Geoscience,* 344**,** 704-722.

Schumm, S. A. 1968. *River adjustment to altered hydrologic regimen, Murrumbidgee River and paleochannels, Australia,* US Government Printing Office, 598 pp.

Shackleton, N. J. & Opdyke, N. D. 1973. Oxygen isotope and palaeomagnetic stratigraphy of Equatorial Pacific core V28-238: Oxygen isotope temperatures and ice volumes on a 105 year and 106 year scale. *Quaternary research,* 3**,** 39-55.

Shao, J., Yang, S. & Li, C. 2012. Chemical indices (CIA and WIP) as proxies for integrated chemical weathering in China: inferences from analysis of fluvial sediments. *Sedimentary Geology,* 265**,** 110-120.

Sharp, M., Creaser, R. A. & Skidmore, M. 2002. Strontium isotope composition of runoff from a glaciated carbonate terrain. *Geochimica et Cosmochimica Acta,* 66**,** 595-614.

Sharp, Z. 2017. Principles of stable isotope geochemistry.

She, Z., Ma, C., Mason, R., Li, J., Wang, G. & Lei, Y. 2006. Provenance of the Triassic Songpan–Ganzi flysch, west China. *Chemical Geology,* 231**,** 159-175.

Shibata, T., Yoshikawa, M. & Tatsumi, Y. 2003. An analytical method for determining precise Sr and Nd isotopic compositions and results for thirteen rock standard materials. *Frontier Research on Earth Evolution,* 1**,** 363-367.

Sims, K. W., Gill, J. B., Dosseto, A., Hoffmann, D. L., Lundstrom, C. C., Williams, R. W., Ball, L., Tollstrup, D., Turner, S. & Prytulak, J. 2008. An inter-laboratory assessment of the thorium isotopic composition of synthetic and rock reference materials. *Geostandards and Geoanalytical Research,* 32**,** 65-91.

Singer, A. 1980. The paleoclimatic interpretation of clay minerals in soils and weathering profiles. *Earth-Science Reviews,* 15**,** 303-326.

Singer, A. & Stoffers, P. 1980. Clay mineral diagenesis in two East African lake sediments. *Clay Minerals,* 15**,** 291-307.

Singh, A. K. & Hasnain, S. I. 1998. Major ion chemistry and weathering control in a high altitude basin: Alaknanda River, Garhwal Himalaya, India. *Hydrological sciences journal,* 43**,** 825-843.

Singh, S. K., Rai, S. K. & Krishnaswami, S. 2008. Sr and Nd isotopes in river sediments from the Ganga Basin: sediment provenance and spatial variability in physical erosion. *Journal of Geophysical Research: Earth Surface,* 113.

Small, J. 1994. Fluid composition, mineralogy and morphological changes associated with the smectite-to-illite reaction: An experimental investigation of the effect of organic acid anions. *Clay Minerals,* 29**,** 539-554.

Stromsoe, N., Callow, J. N., Mcgowan, H. A. & Marx, S. K. 2013. Attribution of sources to metal accumulation in an alpine tarn, the Snowy Mountains, Australia. *Environmental pollution,* 181**,** 133-143.

Summerfield, M. & Hulton, N. 1994. Natural controls of fluvial denudation rates in major world drainage basins. *Journal of Geophysical Research: Solid Earth,* 99**,** 13,871-13,871.

Sun, J. 2005. Nd and Sr isotopic variations in Chinese eolian deposits during the past 8 Ma: Implications for provenance change. *Earth and Planetary Science Letters,* 240**,** 454-466.

Suresh, P., Dosseto, A., Hesse, P. & Handley, H. 2013. Soil formation rates determined from Uranium-series isotope disequilibria in soil profiles from the southeastern Australian highlands. *Earth and Planetary Science Letters,* 379**,** 26-37.

Tachikawa, K., Jeandel, C. & Roy-Barman, M. 1999. A new approach to the Nd residence time in the ocean: the role of atmospheric inputs. *Earth and Planetary Science Letters,* 170**,** 433-446.

Tanaka, T., Togashi, S., Kamioka, H., Amakawa, H., Kagami, H., Hamamoto, T., Yuhara, M., Orihashi, Y., Yoneda, S. & Shimizu, H. 2000. JNdi-1: a neodymium isotopic reference in consistency with LaJolla neodymium. *Chemical Geology,* 168**,** 279-281.

Tang, Y.-J., Zhang, H.-F., Nakamura, E., Moriguti, T., Kobayashi, K. & Ying, J.-F. 2007a. Lithium isotopic systematics of peridotite xenoliths from Hannuoba, North China Craton: implications for melt–rock interaction in the considerably thinned lithospheric mantle. *Geochimica et Cosmochimica Acta,* 71**,** 4327-4341.

Tang, Y.-J., Zhang, H.-F. & Ying, J.-F. 2007b. Review of the lithium isotope system as a geochemical tracer. *International Geology Review,* 49**,** 374-388.

Taylor, G. Glaciation in the southwest Pacific. Proceedings of the Third Pan-Pacific Science Congress, 1926. 1819-1825.

Taylor, L. L., Quirk, J., Thorley, R. M., Kharecha, P. A., Hansen, J., Ridgwell, A., Lomas, M. R., Banwart, S. A. & Beerling, D. J. 2016. Enhanced weathering strategies for stabilizing climate and averting ocean acidification. *Nature Climate Change,* 6**,** 402-406.

Taylor, T. I. & Urey, H. C. 1938. Fractionation of the lithium and potassium isotopes by chemical exchange with zeolites. *The Journal of Chemical Physics,* 6**,** 429-438.

Teng, F.-Z., Mcdonough, W. F., Rudnick, R., Dalpé, C., Tomascak, P., Chappell, B. W. & Gao, S. 2004. Lithium isotopic composition and concentration of the upper continental crust. *Geochimica et Cosmochimica Acta,* 68**,** 4167-4178.

Teng, F.-Z., Mcdonough, W. F., Rudnick, R. L. & Walker, R. J. 2006. Diffusion-driven extreme lithium isotopic fractionation in country rocks of the Tin Mountain pegmatite. *Earth and Planetary Science Letters,* 243**,** 701-710.

Teng, F.-Z., Li, W.-Y., Rudnick, R. L. & Gardner, L. R. 2010. Contrasting lithium and magnesium isotope fractionation during continental weathering. *Earth and Planetary Science Letters,* 300**,** 63-71.

Tessier, A., Campbell, P. G. & Bisson, M. 1979. Sequential extraction procedure for the speciation of particulate trace metals. *Analytical chemistry,* 51**,** 844-851.

Thamban, M. & Rao, V. P. 2005. Clay minerals as palaeomonsoon proxies: Evaluation and relevance to the late Quaternary records from SE Arabian Sea. *In:* S. Rajan, P. C. P. (ed.) *Antarctic Geoscience: Ocean–atmosphere Interaction and Paleoclimatology.* Goa, India: National Centre for Antarctic & Ocean Research, 198-215.

Thienemann, M., Masi, A., Kusch, S., Sadori, L., John, S., Francke, A., Wagner, B. & Rethemeyer, J. 2017. Organic geochemical and palynological evidence for Holocene natural and anthropogenic environmental change at Lake Dojran (Macedonia/Greece). *The Holocene,* 0**,** 1-12.

Thiry, M. 2000. Palaeoclimatic interpretation of clay minerals in marine deposits: an outlook from the continental origin. *Earth-Science Reviews,* 49**,** 201-221.

Thompson, D. W. & Wallace, J. M. 2000. Annular modes in the extratropical circulation. Part I: Month-to-month variability. *Journal of climate,* 13**,** 1000-1016.

Thompson, L. O., Yao, T., Davis, M., Henderson, K., Mosley-Thompson, E., Lin, P.-N., Beer, J., Synal, H.-A., Cole-Dai, J. & Bolzan, J. 1997. Tropical climate instability: The last glacial cycle from a Qinghai-Tibetan ice core. *Science,* 276**,** 1821-1825.

Tipper, E., Galy, A. & Bickle, M. 2006. Riverine evidence for a fractionated reservoir of Ca and Mg on the continents: implications for the oceanic Ca cycle. *Earth and Planetary Science Letters,* 247**,** 267-279.

Tipper, E. T., Galy, A. & Bickle, M. J. 2008. Calcium and magnesium isotope systematics in rivers draining the Himalaya-Tibetan-Plateau region: Lithological or fractionation control? *Geochimica et Cosmochimica Acta,* 72**,** 1057-1075.

Tipper, E. T., Gaillardet, J., Louvat, P., Capmas, F. & White, A. F. 2010. Mg isotope constraints on soil pore-fluid chemistry: evidence from Santa Cruz, California. *Geochimica et Cosmochimica Acta,* 74**,** 3883-3896.

Tipper, E. T., Calmels, D., Gaillardet, J., Louvat, P., Capmas, F. & Dubacq, B. 2012. Positive correlation between Li and Mg isotope ratios in the river waters of the Mackenzie Basin challenges the interpretation of apparent isotopic fractionation during weathering. *Earth and Planetary Science Letters,* 333**,** 35-45.

Tomascak, P. & Langmuir, C. 1999. Lithium isotope variability in MORB. *Eos,* 80**,** F1086-F1087.

Tomascak, P. B., Tera, F., Helz, R. T. & Walker, R. J. 1999. The absence of lithium isotope fractionation during basalt differentiation: new measurements by multicollector sector ICP-MS. *Geochimica et Cosmochimica Acta,* 63**,** 907-910.

Tomascak, P. B., Ryan, J. G. & Defant, M. J. 2000. Lithium isotope evidence for light element decoupling in the Panama subarc mantle. *Geology,* 28**,** 507-510.

Tomascak, P. B., Widom, E., Benton, L. D., Goldstein, S. L. & Ryan, J. G. 2002. The control of lithium budgets in island arcs. *Earth and Planetary Science Letters,* 196**,** 227-238.

Tomascak, P. B. 2004. Developments in the understanding and application of lithium isotopes in the earth and planetary sciences. *Reviews in Mineralogy and Geochemistry,* 55**,** 153-195.

Ummenhofer, C. C., England, M. H., Mcintosh, P. C., Meyers, G. A., Pook, M. J., Risbey, J. S., Gupta, A. S. & Taschetto, A. S. 2009. What causes southeast Australia's worst droughts? *Geophysical Research Letters,* 36.

Urey, H. C. & Korff, S. A. 1952. The planets: their origin and development. *Physics Today,* 5**,** 12-12.

Valeriano, C., Vaz, G., Medeiros, S., Neto, C., Ragatky, C. & Geraldes, M. The Neodymium isotope composition of the JNdi-1 oxide reference material: results from the LAGIR Laboratory, Rio de Janeiro. VI South American Symposium on Isotope Geology, 2008. 1-2.

Van Daele, M., Moernaut, J., Silversmit, G., Schmidt, S., Fontijn, K., Heirman, K., Vandoorne, W., De Clercq, M., Van Acker, J. & Wolff, C. 2014. The 600 yr eruptive history of Villarrica Volcano (Chile) revealed by annually laminated lake sediments. *Bulletin,* 126**,** 481-498.

Van De Flierdt, T., Frank, M., Lee, D.-C. & Halliday, A. N. 2002. Glacial weathering and the hafnium isotope composition of seawater. *Earth and Planetary Science Letters,* 201**,** 639-647.

Vance, D., Teagle, D. A. & Foster, G. L. 2009. Variable Quaternary chemical weathering fluxes and imbalances in marine geochemical budgets. *Nature,* 458**,** 493-496.

Verney-Carron, A., Vigier, N. & Millot, R. 2011. Experimental determination of the role of diffusion on Li isotope fractionation during basaltic glass weathering. *Geochimica et Cosmochimica Acta,* 75**,** 3452-3468.

Veth, P., Smith, M., Bowler, J., Fitzsimmons, K., Williams, A. & Hiscock, P. 2009. Excavations at Parnkupirti, Lake Gregory, great sandy desert: OSL ages for occupation before the last glacial maximum. *Australian Archaeology,* 69**,** 1-10.

Viers, J., Dupré, B., Polvé, M., Schott, J., Dandurand, J.-L. & Braun, J.-J. 1997. Chemical weathering in the drainage basin of a tropical watershed (Nsimi-Zoetele site, Cameroon): comparison between organic-poor and organic-rich waters. *Chemical Geology,* 140**,** 181-206.

Viers, J., Dupré, B., Braun, J.-J., Deberdt, S., Angeletti, B., Ngoupayou, J. N. & Michard, A. 2000. Major and trace element abundances, and strontium isotopes in the Nyong basin rivers (Cameroon): constraints on chemical weathering processes and elements transport mechanisms in humid tropical environments. *Chemical Geology,* 169**,** 211-241.

Vigier, N., Burton, K., Gislason, S., Rogers, N., Duchene, S., Thomas, L., Hodge, E. & Schaefer, B. 2006. The relationship between riverine U-series disequilibria and erosion rates in a basaltic terrain. *Earth and Planetary Science Letters,* 249**,** 258-273.

Vigier, N., Decarreau, A., Millot, R., Carignan, J., Petit, S. & France-Lanord, C. 2008. Quantifying Li isotope fractionation during smectite formation and implications for the Li cycle. *Geochimica et Cosmochimica Acta,* 72**,** 780-792.

Vigier, N., Gislason, S. R., Burton, K., Millot, R. & Mokadem, F. 2009. The relationship between riverine lithium isotope composition and silicate weathering rates in Iceland. *Earth and Planetary Science Letters,* 287**,** 434-441.

Vigier, N. & Godderis, Y. 2015. A new approach for modeling Cenozoic oceanic lithium isotope paleo-variations: the key role of climate. *Climate of the Past Discussions,* 11**,** 635-645.

Vogel, H., Wagner, B., Zanchetta, G., Sulpizio, R. & Rosén, P. 2010. A paleoclimate record with tephrochronological age control for the last glacial-interglacial cycle from Lake Ohrid, Albania and Macedonia. *Journal of Paleolimnology,* 44**,** 295-310.

Vogt, T. 1927. *Sulitjelmafeltets geologi og petrografi,* Norges Geologiske Undersokelse, 560 pp.

Von Blanckenburg, F., O'nions, R. K., Belshaw, N. S., Gibb, A. & Hein, J. R. 1996. Global distribution of beryllium isotopes in deep ocean water as derived from Fe-Mn crusts. *Earth and Planetary Science Letters,* 141**,** 213-226.

Von Blanckenburg, F. & O'nions, R. K. 1999. Response of beryllium and radiogenic isotope ratios in Northern Atlantic Deep Water to the onset of northern hemisphere glaciation. *Earth and Planetary Science Letters,* 167**,** 175-182.

Von Blanckenburg, F. & Nägler, T. F. 2001. Weathering versus circulation-controlled changes in radiogenic isotope tracer composition of the Labrador Sea and North Atlantic Deep Water. *Paleoceanography,* 16**,** 424-434.

Von Blanckenburg, F., Bouchez, J., Ibarra, D. E. & Maher, K. 2015a. Stable runoff and weathering fluxes into the oceans over Quaternary climate cycles. *Nature Geoscience,* 8**,** 538.

Von Blanckenburg, F., Bouchez, J., Ibarra, D. E. & Maher, K. 2015b. Stable runoff and weathering fluxes into the oceans over Quaternary climate cycles. *Nature Geoscience,* 8**,** 538-542.

Von Strandmann, P. a. P., Burton, K. W., James, R. H., Van Calsteren, P., Gislason, S. R. & Sigfússon, B. 2008. The influence of weathering processes on riverine magnesium isotopes in a basaltic terrain. *Earth and Planetary Science Letters,* 276**,** 187-197.

Walker, J. C., Hays, P. & Kasting, J. F. 1981. A negative feedback mechanism for the long-term stabilization of Earth's surface temperature. *Journal of Geophysical Research: Oceans,* 86**,** 9776-9782.

Wan, S., Toucanne, S., Clift, P. D., Zhao, D., Bayon, G., Yu, Z., Cai, G., Yin, X., Révillon, S. & Wang, D. 2015. Human impact overwhelms long-term climate control of weathering and erosion in southwest China. *Geology,* 43**,** 439-442.

Wang, Q.-L., Chetelat, B., Zhao, Z.-Q., Ding, H., Li, S.-L., Wang, B.-L., Li, J. & Liu, X.-L. 2015. Behavior of lithium isotopes in the Changjiang River system: sources effects and response to weathering and erosion. *Geochimica et Cosmochimica Acta,* 151**,** 117-132.

Weiland, F. S., Lopez, P., Van Dijk, A. & Schellekens, J. Global high-resolution reference potential evaporation. MODSIM 2015, Conference Proceedings, Broadbeach, Queensland, Australia, 2015.

Weis, D., Kieffer, B., Maerschalk, C., Barling, J., De Jong, J., Williams, G. A., Hanano, D., Pretorius, W., Mattielli, N. & Scoates, J. S. 2006. High-precision isotopic characterization of USGS reference materials by TIMS and MC-ICP-MS. *Geochemistry, Geophysics, Geosystems,* 7.

West, A. J., Galy, A. & Bickle, M. 2005. Tectonic and climatic controls on silicate weathering. *Earth and Planetary Science Letters,* 235**,** 211-228.

Weynell, M., Wiechert, U. & Schuessler, J. A. 2017. Lithium isotopes and implications on chemical weathering in the catchment of Lake Donggi Cona, northeastern Tibetan Plateau. *Geochimica et Cosmochimica Acta*.

White, W. M. 2013. *Geochemistry,* John Wiley & Sons, pp.

Willenbring, J. K. & Von Blanckenburg, F. 2010. Long-term stability of global erosion rates and weathering during late-Cenozoic cooling. *Nature,* 465**,** 211.

Willenbring, J. K. & Jerolmack, D. J. 2016. The null hypothesis: globally steady rates of erosion, weathering fluxes and shelf sediment accumulation during Late Cenozoic mountain uplift and glaciation. *Terra Nova,* 28**,** 11-18.

Williams, L. B. & Hervig, R. L. 2005. Lithium and boron isotopes in illite-smectite: the importance of crystal size. *Geochimica et Cosmochimica Acta,* 69**,** 5705-5716.

Wimpenny, J., James, R. H., Burton, K. W., Gannoun, A., Mokadem, F. & Gíslason, S. R. 2010a. Glacial effects on weathering processes: new insights from the

elemental and lithium isotopic composition of West Greenland rivers. *Earth and Planetary Science Letters,* 290**,** 427-437.

Wimpenny, J., Gíslason, S. R., James, R. H., Gannoun, A., Pogge Von Strandmann, P. A. & Burton, K. W. 2010b. The behaviour of Li and Mg isotopes during primary phase dissolution and secondary mineral formation in basalt. *Geochimica et Cosmochimica Acta,* 74**,** 5259-5279.

Wimpenny, J., Colla, C. A., Yu, P., Yin, Q.-Z., Rustad, J. R. & Casey, W. H. 2015. Lithium isotope fractionation during uptake by gibbsite. *Geochimica et Cosmochimica Acta,* 168**,** 133-150.

Wurts, W. A. & Durborow, R. M. 1992. Interactions of pH, carbon dioxide, alkalinity and hardness in fish ponds.

Yang, Y.-H., Chu, Z.-Y., Wu, F.-Y., Xie, L.-W. & Yang, J.-H. 2011. Precise and accurate determination of Sm, Nd concentrations and Nd isotopic compositions in geological samples by MC-ICP-MS. *Journal of Analytical Atomic Spectrometry,* 26**,** 1237-1244.

Yang, Y., Wu, F., Xie, L. & Zhang, Y. 2009. High-precision measurements of the 143Nd/144Nd isotope ratio in certified reference materials without Nd and Sm separation by multiple collector inductively coupled plasma mass spectrometry. *Analytical Letters,* 43**,** 142-150.

You, C.-F. & Chan, L.-H. 1996. Precise determination of lithium isotopic composition in low concentration natural samples. *Geochimica et Cosmochimica Acta,* 60**,** 909-915.

Zack, T., Tomascak, P. B., Rudnick, R. L., Dalpé, C. & Mcdonough, W. F. 2003. Extremely light Li in orogenic eclogites: the role of isotope fractionation during dehydration in subducted oceanic crust. *Earth and Planetary Science Letters,* 208**,** 279-290.

Zhang, H., Gao, S., Zhong, Z., Zhang, B., Zhang, L. & Hu, S. 2002. Geochemical and Sr–Nd–Pb isotopic compositions of Cretaceous granitoids: constraints on tectonic framework and crustal structure of the Dabieshan ultrahigh-pressure metamorphic belt, China. *Chemical Geology,* 186**,** 281-299.

Zhang, L., Chan, L.-H. & Gieskes, J. M. 1998. Lithium isotope geochemistry of pore waters from Ocean Drilling Program Sites 918 and 919, Irminger Basin. *Geochimica et Cosmochimica Acta,* 62**,** 2437-2450.